Doctoral Dissertation
Doctoral Program in Energy Engineering (34th Cycle)

An experimental and modelling approach to study the performance and degradation of low temperature electrolyzers

By

Mohsen Mansourkiaei
******

Supervisor:
Prof. Massimo Santarelli

Doctoral Examination Committee:
Prof. Kyrre Sundseth , Referee, SINTEF AS

Prof. Gabriel Correa Perelmuter , Referee, centro regional de energía y ambiente para el desarrollo sustentable

Prof. Gianluca Valenti, Politecnico di Milano

Prof. Alessandro Monteverde, Politecnico di Torino

Prof. Marta Gandiglio, Politecnico di Torino

Politecnico di Torino
2022

Declaration

I hereby declare that, the contents and organization of this dissertation constitute my own original work and does not compromise in any way the rights of third parties, including those relating to the security of personal data.

Mohsen Mansourkiaei

June 2022

* This dissertation is presented in partial fulfilment of the requirements for **Ph.D. degree** in the Graduate School of Politecnico di Torino (ScuDo).

Dedication

I would like to dedicate this thesis to my family…

Acknowledgment

First of all, I would like to thank my supervisor, Professor Massimo Santarelli that gave me the possibility of doing this thesis and guided me through the right way whenever I needed support. I would also like to thank the reviewers, Prof. Kyrre Sundset and Prof. Gabriel Correa Perelmuter.

I would like to extend my sincere gratitude to all the members of STEPS research group, specially Paolo, Domenico, Marta, and Salvatore for the scientific discussions, collaborations and advices. I would also like to thank the management and the staff of Environmental park of Turin -where the CO_2 Circle lap is built at- specially Eng. Marco Fausone for his technical assistance in solving the test bench's issues.

Finally, I would like to thank my family and friends for all the support they provided during these years of studies; without whom this work would have not been possible.

Abstract

The energy transition toward a decarbonized civilization has to be driven by renewable energy sources (RESs). Their installed capacity is anticipated to expand significantly to solve the issues of the depletion of fossil fuels and the mitigation of greenhouse gas emissions. However, the fluctuating behaviour of variable RESs makes it difficult to integrate them into electrical networks. Electrical energy storage hence becomes essential to address the RES-related difficulties. H_2 is becoming one of the most prominent choices for energy storage. Consequently, green H_2 production using water electrolysis has become the subject of many recent researches. Studies are mainly focused on cost reduction via performance improvement and degradation limitation.

In the current work an experimental test rig was built at Environmental Park of Turin. It aims at the characterization of electrochemical devices for the production of hydrogen. This electrochemical test station is designed to enable testing of low temperature electrolytic devices (up to 150°C and 30 bar) both with anionic and cationic electrolyte cells and from individual electrolytic cells to small-assembled cells called stacks.

To be able to deeply study the degradation phenomena starting from the technology level in each P2P system component, accelerated experimental degradation tests were designed and series of tests have been arranged on low-T PEM cells. In order to have all the necessary information about the cells, commercial MEA with acidic chemistry were chosen and assembled in the laboratory using the separated anode and cathode side. Industry standard Nafion membranes (Nafion 115 and 117) and gas diffusion layers were used. The 5X5cm single cells were put under test inside a housing connected to the electrochemical test bench which can control the relevant test variables such as temperatures, mass flow rates and pressures. Cells were characterized by the resultant voltage-current polarization curves and electrochemical impedance spectroscopy (EIS).

A 0D MATLAB model has also been developed that fits the voltage-current curves very well and it can predict the behaviour of the cell in different conditions as well as giving the possibility to study the effect of various electrochemical and physical variables -such as T, P, current densities at anode and cathode i.e. $I_{0,anode}$ $I_{0,cathode}$, etc- on the cell performance. At the same time the hydrogen production rate was also investigated, and the experimental production rate was found to be within 99.5% of theoretical production.

Furthermore, using the COMSOL Multiphysics® environment 2-D and 3D Multi-Phase Multiphysics Model (Bubbly Flow, k-ω) of the PEM electrolytic cell was developed to simulate the main involved physics with special consideration on biphasic anodic mixture interactions within the system. The effect of different variables such as temperature gradient at anode and cathode, bubbles overpotential and oxygen and hydrogen concentration at electrode interface on the system were modelled.

Since the designed electrochemical test bench has the possibility to send liquid to both anode and cathode electrodes, an array of open versus closed cathode experiments were done to compare the difference between the performance in these cases. The improvements in the performance in open vs closed cathode case can be related to the more homogeneous temperature distribution inside the housing and better hydration of the MEA and gas removal from the reaction sites. Besides, EIS tests have also been performed in these experiments to investigate the trend of changes in each cell characteristics such as ohmic resistance (R_{ohm}) or charge transfer resistance (R_{ct}) of the cell. To study these results in depth, they are modelled with equivalent electrical circuits (EEC) in which each element represents an electrical contribution related to a physical phenomenon. A comparison of the results in open vs closed cathode experiment presents the approximately constant ohmic resistance and a decreasing trend of the charge transfer resistance while increasing temperature.

Lastly a series of accelerated degradation tests have been performed on the cells. These tests give insights on the comparison of constant current working with respect to profiles with frequent variations and shutdowns. Meanwhile during the experiments, the circuit water (demineralized water) was analysed for its thermal conductivity continuously and for fluoride ion quantities by sampling at specific time steps. After the degradation tests on the mentioned cells, they undergo post-mortem analysis using SEM, and XRD methods too.

Table of contents

List of abbreviations

0D model:	zero dimensional (time dependent)
AC :	Alternating Current
APU :	Auxiliary Power Units
ASC :	Anode Supported Cell
AWE :	Alkaline Water Electrolysis
BoP :	Balance of Plant
CAD :	Computer-Aided Design
CAPEX:	Capital Expenditures
CPE :	Constant Phase Element
CNLS :	Complex Non-Linear Least Squares
CSC :	Cathode Supported Cell
CSMUI:	Catalyst Sprayed Membrane Under Illumination
CTE :	Coefficient of Thermal Expansion
DC :	Direct Current
DENERG:	Department of Energy of polytechnic of Turin (PoliTo)
DISAT:	Department of Applied Science and Technology of PoliTo
ECM :	Electrical Circuit Modelling
EDS :	Energy Dispersive X-Ray Spectroscopy
EEC :	Equivalent Electrical Circuit
ESC :	Electrolyte Supported Cell
EU :	Europe
FCH2JU:	Fuel Cells and Hydrogen 2 Joint
FRA :	Frequency Response Analyser
HER :	Hydrogen Evolution Reaction

HHV	:	Higher Heating Value
HPU	:	Hydrogen Processing Unit
HSM	:	Hot Stage Microscopic Analysis
HT	:	High Temperature
HTE	:	High Temperature Electrolysis/Electrolyzer
KK	:	Kramers-Kroning
LHV	:	Lower Heating Value
Lin-KK:		Linear Kramers-Kroning
NML	:	Noble Metal Loading
OPEX	:	Operational Expenditures
OER	:	Oxygen Evolution Reaction
PEM	:	Polymer Electrolyte Membrane
PEMWE:		Proton Exchange Membrane Water Electrolysis
Pk-Pk	:	Peak To Peak
RC	:	Resistor Capacitor
RES	:	Renewable Energy Sources
rSOC	:	Reversible Solid Oxide Cell
SEM	:	Scanning Electron Microscopy
S/N	:	Signal-To-Noise Ratio
SOEC	:	Solid Oxide Electrolyzer Cell
SOWE	:	Solid Oxide Water Electrolysis
SPSf	:	Sulfonated Polysulfone
TEM	:	Transmission Electron Microscopy
TF	:	Transfer function
TPB	:	Three Phase Boundary
XRD	:	X- Ray Diffraction

List of figures

List of tables

Chapter 1. Introduction

The European Commission's energy and environmental policies throughout the past few decades have proven the requirement of decarbonizing processes and subsequently reducing greenhouse gas emissions (GHG) in order to electrify systems and improve energy efficiency[1] Because of the rising usage of fossil fuels and changing standards of living, there has been an increase in both global energy consumption and global warming.[2] For this reason, the Paris Agreement was signed by the 195 nations in the 21st Conference of the Parties (COP21).[3] It suggests cutting greenhouse gas emissions by 40% in 2030 compared to 1990 levels in order to keep the rise in the world average temperature below 2 °C and get it down to 1.5 °C in the future years.[4] It's crucial to minimize greenhouse gas emissions in order to obtain net zero CO2 by 2050 if we want to accomplish this aim. This entails a phase of decarbonization and a decline in energy use. [3] Since fossil fuels are still a major part of the world's energy output, the path to accomplishing this objective will be quite challenging.[4] A policy built on a long-term transformation of the energy industry becomes crucial as a result. The shift focuses on renewable energy sources (RES) and low-carbon technologies including carbon capture and sequestration (CCS).[5] These are crucial toward the transition to a more sustainable, attractive, and safe world and play an important part in it.[1] Through the use of CCS, CO2 from industrial processes is separated and captured before being delivered to long-term underground storage facilities. This facilitates a decrease in CO2 emissions and speeds up the process of environmental protection. On the other hand, RES have the potential to create a sustainable world that is not dependent on fossil fuels.[5] But in order to satisfy demand, these have sporadic properties that call for the usage of energy storage devices.[6] Energy storage technology can provide an excellent way to complete

the electrification process, increase the grid's performance, and achieve both grid independence and electrification. Since the generated energy is stored and used as needed, this technology can actually be linked with the primary energy production techniques to meet energy demand at any time.[5] Power-to-Hydrogen technology is the finest option in this regard because it allows for the storage of generated electricity as hydrogen. This is how the coupled system of RES and energy storage can help to reduce greenhouse gas emissions and offer a reliable and affordable energy source.[7]

1.1. Energy storage and hydrogen

The growing use of renewable energy sources and the general trend toward increased electrification necessitate the creation of more complex and effective power grid management and energy storage systems. Electrical energy storage (EES) systems are anticipated to become important energy infrastructures for both grid-connected and off-grid applications as they improve their ability to handle the fluctuating and unpredictable character of new renewable sources (i.e., wind and solar). The primary roles the EES will focus on are storing electricity during off-peak hours and supplying it during peak hours, which can cut overall generating costs. It is also possible to maintain power quality, voltage, and frequency by supplying or absorbing power from the EES as needed. reducing network congestion, supplying reliable electricity for off-grid installations and supplying power during a power outage.

Mechanical, electrochemical, chemical, electrical, and thermal storage systems are the different types of EES systems.[8][9] The most popular mechanical storage technologies are flywheel energy storage (FES), compressed air energy storage, and pumped hydro storage (PHS). Lead-acid, NiCd/NiMH, Li-ion, metal air, sodium sulfate, and sodium nickel chloride are examples of secondary batteries. Redox flow and hybrid flow are examples of flow batteries. The hydrogen atom serves as the foundation for chemical energy storage. Once hydrogen is produced, it can serve as a versatile energy carrier, and further conversion processes enable the storage of energy in a variety of gaseous and liquid synthetic fuels and chemicals in accordance with certain power-to-X (P2X) routes. The electrical-type of storage includes superconducting magnetic energy storage (SMES) and double-layer capacitors (DLCs). The storage of sensible heat, storage of latent heat, and thermo-chemical adsorption/desorption processes are the final three categories of thermal storage systems. The EES systems that were just briefly discussed each have unique characteristics in terms of storage capacity, energy

density, power density, discharge time, self-discharge rate, and cyclability that make them each suited for a particular application[10][11]. The various EES typologies are thus complimentary rather than competitive possibilities to supply storage services in various application areas.

When compact and short-term energy storage are required, batteries are the best option. Instead, chemical storage is anticipated to be used primarily for large-scale and longer-term energy storage solutions, which will most likely be needed in the coming years where a significant introduction of RES is anticipated. In more detail, the following characteristics distinguish the chemical storage option as a promising tactic: high storage capacity, high volumetric storage density, provision of system stabilization services, negligible self-discharge losses, flexibility to site topography, and potential for decentralized applications. With regard to the conventional long-term, high capacity PHS solution, the last two characteristics represent the greatest benefit. The power-to-hydrogen (P2H) route, which is the initial part of the entire power-to-X system, may produce hydrogen, which is the simplest energy carrier.[12][13]

Hydrogen is the most important energy carrier as it is clean and sustainable. Its energy density is 140 MJ/kg -higher heating value (HHV)- which is almost three times of solid fuels (50 MJ/kg).[6] Depending on the various production processes, hydrogen can be distinguished by its various hues. Green hydrogen, blue hydrogen, gray hydrogen, and turquoise hydrogen. [14] Gray hydrogen is produced from fossil fuels, such as coal or steam methane reforming (SMR). In order to lower CO2 emissions, SMR also uses CCS to produce blue hydrogen. It promotes the growth of the hydrogen market over gray hydrogen generation. Starting with the pyrolysis of natural gas, turquoise hydrogen is created without the creation of carbon dioxide. Through the electrolysis procedure, green hydrogen is created from RES.[5] [15] It follows that green hydrogen is the greatest option because it is clean and doesn't produce the emissions that other hydrogen generation methods do.[15] Since it can be produced using renewable power, it can aid in integrating significant amounts of variable renewable energy (VRE) into the energy system since hydrogen serves as an energy storage medium. The cost of production will decrease in the future because to ongoing research and development, although hydrogen is not yet that economically competitive. The primary component in an energy shift that starts with the generation of renewable electricity will be hydrogen. As a result, it will be possible to produce the hydrogen needed for the decarbonization process.[4] In industrial operations like fuel cells, the chemical industry, and the refining of petroleum, hydrogen is used in significant amounts. The many methods

for producing hydrogen are depicted in Figure 1.1[2]. Most recently, non-renewable energy sources like SMR have been used to produce hydrogen. However, as the hydrogen produced via these processes has a low purity, other technologies, including water electrolysis (WE), are being improved. [2] [4] [16]

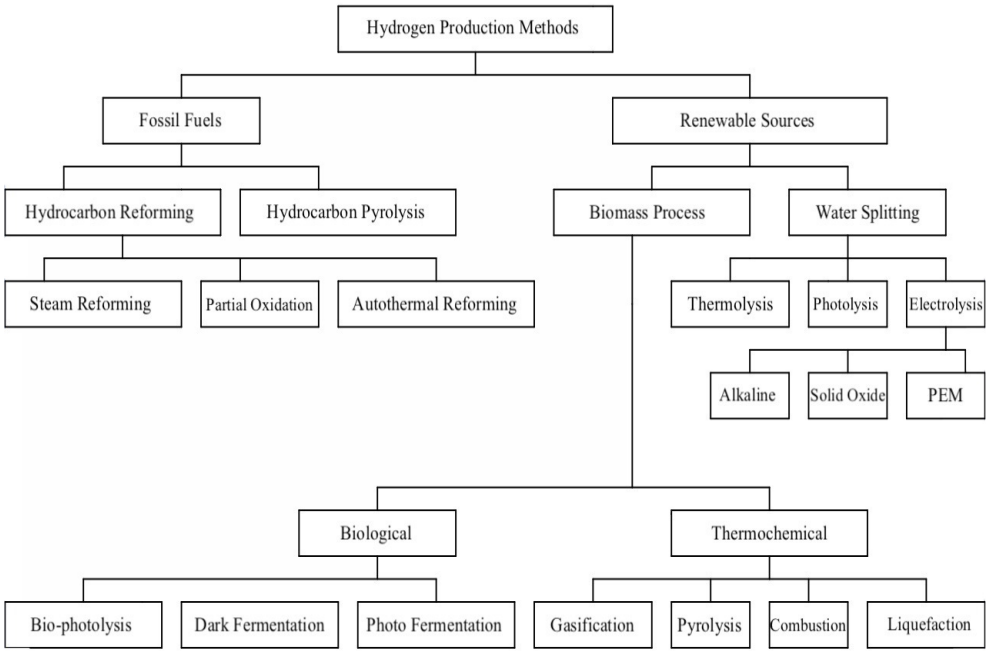

Figure 1.1 Different Hydrogen production method [2]

1.2. Electrolysis

The theory of water electrolysis came out from the work of Alessandro Volta when invented the pila in 1800. [17] The WE is an endothermic process that involves introducing a water molecule into a cell and using electricity to cause electrochemical water splitting, which results in the creation of a molecule of H2 and one-half of an O2 molecule. At first, it wasn't utilized for the commercial production of hydrogen. Instead, WE attracted a lot of attention in relation to PEM electrolyzers to produce oxygen for the use in spacecrafts and submarines. Actually, due to the Suez oil crisis (1956-7), which stimulated interest in alternative energy, the first hydrogen synthesis via electrolysis reaction appeared in 1960.[18][19] In those years, General Electric overcame the AWE issues by researching a novel design of WE cells based on a solid polymer electrolyte (SPE).[20] PEM water electrolysis is yet another name for what they found; a

cathode and anode-based electrochemical device that allow the reaction to take place in .[21] As it is possible to see in reaction 1.1.

$$H_2O \rightarrow H_2 + \frac{1}{2}O_2 \qquad 1.1$$

In this case, the purity of produced Hydrogen can arrive to 99.99%, but the obtained H2 from electrolysis is around 4% due to economic issues. [1] [2] Due to the low production efficiency, which is an issue for WE, researchers are looking at various technologies in an effort to raise the efficiency level. [2]

Depending on the cell's utilized electrolytes, there are three types of technologies. [6] Which are:

- Alkaline Water Electrolysis (AWE);
- Solid Oxide Water Electrolysis (SOWE);
- Proton Exchange Membrane (PEM) Water Electrolysis.

These systems use different types of materials and condition, but the operations are equal in principle. [6] They are based on the Electrolyzer Galvanic cell, a device that uses electricity to split water into hydrogen and oxygen.[4] Water is thus fed into the cell, which consists of an anode, a cathode, and an electrolyte. The oxidation reaction takes place in the anode, whereas the reduction reaction takes place in the cathode. Instead, the electrolyte is the component where ionic conduction takes place. The anode to the cathode conducts positive ions as a result. The AWE is a device that uses two molecules of an alkaline solution—such as KOH or NaOH—inserted in the cathode chamber to create hydrogen. One molecule of H2 is removed from the solution, and two ions of OH are also created. Due to the impact of current flowing in the external circuit, the H2 is recombined into gaseous form, and the ions of OH are transmitted to the anode through the porous diaphragm. O2 recombines and leaves the chamber when it is present on the anode side along with one H2O molecule. The electrolyte content is between 20 and 30 percent, and the usual operating range is between 40 and 90 degrees Celsius.[2] Compared to other types of electrolyzers, the SOWE operates at higher temperatures and pressures. It is made up of one solid-ionic conducting electrolyte, such as nickel or yttria stabilized zirconia, and two porous electrodes. As a result, water is pumped into the cathode side in the form of steam, and the electrolyte yields O2 conductors. Here, hydrogen is created by starting with water and using electrons created on the anode side. The O2 conductors are oxidized on the anode side, yielding two electrons and half an oxygen molecule. These are moved to the

cathode side, where water is reduced to create H2.[2] [17] The main benefit of this type of electrolyzer is that it operates at a higher temperature than low temperature electrolyzers, but it also has stability and degradation issues.[2] PEM fuel cell and PEM water electrolysis are both very similar technologies. This technology is appropriate since it works to balance the electricity grid as a result of RES fluctuation. Because of its flexibility, it can run on a variety of loads.[17] Today, the PEM water electrolysis represents one of the best solutions for the future. [7] It operates at a higher current value than AWE and enables the use of thinner membrane allowing lowering costs. As a result, the PEM has the advantage of working at higher current and voltage levels, resulting in a faster grid system response. The problem with this technology is the high cost of the components that make up the entire cell, as well as the corrosive acid regime in which it operates.[21]

As previously stated, the commercially available electrolysis technologies are PEMWE and AWE, with SOEC still in the early stages of development. AWE, in particular, is a more mature technology than others, but it has several disadvantages that contribute to the adoption of PEM technology for both O2 and H2 production. [2]

At the moment, AWE is the simplest, most developed, and cheapest technology for producing Hydrogen and Oxygen, but it has some efficiency issues. Because of this, research is focused on improving the system's robustness, safety, and reliability. The corrosive environment in which the AWE functions is the primary issue, and the increased use of PEMWE over the past few decades is largely attributable to this element as well as the rise in hydrogen production purity. However, compared to the other two, PEM is the most efficient and secure technology because, unlike AWE, it does not employ potassium or salt as an electrolyte and because its working temperature is lower than that of SOEC. Additionally, PEMWE is a dependable and affordable solution that enables to get beyond some challenges related to the other two types of electrolysis procedures. [22] AWE technology has a lower current density than PEMWE, which is the main disadvantage, along with the low purity hydrogen produced. However, PEMWE is a more expensive technology, and as a result, cost components must be reduced. In laboratory tests, SOWE, on the other hand, performed better than the other technologies. However, because SOWE technologies require higher temperatures and specific operating conditions, they will be advantageous for centralized and large-scale hydrogen production plants. At the moment, research is focused on developing materials that can extend both the lifespan and performance of plants.

In this regard, the primary goal is to reduce system complexity.[23] PEM electrolyzers have advantages over alkaline devices in that they are less caustic, can be reversible, and can operate at lower cell voltages, higher current densities, higher temperatures, and pressures, resulting in higher efficiencies (80 and 90 percent). The main drawbacks are high material costs, cross permeation phenomena that increase with pressure, and the presence of water vapor alongside the produced hydrogen, which necessitates hydration.[21] [24] [25] The main features of the different water electrolysis technologies are reported in Table 1.1. [2] [21] [23]

Table 1.1 Comparison of three technologies

Specifications	**AWE**	**PEMWE**	**SOWE**
Maturity	Mature	Commercial	Demonstration
Electrolyte	NaOH/KOH	Polymer Electrolyte	Ceramic
Electrode	Ni	Pt-Ir	Ni - cermet
Current density [A/cm2]	0.3 - 0.5	0 - 2	0.5 - 1
Operating Temperature [◦C]	40 - 90	30 - 80	700 - 1000
Operating Pressure [bars]	1 - 30	1 - 300	1 - 50
Hydrogen Purity [%]	99.5 - 99.9988	99.9 - 99.9999	99.9
Degradation Rate [µV/h]	<3	<14	
Efficiency [%]	68 - 77	80 - 90	89

1.3. PEM water electrolysis

The PEM electrolyzer can split water into H2 and O2 thanks to electrochemical reactions driven by electricity. [23] [26] The water is fed into the anode side and the reaction of reduction occurs forming the O2 and H+ and two electrons. The H+ ions pass into the cathode side through the membrane and the electrons through the external circuit. In the cathode the oxidation reaction occurs with the formation of H2.[2] [6] The overall is stated in reaction 1.1.

It is the global reaction that can be considered as the sum of the two reactions: the Hydrogen Evolution Reaction (HER) 1.3 and Oxygen Evolution Reaction (OER) 1.2[2]

$$H_2O \rightarrow 2H^+ + \frac{1}{2}O_2 + 2e^- \qquad 1.2$$

$$2H^+ + 2e^- \rightarrow H_2 \qquad 1.3$$

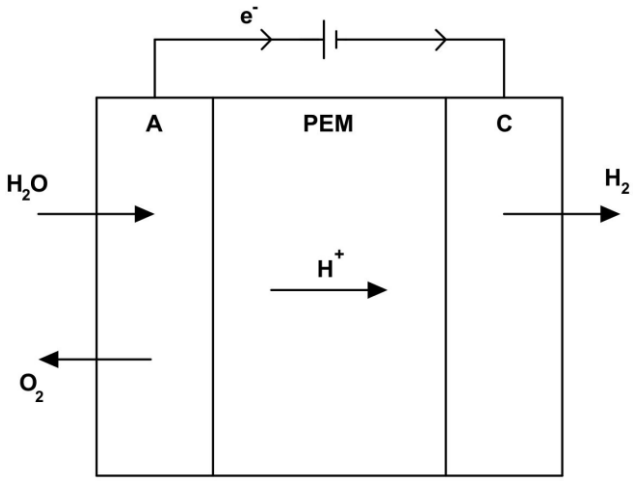

Figure 1.2 Simple scheme of PEMWE

A simple scheme of PEMWE is reported in Figure 1.2 . The structure of the cell is composed by Membrane Electrode Assembly (MEA), Gas Diffusion Layer (GDL), Bipolar Plate (BP) and End Plates. In the BPs the channels are present, and they are important elements for the cell performance. Between the BPs the Gasket is present. Figure 1.3 shows the general structure.

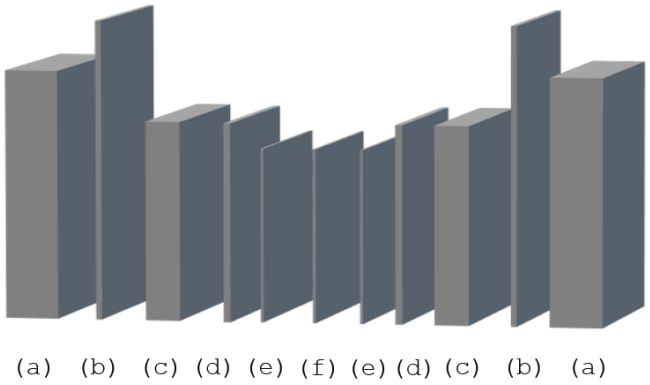

Figure 1.3: Exploded view of PEMWE: (a) End Plate, (b) Current collector, (c) Bipolar Plate, (d) Gasket, (e) Gas Diffusion Layer, (f) MEA

This technology is made up of a number of components that are still being researched in an effort to find better solutions and, primarily, to lower the system's overall cost. BPs in particular stand for the cell's most expensive component. These are being investigated in order to find materials that are less expensive but nevertheless work satisfactorily.

1.3.1. Membrane Electrode Assembly

The MEA is a structure formed by the proton conducting membrane put in between the cathode and anode electrocatalysts. [2] The membrane inside the electrolytic cell is the perfluoro sulfonic acid polymers (PFSA) called Nafion®. These membranes have a thickness that varies in the range of 50-200 μm. [22] Positive aspects include good chemical, mechanical, and thermal properties, as well as the prevention of cell corrosion. This membrane is well-known for its high proton conductivity. [21] [27] However, because they contain the fluorine group, they also have a disposal issue. [21] These MEAs are created by joining an HSO3-terminated lateral branch with a Teflon molecule that has sulfonic acid groups as its termination. The weak connection between H+ and SO3- contributes to the increase in H+ ion mobility. The mobility mechanism and the Grotthuss mechanism are the two mechanisms that govern proton conductivity. The first transports the ions using molecule carriers that in this case are the water molecules. The second refers to the jump of the protons from the group H_3O+ to the near water molecule. And so it results in a continue bond breaking.[28][29] The efficiency of the mechanism is good if the membrane is wet. For this reason, membrane must be

maintained well hydrated and so, the temperature must be lower than the evaporation temperature of water. In particular, this type of membrane suffers the temperature above 80◦C that compromise the proton conductivity and the increase of degradation effects. So, the optimal range of temperature is 30-80◦C. The hydration of the cell is very good since in electrolyzer it is in direct contact with the water fed into the anode side. The proton conductivity of membrane is function of degree of humidification λ and temperature and it can be expressed as in Equation 1.4.[30]

$$\sigma_{\mathrm{mem}} = (0.005139 * \lambda - 0.00326)\exp\left[1268 * \left(\frac{1}{303} - \frac{1}{\mathrm{T_{cell}}}\right)\right] \qquad 1.4$$

- λ is the degree of humidification of the membrane expressed in $\mathrm{mol_{H_2O}}/\mathrm{mol_{SO_3^-}}$.

The researchers are also studying other types of membranes able to improve the ion exchange characteristics and to reduce the costs to produce them. [21]When the H+ ions pass through the membrane, the water drives these ions if an electrical field is applied. This phenomenon is called electro-osmosis. And the electro-osmotic drag can be defined as the number of water molecules that are transported with the protons. [31] This parameter depends only on temperature and can be calculated by Equation 1.5. [30] [31]

$$n_{\mathrm{d}} = 0.0134 * T + 0.03 \qquad 1.5$$

Because, the system works at low temperature, low rates of electrochemical reaction are involved. To overcome this problem, electrocatalysts layer are used. They are the place in which the main reactions (HER and OER) happen. [2] The electrocatalysts are implemented on the membrane to promote the charge transfer kinetics in order to diminish the activation energy and to decrease the mass transfer resistance. They are also responsible of creating the Three Phase Boundary (TPB). The TPB is the place in which three different pathways coexist: electrons, reactants and products. [32] The used materials must be appropriate in order to avoid the cell corrosion, for this reason precious metals are implemented as electrocatalyst in order to conducts both electrons and protons. [2] [21] In particular, anode electrocatalysts materials are iridium oxide (IrO2) or mixtures between iridium/iridium oxide and ruthenium. Cathode electrocatalysts are, instead, Platinum/Carbon-based materials. In the state of art, the anode electrocatalysts loading goes from 0.5 to 2 mg/cm2 and the cathode electrocatalysts loading goes from 0.5 to 1 mg/cm2. [2] In these years, the research on PEM water electrolysis were focused to find performant material for electrocatalysts in order to mitigate

the drawback of the OER irreversibility and slowness. [20] In fact, the OER governs the efficiency of the cell due to the fact that it has a great amount of overpotential loss of anode electrochemical process if compared to the cathode. [33] Durability is an important element of the electrocatalysts. In fact, the electrocatalyst layer has problems related to the degradation. The first degradation is due to the Pt agglomeration or loss of activation sites. As a result, to understand how to overcome this problem becomes important. In addition, electrocatalysts are often very thin, but not enough, in fact they may be subjected to mass transport limitation or a considerable ohmic losses. Regarding this aspect, further research is necessary in order to reduce the thickness and so, improving the performance. [34]

1.3.2. Gas Diffusion Layer

The GDL is composed of a microporous substrate and that can or cannot be attached with a Micro Porous Layer (MPL). [24] The GDL and MPL play important roles, like electronic connection between bipolar plate and the electrode, transition for reactant transport, remover of heat and water, support for MEA and preservation of electrocatalyst layer from corrosion. [24] [34] Carbon matrix or carbon paper are the materials used in conventional PEM Fuel cells. However, because carbon oxidizes during water electrolysis, these are not suitable for the anode side of PEMWE. Titanium is the only material that can function in the acidic environment of the anode side. However, these are frequently coated with platinum to achieve the desired conductance as well as Titanium's high contact resistance. Porous carbon material or porous carbon stainless steel are used on the cathode side.[22] The researchers are presently focused on improving the performance of the electrolyzers by modifying the structure of GDL. Improving water management is one example of an improvement. The GDLs are optimized with a coating of PolyTetraFluoroEthylene (PTFE) or with an implementation of MPL on the surface because it allows for electrolytic cell water management. As a result, the water is removed, and the flow of the reactant is improved. [24] If this is not taken into account, some negative phenomena may occur, resulting in decreased durability and performance. GDLs, on the other hand, can degrade after long-term tests because the PTFE fibers can be destroyed. As a result, it has the potential to increase the overcapacity of mass transportation.[35] In the next years, the studies will investigate new materials of GDLs in order to have a reduction of the negative phenomenon and to increase the electrical conductivity.

1.3.3. Bipolar Plate

In PEMWE stack, a number of cells are connected together in series in order to increase the production of gases. The connection of the different cells is obtained considering a part of the system that is the Bipolar Plate (BP). The BP are used to conduct electrons from the anode side to the cathode side, to separate

1.3.3.1. Channels

The channels are usually printed on BPs in order to transport the water and to permit the water splitting reaction. Channels together with the GDLs represent the so-called flow field. They are also used to lower the temperature, thereby acting as a heat remover. Various types of channels, such as serpentine, zig-zag, parallel, and pin-type, have been developed over time. The choice of one over the other affects the electrolyzer's performance.[34] The reason for this influence is the fact that the channels are responsible of the distribution of reactants on electrodes. It also affects the hydraulic resistance, the pressure drop and the entire cost of assembly. [35] In particular, the different configurations have been studied in order to evaluate the behaviour of them and the better configuration was resulted in the serpentine type, because it represents the best solution in terms of hydrogen production and thermal distribution.[36]

1.3.3.2. End Plates

The last components are End plates. They are one of the main components which have important roles in the structure, such as combining various components like MEA, GDL, BP, etc, in order to realize a stack and to provide a uniform pressure distribution between all these components. In this sense, the aim is to decrease ohmic resistance as low as possible to increase the efficiency of cell. So, it is the most important role of this component, in fact it decreases the contact resistance between MEA and BPs as well as BPs and current collectors and so enhance efficiency and hydrogen productivity. As a result, they keep all the elements together by using clamping bolts that bring the entire mechanical load on the cell. [37][38] They provide the passages for reactant gases and coolant fluid and ensuring good sealing at various interfaces. End plate materials are divided into two main categories: non-metallic materials and metallic materials. The non-metallic materials such as engineering plastics, polysulfons, etc. have not sufficient thermal stability and may be damaged at high operating temperature. The metallic

materials such as steel, aluminum and titanium have high mechanical properties and thermal stability, but they present problems related to the low corrosion resistance and electrical insulation. [39]

1.3.4. Gasket

Sealing gaskets are materials that in PEMWE cells are placed between BPs and the MEA. The main function of them is to prevent the leaking of water inserted inside the cell and avoid the not-correct passage of water needed to cool the cell. They also serve as electrical insulators between the two BPs (Anode and Cathode). Polymeric materials, in general, can be used due to the low operating temperature. Because many individual cells in a stack are connected in series, some studies indicate that elastomer gaskets must be used. In fact, they are beneficial in preventing water leaks, allowing the electrolysis reaction to proceed normally. [40] [41]

1.3.5. Thermodynamics

An electrolyzer's thermodynamic analysis is critical because it is inextricably linked to its heat, work, and energy streams. In this sense, the main concepts are illustrated in order to better understand the mechanisms at work.[42] An electrolytic cell is a device in which non-spontaneous reactions- $\Delta G > 0$- are driven by electrical power. So, electrical energy is transformed into chemical energy associated to a chemical element or compound. It is clear that the occurred reaction influences the efficiency of entire system. Furthermore, an important parameter is the Open Circuit Voltage (OCV), which was presented in mathematical form in 1887 by Nernst, combining the two laws of thermodynamics, equations 1.6 and 1.7, and the Faraday Law, Equation 1.8.[43] The first law of thermodynamics that is shown in equation 1.6 is considered for a system having the reactants as input and products -shown with the subscript p- as output. The reactants include the fuel -shown with the subscript f- and the oxidant -shown with the subscript ox- and heat and work are shown with the $\Phi_{th}$and W_{el}. In the second law of thermodynamics in equation 1.7 the same convention is kept. Σ_{irr} is referred to all the irreversibilities.

$$\Phi_{th} - W_{el} = \dot{n}_p \cdot \bar{h}_p(T, p_i) - \dot{n}_f \cdot \bar{h}_f(T, p_i) - \dot{n}_{ox} \cdot \bar{h}_{ox}(T, p_i) \quad 1.6$$

$$\frac{\Phi_{th}}{T} - \Sigma_{irr} = \dot{n}_p \cdot \bar{s}_p(T, p_i) - \dot{n}_f \cdot \bar{s}_f(T, p_i) - \dot{n}_{ox} \cdot \bar{s}_{ox}(T, p_i) \quad 1.7$$

$$\dot{n}_r = \frac{I}{z_r \cdot F} \tag{1.8}$$

Solving the equation and considering the correct assumptions as:

- Σ_{irr}=0, in reversible conditions.
- Steady-state conditions.
- Equilibrium condition.

The solution is reported in Equation 1.9.

$$\bar{l}_{el} = \frac{W_{el}}{\dot{n}_f} \tag{1.9}$$

It is the work injected in the system, that is generally negative by convention and in reversible conditions is like in Equation 1.10 [44] :

$$\bar{l}_{el} = -\Delta\bar{g}_r \tag{1.10}$$

In this case, it is intrinsically positive since the reaction is non-spontaneous. Considering the Equations obtained before, the OCV is found through Equation 1.11. [21] [42]

$$OCV = \frac{\Delta\bar{g}_r(T,p)}{z_r \cdot F} \tag{1.11}$$

The OCV depends on temperature and pressure since $\Delta g_r(T, p)$ depends on them but also on z_r, that is the number of electrons exchanged in the electrochemical reaction of the r-th specie per molecule. So, it is strongly dependent on the reaction and on the type of compound. Knowing the partial pressures, the potential of electrolytic cell can be determined, and it is reported in Equation 1.12. [44]

$$OCV = \frac{\Delta\bar{g}_r(T,p_0)}{z_r \cdot F} + \frac{\bar{R} \cdot T}{z_r \cdot F} \cdot \ln\left(\frac{\Pi_i^p \left(\frac{p_i}{p_0}\right)^{\nu_i}}{\Pi_i^r \left(\frac{p_i}{p_0}\right)^{\nu_i}}\right) \tag{1.12}$$

In Equation 1.12, temperature and partial pressures of reactants and products are present, together with the standard Gibbs Free Energy of the reaction. It can be expressed also in terms of concentration of chemical species and in terms of activity. In particular, this equation depends on temperature, if it increases the reversible voltage decreases due to the decrease in the Gibbs Free Energy at

standard conditions. Otherwise increases with a consequent increment in the absorbed power. A particular case is shown in Equation 1.13 and it happens when there is not an external heat source. In this case the entire energy for the reaction must be supplied by electrical energy and so, the voltage is higher and called thermoneutral. [44]

$$V_{th} = \frac{\Delta \bar{h}_{\text{react}}(T,p)}{z_r \cdot F} \qquad 1.13$$

It means that the cell is not only able to drive the reaction but also to compensate the thermal needs of the cell.

1.3.6. Kinetics

The OCV represents the potential drop under ideal conditions at open circuit, or when no current circulates within the circuit. It means that the circuit is closed and current begins to flow inside the cell; the system is no longer in ideal conditions, but rather in real ones. The differences between the real and ideal functioning arise from the occurrence of mass and charge transport phenomena, which characterize the system's real functioning. These phenomena cause an increase in voltage. [42] According to this, a relationship between the potential drop across the cell and the intensity of the current flowing in the cell can be created and its name is Polarization curve. In an electrolytic cell, with an increase of current there is an increase of voltage, due to the irreversibility. [21] Considering a generic Polarization curve, three main sections are visible, and they are the three main mechanisms that create losses in the cell :

- Charge transfer related to kinetic behaviour of the electrochemical reaction at the anode and the cathode.
- Charge conduction related to ion conduction in the electrolyte and electron conduction in electrodes and the external circuit.
- Mass transport related to molecules diffusion through the electrode's pores.

These phenomena can be also sub-divided in two main categories:

- Faradaic losses, which belong the first mechanism. These irreversibilities are caused by the direct transfer of electrons between redox reactions at interface between electrode and electrolyte.
- Non-Faradaic Losses, which belong the other two mechanism.

These irreversibilities are caused by mass transport phenomena and the resistance affecting the current flow in the cell.

The cell voltage in Equation 1.14 is reported. [44]

$$V_c(T,p) = OCV + \sum_{n=1}^{3} \eta_n(i) \qquad 1.14$$

In which the η indicates the value of losses inside the cell. The Equation 2.15 is re-written in the form of Equation 1.15. [21] [42]

$$V_c(T,p) = OCV + \eta_{\text{act}}(i) + \eta_{\text{ahm}}(i) + \eta_{\text{diff}}(i) \qquad 1.15$$

The first contribute is the activation losses related to slow electrode reaction kinetics. These are predominant at low current densities. To take place, a chemical reaction must overcome an initial energy barrier. The energy required to overcome this barrier is called Activation Energy. This is indicated with Ea. The general reaction constant k(T) can be estimated through an Arrhenius type equation 1.16. [44] [42]

$$k(T) = A \cdot \exp\left(-\frac{E_a}{R \cdot T}\right) \qquad 1.16$$

Where:

- A is the pre-exponential factor.
- E_a is the Activation Energy.
- R is the molar gas constant.
- T the temperature.

In case of an electrochemical reaction, that takes place as two different half electrochemical reactions occurring separately at the two electrodes, the reaction rate not only depends on temperature, as in the common reactions, but also on the potential gradient in the electrodes η. It is expressed through the Equation 1.17. [44]

$$r(T,\eta) = k(T) \cdot \exp\left(\frac{\alpha \cdot F}{R \cdot T} \cdot \nu_i \cdot z_i \cdot \eta\right) \qquad 1.17$$

Where:

- F is the Faraday Constant.

- α is the Charge Transfer Coefficient (CTC) and it is function of the Symmetry factor β and of the Number of electrons exchanged in the Rate Determining Step of the reaction n_{rds}.
- νi is the stoichiometric coefficient of the i-th specie.
- zi is the Charge Number of the i-th specie.

It is possible to express a relationship between the current density and the Over- voltage across the electrodes through the so-called Butler-Volmer Equation 1.18, using the rate of reaction of forward and backward reaction. [21] [42]

$$i = i_0 \cdot \left\{ \exp\left[\frac{n_{rds} \cdot \beta \cdot F}{R \cdot T} \cdot \eta_{act}\right] - \exp\left[-\frac{n_{rds} \cdot (1-\beta) \cdot F}{R \cdot T} \cdot \eta_{act}\right]\right\} \qquad 1.18$$

Where:

- η_{act} is the Activation Overvoltage. It represents the voltage drop spent in order to activate the electro-chemical reaction by increasing its rate of reaction.
- i_0 is the Exchange Current Density. It is the current exchanged when the electrochemical reaction is in equilibrium, it depends on the catalyst and on temperature but mainly on Three Phase Boundary Length, l_{TPB}. It is a parameter that takes into account the surface over the reaction occurs, the nanostructure of the catalyst and the temperature.
- F is the Faraday Constant.
- R is the molar gas constant.
- T is the Temperature.

Considering the approximation β≈ (1-β), the Activation Overvoltage is found, and it is reported in Equation 1.19.

$$\eta_{\text{act}} = \frac{R \cdot T}{\beta \cdot F \cdot n_{rds}} \cdot \sinh^{-1} \cdot \left(\frac{i}{2 \cdot i_0}\right) \qquad 1.19$$

The equation 1.19 is valid for both anode and cathode side. The second contribution is related to ions and electrons transport phenomena which are responsible for the Ohmic overvoltage. The voltage drop is due to the conduction of protons in the electrolyte and electrons in the electrodes and in external circuit. They are resulting from the resistance of the flow of electrical current. The Equation 1.20 is found through the Ohm's Law.

$$\eta_{\text{ohm}} = I \cdot \sum R(T) \qquad 1.20$$

Where:

- R represents the overall resistance of the electrolytic cell that is mainly linked ion conduction since ion conductivity is much lower than the electronic one. It is the sum of electrical and ionic resistances.
- I is the current flowing the cell.

The Equation 1.20 can be also written in terms of Area Specific Resistance (ASR) and current density i. ASR can be expressed as the product between the resistivity ρ, function of the material and temperature, and the mean ion path length, l_{path}. In this way, the Equation 1.21 is obtained.

$$\eta_{\text{ohm}} = \text{ASR(T)} * \text{i} \qquad 1.21$$

The third contribution is related to molecular diffusion processes that affect the quantity of reactants that are useful for the reaction itself. Considering a certain molar flow rate of a reactant specie, the diffusive process that allows the molecules to diffuse across the porous electrode and reach the reaction point will determine the concentration at the TPBs, thus it is important to consider diffusivity effects to understand the potential increase due to concentration losses. It is possible to obtain the diffusion overvoltage as function of current density using the Fick's Law 1.22 and the Faraday's Law 1.23.

$$\frac{z_r}{S} = D^{eff} \cdot \nabla \cdot C \qquad 1.22$$

$$\dot{n}_r = \frac{I}{z_r \cdot F} \qquad 1.23$$

In this case I=i.S where the S is the area, z_r is the Charge Number of the r-th specie. Under the hypothesis of diffusion prevailing on one dimension, the Equation

1.24 is obtained.

$$i = z_r \cdot F \cdot D^{eff} \frac{C_{bulk} - C_{cat}}{t} \qquad 1.24$$

In the limiting situation in which concentration in cathode flow is zero C_{cat} = 0, the limiting current is obtained as reported in Equation 1.25, that is function of the reactant molecular species inside the electrodes. Where:

$$i_l = z_r \cdot F \cdot D^{eff} \frac{C_{bulk}}{t} \qquad 1.25$$

- D^{eff} is the effective diffusion coefficient in m2/s, function of porosity ϵ and tortuosity τ coefficients.
- C_{bulk} is the concentration in the Bulk Flow in mol/m3.
- t is the transport length in m.

The diffusion overvoltage equation 1.26 is obtained.

$$\eta_{\text{diff}} = \left| \frac{R \cdot T}{z_r \cdot F} \cdot \ln\left(\frac{C_{cat}}{C_{\text{bulk}}}\right) \right| \qquad 1.26$$

And the Equation 2.27 can be written in the form of Equation 1.27, function of i_l.

$$\eta_{\text{diff}} = \left| \frac{R \cdot T}{z_r \cdot F} \cdot \ln\left(1 - \frac{i}{i_l}\right) \right| \qquad 1.27$$

Considering the three contributions, the voltage Equation 1.15 can be written in the form of Equation 1.28.

$$V_c(T,p) = OCV(T,p) + \eta_{act,a}(i) + \eta_{act,c}(i) + \eta_{ohm}(i) + \eta_{\text{diff},a}(i) + \eta_{\text{diff,c}}(i) \qquad 1.28$$

The Equation 1.28 shows the Polarization Curve in its more general form, considering the different contributes both at the anodic and cathodic sides. A generic curve is reported in Figure 1.4, in which the different sections are present.

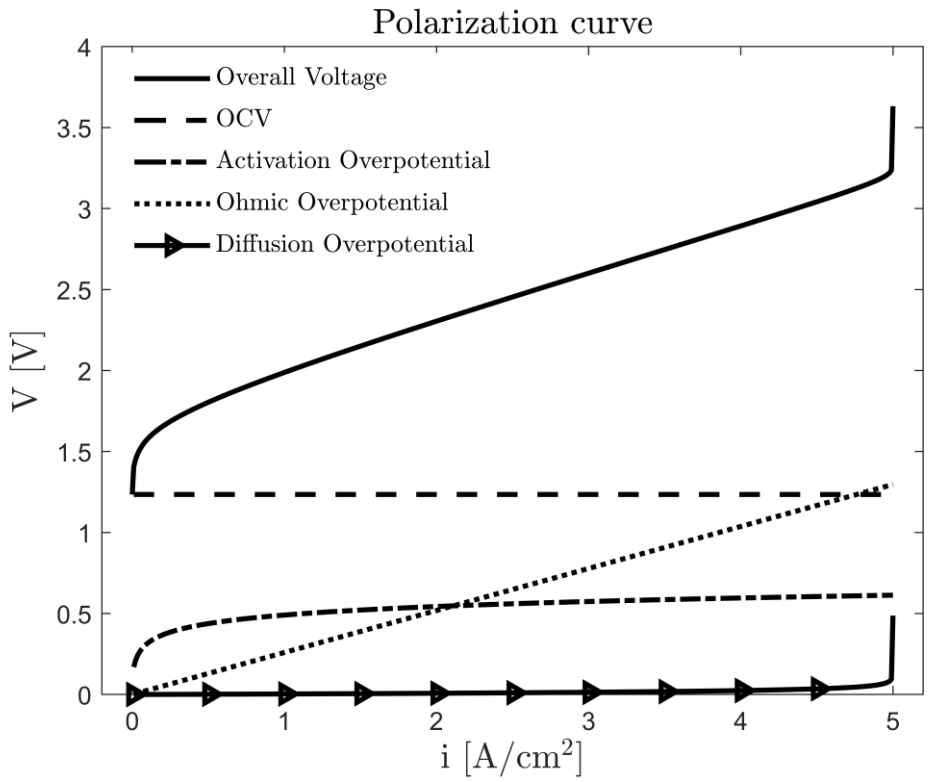

Figure 1.4Different contributions of polarization curve [44]

1.3.7. Water management

Water is the primary element used in the electrolysis process to produce hydrogen and oxygen. Water management is important in this context because it allows for the prediction of water consumption and the associated production of oxygen and hydrogen. The water is oxidized at the anode, producing oxygen, electrons, and protons. By carrying out a balance on the anode side, the Equations 1.29 and 1.30 are obtained.

$$\frac{dN_{O_2}}{dt} = \dot{N}_{O_2}^{in} - \dot{N}_{O_2}^{out} + \dot{N}_{O_2}^{gen} \qquad 1.29$$

$$\frac{dN_{H_2O}}{dt} = \dot{N}_{H_2O}^{in} - \dot{N}_{H_2O}^{out} - \dot{N}_{H_2O}^{mem} - \dot{N}_{H_2O}^{cons} \qquad 1.30$$

where $\dot{N}_{O_2}^{in}$ in and$\dot{N}_{O_2}^{out}$ out are molar flow rates of oxygen of anode inlet and outlet, $\dot{N}_{H_2O}^{cons}$ is the molar flow rate of water consumed, $\dot{N}_{H_2O}^{in}$ and $\dot{N}_{H_2O}^{out}$ are molar flow rates of water of anode inlet and outlet, $\dot{N}_{O_2}^{gen}$ is the molar flow rate of oxygen generated, and $\dot{N}_{H_2O}^{mem}$ is molar flow rate of water passing through membrane. [44]

[45] Using Faraday's Law it is possible to write the quantity of water consumed, reported in the Equation 1.31 , and the quantity of oxygen produced, reported in the Equation 1.32.

$$N_{\mathrm{H_2O}_{an,cons}} = \frac{I}{4 \cdot F} \quad 1.31$$

$$N_{O_{2an,gen}} = \frac{I}{4 \cdot F} \quad 1.32$$

At the cathode, on the other hand, the reduction reaction takes place with the relative production of hydrogen. As in the case of the anode, the Equations 1.33 and 1.34 are obtained by carrying out a balance at the cathode chamber.

$$\frac{dN_{H_2}}{dt} = \dot{N}_{H_2}^{in} - \dot{N}_{H_2}^{out} + \dot{N}_{H_2}^{gen} \quad 1.33$$

$$\frac{dN_{H_2O}}{dt} = \dot{N}_{H_2O}^{in} - \dot{N}_{H_2O}^{out} + \dot{N}_{H_2O}^{mem} \quad 1.34$$

where $\dot{N}_{H_2}^{in}$ and $\dot{N}_{H_2}^{out}$ are molar flow rates of hydrogen of anode inlet and outlet, $\dot{N}_{H_2O}^{in}$ and $\dot{N}_{H_2O}^{out}$ are molar flow rates of water of anode inlet and outlet, $\dot{N}_{H_2}^{gen}$ is the molar flow rate of hydrogen generated, and $\dot{N}_{H_2O}^{mem}$ is molar flow rate of water passing through membrane from anode side to cathode side. [44] [45] Applying Faraday's Law the quantity of Hydrogen produced is calculated through the Equation 1.35.

$$N_{H_{2an,gen}} = \frac{I}{2 \cdot F} \quad 1.35$$

The water passing through membrane is described by Equation 1.36.

$$N_{\mathrm{H_2O_{mem}}} = N_{\mathrm{H_2O_{diff}}} + N_{\mathrm{H_2O_{eod}}} + \mathrm{N_{H_2O_{pe}}} \quad 1.36$$

in which $N_{\mathrm{H_2O_{diff}}}$ is the molar flow rate referred to the diffusion contribution, due to the fact that there is a concentration gradient across the membrane. It refers to transport of water from high concentration zone (anode) to low concentration zone (cathode). $N_{\mathrm{H_2O_{eod}}}$ is molar flow rate due to the electro-osmotic drag, it tends to increase because the H^+ ions drag with themselves water molecules through membrane. $\mathrm{N_{H_2O_{pe}}}$ is the molar flow rate due to pressure gradients between anode side and cathode side. [30] [45] The water management is extremely important for PEMWE. Considering a cell, if it is not well hydrated, it means a lower content of water inside the cell with consequent reduction of proton conductivity and higher ohmic losses. So, it is clear as the water management plays an important role in the

performance of the cell. However, the opposite case can occur, i.e., an excess of water sent in the anode side can compromise the correct functioning of the cell, with an increase of mass transport loss, with consequent voltage drop. [46][47]

1.3.8. Thermal management

Thermal fluxes management is an important aspect to analyse. Thermal fluxes are generated by the reactions and by the overvoltage effects. Considering the electrolytic cell in which a not spontaneous reaction occurs ($\Delta \bar{g}_r > 0$) through the injection of electricity, there are two effects. The first effect tends to increase the entropy of the system ($\Delta s > 0$) and absorbs a heat flux as can be seen from the Equation 1.37, while the second one is related to the exothermic flux ($\Phi_{irr} > 0$) generated by overvoltages, as reported in the Equation 1.38. [44]

$$\Phi_{react} = \left(\frac{T \cdot \Delta \bar{s}_{react}}{z_f \cdot F} \right) \cdot I > 0 \qquad 1.37$$

$$\Phi_{irr} = -\sum_j \eta_j \cdot I > 0 \qquad 1.38$$

The Total Thermal Flux Φ_{tot} can be expressed as the algebraic sum between the Equation 1.38 and 1.39. A certain amount of external energy must be provided to the system in order for the water splitting reaction to occur. This energy is the reaction enthalpy ΔH_r. Through Equation 1.39 the enthalpy of reaction is found.

$$\Delta H_r = \Delta G_r + T\Delta S_r \qquad 1.39$$

Inverting the Equation 1.39, $T\,\Delta S_{react}$ is found and reported in Equation 1.40.

$$T\Delta S_r = \Delta H_r - \Delta G_r \qquad 1.40$$

The Φ_{tot} is found through Equation 1.41.

$$\Phi_{tot} = \left(\frac{\Delta \bar{h}_{react}(T,p)}{z_f \cdot F} - V_c(T,p) \right) \cdot I \qquad 1.41$$

Considering the equation three behaviours can be identified for the electrolyzer:

$$\frac{\Delta \bar{h}_{react}(T,p)}{z_f \cdot F} - V_c(T,p) \qquad 1.42$$

- If $\frac{\Delta \bar{h}_{react}(T,p)}{z_f \cdot F} > V_c(T,p)$, the electrolyzer has an endothermic behaviour.

- If $\frac{\Delta\bar{h}_{\text{react}}(T,p)}{z_f \cdot F} > < V_c(T,p)$, the electrolyzer has an exothermic behaviour.
- If $\frac{\Delta\bar{h}_{\text{react}}(T,p)}{z_f \cdot F} > = V_c(T,p)$, the electrolyzer has a thermoneutral behaviour.

In the first case the reaction needs heat to be supplied; while in the second, heat to be removed, and in third it is at Thermoneutral conditions. [44] In general, the cell performance decreases at both low and high temperatures. [48] Low temperatures can cause issues due to the freezing of the water content in the cell, which can cause different problems to the entire system, such as mechanical damage to the components. However, it can be demonstrated that high operating temperature permits to achieve good performance. Nevertheless, this operating condition requires an enhanced water management and cooling. However, considering the effect temperature, the degradation rate is accelerated, and the long-time performances are decreased. [49]

1.3.9. Efficiency

The efficiency of an electrolysis system is a Key Performance Indicator (KPI). A KPI permits to understand how much a solution is far from the ideal one and, focusing on the performance, how much they are different. The efficiency of an energy system is defined through Equation 1.43.

$$\eta = \frac{\text{useful energy}}{\text{available energy}} \qquad 1.43$$

In case of electrolyzer systems, the efficiency depends on the operating conditions of this one and it can be calculated in three ways, considering three main effects: the faradaic effect, the voltage effect and the thermodynamic effect. The Faradaic type is reported in Equation 1.44. [44]

$$\eta_F = \frac{\dot{n}_{H_2,\,\text{real}}}{\dot{n}_{H_2,\,\text{Faraday}}} \qquad 1.44$$

This considers the relationship between the real and the ideal hydrogen production. The ideal one can be calculated considering Faraday's Law. [44] The Voltage type is reported in Equation 1.45 and Equation 1.46.

$$\eta_v = \frac{E_{rev}}{V_c} \qquad 1.45$$

$$\eta_F = \frac{E_{TN}}{V_c} \qquad 1.46$$

The Equation 1.45 considers the relationship between the Reversible Voltage and the real voltage, while the Equation 1.46 between the Thermoneutral Voltage and the real voltage. [44] Whereas the third formulation is found through the Equation 1.47.

$$\eta_T = \frac{\overline{LHV}_{H_2}}{\Delta \bar{h}_{\text{react}}\,(T,p)} \qquad 1.47$$

The Equation 1.47 represents the ratio between the molar LHV H2 of the hydrogen and the $\Delta h_{react}(T, p)$. This one is usually used to compare hydrogen production technology and to understand how much input energy is transferred in terms of chemical energy to the final products. [44] In general, the efficiency can be improved increasing the temperature and pressure but obviously, it is important to consider the operating conditions in order to understand how much this can be increased.

1.3.10. Operating conditions

The operating conditions are important as they influence the thermodynamics of PEMWE in different ways. Optimization of these is very important because they ensure high efficiency and good life to device. So, the main parameters, such as voltage, current density, pressure and temperature, and their influence on PEMWE, are illustrated.

1.3.10.1. Voltage

The voltage is an important parameter to characterize the electrolyzer device. It determines the electricity efficiency and the energy consumption. In this sense, for an electrolyzer the voltage must be as low as possible, since a high value would result in low production efficiencies and a high power required. The voltage is a parameter that depends on other operating conditions such as temperature and pressure. So, improving these means improving the performance of entire system. In general, for PEMWE the voltage is 1.8-2.2 V. [20]

1.3.10.2. Current density

Current density is the parameter that has inverse relation to the energy efficiency. In fact, the higher operating current density the higher reaction rate and so the higher production rate. But it can create problems, like the gas bubble generation. An increase of gas bubble can compromise the performance of entire cell due to

the fact that mass transport limitations occur. According to this, the current density must be maintained under a certain value in order to have a good production rate and to avoid the rapid gas bubble formation. [20] [50] The good value in which PEMWE can operate is 2 A/cm2.[51]

1.3.10.3. Temperature

Temperature is an important parameter that can affect thermodynamics. The PEMWE is a device that can obtain good performance only under certain value of temperature. The temperature influences the voltage of the cell, in fact working at low value of this can reduce the proton conductivity with the consequent increase of overvoltages. Temperature results a good indicator in terms of performance of electrolyzer and so, an increase of this parameter reduces the Gibbs free energy of the electrochemical reaction, increasing the ionic conductivity, and so the performance of electrolytic cell. In fact the kinetic of reaction is favoured at high value of temperature. [52] The working temperature range is 30 to 80 degrees Celsius. It has been studied that the electrolysis voltage can be reduced by increasing the temperature. In particular, it has been demonstrated in one study that working at high temperatures can reduce the voltage of the cell by 2.5mV for every Kelvin increase, reducing the amount of power required by the system. [53] However, PEMWE has one limitation connected to maximum working temperature due to the fact that the MEA must be very well hydrated in order to avoid the reduction of proton conductivity of this one and as consequence the reduction of performance. Furthermore, higher temperature values can cause degradation of the MEA. The latter issue arises from the fact that at high temperatures, there is a risk that the MEA will not be adequately wet, as well as a lack of water supplied inside the cell. These two issues have the potential to harm the MEA, causing it to fail to complete the operation or, in extreme cases, to break.[54]

1.3.10.4. Pressure

The pressure, like the temperature, plays a big role for electrolyzer thermodynamics and functioning. The electrolyzer is a device able to work from the ambient pressure to higher value. [30] Today, commercial electrolyzers work up to high value of pressure. The reason is that high operating pressure permits to overcome the gas bubble generation that occurs to high temperature during the electrolysis reaction. In this sense, the investigations were concentrated into study

some commercial electrolyzers at 70 bars and the results were excellent. In fact, this technology permits to have a production of Oxygen and Hydrogen with high efficiencies. Considering the commercial PEMWE, an optimal range of operating pressure was found around 30-45 bars. In this context, the functioning of an electrolyzer with different pressure between the cathodic and anodic chamber was also demonstrated. [30] Another reason for using high operating pressure is that it allows to directly store the produced hydrogen instead of using external power to compress it.[55] However, the high operating pressure can demand some particular requirements to the system in order to avoid safety problems, in fact when an electrolyzer works to high pressure, the production of gases can reach critical levels, for this reason it is important to reduce the gas cross-permeation, since explosive mixture can be created. [56] Gas recombiners can be used in order to maintain the hydrogen under a certain content avoiding the explosions. Other safety systems can be installed in the experimental bench. [56] If the pressure is considered for the level of a stack, which can reach operating pressure of 700 bars, it is simple to understand that these systems will require a very high external power. For this reason, in the last years, more and more researches were concentrated on to develop materials constituting the cell able to resist to high pressure. However, the compression work of the produced hydrogen can be calculated through the Equation 1.48.

$$l_c = c_p \cdot T_{in} \cdot \left(\beta^{\frac{\gamma-1}{\gamma}}\right) \cdot \frac{1}{\eta_{is}} \qquad 1.48$$

The compression work depends on β; the higher β the higher compression work. So, it is better to work at high pressure rather that compress the produced gases. As seen previously, the pressure affects the value of OCV, as it is possible to see in Equation 1.49.

$$OCV = \frac{\Delta \bar{g}_r(T, p_0)}{z_r \cdot F} + \frac{\bar{R} \cdot T}{z_r \cdot F} \cdot \ln\left(\frac{p_{H_2} \cdot p_{O_2}^{0.5}}{p_{H_2O}}\right) \qquad 1.49$$

An increase of partial pressure of two produced elements makes an increase of OCV. So, it is clear that it is important to make a trade-off between the electrical power spent to make water splitting and the electrical power used to compress the produced hydrogen in order to understand how it is better to proceed, considering also the purposes to do this. [44]

1.4. Research questions addressed

The research brought in this thesis is inspired by the quest for getting the most out of low temperature electrolysers while having the least degradation.

The European Commission introduced its "Hydrogen strategy for a climate-neutral Europe"[57] in 2020, outlining the prerequisites and steps for mainstreaming clean hydrogen as well as goals for the installation of renewable hydrogen electrolysers by 2024 and subsequently 2030. In order to enable the high-volume production of electrolysers, it is fundamental to have a thorough understanding of the electrolysers, their performance and testing method, as well as the degradation issues. Hence it is necessary to create standardized degradation tests coming from real usage data based on variable dynamic operation of electrolysers. Furthermore, the use of computational modelling is of paramount importance in order to be able to predict the behaviour of the electrolysers without going through exorbitant testing each time.

Considering the shortcomings of the state of the art both regarding a flexible experimental test setup to study different variables that affect the performance of the low temperature electrolyser and its degradation -from cells to stacks- and lack of presence of a Multiphysics model with detailed biphasic flow condition that preciously predicts the behaviour and the limits of the low temperature PEM electrolyser, it was evident that improvement in each of the these areas would be indispensable.

The goals mentioned in the second paragraph and the research gaps explained subsequently led to the following research questions:

1. How is it possible to build a flexible test bench that is able to evaluate a vast range of low temperature electrolysers and perform degradation tests?
2. How is it possible to benchmark different cells -PEM and Alkaline, single cells to short stacks- in one validated test setup to have standardized comparable results? How does the presence of water flow on the cathode side influence the performance of electrolyser?
3. How is it possible to diagnose the origin of performance variations during the normal functioning and accelerated degradation of the cells in a non-destructive non-disruptive way?
4. How is it possible to accurately predict the behaviour of the electrolytic cells under different physical conditions such as pressure, temperature, mass flow rate?

5. How the bi-phasic flow affects the performance of low temperature electrolysers and how to parametrize an accurate multiphysics model for it?

To **summarize** the consecutive steps that are followed to develop this thesis are:

Initially an electrochemical test bench was built that is able to test low temperature electrolytic devices up to high pressures and temperatures (1st and 2nd research questions). Different cathode configurations were analysed for a single cell PEM, considering experimental and modelling comparison. Degradation experiments were designed and performed in order to compare the effect of variable conditions on the cells. During the experiments, EIS was performed; and online water conductivity and measurement of fluoride ion chromatography were used to control the degradation (3rd research question). Subsequently, a 0D model, and 2D/3D Multiphysics models of the PEMWE was developed. These models were validated with the experimental results from the test bench (4th and 5th research questions). At the end, degraded samples were studied using SEM-XRD analysis to find out more about the degradation phenomena. Finally, to consider the safety and degradation issues, the hydrogen in Oxygen percentage was controlled throughout the tests.

1.5. Layout of the work

The current work is an effort to tackle the mentioned research questions. To address the questions properly, the work is divided in 7 chapters:

The **1st chapter** gives an overall introduction on energy storage and more specifically Hydrogen as a storage medium. Subsequently, a literature review on electrolysis and PEM water electrolysis is brought which would be the basis for the subsequent chapters.

2nd chapter presents the test bench that has been built and the experiments that have been done. This chapter addresses the first and second research questions.

3rd chapter brings the models that were built for the analysis of the PEM water electrolyser. The first part is dedicated to the 0D MATLAB model, and the second part to the Multiphysics model. This chapter addresses the fourth and fifth research questions.

4th chapter combines the results of the experiments and the models that were brought in chapter 3, and presents a validation of the models.

5th chapter discusses the Electrochemical impedance spectroscopy and its equivalent electrical circuit modelling approach for a better analysis on the phenomena happening inside the test cells during the experiments. This chapter addresses the third research question.

6th chapter brings the experimental and modelling results from the tests of chapter 2 and 5, and discusses them together. Since the content in this chapter put the results together, it contributes to responding to all of the research questions. In this chapter the tests regarding a comparison between the open and closed cathode configuration and the degradation test which come from the second research question is highlighted too.

Finally in the **last chapter**, some conclusions are brought, addressed research questions are highlighted and possible future works are discussed.

1.5.1. Award

The research work described in this thesis contributed to the achievement of **"Premio Qualità"** , Quality Award for PhD in Energetics, class of 2022 (among 34th cycle PhD candidates of Polytechnic of Turin).

Introduction

"Premio Qualità" is the prize awarded once a year to the three best performing PhD candidates by Polytechnic of Turin.

Chapter 2. Experimental

2.1. Electrochemical test bench

The experimental measurements were carried out on a PEM electrolyzer located at the CO2 circle lab. This laboratory contains test benches for the research on hydrogen production technologies, as a part of Polytechnic of Turin, located at the Environment Park in Turin. The latter is a science and technology park dedicated to the Environment and Clean Technologies.

Figure 2.1 Environment park- CO2 circle Lab

2.1.1. Test bench description

The experimental test bench, aims to carry out the characterization and evaluation of performance of electrochemical devices for the production of hydrogen. In particular, the goal is that of testing both single electrolytic cells and small assemblies of multiple cells (stack). There Hydrogen production occurs by feeding the devices with demineralized water and supplying them electric energy. The characterization of the devices will consist in evaluating the voltage-current curves (polarization) as well as in subjecting the cells to electrochemical impedance spectroscopy (EIS) analysis. The aim is to examine the performance of the cells through the phenomena of irreversibility that arise during operation. In addition, the devices will be subjected to long-term tests to analyze any degradation phenomena (with consequent loss of performance). The test bench must allow experimental activity on devices low temperature electrolytics (up to a maximum of 150°C) and with anionic electrolyte (alkaline cells) and with cationic electrolyte (PEM). In the Figure 2.2 is reported the Test Bench in which are conducted the tests.

Figure 2.2 Test Bench

In the Figure 2.3 the P & I of the testing station is reported.

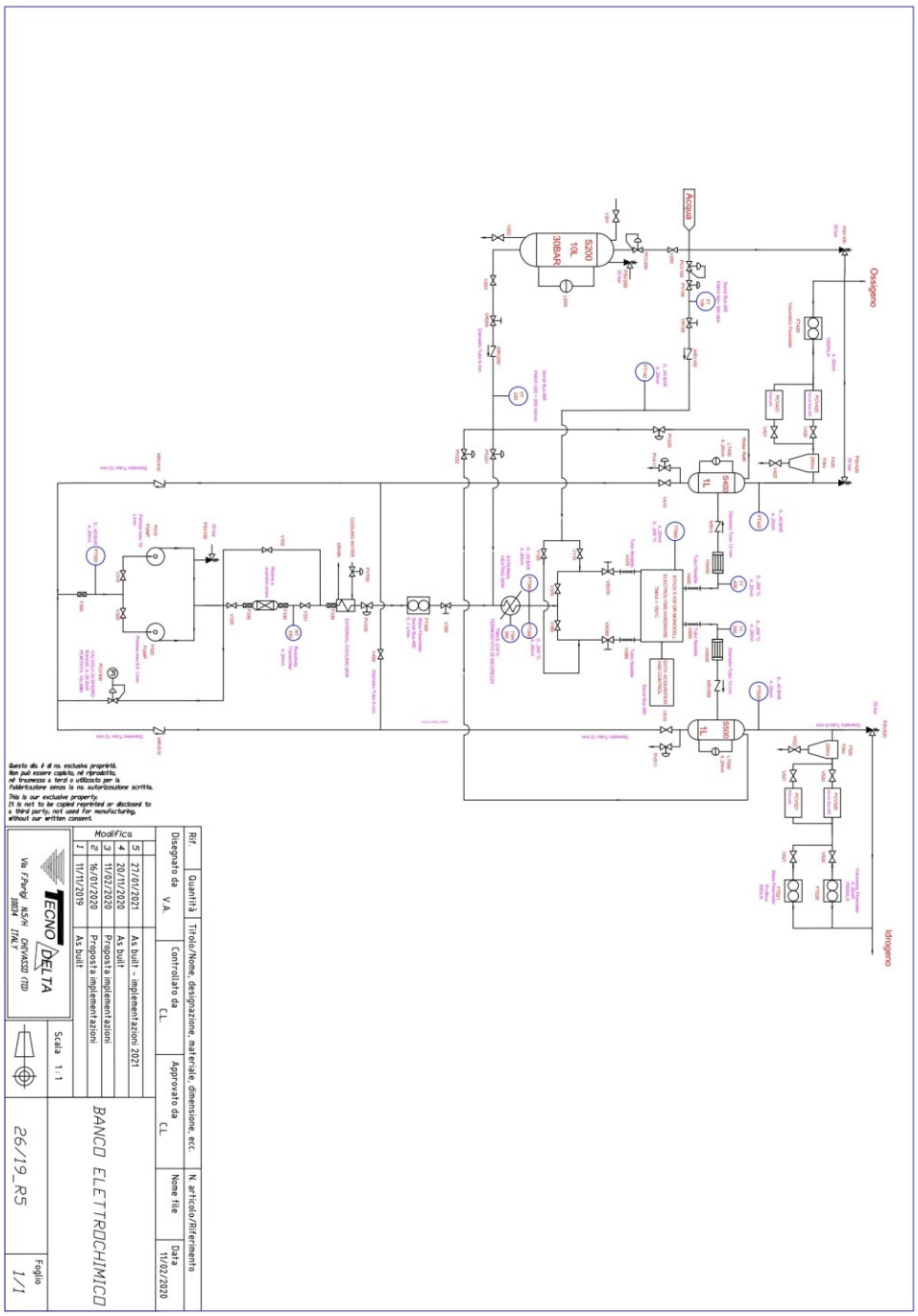

Figure 2.3 P&I of test bench

There are two external supply line, one for nitrogen and one for compressed air. The first is needed for cleaning and pressurization purposes, while the second for the correct operation of the pneumatic valves. Since electrolysis reaction needs

a huge amount of demineralized water, a water storage of 10 liters is located into the system. The function of tank is not only related to water storage but through the nitrogen line keeps the system pressurized. Water is further demineralized thanks to ion exchange resin that are present downstream the pumping system and the conductivity is kept <1 μS/cm. The tank feeds the electrochemical cell thanks to two main loops, one for the anode side and one for cathode side, obviously the water sent to the cathode side is not needed for the electrolysis reaction but only for cooling. At the anodic and cathodic outlet, the biphasic mixtures need to be separated. The separation occurs in two subsequent stages. The first stage is cooling, it takes place by means of condensers placed immediately at the exit of the respective channels. The condensers are of the tube-in-tube type, with the hot mixture flowing in the internal tube while refrigerating water from the water mains flows in the annular region. The second stage is the actual separation, it takes place in the gas / liquid separators tanks. They are two one-liter containers with two outlets, one in the upper part for the gas-rich mixture and one in the lower part for the liquid-rich mixture. The two separators are placed at the same height in order to have an optimal control of the quantity of demineralized water present in the process. The separators are connected with two 250 ml tanks placed above them in order to optimize the separation process. The water is pumped into the circuit through a volumetric pump that is able to treat a maximum flow rate of 10 L/min. In the system is present another volumetric pump with higher maximum flow rate both for redundancy and stack operations. The pumped water is heated up through an external electrical heater in order to reach the desired operating temperature. The heat is transferred to the fluid with a plate heat exchanger and temperature is kept almost constant thanks to a PID controller. To keep temperature and pressure, main thermodynamics parameters, as desired, several devices are inserted into the system:

- Back pressure controller, anode and cathode side;
- Mass flow meter for demineralized water;
- Level physical indicators, one for each separator;
- Temperature transducer;
- Pressure transducer;
- Valves;
- Conductivity probe.

· A general control system for the test bench was developed in LabVIEW (National instruments, LabVIEW 2009). It was interfaced with the power supply, instruments and hood and allowed the system variables, voltage and current to be controlled. It collects and stores data that can be viewed in an easy to read format. The LabVIEW system comprised of a front panel and a block diagram as shown in Figure 2.4.

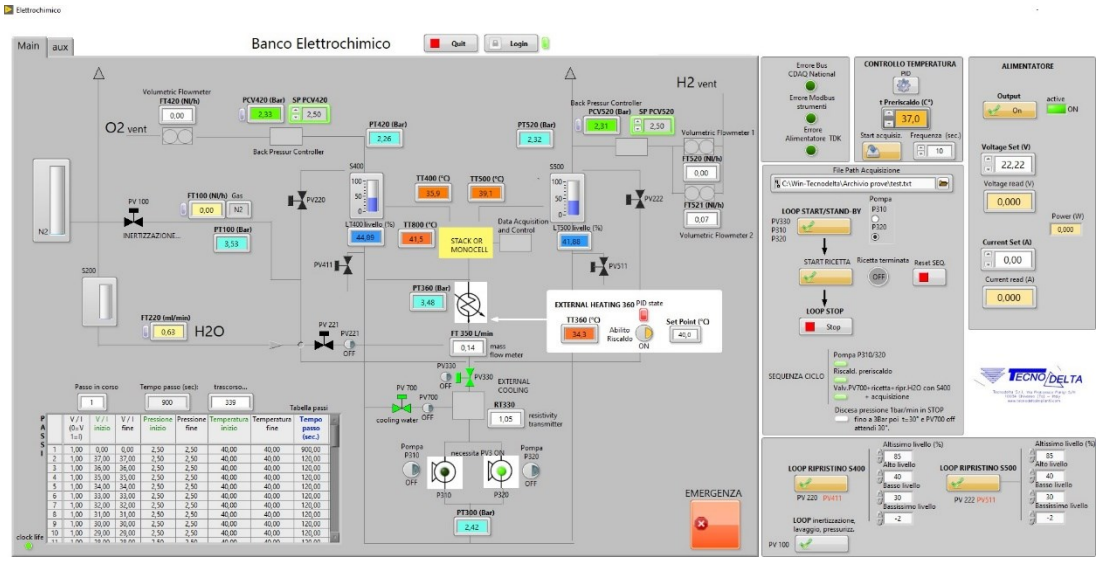

Figure 2.4 Software interface

The front panel displays the values of the variables in real time and the data collected from the system. The water can be supplied to the anode or cathode side and most PEM electrolyzers operate with a water anode feed because water is consumed at this side. In test bench considered the water is supplied both anode and cathode side, to analyse the industrial behaviour of PEM electrolyzer.

2.1.2. Novelty and comparison with other test stations

In the literature there are few documents that go into details of the balance of plant for the low temperature electrolysers.

In a recently published document by JRC, EU harmonised protocols for testing of low temperature water electrolysers, a similar plant of AEW is put in evidence as a comprehensive reference for the electrolysis test stations.[58]

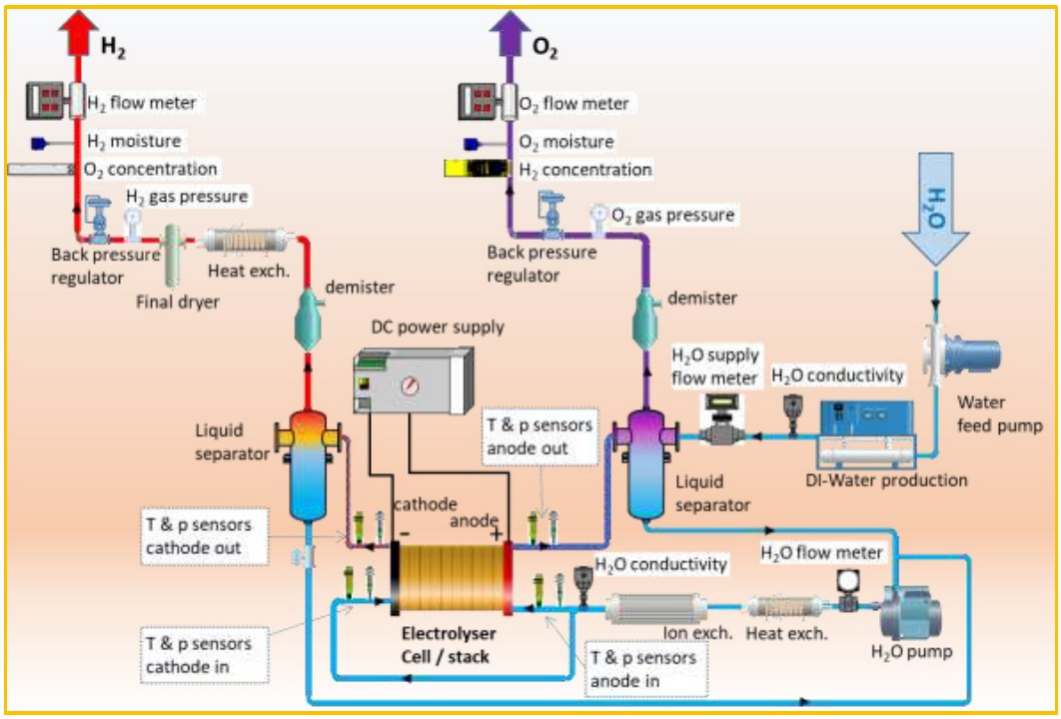

Figure 2.5 Scheme of AEMW electrolyser with the position of monitoring devices

Figure 2.5 shows a scheme with the location of the instrument measuring points for an AEM water electrolysis experimental set-up suggested by the JRC. In comparison with the test rig that is designed for this thesis, although this report refers to a more recent work , our test bench is equipped with all of the necessary monitoring devices. In addition to the devices presented by JRC, our test bench benefits from the presence of additional sensors for pressure and temperature in different points, additional conductivity meter for the liquid at the exit of cathode/anode, gas analyzers, mass spectrometers and additional doubled piping, pumps and sensors in order to be able to test the electrolytic cells up to the dimension of short stacks. Furthermore, suggested parameters by JRC to be measured consist in Current [A], Temperature [°C], Cell/stack voltage [V], Pressure [kPa], Water Flow rate [L.min-1], Gas Flow rate [L.min-1], Gas concentration [%] which are all measured in our test bench with the suggested accuracy.

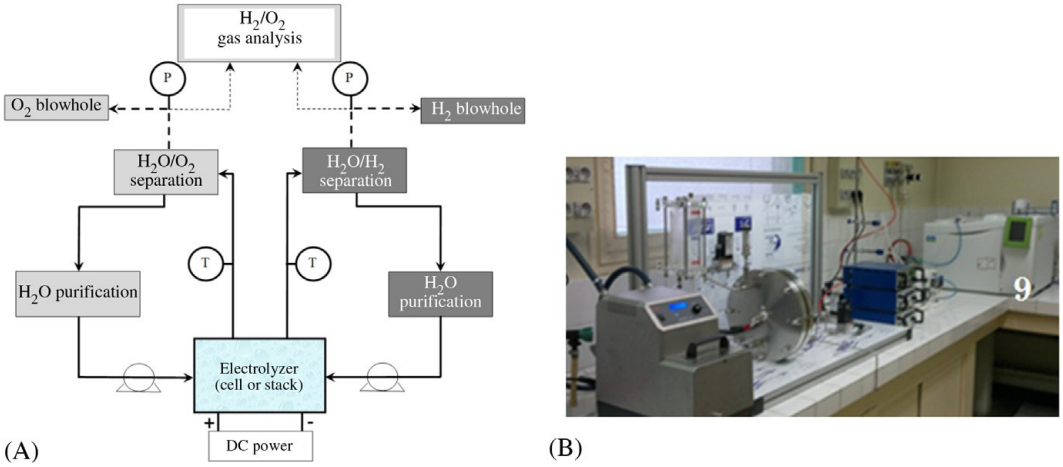

Figure 2.6 an example of PEM water electrolysis laboratory setup (A) Schematic diagram. (B) Photograph of a plant

Bessarbov et al have studied a considerable number of different PEM plants with their relative BoP and as a result they identified the main units for the PEM plant.[59] Among the main units the power supply, liquid-gas separation, water purification, gas treatment and process monitoring are the most important ones to be present in a PEM electrolysis plant. In comparison, our laboratory scale plant does not need a gas treatment unit as the produced hydrogen is not used afterwards.

Bessarbov et al state that the laboratory scale electrolysis plant -e.g. the one brought in Figure 2.6- should be placed in a specific environment for effective operation. it is necessary to continuously provide water of adequate purity and to supply that water to the cell/stack to feed the reaction but also to remove the excess heat produced by internal dissipation during operation at nonzero current density. Another factor is adequate control of operating temperature and pressure. Using two different water circulation loops facilitates gas removal and isothermal operating conditions. In comparison with the proposed condition, our plant has the mentioned necessary units and specifications and also includes more controls and sensors.

Regarding our newly constructed test bench, one of the most important novelties is the focus on its flexibility. Critical control and measurement devices such as mass flow meters, recirculation pump, backpressure controller and valves and piping system have been chosen in a way that permits the testing of electrolytic devices from ambient temperature to 150C and up to 30Bar of pressure resistant to both Alkaline and PEM liquid recirculation. In case, some devices are doubled to have the capacity of supplying both the single cells and stacks. An example is the

deionized water recirculation pump. Because of the flexibility of the measurement devices, we have the possibility of performing different studies. All of these studies are possible on different kinds of cells (PEM or alkaline), at different power levels (from single cell to short stack) in different T and P conditions and at different points of V and I, and in an automated mode (both for testing and data acquisition):

-Possibility of study of water consumption, because of the presence of liquid level on the tanks (digital value on the software)

-Possibility of study of Hydrogen (and oxygen) production quantity as the flow meter is present

-Possibility of studying the degradation of the membrane based on the conductivity sensor

-Possibility of study on crossover, the percentage and amount of hydrogen in oxygen and oxygen in hydrogen : there are both gas analyzer and the mass spectrometer available for use

-possibility of performing the EIS and Study the effect of different physical variables on parameters coming from the electrochemical impedance spectroscopy, such as double layer capacitance, resistances,….

-Study of clamping pressure of the cell housing using different types of pressure papers.

-Study on efficiencies of the cell/ stack such as a study on the mapping of effect of number of cells on the voltage of the stack, …

-Study on different geometries of the cell/stack (no limit on the geometry in this test bench)

These mentioned examples are only to show the vast possibility of performing experiments on this test bench.

2.1.3. Electrochemical cell

Electrochemical measurements were made on a 25 cm2 cell. The MEA was bought from QuinTech and composed by Nafion® 117 membrane, anode catalyst layer with 2 mg Ir/cm2 and cathode catalyst layer made of advanced carbon with 1 mg Pt/cm2. It is reported in Figure 2.7.

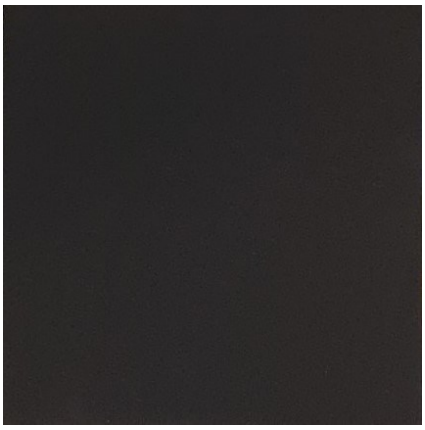

Figure 2.7 MEA composed by Nafion 117

It was sandwiched between Ti mesh GDL of 180 µm thickness on the anode side and Freudenberg H23C6 carbon paper GDL with MPL of 250 µm on the cathode side. These are reported respectively in Figure 2.8.

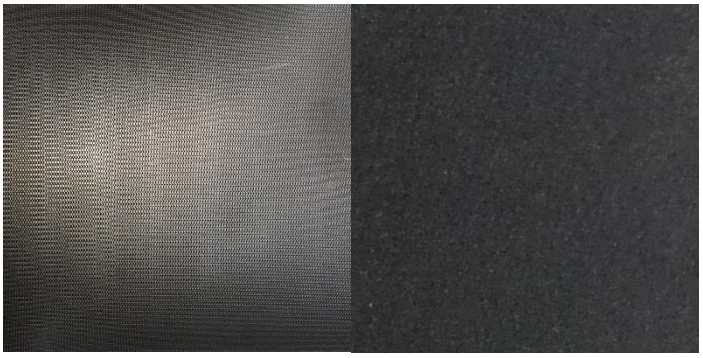

Figure 2.8 left :Titanium GDL – right:H23C6 Carbon paper GDL

The housing was bought from Fuel Cell Technologies, USA. The anode BP of 8.47mm thickness is a Titanium Block and the cathode BP is a Graphite Block of 12.45mm thickness, both with pyro-sealed triple serpentine flow pattern printed on them. The current collectors are made of gold plated copper and are equipped with high current connectors. Their thickness is of 0.6 mm. Moreover, they are electrical isolated from End Plates through a layer of Teflon coated with fiber-glass tape. The End Plates are made by aluminum alloy and the thickness is about 18.65 mm. The function is to keep together all the components using 8-bolt patterns. The entire structure equipped with BPs and current collectors for anode and cathode side is reported in Figure 2.9.

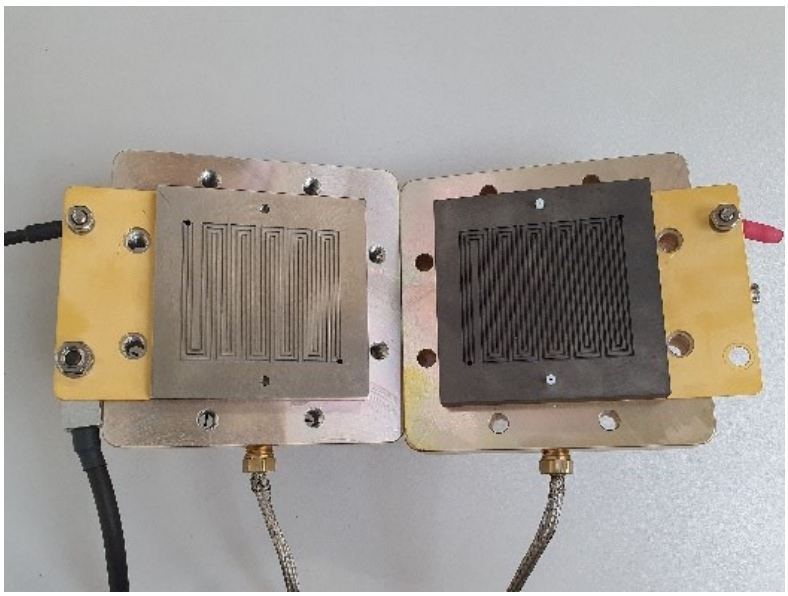

Figure 2.9 Housing composed by: Anode side with Titanium BP and current collector and Cathode side with Graphite BP and current collector

Figure 2.10 Temperature controller installed for control on cell housing

The entire housing is equipped with a Love Controls 16A Series, which is a microprocessor based temperature/process control. The controller is reported in Figure 2.10. It uses a PID in order to keep constant the operating temperature of the cell. It is constituted by two heater cartridge that are inserted in the housing.

2.1.4. Preparation of setup

Testing of single cells aims to characterize the performance and the durability of the materials and components under experimental conditions that can give relevant information about their behaviour when inserted in electrolyzer systems. To characterize the performances of the electrolytic cell and the test bench a preparation is necessary. Preparation consists of a procedure that must be performed for both the cell and the test bench. For the cell, all the components are

washed and then assembled. As regards the test bench, however, the PID must be set, and a thermocouple calibration must be performed. Some tests are conducted on the housing to avoid the increases of degradation effects. In this context, the right sealant has to be chosen and pressure paper technique was used.

2.1.4.1. Pressure paper technique

To prevent gas and water escaping during high pressure operation, uniform and homogeneous compressive forces on the sealants are essential and above all that the surface is smooth and free of defects. For this reason, it is important to understand what the correct technique is to close the entire structure. The structure, in fact, must be closed with bolts, which must be properly tightened. A high or an excessive compression means a big force on all the materials constituting the cell, with the creation of a mechanical degradation over time. To verify the pressure distribution inside the cell the pressure paper techniques was used. It consists of different pressure sensitive film (Prescale, Fujifilm) which are placed between the BPs and the Gasket with a pressure that must be maintained for two minutes. Some tests were conducted on the cell and different types of pressure papers were used, from the less to the most sensitive, and they were: LOW (LW), SUPER LOW (LLW) and ULTRA SUPER LOW (LLLW). These are two-sheet type, one is coated with a layer of micro-encapsulated color forming material and the other with a layer of the color developing material. These must be put in contact and when pressure is applied, the micro-capsules are broken and the color forming material reacts with color developing one to make red color. Looking at the red color is possible to check the pressure distribution. In fact, if the color density is high it means the pressure is high, vice-versa if the color density is low the pressure applied is low. So, the pressure paper was compared with the pressure chart, given by supplier, in order to understand the value of pressure applied, considering the temperature and humidity condition. An application of pressure paper in housing with correct sealants is reported in Figure 2.11. In these the pressure paper application before and after those bolts are tightened, are shown.

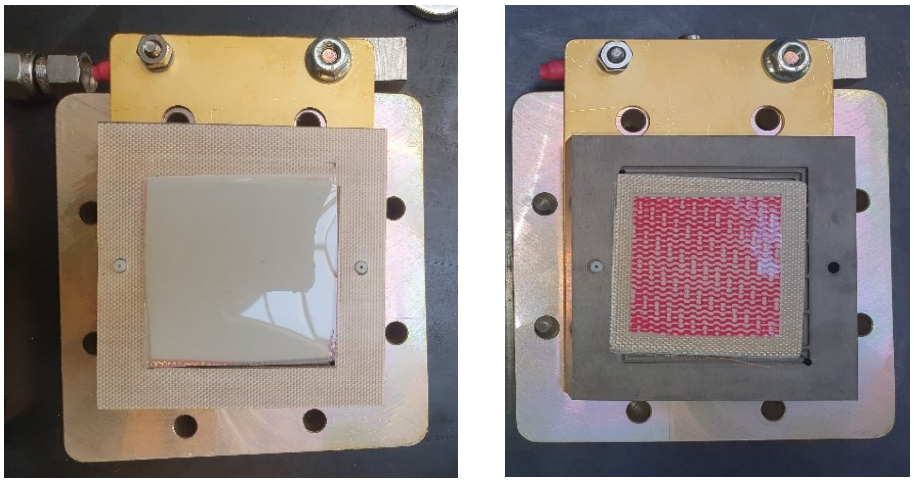

Figure 2.11 left: Pressure distribution inside the electrolytic cell before the closing – right: Pressure distribution inside the electrolytic cell after the closing

In this case, the "star" mode to close the cell, also defined as alternating, is analysed. The cell is tested with 6Nm, 10Nm applied on the bolts. The test results made in different type of pressure paper and the results are reported in Figure 2.12 and Figure 2.13.

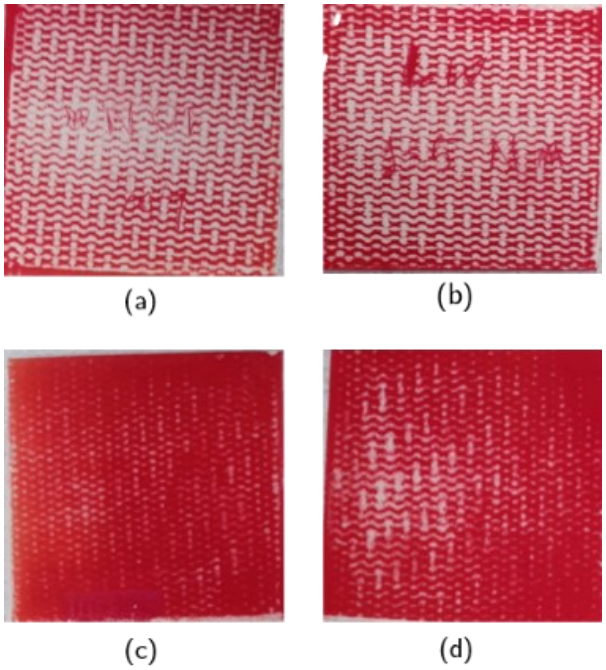

Figure 2.12 Pressure distribution analysis on 7.5x7.5cm2 area: (a) LW pressure paper with 6 Nm applied, (b) LW pressure paper with 10 Nm applied, (c) LLW

pressure paper with 6 Nm applied, (d) LLW pressure paper with 10 Nm applied, (e) LLLW pressure paper with 6 Nm

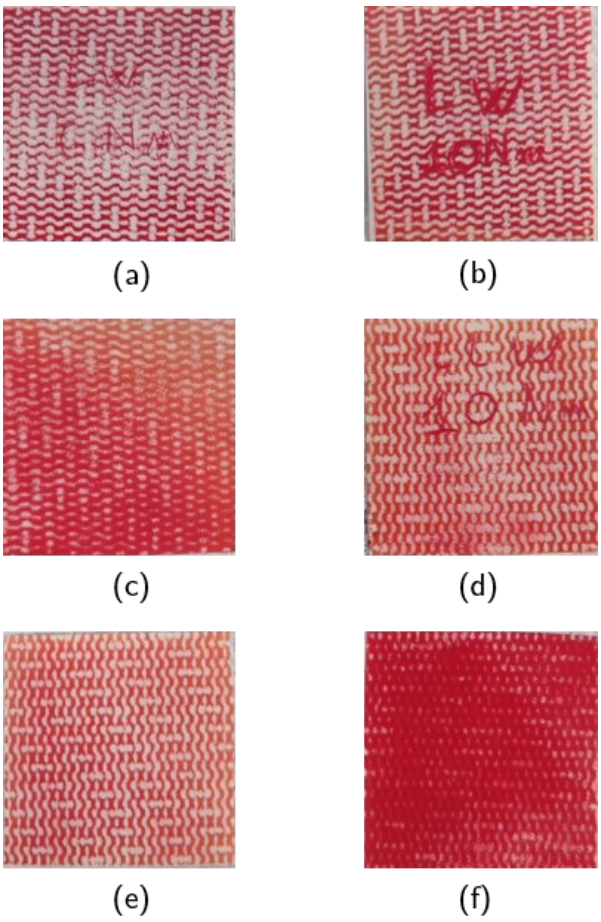

Figure 2.13 Pressure distribution analysis on 5x5cm2 area: (a) LW pressure paper with 10 Nm applied, (b) LW pressure paper with 13.5 Nm applied, (c) LLLW pressure paper with 6 Nm applied, (d) LLLW pressure paper with 10 Nm applied

The results show that with this procedure the pressure exerted on the components is homogeneous and not too high.

2.1.4.2. Cell assembly

2.1.4.2.1. Ultrasonic cleaning

Before the cell assembling was needed to do a correct cleaning of the main elements composing the internal part of electrolyzer. In this sense, the elements to clean are: Gasket, GDL and BPs. The methods to clean them can be different but,

in the case of electrolyzer the Ultrasonic Cleaning was chosen. The reason is that the normal cleaning in which the water is sprayed on the material is not as effective as the ultrasonic cleaner. An ultrasonic cleaner is composed by several parts. The system is closed through a lid. Opening the lid, the first part that is seen is the stainless steel tank, in this the items that must be cleaned are placed. It also has transducers, which are made of piezoceramic materials, and are placed on the side or bottom of the tank. The transducers react when hit by an electrical charge and due to the energy applied to them, their size and shape change. These changes cause the vibration of tank with consequent cavitation bubbles formed in the cleaning bath. However, the bubbles are formed only if the current applied to transducers has a frequency between 40 kHz and 59 kHz. The used ultrasonic cleaner is reported in Figure 2.14.

Figure 2.14 Ultrasonic Cleaner used in cell preparation.

The formed bubbles have a great action on the contaminants present on the surface. In fact, they tend to implode removing contaminants from objects in the tank. Even if the bubbles are small, their implosions are extremely powerful. In fact, they hit the contaminants making the formation of grains and later the deposition in the bottom of the tank. Another element that promotes the removing of contaminants is the temperature. This can be set in order to facilitate the elimination due to the fact that degases the tank. The cleaning procedure is made setting the temperature equal to ambient temperature (25◦C) and the current frequency to 59 kHz. The procedure was made for 5 minutes and repeated until the elements were cleaned. The result was very good, because the elements were cleaned, and the surface was free of contaminants. In Figure 2.15 an example of cleaning process is reported.

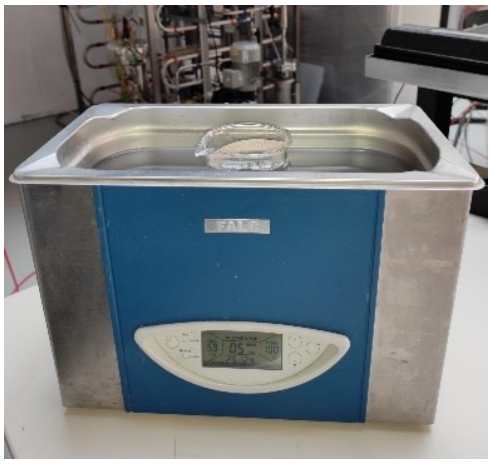

Figure 2.15 Cleaning process of GDLs and Sealant

2.1.4.2.2. Assembly procedure

To prevent gas and water escaping during high pressure operation, the correct configuration of sealants must be chosen. In this sense, different configurations were tested in order to find the correct one. Different types of materials were used, like silicon sealants and Teflon coated with glass fiber. The better solution was represented by two silicone sealants of 180 µm. Also, other type of sealants was used to make tests but the results are not good. In fact, the leakage of water and gases occurred and the values obtained were different from the expected one. The procedure consists into cut the sealants with the same dimensions of housing and after a cleaning in ultrasonic cleaner. The cut procedure is reported in Figure 2.16.

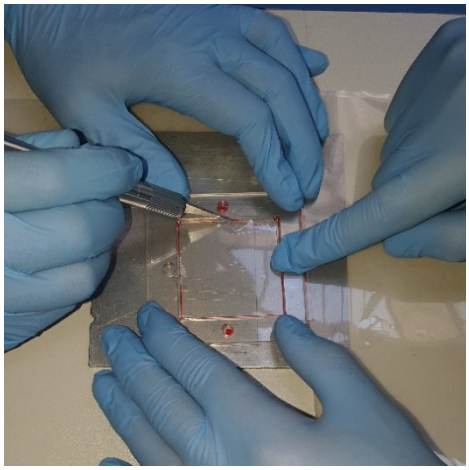

Figure 2.16 Cutting procedure of sealants

The procedure must be repeated until the quantity of sealants needed is reached. At the end of the cleaning phase, after choosing the correct sealants and checking that the force applied to the bolts is correct, the installation of the membrane (MEA) with the relative GDLs was foreseen both for the anode and the cathode side. However, the chosen method to make the installation was the "layered" method. It consists, into insert the different elements one by one on the chosen flow field plate. In this case, the chosen flow field plate was the anode side, due to the fact that Titanium GDL was used and so to avoid its movement, it was better to place the other elements on its. Moreover, the bolts can be inserted from cathode end plates and they are a guide to avoid the movement of all elements constituting the cell. Therefore, the first step consists of inserting the sealant on the anode side as it is possible to see in Figure 2.17.

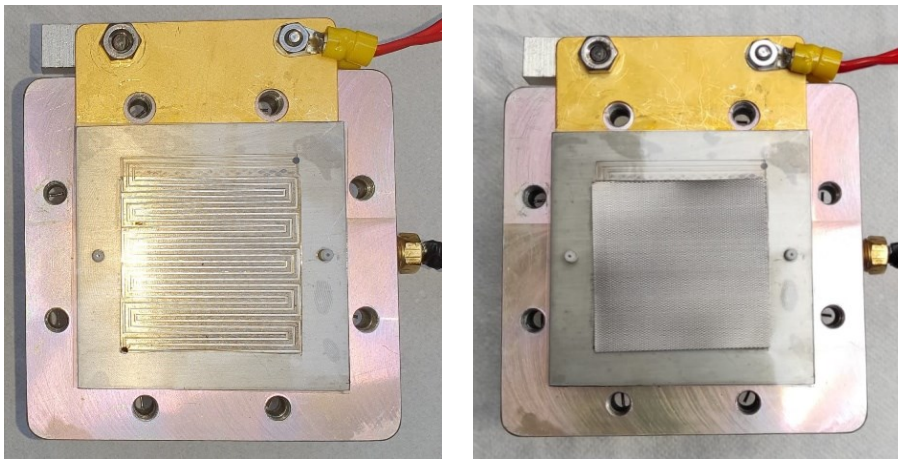

Figure 2.17 left: Assembly procedure in which sealant is placed on anode side – right: Assembly procedure in which Titanium GDL is placed on anode side

As said, the sealants have different dimensions and the chosen depends on an appropriate calculation that must be done in order to have the correct thickness of sealants which must be congruent with MEA thickness. Later, the GDL of anode was inserted, as reported in Figure 2.17.

The MEA was placed above it as is possible to see in Figure 2.18.

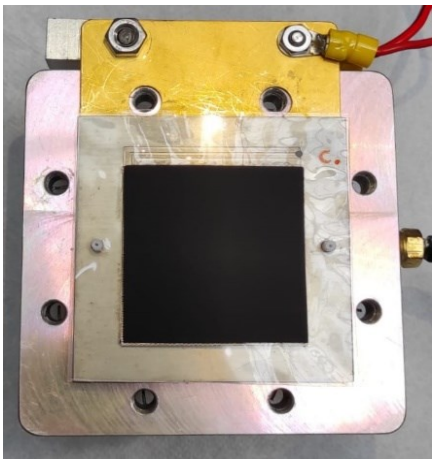
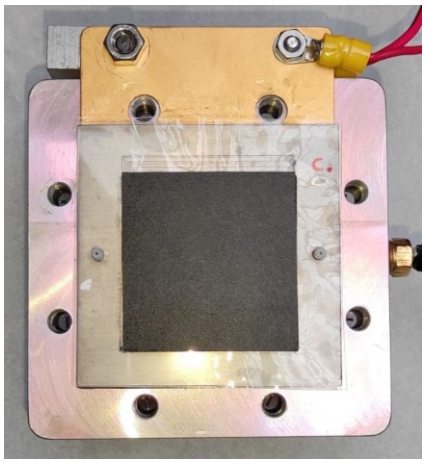

Figure 2.18 left: Assembly procedure in which MEA is placed above Titanium GDL _ right: Assembly procedure in which H23C6 GDL is placed above MEA

For the installation of the MEA, an appropriate humidification, spraying demineralized water over the surface, is important to ensure that it adheres well to the structure. The GDL for cathode side was after installed over the MEA, as in Figure 2.18.

Placing these elements, the flow field plate, also humidified, was placed above them and the structure was closed by means of End Plates and with the help of 8 bolts, as said. The last procedure is reported in Figure 2.19.

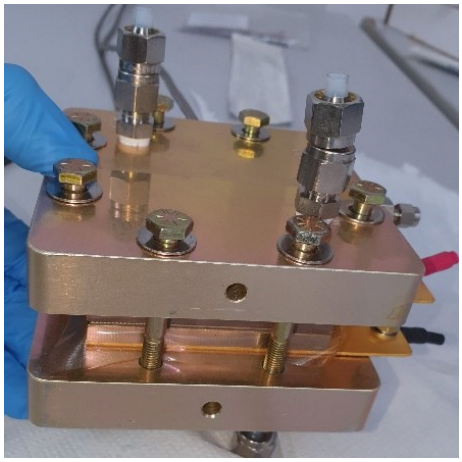
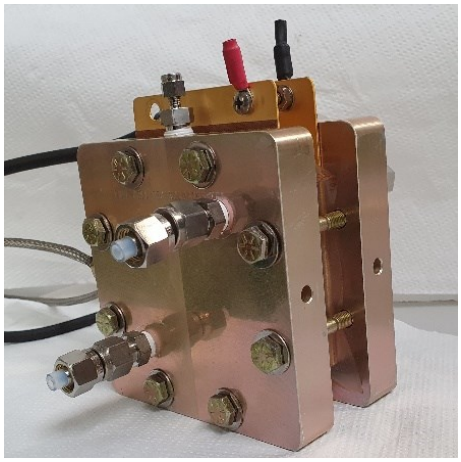

Figure 2.19 left: Final procedure with closure of housing – right: Housing closed and correctly tightened

The bolts must be properly tightened, because, as said, incorrect compression of the cell leads to degradative effects on the cell. After closing, the cell was placed on the experimental bench and connected with the latter. In this sense, there are 2

tubes per anode side and 2 tubes per cathode side, two for inlet and two for outlet. The cables necessary to supply the electrical power were also attached to the cell. Finally, the cell heating systems were also installed, in order to reach the desired temperature and maintaining it in steady-state condition for carrying out the tests, as it is possible to see in Figure 2.20.

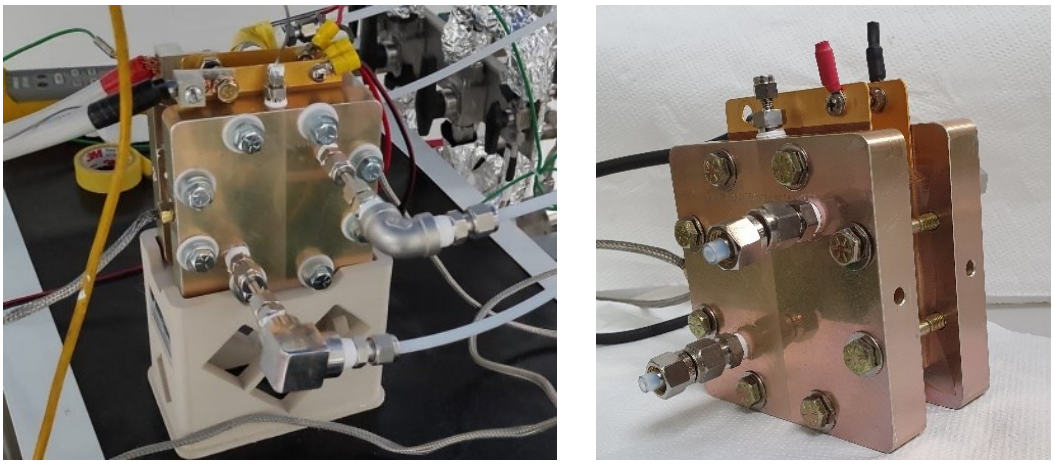

Figure 2.20 left: Housing placed on Test Bench with inserted cartridge - right: Housing placed on Test Bench with power supply connected

Obviously, the connection of thermocouple must be done in order to have the correct visualization of temperature from software interface that permits to understand when the system reaches the correct value or when the system is too heated.

2.1.4.3. Thermocouples and temperature Controller setup

After the first step of cell assembling, the temperature controller is set in order to have a right control of cell temperature. The setting is made on the Controller Love 16A that is reported in Figure 2.21.

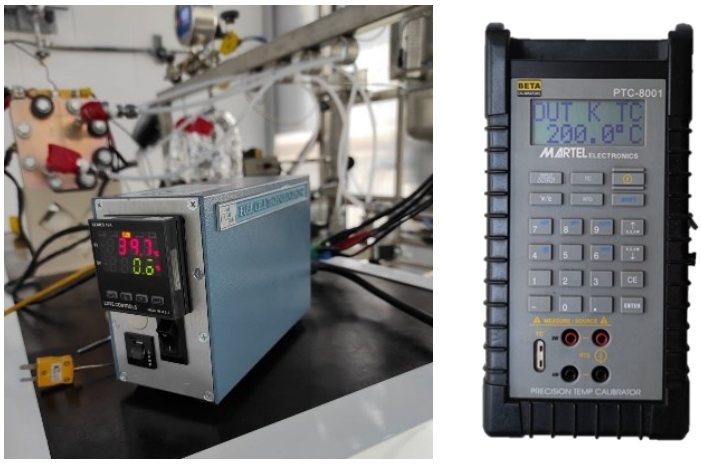

Figure 2.21 left: Temperature controller – right: Instrument used for the thermocouple calibration

The device presents different characteristics like Self-Tune PID or Fuzzy Logic. It is used in order to avoid the temperature oscillations that can occur in the system. Two temperature levels are set, the Set Point 1 (SP1) and Set Point 2 (SP2).

These are used to maintain the cell temperature in the range of the values imposed. The system reads the cell temperature through a thermocouple that is connected both to controller and to cell. In this sense, the response of system changes if the thermocouple changes. So, the type of thermocouple used must be specified. In Input type the right thermocouple is selected. In the controller type K thermocouple is set, considering that in the system type K thermocouples are installed. However, in controller must be defined the Output selection. Different type of tuning can be chosen, like SELF, PID or On-Off. In this case, SELF control is chosen since it is able to evaluate the process and select the PID values to maintain the correct control. However, it is coupled with a LEARN command. When this is activated the learning process start to operate in order to find automatically the best PID. An important parameter that can be imposed is DAMPING factor. It varies from 1 to 7. Low values have a fast response, high value have a slower response. The correct value for right functioning of system has been found in 3. The value is shown in the system in ◦C and with one decimal digit.

Thermocouple calibration: thermocouples are important elements of test bench. The thermocouples are temperature transducers that in the system are useful to have a correct measurement of cell temperature. As said, in the system type K thermocouples are installed. The type K thermocouple operates in the temperature range -200°C and +1350°C. However, thermocouples read the cell temperature and

is subsequently reconverted into a current signal. This current signal is elaborated by the PLC and sent the values on software of test bench (LabView), that is programmed to analyze all the current signal in 4-20mA setting. Therefore, it is necessary to know the minimum value and the full scale of the instrument. Based on this, by means of the Martel PTC-8001 instrument, a thermocouple calibrator, it is possible to perform a calibration in order to have an affordable instrument through which measure the cell temperature. It is brought in Figure 2.21.

The procedure aims to find the minimum value and the full-scale value of the thermocouple. The procedure was conducted and repeated until the values were found. This consists in setting different value of temperature and to find the correct value of minimum and maximum. So, the lowest value is set in order to have a signal of 4mA and the higher value is set in order to have a signal of 20mA. In Figure 2.22 an example of calibration made on test bench is reported.

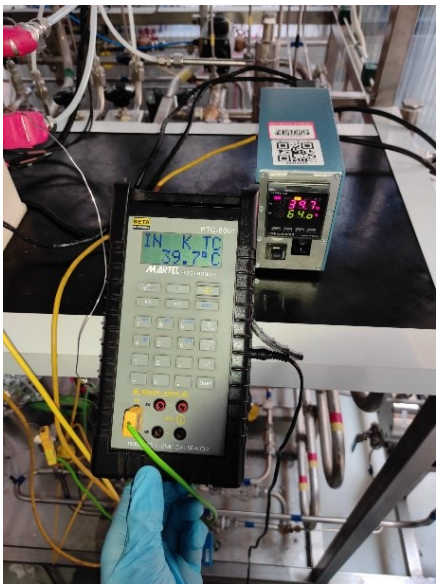

Figure 2.22 Calibration of thermocouple on test bench

2.2. Experimental result validation

The tests, as mentioned, were carried out on an electrochemical bench in which the electrolytic cell -of the PEM type- was installed. The general procedure consists in filling the 10-liter tank with demineralized water, then the system is pressurized through the nitrogen line, which also has the purpose of washing the circuits. Finally, the compressed air line opens, in order to have the correct functioning of the pneumatic valves. Before switching on the system, it is advisable to check all

the control systems, such as valves, back pressure controllers and emergency auxiliary systems. On the software side, the parameters to be controlled are set in order to carry out the tests. In this case, the preliminary experimental measurements consist of polarization tests. However, before carrying out the tests, the MEA must be hydrated and subsequently activated, in fact these are used to ensure that the cell operates in the correct way by ensuring that the voltage stabilizes. Hydration is a step that is carried out on the MEA and consists in circulating the water in the electrolyzer at least for 4 hours. Hydration plays an important role on the proton conductivity, which allows reaching high efficiency values of the electrochemical reactions. It was performed considering a current value of 0 A and the ambient temperature. The activation of the MEA, on the other hand, is the next step after hydration necessary to ensure that the voltage stabilizes. This was done considering 10 minutes time-steps in which the current density was made to rise from 0.5 to 1.5 A/cm2 and fall from 1.5 to 0.5 repeatedly. The activation procedure is reported in Figure 2.23.

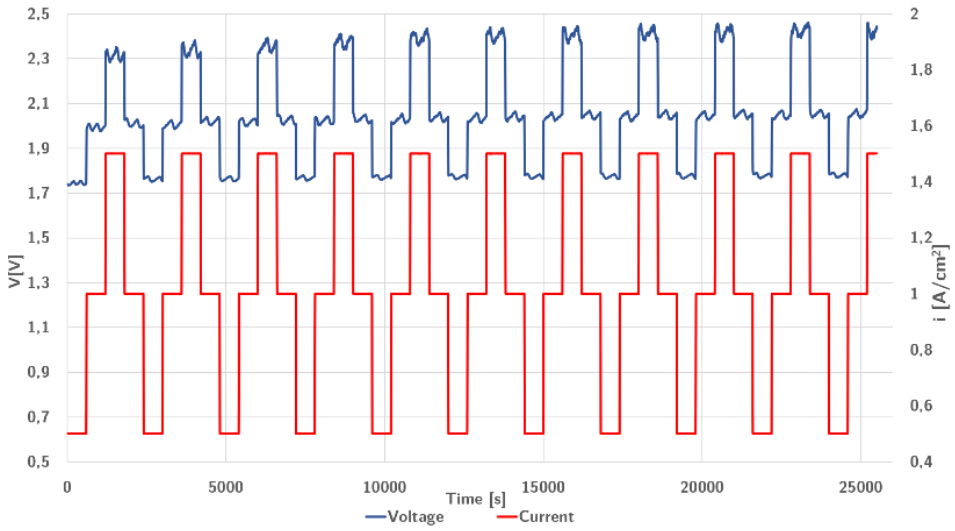

Figure 2.23 Activation procedure performed on the cell

Following the instructions of the membrane producer and in order to double check the stability of the test results after the hydration and activation stages, it is possible to keep the voltage as a constant value for a specific period of time to see the results of voltage change in time. For this reason the stabilization process was conducted considering a constant value of current density equal to 0.8 A/cm2 and the result is reported in Figure 2.24.

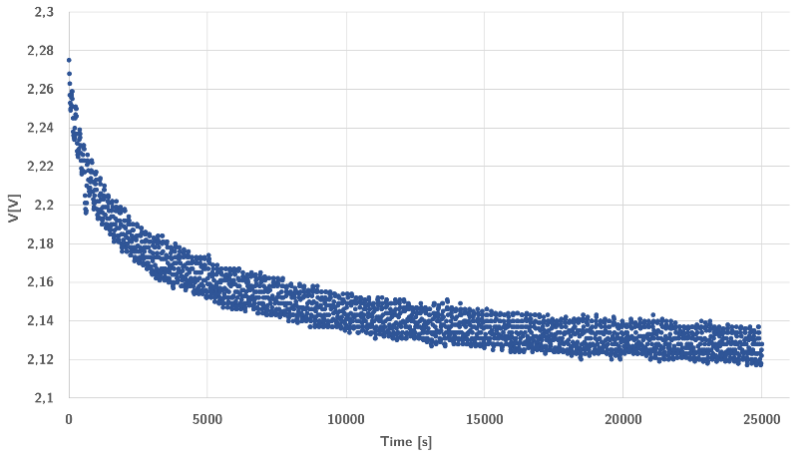

Figure 2.24 Stabilization procedure performed on the cell

2.2.1. Polarization

After hydration and activation, the polarization curve can be performed. The main objective of the polarization curve measurement is to carry out an electrochemical characterization of MEA. In this sense, the change in the cell voltage generated by the variation in the supplied current under steady-state conditions was analyzed, and in particular at a constant cell temperature and a gases constant outlet pressure. The polarization measurements were made through the coupling of power supply and the user interface by setting the main parameters: current, pressure, temperature for each step. A step consists of a defined interval of time in which is measured the voltage keeping constant all the other parameters. These procedures were done until the voltage reaches the steady-state condition, so the time-step is also an important parameter for the measurements. The chosen timestep is 120s, that is higher than the timestep chosen by Malkow et al. [60] In fact, it was experimentally checked that the cell voltage is stabilized after this time. All tests were conducted fixing pressure, temperature and time-step and varying the input current from 0 to 37 A and from 37 to 0 A. An example of steps is reported in the Table 2.1.

Table 2.1 Step set on LabView

Step	Current [A]	Pressure [bar]	Temperature [°C]	Timestep [s]
1	0,1	5	65	120
2	0,2	5	65	120

3	0,3	5	65	120
4	0,4	5	65	120
. . .	. . .	. . .	. . .	120
49	37	5	65	120
50	36	5	65	120
51	35	5	65	120
. . .	. . .	. . .	. . .	. . .
99	0,2	5	65	120
100	0,1	5	65	120

This procedure of ascending and descending the current was made in order to stabilize the voltage curve. If there is a difference between the two curves obtained it means that a hysteresis is present and it provides information on thermal equilibrium during the measurements, as it is possible to see in Figure 2.25 Hysteresis occurred in a test with T=40°C and p=5 barg.

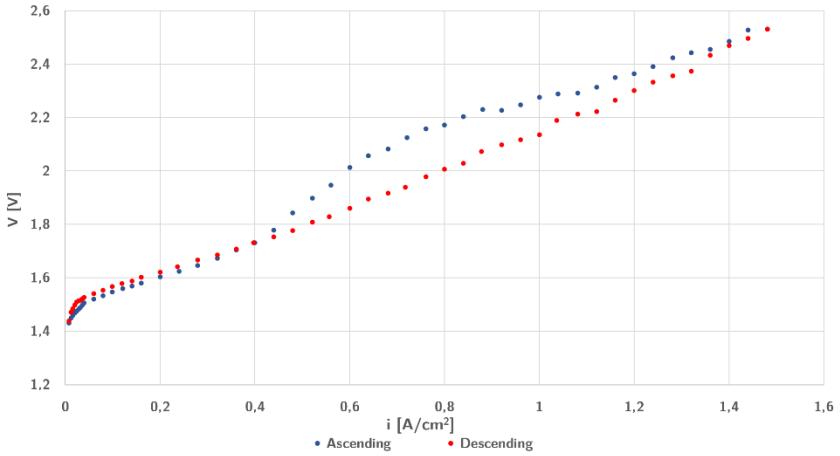

Figure 2.25 Hysteresis occurred in a test with T=40°C and p=5 barg

Since the output values of measurements were obtained in a .txt file a further data processing in Excel environment was needed in order to extrapolate the polarization curve.

Generally the tests are conducted considering two types of configurations, one with anode inlet valve opened and cathode inlet valve opened variably and one with anode inlet valve opened and cathode inlet valve closed.

Table 2. Different cathode configurations

configuration	Anode valve	Cathode valve	Details
Type 1	open	open	Type 1.1: cathode valve completely open Type 1.2: cathode valve partially open to account for different variables such as the different pressure drops in cathode and anode side of the test rig and electrolyser
Type 2	open	closed	This configuration is similar to the dead end mode in the fuel cells

In the current subsection, the Polarization results are reported according to the two configurations. In the next subsection, the Hydrogen production results are reported, relatively to the second configuration.

The results of first configuration are shown in the Figure 2.26, Figure 2.27, Figure 2.28, Figure 2.29. In Figure 2.26 the influence of the operating temperature at constant pressure equal to 2.5barg is represented. In this sense, the higher the temperature the lower the polarization curve.

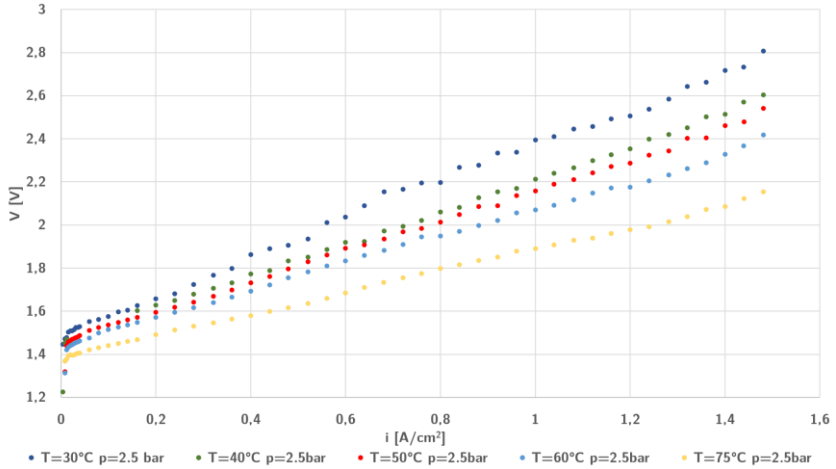

Figure 2.26 Polarisation curves in different temperatures with fixed pressure equal to 2.5barg

Looking at the figure some variations in voltage are present. Generally, the automatic back pressure controllers installed in the system are more precious to

control higher pressures such as 10 or 15barg. For the pressures below 3 bars the manual valves are used. The oscillations in graphs are a normal behaviour of the system response and the obtained result are discrete. Furthermore, the main parameters that can influence the polarization curve are analyzed and no problems occurred during the tests. So, further investigation can be conducted to understand the nature of high value of polarization and in this way, justify the behaviour. Also Figure 2.27 shows the influence of the operating temperature at constant pressure, with the operating pressure set to 5barg. In Figure 2.26 and Figure 2.27 the influence of temperature for different operating pressures, considering anode inlet valve completely opened and cathode inlet valve partially opened is represented.

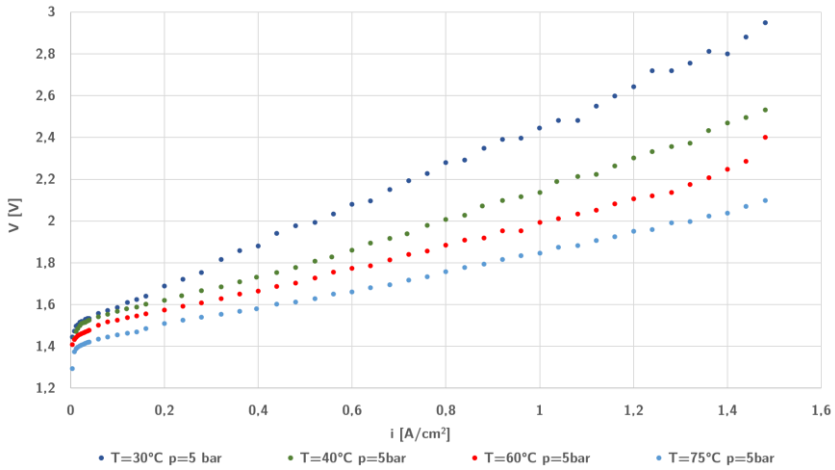

Figure 2.27 Polarization curves in different temperatures with fixed pressure equal to 5barg

Instead, in Figure 2.28 and Figure 2.29 the influence of pressure at the higher operating temperature equal to 75◦C is represented.

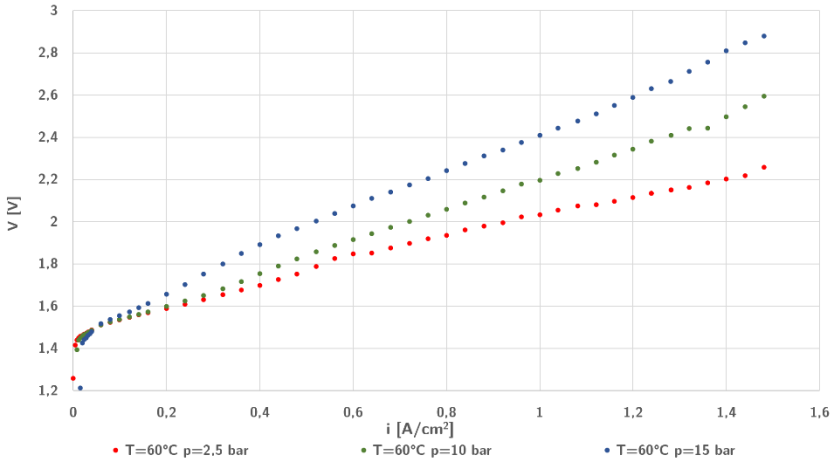

Figure 2.28 Polarization curves in different pressure with fixed temperature equal to 60°C

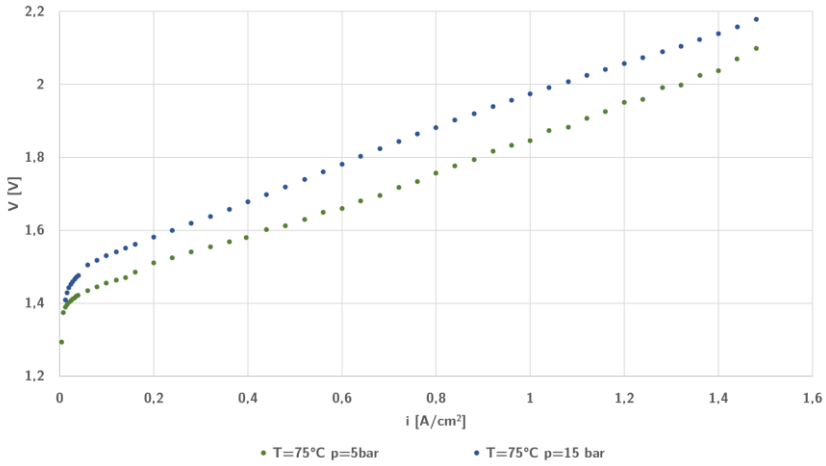

Figure 2.29 Polarization curves in different pressure with fixed temperature equal to 75°C

Analyzing the graphs, as expected, the higher the pressure the higher the polarization curve. However, the pressure is an important parameter, since the hydrogen produced is already pressurized avoiding the high cost connected with the later pressurization of hydrogen. As can be seen from Figure 2.29, differently from other Figures, the polarization curves present flatter profiles. The reason behind this is due to the fact that temperature is higher and the response of the system results better. In this sense, the temperature control is optimal.

Another configuration is tested, substituting the main components MEA, GDLs and sealants with new ones of the type discussed in the experimental section

and closing the cathode inlet valve completely. In Figure 2.30 and Figure 2.31 the pressure influences on the polarization curves for two defined operating temperatures, equal to 40◦C, 60◦C and 80◦, in the new configuration are represented. In the Figures 5.5 and 5.6 are shown the results of closed cathode configuration for low (40°C) and medium (60°C) temperatures. Instead, in Figure 2.32 the high temperature (80°C) tests are reported.

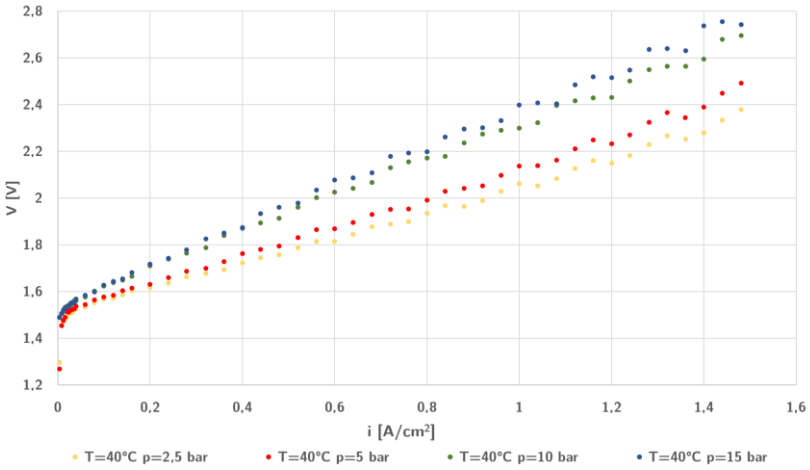

Figure 2.30 Polarization curves in different pressure with fixed temperature equal to 40°C with closed cathode

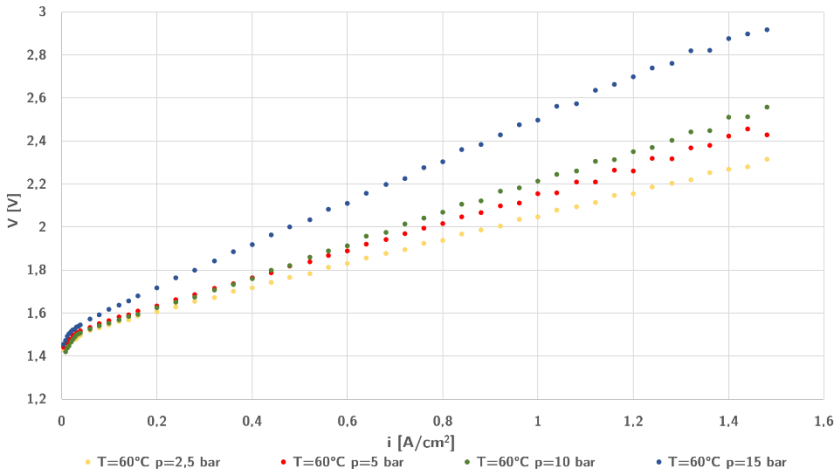

Figure 2.31 Polarization curves in different pressure with fixed temperature equal to 60°C with closed cathode

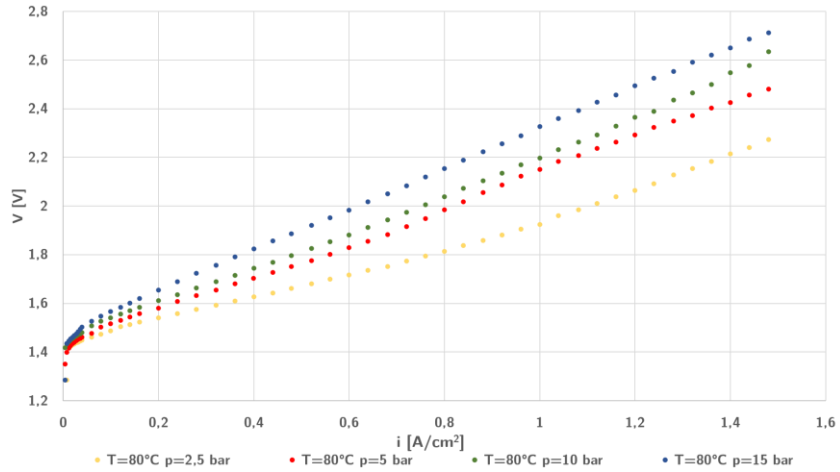

Figure 2.32 Polarization curves in different pressure with fixed temperature equal to 80°C with closed cathode

Analyzing these graphs, as before, the main oscillations are in low and medium temperature tests. As said, further investigations are required because the main analysis conducted on the parameters that influence the polarization curve trend are good and the reasons of this behaviour can be different and mainly due to the system response. However, in this case, the polarization curves are a little bit higher than the first configuration. The behaviour must be investigated in order to find the reason. In fact, with this configuration the cathode valve is closed, and cooling of the cathode side does not occur. It means that temperature should be a little bit higher with consequent lower polarization curve. So, temperature should be controlled in well manner avoiding the variation and the relative oscillations.

2.2.2. Hydrogen production rate

One of the most important experimental results that can be extracted from the Test Bench is the produced H2 during the electrolysis process. Using these values, the process efficiency can be calculated and compared to the values available in literature. To correctly measure the Hydrogen production, the chosen configuration is the one with the cathode inlet valve closed. The reason way is that the hydrogen flow meter is placed at the outlet of the hydrogen separator and so, in the case of the cathode inlet valve opened, the outlet gaseous mixture of the separator has a great content of water vapor (and nitrogen). Therefore, the quantity measured by the flow meter do not reflect the real hydrogen quantity. For this reason, it is chosen the configuration with cathode closed inlet valve to have an H2 richer outlet mixture to better measure the H2 flow and subsequently, the produced H2. All the

considerations on the outlet mixtures are seen through the help of a mass spectrometer that is occasionally connected to the outlet of the hydrogen separator, in order to analyze the outlet gas mixture. In Figure 2.33, Figure 2.34 and Figure 2.35 the hydrogen production trends with the respective theoretical trends are presented. The graphs report only second half of experiment from higher to lower current values (1.5-0A/cm2) due to the fact that in the first part of the curve the system is still in stabilization process.

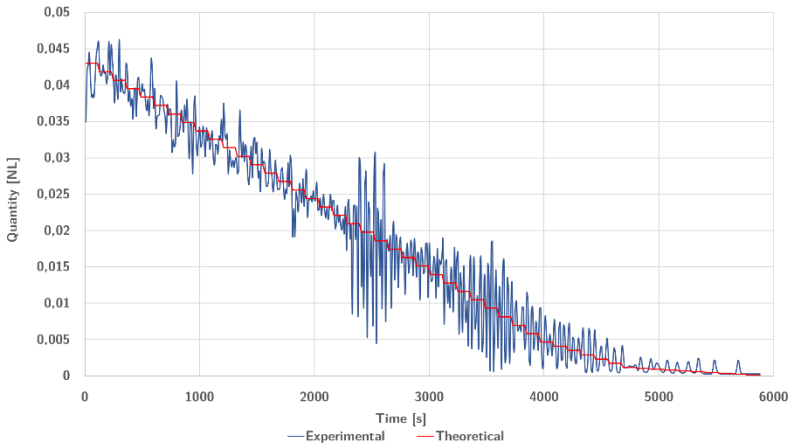

Figure 2.33 Hydrogen production graph for fixed temperature equal to 40°C and fixed pressure equal to 2.5barg

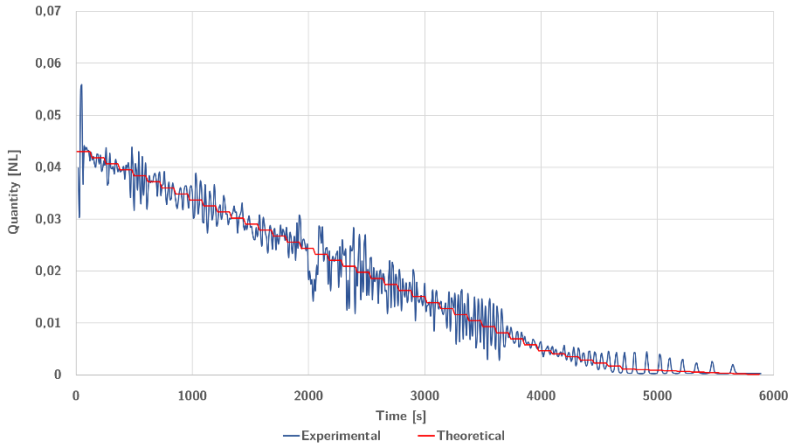

Figure 2.34 Hydrogen production graph for fixed temperature equal to 60°C and fixed pressure equal to 2.5barg

As can be seen from Figure 2.34 the Experimental values presents some oscillations that are connected to the working principle of the Back Pressure Controller. In fact, as mentioned, the system is pressurized thanks to the injection

of N2 and kept constant through the Back pressure controllers, placed downstream each separator but upstream each flow meter. Generally, the pressure tends to increase due to the physics behind the production of gas. To control this at certain value, the controllers open and release the mixture of gas at the outlet of the separators creating the oscillations that are present on the Figure. The Theoretical one, instead, is calculated according to Faraday Law, for this reason, it is constant for a fixed current value.

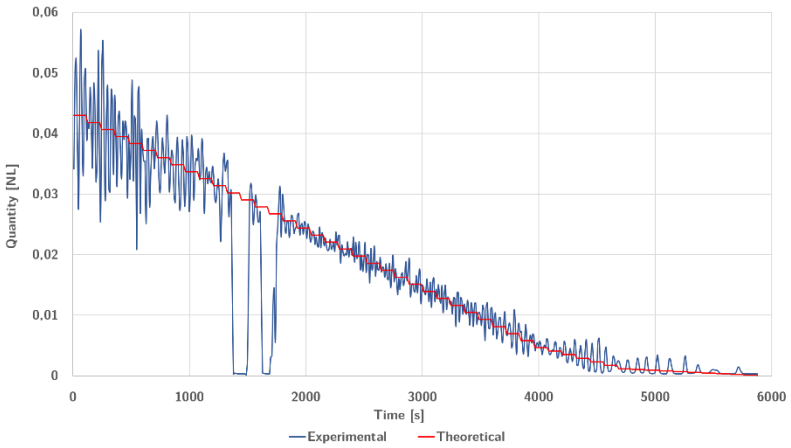

Figure 2.35 Hydrogen production graph for fixed temperature equal to 80°C and fixed pressure equal to 2.5barg

In Figure 2.33, Figure 2.34 and Figure 2.35 the hydrogen production at p=2.5barg for three different temperatures (40◦C, 60◦C, 80◦C) is represented. Some oscillations are present in the graphs due to physics of Back Pressure Controller. The reason is that the system has been pressurized with Nitrogen and at each time in which the imposed pressure was overcame, the system released the gases. The released quantity was different for each timestep considered and so, the oscillations appeared. In Table 2.3, the integral values of hydrogen production, found with experimental and theoretical approaches are represented.

Table 2.3 Hydrogen production quantity

T [°C]	Experimental Quantity [NL]	Theoretical Quantity [NL]
40	9,887,516,667	9,945,583,836
60	9,930,709,722	9,945,583,836
80	9,242,655,556	9,945,583,836

As reported in 2.4, the theoretical quantity can be calculated using the Faraday Law and this does not depend on temperature and pressure. Looking at the Table 2.3, it is possible to see that the theoretical value is equal for the three temperatures. Since time-step chosen to calculate the theoretical hydrogen quantity is equal, also the theoretical value is equal. It depends only on current defined for each time-step. Analyzing the 80°C experimental integral values, it is lower than the theoretical one, but this behaviour is due to the lack of registered values between 1000 and 2000 seconds. However, looking at the theoretical integral values and experimental integral values, for the three temperatures, appears that the Faradaic Efficiency is close to unit.

A second verification has been done using the mass spectrometer:

To measure the composition of the gases it is possible to use a mass spectrometer. The Hiden HPR-20 QIC R&D (Hiden analytical, Warrington, United Kingdom) is designed for continuous analysis of gases and vapors at pressures near atmosphere. It has a mass range of 200 AMU and a detection capability from 100% to less than 5 ppb. It is a Bench-top triple filter quadrupole mass spectrometer gas analysis system that has a very fast response of less than 300 ms response time for to permanent gases and vapors. A picture of the mass spectrometer (without the turbo pump) is presented in Figure 2.36.

Figure 2.36 Hiden mass spectrometer overview[61]

In the current experiment mainly the void pump of the mass spectrometer is used to create void in the sample in order to see if the glass ceramic sealant is healthy or not. In case that the glass ceramic sealant has cracks, the void cannot be created by the mass spectrometer and the void pressure level on the monitor remain at high amounts. This means that there is no void created inside the sample and the piping and the glass ceramic sealant is not functioning.

A schematic of mass spectrometer void is presented in Figure 2.37.

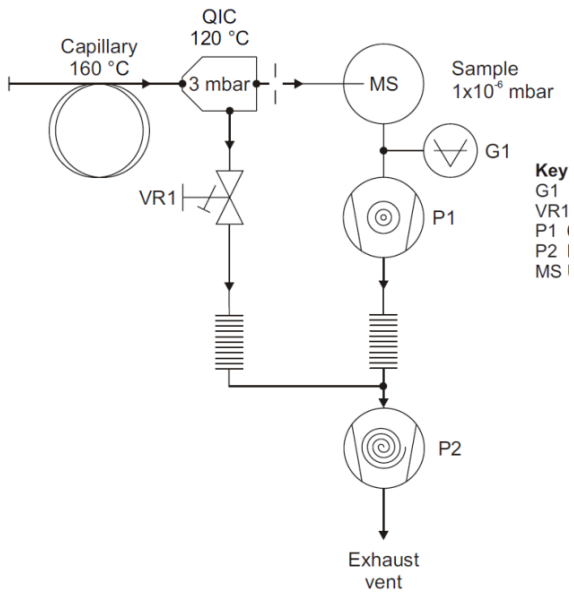

Figure 2.37 Vacuum Schematic of the mass spectrometer [61]

G1 is the penning gauge, VR1 is the QIC inlet bypass control valve, P1 is the 60l/s turbo drag pump, P2 is the backing and bypass scroll pump and MS UHV housing shows the mass spectrometer chamber.

The supplied software package for quantitative gas and vapor analysis can provide real time continuous analysis of up to 32 species with concentrations measured in the range 0.1PPM to 100%. It also has automated calibration system and a mass spectral library with intelligent scan feature. Moreover, it can support multi stream of gases.

In the present case the analysis of cathode gas output has been done with the mass spectrometer at the start of each series of experiments when the new cells are put in the housing for the tests , and the test results showed a production of more than 99% H2 on the cathode side.

Chapter 3. Modelling

3.1. 0D MATLAB model

Analytical models is a satisfactory tool to understand the effect of the main variables on electrolyzer performance. It works on the basis of simplified considerations to simulate a reasonably accurate polarization curve. Models permit the prediction of the electrolyzer behaviour as a function of operating conditions using simple empirical equations. A summary of the equations used to calculate the electrolyzer voltage is presented. [25][62]

3.1.1. Theoretical basis

3.1.1.1. voltage

A model of a PEM electrolyzer cell was developed including electrochemical mechanism at the anode, cathode and in the membrane. The theoretical model has the aim to express the relationship present between the electrolytic cell voltage and cell current and after this model is implemented on MATLAB. Generally, the Voltage is expressed through Equation 3.1. [63]

$$V_c(T,p) = OCV(T,p) + \eta_{\text{act}}(i) + \eta_{\text{ohm}}(i) + \eta_{\text{diff}}(i) \qquad 3.1$$

Where:

- OCV is the open circuit voltage measured in V;
- ηact is the activation overpotential measured in V.
- ηohm is the ohmic overpotential measured in V.
- ηdiff is the diffusion overpotential measured in V.

3.1.1.1.1. Open circuit voltage

An electrolyzer OCV is typically determined using the Nernst equation, or by evaluating the Gibb's Free Energy. The OCV is expressed through Equation 3.2. [63]

$$\text{OCV} = \frac{\Delta \text{G}}{2 * \text{F}} \qquad 3.2$$

Where: F is the Faraday constant, equal to 96485 C/mol;

ΔG is the Gibbs free energy and it is described by the Equation 3.3[63] .

$$\Delta G = \Delta G^* + R * Tcell * \ln\left(\frac{pH_2\sqrt{pO_2}}{PH_2O}\right) \quad 3.3$$

And ΔG^* is calculated through Equation 3.4. [63]

$$\Delta G^* = \left[H_{H_2}(T_{cat}) + \frac{1}{2}H_{O_2}(T_{an}) - H_{H_2O}(T_{an})\right] - T_{cell}\left[S_{H_2}(T_{cat}) + \frac{1}{2}S_{O_2}(T_{an}) - S_{H_2O}(T_{an})\right] \quad 3.4$$

In which:

· T_{cell} is temperature of the cell in K;

· H is the enthalpy in J/kg, described by:

$$H(T) = a_j T + \frac{4}{5}b_j T^{\frac{4}{5}} + \frac{2}{3}c_j T^{\frac{3}{2}} + \frac{4}{7}d_j T^{\frac{7}{4}} \quad 3.5$$

S is the entropy in J/ (kg K), described by:

$$S(T) = a_j \ln T + 4b_j T^{\frac{1}{4}} + 2c_j T^{\frac{1}{2}} + \frac{4}{3}d_j - T^{\frac{3}{4}} - R\ln P \quad 3.6$$

These two equations are valid in the range between 300 and 4000 K. The values of the previous unknows are reported in the following table. [63]

Table 3.1 formula parameters

	Substances	a_j	b_j	c_j	d_j
j=1	Water	180	-85.4	15.6	-0.858
j=2	Hydrogen	79.5	-26.3	4.23	-0.197
j=3	Oxygen	10.3	5.4	-0.18	0

The pressure PH_2O, pH_2, pO_2 are calculated through Equation 3.7, Equation 3.9 and Equation 3.10 and x is expressed through Equation 3.8.. [52]

$$P_{H_2O} = 10^x \quad 3.7$$

$$x = -2.1794 + 0.02953 * (T_{cell} - 273.15) - 9.1837 * 10^{-5} * (T_{cell} - 273.15)^2 + 1.4454 * 10^{-7} * (T_{cell} - 273.15)^3 \quad 3.8$$

$$p_{H_2} = 0.5 * \left(\frac{\left(P_{H_2}\right)}{e^{\left(1.653 * \frac{i}{T_{cell}{}^{1.334}}\right)}} - P_{H_2O} \right) \quad 3.9$$

$$p_{O_2} = \left(\frac{\left(P_{O_2}\right)}{e^{\left(4.192 * \frac{i}{T_{cell}{}^{1.334}}\right)}} - P_{H_2O} \right) \quad 3.10$$

3.1.1.1.2. Activation overpotential

The activation overvoltage, η_{act} is the voltage loss attributed to driving the electrochemical reaction and is necessary to overcome the molecular bonds. [20] Thanks to the equation of current density of Butler-Volmer Equation 3.11

$$i = i_0 * \left[\exp\left(\frac{\alpha_1 * F}{R * T_{cell}} * \eta_{act} \right) - \exp\left(-\frac{\alpha_2 * F}{R * T_{cell}} * \eta_{act} \right) \right] \quad 3.11$$

and considering the same value of α, it is possible to obtain the value of η_{act}, through Equation 3.11. It is evaluated as in the Equation 3.12. [44]:

$$\eta_{act} = \frac{R * T_{cell}}{\alpha_j * F} \operatorname{arcsinh}\left(\frac{i}{2 i_{0_j}} \right) \quad 3.12$$

Where:

- j indicates the anode and cathode side;
- R is the universal constant of gases in J/ (mol K);
- T is the temperature in K;
- α_j is the transfer coefficient;
- i_0 is the exchange current density in A/cm^2 expressed through the Equation 4.13. [20][64][65] In this case the Equation 3.13 is a modification of the real equation, in order to take into account only the effect of the materials. So, the equation is written as function of pressure ratio and temperature.

$$i_0 = i_{0,\,\mathrm{ref}} \cdot \left(\frac{P}{P_{\mathrm{ref}}} \right)^{\gamma} \cdot \exp\left[-\frac{E_a}{R} \cdot \left(\frac{1}{T} - \frac{1}{T_{\mathrm{ref}}} \right) \right] \quad 3.13$$

in which $i_{0,ref}$ is the exchange current density considered at reference temperature, T_{ref} , E_a is the activation energy and R is the universal gas constant.

However, some authors use different equations to evaluate the Activation Overvolt- age, like Equation 3.14

$$\eta_{act} = \frac{R \cdot T}{2 \cdot \alpha_j \cdot F \cdot} \cdot \sinh^{-1} \cdot \left(\frac{i}{2 \cdot i_{0_j}} \right) \qquad 3.14$$

It is a similar expression to Equation 3.12 but with a factor of 2 coupled to the charge transfer coefficient. The reason is that the Butler-Volmer equation appears not consensual. [20]

In this model, the Equation 3.12 is used.

3.1.1.1.3. Diffusion overpotential

The diffusion overpotential ηdiff , or concentration overpotential, considers the mass transport limitations that occurs at high current densities. The losses due to mass transfer are caused by flow restriction to the catalyst sites such as current collector and separator plate morphology as well as gas bubbles formed from the reaction products. In the cases of water electrolysis, the electrochemical reaction needs water to be supplied to the reaction site, and hydrogen and oxygen to be removed. If hydrogen and oxygen are not removed quickly, their concentration will increase, and the kinetics will become slowly. [3] The value of η_{diff} is calculated through Equation 3.15.

$$\eta_{\text{diff}} = \frac{\text{R} * \text{T}_{\text{cell}}}{\text{Z} * \text{F}} * \log\left(1 - \frac{\text{i}}{\text{i}_{\text{l}}}\right) \qquad 3.15$$

Where:

- z_r is the number of electrons, that in case of cathode is equal to 2 and for anode is equal to 4.
- i_l is the limiting current density in A/cm2.

The limiting current density is a parameter connected to the concentration over- potential at the electrodes, it is significant just at high load values. It changes if thermodynamics change, like temperature and pressure. However, the diffusion overpotential cannot be considered until lower operating current densities, like 1.6 A/cm2. So, for this reason, in this model these losses can be neglected and significant errors in polarization curve are not found. [25]

3.1.1.1.4. Ohmic overpotential

The Ohmic overpotential η_{ohm} is typically modelled using a standard Ohm's Law and it is related to the materials resistance to the protons flux. It is described by the following equation and there are different equations for each part of the cell. In the case of the membrane, the Ohmic contribute is found through the Equation 3.16.

$$\eta_{ohm} = ASR*i \quad 3.16$$

Where ASR is the area specific resistance and I is the current density. But, considering the total resistance, the Ohmic overpotential is found through Equation 3.17. [44]

$$\eta_{ohm} = R_{tot}*I \quad 3.17$$

in which:

- I is the current in A.
- R_{tot} is the total resistance of the cell (catalyst and anode side), in **Ω** and it is obtained considering the Equation 3.18. [79]

$$Rtot = R_{el} + R_{pl} + R_{mem} \quad 3.18$$

Applying Ohm's law to the electrode and the flow field plate, the Equation 3.19 is obtained. [63]

$$R_{el,pl} = \rho_{eff} \cdot \frac{l}{A} \quad 3.19$$

- A is the cross-section of the conductor in cm2.
- l is the length of the electrons path in cm.
- ρ_{eff} is the is the effective resistivity of the electrode.

The value of l and ρ_{eff} are found through Equations 3.20 and 3.21. [63]

$$l = \frac{\omega_s + \omega_c}{4} \quad 3.20$$

$$\rho_{eff} = \frac{\rho_e l}{(1-\epsilon)^{1.5}} \quad 3.21$$

in which:

- ωs and ωc are the channel support width and the channel width, respectively, in cm.
- ϵ is the porosity of electrode.

So, the average resistance in the electrodes are reported in Equations 3.22 and 3.23. [30][63]

$$R_{el,an} = \rho_{eff} \cdot \frac{\omega_{s,an}+\omega_{c,an}}{4 \cdot L \cdot \delta_{el,an} \cdot n_{el,an}} \quad 3.22$$

$$R_{\text{el,cath}} = \rho_{eff} \cdot \frac{\omega_{s,\text{ cath}} + \omega_{c,\text{ cath}}}{4 \cdot L \cdot \delta_{\text{el,cath}} \cdot n_{el,\text{ cath}}} \quad 3.23$$

Where:

- L is MEA length in cm.
- δel,an and δel,an are anode and cathode thickness in cm.
- $n_{el,an}$ and $n_{el,\text{ cath}}$ are anode and cathode channel support quantities.

The total resistance of electrode is found and it is reported in Equation 3.24. [63]

$$\mathrm{R_{el}} = \frac{\rho_{\mathrm{eff}}}{8 * \mathrm{L}} * \left[\frac{(\omega_{\mathrm{s,an}} + \omega_{\mathrm{c,an}})}{\delta_{\mathrm{el,an}} * \mathrm{n_{el,an}}} + \frac{(\omega_{\mathrm{s,cath}} + \omega_{\mathrm{c,cath}})}{\delta_{\mathrm{el,cath}} * \mathrm{n_{el,cath}}}\right] \quad 3.24$$

The resistance of the flow field plate is found and it is reported in Equation 3.25.

$$\mathrm{R_{pl}} = \left(\mathrm{R_{PS,an}} + \mathrm{R_{PS,cath}}\right) + \left(\mathrm{R_{PR,an}} + \mathrm{R_{PR,cath}}\right) \quad 3.25$$

Each resistance in Equation 3.25 can be calculated through Equation 3.26 and 3.27.

$$\mathrm{R_{PS,an}} = \rho_{\mathrm{pl,an}} * \frac{\mathrm{h_{c,an}}}{\frac{\omega_{\mathrm{s,an}}}{2} * \mathrm{L}} \quad , \quad \mathrm{R_{ps,cat}} = \rho_{\mathrm{pl,cath}} * \frac{\mathrm{h_{c,cath}}}{\frac{\omega_{\mathrm{s,cath}}}{2} * \mathrm{L}} \quad 3.26$$

$$\mathrm{R_{PR,an}} = \rho_{\mathrm{pl,an}} * \frac{\mathrm{h_{p,an}}}{\mathrm{A}} \quad , \quad \mathrm{R_{PR,cath}} = \rho_{\mathrm{pl,cath}} * \frac{\mathrm{h_{p,cath}}}{\mathrm{A}} \quad 3.27$$

Where:

- ρpl,an and ρpl,cath are the anode and cathode electrode resistivities in Ωcm.
- hc,an and hc,cath are anode and cathode channel height in cm.
- hp,an and hp,cath are the distances from the outside border of the plate to the channel surface of anode and cathode side in cm [30].

The dominant contribution to ηohm is the ionic loss, caused by resistance to the ion flow through the membrane. [45] The Equation 3.28 permits to find the resistance of membrane.

$$R_{mem} = \frac{\delta_{mem}}{\sigma_{mem}} \quad 3.28$$

in which:

- δmem is the membrane thicknes in cm.
- σmem is the membrane conductivity in S/cm, calculated through Equation 3.29. [63]

$$\sigma_{mem} = (0.005139 * \lambda - 0.00326)\exp\left[1268 * \left(\frac{1}{303} - \frac{1}{T_{cell}}\right)\right] \quad 3.29$$

with λ that is the degree of humidification of membrane expressed in molH2O/molSO3– .

3.1.1.2. mass flow in the cell

Another model as developed to establish the water mass flow inside the cell. In the anode side of the cell, four moles of oxygen are generated for each electron. So, it is possible to define the molar flow rate of oxygen generated using the Faraday's law. [66] The Equation 3.30 express the molar flow rate.

$$N_{O_{2,an_{gen}}} = \frac{I}{4 * F} \quad 3.30$$

And according to the same law, it is possible to calculate the molar flow rate of water consumed considering that for each electron are consumed two moles of water. It is expressed in Equation 3.31.

$$N_{H_2O_{an_{cons}}} = \frac{I}{2 * F} \quad 3.31$$

Instead, in the cathode chamber, hydrogen is generated by electrochemical reaction. And similarly to the equation used in the anode side is possible to calculate the quantity of hydrogen generated through Equation 3.32.

$$N_{H_2cath_{gen}} = \frac{I}{2 * F} \quad 3.32$$

The net water passing through the membrane is expressed through the Equation 3.33. [52]

$$N_{H_2O_{mem}} = N_{H_2O_{diff}} + N_{H_2O_{eod}} - N_{H_2O_{pe}} \quad 3.33$$

In which there are some terms that are:

- NH2Odiff is the molar flow rate referred to the diffusion contribution.
- NH2O is molar flow rate due to the electro-osmotic drag.

- NH2Ope is the molar flow rate due to pressure gradients between anode side and cathode side.

3.1.1.2.1. Water diffusion

$N_{H_2O_{diff}}$ is the term due to the diffusion and it can be described by the Fick's Law. And it is:

$$N_{H_2O_{diff}} = A * \frac{D_w}{L} * \left(C_{H_2O_{mem_{cath}}} - C_{H_2O_{mem_{an}}}\right) \quad 3.34$$

In which:

- A is the area of membrane in cm^2;
- D_w is the membrane water diffusion coefficient in m^2/s;
- L is the membrane thickness in cm;
- $C_{H2O_{mem_{cath}}}$ is the water concentration at the electrolyte and cathode interface in mol/l;
- $C_{H2O_{mem_{an}}}$ is the water concentration at the electrolyte and anode interface in mol/l.

The last two terms are calculated through Equations 3.35 and 3.36. [52]

$$C_{H2O_{mem_{cath}}} = C_{H_2O_{ch_{cath}}} + \delta_{el_{cath}} * \frac{\dot{n}_{H_2O_{cath}}}{D_{eff_{cath,H_2-H_2O}}} \quad 3.35$$

$$C_{H2O_{mem_{an}}} = C_{H_2O_{ch_{an}}} - \delta_{el_{an}} * \frac{\dot{n}_{H_2O_{an}}}{D_{eff_{an,O_2-H_2O}}} \quad 3.36$$

Where δel,cath and δel,an are the thickness of cathode and anode side in cm, n˙H2Ocath and n˙ H2Oan are the molar flow rate of water in cathode and anode side in mol/(s.cm2) and they can be calculated through Equations 3.37 and 3.38.

$$\dot{n}_{H_2O,an} = D_{eff_{an,O_2-H_2O}} * \frac{\left(C_{H_2O_{ch_{an}}} - C_{H2O_{mem_{an}}}\right)}{\delta_{el_{an}}} \quad 3.37$$

$$\dot{n}_{H_2O,cath} = D_{eff_{cath,H_2-H_2O}} * \frac{\left(C_{H2O_{mem_{cath}}} - C_{H_2O_{ch_{cath}}}\right)}{\delta_{el_{cath}}} \quad 3.38$$

the value of CH2Och,cath and CH2Och,an are the concentration of liquid water inside the channel of cathode and anode side in mol/l, calculated through Equations 3.39 and 3.40.

$$C_{H_2O_{ch_{cath}}} = \frac{\rho_{H_2O}(T_{cath})}{M_{H_2O}} \quad 3.39$$

$$C_{H_2O_{ch_{an}}} = \frac{\rho_{H_2O}(T_{an})}{M_{H_2O}} \quad 3.40$$

in which there is the value of water molar mass MH2O in g/mol and the value of water density in kg/m3 calculated through 3.41.

$$\rho_{H_2O} = \frac{A}{B^{1+\left(1-\frac{T_c}{C}\right)^D}} \quad 3.41$$

A, B, C and D are experimental parameters, and the values are reported in Table 3.2. [52]

Table 3.2 Table of experimental parameters for water density

A	B	C	D	Tmin [K]	Tmax [K]
0.14395	0.0112	649.727	0.05107	273	685

The effective binary diffusion coefficients are calculated as- cm2/s- Equations 3.42 and 3.43. :

$$D_{eff,O_2-H_2O} = D_{O_2-H_2O} * \varepsilon * \left(\frac{\varepsilon - \varepsilon_p}{1-\varepsilon}\right)^{\alpha} \quad 3.42$$

$$D_{eff,H_2-H_2O} = D_{H_2-H_2O} * \varepsilon * \left(\frac{\varepsilon - \varepsilon_p}{1-\varepsilon}\right)^{\alpha} \quad 3.43$$

in which ϵ is the porosity, ϵp is the percolation threshold and α is an empirical coefficient. The binary diffusion coefficient depends on thermodynamic conditions, pressure and temperature, of two gases and it is calculated through Equations 3.44 and 3.45. [63]

$$D_{O_2-H_2O} = \left(a * \left(\frac{T}{\sqrt{T_{c_{H_2}} * T_{c_{O_2}}}}\right)^b * \left(p_{c_{H_2}} * p_{c_{O_2}}\right)^{\frac{1}{3}} * \left(T_{c_{H_2}} * T_{c_{O_2}}\right)^{\frac{5}{12}} * \left(\left(\frac{1}{M_{O_2}} + \frac{1}{M_{H_2}}\right)^{\frac{1}{2}}\right)\right) * \frac{1}{P} \quad 3.44$$

$$D_{H_2-H_2O} = \left(a * \left(\frac{T_c}{\sqrt{T_{c_{H_2}} * T_{c_{O_2}}}} \right)^b * \left(p_{c_{H_2}} * p_{c_{O_2}} \right)^{\frac{1}{3}} * \left(T_{c_{H_2}} * T_{c_{O_2}} \right)^{\frac{5}{12}} * \left(\left(\frac{1}{M_{O_2}} + \frac{1}{M_{H_2}} \right)^{\frac{1}{2}} \right) \right) * \frac{1}{P} \quad 3.45$$

Where a and b are fixed dimensionless coefficients reported in table of parameters, Tc is the critical temperature in K defined for the two species and Pc is the critical pressure in atm defined for the two species.

3.1.1.2.2. Electro-osmotic drag

The molar flow rate due to the electro-osmotic drag is calculated through Equation 3.46.

$$N_{H2O_{eod}} = n_d * \frac{I}{F} \quad 3.46$$

In which the term nd is defined as function of temperature of cell and calculated through Equation 3.47.

$$n_d = 0.0134 * T_c + 0.03 \quad 3.47$$

It represents the number of water molecules carried by each hydrogen ions.[67]

3.1.1.2.3. Hydraulic pressure

The molar flow rate due to pressure gradients is reported in Equation 3.48. [52]

$$N_{H_2O_{pe}} = K_{darcy} * \frac{A * \rho_{H_2O}}{L * \mu_{H_2O} * M_{H_2O}} * \Delta P \quad 3.48$$

in which:

- Kdarcy is the membrane permeability to water in cm2.
- μH2O is the viscosity in g/cm s

3.1.2. Model parameters

In the Table 3.3 are reported the main parameters used to build the polarization curve. [45] [63]

Table 3.3 Table of parameters

Parameter	Value	Unit	Reference
A	25	cm2	
a	3.64*10^−4	-	[63]
b	2.334	-	[63]
Dw	1.28*10^−10	cm2/s	[63]
Tcell	313.15	K	
Tc,H2	33.3	K	[63]
Tc,O2	154.4	K	[63]
R	8.314	J/(molK)	
pH2	5	bar	
pO2	5	bar	
pc,H2	12.8	atm	[63]
pc,O2	49.7	atm	[63]
α_{an}	2	-	[63]
α_{cath}	0.5	-	[63]
i0,an	10^−7 ÷ 10^−12	A/cm2	[63]
i0,cath	10^−1 ÷ 10^−5	A/cm2	[63]
δ_{mem}	0.0584	cm	
λ	14÷25	molH2O/molSO3−	[63]
ϵ	0.3	-	[45]
ϵ_p	0.11	-	[63]
α	0.785	-	[63]
Kdarcy	1.58*10^-14	cm2	[63]
µH2O	1.1*10^-2	gm/(cm.s)	[63]
ρ_{el}	10.6*10^-6	Ω *cm*	[45]

$\rho_{pl,an}$	43.1*10^-6	Ω *cm*	[45]
$\rho_{pl,cath}$	16*10^-3	Ω *cm*	[45]
$\omega_{c,an}$	0.1	cm	
$\omega c,cath$	0.1	cm	
$\omega_{s,an}$	0.1	cm	
$\omega s,cath$	0.1	cm	
$E_{a,an}$	76	kJ/mol	[52]
$E_{a,cath}$	4.3	kJ/mol	[52]
$\delta el,an$	0.008	cm	[45]
$\delta el,cath$	0.008	cm	[45]

3.1.1. Model results

The first curve obtained by the theoretical model with the help of MATLAB function is reported in Figure 3.1.

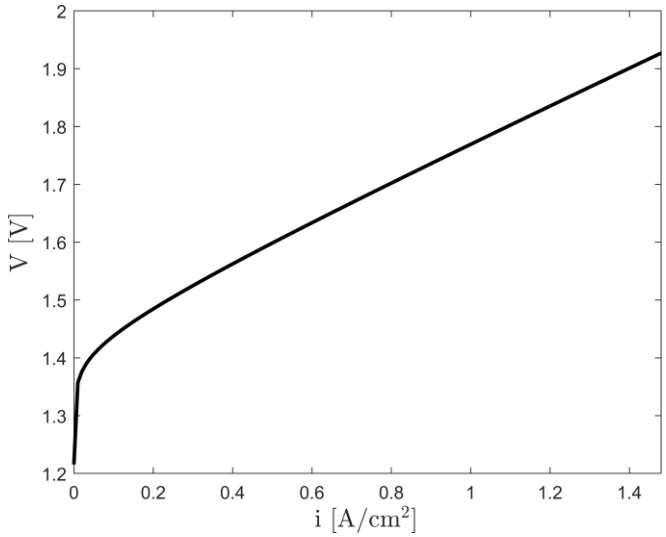

Figure 3.1 Polarization curve of model

The main contributions of voltage are reported in Figure 3.2.

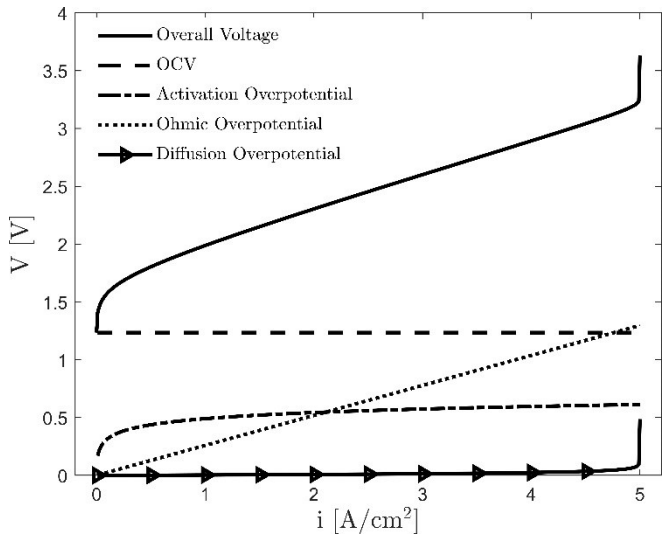

Figure 3.2 Polarization curve with the main contributions

However, as said, some parameters influence the polarization curve results. The main parameters having a great contribution in this sense are: temperature, pressure and exchange current densities. In Figure 3.3 it is possible to see the influence of temperature and how the polarization changes, while in Figure 3.4 the influence of pressure is reported.

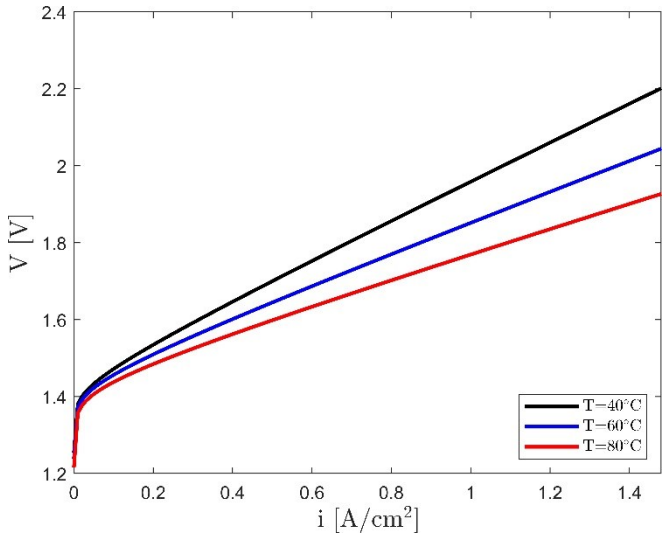

Figure 3.3 Influence of temperature on polarization curve of cell

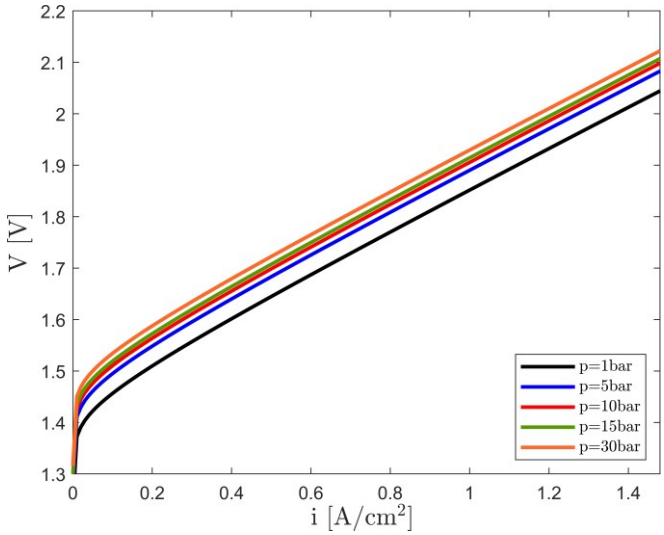

Figure 3.4 Influence of pressure on polarization curve of cell

As expected, the polarization curves increase when the cell operates at low temperatures or high pressure. It means worse results in terms of efficiency. [68] The exchange current densities are, however, unknown parameters, but their determination is very important: in fact, their values have a great influence on the final polarization curve. [63]In the Figure 3.5 the behaviour of polarization curve while changing the value of i0,an is reported. The result is that a decreasing value of i0,an tends to translate the curve to higher value of V.

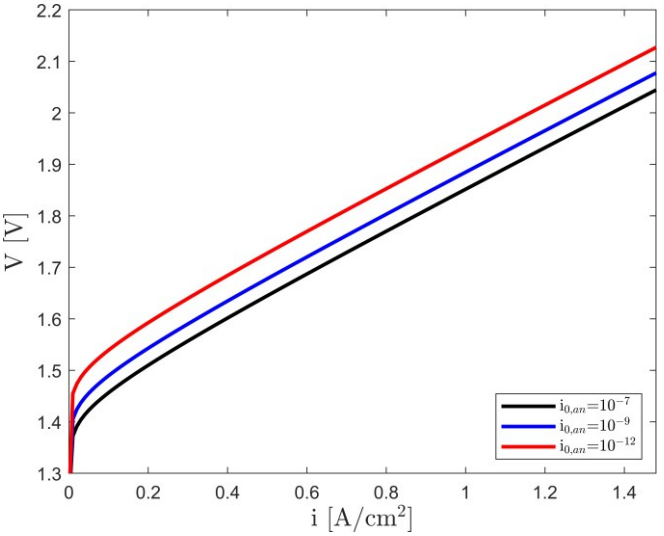

Figure 3.5 Influence of i0,an on polarization curve of cell

The same thing happens changing the value of i0,cath and it is possible to see this behaviour in the Figure 3.6

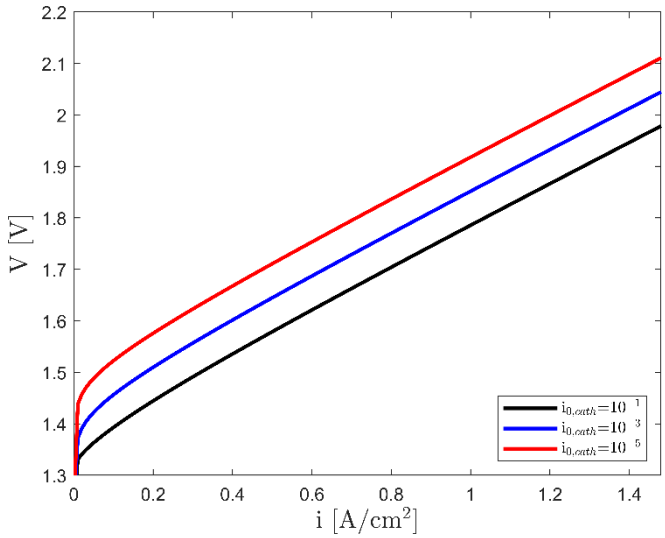

Figure 3.6 Influence of i0,cath on polarization curve of cell

3.2. Multiphase model

During the last half century several multiphase flow models have been employed in the industrial sector to predict the motion of the multiphase flows involved in production processes. As definition a multiphase flow is referred to a fluid flow in which more than one phase is present. Thus, the flow is composed by more than one uniform quantity of matter that can be separated mechanically from a non-homogeneous mixture.

3.2.1. Motivation and novelty

The need for a more precious model to predict the behaviour of the electrolytic cell was the initial motivation to start the multiphase modelling. Based on the literature review, electrolysis process creates a large number of relatively small bubbles at electrodes interface. In this case, bubble dynamics has significant impact on the fluid flow and the performance of electrolyser. An example of this effect is the overpotential related to the presence of bubbles. Besides, the possibility of modelling electrochemistry, transport of diluted species, free and porous media flow, heat transfer in porous media and biphasic bubbly flow physics at the same time , gives us a much more reliable and real results compared with previous simpler models.

Considering the lack of a precious 3D model that predicts the behaviour of the electrolytic cell with our specific geometry, creating a multiphase model gives us full understanding of the processes happening at the level of the cell.

More specifically it is possible to analyze the difference between the Voltage, temperature distribution, hydrogen and oxygen concentration in this new model and compare it with the traditional ones.

3.2.2. General models and instabilities

The models that can be used to describe the behaviour of the phases and their interaction with the boundaries of the system can be classified in two macro classes: Disperse and Separated flow models. The first class is characterized by an inter-phasal momentum transfer much greater than the momentum transfer between each fluid and the environment. This class is usually divided into two subclasses: homogeneous and bubbly flow. In the first subclass of the Disperse flow models, the dispersed phase is the gaseous one and it is distributed as an infinite number of infinitesimally small particles, it is transported by the continuous phase, the liquid on. The i-th phase velocity coincides with the liquid phase velocity and the flow is considered as single phase. In this model the relative motion between the phases, that is usually modelled through the slip velocity, is not considered. The second sub class, bubbly flow, instead considers the slip velocity different from zero, this is one of the two most important differences between the two Dispersed flow sub models. The second difference is linked to the particle/droplet/bubble dimension, although in bubbly flow model the particle size of the dispersed phase is much smaller respect to pipe/duct dimension, it is not infinitesimally dispersed and smaller. [69] The second macro class, Separated Flow Models, is characterized by considering a finite interphase transport rate and thereby allowing the two phases to have different velocities independent one from the other. As the first, also the second class can be divided into two additional subclasses: annular or film flow and fully separated flow. In the first subclass the dimension of droplets/bubbles is relevant to be treated as dispersed phase that interacts with the external boundaries. Thus, the phases can be regarded as partially separated and their phases motion is evaluated via two transport equations. The second subclass consists of two single phase streams in which each phase is considered separately through two sets of conservation equations. The above-mentioned difference between the models subclasses are reported in Table 3.4 Despite the large differentiation of the models employed for different applications and operating conditions, there are some instabilities that lead to multiphase

transitions, in particular Disperse to Separated transitions [D → S] and the opposite one [S → D]. The first [D → S] is mainly due to two effects: turbulent mixing and wave perturbations. Both destroy the dispersed phase nature, in fact the turbulent mixing can cause coalescence and wave perturbation can create phase separation due to the internal instability caused by gravitational-induced relative motion (Jackson Instability). The second [S → D] multiphase instability is related to the Kelvin-Helmotz waves [70], these waves form at the interphasial boundary and make the interface unstable. Kelvin-Helmotz waves are driven by Rayleigh-Taylor instability that is linked to buoyancy effects and Bernoulli instability thus, related to pressure gradients created by the change in the slip velocity. [69] [70]

Table 3.4 Multiphase models main difference.

<table>
<tr><td colspan="3">Multiphase Models</td></tr>
<tr><td>Disperse Flow Models</td><td colspan="2">Separated Flow Models</td></tr>
<tr><td>Homogeneous Flow $u\Phi l = u\Phi g$</td><td>Annular/Film flow</td><td rowspan="2">uΦl ≠ uΦg</td></tr>
<tr><td>Bubbly Flow $u\Phi l = u\Phi g + uslip$</td><td>Fully Separated</td></tr>
</table>

Since electrolysis process creates a large number of relatively small bubbles at electrodes interface, the study of Multiphase flow has gained interest due to the significant impact of bubble dynamics interaction with fluid flow. Moreover, the role of gas flow in water displacement in porous media needs to be studied more in depth to give a more thorough explanation on how gas and water interact in capillaries. Among the earliest works studying two-phase flows, the article of Bretherton [71] and Nicklin [72] can be considered as two milestones. Both articles deal with bubble motion in vertical pipes. The first takes into account also bubble motion through capillarities while the second focuses on “energy loss due to slip” associated with two-phase gas-liquid flow.

In PEMEC microchannels, there are usually four types of two-phase flow regimes, in particular dispersed bubbly, plug, slug, churn and annular.[73] In the dispersed bubbly flow the dispersed phase is represented by the gas phase while the continuous one is represented by liquid water. Usually, the condition that declare this type of flow is related to the comparison between the bubble diameter (db) and the equivalent hydraulic diameter of the channel (dch), thus, if db < dch the flow is considered dispersed bubbly else it is considered plug (db > dch). When the gas bubble diameter is far larger than channel equivalent diameter (db dch) the type of flow is called slug flow.[74] Slug and churn flow are characterized by an elongated profile due to coalescence phenomena; in these types of flows can

happen that bubbles break off creating a triple layer bubble/liquid/bubble in the channel with a thin film of liquid on the wall side with the last that can dry out if the bubbles are too long. The annular flow instead is characterized by bubble diameter almost equal to the channel diameter so only a thin film of liquid is present in the channel in the annular region.

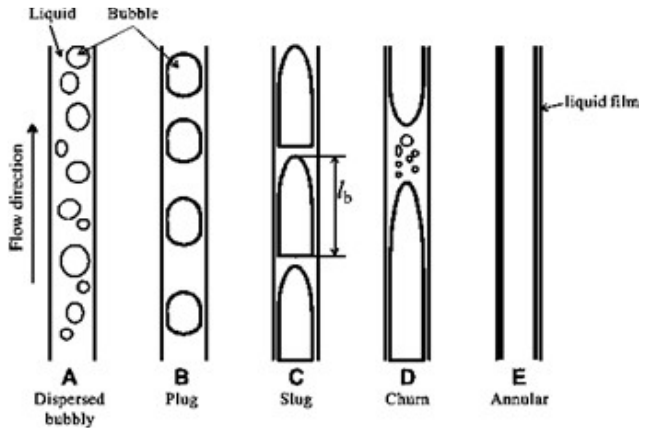

Figure 3.7 Flow regimes [75]

Also Hui Liu et al. [76] observed four distinct flow regimes performing experiments in vertical capillaries of circular and square cross section: bubbly, slug-bubbly, Taylor, and churn. A fifth regime, the annular flow regime, was found at excessively high gas fluxes and low liquid velocities. They demonstrated that when the ratio U_G/U_T P < 0.5, so when the ratio between the gas velocity and the two phase velocity approaches a value of unity, it indicates an homogeneous flow while for U_G/U_T P ≤ 0.5 indicates significant deviation from homogeneous flow. Moreover, they found a correlation for predicting bubble rise velocity in vertical-capillary two-phase flow and a correlation for estimating the liquid slug length.

Despite the wide variety of combinations of phases and flow regimes encountered in multiphase flows, they are all governed by the same fundamental conservation laws of mass, momentum and energy. In order to evaluate the impact of multiphase flow in PEM water electrolysis bubbly flow will be considered since the typical water inlet velocities inside the PEM electrolyzer channels are typical of bubbly flow regime [77] even if other parameters may affect the type of regime such as the current density, geometry, pressure, temperature and different flow fields [78] that can cause coalescence forming slugs. Different authors studied how each two-phase flow regime can have different transport properties, for example Muhao Zhang et al.[79] studied the phenomenon of bubbly to slug flow regime transition correlating void fraction with rising bubble velocity. Their two-phase

flow correlation was then validated with experimental measurements in a vertical air-water upward/downward flow experimental facility. Ishii published one of the first and most widely used two-phase flow models [80], which was later used to draw a flow-regime map that predicts the flow regime as a function of the individual gas and liquid velocities.

To better understand the dynamics of the multiphase regime it is appropriate to make a small reference to the growth and nucleation of bubbles. According to Andrea Angulo and colleagues [81] bubbles nucleate at electrode microcracks due to the increasing in chemical potential of the dissolved gas molecules created by the electrochemical processes. Thus, considering homogeneous nucleation, the bubbles attached at the electrode surface grow until they reach their critical radius, which coincides with the maximum of the Gibbs Free Energy. Bubbles growth is related to the sum of the interfacial and volumetric energy, the critical radius is found at the maximum of the sum the two contributions as can be seen from the Figure (1.9)[78] After reaching the critical radius, bubble detaches from the surface

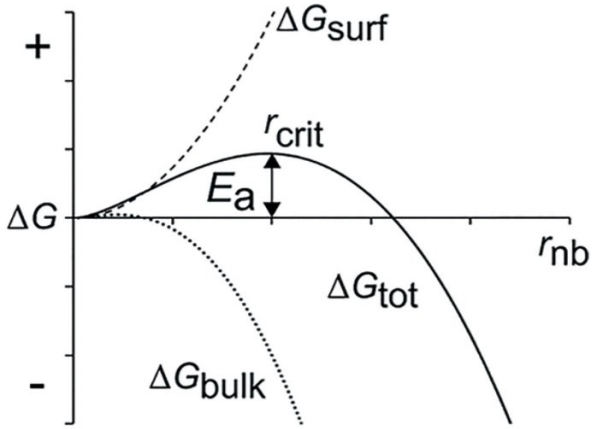

Figure 3.8 Bubble Growth [78]

of the gas-evolving electrode due to the work of the resultant forces acting on the bubble, these forces can be treated with different approaches. Syed Sahil Hossain et al.[82] discussed about Marangoni effect due to surface tension gradients and capillary effects while J.C. Garcia-Navarro et al. [83] proposed a force balance model for the single bubble detachment and ascertained that the bubble detaches when the forces normal to the electrode are at equilibrium so the only forces that act on the bubble are caused by the fluid flow that tend to detach and drag them away.

Garcia Navarro et al. [83] investigated gas permeation water within a PTL and found that water exerts a shear stress proportional to its kinetic energy on the gas flowing through the PTL.

3.2.3. Bubbles' impact on PEM electrolysis

Since a large amount of gas bubbles are produced during the water electrolysis, an ineffective removal may lead to pore blockage and catalyst layer deactivation due to coverage phenomena that will impede the transport of liquid water from the flow fields to the catalyst layer. This may lead to a reduced number of reaction sites and poor performance with a subsequent increase in the power injection and energy consumption [84] due to bubble attachment that creates an additional resistance and so a higher overpotential.[85]

Several publications have asserted bubble overpotential and the subsequent role of the multiphase flow, Amin Nouri-Khorasani et al. found that the overpotential due to bubbles is mainly related to temperature, pressure, current density and bubble diameter [86]. Specifically, bubble diameter and current density slightly affects the overpotential but strongly reduces bubbles lifetime, while pressure and temperature affect the overpotential differently, as the pressure increases, the overpotential decreases while the overpotential increases as the temperature increases. Ito and colleagues [87] found that the two-phase flow affects mass transport mechanism especially if the multiphase flow is slug or annular. They also found that higher gas content in the multiphase mixture imply higher pressure drop supposing the flow as laminar and serpentine anodic channels. Chung Hyuk Lee et al.[88] analysed the relative impact of mass transport losses identifying its major contributes. They assessed that during operation the losses due to oxygen starvation and accumulation in PTLs, potentially dominates the other contributes especially if the PTL pores have larger dimension respect to bubbles. Higher pore dimension means higher growth possibility forming slugs. Ito et al. debated that bubble induced overpotentials only appear in the anode, the O2-evolving electrode, thus water circulation in the cathode does not significantly affect cell operation [87]. Nagai [89] found that void fraction between electrodes decrease the electrolysis efficiency. The last was treated as function of current, but does not go deep into detail regarding bubble evolution. Aldas et al. [90] developed a two-phase flow model which solves transport equation for both liquid and gaseous phases and compared with experimental results of void fraction to validate and improve the mathematical model. The local void fraction was measured thanks electrical resistivity measurements correlated to the presence of bubbles in the

system. In this context a comprehensive study of Yan et al.[91] identified over 46 void fraction correlations available in literature and they classified these correlation into five categories i.e. drift flux model, slip ratio correlation, Kb correlation, Lockhart-Martinelli parameter based correlations and general correlations. Ito et al[87] based their work off the works of Mishima and Ishii model for round tubes [92] and measured a flow regime map of a PEM electrolyzer, where they assessed the effect of different flow fields on the pressure drop. Ito et al. [87] found that there is a relationship between circulating water in the channel and the electrolysis performance. They observed that when the two-phase flow at the anode is slug or annular, mass transport of water for the anode reaction is almost prevented and the concentration overvoltage increases especially at higher current density. Roy and colleagues [93] studied electrode activation and Ohmic losses at various operating pressure, from ambient up to 700 atm. They found that the gas production and so also void fraction increases at high operating current density, due to presence of more gas bubbles. The increased void fraction affects the voltage due to the 'bubble voltage loss'. Ito and colleagues [94] found a source of overpotential linked to pore structure of the anode current collector. The results of the polarization curves revealed that produced gas bubbles hinder the water supply to the electrode limiting the reactions in the anodic compartment. Moreover, they also found that an enhancement in the contact between the porous transport layer and the electrode reduces both the contact resistance and the activation overpotential. In the context of PTL Grigoriev et al.[95] reviewed the effect of the PTL properties on the PEM electrolyzer since microstructure of porous titanium plates used as das diffusion layers in PEM water electrolysis cells plays a significant role on the overall cell efficiency and requires an optimization in terms of porosity and mean pore size value operation. They hypothesized that large pores are inhabited by gas and small pores are inhabited by liquid; mass transport limitations are found to depend on small pores. According to Grigoriev and colleagues, pore size has two effects: large pores are necessary for good mass transport while small pores are required for good conductivity. They also ascertained that neither the gas permeability nor the porosity affects the performance. Dedigama et al. [96] modelled through EIS the mass transport losses due to bubbles. The low frequency arc was validated through experiments that showed an increasing size of oxygen bubbles and increasing regularity of their occurrence in anode membrane electrode interface increasing current density. From their study the size of the bubbles decreases significantly increasing flow rates of water due to the fact that bubbles are discharged from the electrode surface when their diameter reaches the critical radius. Vogt [97] assessed that the size of gas bubbles at the moment of detachment from the

electrode, is the most essential quantity in estimating heat and mass transfer rates at gas-evolving electrodes. Thus, he developed an intrinsic relationship between gas departure and the electrode shielding by bubbles. The last is a function of current density and surface properties of the electrode. Vogt also discovered that the average bubble diameters across different gas evolving electrodes lies between 50 and 100 µm. Ito and colleagues [98] found that bubble diameter reduces increasing mass flow rate in the compartments promoting the production efficiency and so reducing the overpotential caused by bubbles. Moreover, they fund that pressure does not affect the bubble diameter. Vogt et al. [99] found that the fractional bubble coverage is not only dependent on the current density, but also on temperature and pressure and indirectly by the break-off diameter, by the diffusion coefficient and the supersaturation with dissolved gas reflecting the mass transfer conditions. Figure 3.9 shows qualitatively the multi-phase interaction and the obstruction problems. H. Vogt and R.J. Blazer [99] found

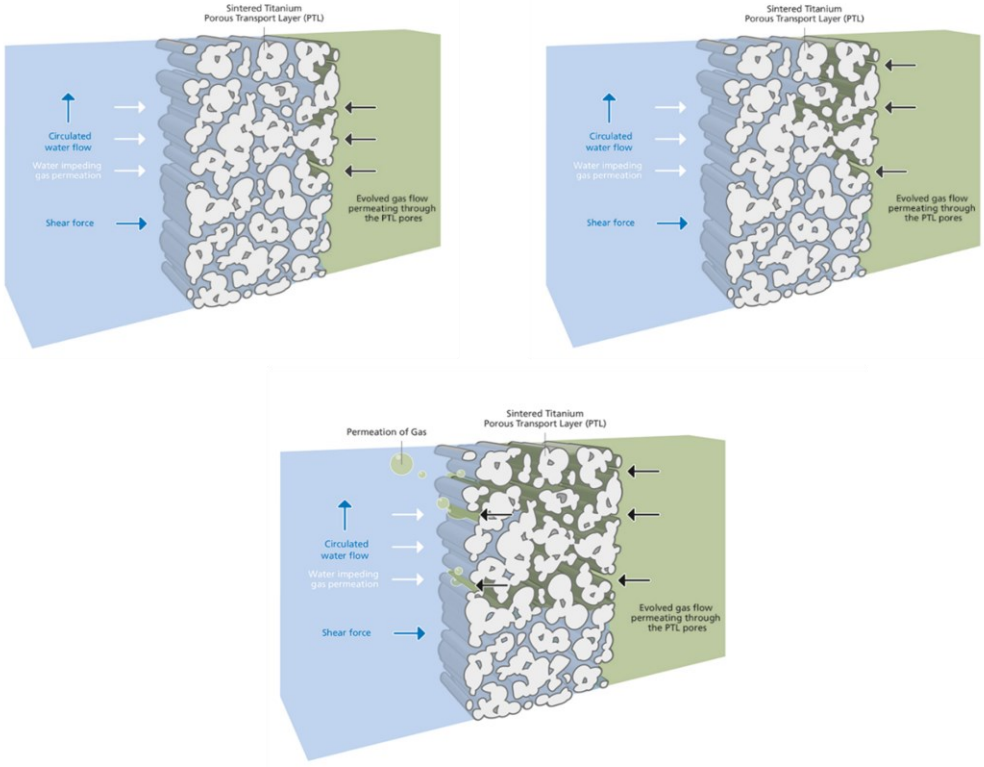

Figure 3.9 Gas transport in porous transport layers and its effects on gas permeation in time [83]

a relationship between current density and bubble coverage taking into account different parameters such as temperature, time, Reynolds number and gas evolution efficiency. Bubble coverage is a helpful parameter to describe the surface area covered by adhering bubbles, a higher value of bubble coverage implies higher mass transport overpotential also at low current densities. For this reason, bubble coverage problem has been investigated also by Quian and colleagues[85], they identified a linear relationship between bubble coverage and bubble resistivity ratio during electrolysis, the higher the bubble coverage the higher the resistivity induced by bubbles. It was seen that the bubbles moving up the flow field channels grew in size with increasing current density indicating increase in gas void fraction and a transition from bubbly to slug flow was also observed at higher current densities. However, the opposite was observed with increasing water flow rate. Transition from bubbly to slug flow enhances mass transport in the electrolyzer.

Dedigama et al. [96] measured current density through optical in the channels of a PEM electrolyzer. They found that current density increased up the channel and the highest current density was observed at the segment closest to the exit. The difference between the current densities observed across each segment decreased with increasing water flow rate. The size of bubbles increased with increasing operating potential as expected due to greater gas generation at higher potentials. Furthermore, it was observed that the size of the bubbles increased along the channel forming Taylor bubbles toward the exit of the channel that explains the improved performance of the segments closer to the exit. Two-phase flow observations indicate that the size of gas bubbles increase with increasing current but decrease with increasing water flow rate due to decrease in gas void fraction. They also found that larger bubbles create a greater turbulence in the liquid water when rising the channel that sweeps smaller bubbles off the electrode surface, increasing the mass transport of the cell as can be seen in Figure 3.10. Furthermore, bigger bubbles moving up a channel have a higher tendency to coalescence with smaller bubbles removing them from the electrode surface, which results in increased mass transport.

Under a thermo-fluid dynamic point of view the presence of bubbles in gas evolving electrodes can induce a transition from quasi-steady flow to a pseudo-turbulent one, especially if the gas production rate is high and the bubble dimension is relatively small. [100] Nie and Chen [101] modelled the two-phase laminar flow through the anode of a PEM electrolyzer using a CFD-based model. They assessed the velocity and pressure drop on the basis of oxygen generation. When the oxygen generation is relatively low, the velocity profiles resulted similar to each other for

different locations along the y-coordinate of the channels while velocity distribution was non-uniform. Otherwise, when the mass flow rate of oxygen generation increases, a locally minimum velocity magnitude is observed for the velocity profiles near the outlet port section. Considering the pressure drop over the flow field it becomes higher as the flow rate of oxygen increases. Since the volume fraction of oxygen is not uniform within the studied flow field plate, in the regions with higher oxygen volume fraction a reverse flow in some channels can occur.

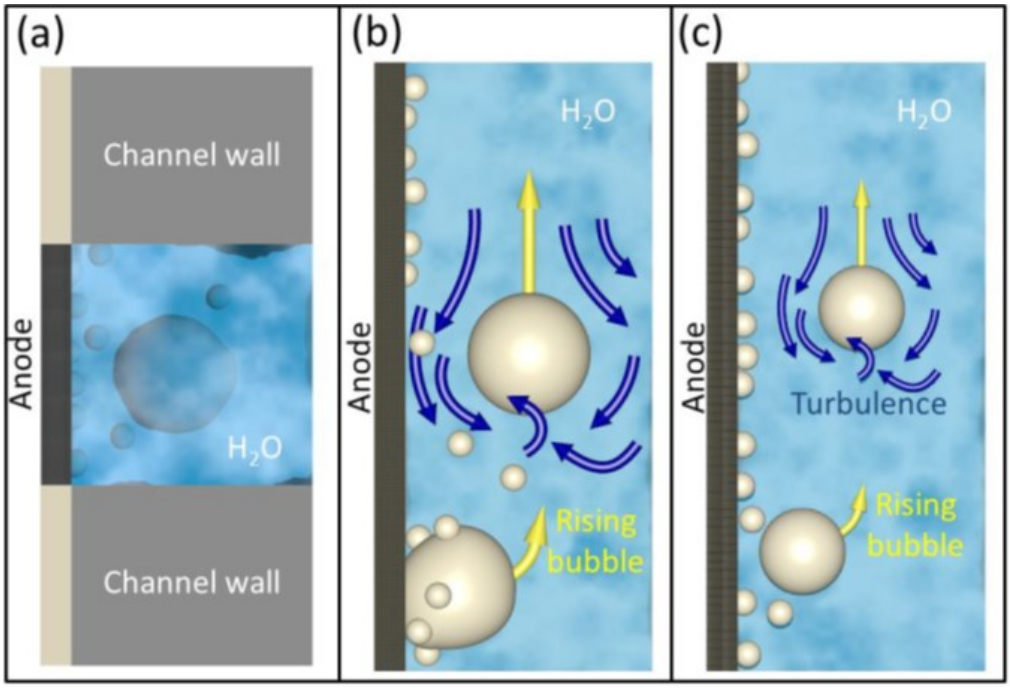

Figure 3.10 Bubble induced turbulence [96]

Cheng Lin-Liu and colleagues investigated gas evolving electrodes two-phase flow systems to find that the flow field can be transformed from laminar to turbulent due to bubble evolution.[102] Moreover in the most of the cases the cooling in PEM system is achieved by feeding the cell with an excess of water, so under nominal conditions the flow may become turbulent as in the study of Olesen et al. [103] The turbulence created in the flow field may depend on different parameters such as bubble radius, inlet velocity, temperature and flow field geometry; Alhassan Salami Tijani et al. [104] studied three different flow field patterns of a PEM Bipolar plate with a pseudo turbulent flow (Re=4000). They found through simulations that the parallel flow pattern minimized the internal turbulence while the serpentine one increased the internal turbulence especially due

to the higher velocity magnitude that can be caused by the missing manifold. In this context, the knowledge of the characteristics of bubbly flows is important to model the system through computational fluid dynamics methods that allow to solve multi-dimensional systems. As the computer power increases each year, the use of advanced models should be able to account for effects as turbulence or strong interaction between phases and multi-dimensionality. Fritz et al. [105] derived a new mass transport model due to considering also that the production of the oxygen gas phase creates additional flow restrictions respect to the conventional one limiting the water needed to sustain the reactions at catalyst layer. The new model is based on two additional parameters that are the ratio between the molar flow rate of produced oxygen and supplied water and another parameter based on the mean pore diameter and the critical film thickness.

Several bubbly turbulent models can be employed to solve the multi-physics PEM electrolyzer systems and their availability depend on the commercial Software utilized. For the purpose of this thesis work, COMSOL Multiphysics software was used to model together the different physics involved. Thus, according to the CFD module user guide, to enhance the contemporary study of the different modules, it is appropriate to treat the multiphase flow at the channels as a dispersed bubbly flow since bubbles are created at the porous electrodes and are transported by the flow. The relative bubble velocity is described with an equation that balances drag and pressure gradient and bubbles motion, through the flow field, is ruled by a balance between the buoyancy/gravity forces and the hydrodynamic forces.[106] Under the dispersed bubbly flow physics section, the most part of the models belong to RANS pattern. The models present in the section are: Algebraic, L-VEL, k −ε_, k − ω, Spallart-Almaras, SST, Low Reynolds k − ε and v2-f. The model chosen for this work is k − ω because, it not only matches all the aforementioned requirements but also it is the best in terms of trade-off between accuracy and computational time. The CFD model will be discussed in detail in the next sub-Chapter together with the chemical species transport, permeation, electrochemistry and thermal models.

3.2.4. Modelling assumptions

In the context of this work, the model has been focused directly on the electrolytic cell, used for the experiments, and indirectly on the test bench through boundary conditions.

The model was implemented in Comsol Multiphysics environment and was developed both for 2D and 3D geometry. The model is composed by general assumptions, mathematical formulation, computational domain, geometry and mesh, boundary conditions, numerical implementation and calculation procedure. The different sections will be analyzed in the next paragraphs.To derive a closed form of expressions for the electrolytic cell model, the following assumptions are made:

• All gases in the simulation are treated as ideal. For a real gas to be considered as an ideal gas oftentimes the temperature needs to be high and the pressure low. This is a reasonable assumption given the compressibility factor of oxygen and hydrogen is approximately equal to that of an ideal gas at the pressures and temperatures used to in this simulation.

• When the Butler-Volmer equation was used for concentration dependent kinetics, it was assumed that the kinetics had the reaction order of unity with respect to all species.

• The reactions are assumed to take place at electrode/membrane interfaces and so local currents has been considered generated at interfaces.

• The simulation was performed at steady-state conditions.

• The pores are considered isotropic since all the parameters are constant in all directions including the diffusivity, thermal conductivity and permeability.

• The electroosmotic drag coefficient is assumed to be constant dependant on temperature.

3.2.5. Mathematical formulation

In this section the mathematical formulation that is used inside the Comsol model is brought. It is noteworthy that some of these formulas have already been mentioned in a similar or a simpler way in the theoretical basis for MATLAB model, but they are brought here in the form that they have been implemented in the Multiphysics environment for the sake of complicity and clarity.

3.2.5.1. Charge transport and conservation

Charge transport and conservation are defined in electrodes and electrolyte by imposing Ohm's Law in combination with the charge balance for electrons and ions:

$$\nabla i_s = 0 \quad 3.49$$

$$i_g = -\sigma_{seq} \nabla \phi_s \quad 3.50$$

$$\nabla i_l = 0 \quad 3.51$$

$$i_l = -\sigma_l \nabla \phi_l \quad 3.52$$

The parameter i_s represents the electronic current density while i_l represents the ionic one. $\sigma_l$is the conductivity of the electrolyte and σ_{seq} is the equilibrium electrical conductance. the φs and φl are the electronic and ionic potential that are also the two unknowns of the selected physics interface. The overall Voltage of the cell Vc is evaluated as in the equation :

$$V_c(T,p) = OCV(T,p) + \eta_{act,an}(i) + \eta_{act,cat}(i) + \eta_{\text{ohm}}(i) + \eta_{diff,an}(i) + \eta_{\text{diff},cat}(i) \quad 3.53$$

In order to find the dependent variables, φs and φl, the conductivity of the electrolyte was evaluated as:

$$\sigma_l = \frac{F^2 C_{H^+} D_{H^+}}{RT} \quad 3.54$$

- F = 96485.3329 [C/mol], Faraday Constant.
- CH+ [mol/m3], H+ concentration in the membrane.
- DH+ [m2/s], H+ Diffusivity.
- R = 8.3145 [J/mol K], Ideal Gas Constant.
- T [K], Absolute Operating Temperature.

The C_{H+} value was referred to the work of Ferrero et al. [107] while D_{H+} value was obtained from the fitting procedure. The electrical conductance σ_{seq} was obtained by solving the equivalent circuit of the cell as indicated from Marangio et al.[108]. In their study, they considered several contact resistances between the inner components as showed in equations bellow. The overall resistance of the cell, Rtot, was considered the most important indicator to evaluate the ohmic contribute.

$R_{tot} = R_{eq,an} + R_{eq,cath}$

And the components are :

$$R_{ES,an} = \rho_{el,an}\frac{\delta_{el,an}}{\frac{\omega_{s,an}}{2}L} R_{ES,\text{ cath}} = \rho_{el,cath}\frac{\delta_{el,cath}}{\frac{\omega_{s,c\text{ cath}}}{2}L}$$
$$R_{EC,an} = \rho_{el,an}\frac{\delta_{el,an}}{\omega_{c,\text{ an}}L} R_{EC,\text{ cath}} = \rho_{el,cath}\frac{\delta_{el,cath}}{\omega_{c,\text{ cath}}L}$$
$$R_{ED,an} = \rho_{el,an}\frac{\frac{\omega_{c,an}}{4}}{L\delta_{el,an}} R_{ED,\text{ cath}} = \rho_{el,cath}\frac{\frac{\omega_{c,\text{ cath}}}{4}}{L\delta_{cl,cath}} \quad 3.55$$
$$R_{PS,an} = \rho_{pl,an}\frac{h_{c,an}}{\frac{\omega_{s,}an}{2}L} R_{ps,cat} = \rho_{pl,\text{ cath}}\frac{h_{c,cath}}{\frac{\omega_{s,cath}}{2}L}$$
$$R_{PR,an} = \rho_{pl,an}\frac{h_{p,an}}{A} R_{PR,\text{ cath}} = \rho_{pl,cath}\frac{h_{p,cath}}{A}$$

In which:

- ρel,an and ρel,cath are the anode and cathode material resistivity in ωcm.
- ωs, an and ωs, cath are the anode and cathode channel support width in cm.
- ωc, an and ωc, cath are the anode and cathode channel width in cm.
- δel,an and δel,cath are the anode and cathode thickness in cm.
- ρpl,an and ρpl,cath are the anode and cathode electrode resistivity expressed in ohm.cm.
- hc,an and hp,cath are the anode and cathode channel height in cm.
- L is the Membrane Electrode Assembly (MEA) length in cm.

The kinetic electrode type was set on Butler-Volmer Equation as reported so the homonymous equation was utilized. In this case a pre-exponential factor was implemented to include different conditions respect to the reference one, the corrected Butler-Volmer Kinetic Equations are reported bellow:

$$i_{\text{loc,an}} = i_{0,an}\left(\frac{C_{O_2}}{C_{O_2,\text{ ref}}}\right)^{k_{O_2}}\left[\exp\left(\frac{\alpha_{an}F}{RT}\eta_{act,an}\right) - \exp\left(-\frac{\alpha_{an}F}{RT}\eta_{act,an}\right)\right]$$
$$i_{\text{loc, cat}} = i_{0,cat}\left(\frac{C_{H_2}}{C_{H_2,ref}}\right)^{k_{H_2}}\left[\exp\left(\frac{\alpha_{cat}F}{RT}\eta_{act,cat}\right) - \exp\left(-\frac{\alpha_{cat}F}{RT}\eta_{act,cat}\right)\right] \quad 3.56$$

Where:

- CO2 and CH2 are the Oxygen and Hydrogen concentrations at electrode/membrane interface expressed in [mol/m3]
- CO2,ref and CH2,ref are the Oxygen and Hydrogen reference concentrations at electrode/membrane interface expressed in [mol/m3]
- kO2and kH2 are empirical parameters set to 0.5 and 0.25 according to Marangio et al. [108], αi is i-th transfer coefficient.
- i0,i is the i-th exchange current density expressed in [A/cm2].
- ηact,i is the i-th activation overvoltage. It represents the voltage spent to activate the electro-chemical reaction by increasing its rate of reaction and it is expressed in [V].

The activation overvoltage was evaluated through the following expression:

ηact = φs − φl − Eeq

Where:

- φs is the Electronic Potential [V].
- φl is the Ionic Potential [V].
- Eeq is the Equilibrium Potential [V];

The equation is applied to both the electrodes and the Equilibrium Potential was calculated considering the equation

$$E_{REV} = \frac{\Delta \bar{g}_r(T, p_0)}{z_r F} + \frac{\bar{R}T}{z_r F} \ln \left[\frac{\prod_i^p \left(\frac{p_i}{p_0}\right)^{-\nu_i}}{\prod_i^r \left(\frac{p_i}{p_0}\right)^{-\nu_i}} \right] \quad 3.57$$

Which is applied to the two semi reactions:

$$E_{eq,an} = \frac{\Delta \bar{g}_r(T, p_0)}{z_r F} + \frac{\bar{R}T}{z_r F} \ln \left(\frac{p_{O_2}^{0.5}}{p_{H_2O}} \right) \quad 3.58$$

$$E_{eq,cat} = \frac{\Delta \bar{g}_r(T, p_0)}{z_r F} + \frac{\bar{R}T}{z_r F} \ln (H_2) \quad 3.59$$

Where:

- Δ¯gr(T,p0) is the Gibbs Free Energy variation at Standard Conditions expressed in [kJ/kgmol].

- zr is the number of e− exchanged in the electrochemical half-reactions.
- F = 96485.3329 [C/mol].
- •R¯ = 8.3145 [J/Kmol].
- T is the Absolute Temperature [K].

The values of the Gibbs Free Energy variations were obtained from the following relationship:

$\Delta g0 = g0_{products} - g0_{reactants}$

3.2.5.2. Mass and momentum conservation

Mass and momentum conservation was used to describe the flow in open regions. Navier Stokes Equations are written below:

$$\rho(u \cdot \nabla u) = \nabla \cdot [-pI + \mu(\nabla u + (\nabla u)^T)] \quad 3.60$$

In the porous regions Brinkman Equations were utilized:

$$\frac{\rho}{\varepsilon}\left((u \cdot \nabla)\frac{u}{\varepsilon}\right) = \nabla \cdot \left[-pI + \frac{\mu}{\varepsilon}(\nabla u + (\nabla u)^T) - \frac{2\mu}{3\varepsilon}(\nabla \cdot u)I\right] - \left(\frac{\mu}{k} + \frac{Q}{\varepsilon^2}\right)u \quad 3.61$$

Where:

ρ is the density, u is the velocity vector, P is the pressure, μ is the viscosity, ε is the porosity and k is the Thermal Conductivity.

The equations are solved together with the continuity equation:

$$\rho \nabla.u = Q \quad 3.62$$

The term Q is the mass volumetric source, and it was set equal to zero.

3.2.5.3. Transport of diluted species in porous media

Transport of Diluted Species (TDS) physics provides a predefined environment for studying the evolution of chemical species transported by diffusion and convection as well as migration due to an electric field. The physics interface assumes that all the species are diluted so their concentration is small compared to a solvent fluid or solid. The gases, both oxygen and hydrogen, are considered diluted in water.

The TDS interface supports the simulations of chemical species transport by convection, migration, and diffusion utilising Fick's Law to govern the diffusion of the solutes, dilute mixtures and solutions. Steady state conditions Fick's Law is reported below:

$$\nabla \cdot Ji + u \cdot \nabla ci = Ri \qquad 3.63$$

Where:

- Ji is the Diffusive Flux vector of the i-th specie.
- u is the mass averaged velocity.
- ci is the concentration of the i-th specie.

The diffusive mass flux vector is expressed as follow:

$$Ji = -D_i \nabla c_i \qquad 3.64$$

Where:

Ji, is the Diffusive mass flux, ∇ci, is the concentration gradient, and D_i denotes the diffusion coefficient of the i-th specie. Since the mixtures considered are H2O/O2 and H2O/H2 the value of D_i coincides with the binary diffusion coefficients of the mixtures:

$$D_i = \frac{a}{p}\left(\frac{T}{\sqrt{T_{c,a} \cdot T_{c,b}}}\right)^b \cdot \left(p_{c,a} \cdot p_{c,b}\right)^{\frac{1}{3}} \cdot \left(T_{c,a} \cdot T_{c,b}\right)^{5/12} \cdot \left(\frac{1}{M_a} + \frac{1}{M_b}\right)^{\frac{1}{2}} \qquad 3.65$$

Where:

- a and b are dimensionless empirical coefficients.
- p [atm] is the pressure.
- Tc,i and pc,i [K],[atm] are the critical temperatures and critical pressures.

3.2.5.4. Water transport model in the membrane

Since Proton Exchange membrane is the most sensible component of the system, its capability to be a semipermeable polymer makes the water transport phenomenon one of the most relevant for the economy of the process as already discussed before. Water transport phenomenon can be considered mainly driven by three different physics: Diffusion, Electroosmotic-drag and Hydraulic pressure. The equation of water balance across the membrane is the following:

$$\dot{N}_{\mathrm{H_2O},mem} = \dot{N}_{\mathrm{H_2O,\,diff}} + \dot{N}_{\mathrm{H_2O},eo} - \dot{N}_{\mathrm{H_2O,hp}} \qquad 3.66$$

The term N˙H2O,diff is the molar flow rate due to Diffusion and is expressed as:

$$\dot{N}_{H_2O,\,\mathrm{diff}} = \frac{A}{\delta_{\mathrm{mem}}} \int_{C_w\ \mathrm{anode}}^{C_w^{\mathrm{cathode}}} D_w dy \qquad 3.67$$

And the water diffusion coefficient can be evaluated with the following experimental formula:

$$D_w = 1.25 \cdot 10^{-10} e^{\left(2416 \cdot \left(\frac{1}{303} - \frac{1}{T}\right)\right)} \qquad 3.68$$

$\dot{N}_{\mathrm{H_2O},eo}$is the Electroosmotic drag term, it represents the moles per second of water molecules which are dragged by each mole of hydrogen ions through the membrane. It is proportional to the osmotic drag coefficient and to the hydrogen ions.

$$\dot{N}_{\mathrm{H_2O},eo} = \frac{n_d I}{F}$$

Where:

- $n_d = 0.025Pc - 1.9073i + 0.0189Tm - 2.7892$, Electroosmotic drag Coefficient, represents the ratio between H2O and H+ moles. Pc is the critical pressure, Tm membrane thickness (cm), and i is the current density. [63][30]
- I [A] is the local current.
- F = 96485 is Faraday Constant.

$\dot{N}_{\mathrm{H_2O,hp}}$ is the water transport term due to pressure. It is generated when there is a gradient between anode porous layer and cathode porous layer. For the purpose f this work it was modelled with Darcy Permeability Model:

$$\dot{N}_{\mathrm{H_2O},hp} = k_{\mathrm{Darcy}} \frac{A \rho_{\mathrm{H_2O}}}{\delta_{\mathrm{mem}}\, \mu_{\mathrm{H_2O}} M_{\mathrm{H_2O}}} \Delta p$$

Where:

- k_{Darcy} [m2], is the Darcy Constant.
- A [m2], is the Active area.
- ρ_{H2O} [kg/m3], is the density of water
- μ_{H2O} [Pa s], is the cinematic viscosity.
- Δp [Pa], is the pressure difference.
- M_{H2O} [kg/mol], is the water molar mass.

3.2.5.5. Heat Transfer and Energy Conservation

Temperature of the electrolyzer is influenced by the heat of reaction both in the anodic and in the cathodic side as discussed in chapter 2. The equation used for the thermal analysis is the Energy Conservation Equation:

$$\nabla \cdot (\rho c_p u T) = -\nabla \cdot (k_{eq} \nabla T) + Q_v \qquad 3.69$$

In a solid domain k_{eq} is the thermal conductivity of the material. Since in the porous electrodes not all the volume is solid, a k_{eq} expression that considers the porosity of the material is used:

$$k_{eq} = k_s \cdot (1 - \varepsilon) + k_f \cdot \varepsilon \qquad 3.70$$

Where:

- Ks , thermal conductivity of the solid domain.
- kf,thermal conductivity of the fluid domain.
- ε , porosity.
- Qv , heat source term.

The heat source term is obtained by overlapping the three main heat source/sinks phenomena:

1-Heat due to irreversibility during the redox reactions, respectively:

$$Q_{th,R_{an}} = \frac{T\Delta S_{R,an}}{2F} \cdot i_{loc,an}$$
$$Q_{th,R_{cat}} = \frac{T\Delta S_{R,cat}}{2F} \cdot i_{loc,cat}$$

The values of Entropy were evaluated with experimental formula:

$$S(T) = a_j \ln T + 4b_j T^{\frac{1}{4}} + 2c_j T^{\frac{1}{2}} + \frac{4}{3} d_j - T^{\frac{3}{4}} R \ln P$$

These two equations are valid in the range between 300 and 4000 K. The values of the previous unknows are reported in the Table 3.5.

2-Heat due to Activation of the reactions:

$$Q_{th,act_{an}} = \eta_{act,an} \cdot i_{loc,an}$$
$$Q_{th,act_{cat}} = \eta_{act,cat} \cdot i_{loc,cat}$$

Since the reactions sites are located at electrode/membrane interfaces by hypothesis, $\eta_{act,an}$ and $\eta_{act,cat}$ are Activation Overvoltages while $i_{loc,cat}$ and $i_{loc,an}$ are the Local Current Densities at the respective interfaces.

3-Heat due to Joule effect, thus, to heat generated by the passage of current in a conductor:

$$Q_{\text{joule}} = -(i_s \nabla \cdot \phi_s + i_l \nabla \cdot \phi_l) \qquad 3.71$$

It is worth to point out that there is a strong interaction between the electrokinetic and thermal phenomena due to the electric resistivity dependance on temperature. Considering the formula, is and il are the ionic and electronic current densities while φs,φl are the electronic and ionic potential.

Table 3.5 Experimental parameters for Equation 3.71

j	Substance	aj	bj	cj	dj
1	Water	180	-85.4	15.6	-0.858
2	Hydrogen	79.5	-26.3	4.23	-0.197
3	Oxygen	10.3	5.4	-0.18	0

3.2.5.6. Multi-phase flow transport model

This section is devoted to two-phase flow mathematical model formulation of the anodic compartment. The flow can change from laminar to turbulent throughout the length of the cell. Thus, it is necessary to establish Reynolds Number for each phase the formulation used is the Blasius Equation as suggested from H. Ito et al. and others : [109] [110] [111]

$$Re_i = \frac{G_i D_{eq}}{\mu_i} \qquad 3.72$$

The term D_{eq} represents the hydraulic equivalent diameter for a rectangular/square duct, can be expressed as : [83]

$$D_{eq} = \frac{4LB}{2(L+B)} \qquad 3.73$$

Where L is the channel thickness, B is the channel height, Gi is the Mass flow rate over the surface of the i-th phase and μi is the viscosity of the i-th phase. The two-phase fluid/gas transport model for gas bubbles/water flow in the microchannels, was modelled with Navier-Stokes Bubbly Turbulent Flow Equations. This model pattern was chosen to take into account the interaction between the fluid flow and gas bubbles, in fact the eddies created in the channels

are responsible of additional momentum transfer to the fluid flow. The fluid layers experience additional shear stresses thus the velocity, in its more general form, can be expressed as:

$$u = U + \tilde{u}$$

The term U is the average value of the velocity and u˜ is the oscillating component around the average. Thus, to solve the Navier Stokes Equations and model eddies at 'Kolmogorov scale' a turbulent model is necessary. The turbulent model selected for the simulation was the k − ω model for compressible/incompressible flows. This model belongs to the family of RANS models and considers two additional equations respect to the usual Navier-Stokes set of equations: the Turbulent Kinetic Energy (k) Equation and the Specific Dissipation Rate Equation (ω). Another important remark about this model, is related to the formulation of the eddy viscosity μt, it considers both of k and ω. Compressibility effects were neglected both for gas and fluid flow and Continuity equation was applied to ensure the mass conservation. Below are reported the equations for the turbulent bubbly flow:

$$\begin{gathered}
\phi_l \rho_l (\nabla \cdot u_l) u_l = \nabla \cdot [-\rho I + K] + \phi_l \rho_{lg} + F \\
\nabla \cdot \left(\phi_l \rho_{l u_l} + \phi_g \rho_{g u_g} \right) = 0 \\
K = \phi_l (\mu_l + \mu_t) \left(\nabla u_l + \nabla u_t^T - \frac{2}{3} (\nabla u_l I) - \frac{2}{3} \phi_l \rho_l K I \right) \\
\nabla \cdot N_{\phi_g \rho_g} = -m_{gl} \\
u_l = u \\
u_g = u_l + u_{slip} - \mu_t \frac{\nabla \phi_g}{\rho_l \phi_g} \\
\rho_l (\nabla \cdot u_l) k = \nabla \cdot [(\mu_l + \mu_t \sigma_k{}^*) \nabla k] + P_k - \beta_0{}^* \rho_l \omega_k \\
\rho_l (\nabla \cdot u_l) \omega = \nabla \cdot [\mu_l + \mu_t \sigma_\omega \nabla \omega] + \alpha \frac{\omega}{k} - \rho_l \beta_0 \omega^2 + \alpha_k s_k \frac{\omega}{k} \\
\mu_t = \rho_l \frac{k}{\omega} = -c_k \phi_g \nabla p \cdot u_{slip} \\
P_k = \mu_t \left[\nabla \mu_l : \left(\nabla \mu_l + (\nabla \mu_l)^T - \frac{2}{3} \nabla \mu_l^2 \right) \right] - \frac{2}{3} \rho_l k \nabla \cdot u_l \\
k = \frac{1}{2} (\tilde{u}^2 + \tilde{v}^2 + \tilde{z}^2)
\end{gathered} \qquad 3.74$$

Where :

- ρ_l is the liquid-phase density
- u_l is the liquid-phase velocity

- p is the pressure
- Φ_l is the volume fraction of the liquid phase
- g is the gravity acceleration
- k is the turbulent kinetic energy
- μ_t is the eddy viscosity
- ρ_g is the gas-phase density
- Φ_g is the gas phase volume fraction
- u_g is the gas-phase velocity
- u_{slip} is the slip velocity. For the evaluation, is assumed that the pressure forces on a bubble are balanced by the drag force.
- The Turbulence model parameters for the RANS model are:
  - $\alpha = \frac{13}{25}$
  - $\sigma_k = \frac{1}{2}$
  - $\sigma_\omega = \frac{1}{2}$
  - $\beta_0 = \frac{9}{125}$
  - $k_v = 0.41$
  - $B = 5.2$
  - $\sigma_t = 1$
  - $C_k = 0.505$
  - $\alpha_\omega = 0.46$

The slip velocity selected was based on Pressure-Drag Balance model and the drag coefficient was established in view of Hadamard and Rybdczynski work, thus Small Spherical Bubbles were considered. The parameter φi, that represents the volume fraction of the i-th phase, was solved together with the Turbulent kinetic Energy k and Dissipation rate ω on the whole segregated step, while pressure and velocity field were solved in another segregated step. The initial values for the simulation were set the same of the previous model, except for the values of k and ω. The reason is related to the fact that the new turbulent model formulation was substituted with the Mass and Momentum Conservation laminar single phase flow discussed before.

3.2.5.7. Potential increment due to bubbles

The potential rise across the cell was modelled to better understand the impact of the bubbles. The potential is made up by the sum of activation, ohmic and concentration overvoltage. The effects of the bubbles need to be considered in all

the overpotential components. Andrea Angulo et al. [81] suggest that nucleation and growth of the bubbles, attached on the electrode surface, affects the activation overpotential due to the decrease in the electrocatalytic area needed for the redox reactions. Furthermore, block the passage of the ions with a consequent creation of an additional contact resistance, increasing the ohmic overvoltage. Regarding the diffusion overpotential, bubbles attached to the electrodes can also absorb the gaseous products decreasing supersaturation levels on the electrolyte. Amin Nouri-Khourasani et al. [86] studied the coverage impact of the bubbles as bubble overvoltage source. The formulation is reported in the following equation:

$$\eta_{\text{bubbles}} = -\frac{RT}{\alpha_a F}\log\left(1-\xi_b\right) \qquad 3.75$$

Where:

- R is the universal gas constant.
- T is the absolute temperature.
- F is the Faraday constant
- αa is the anodic transfer coefficient.
- ξb is the fraction of the electrode covered by the bubbles

The Turbulent Bubbly Flow k−ω Model is used as input for the 'Transport of Diluted Species' section in substitution of the previous 'Free and Porous Media Model'. Some differences arise comparing the new multiphysics model with previous one. The presence of bubbles influences the local current density at electrode interface. Aubras et al[112] modelled this influence as reported in the following equation:

$$i_{loc,an} = i_{0,an}\left[\exp\left(\frac{\alpha_{an}F}{RT}\eta_{act,an}\right)\frac{\lambda}{\lambda_{sat}} - \exp\left(-\frac{\alpha_{an}F}{RT}\eta_{act,an}\right)\right] \qquad 3.76$$

The local current is reduced a priori as the ratio $\frac{\lambda}{\lambda_{sat}} \leq 1$. The parameter λ represents the humidification coefficient of the membrane, it is an important parameter used to determine the ionic conductivity of the membrane thus it can be used to estimate the Ohmic Overvoltage. The other parameter λsat is humidification coefficient considering saturation conditions, in fact in order to simulate mass transfer, critical saturation processes were considered. The humidification coefficient was estimated as follows:

$$\lambda = 0.3 + 10.8\left(\frac{C_{H_2O}}{C_{H_2O,sat}}\right) - 16\left(\frac{C_{H_2O}}{C_{H_2O,sat}}\right)^2 + 14.1\left(\frac{C_{H_2O}}{C_{H_2O,sat}}\right)^2 \quad 3.77$$

The saturation concentration was calculated considering the following equations:

$$C_{H_2O,sat} = \frac{P_{sat}(T)}{RT} \quad 3.78$$

Where Psat(T) was treated with the following experimental formula:

$$P_{sat}(T) = \exp\left(23.1964 - \left(\frac{3816}{T} - 46.15\right)\right)[Pa] \quad 3.79$$

3.2.6. Geometry

The geometry was obtained entirely in the Comsol Multiphysics environment with real scale proportions, in order to faithfully reproduce the dimensions of the cell, the channels and the components required for the simulation. Figure 3.11 shows a 3D representation of the system analyzed.

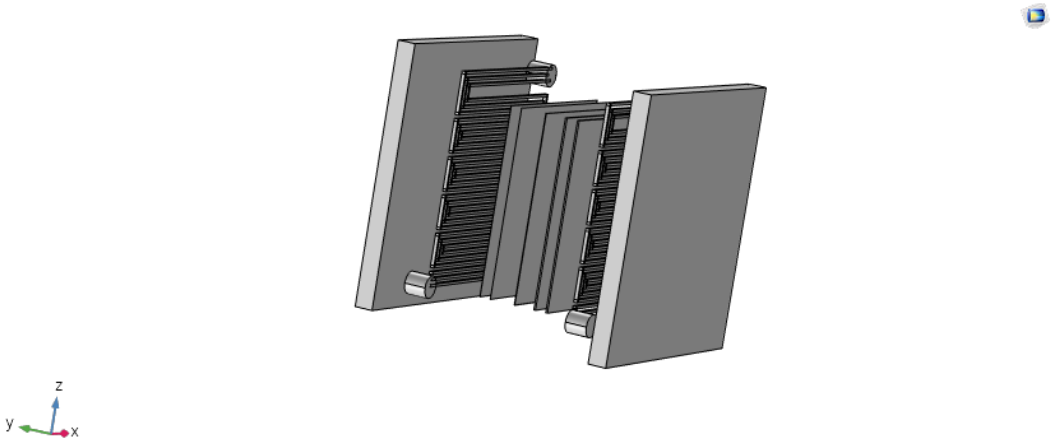

Figure 3.11 3D Geometry

Figure 3.12 reports a larger magnification of the channels which faithfully replicates the triple serpentine pattern of the real bipolar plates.

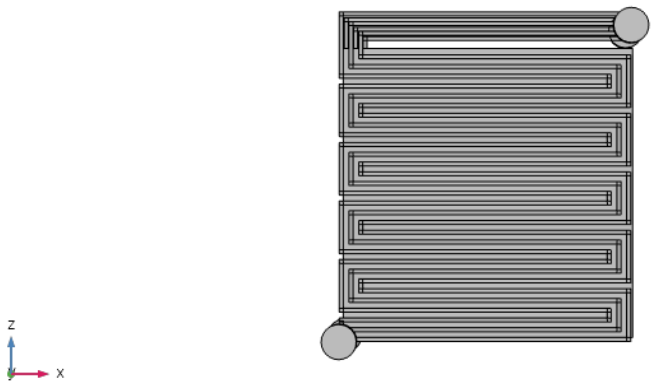

Figure 3.12 Channel geometric pattern

As can be seen from the Figure 3.11 the components considered for the simulation are the two bipolar plates, anodic and cathodic channels, anode GDL, anode catalyst layer, cathode GDL with its relative catalyst layer and obviously the Nafion membrane. The simulation was also carried out in 2D dimension, Figure 3.13 shows the 2-D geometry used for the simulations. Also, in this case the dimensions faithfully reproduce the real ones. It consists of Anodic and Cathodic Bipolar plates made of Titanium (Anodic) and Graphite (Cathodic), Anode Electrode, PEM Electrolyte and Cathode Electrode.

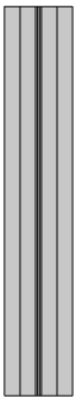

Figure 3.13 Channel geometric pattern.

The 2-D geometry is simpler respect to the 3-D one. It consists of rectangular blocks, as can be seen from the exploded geometry shown in Figure 3.14.

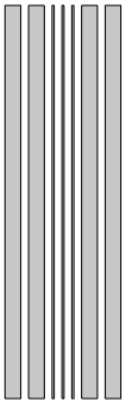

Figure 3.14 Exploded geometry in 2D.

3.2.6.1. 2-D Mesh

For the 2-D case, a cartesian grid block-structured mesh was used. It is characterized by different domains as can be seen from Figure 3.15.

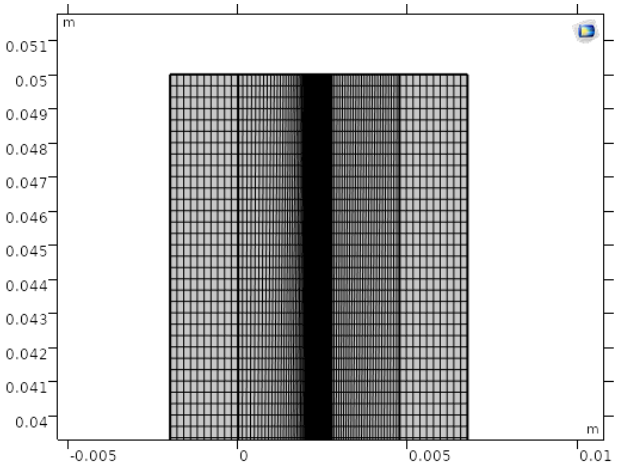

Figure 3.15 2D block-structured Mesh.

Figure 3.16 reports a larger magnification of the mesh utilized. As can be noticed, the mesh density increases going towards the electrode/electrolyte interfaces from both sides. This is due to the fact that the electrochemical reactions occur in these regions so finer mesh is needed to better represent the phenomena involved. The size of the elements and the growth factor were chosen considering a trade-off between accuracy and computational time.

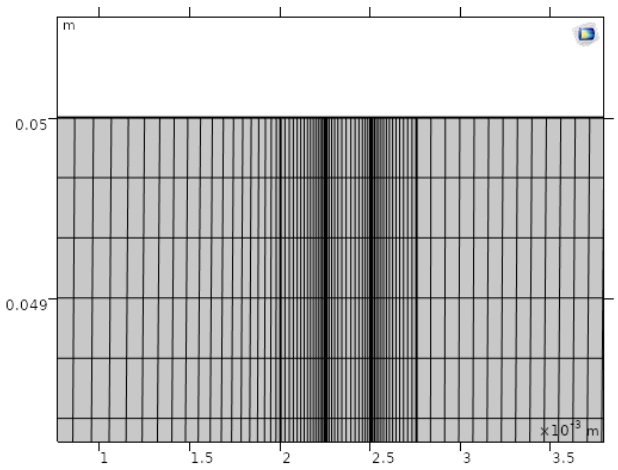

Figure 3.16 Magnification of 2D block-structured Mesh.

3.2.6.2. 3-D Mesh

The 3-D mesh was implemented with Comsol MultiPhysics adaptive mesher to better match the optimum value between accuracy and computational time. Figure 3.17 shows the mesh used for the 3-D geometry:

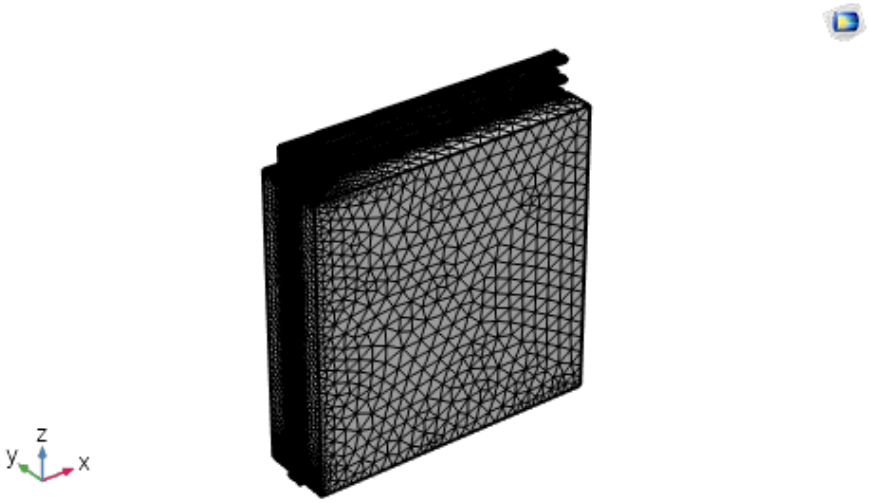

Figure 3.17 3-D Free tetrahedral mesh.

As can be seen from the Figure 3.18, also in this case, the density of elements that compose the mesh is higher going toward the inner part of the cell, especially in MEA neighbourhood and in the corners of the triple serpentine flow field.

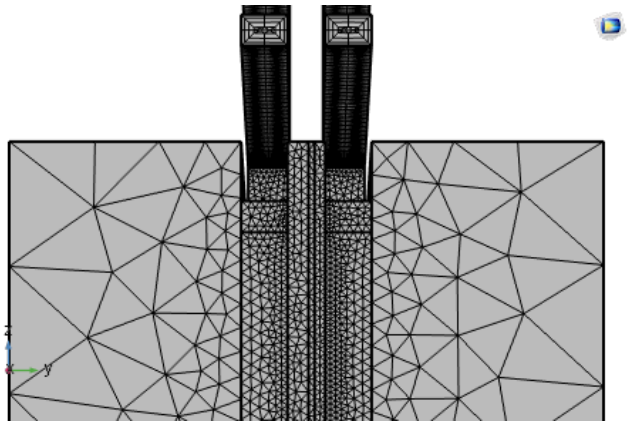

Figure 3.18 Higher magnification of 3-D Free tetrahedral mesh with a focus on the membrane electrolyte assembly and channels.

3.2.6.3. Mesh II

Since a new physics is involved in the treatment, an updated mesh is needed to model the system. The new mesh was obtained by the automated mesh of COMSOL Multiphysics software. In this case a physics-controlled mesh was used in order to enhance convergence. In this regard the boundary conditions and the physics were set before meshing to facilitate the mesh creation. The mesh used presents tetrahedral core cells with a predefined base size and is characterized by having an increasing growth rate from the solid walls to the centre. A prism layer mesh was used near the walls to solve viscous and buffer layers.

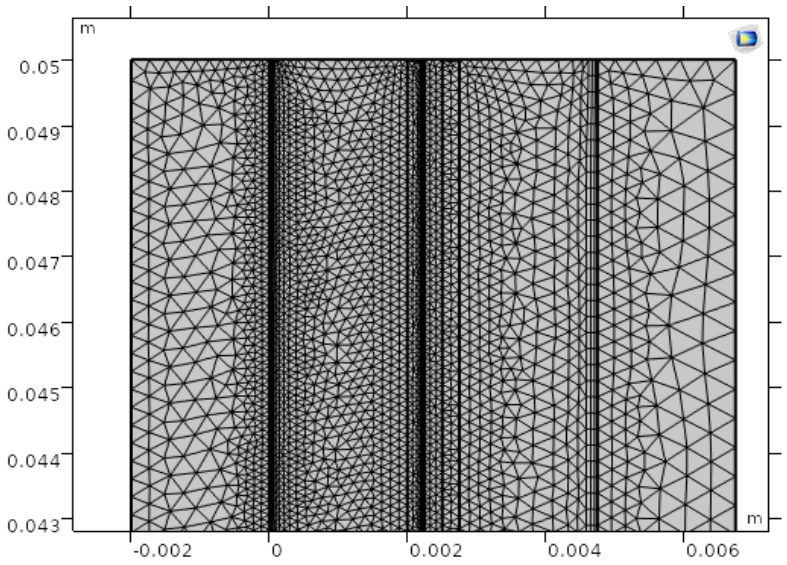

Figure 3.19 Magnification of 2D Mesh.

from the mesh plot that the anode channel mesh results finer respect to the cathode side due to the selected physics interface is observable.

3.2.7. Boundary conditions

In order to assign the proper boundary conditions (BCs) to the relative boundaries, in the first part of the paragraph some intuitive 2-D and 3-D representation are reported, as can be seen in Figure 3.20 and Figure 3.21.

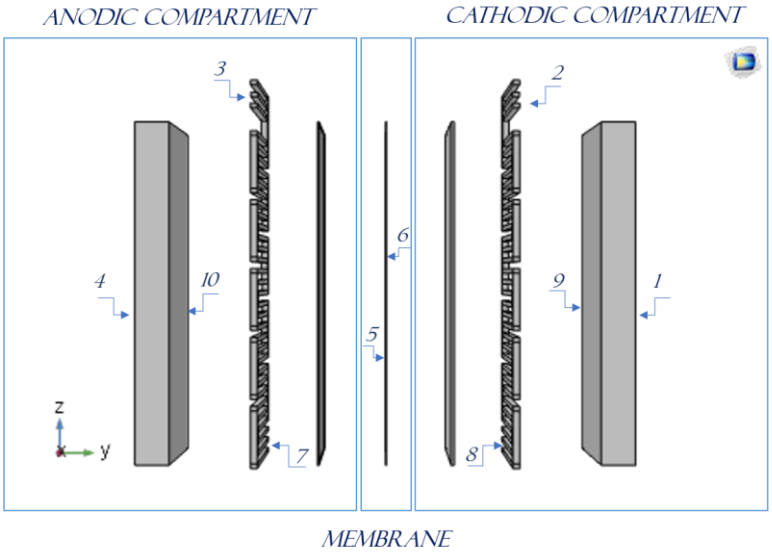

Figure 3.20 3-D Boundary numeration.

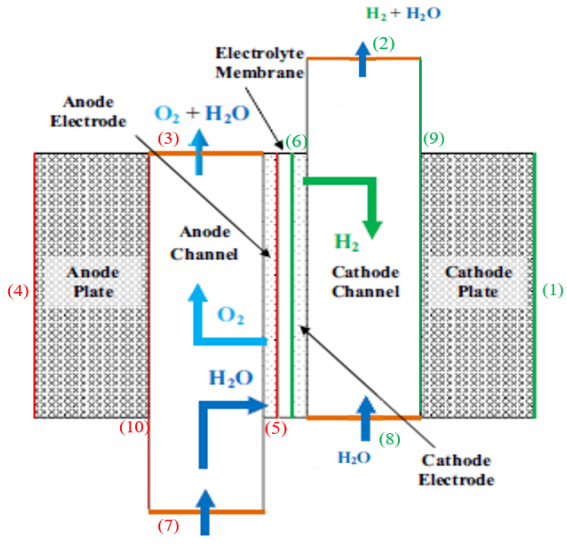

Figure 3.21 2-D Boundary numeration.

In the following table the boundary conditions utilized for the simulation both for 2-D and 3-D models are shown:

Table 3.6 Boundary Conditions for both 2-D and 3-D models.

Boundary Conditions		
Type	Formulation	Boundary
Electric Potential	$\phi_s = V_{\text{cell}}$	4
Electric Ground	$\phi_s = 0$	1
Insulated Boundaries	$-i_s \cdot n = 0$	all others
Insulated Boundaries	$-i_l \cdot n = 0$	all others
Interface	$\mathrm{t} - i_s \cdot n = -i_{\text{tot}}$	5,6
Interface	$-i_l \cdot n = -i_{\text{tot}}$	5,6
Interface	$i_{\text{tot}} = \sum_j i_{loc,j}$	5,6
H2O Concentration	$C_{H_2O,an,in} = \frac{\rho_{H_2O}(T_{an,in})}{M_{H_2O}}$	7
O2 Concentration	$C_{O_2,an,in} = \frac{\rho_{O_2(T_{an,in})}}{M_{O_2}}$	7
H2O Concentration	$C_{H_2O,cat,in} = \frac{\rho_{H_2O}(T_{\text{cat,in}})}{M_{H_2O}}$	8
H2 Concentration	$C_{H_2,cat,in} = \frac{\rho_{H_2}(T_{\text{cat},in})}{M_{O_2}}$	8
Pure Convective Outflow	$-n \cdot D_i \nabla C_i = 0$	2,3
Mass Flow Inlet	$-d_c \int \rho(u \cdot n) dA = \dot{n}_{H_2O,an} \cdot M_{H_2O}$	7
Outlet Pressure	$p = p_{an,out}$	3
Mass Flow Inlet	$-d_c \int \rho(u \cdot n) dA = \dot{n}_{H_2O,cat} \cdot M_{H_2O}$	8

Outlet Pressure	$p = p_{\text{cat,out}}$	2
Interface	$u = -\frac{n}{\rho}\sum_j \sum_i \left(R_{i,j}M_i + \dot{N}_{H_2O,j}M_{H_2O}\right)$	5,6
No slip	U=0	9,10
Symmetry	$-n \cdot (k\nabla T) = 0$	1,4
Fixed Temperature	$T = T_{an,in}$	7
Fixed Temperature	$T = T_{\text{cat , out}}$	8
Pure Convection	$-n \cdot (k\nabla T) = 0$	2,3
Heat Source	$-n \cdot (k\nabla T) = Q_{th,R_{an}} + Q_{th,Act_{an}}$	5
Heat Source	$-n \cdot (k\nabla T) = Q_{th,R_{\text{cat}}} + Q_{th,Act_{cat}}$	6
Thermal Insulation	$-n \cdot (k\nabla T) = 0$	all others

It is apparent from both Figure 3.20 and Figure 3.21 that the boundary condition were enumerated as follow: 1 is referred to the surface outer surface of the cathodic BP, 4 is referred to the surface outer surface of the anodic BP, 2 is referred to the outlet of the cathodic channels, 3 is referred to the outlet of the anodic channels, 5 is referred to the interface anode/membrane, 6 is referred to the interface cathode/membrane, 7 is referred to the inlet of the anodic channels, 8 is referred to the inlet of the cathodic channels, 9 is referred to the surface inner surface of the cathodic BP and 10 is referred to the surface outer surface of the anodic BP.

3.2.8. Multi-Phase Flow Boundary Conditions

Below are reported the Boundary Conditions used for the Turbulent Bubbly Flow Model in the anodic compartment:

Table 3.7 Boundary Conditions Multi-phase flow only

Boundary Conditions		
Type	Formulation	Boundary
Water velocity Field		10

Water velocity Field	$u_l \cdot n = 0$	10
Specific Dissipation Rate	$u_{l,\,\text{tang}} = u_l - (u_l \cdot n)n$	10
Pressure	$\omega = \frac{\rho_l k}{\kappa_v \delta_w^+ u_l}$	3
Specific Dissipation Rate	$[-p \cdot I + K]n = -p_0 n$	3
Turbulent Kinetic Energy	$\nabla\omega \cdot n = 0$	3
Water Velocity Field	$\nabla k \cdot n = 0$	7
Water Velocity Field	$u_l = u_0$	7
Turbulent Kinetic Energy	$u_0 = \|u_{ref}\|$	7
Specific Dissipation Rate	$k = \frac{3}{2}(u_{ref,} \cdot I_t)^2$	7
Gas Flux	$\omega = \frac{k^{0.5}}{((\beta_0 *)^{0.25})LT}$	5
Specific Dissipation rate	$N_{\phi_g \rho_g} = \frac{jM_{O_2}}{z \cdot F}$	5
	$\omega = \frac{\rho_l k}{\kappa_v \delta_w^+ u_l}$	

The channel walls were also considered as no-slip walls for both the two phases and no gas flux walls. The Electrode/Electrolyte Interface was considered as gas flux wall with no-slip condition for the liquid phase. All the remaining boundary conditions were set as the previous model. During the simulation, roughness effects were not considered, and the mixing length parameter were set to a default value. The turbulent parameters were also set to its own default values in order to enhance stability of the solution.

3.2.9. Results

3.2.9.1. Parameter list

Initial parameters list used for the 2D models are brought in the table bellow:

Table 3.8 parameters list

Parameters		
Name	**SI Unit**	**Details**
S	1E6 1/m	Active Surface
L	0.05 m	Cell length

m_w	5.0926 mol/s	Molar flow
k_el	1.3 W/(m·K)	*k* Electrodes
k_mem	0.16 W/(m·K)	*k* Nafion
rho_mem	1980 kg/m3	*ρ* Nafion
Cp_mem	1300 J/(kg·K)	c_pNafion
h_an	2.5E-4 m	Anode width
h_cat	2.5E-4 m	Cathode width
h_m	1.954E-4 m	Nafion width
h_c	0.002 m	Channel width
eta	0.3	Electrode porosity
eta_p	0.11	Percolation threshold.
rho_an	5E-5 Ω·m	ρ_{el} Anode
rho_cat	5E-5 Ω·m	ρ_{el} Cathode
i0a	1.6 A/m2	Exch. Current Density
A	0.025 m2	MEA area
V_cell	1.7 V	Cell Voltage
p_an	5E5 Pa	Anode Pressure
p_cat	5E5 Pa	Cathode Pressure
T_an	314.7 K	Anode Initial T
i0c	2800 A/m2	Cath. exch. current
nd	2.165	Electro osm. Coeff
F	96485 C/mol	Faraday Constant
M_O2	0.032 kg/mol	O2 Molar Mass
M_H2	0.002 kg/mol	H2 Molar Mass
M_H2O	0.018 kg/mol	H2O Molar Mass
y_O2	0.2451	Initial Mol. Frac.

y_H2	0.64934	Initial Mol. Frac.
y_H2Ocat	0.35066	Initial mol. frac.
y_H2Oan	0.7549	Initial mol. frac.
w_H2	0.17064	Initial Mass frac.
w_O2	0.36596	Initial Mass frac.
w_H2O_cat	0.82936	Initial mass frac.
w_H2O_an	0.63404	Initial mass frac.
K_darcy	7.14E-20 m2	Darcy Constant
p_ref	1E5 Pa	Reference Pressure
alpha_an	2	Anode exch. coef.
alpha_cat	0.5	Cathode exch. coef.
C_ioniH	1000 mol/m3	H^+ Concentration
D_ioniH	1.73E-9 m2/s	H^+ Diffusivity
a_H2O	32.2 J/(mol·K)	H_2O Coefficients
b_H2O	0.0019 kg·m2/(s2·K2·mol)	
d_H2O	1.06E-5 kg·m2/(s2·K3·mol)	
e_H2O	-3.6E-9 kg·m2/(s2·K3·mol)	
dens_an	992.57 kg/m3	Anode Density
dens_cat	992.66 kg/m3	Cathode Density
C_O2_ch	4.4759 mol/m3	Initial mol. conc.
C_H2_ch	33.303 mol/m3	Initial mol. conc.
R	8.314 J/(mol·K)	Ideal Gas Costant
R_an	1.4333E-5 Ω	Anode Resistance
R_cat	1.4333E-5 Ω	Cathode Resistance
R_m	0.0030819 Ω	Nafion resistance
T_cat	314.48 K	Cathode Initial T

a_H2	27.1 J/(mol·K)	H_2 Coefficients
b_H2	0.0093 kg·m2/(s2·K2·mol)	
d_H2	-1.38E-5 kg·m2/(s2·K3·mol)	
e_H2	7.65E-9 kg·m2/(s2·K3·mol)	
a_O2	28.1 J/(mol·K)	O_2 Coefficients
b_O2	0 kg·m2/(s2·K2·mol)	
d_O2	1.75E-5 kg·m2/(s2·K3·mol)	
e_O2	-1.07E-8 kg·m2/(s2·K3·mol)	

3.2.9.2. 2D Single-phase Laminar flow model

Several operating conditions can be found in PEM applications as reported the second chapter under the operating conditions, thus, to derive the characteristic curve the standard test temperature of 60[◦C] was selected and a pressure of p=10[bar] was set both for the two compartments. The voltage was increased from OCV to 2.25[V] and the current was measured with a Domain Probe on both the electrodes. Figure 3.22 reports the corresponding polarization curve. Other probes were inserted in the critical points of the system to measure the desired parameters such as Concentrations of both reactants and products, local currents and water flows. The last simulation results are crucial to understand water consumption related to predefined operating conditions, since it is considered by many authors the "Achilles heel" of the electrolysis technology.[113] A plethora of interesting results can be analysed to better understand the phenomena involved, two of these are certainly voltage and current density distribution both in the electrodes and in the membrane as can be seen from Figure 3.23.

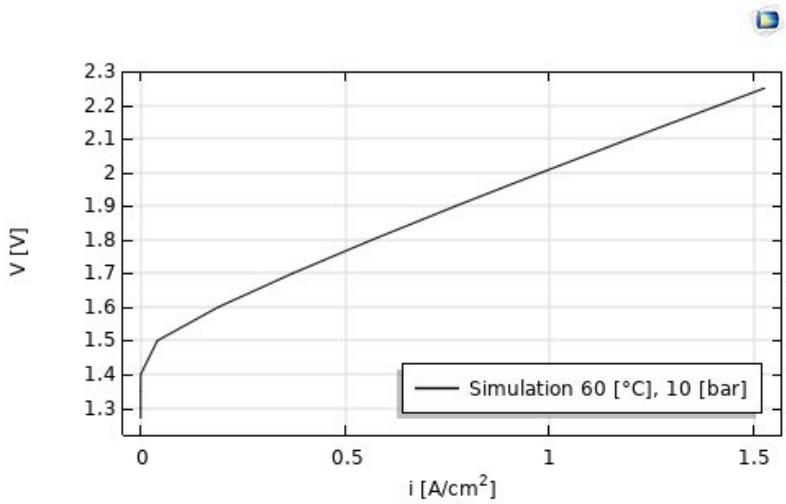

Figure 3.22 Polarization Curve at T = 60[◦C] and p = 10[barg].

The electrodes voltage results constant in the in both x and y directions across the electrodes while the electrolyte voltage distributions present different values along x-direction. One of the most important results is that it is reversed at OCV due to Nernstian physics. When the applied voltage across the terminals of cell increases respect to the OCV value, the Electric Field Vector at Electrolyte change direction and aligns with the Electric Field Induced by the external bias. Figure 3.24 shows that the concentration distributions present the same shape for different values of Voltage. One reason is related to the fact that the pressure distributions remain almost the same in both compartments. To better analyse the two distributions, it is better to explore concentrations evolution with line graphs, in the critical points of the system, such as Anode/Electrolyte interface and Cathode/Electrolyte interface. The behaviour of the oxygen concentration is strongly dependent on the local current density in the porous Anode, on the stoichiometric coefficient and on the height of the channel. The O2 molar concentration increases with the increase of the height of the channel as can be seen from Figure 3.25. In particular, the higher the applied voltage as well the height the higher the increase in the concentration. The increment is due to the increase of the local current at the interface as is shown in Figure 3.26.

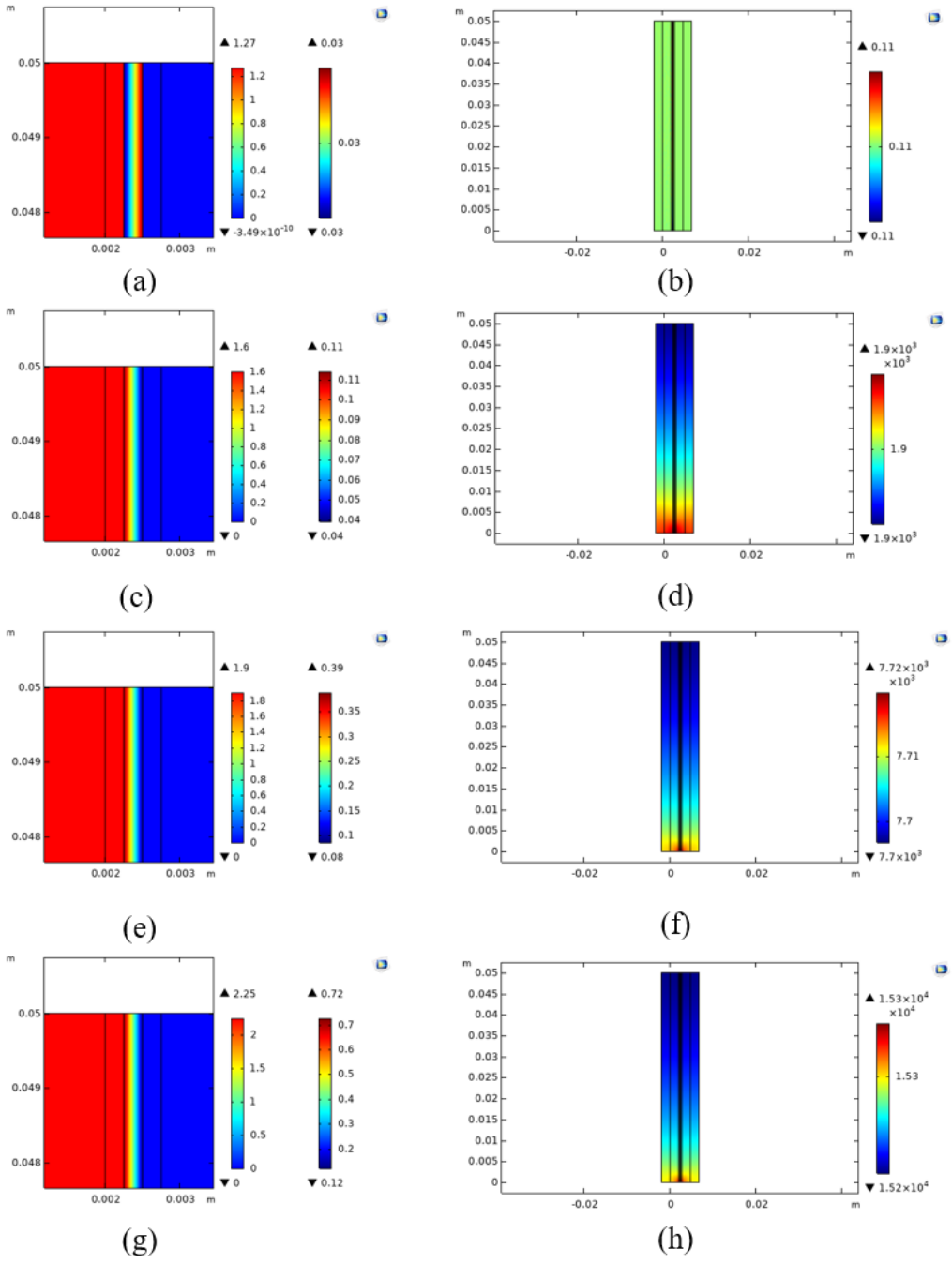

Figure 3.23 Voltage and Current Density 2-D snapshots from Multiphysics Simulation for different input voltages expressed respectively in in [V] and in [A/cm2]. Figure (a) and (b) is obtained selecting OCV condition from the parametric study while the pairs (c)-(d), (e)-(f), (g)-(h) snapshots are extracted selecting respectively 1.6, 1.9 and 2.25 Volts.

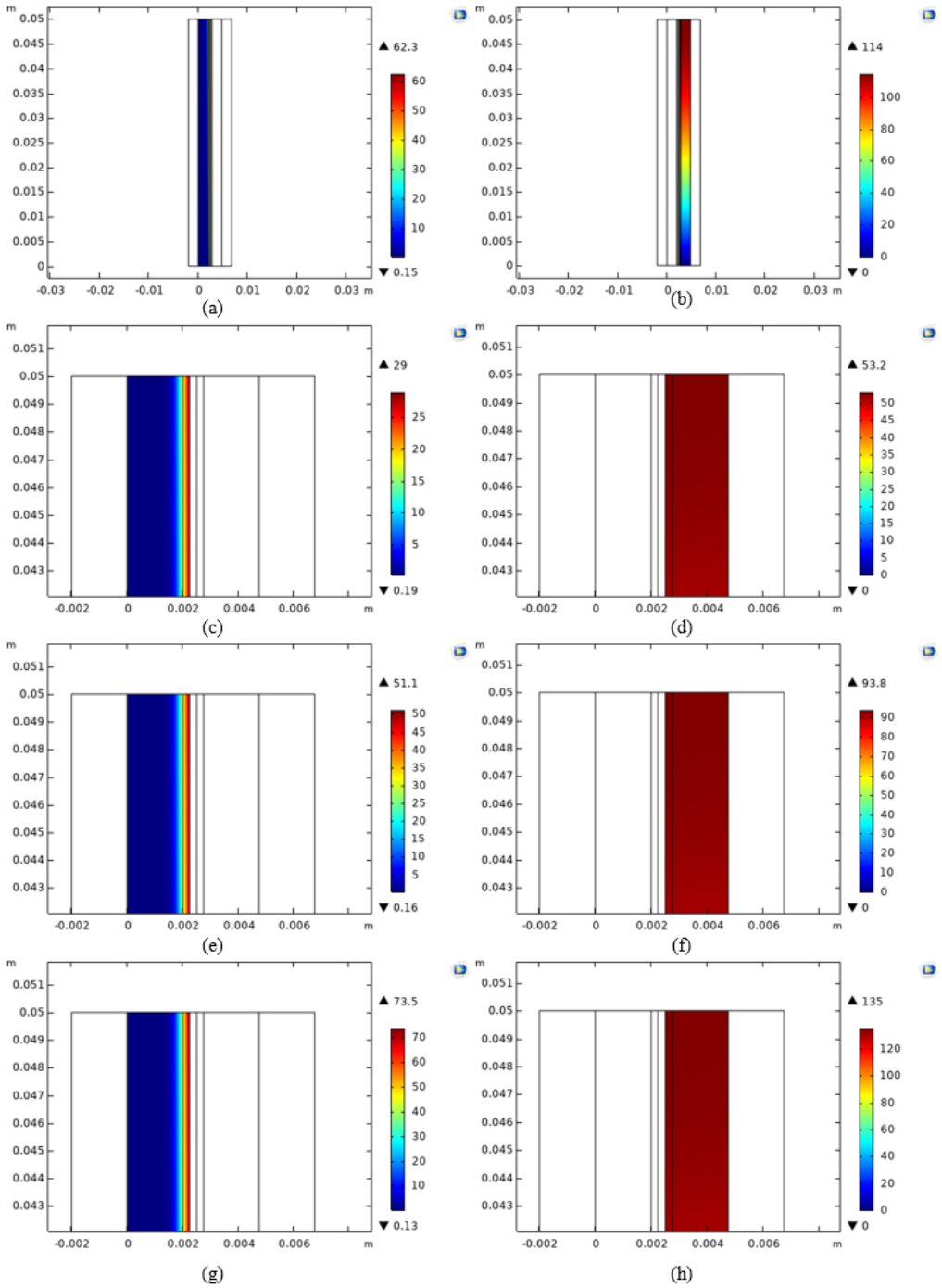

Figure 3.24 CO2 and CH2 2-D snapshots from Multiphysics Simulation for different input voltages expressed in in [mol/m3]. Figure (a) and (b) shows the complete distribution of the two species along the cell with an input voltage of 2 [V] while the pairs (c)-(d) ,(e)-(f) and (g)-(h) show the top part of the channel at respectively 1.7, 1.9 and 2.1 Volts.

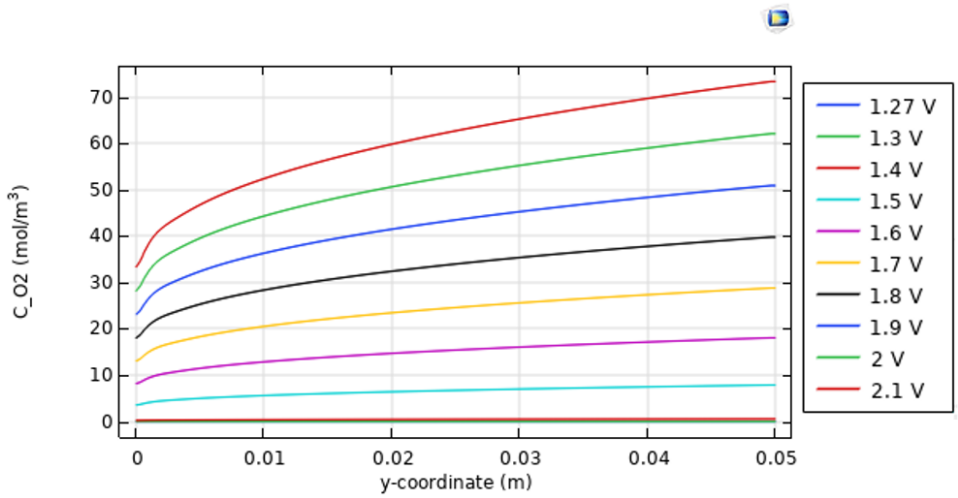

Figure 3.25 C_{O2} evolution along the y-direction.

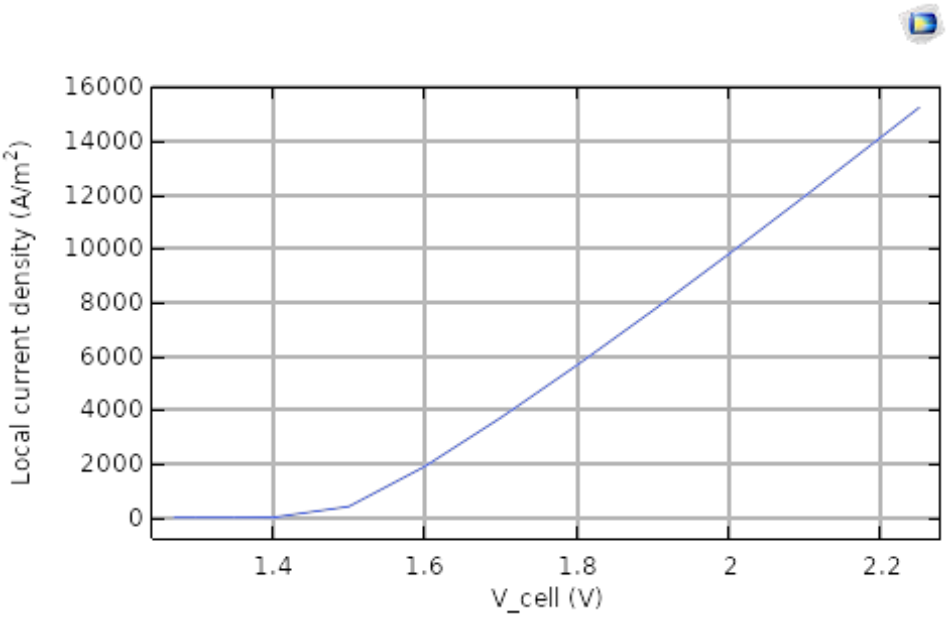

Figure 3.26 $i_{loc,an}$ behaviour along y-direction at anode/membrane interface.

Figure 3.27 shows the H2O Concentration Distribution in the Anodic Compartment. It easy to understand that the water concentration distribution field is the "dual" respect to the O2 one thanks to the fact that H2O and O2 are reactants and products of the same half-reaction.

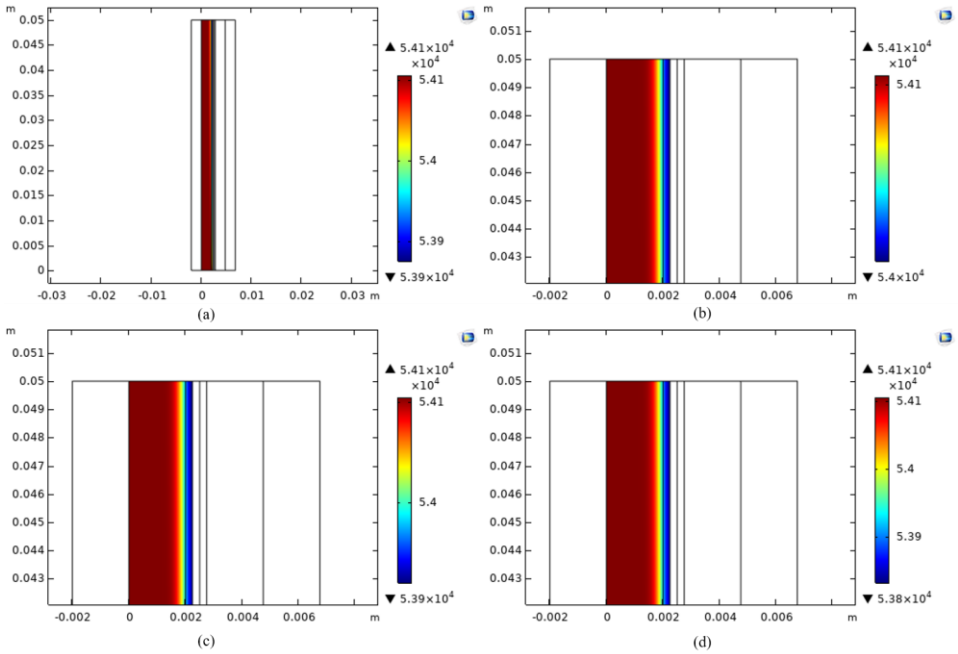

Figure 3.27 $C_{H2O,an}$ 2-D snapshots from Multiphysics Simulation expressed in in [mol/m3]. Figure (a) shows the entire profile at V=2[V] while (b),(c),(d) show the top part of the anodic channel respectively at V=1.7, 1.9 and 2.1 [V]

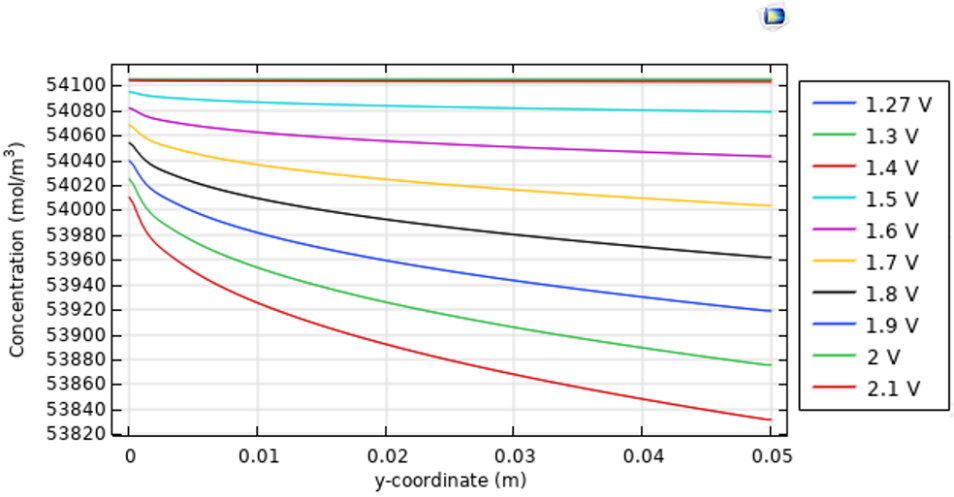

Figure 3.28 $C_{H2O,an}$ behaviour along y-direction at anode/membrane interface.

The shape of the concentration field of water is influenced by the voltage through the influence of the local current density. Moreover, it is influenced by the stoichiometric coefficient and the height of the channel. Regarding the cathodic

side, Figure 3.29 shows a parametric plot of Hydrogen concentration along the y-coordinate at the Electrode/Electrolyte interface.

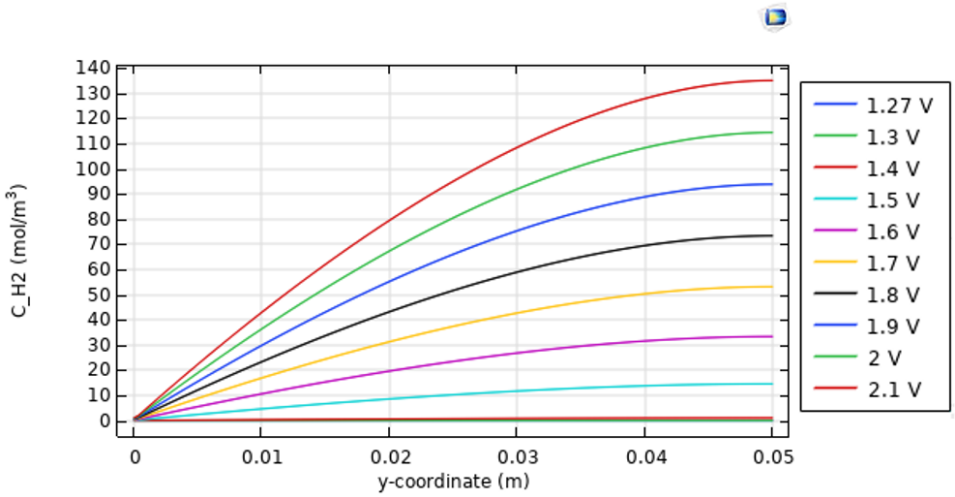

Figure 3.29 C_{H2} behaviour along y-direction at anode/membrane interface.

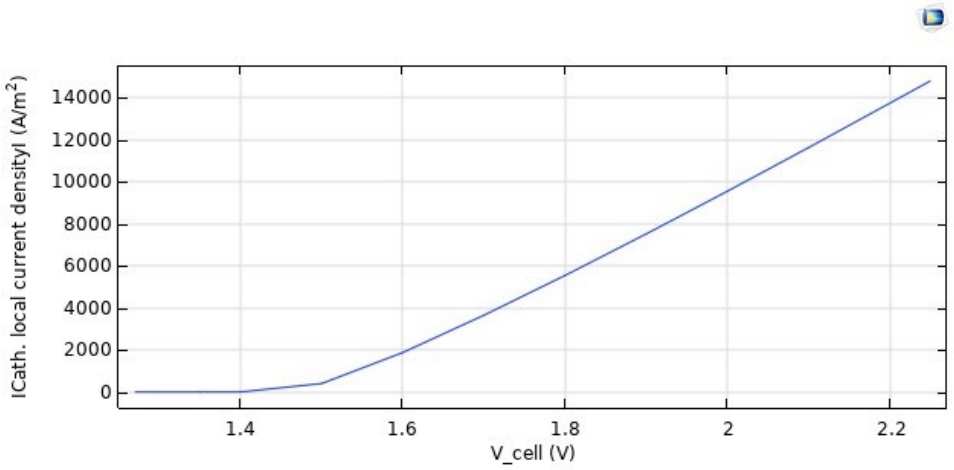

Figure 3.30 $|i_{loc,cat}|$ behaviour along y-direction at anode/membrane interface.

As can be seen from the Figure 3.29 Hydrogen concentration increases with both voltage and height increase. Also, in this case they are the same of the oxygen. In Figure 3.29 is reported the graph of the absolute value of the local current density at the Cathode/Electrolyte Interface. A further check of the value obtained for the products O2 and H2 is reported in the final part of the chapter. An additional simulation result, useful to understand water management, is linked to water distribution in the cathodic compartment. Obviously, the cathode water is not involved in the half-reaction, it is used only to keep the cell at the desired

temperature. Figure 3.31 shows water concentration distribution for different operating conditions.

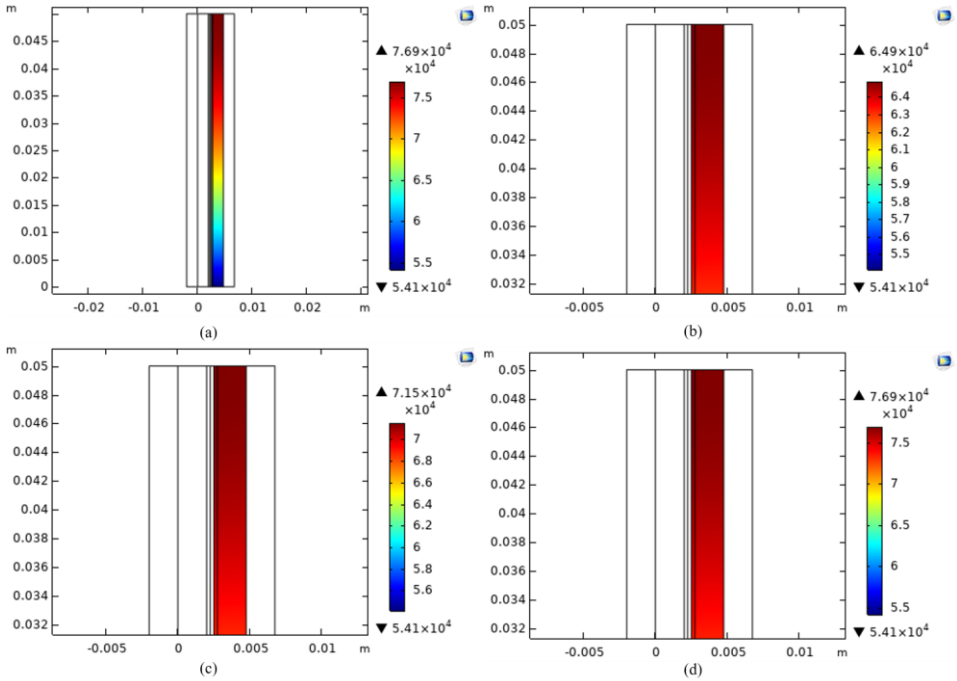

Figure 3.31 $C_{H2O,cat}$ distribution in [mol/m3] along the cathodic channel.

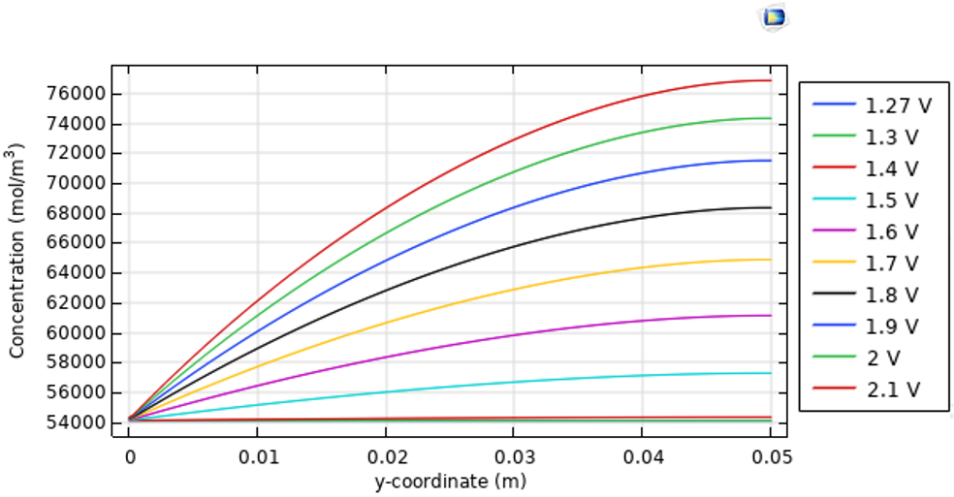

Figure 3.32 $C_{H2O,cat}$ distribution in at Electrode/Electrolyte interface.

The screenshots reported in Figure 3.31 shows that water concentration at cathode side increases even if it is not involved in the reaction. It increases both with the height of the channel and with the applied voltage as shown in Figure 3.32,

this is due to the water transport across the membrane, water crosses the membrane from anodic compartment to the cathodic one and due to electroosmotic drag, diffusion and pressure phenomena. In order to properly simulate the operating conditions of the system, the hydraulic pressure contribute was not taken into account since both anodic and cathodic operating pressure was set to the constant value of 10 bar (p_{an}=p_{cat}=10 [bar]).

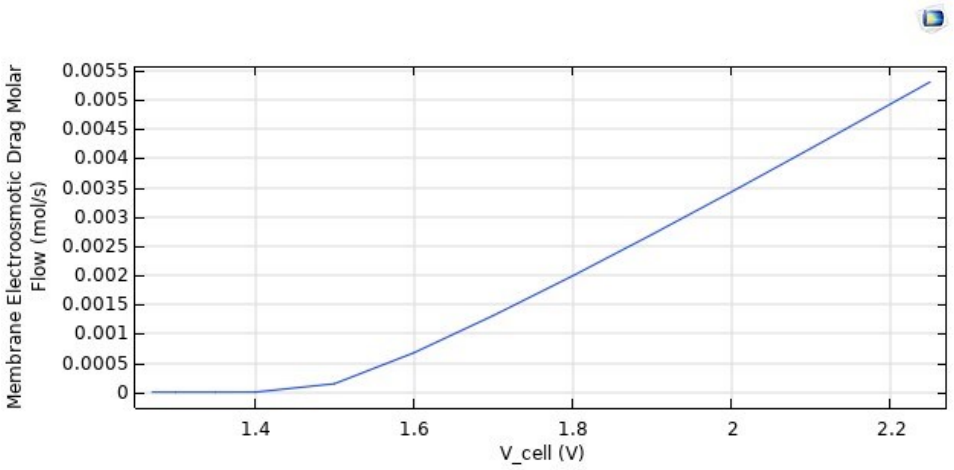

Figure 3.33 Electroosmotic drag contribute to membrane total flow.

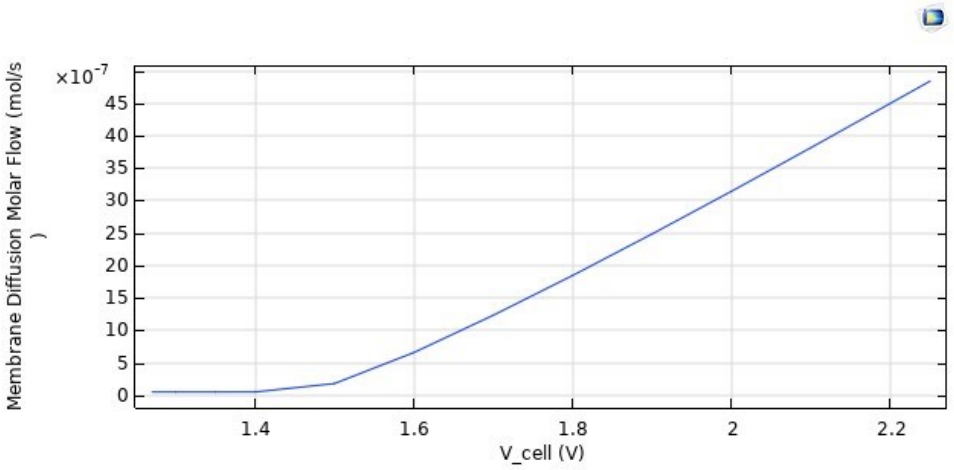

Figure 3.34 Diffusion contribute to membrane total flow.

Considering the diffusion contribute, it assumes higher values near the cathode/electrolyte interface, in the mid-higher part due to the higher concentration gradient.

Since the electro-osmotic contribute is proportional to the local current, most of the membrane total flow is represented by this contribute. Figure 3.33 and Figure 3.34 report the integral values of the two water transport contributes across the membrane for different cell voltage values. Both the contributions are dependent on the anodic local current even if their dependence has different nature. In particular, the electroosmotic one is directly linked to the current while the diffusion one is indirectly linked to the current since the molar water concentration at the anode side undergoes the splitting reaction.

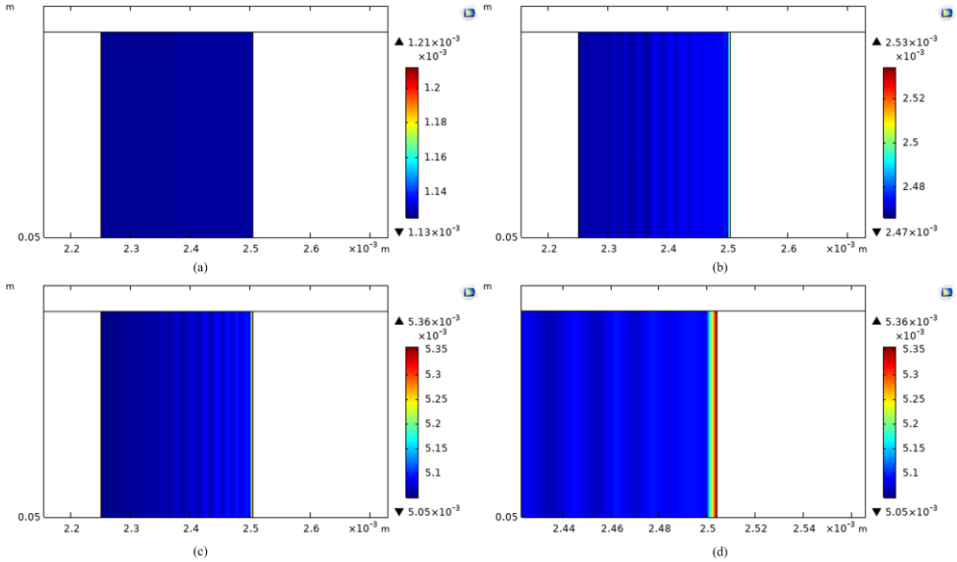

Figure 3.35 2-D water Distribution in the membrane expressed in [mol/s]. Figure (a), (b) and (c) represent water distribution respectively at 1.7, 1.9 and 2.1 [V] while figure (d) show a larger magnification of figure (c).

Is apparent from both Figure 3.33 and Figure 3.34 that the main contribute to the overall flow in the membrane is the electroosmotic one due to its direct dependence on the current. In fact, it is one order of magnitude higher than the diffusion one. In Figure 3.35 is reported the overall water distribution inside the membrane. Figure 3.35 shows an interesting behaviour of water flow rate in the membrane. It is linked to the presence of some waves; these seem to condensate toward the cathodic interface increasing the applied voltage. One of the most important thermodynamic parameters involved in the system is the temperature, it plays a crucial role for the correct operation of the electrolyzer.

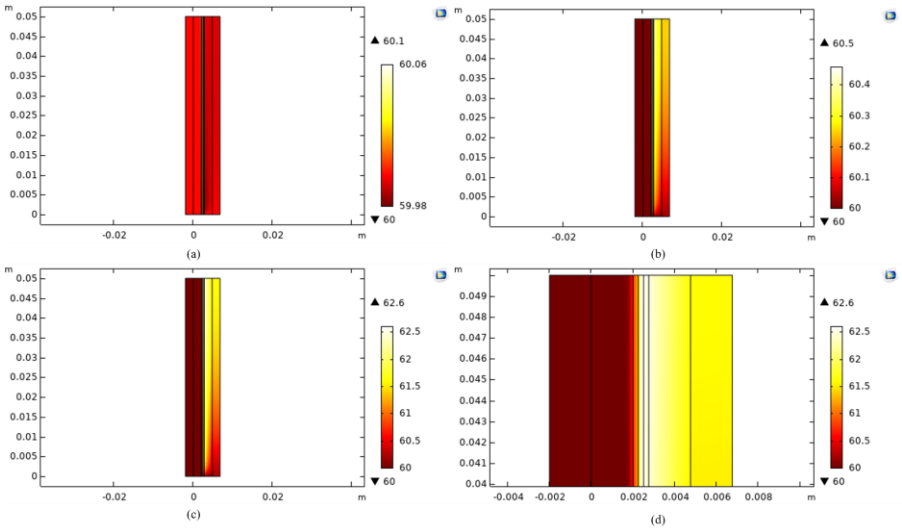

Figure 3.36 2-D Temperature distribution in the membrane expressed in [◦C]. Figure (a), (b) and (c) represent temperature distribution respectively at 1.5, 1.7 and 1.9 [V] while figure (d) shows a larger magnification of figure (c).

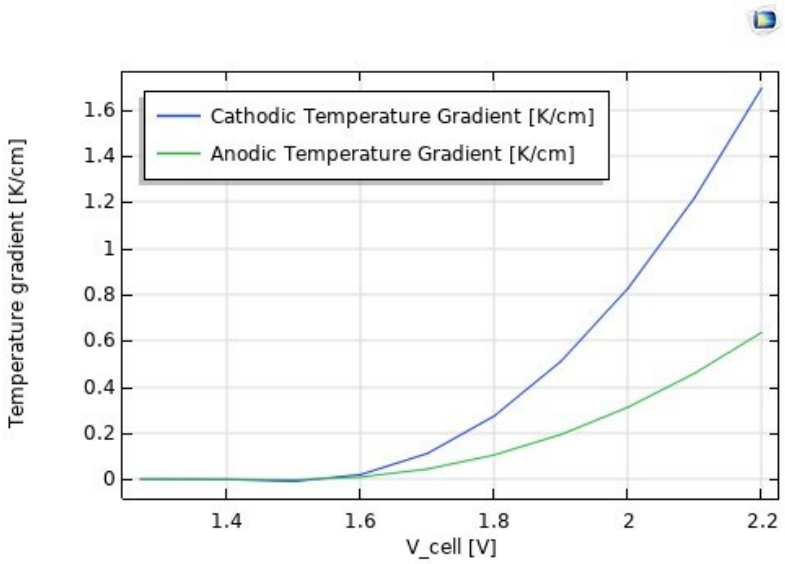

Figure 3.37 Temperature Gradients at both membrane/electrolyte interfaces.

Figure 3.36 shows the temperature distribution for different values of applied voltage. As can be observed, the cathodic part results hotter respect to the anode side, this is mainly due lower water flow in the cathodic compartment respect to the anodic one but also to the overall heat source. In the Anodic compartment the water flow is able to keep the Temperature almost constant except for the porous anode, due to the presence of the reaction sites. Figure 3.37 exhibits the

temperature gradients that the mixtures undergo crossing the channels. It is apparent that the cathodic part has a higher temperature gradient since the water flow rate in the cathodic compartment is lower respect to the anodic one. In the following graphs the Temperature profiles at Anode/Electrolyte Interface and Cathode/Electrolyte Interface are reported:

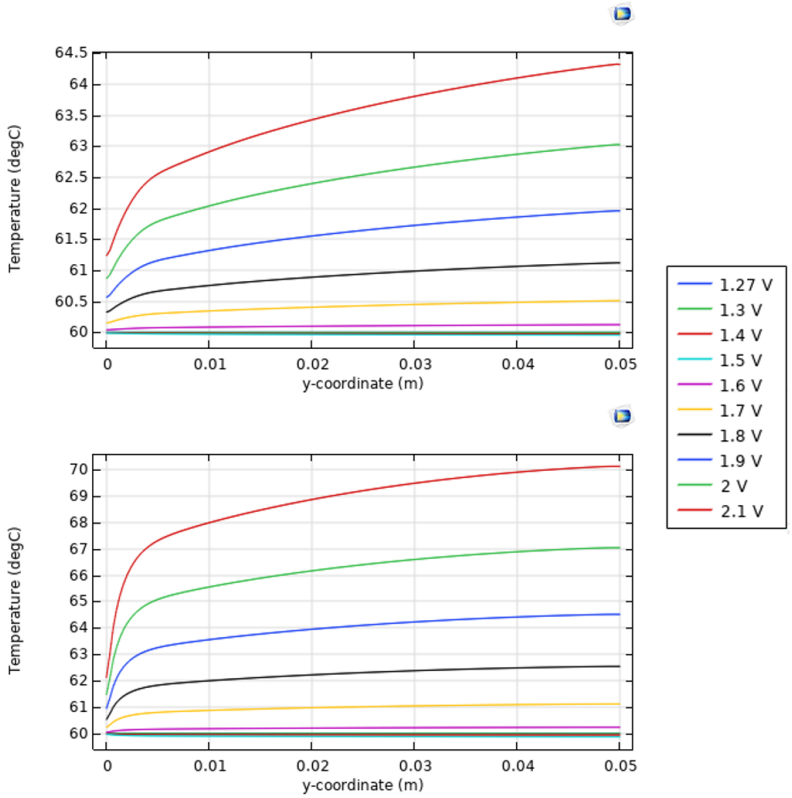

Figure 3.38 Temperature profiles at membrane/electrolyte interface. Figure (a) shows the anodic part while figure (b) shows the cathodic one

Figure 3.38 shows the temperature profiles of the mixtures at the interfaces, further validating the temperature gradients behaviour while also showing the dependence on the vertical coordinate. Finally, to attest the feasibility of the model, it is appropriate to understand the limiting current since it is a performance indicator for gas-evolving electrochemical devices. The limiting current of the model was investigated considering the impact of the diffusion processes in the voltage rise. It was observed that additional onset of voltage appears due to transport phenomena. Figure 3.39 shows the complete polarization curve, as can be observed the maximum allowable current is around [A/cm2].

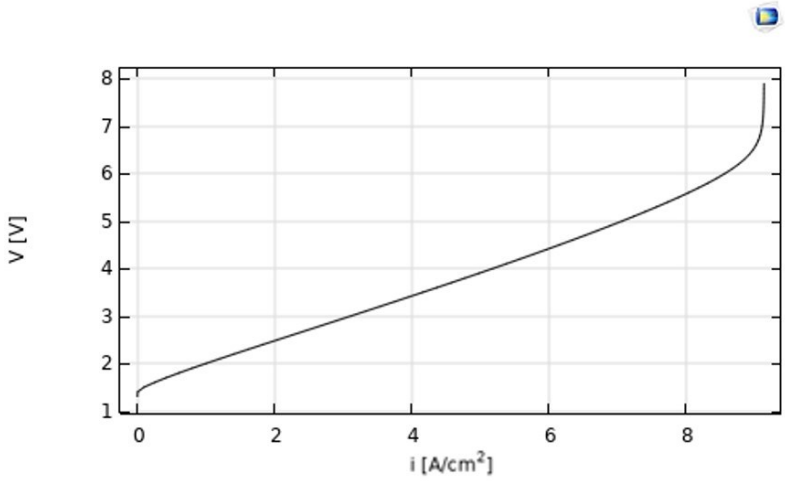

Figure 3.39 Polarization until i_{lim} = 9.84 [A/cm2].

3.2.9.3. 3D Single-phase Laminar flow model

The need of a 3-D model is significant to understand the differences with the other ones due to the change in geometry, especially regarding the hydrogen production compartment. Thus, in this subsection, the main results extracted from the 3-D model are discussed and analyzed.

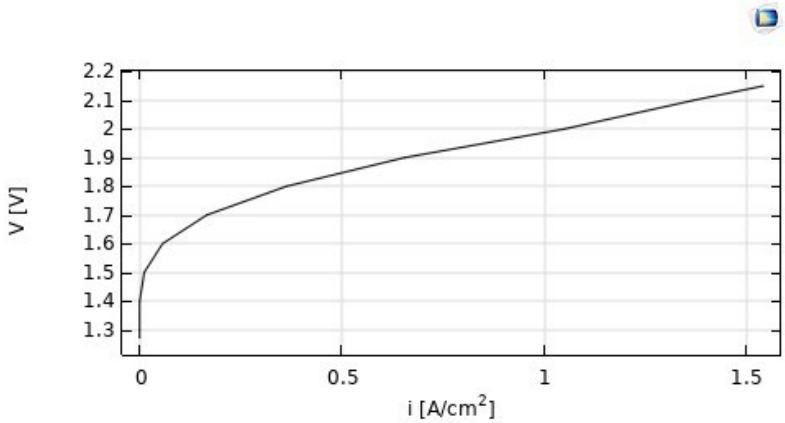

Figure 3.40 Polarization 3-D.

It is worth to say that the main goal of the model is to extract the polarization curve, so for computational reasons, the 3-D model was not implemented as the previous models and some parameters were set as constant values. Figure 3.40 reports the characteristic Polarization curve is reported considering a constant temperature of 60 [˚C] and constant pressure of 10 [bar]. Figure 3.41 shows voltage

distribution of the entire cell at OCV condition while Figure 3.41 and Figure 3.42 show voltage and current density distributions for different values of voltage.

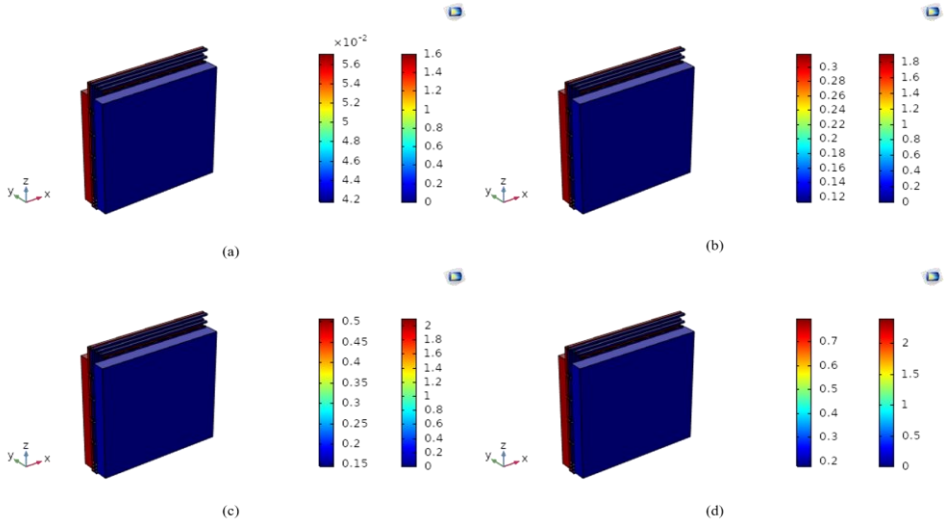

Figure 3.41 Screenshots of the voltage distribution in the entire cell at OCV. Figure (a), (b), (c) and (d) show voltage distributions in the cell at 1.6, 1.9, 2.1 and 2.4 [V]. The first legend is referred to the electrolyte potential while the second to the overall cell.

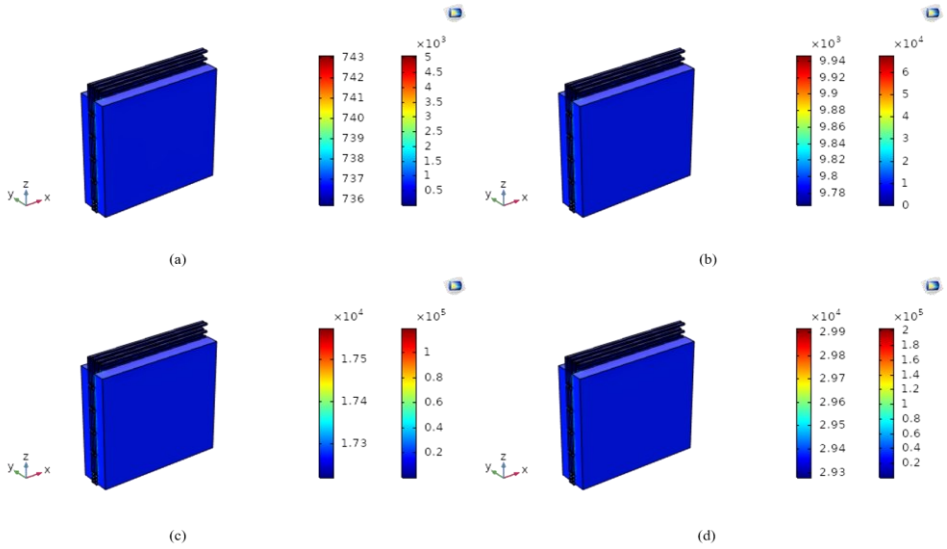

Figure 3.42 Screenshots of the current magnitude distribution in the entire cell. Figure(a), (b), (c) and (d) show current distributions in the cell at 1.5, 1.7, 1.7 and 1.9 [V]. The first legend is referred to the electrolyte current density while the second to the overall cell.

Regarding Hydrogen distribution, Figure 3.43 shows 3-D distribution of hydrogen both in the porous electrodes and channels. As can be observed, hydrogen production increases with the z-coordinate (height) increase while it is constant along the other two directions. Considering the maximum numerical values of hydrogen concentration, they are thicker in the higher part of the porous electrode. Also, the final part of channel presents high values of hydrogen concentration showing the increase of concentration along the triple serpentine. Figure 3.44 shows hydrogen distributions for different values of cell voltage along xz plane.

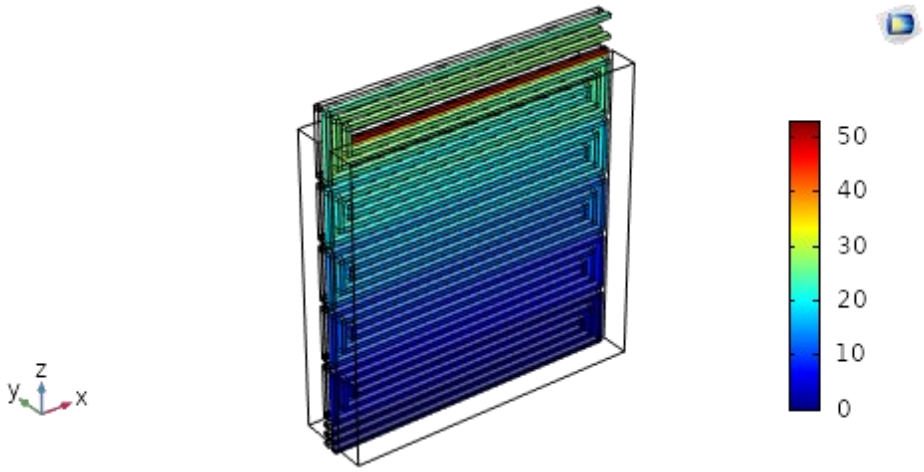

Figure 3.43 3-D H2 distribution in the cathodic compartment at 1.8 [V].

Figure 3.45 shows the parametric plot of H2 concentration at the cathode/membrane interface versus the z-coordinate (height). Through this figure, the influence of the triple serpentine flow field pattern can be caught: hydrogen concentration presents some ripples related to the presence of the characteristic curves of the serpentine that cannot be caught with the previous 2-D simulations.

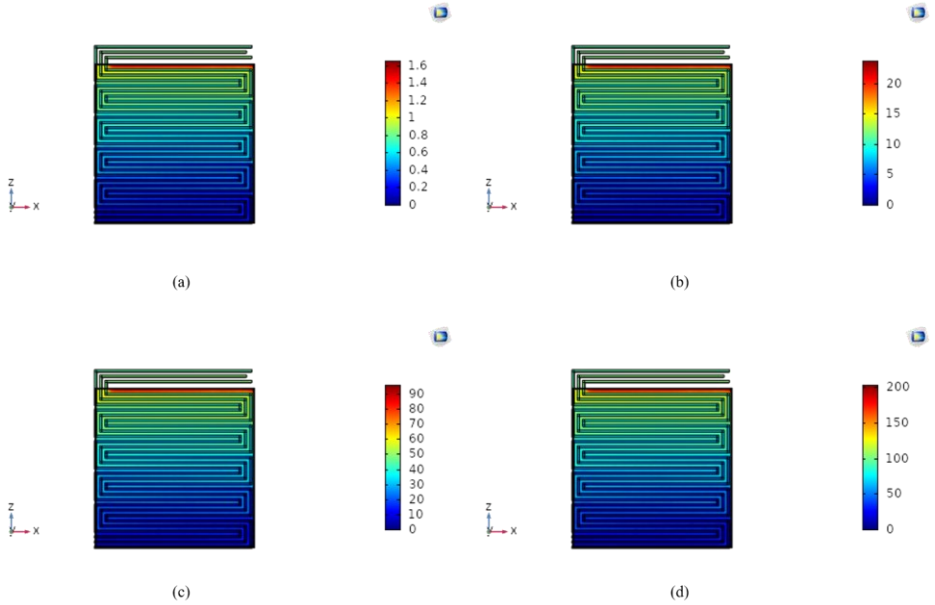

Figure 3.44 Screenshots of H2 distribution in the cathodic compartment. Figure (a), (b), (c) and (d) show H2 distributions in [mol/m3] with cell voltage set to 1.5, 1.7, 1.9 and 2.1 [V].

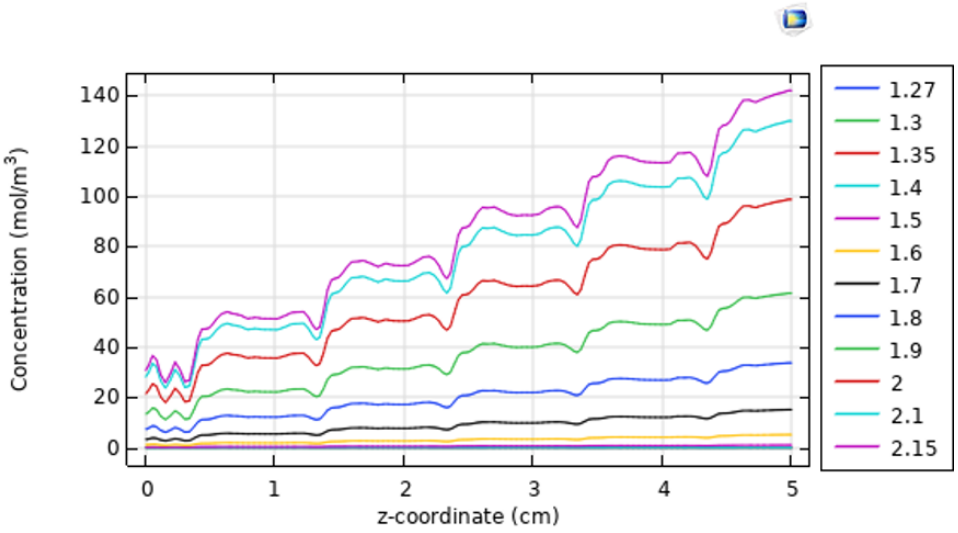

Figure 3.45 H2 distribution in the cathode/electrolyte interface for different values of cell voltage.

3.2.9.4. 2D Multi-phase Turbulent Flow Model

In this subsection the main results of the multi-phase approach are discussed. Bubbles' impact in electrochemical process is a relevant phenomenon that must be

carefully taken under consideration. During this treatment, bubbles influence will be considered through the gaseous volume fraction. The first important result needed to validate the choice of the k − ω Turbulent Model is reported in Figure 3.46, it shows the surface plot of Reynolds Number for both phases along the Anodic channel:

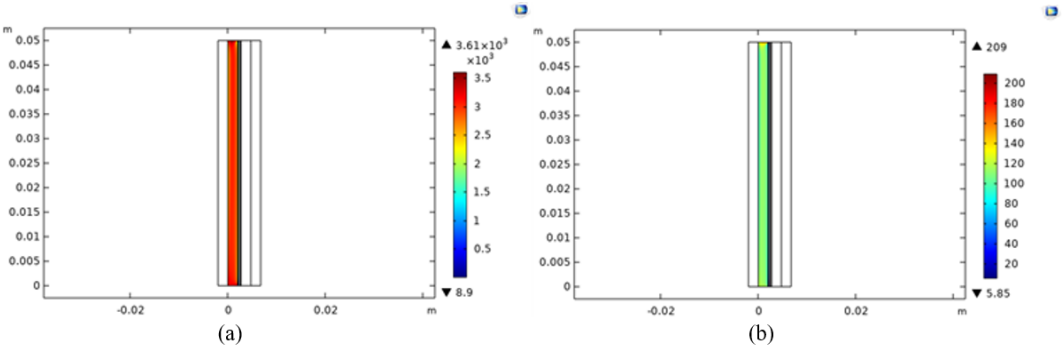

Figure 3.46 Reynolds Number distribution in the anodic channel. Figure (a) shows Re number for the liquid phase (H2O) while Figure (b) shows Re number for the gaseous one (O2).

The liquid phase presents high Re values for the most part of the channel while the gaseous phase presents lower values. Thus, as suggested by Ito et al [87] the flow can be considered as "T_L", turbulent for liquid phase and laminar for the gas phase.

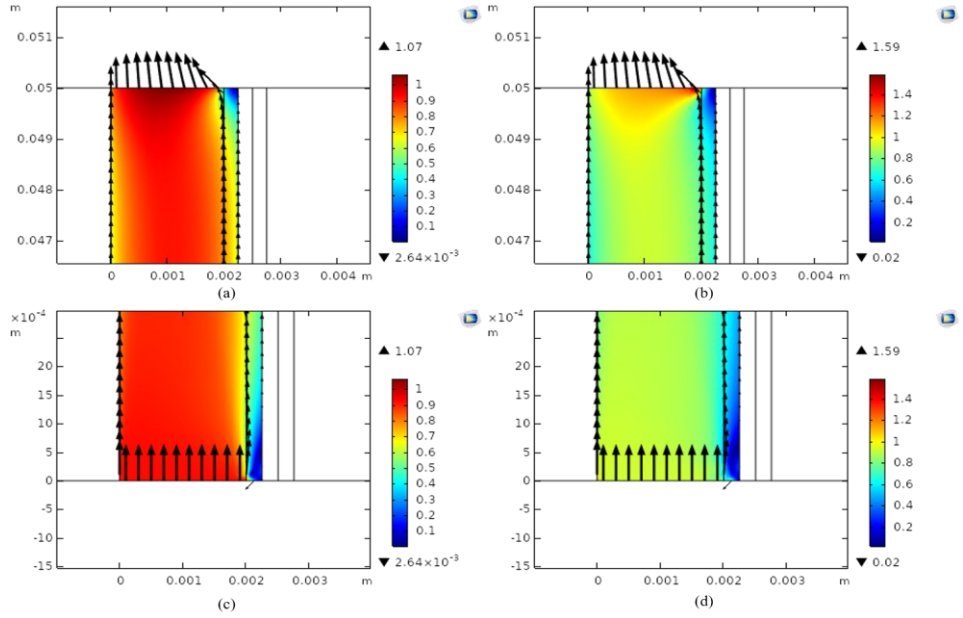

Figure 3.47 Inlet Velocity profiles in the anodic channel inlet. Figure (a) shows the liquid phase velocity (H2O) while Figure (b) shows the gaseous one (O2).

The Reynolds values confirm the choice of the turbulent model to solve the Navier-Stokes Equations since the fluid flow is the pseudo-turbulent region, 2000 < Re < 3000. Figure 3.47 reports the surface plots of the velocity distributions in the inlet and outlet part of the channel for both O2 and H2O. Figure 3.47 shows the influence of the gaseous phase in the channel. Near the channel inlet, next to the interface with the electrolyte, there is a zone in which the velocity direction is reversed indicating the presence of a little vortex. The interaction between fluid flow and bubbles, transfer momentum to the fluid flow creating oscillations on the velocity average values.

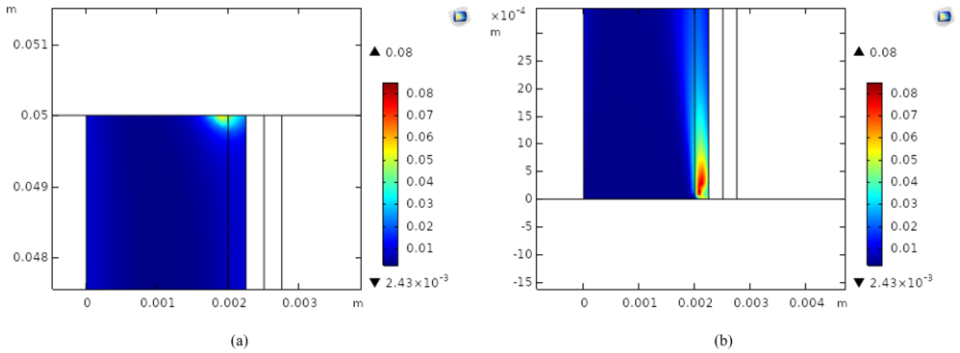

Figure 3.48 Turbulent Kinetic Energy distribution both in the anodic channel inlet (a) and outlet (b) neighbourhood expressed in [m2/s2].

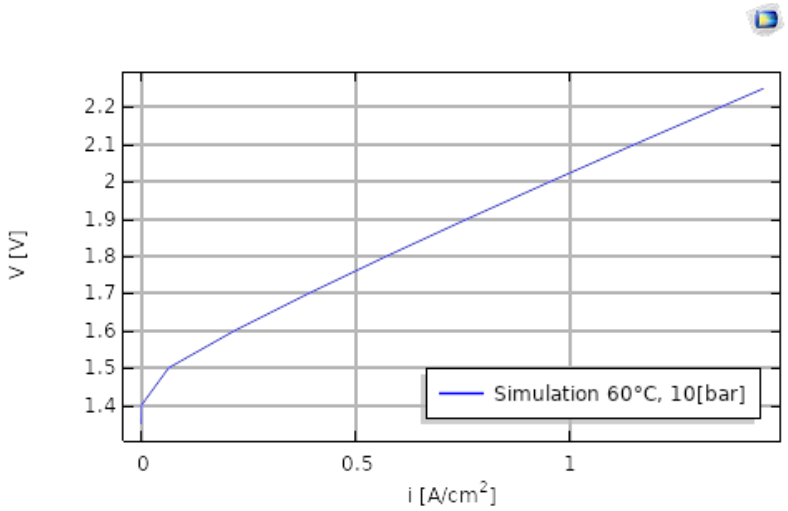

Figure 3.49 Polarization Curve at T = 60 [°C] and p = 10 [bar].

The 2-D distributions reported in Figure 3.48 confirm that the fluctuations are very high in the eddy neighbourhood. It is observable, from Figure (a) and (b), that the exit velocity assumes the highest values for both phases, one possible

reason can be the boundary conditions utilised for the simulation combined with shrinkage of the section. In this case there is no presence of eddies but some fluctuating components in the velocity field are still present. These are located near the top right corner, as can be seen from the Turbulent Kinetic Energy 2-D plot showed in Figure 3.48. To better understand the simulation results, it is useful to report the polarization curve of the corresponding simulation, Figure 3.49 shows the characteristic curve. The conditions in which the data are extracted from the software were set the same to the previous case, to better compare the two models.

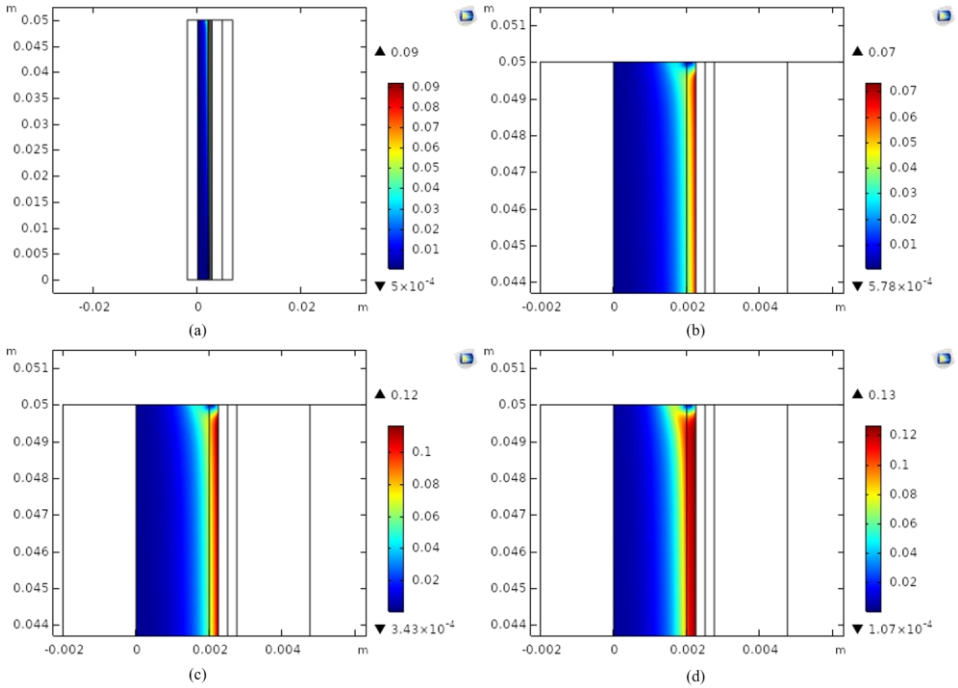

Figure 3.50 O2 Volume fraction in the anodic channel. Figure (a) shows the complete volume fraction distribution at V = 2 [V], while Figure (b), (C) and (d) show O2 Volume fraction in th top part of the anodic compartment respectively at 1.6, 2.1, 2.25

Another interesting result that can be discussed in the new model is the Volume fraction trends of the gaseous phase, O2. It is the major indicator of the presence of the dissolved bubbles in the channel. As can be seen from Figure 3.50, the highest values are located near the electrode/electrolyte interface, the place in which the electrochemical reactions take place. The volume fraction increases both with the increase of the applied voltage and height of the channel.

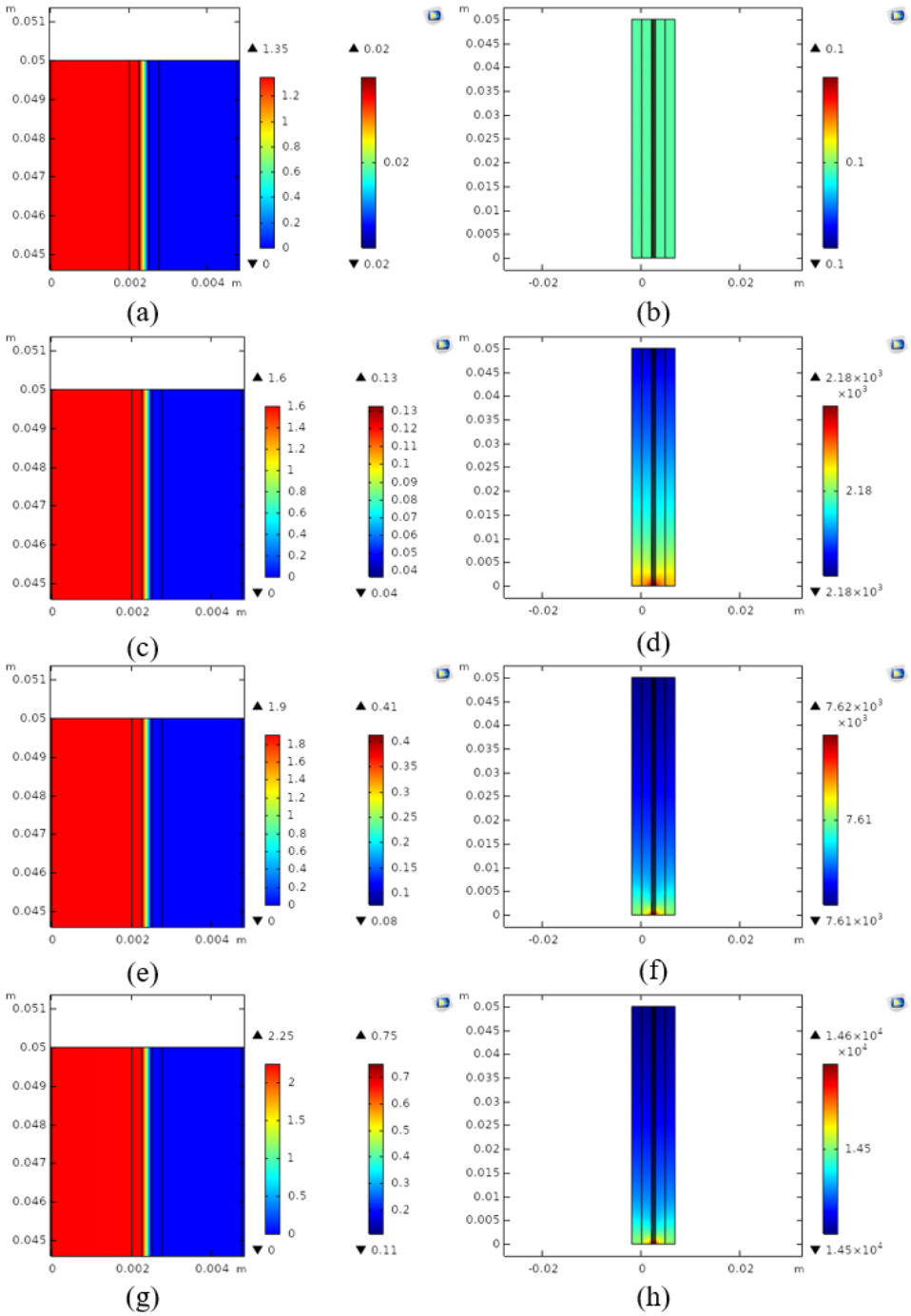

Figure 3.51 Voltage and Current Density 2-D snapshots from Multiphysics Simulation for different input voltages expressed respectively in in [V] and in [A/cm2]. Figure (a) and (b) is obtained selecting OCV condition from the parametric study while the pairs (c)-(d), (e)-(f), (g)-(h) snapshots are extracted selecting respectively 1.6, 1.9 and 2.25 Volts.

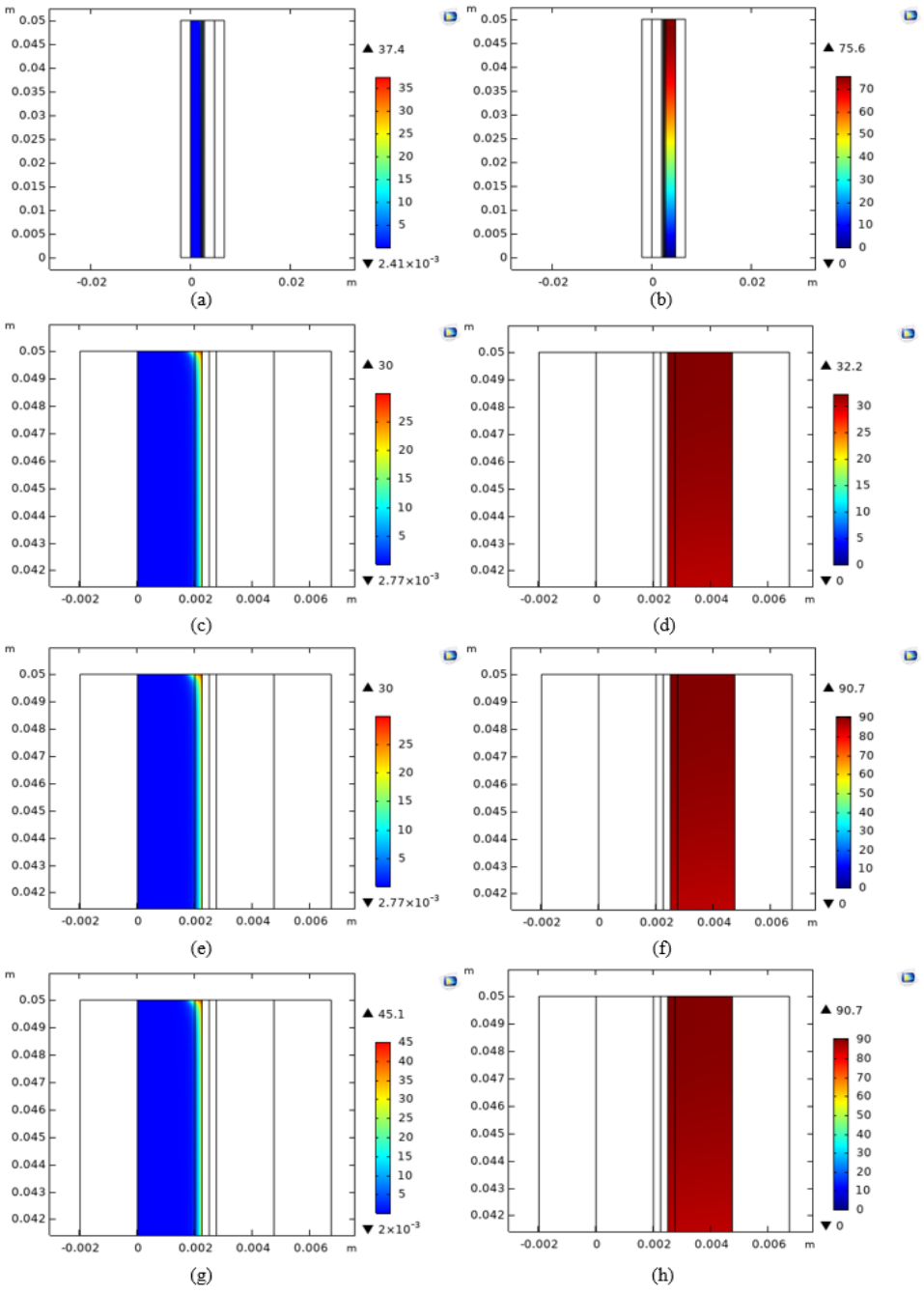

Figure 3.52 C_{O2} and C_{H2} 2-D snapshots from Multiphysics Simulation for different input voltages expressed in in [mol/m3]. Figure (a) and (b) shows the complete distribution of the two species along the cell with an input voltage of 2 [V] while the pairs (c)-(d) ,(e)-(f) and (g)-(h) show the top part of the channel at respectively 1.6, 1.9 and 2.1 Volts.

Figure 3.51 reports voltage and current 2-D distributions in the electrodes. The same considerations discussed in the previous section can be extended also to this case, even if there are some differences with respect to the previous 2-D model results. As can be seen from Figure 3.51, the values of current results almost the same due to the overlapping of the two characteristic curves that is inevitable since the two curves were fitted on the same experimental measurements.

Figure 3.52 shows that the concentration distributions for both of the two gaseous phases. Also in this case, the shape is the same for different applied voltages in the cell, even if there are some differences respect to the results through the single phase model reported in Figure 3.23. Comparing the two distributions, both the shape and the values, the last appears to be different due to the influence of the bubbles in the anodic channel that tend to decrease the amount of reactions at membrane interface. The difference in the two distributions is also linked to the different velocity fields, in fact it is one important factor for the momentum transfer during reactions. Figure 3.53 shows the O2 concentration at the interface for different values of voltage. Comparing the new profiles with those obtained in the previous simulation, shown in Figure 3.24, can be observed that O2 molar concentration presents two peaks at the inlet and outlet of the anodic channel. Moreover, the numerical values obtained are lower respect to the case of Figure 3.24 due to the presence of the above-mentioned differences linked both to the velocity profiles of liquid and gaseous phase, shown in Figure 3.47, but also to the Local current at the anodic interface. The last is decreased due to the bubble presence as can be shown in Figure 3.55.

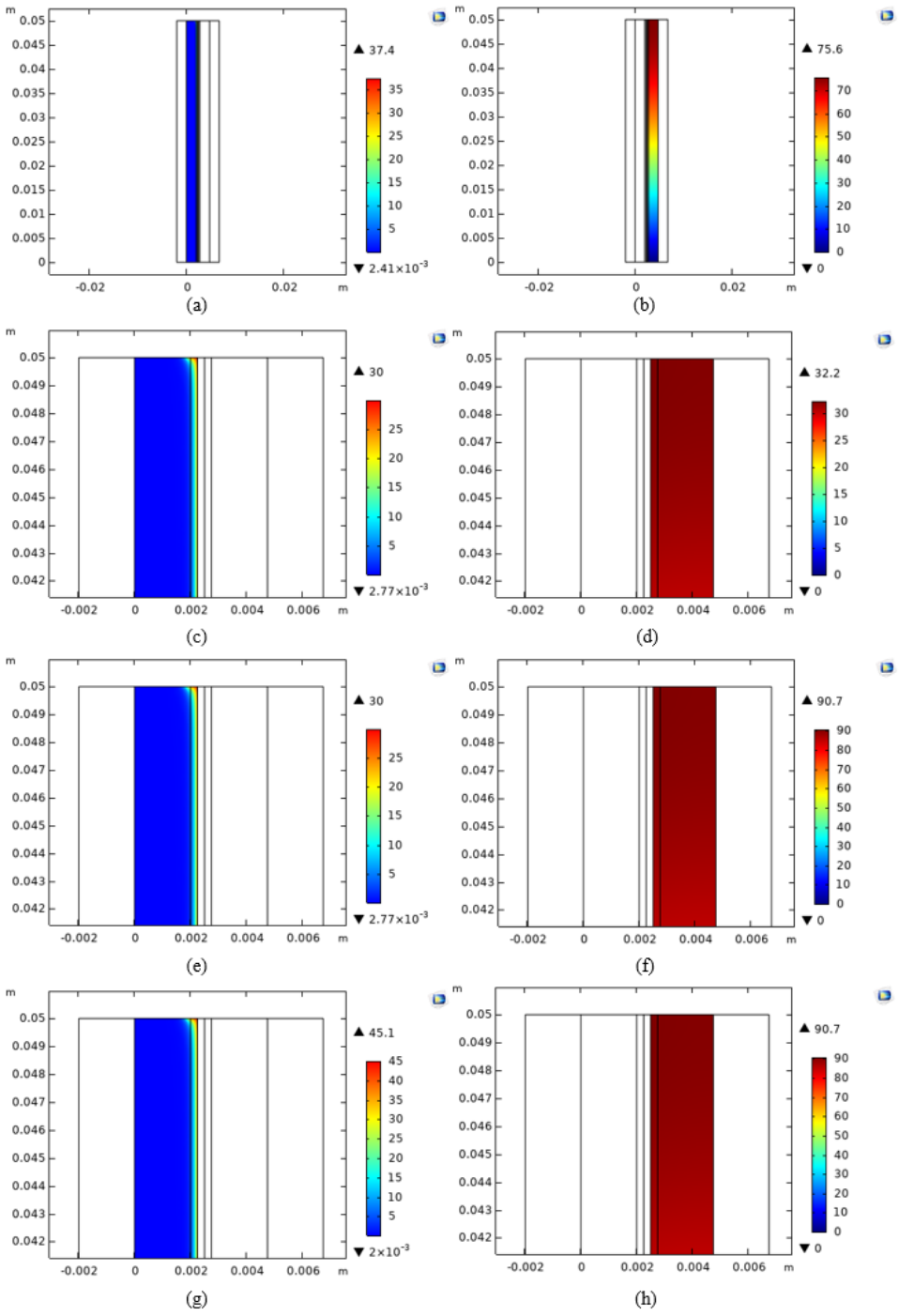

Figure 3.53 C_{O2} evolution along the y-direction for different values of voltage.

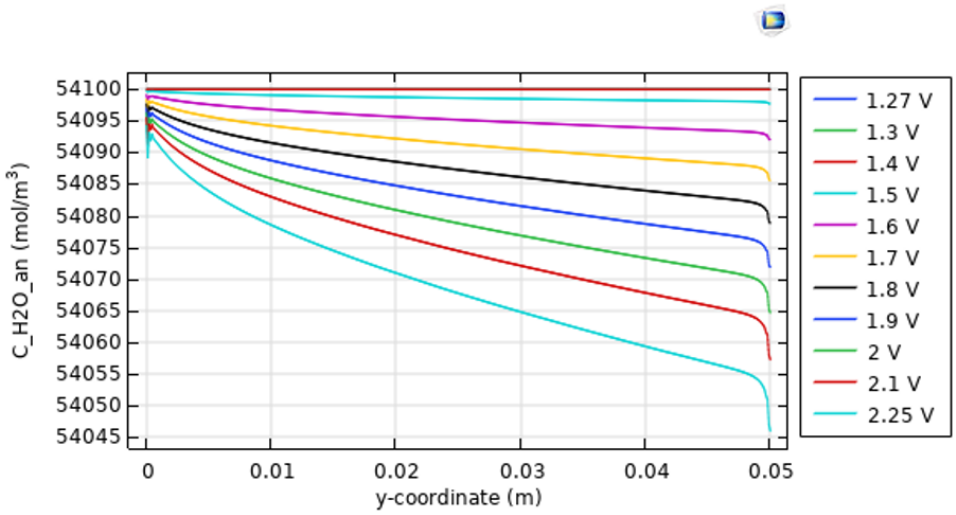

Figure 3.54 C_{O2} evolution along the y-direction of different values of voltage.

Obviously, also in this case, the H2O concentration decreases since it is the dual specie respect to the O2, Figure 3.54 shows the H2O trends at anode/membrane interface. Regarding H2 side, it seems indirectly affected by the presence of bubbles in the anodic compartment. Although the shape is almost equal to those showed both in Figure 3.23 and Figure 3.28, the values are decreased by more than 15%. The main reason can be linked to the fact that the bubbles presence decreases the local current at cathode in absolute value as well, as is shown in Figure 3.57.

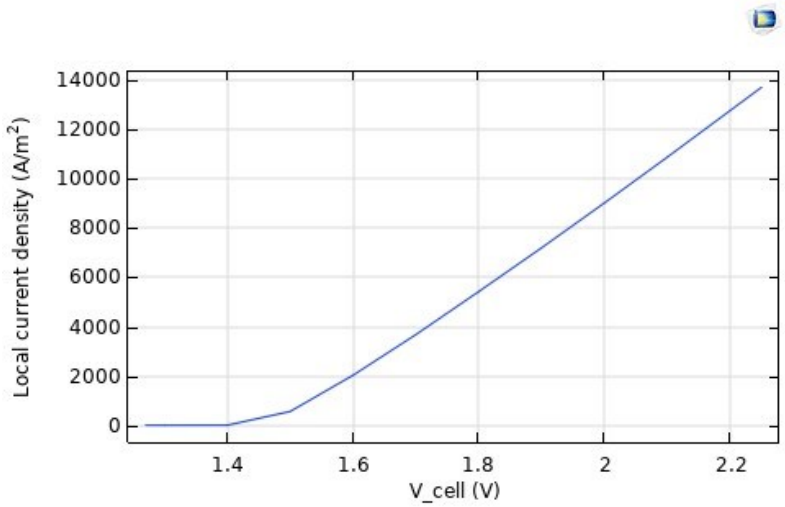

Figure 3.55 $i_{loc,an}$ behaviour along y-direction at anode/membrane interface.

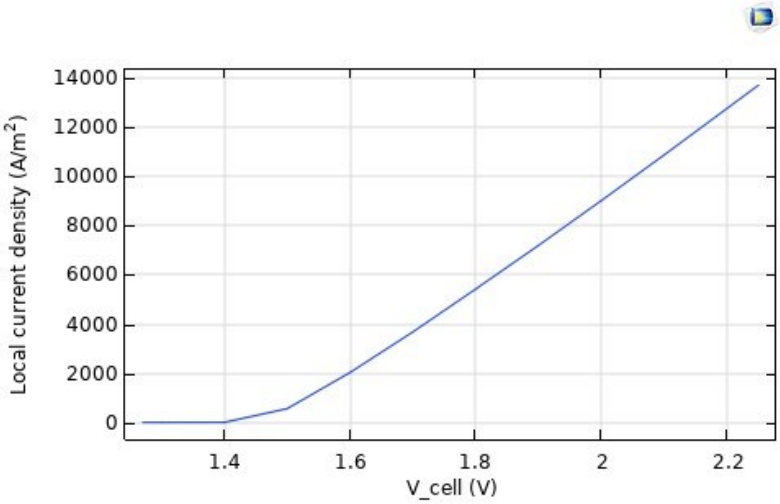

Figure 3.56 C_{H2} evolution along the y-direction for different values of voltage.

Another interesting results that can be discussed regards the cathodic water behaviour at the interface. As can be seen from Figure 3.58 and Figure 3.31, the H2O concentration is almost the same even if is present a little reduction due to the decrease in water transport across the membrane.

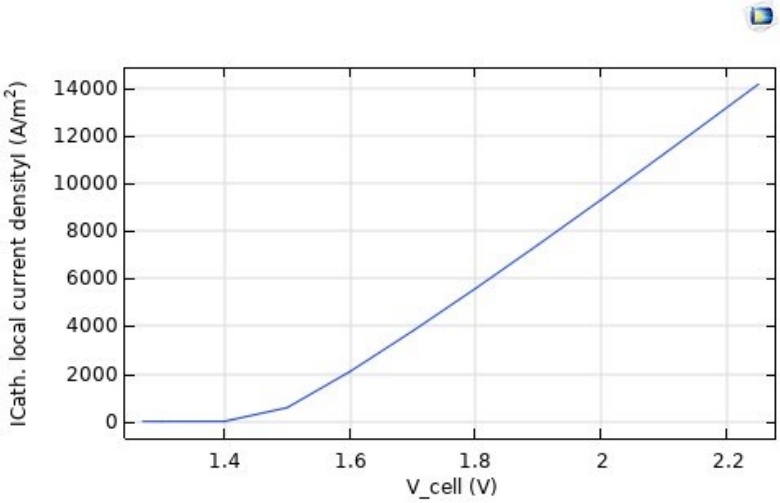

Figure 3.57 $|i_{loc,cat}|$ behaviour along y-direction at anode/membrane interface.

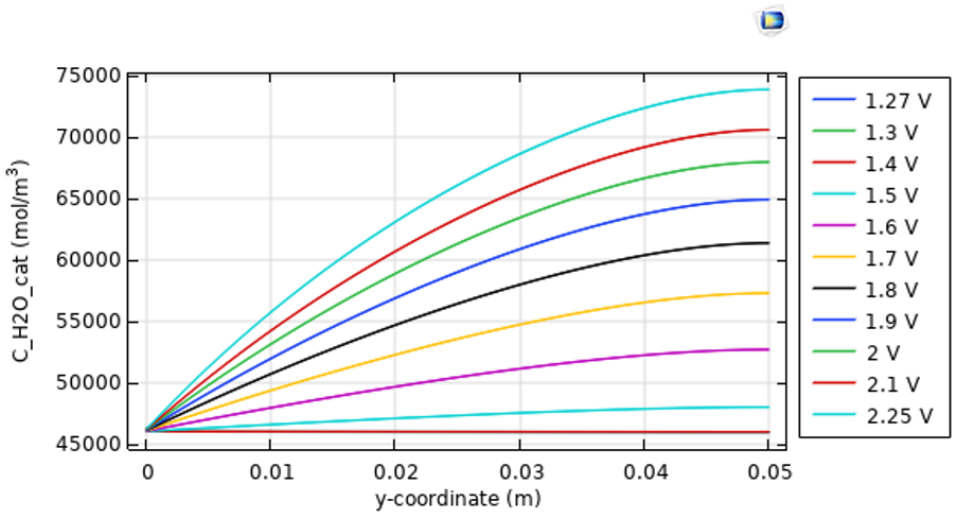

Figure 3.58 C_{H2O} behaviour along y-direction at anode/membrane interface for different values of applied voltage.

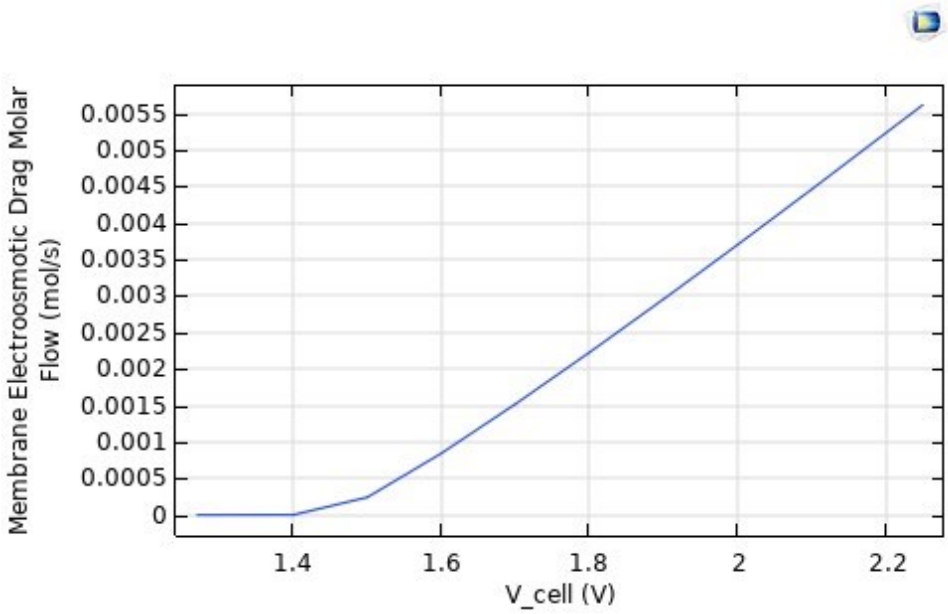

Figure 3.59 C_{H2O} behaviour along y-direction at anode/membrane interface for different values of applied voltage.

As discussed above, water transport across the membrane is reduced since Diffusion contribute is indirectly affected by the presence of bubbles, due to the reduction of H2O concentrations at both interfaces. In general, this reduction does not affect the overall contribute due to the bigger weight of the Electroosmotic drag contribute that results practically the same due to the same currents involved.

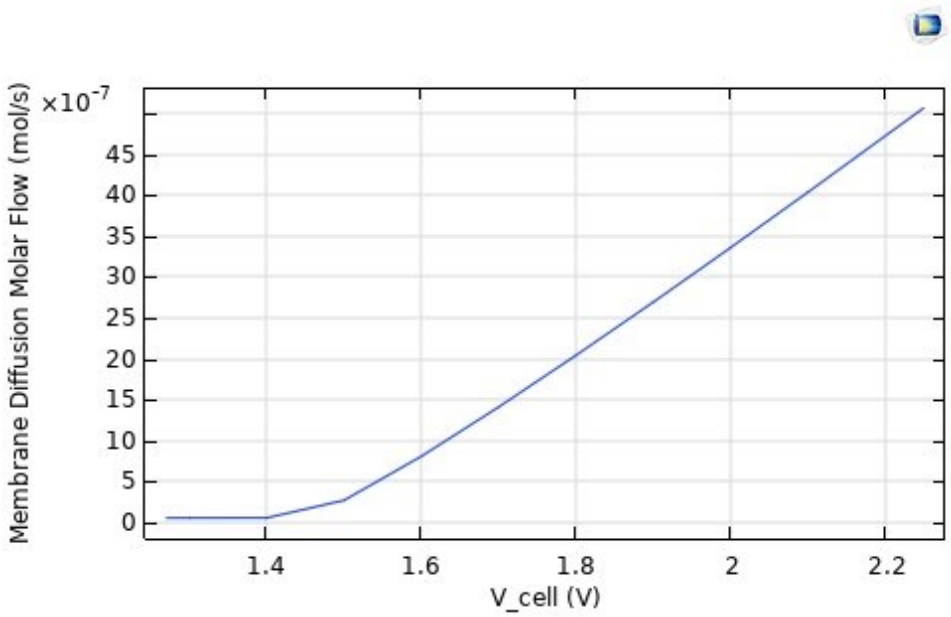

Figure 3.60 C_{H2O} behaviour along y-direction at anode/membrane interface for different values of applied voltage.

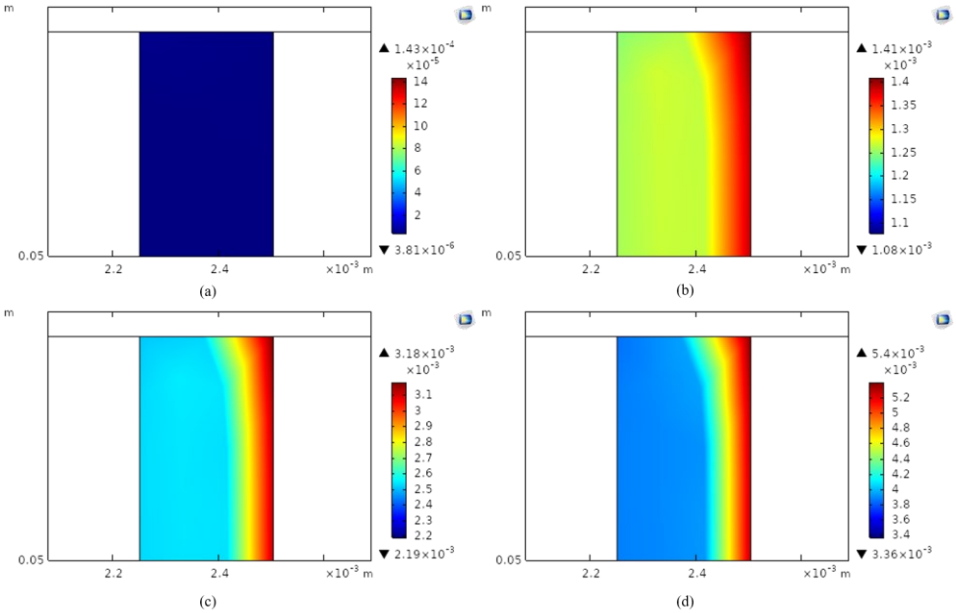

Figure 3.61 2-D water Distribution in the membrane expressed in [mol/s]. Figure (a), (b), (c) and (d) represent water distribution respectively at 1.35, 1.7, 1.9 and 2.1 [V] .

Figure 3.59 and Figure 3.60 show the two contributes while Figure 3.61 shows the 2-D concentration distribution of water in the membrane. Comparing the

new water distribution with the previous one, shown in Figure 3.34, there are some similar aspects such as the quantity of water inside the membrane and the wavy distribution, even if, the last aspect appears to be sharper respect to the previous simulation. Also in this case, one of the most results useful to understand the thermodynamic behaviour of the system is the temperature because it plays a crucial role for the correct operation of the electrolyzer. The temperature profile at the interface of the membrane and electrolyte is another indication for a better analysis. As it can be seen , the temperature in the cathodic part is higher than the anodic one as it is shown in Figure 3.62.

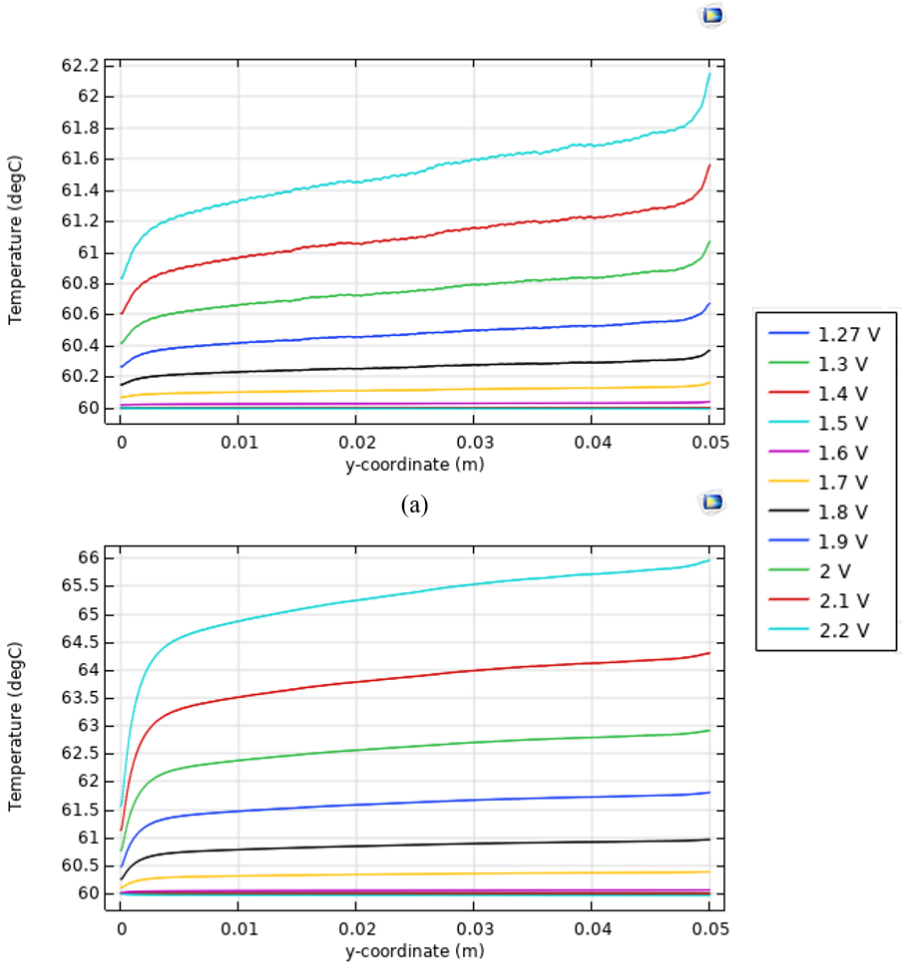

(a)

(b)

Figure 3.62 Temperature profiles at membrane/electrolyte interface. Figure (a) shows the profiles referred to the anodic part while figure (b) shows the cathodic ones one.

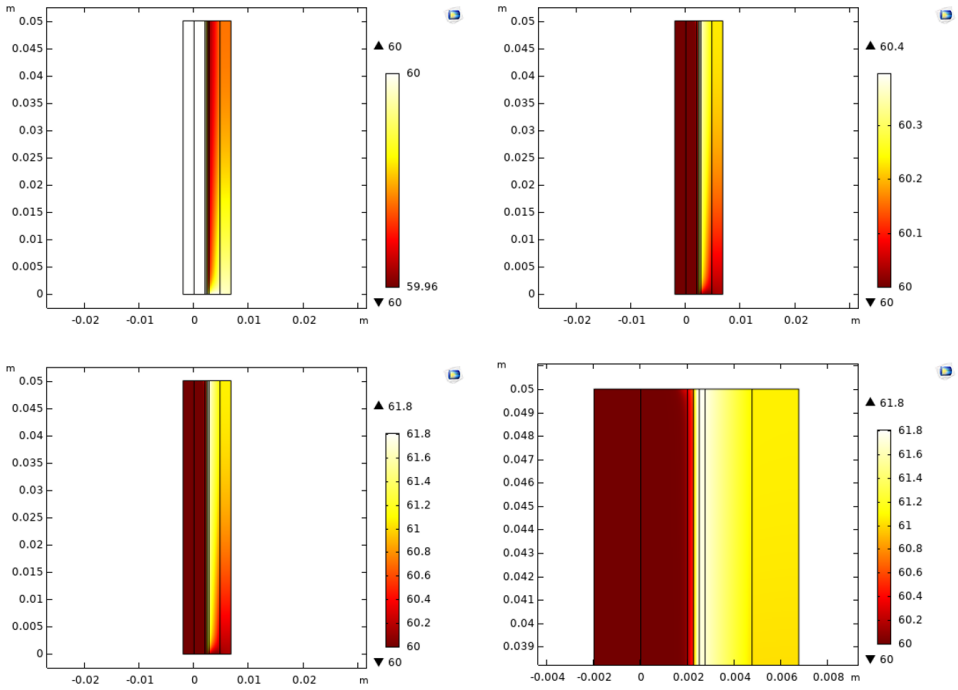

Figure 3.63 2-D Temperature distribution in the membrane expressed in [◦C]. Figure(a), (b) and (c) represent temperature distribution respectively at 1.5, 1.7 and 1.9 [V] while figure (d) shows a larger magnification of figure (c).

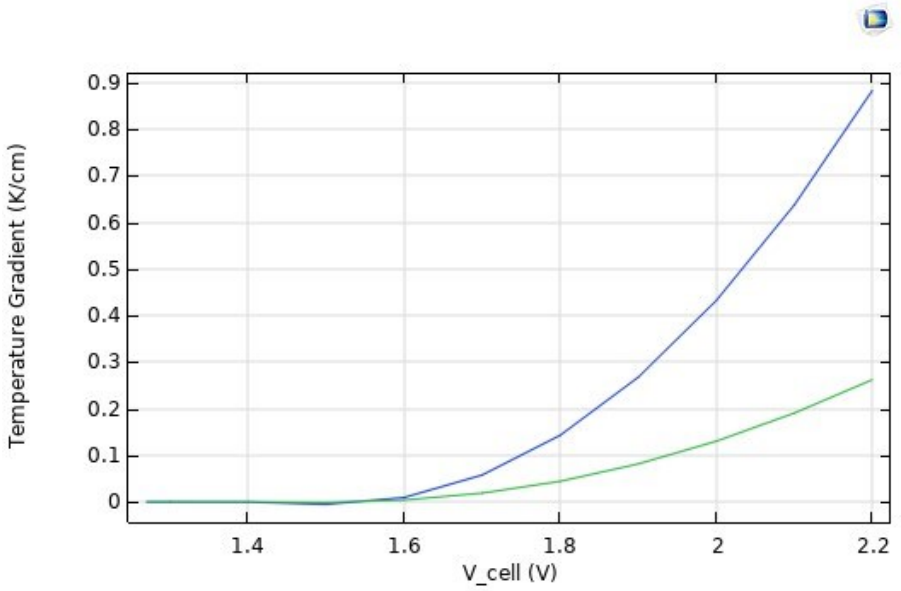

Figure 3.64 Temperature profiles at membrane/electrolyte interface. Figure (a) shows the profiles referred to the anodic part while figure (b) shows the cathodic ones one.

Figure 3.63 shows the temperature distribution for different values of applied voltage. As can be observed, also in this simulation, the cathodic part results hotter respect to the anode side due to the presence of less water in the compartment. Considering Figure 3.35 the temperature distributions results almost 1 [˚C] lower respect to the previous case due to the lower local current densities involved. Figure 3.64 shows the temperature gradients in both the electrode/membrane interfaces. The higher gradient is in the cathodic interface since the flow rate crossing the channel was set with a lower value respect to the anodic one thus the cooling power is lower.

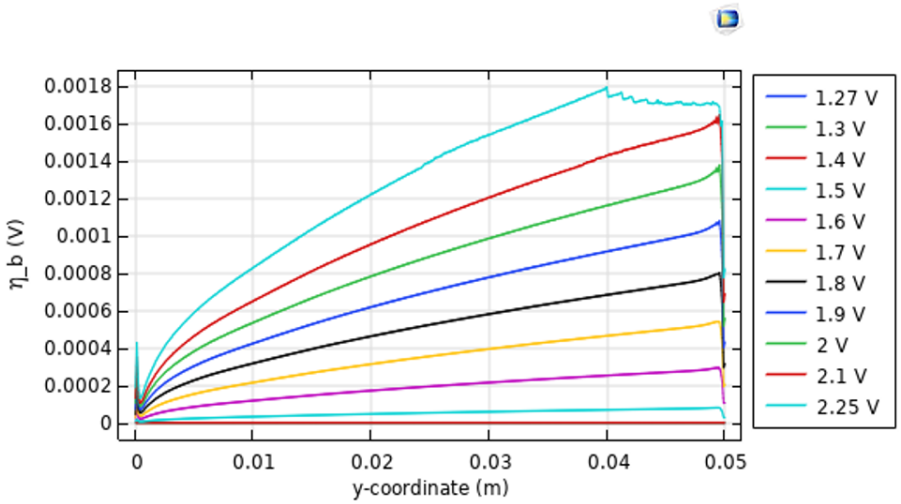

Figure 3.65 Bubble Overpotential.

The goal of the new model is not only related to the analysis of the multi-phase flow itself but also to understand the consequences of the bubble formation. As above mentioned, the bubbles obstruct the pores creating an additional overpotential [86]. The parametric plot shown in Figure 3.65 reports the overpotential vs the y-coordinate for different values of applied voltages. Figure 3.67 shows the Bubble Overpotential integral value along the Electrode/Electrolyte interface versus the applied voltage. A further result, useful to understand the impact of bubbles related to the reduction of the useful electro-active area needed for the splitting reaction is linked to bubble electrode coverage. Figure 3.66 shows the behaviour of bubble volume fraction at electrode for different applied voltages.

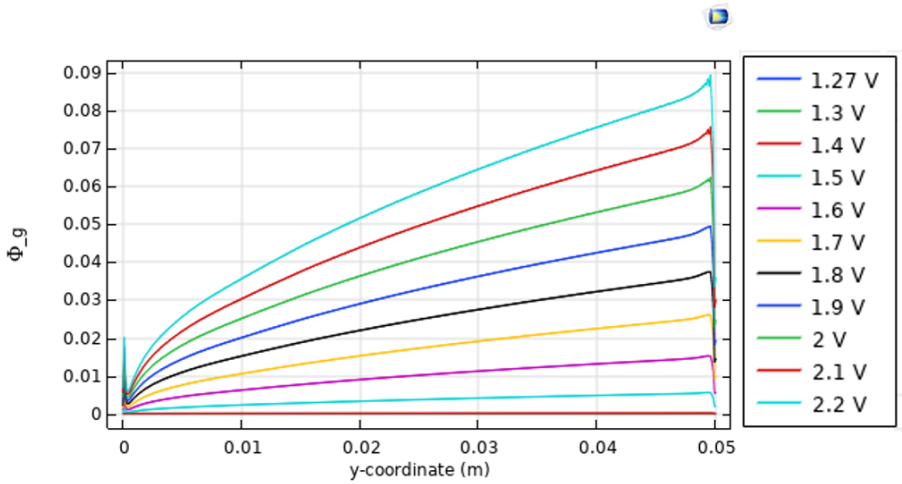

Figure 3.66 Electrode Bubble Coverage.

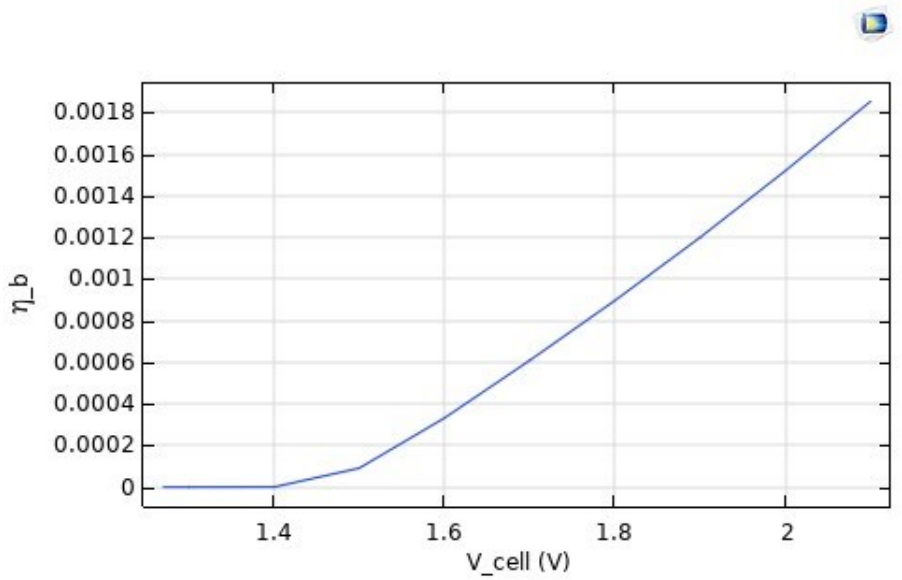

Figure 3.67 Bubble Overpotential.

As can be seen, the shape of the overpotential at electrode is similar to the volume fraction, testifying the strict dependence. The results showed in Figure 3.65, Figure 3.67 and Figure 3.66 were extracted starting from the Gas Volume fraction and applying the formulas presented in section 3.2.5.7. A key result useful to attest the limits of the Multiphase Model is linked to the maximum current density that the model is able to withstand. In order to find the limiting current, another simulation was carried out pushing the input voltage to its highest possible

value. The expectations for the maximum limiting current were linked to the gaseous volume fraction behaviour.

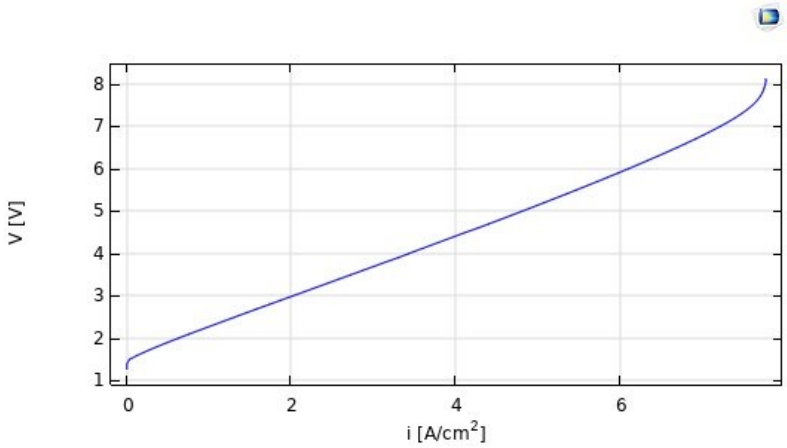

Figure 3.68 Polarization curve until i_{lim} = 8.13 [A/cm2] .

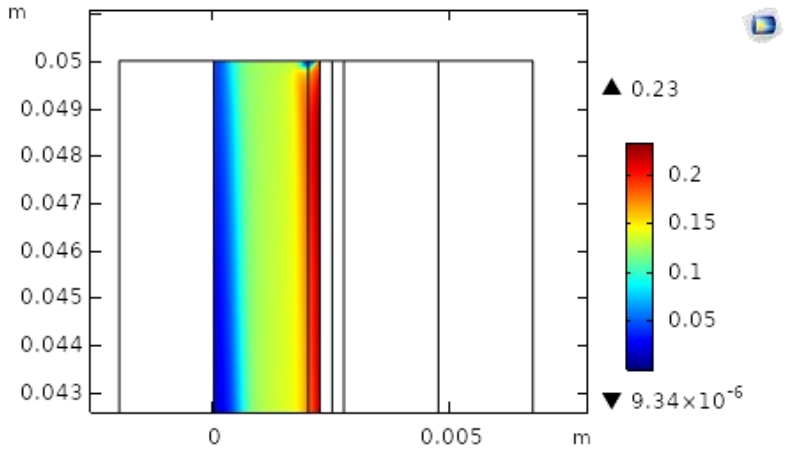

Figure 3.69 O2 volume fraction at i_{lim} = 8.13 [A/cm2] in the top part of the channel.

Since the bubble overpotential is function of the volume fraction, as showed in equations in the section 3.2.5.7. [86] the maximum allowable current is found through the condition $\eta_{bubble} \rightarrow -\infty$, that is true if the bubble volume fraction approaches the value 1. Figure 3.68Figure 3.68 Polarization curve until i_{lim} = 8.13 [A/cm2] . and Figure 3.69 show the polarization curve pushed until i_{lim}=8.13 [A/cm2] and O2 volume fraction distribution in the top part of the channel at i_{lim}=8.13 [A/cm2]. Comparing the limiting current obtained with this Multi-phase approach with the limiting one obtained with the Single phase approach, can be seen that the limiting current results lower thanks to the presence of bubbles that

decrease the concentration of O2 in the bulk flow of the anodic compartment. The parameters used for the Multi-Phase Model were set as the Single-Phase one, that are shown in Table 3.8 parameters list, even if additional parameters were utilised such as: the bubble diameter that was set to the value of 60 [µm] and the turbulent kinetic parameters that were set to their default values.

It is also interesting to have a comparison of the same results with the use of turbulent interface of RANS k-w, used for value of Reynolds number between 2000 and 3000.

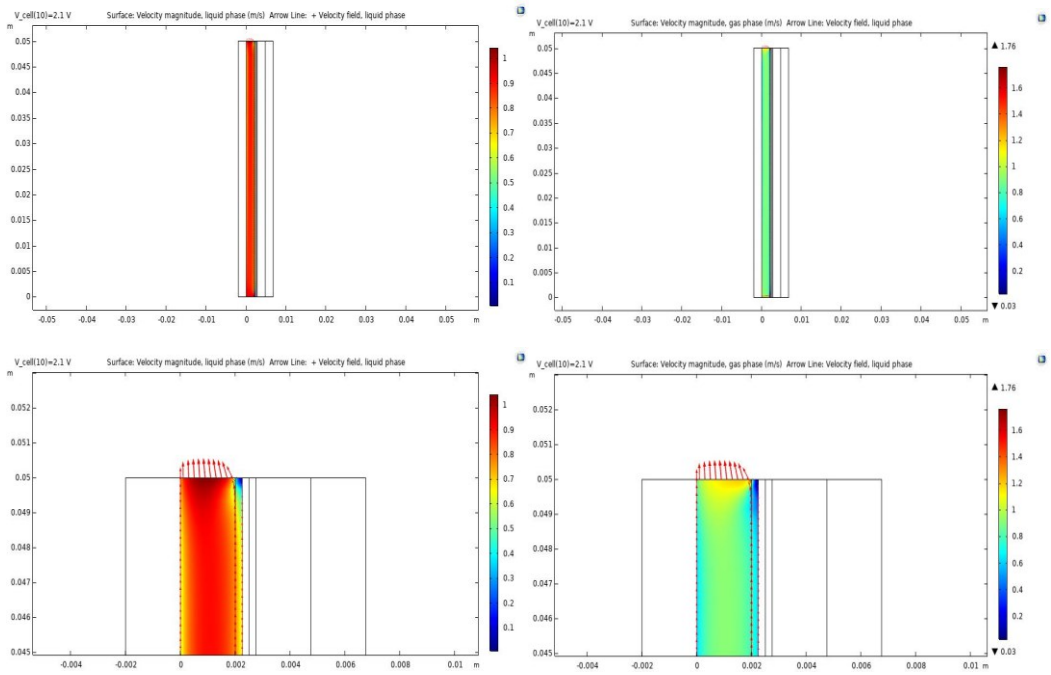

Figure 3.70 Velocity distribution of liquid (left) and gas (right) phase.

In Figure 3.70 the speed of the two phases in the anodic domain, gas phase and liquid one is shown.

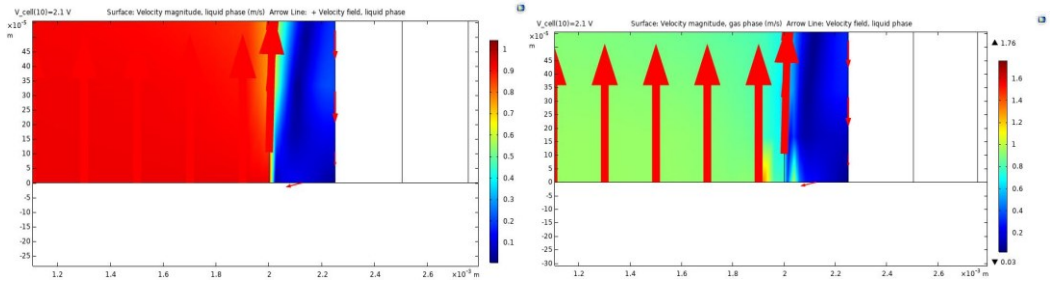

Figure 3.71 Vortex formation

As presented in Figure 3.71 there is a zone at the channel intake, near the electrolyte contact, where the velocity direction is reversed, suggesting the existence of a small vortex, which is due to the turbulences created by the bubbles on the fluid flow.

An important result of the Multiphase model is the fraction of volume occupied by the bubbles, since it is fundamental to understand the size of the bubbles and their impact on the electrodes.

The bubble electrode coverage is important in understanding the influence of bubbles on the lowering of the usable electro-active area required for the splitting process. The behaviour of bubble volume fraction at electrode for various applied voltages is shown:

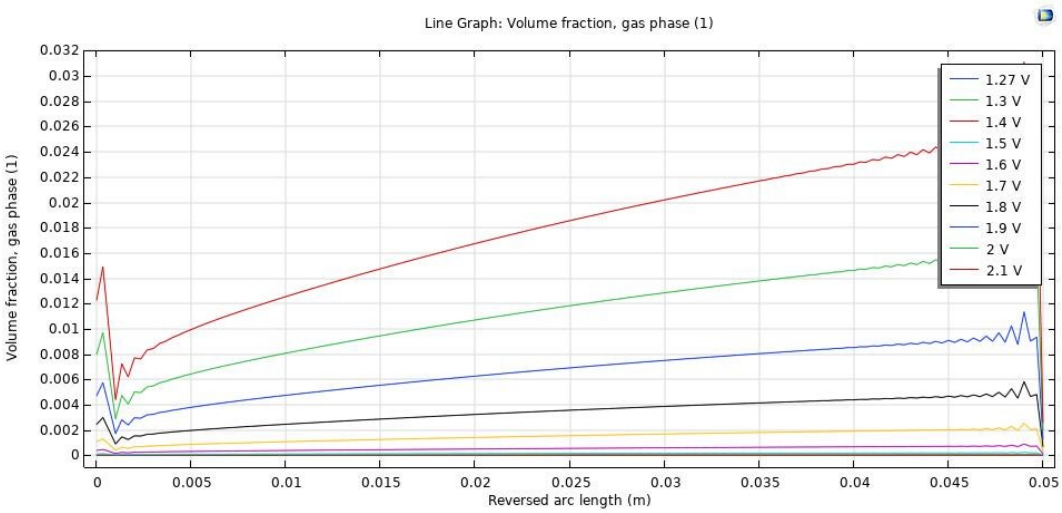

Figure 3.72 Volume fraction in function of the height

The bubbles, clog the pores, resulting in an extra overpotential. Figure 3.73 shows a plot of the overpotential in function of the length of the anodic channel.

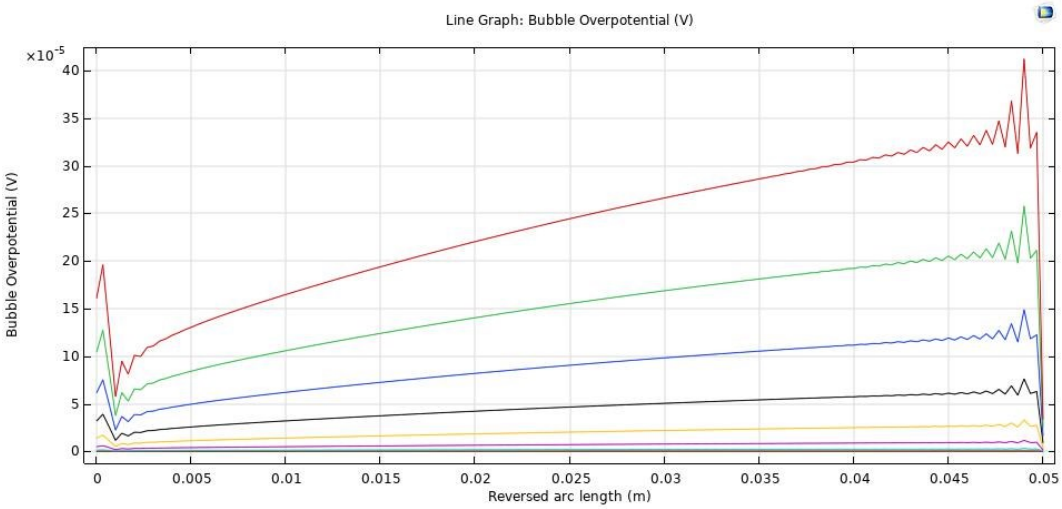

Figure 3.73 Overpotential due to bubble formation

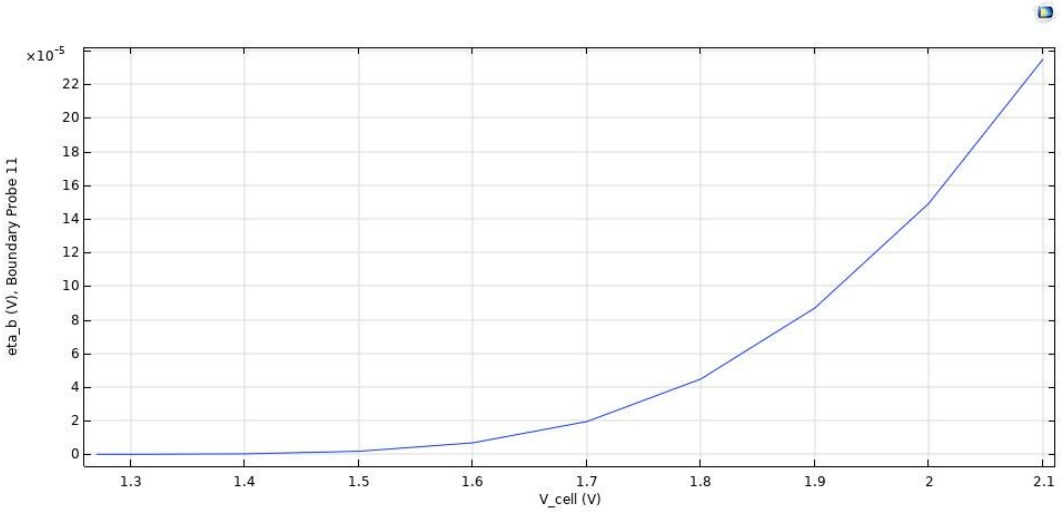

Figure 3.74 Bubble overpotential in function of the applied voltage

The integral value of the Bubble Overpotential at the Electrode/Electrolyte contact vs the applied voltage is shown in Figure 3.74.

3.2.9.5. 3D Single Phase Turbulent Flow Model

In this section, a comparison between 3D turbulent model and 3D laminar model seen above is reported. The turbulent model used in this section is again the RANS k-w. First, a brief report on the turbulent variables is presented.

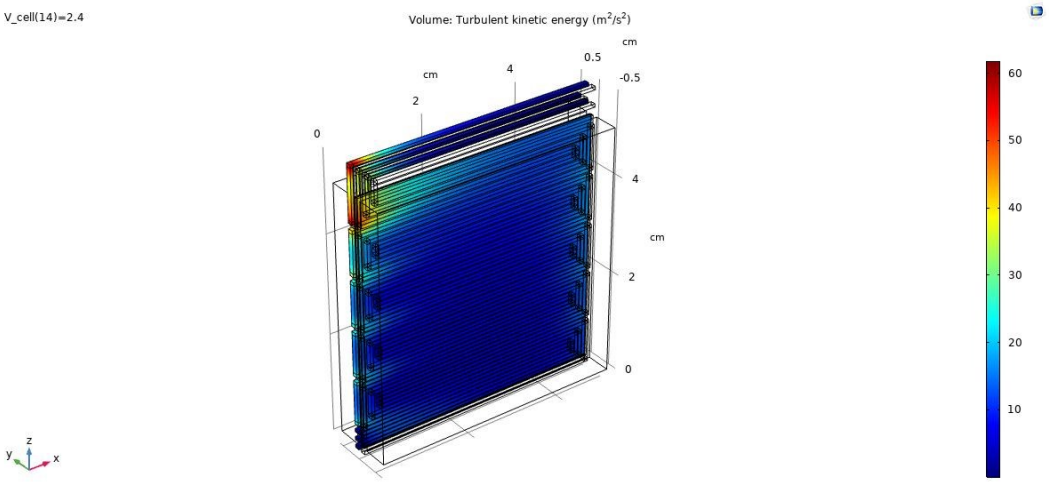

Figure 3.75 Turbulent kinetic energy distribution

Turbulent kinetic energy is simply defined as a mean variation in kinetic energy per unit mass. The root mean square (RMS) fluctuation in the magnitude of the flow velocity is defined as this quantity. The total turbulent kinetic energy is just the sum of the variations in each velocity component since flow velocity is a vector. If the flow was purely laminar along all three orthogonal directions, then the turbulent kinetic energy would be zero, meaning all kinetic energy would be accounted for in laminar flow.

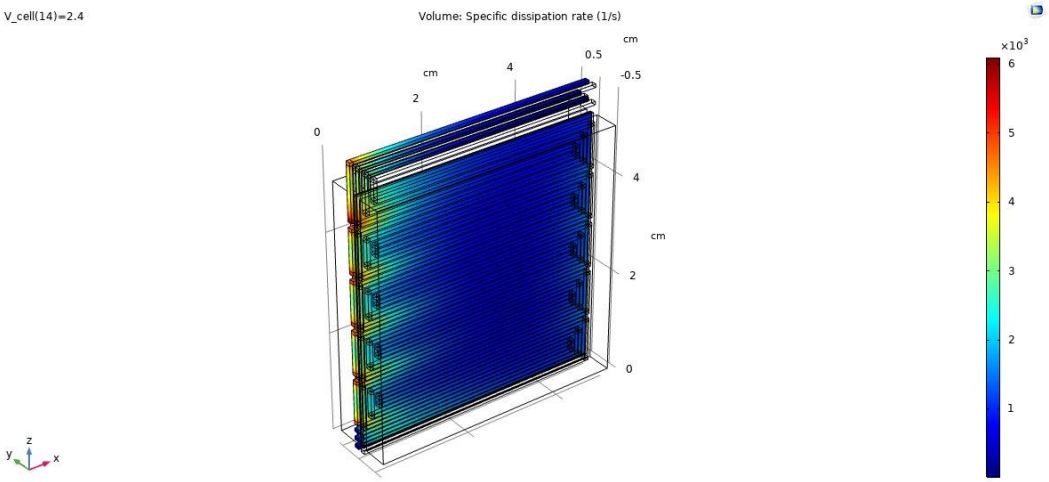

Figure 3.76 Specific dissipation rate distribution

Turbulent flow is made up of eddies of varying sizes, and the size range expands as the Reynolds number rises. Interactional forces between the eddies

cause kinetic energy to cascade down from big to tiny eddies. The energy of the eddies dissipates into heat at a very tiny scale owing to viscous forces. The energy dissipation rate is a parameter that determines how much energy is wasted in a turbulent flow due to viscous forces.

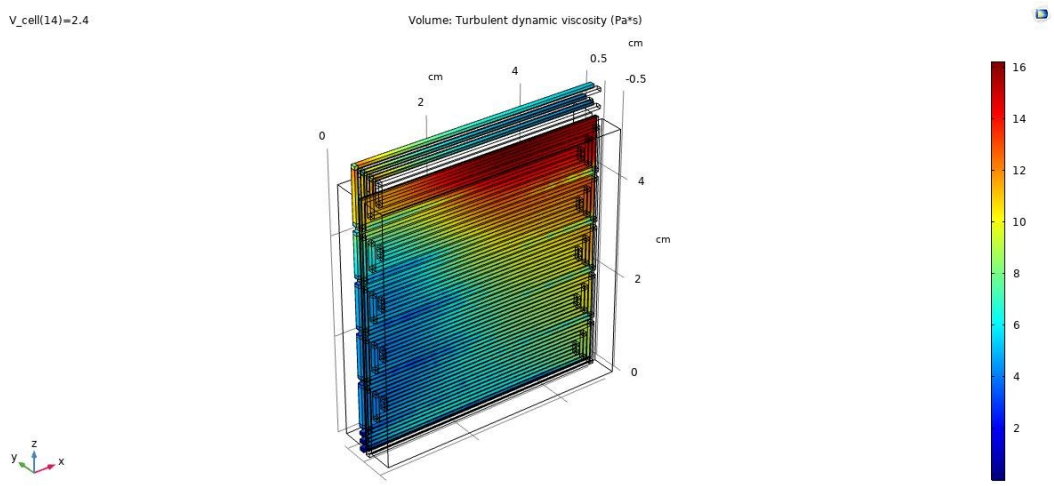

Figure 3.77 Turbulent dynamic viscosity distribution

When the flow is laminar, the sole mechanism for diffusion inside the flow is molecular movements. The metric to quantify this phenomenon is viscosity, which is a diffusion coefficient.

When the flow becomes turbulent, however, the diffusion process is not only done by molecular movements, but also by eddies motions, which are much enhanced. As a result, while utilizing eddy viscosity models to describe turbulence, we must add turbulent viscosity to the molecular viscosity to increase the diffusion coefficient. Both momentum and heat transfer equations will be affected by this coefficient.

3.2.9.6. Differences with laminar model

First difference that can be evaluated from the comparison with the laminar model are the velocity and vorticity magnitude distribution in the anodic channels, where the turbulent RANS model is applied.

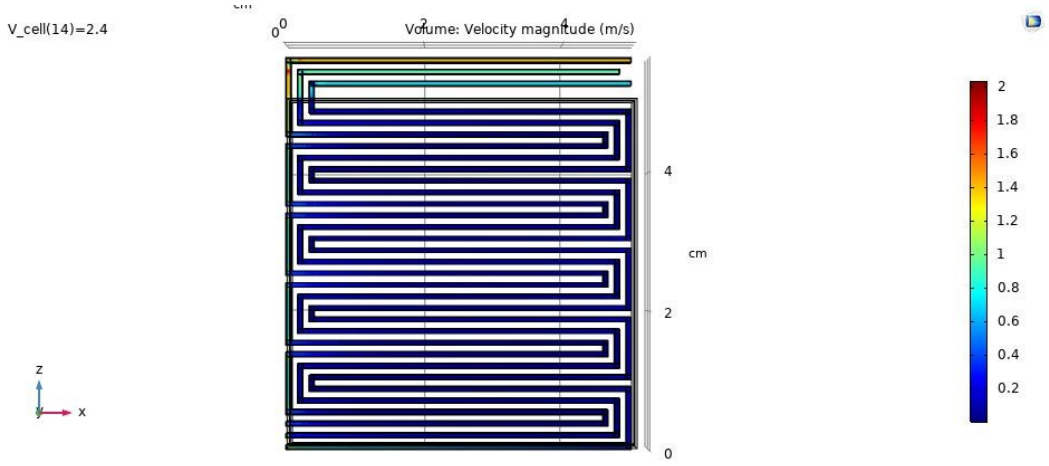

Figure 3.78 Velocity magnitude distribution in turbulent flow model

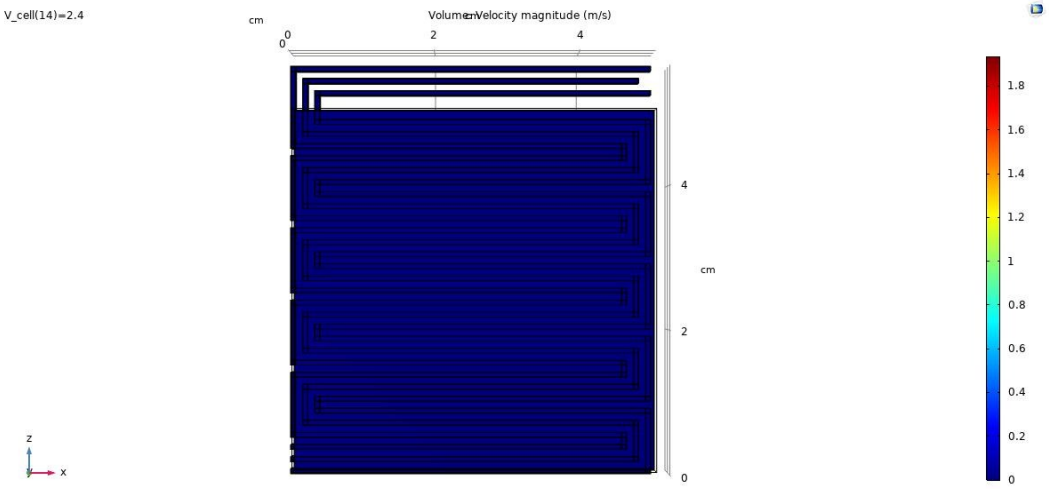

Figure 3.79 Velocity magnitude distribution in laminar flow model

From the comparison between Figure 3.78 and Figure 3.79 it can be noticed that the velocity magnitude is more relevant in the turbulent configuration, especially in proximity of the outlet channels. This is due to the higher amount of kinetic energy in the turbulent flow model and the increase of diffusion processes, caused by the turbulent dynamic viscosity.

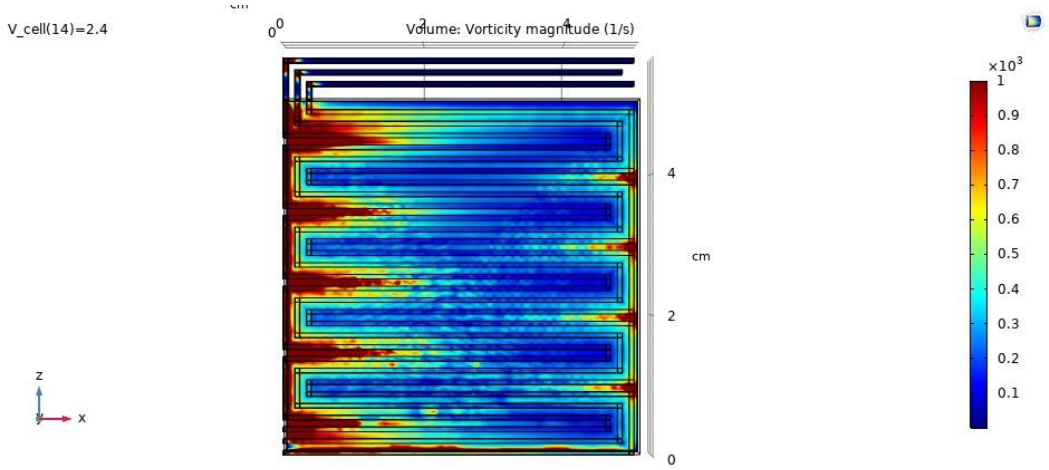

Figure 3.80 Vorticity magnitude distribution in turbulent flow model

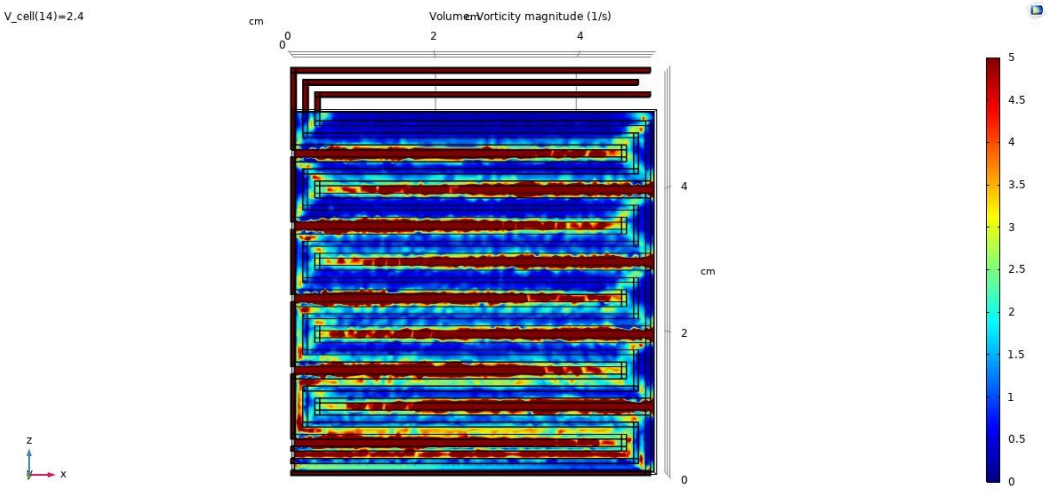

Figure 3.81 Vorticity magnitude distribution in laminar flow model

A comparison of vorticity is reported in Figure 3.80 and Figure 3.81. The vorticity field is twice the rotation rate of fluid particles and is the curl of the velocity field. The vorticity field is a vector field, and vortex lines are calculated using a tangency condition identical to the one used to calculate streamlines in the fluid velocity field.

Vortex lines are transported by the flow and cannot finish inside the fluid, limiting their topology. Vorticity is most often seen near solid borders, where it spreads into the flow due to viscosity. It can be seen that vorticity is two orders of magnitude higher in the RANS model in comparison with the laminar one, especially in corners and edges.

Regarding concentration, the first difference that can be seen with the laminar model is the oxygen concentration at anode.

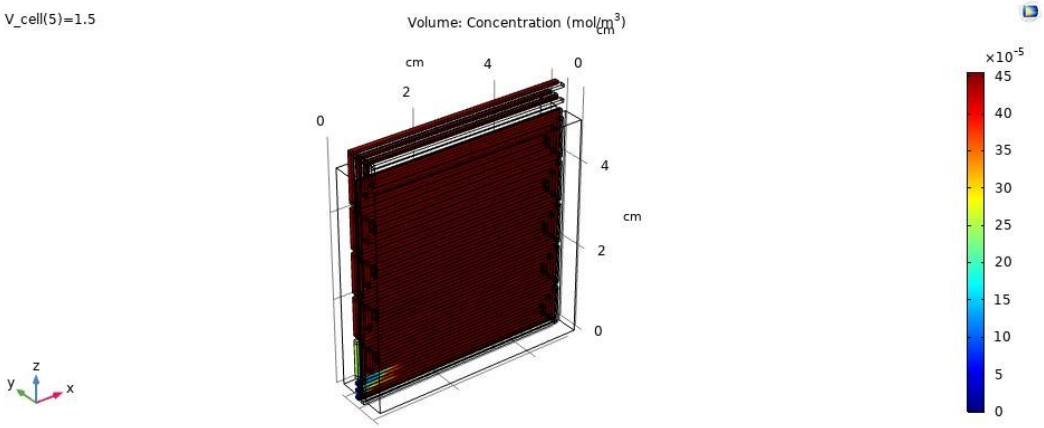

Figure 3.82 Oxygen concentration in turbulent flow model

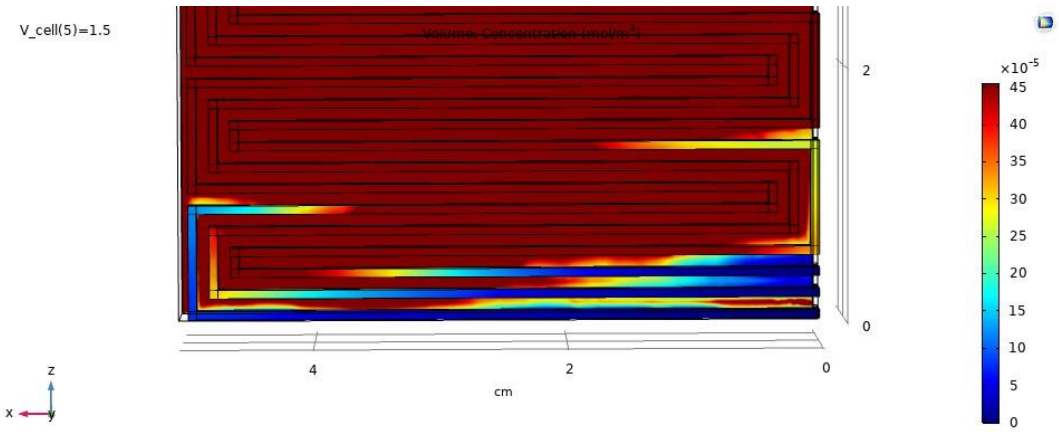

Figure 3.83 Oxygen concentration in turbulent flow model, inlet closeup

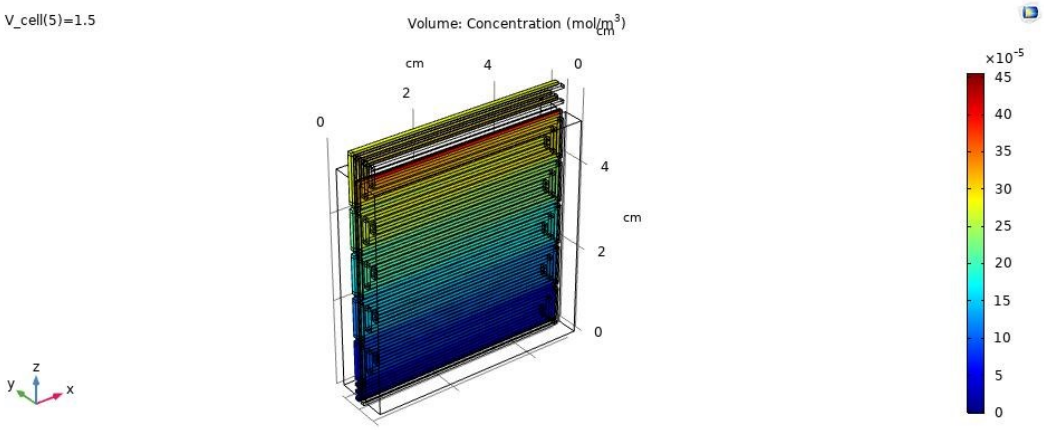

Figure 3.84 Oxygen concentration in laminar flow model

The turbulent concentration of oxygen has a different distribution in the anodic channel from the laminar flow one: is more uniform and presents different values of concentration at the anode inlet (Figure 3.83) caused by the turbulent flow and increase of velocity.

Overall, the concentration of O_2 is higher trough the anodic channel, respect to the laminar model, even if at the interface with the electrolyte (Figure 3.85) the concentration has the same trend, when in function of the channel height.

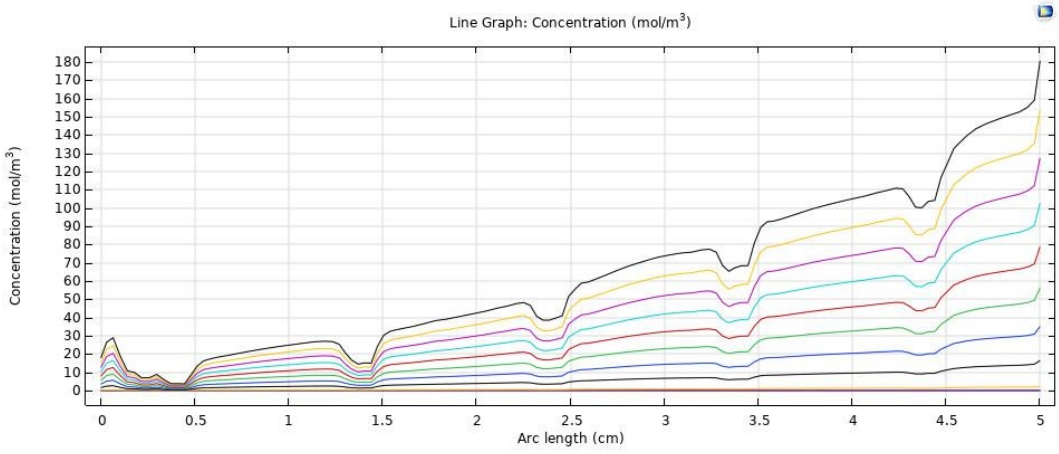

Figure 3.85 Oxygen concentration at interface, in function of arch length

A similar trend can be observed for the water concentration in the anodic channel:

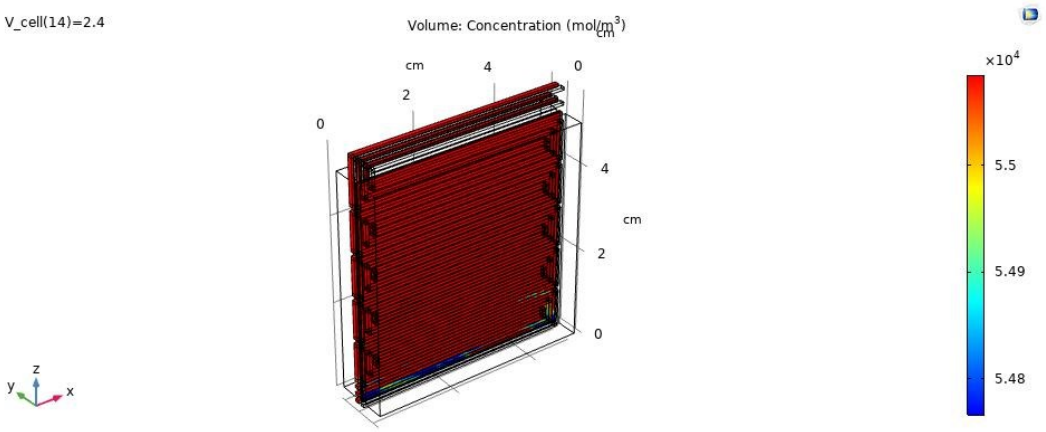

Figure 3.86 Water concentration at anode, turbulent flow model

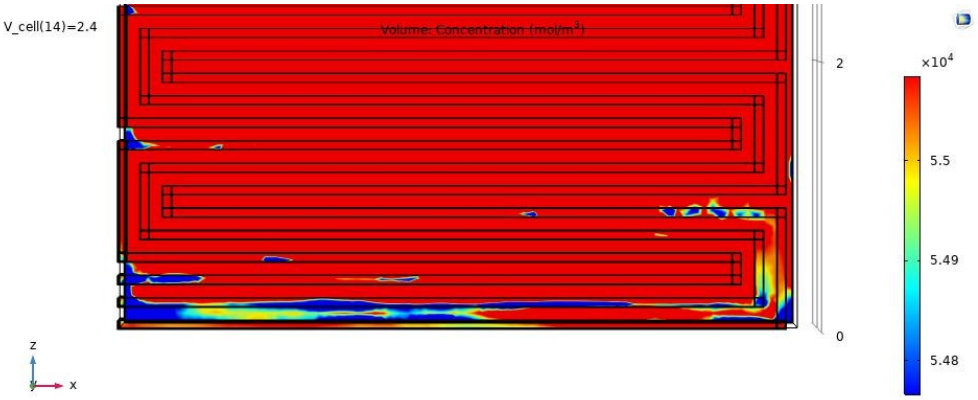

Figure 3.87 Water concentration at anode, turbulent flow model, inlet closeup

Again, at the anode inlet more spread value of water are evidenced.

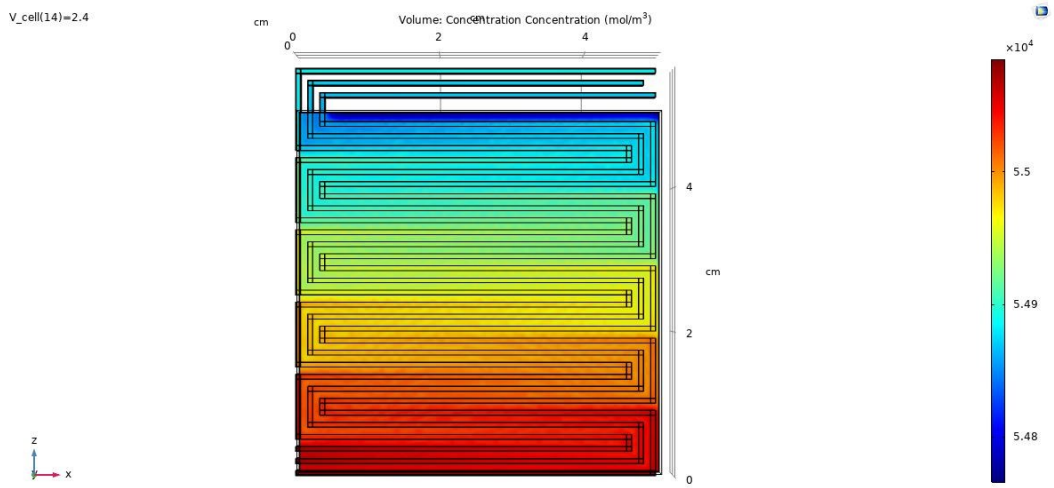

Figure 3.88 Water concentration at anode, laminar flow model

Respect to the laminar flow model, as for the oxygen concentration, the turbulent flow one has a more uniform water concentration, except for the inlet, where the presence of turbulences and vorticity is higher. However, the most interesting value is the difference in the concentration of hydrogen:

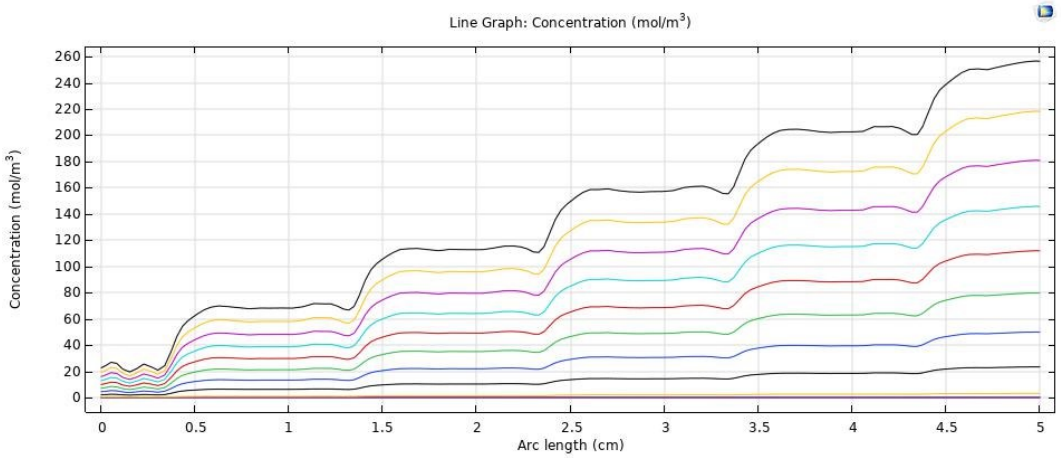

Figure 3.89 Hydrogen concentration at cathode/membrane interface, turbulent flow model

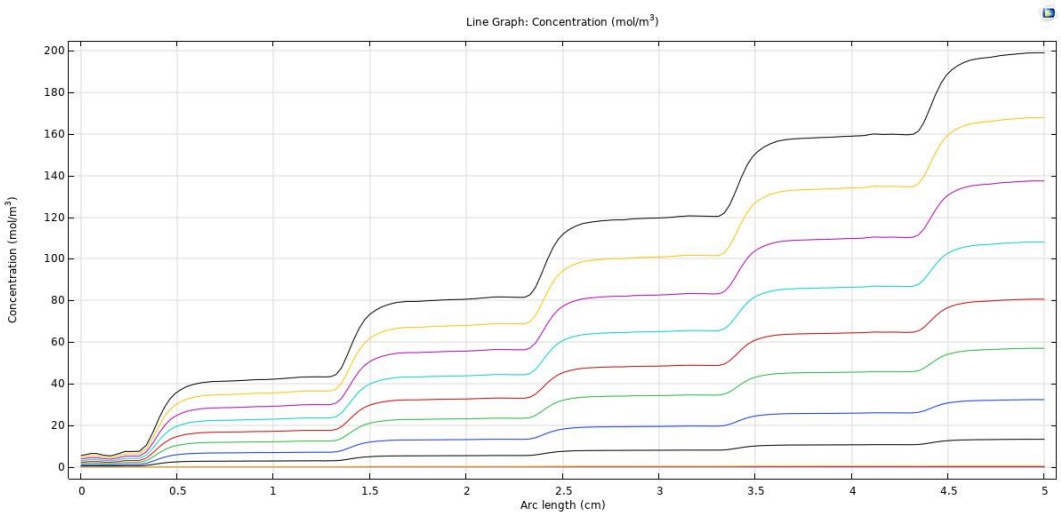

Figure 3.90 Hydrogen concentration at cathode/membrane interface, laminar flow model

In the Turbulent configuration the hydrogen concentration is 30 % more. This can be due to the rise of turbulent kinetic energy at the electrode/electrolyte interface which speeds up the electrolysis reaction:

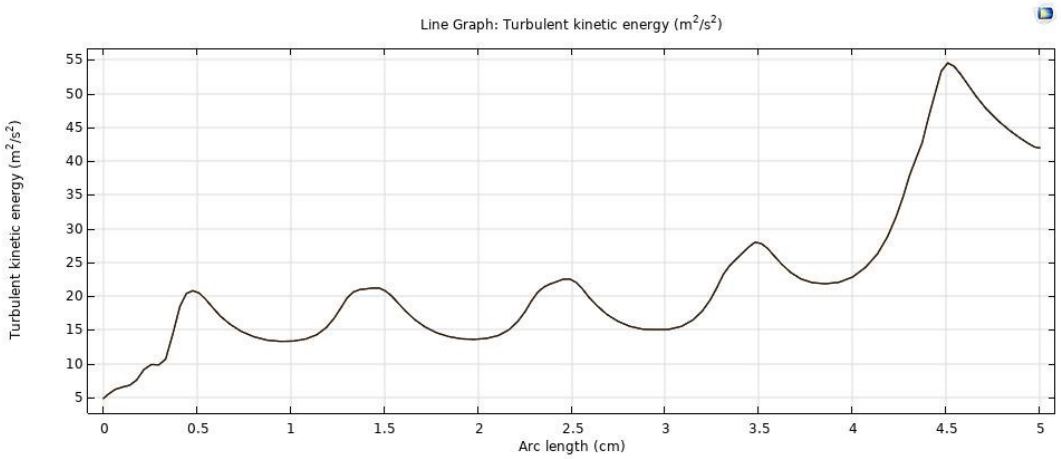

Figure 3.91 Turbulent kinetic energy distribution at interface, in function of arch length

3.2.9.7. 3D Laminar Flow Model Open/Closed Cathode Comparison

In this subchapter the main differences between the open cathode configuration and closed cathode one are analysed. In the closed cathode configuration, as

discussed in the experimental part, the water cathode inlet is closed, to have higher temperature and better electrolysis performance.

The expected results in the closed cathode model are:

- Temperature increased, due to lack of water at cathode side
- Mass flow of hydrogen increased, since high temperatures lower the potential needed to break the water molecule
- Resistance decreases since an increase in temperature favours the molecular collisions between ions of the electrolyte.

First result reported is the difference in water concentration at cathode in the two models:

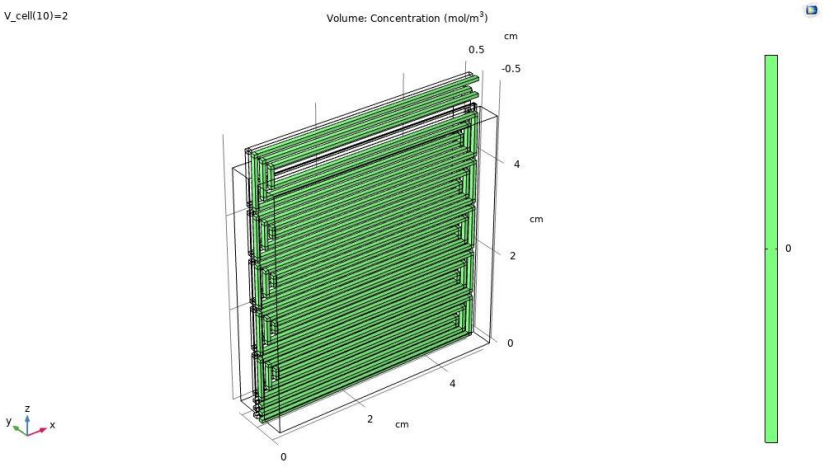

Figure 3.92 Water concentration at cathode, closed cathode configuration

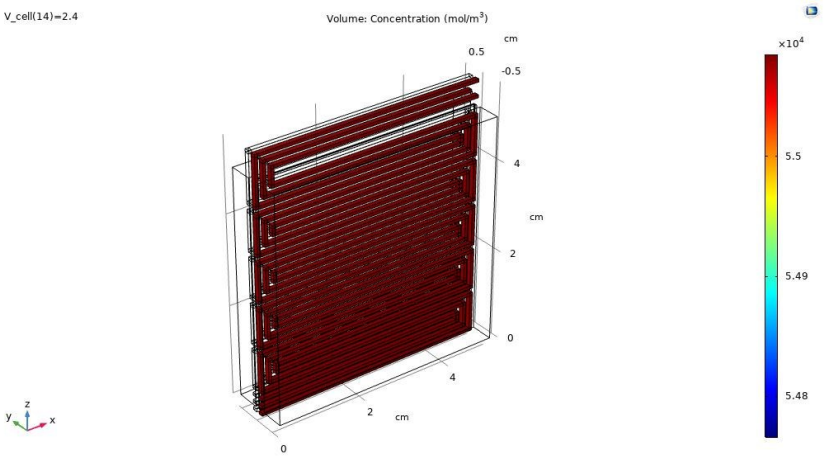

Figure 3.93 Water concentration at cathode, open cathode configuration

Water concentration is zero at the cathode side, in closed cathode model. The temperature distribution is now shown:

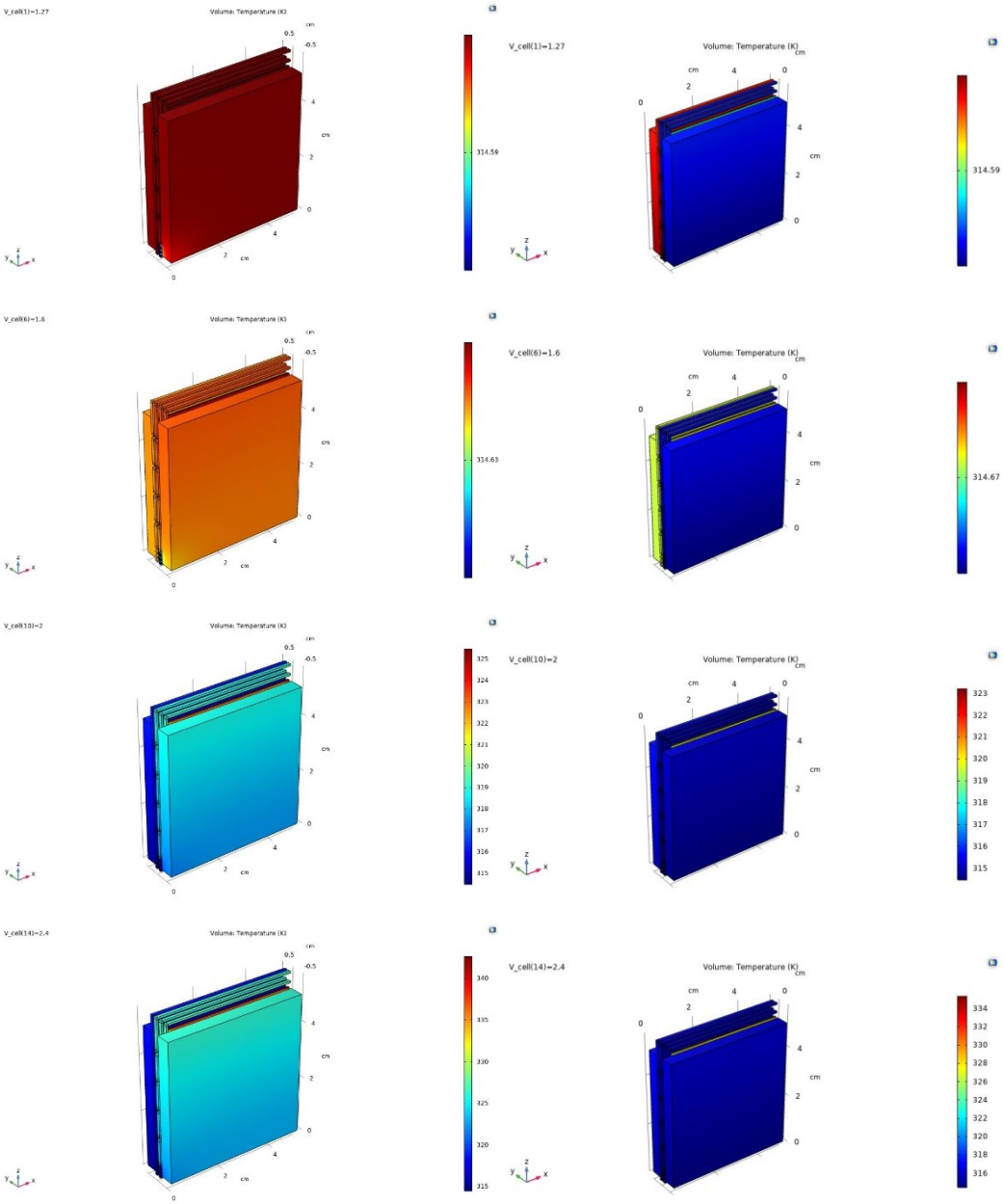

Figure 3.94 Temperature distribution in closed cathode configuration (left) and open (right). Value of voltages, from top to bottom, for each row: 1,27 - 1,6 - 2 - 2,4 V

As expected, the different water concentration at cathode side, whose use is to cool the cell, result in a higher cell temperature in closed cathode configuration,

with maximum average temperature difference of $\Delta T = 10\,°\,C$ for higher values of voltage. At interfaces, the temperature is the sequent:

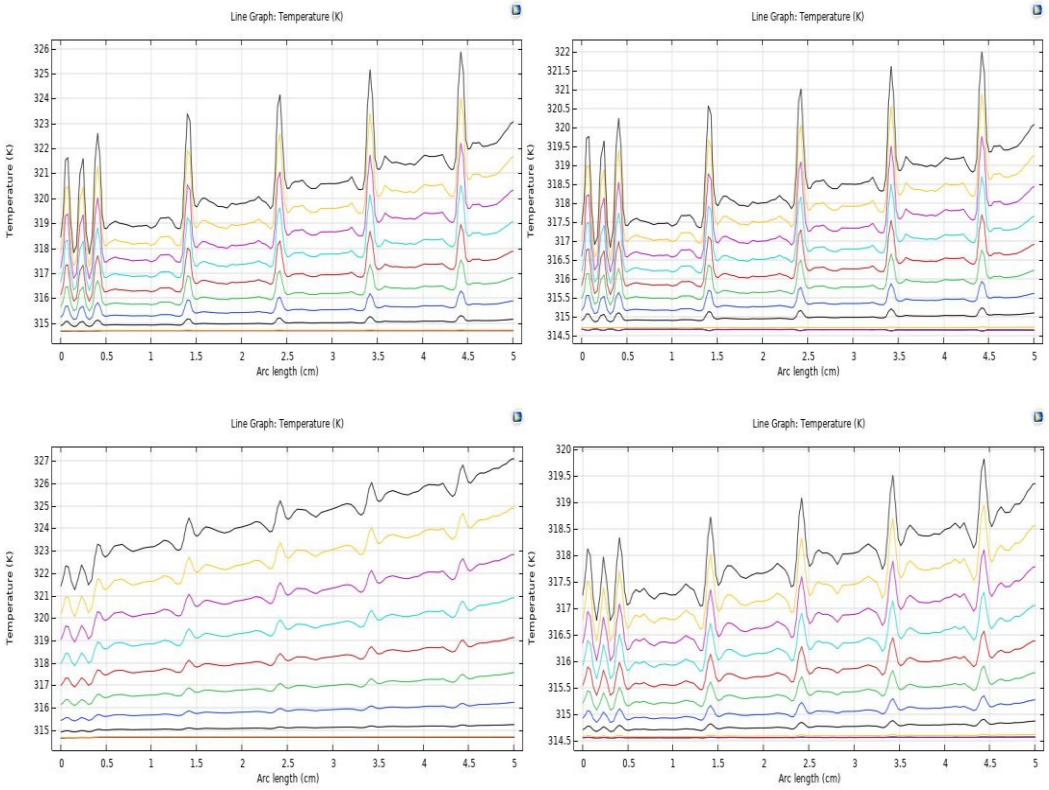

Figure 3.95 Temperature at interfaces. Left column, closed cathode configuration, right column open one. Top row, temperature at anode/membrane interface, bottom cathode/membrane

In Figure 3.95 the temperature trend can be observed clearer. From the plot comparison, a temperature difference of about $\Delta T = 4\,°\,C$ at anode/electrolyte interface is shown, between the open and closed cathode configuration, while in the cathode/electrolyte one differences is of about $\Delta T = 7\,°\,C$ for higher value of voltages.

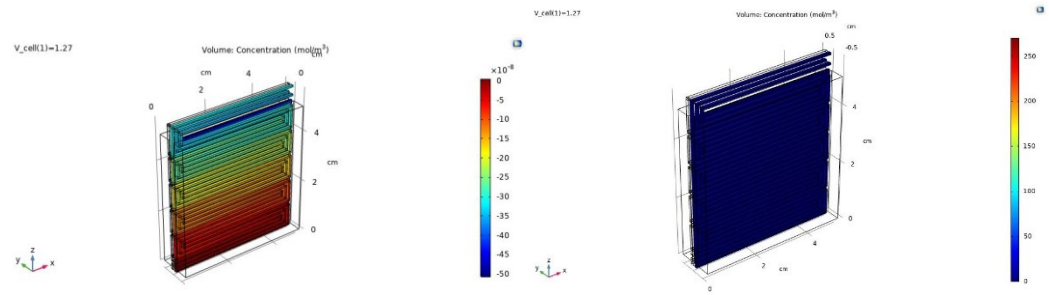

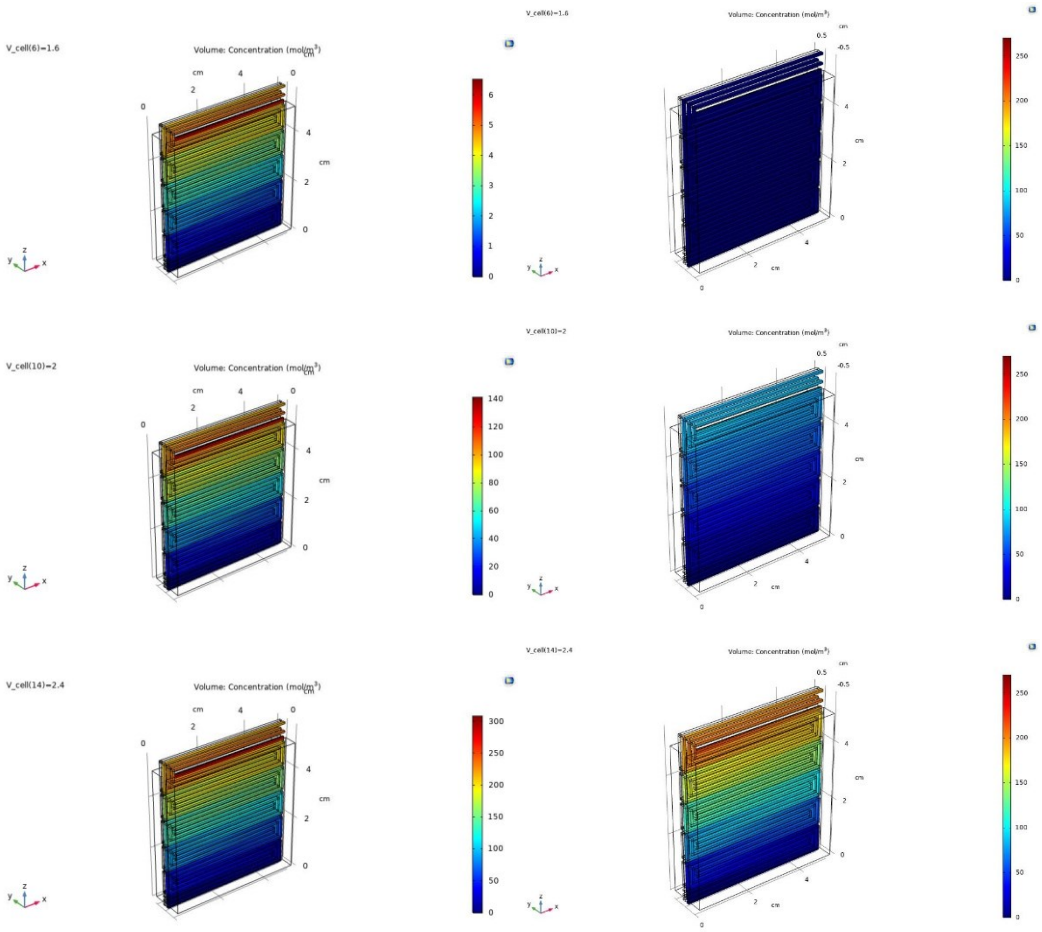

Figure 3.96 Hydrogen concentration in closed cathode configuration (left) and open (right). Value of voltages, from top to bottom, for each row: 1,27 - 1,6 - 2 - 2,4 V

In Figure 3.96 the hydrogen concentration in cathode channels is shown. Overall, the concentration is higher in the closed cathode configuration, again as anticipated. A better view is proposed below analysing the concentration distribution at cathode/membrane interface in function of the z-coordinate, the height of the cathode channel:

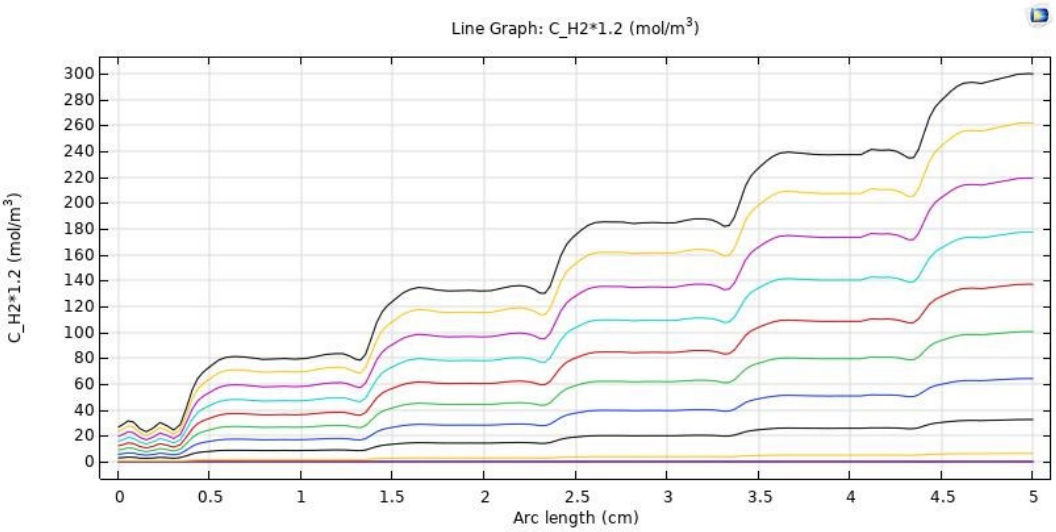

Figure 3.97 Hydrogen concentration at electrode/electrolyte interface, closed cathode configuration

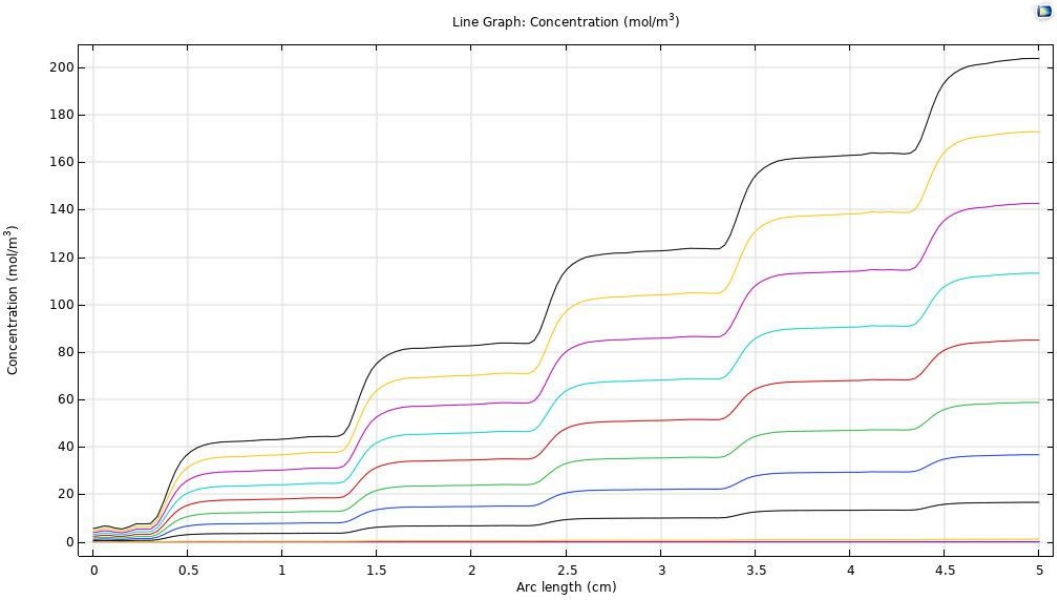

Figure 3.98 Hydrogen concentration at electrode/electrolyte interface, open cathode configuration

The hydrogen concentration is higher of values between 50 % and 60 % in closed cathode configuration since the temperature rises favours the electrolysis, fastening the breaking of the water molecule.

Lastly, some differences can be noticed in the polarization curve as well:

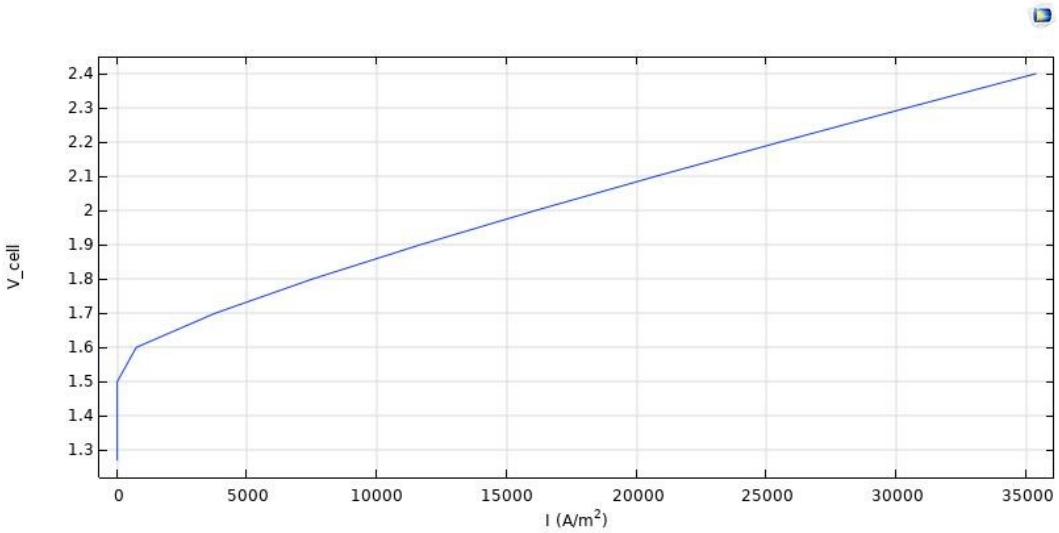

Figure 3.99 Polarization curve, closed cathode configuration, T = 60 ° C, relative pressure = 0.5 bar

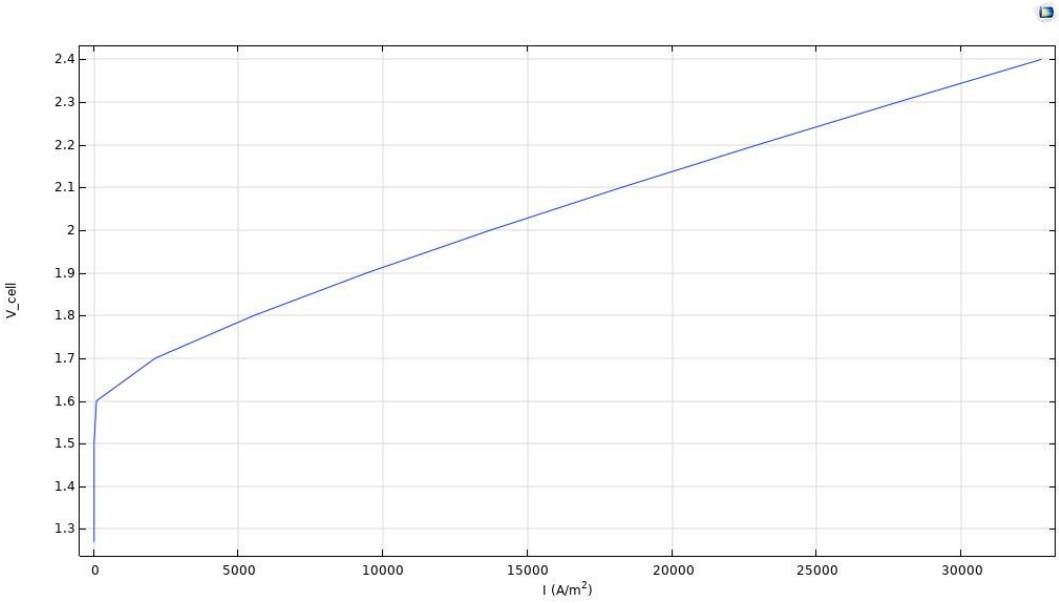

Figure 3.100 Polarization curve, open cathode configuration, T = 60 ° C, relative pressure = 0.5 bar

For same values of voltages input, higher current density is reached, this is due to the decrease in resistance mentioned above.

Chapter 4. Validation

In this chapter the validation of the models in Matlab and Comsol with the experimental results from the test bench are discussed.

4.1. Model Validation

The theoretical model created was after compared with the experimental result came out from the test bench. The validation is performed by using the MATLAB and implementing a function that is able to minimize a certain cost function, namely the so-called Sum Squared Error (SSE) defined as:

$$SSE = \sum_{i=1}^{n} \left(x_{exp,i} - x_{mod,i}\right)^2 \qquad 4.1$$

Where:

- x_{exp} is the reference value taken from experiments;
- x_{mod} is the value obtained by the model.

The cost function minimization is performed at each iteration by varying some parameters in order to understand what are the main differences of the material constituting the PEM electrolyzer cell. In some studies, it was demonstrated that activation and ohmic overvoltages are influenced by temperature. Thus, for the fitting, key parameters able to show this influence, are chosen. The reference exchange current density and change transfer coefficients are the main parameters related to the activation overvoltage. The humidification factor is related to temperature in the ohmic overvoltage relationship. [52]Although, the charge transfer coefficients are influenced by temperature, these are kept constant in order to investigate other parameters, like the pressure exponent coefficient. In conclusion, the parameters considered for the validation are:

- Anode and cathode reference exchange current densities.
- Anode and cathode pressure exponent parameter γ.
- The humidification degree.

The procedure consists of some iterations:

- Define the lower and upper bound in which the parameters must vary.
- Define the relative standard deviation (RSD) as the difference between the potential of the model and the potential of experiment.
- Insert the experimental values (like I, V and Tcell) as input.
- Run the code.

If the value of the SSE is small and close to 0, the procedure is finished whereas the value of this is higher than 0, it is needed to change the initial guess values and run again the code. The procedure is repeated until the SSE is close to 0. The model is validated using the experimental data, considering the two configurations used for conducting the tests.

4.1.1. Configuration 1

Initially, the validation of first configuration is performed and curves at constant temperature and pressure are used. The first validation on experimental curves at constant pressure equal to 2.5bar it is performed

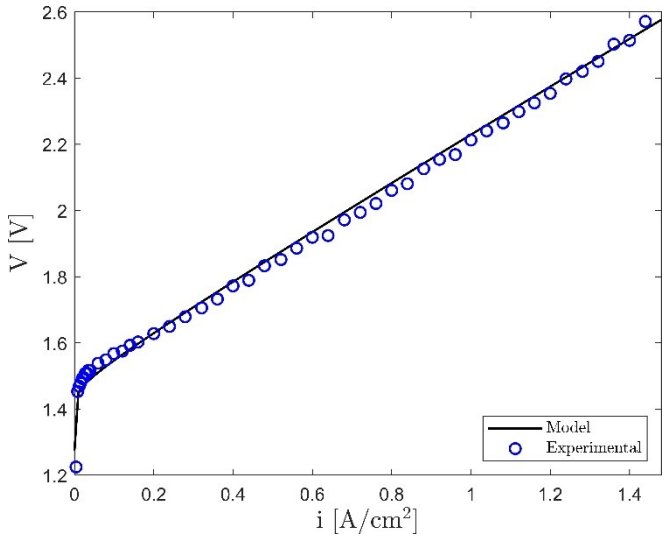

Figure 4.1 Validation with polarization curve at constant temperature equal to 40°C and at constant pressure equal to 2.5barg

In the Figure 4.1 the validation of the model with experimental curve is reported. The experimental curve at constant temperature equal to 40°C is used. The validation is done changing the parameters. In this sense, the values of the key parameters are found and it is possible to see as they changes. These are reported in the Table 4.1.

Table 4.1 Table of fitting parameters for polarization curve at constant temperature equal to 40°C and at constant pressure equal to 2.5barg

Parameter	Value	Unit
$i_{0,ref,an}$	10^{-8}	A/ cm2
$i_{0,ref,cath}$	$2.5*10^{-1}$	A/cm2
γ_{an}	0.5	-
γ_{cath}	1	-
λ	15	mol_{H2O} / mol_{SO3^-}

Generally, with validation and using the parameters obtained, the model polarization curve trend is very similar to experimental polarization curve. Obviously, the fitting can be continued to arrive in a better representation of the model curve. In the Figure 4.2 Validation with polarization curve at constant temperature equal to 60°C and at constant pressure equal to 2.5barg the validation of the model with experimental curve at constant temperature equal to 60°C is reported.

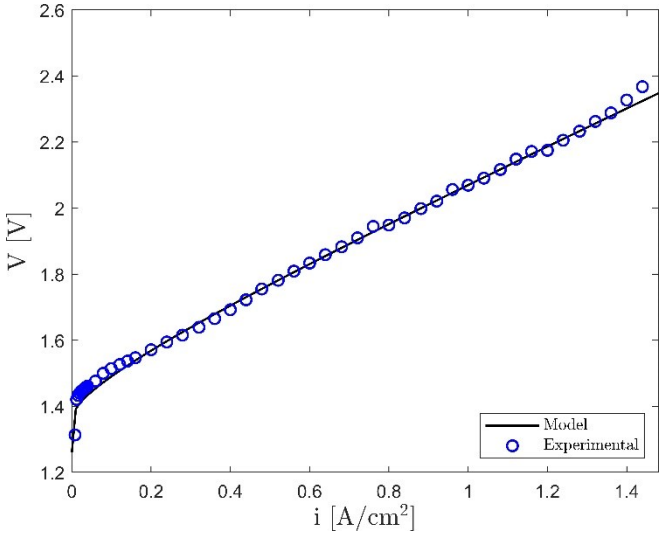

Figure 4.2 Validation with polarization curve at constant temperature equal to 60°C and at constant pressure equal to 2.5barg

It is possible to see that with data fitting of model curve on experimental curve the curve shows very well the behaviour of experimental one. The fitted parameters analyzed are reported in Table 4.2.

Table 4.2 Table of fitting parameters for polarization curve at constant temperature equal to 60°C and at constant pressure equal to 2.5barg

Parameter	Value	Unit
$i_{0,ref,an}$	$9*10^{-8}$	A/ cm2
$i_{0,ref,cath}$	$7.5*10^{-2}$	A/cm2
γ_{an}	0.5	-
γ_{cath}	0.5	-
λ	15	mol_{H2O} / mol_{SO3^-}

The value shown are the best values obtained by the data fitting performed. The value of λ is in the range between 14 and 21. [63] After a validation on experimental curves at constant pressure equal to 5barg it is performed. In the Figure 4.3 Validation with polarization curve at constant temperature equal to 40°C and at constant pressure equal to 5barg the result of model validation for constant temperature equal to 40°C is reported.

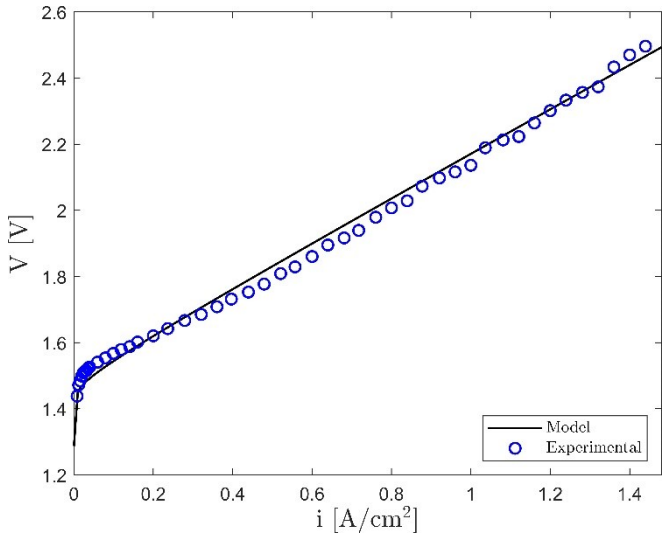

Figure 4.3 Validation with polarization curve at constant temperature equal to 40°C and at constant pressure equal to 5barg

The obtained parameters are reported in the Table 4.3

Table 4.3 Table of fitting parameters for polarization curve at constant temperature equal to 40°C and at constant pressure equal to 5barg

Parameter	Value	Unit

$i_{0,ref,an}$	10^{-8}	A/ cm2
$i_{0,ref,cath}$	$5*10^{-1}$	A/cm2
γ_{an}	0.75	-
γ_{cath}	0.75	-
λ	16	mol_{H2O} / mol_{SO3^-}

In the Figure 4.4 Validation with polarization curve at constant temperature equal to 60°C and at constant pressure equal to 5barg the validation of the model with experimental curve at constant temperature equal to 60°C is reported.

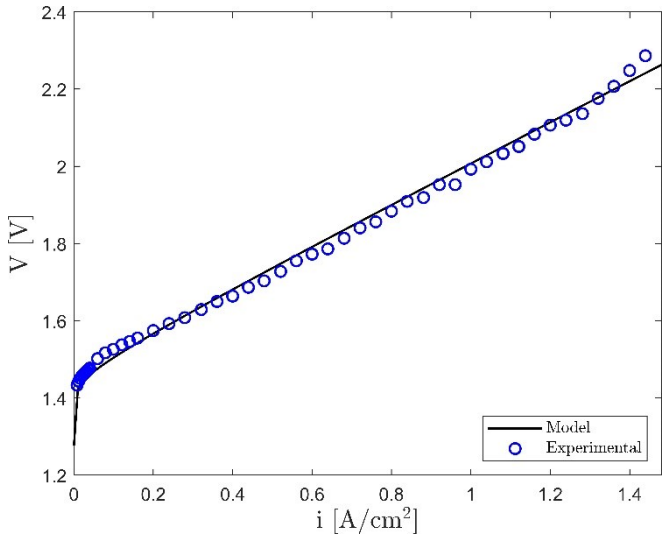

Figure 4.4 Validation with polarization curve at constant temperature equal to 60°C and at constant pressure equal to 5barg

And the fitted parameters are reported in Table 4.4.

Table 4.4 Table of fitting parameters for polarization curve at constant temperature equal to 60°C and at constant pressure equal to 5barg

Parameter	Value	Unit
$i_{0,ref,an}$	$7.5*10^{-9}$	A/ cm2
$i_{0,ref,cath}$	$7.5*10^{-1}$	A/cm2
γ_{an}	1	-
γ_{cath}	0.75	-
λ	16	mol_{H2O} / mol_{SO3^-}

In the Figure 4.5 the validation of the model with experimental curve at constant temperature equal to 75°C is reported.

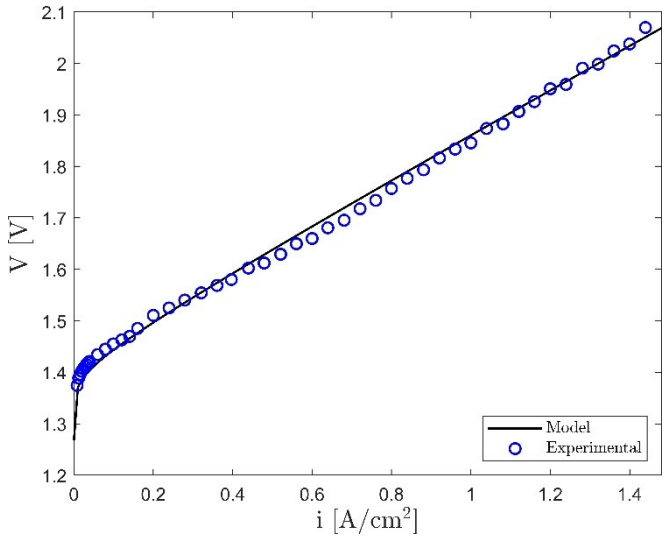

Figure 4.5 Validation with polarization curve at constant temperature equal to 75°C and at constant pressure equal to 5barg

The fitted parameters obtained after validation are reported in Table 4.5.

Table 4.5 Table of fitting parameters for polarization curve at constant temperature equal to 75°C and at constant pressure equal to 5barg

Parameter	Value	Unit
$i_{0,ref,an}$	$1.5*10^{-7}$	A/ cm2
$i_{0,ref,cath}$	$5*10^{-1}$	A/cm2
γ_{an}	0.5	-
γ_{cath}	0.5	-
λ	17	mol_{H2O} / mol_{SO3-}

The last validation is made, for first configuration, using the curve with high pressure and high temperature. In this sense, the experimental polarization curve at constant temperature equal to 75°C and at constant pressure equal to 15barg is used. In the Figure 4.6 the validation result is reported.

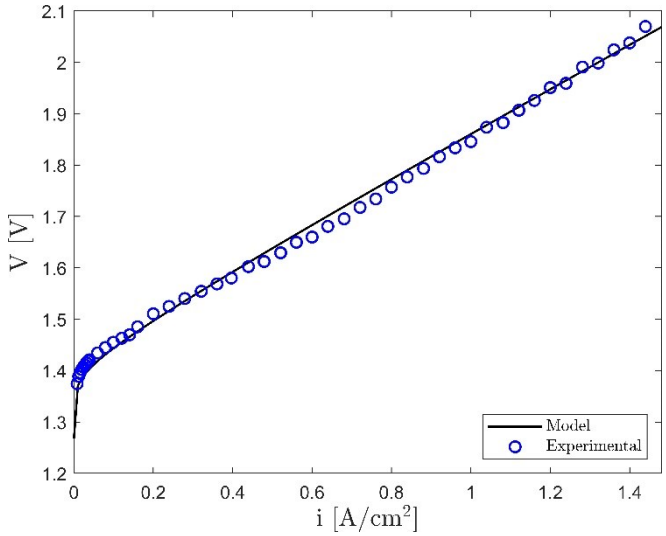

Figure 4.6 Validation with polarization curve at constant temperature equal to 75°C and at constant pressure equal to 15barg

The fitted parameters obtained after validation are reported in:

Table 4.6 Table of fitting parameters for polarization curve at constant temperature equal to 75°C and at constant pressure equal to 15barg

Parameter	Value	Unit
$i_{0,ref,an}$	$2.5*10^{-7}$	A/ cm2
$i_{0,ref,cath}$	$1.25*10^{-1}$	A/cm2
γ_{an}	0.9	-
γ_{cath}	0.8	-
λ	17.5	mol_{H2O} / mol_{SO3^-}

4.1.2. Configuration 2

From second configuration, the experimental results at different operating temperature and pressure are obtained. The performed validations are reported. In the Figure 4.7 the validation of the model with experimental curve at constant temperature equal to 40°C and at constant pressure of 10barg is reported.

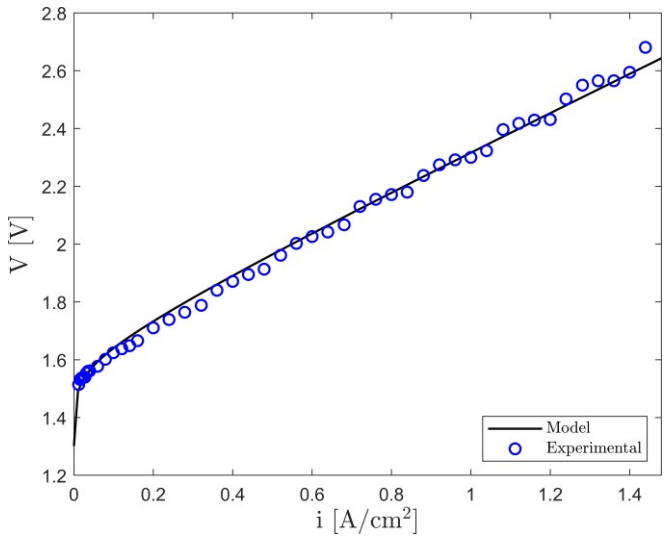

Figure 4.7 Validation with polarization curve at constant temperature equal to 40°C and at constant pressure equal to 10barg

The fitted parameters obtained after validation are reported in :

Table 4.7 Table of fitting parameters for polarization curve at constant temperature equal to 40°C and at constant pressure equal to 10barg

Parameter	Value	Unit
$i_{0,ref,an}$	$7.5*10^{-7}$	A/ cm2
$i_{0,ref,cath}$	$2.5*10^{-4}$	A/cm2
γ_{an}	0.7	-
γ_{cath}	0.5	-
λ	16	mol_{H2O} / mol_{SO3^-}

In the Figure 4.8 the validation of the model with experimental curve at constant temperature equal to 40°C and at constant pressure of 15barg is reported.

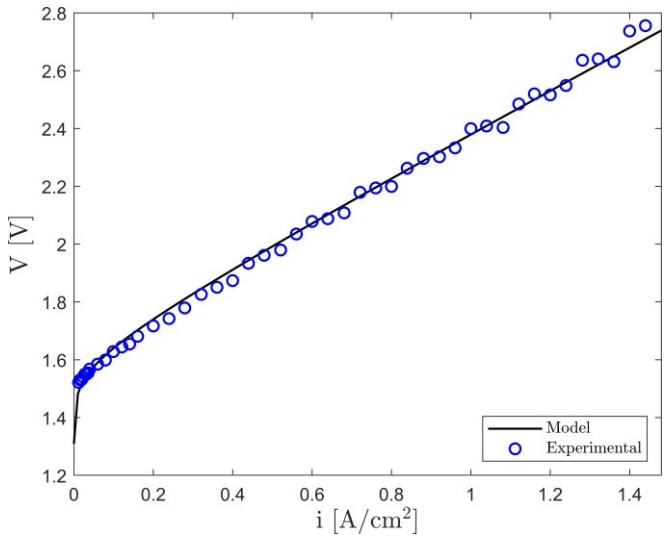

Figure 4.8 Validation with polarization curve at constant temperature equal to 40°C and at constant pressure equal to 15barg

The fitted parameters obtained after validation are reported in:

Table 4.8: Table of fitting parameters for polarization curve at constant temperature equal to 40°C and at constant pressure equal to 15barg

Parameter	Value	Unit
$i_{0,ref,an}$	$5*10^{-7}$	A/ cm2
$i_{0,ref,cath}$	$5*10^{-4}$	A/cm2
γ_{an}	0.5	-
γ_{cath}	0.5	-
λ	14.5	mol_{H2O} / mol_{SO3^-}

In the Figure 4.9 the validation of the model with experimental curve at constant temperature equal to 60°C and at constant pressure of 5barg is reported.

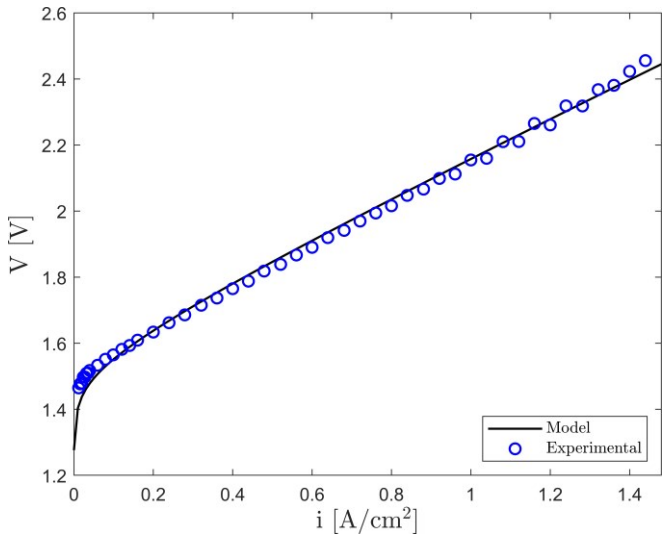

Figure 4.9 Validation with polarization curve at constant temperature equal to 60°C and at constant pressure equal to 5barg

The fitted parameters obtained after validation are reported in:

Table 4.9 Table of fitting parameters for polarization curve at constant temperature equal to 60°C and at constant pressure equal to 5barg

Parameter	Value	Unit
$i_{0,ref,an}$	$5*10^{-7}$	A/ cm2
$i_{0,ref,cath}$	$9*10^{-4}$	A/cm2
γ_{an}	1	-
γ_{cath}	1	-
λ	14.5	mol_{H2O} / mol_{SO3-}

In the Figure 4.10 the validation of the model with experimental curve at constant temperature equal to 60°C and at constant pressure of 5barg is reported.

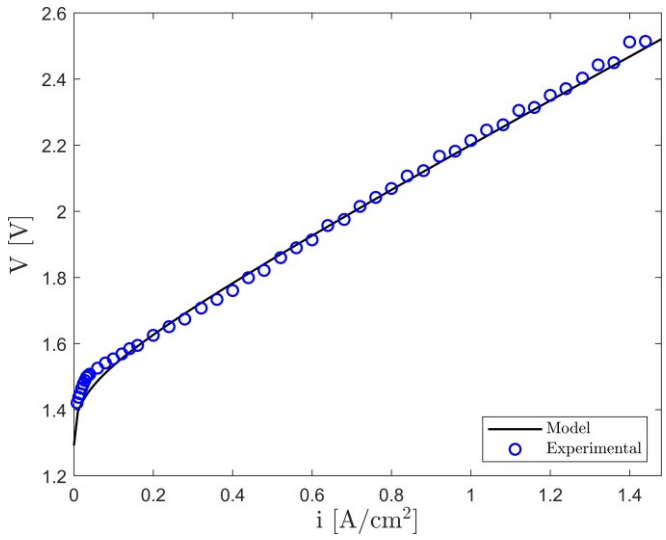

Figure 4.10 Validation with polarization curve at constant temperature equal to 60°C and at constant pressure equal to 10barg

The fitted parameters obtained after validation are reported in :

Table 4.10 Table of fitting parameters for polarization curve at constant temperature equal to 60°C and at constant pressure equal to 10barg

Parameter	Value	Unit
$i_{0,ref,an}$	$5*10^{-7}$	A/ cm2
$i_{0,ref,cath}$	$6.5*10^{-3}$	A/cm2
γ_{an}	0.6	-
γ_{cath}	0.5	-
λ	13	mol_{H2O} / mol_{SO3^-}

In the Figure 4.11 the validation of the model with experimental curve at constant temperature equal to 80°C and at constant pressure of 2.5barg is reported.

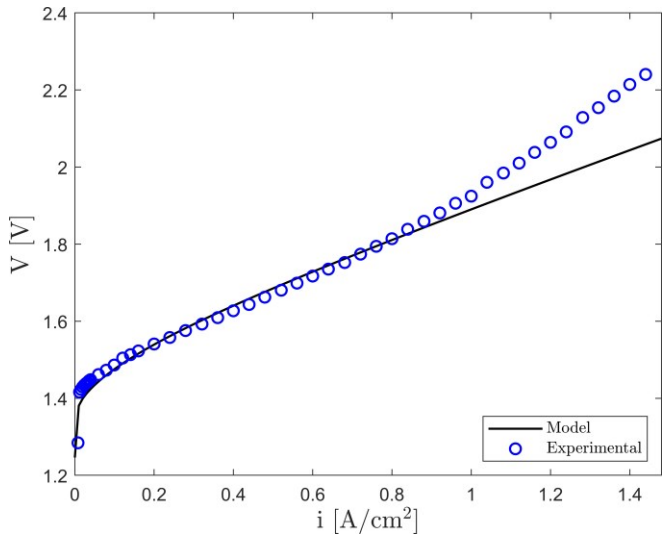

Figure 4.11 Validation with polarization curve at constant temperature equal to 80°C and at constant pressure equal to 2.5barg

The fitted parameters obtained after validation are reported in:

Table 4.11 Table of fitting parameters for polarization curve at constant temperature equal to 80°C and at constant pressure equal to 2.5barg

Parameter	Value	Unit
α_{an}	1.7	-
$i_{0,ref,an}$	$5*10^{-7}$	A/ cm2
$i_{0,ref,cath}$	$6.5*10^{-3}$	A/cm2
γ_{an}	0.6	-
γ_{cath}	0.5	-
λ	13	mol_{H2O} / mol_{SO3^-}

In this last case, also the anode charge transfer coefficient is changed. This is due to the fact that the curve presents a trend very strange. It must be investigated but probably this trend is due to the birth of degradation mechanisms.

In the Figure 4.12 the validation of the model with experimental curve at constant temperature equal to 80°C and at constant pressure of 15barg is reported.

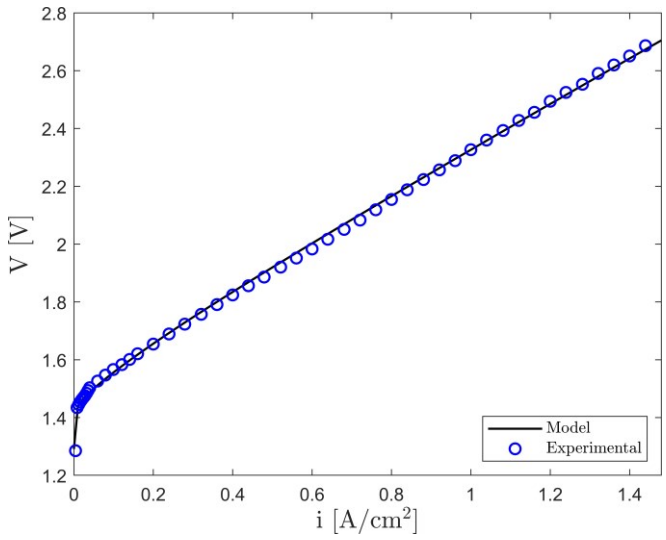

Figure 4.12 Validation with polarization curve at constant temperature equal to 80°C and at constant pressure equal to 15barg

The fitted parameters obtained after validation are reported in :

Table 4.12 Table of fitting parameters for polarization curve at constant temperature equal to 80°C and at constant pressure equal to 15barg

Parameter	Value	Unit
$i_{0,ref,an}$	$5*10^{-9}$	A/ cm2
$i_{0,ref,cath}$	$2.5*10^{-2}$	A/cm2
γ_{an}	0.5	-
γ_{cath}	0.6	-
λ	9	mol_{H2O} / mol_{SO3^-}

The only problem of this validation is the low humidification degree. Generally, this must have values included in the range 14-21.

4.1.3. Chosen fitting parameters

On the basis of the parameter values found, considering the opened valve cathode configuration, an analysis of the same parameters was carried out to find those suitable to ensure that the validation of the model at different temperatures can be carried out. In particular, the main parameters were changed due to the fact that these had to fit changing the temperature. This means that the values found are

valid for three different temperature values, in this case 40, 60 and 75◦°C. By changing the temperature and keeping the parameters constant, the model fits the experimental curves found by means of the test bench. The model was therefore validated. In Figure 4.13 the validated model curve are reported.

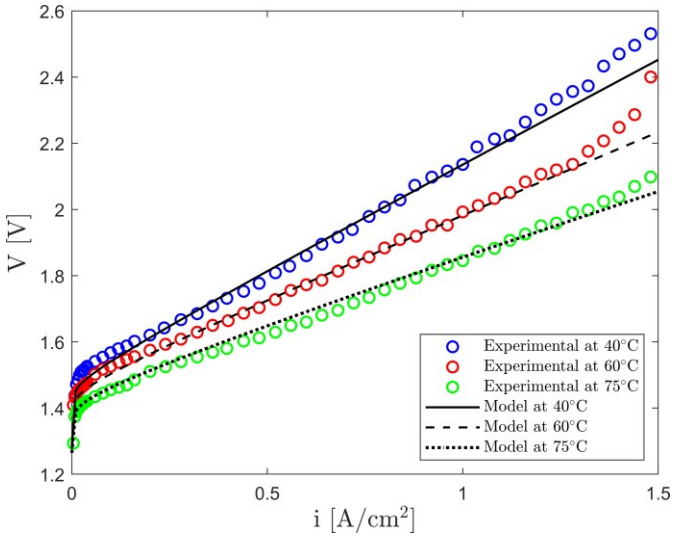

Figure 4.13 Validation with experimental curves at different temperatures (40, 60, 75◦C) and at constant pressure equal to 5barg

In the Table 4.13 the fitted parameters are reported.

Table 4.13 Table of fitting parameters for polarization curve at constant pressure equal to 5barg

Parameter	Value	Unit
$i_{0,ref,an}$	$1.5*10^{-8}$	A/ cm2
$i_{0,ref,cath}$	$2.5*10^{-1}$	A/cm2
γ_{an}	0.5	-
γ_{cath}	1	-
λ(T=40-60◦ C)	17	mol_{H2O} / mol_{SO3^-}
λ (T=75◦ C)	18	mol_{H2O} / mol_{SO3^-}

Looking at the Table 4.13, all the values are kept constant for the three curve. The only parameter changed is the humidification degree. In fact, in the case of 75◦C curve, λ is different respect to 40 and 60◦C curves. The reason is due to the fact that the curves have a different slope. This difference depends on the Ohmic

resistance. In particular, the Ohmic resistance was found through Equation 4.28 and this depends mainly on the membrane resistance which depends on the degree of humidification. An increase of λ tends to decrease the slope of the curve. However, also temperature is an important element, since an increase of temperature tends to decrease the polarization curves, but in this case, it is fixed at 75◦. So, being at high temperature the curve results lower. To decrease the slope of the curve, the only value that can be changed is the degree of humidification. In conclusion, the difference of the degree of humidification is dictated by the high operating temperature. The same operation was done for the closed cathode valve configuration but only for the two curves at fixed pressure equal to 15 barg. The results are shown in Figure 4.14.

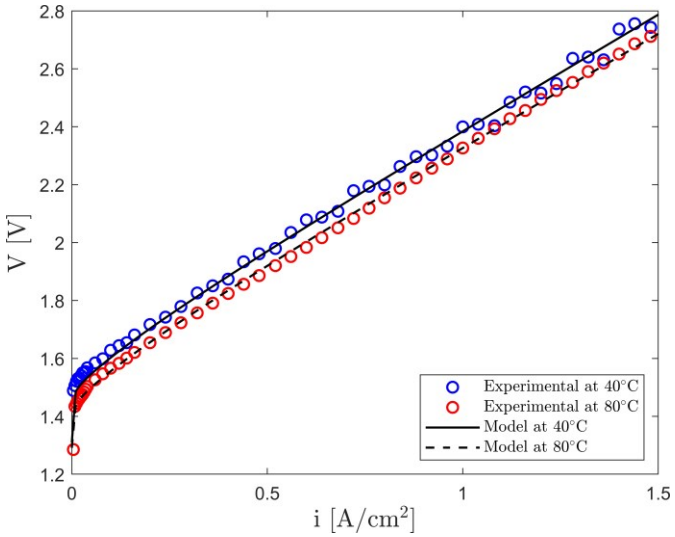

Figure 4.14 Validation with experimental curves at different temperatures (40, 80◦C) and at constant pressure equal to 15barg

In the Table 4.14 the fitted parameters are reported.

Table 4.14 Table of fitting parameters for polarization curve at constant pressure equal to 15barg

Parameter	Value	Unit
$i_{0,ref,an}$	10^{-9}	A/ cm2
$i_{0,ref,cath}$	$5*10^{-2}$	A/cm2
γ_{an}	0.75	-
γ_{cath}	0.5	-

λ(T=40-60◦ C)	13.5	mol_{H2O} / mol_{SO3^-}
λ (T=75◦ C)	19	mol_{H2O} / mol_{SO3^-}

In this case, the values are a little bit different due to strange behaviour of experimental polarization curves. The reference exchange current densities are similar to literature values but the humidification degree values are different. The reason is the slope of the curve, that as said, is influenced by λ. So, to fit the model according the experimental curve the value of 13.5 for 40◦C and 9 for 80◦ are fixed. But, according to Marangio et al. [30] the value must be in the range of 14-21 mol_{H2O} / mol_{SO3^-}. However, this configuration must be analyzed more in detail.

4.2. Validation of Multiphysics models

Experimental data are important to represent materials properties or performances so to understand if the model is well calibrated a comparison between the two is necessary. In this section, polarization curve obtained with the COMSOL models will be compared with experimental data. The goal of applying the procedure is to fit the Polarization curves, extracted from the simulation, to the experimental measurements through the help of fitting parameters. The curve fitting procedure is treated as a minimization problem. Thus, it is analysed considering the "Global least squares method", it consists in minimizing the sum of the squares of the residuals between raw data and simulation data. In mathematical terms:

$$R^2 \equiv \sum_i [y_i - f(x_i, a_1, a_2, \dots, a_n)]^2 \qquad 4.2$$

Where:

- R^2 is the square of the vertical residuals.
- yi are the raw data points.
- f(xi,a1,a2,...,an) are the points obtained with COMSOL software.
- a_i are the parameters used.

The condition used in the minimization problem is:

$$\frac{\partial R^2}{\partial a_i} = 0$$

To better fit the simulation curves on the experimental ones and to understand the influence of pressure and temperature on the curves, the fitting parameters used were the two Exchange Current Coefficients, αan and αcat, the Protonic

Diffusivity, DH+ and the two Exchange Current Densities i0an and i0cat. The last two were treated with an Arrhenius type expression in order to consider the influence of temperature and pressure. The expression for the generic exchange current density is reported in the equation bellow:

$$i0 = i0_{ref} \cdot \left(\frac{p}{p_0}\right)^{\gamma} \cdot e^{\frac{-E_a}{RT}\left(\frac{1}{T}-\frac{1}{T_{ref}}\right)} \qquad 4.3$$

From this formulation, the fitting parameters considered were both i0ref,an and i0ref,cat but also the two Activation Energies, Ea_{an} and Ea_{cat}. γ_{an} and γ_{cat} were not considered as fitting parameters since the pressure was set constant for the fitting procedure.

In comparison with the other graphs that are brought in sub-chapter 4.1 , the graphs in this part show the polarization model coming from multiphase Multiphysics model.

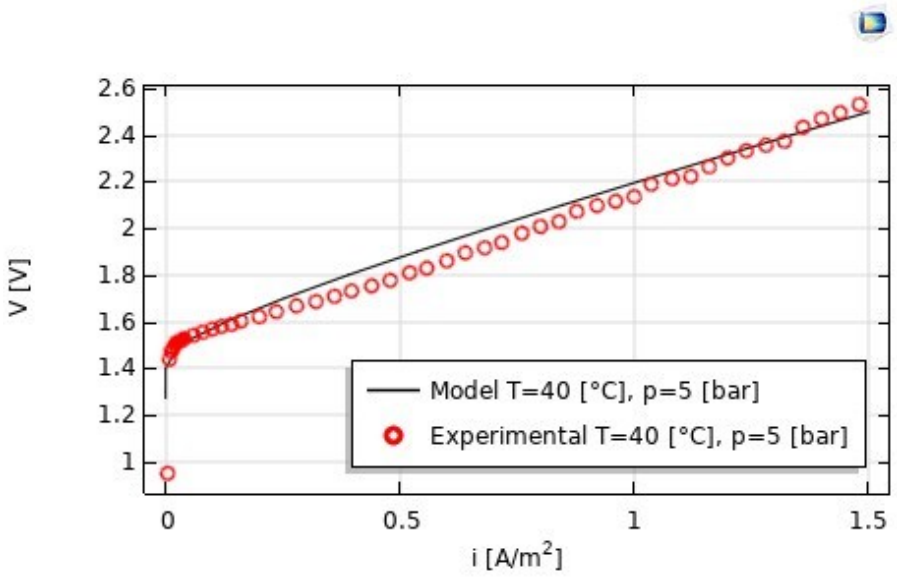

Figure 4.15 Simulation and experimental polarization curves at 40[°C] and 5 [bar_g].

Figure 4.15, Figure 4.16 and Figure 4.17 show the fitted model curves and the corresponding simulation for three different operating conditions for the Single phase 2-D model.

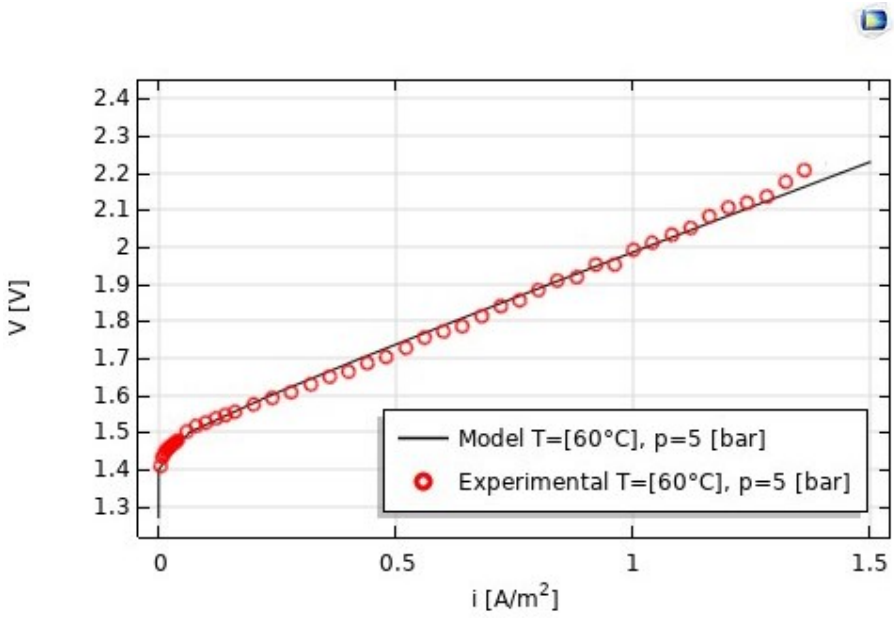

Figure 4.16 Simulation and experimental polarization curves at 60[°C] and 5 [bar_g].

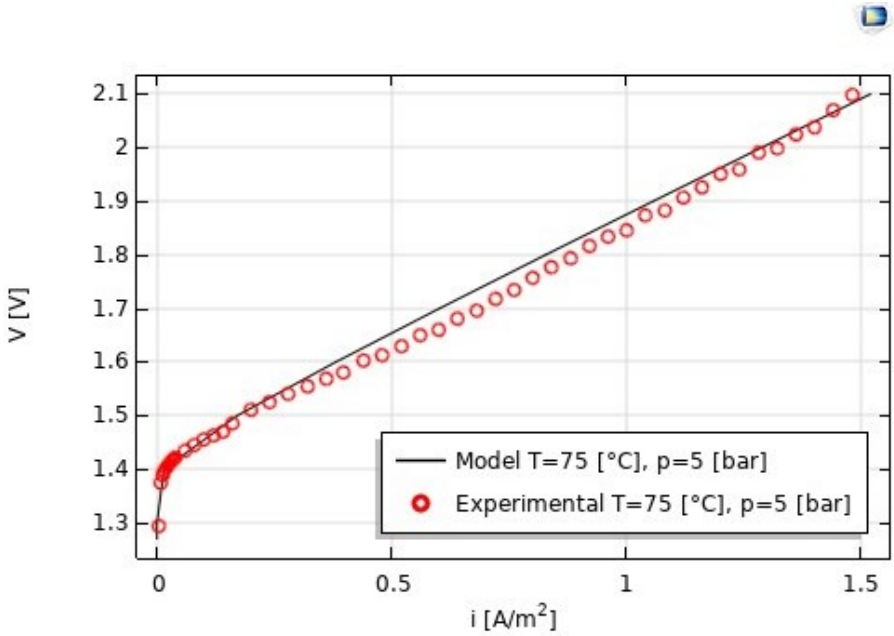

Figure 4.17 Simulation and experimental polarization curves at 75[°C] and 5 [bar_g].

Figure 4.18, Figure 4.19 and Figure 4.20 show the fitted model curves and the corresponding simulation for two different operating conditions for the Multi-phase 2-D model.

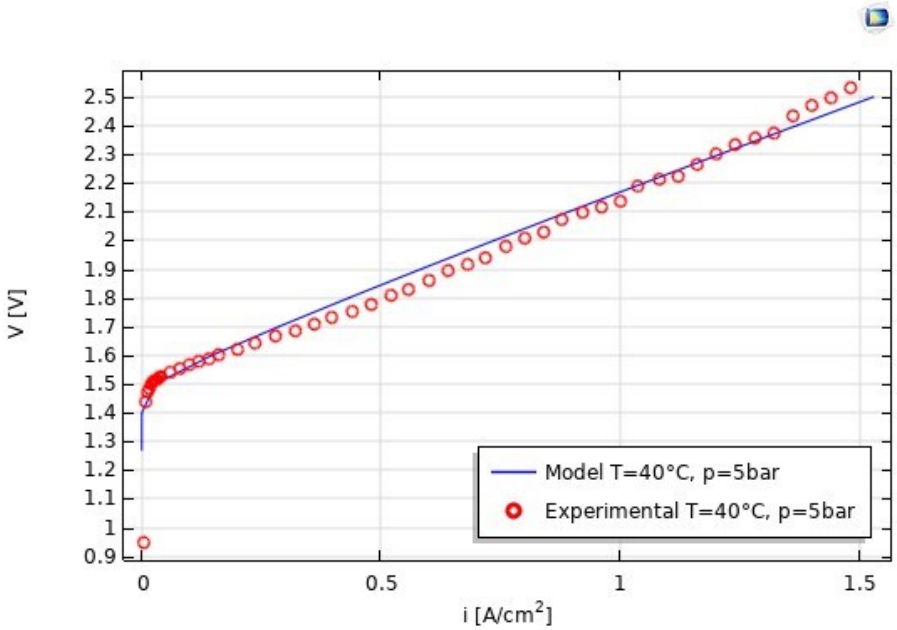

Figure 4.18 Simulation and experimental polarization curves at 40[°C] and 5 [bar$_g$].

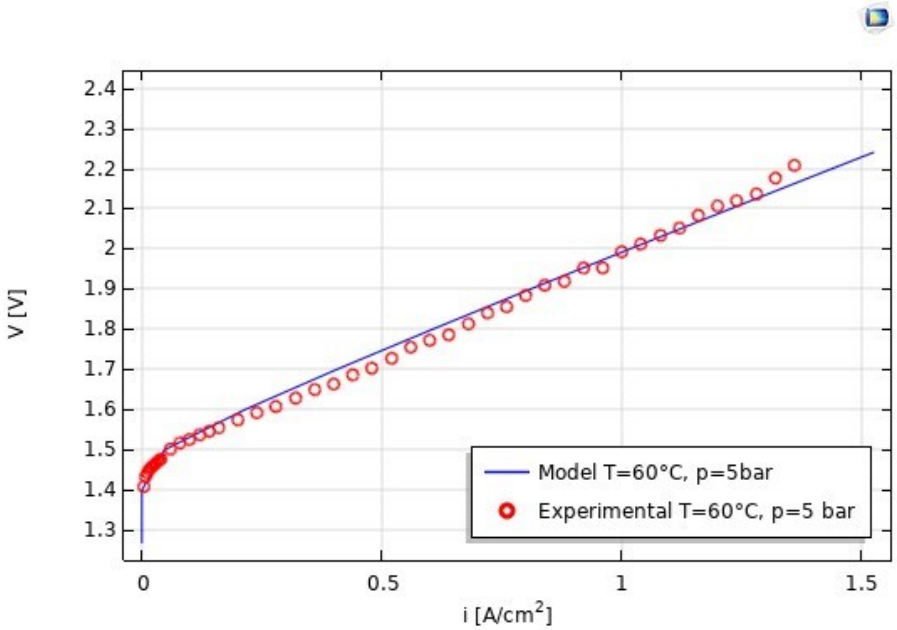

Figure 4.19 Simulation and experimental polarization curves at 60[°C] and 5 [bar_g].

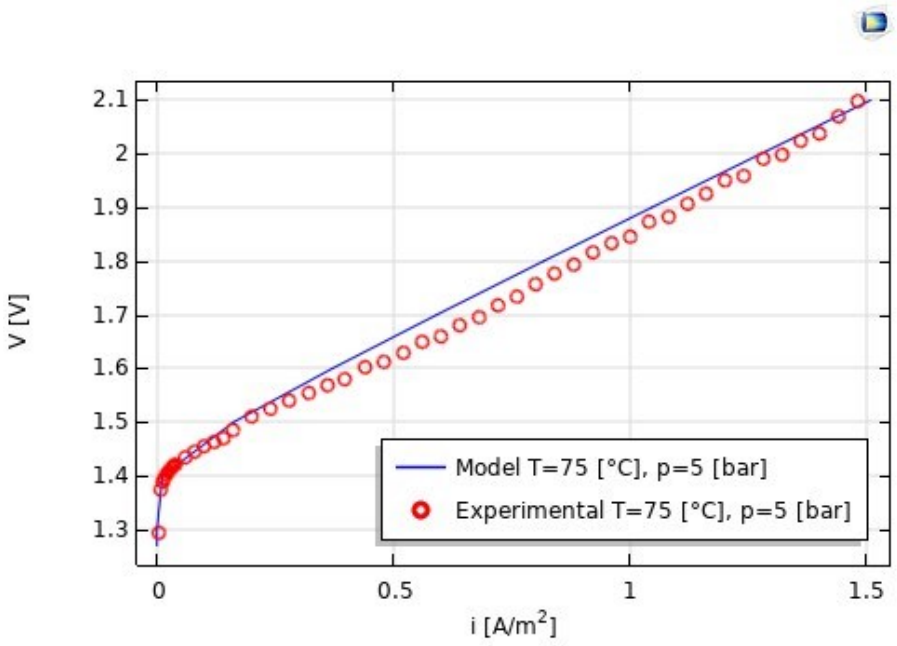

Figure 4.20 Simulation and experimental polarization curves at 75[°C] and 5 [bar_g].

The fitting parameters used to fit the model are reported in the following Table.

Table 4.15 Fitted Single Phase 2-D Model parameters

Fitting Parameters		
Parameter	**Value**	**Unit**
i0ref,an	2.49 · 10−8	[A/cm^2]
^{i}0ref,cat	0.0642	[A/cm^2]
αan	2	−
αcat	0.5	−
Ea_{an}	76	[kJ/mol]
Ea_{cat}	4.3	[kJ/mol]
D_{H^+}(T = 40°C)	1.43 · 10−9	[m^2/s^2]
D_{H^+}(T= 60◦C)	1.68 · 10−9	[m^2/s^2]

D_{H}+(T= 75◦C)	2.15 · 10−9	[m^2/s^2]

Table 4.16 Fitted Multi-Phase 2-D Model parameters.

Fitting Parameters		
Parameter	**Value**	**Unit**
$i0_{ref,an}$	2.29 · 10−8	[A/cm^2]
$^{i}0_{ref,cat}$	0.08036	[A/cm^2]
αan	2	–
αcat	0.5	–
Ea_{an}	76	[kJ/mol]
Ea_{cat}	4.3	[kJ/mol]
D_{H}+($T = 40^{\circ}C$)	1.38 · 10−9	[m^2/s^2]
D_{H}+($T = 60◦C$)	1.79 · 10−9	[m^2/s^2]
D_{H}+($T = 75◦C$)	2.21 · 10−9	[m^2/s^2]

Both Table 4.15 and Table 4.16 show the fitting parameters. The i0ref,an is quiet similar for both the two models testifying the effectiveness of the equation applied to model the bubble overpotential on anode side. Also i0ref,cat, DH+(T = 40◦C) and DH+(T = 75◦C) results almost the same while a bigger difference can be seen in the values of DH+(T = 60◦C).

Chapter 5. EIS and ECM

5.1. EIS basics

The objective of the present chapter -electrochemical impedance spectroscopy and equivalent circuit modelling- is to investigate the performance of PEM electrolytic cell by carrying out electrochemical impedance spectroscopy measurements.

The impedance spectroscopy technique is a powerful diagnostic method applied to electrochemical system for understanding and estimating its performance under different operating conditions. As the name mentions, it characterises the impedance of the system under investigation. Considering the analogy with electrical circuit, the impedance provides the measure of the opposition to current flow through the cell which derives from activation, ohmic and diffusion losses. Therefore, characterising impedance is an important task to characterise, control and enhance the cell behaviour.

The methodology for the system's characterization depicted in the flow chart is based on two steps, the experimental procedure and the model development. In the first step several tests under different operating conditions are performed. Accordingly, the main variables identified in potential, current density, temperature and pressure, which affect differently each process occurring within the cell, are varied. During operation at steady state condition, EIS tests are carried out and data are collected. Prior to the second step, data quality check is needed to remove wild points, data affected by inductive effects of cables and noise. Then, the equivalent circuit model (ECM) is chosen to simulate the impedance spectra trying to minimize the deviation between experimental results and fitting. The electrochemical parameters (double layer capacitance, polarization resistance, ohmic resistance) are estimated by CNLS analysis of the ECM model. To verify the validity of the results obtained from the impedance spectroscopy a comparison with the findings of the polarization curve is done.

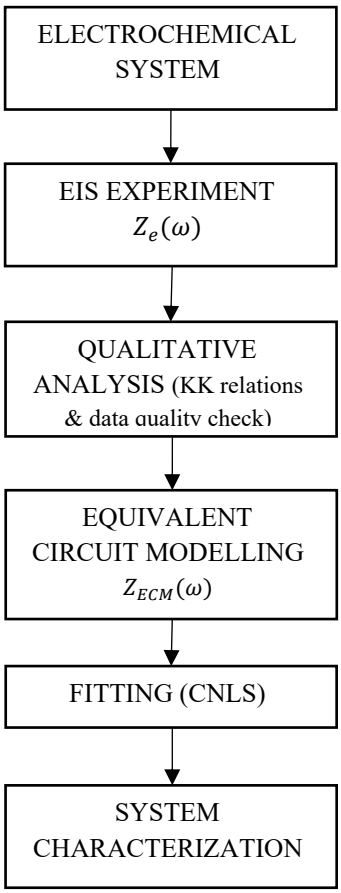

The following section will describe the basic concepts of electrochemical impedance spectroscopy. The first part gives a brief description of the fundamental principles of EIS. Thereafter, data validation with Kramers-Kroning relations is discussed. The latter argument will focus on the modelling of the experimental impedance data and the parametrical identification with Complex Non-linear Least Squares analysis.

5.1.1. Introduction to electrochemical characterization methods and EIS

The polarization curve is the most used method for the characterization of PEM water electrolyser because it allows to estimate the effects of many parameters such as temperature, pressure, composition, relative humidity on the cell performance. In general, the polarization curve has three characteristic regions, as depicted in Figure 5.1, related to the major internal irreversibilities within the cell.

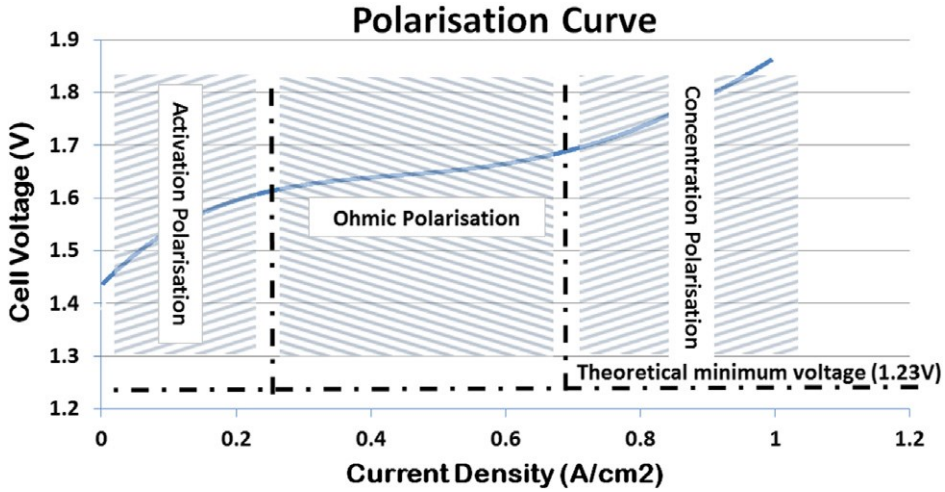

Figure 5.1 Experimental polarization curve of a PEM electrolyser [114]

The shape of the polarization curve is dictated by the several loss mechanisms aforementioned. At low current density, it assumes a logarithmic behaviour due to charge-transfer phenomena at the anode and the cathode; moreover, the anodic overvoltage is outweighed with respect to the cathodic one because the kinetics of the OER is slower than that of the HER. With increasing current densities, the shape becomes linear because activation losses are less relevant with respect to ohmic losses. Meanwhile, at high current densities the mass transfer processes are dominant giving to the cell voltage a non-linear behaviour. The polarization curve enables the identification of the overall loss of the cell making difficult to separate the different contributions of the loss mechanisms to the cell performance. In contrast to the I-V curves, the electrochemical impedance spectroscopy (EIS) is a very promising technique to analyse complex electrochemical systems like PEM water electrolysers.

Electrochemical impedance spectroscopy (EIS) is a powerful and non-invasive in-situ diagnostic method for the characterization of electrochemical processes and devices. It is mainly used to study and evaluate the different phenomena in a separate way, taking advantage from the fact that the polarization losses occurring within the cell exhibit different characteristic time constants and frequency response.

The measurement approach consists of applying a sinusoidal current (galvanostatic mode) or voltage (potentiostatic mode) of a certain amplitude and frequency superimposed on the normal operating DC current/voltage and measuring the amplitude and phase shift of the output voltage-in case of current

control mode- or current when a voltage control mode is applied. This procedure is repeated for a discrete quantity of frequency values over kHz-mHz range, thereby generating a characteristic impedance spectrum. The impedance or the admittance (inverse of impedance), for galvanostatic and potentiostatic modes respectively, is obtained by the ratio between the response (output) and the perturbation (input) according to 5.1 and 5.2 [115].

$$Z(f) = \frac{U_{AC}(f)}{I_{AC}(f)} = |Z(f)| * e^{i\theta(f)} \qquad 5.1$$

$$Y(f) = Z(f)^{-1} = \frac{I_{AC}(f)}{U_{AC}(f)} = |Z(f)|^{-1} * e^{-i\theta(f)} \qquad 5.2$$

Generally, the impedance spectrum can be presented in Nyquist and Bode plots, which are representations of the impedance as a function of frequency. Nyquist plot- where imaginary part is plotted against the real part- consists of two or more (depressed) semicircles representing the different processes taking place in the WE cell such as charge transfer, electronic and ionic conduction, diffusion and transport processes [115]. In particular, it is possible to identify three domains as in the polarization curve.

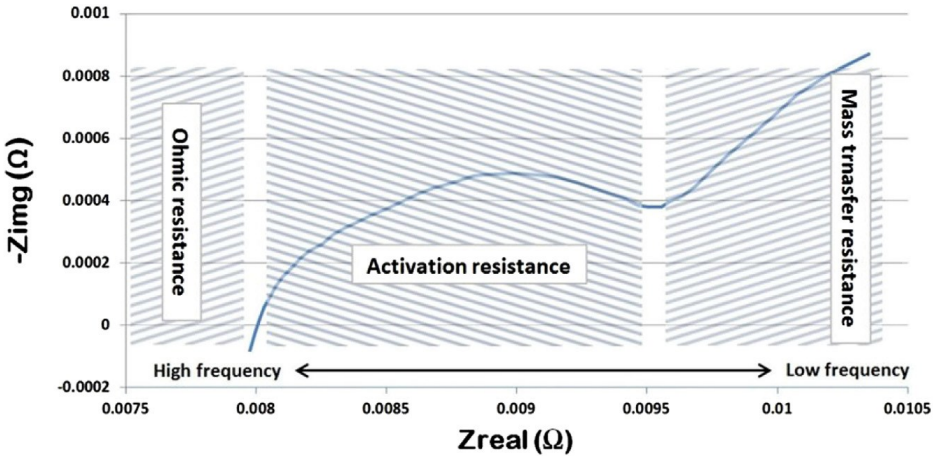

Figure 5.2 Characteristic impedance spectrum [114].

In the Bode graph each semicircle of the Nyquist representation- characterized by a specific time constant- is represented by a peak of the phase angle as function of frequency. When semicircles merge, it means that processes have time constants with same order of magnitude and this, translated to the Bode plot, is graphically shown by merging peaks as well, but these are still pronounced

and distinguishable even if merged. In these cases, the individuation and separation of the phenomena becomes challenging and troublesome.

The Nyquist plot is the most used graphical representation of the impedance data since from a visual inspection it allows to individuate some important features- high frequency, mid frequency and low frequency features- directly correlated to the main sources of losses in the cell. The high frequency intercept with the real axis corresponds to the sum of the internal ohmic resistances, including the electrolyte, active material, current collectors and electrical contacts. Hence, it gives an insight of the ohmic losses within the cell. The arcs appearing in the mid-frequency region- which can approximately be defined and usually it appears as two merged semicircles- are primarily due to the electrochemical processes occurring at the electrolyte/electrode interfaces inside the cell, which combine resistive and capacitive effects. These are OER at the anode and HER at the cathode, but mostly of the time the charge transfer reaction of the anode dominates due to its sluggish kinetics. Finally, the low-frequency range reflects mainly mass transport limitations in the active material of the cell electrodes.

It is important to point out that the impedance is defined for those systems that are compliant with the condition of causality, linearity and time-invariance. These are the conditions to get good impedances. Although PEM electrolysers, and in general electrochemical systems, are non-linear, the condition of linearity can be achieved if the amplitude of the perturbating signal is small enough to determine a linear response from the system under study [115]. As a consequence, the impedance data obtained are numerically validated through the use of the Kramers-Kroning relations which describe the correlation between the real and imaginary parts of the impedance. More details will be discussed in the next sections.

The analysis of the impedance spectrum is made by fitting the experimental data with a suitable equivalent electrical circuit (EEC) model composed of a combination of resistances, capacitors, inductors, Warburg elements and constant phase elements. These impedance elements are connected in parallel and/or in series to closely simulate the impedance spectrum and thus for describing the different processes characterized by different time constant.

For PEM electrolyser a common ECM used for the fitting procedure is shown in the figure below.

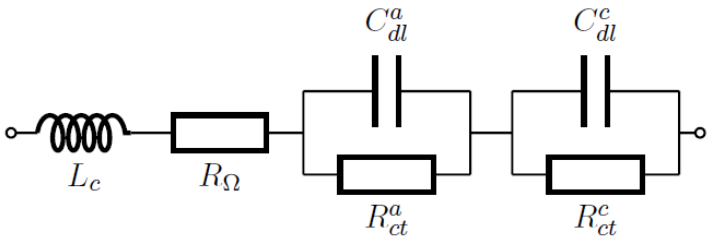

Figure 5.3 General ECM to simulate the impedance spectrum of a PEMWE[115].

The resistor R_Ω in series with the inductor L_C represent the resistance of the electrolyte membrane and the inductance of cables/wires used in the test, respectively. Thereafter, the subsequent two impedance elements consist of an ideal capacitor C_{dl} in parallel with an ideal resistor R_{ct}. These parallel connections account for the electrode/electrolyte interface at the anode and the cathode; the capacitance represents the double layer charging at the electrode interface whereas the resistance, commonly called charge-transfer resistance, accounts for the effective resistance for the electrode reaction.

More elaborate models substitute the capacitance with constant phase element (CPE) to simulate the fractal and porous nature of the electrodes [115] and add a Warburg element to consider the diffusive processes occurring in both electrodes.

Finally, the unknown values of the ECM, such as R_{ct}, R_Ω, CPE, are evaluated by a Non-linear Least Squares (CNLS) analysis. The CNLS-fit of the impedance data is carried out with commercially available software. It is an iterative process so once those good initial values of the parameters are estimated, the software will adjust them until the goodness of the fit is satisfactory. When the fit looks inappropriate, i.e. the simulation of the impedance spectrum results poorly close to the experimental data, the reason may be the wrong choice of the ECM or incorrect estimation of the initial values. Therefore, in these cases the procedure should be repeated [116].

5.1.2. Mathematical formulation

In the EIS experiment, the electrochemical system considered is perturbed with an input signal $x(t)$ and the response is measured as an output signal $y(t)$. The conversion of the time domain input and output signals to gain a quantity, that is function of the frequency, is based on the *Transfer Function (TF) method* which involves the use of the Laplace Transforms. Under the hypotheses of steady-state

system, Laplace transforms are replaced with simple Fourier Transforms. In this case, the TF takes the form of the ratio of the response to the input signal obtained in the frequency domain and moreover it describes entirely the properties of linear and steady-state systems [117].

In case of linear system, if $x(t)$is a sine wave input

$$x(t) = Asin(\omega t) \quad 5.3$$

the response is also a sine wave

$$y(t) = Bsin(\omega t + \phi) \quad 5.4$$

From a theoretical point of view the perturbation signal can be of different nature- white noise, step, pulse, etc.- however the sinusoidal wave signal is considered the most appropriate for EIS technique [118].

The relation between the system and the response to a perturbating signal is quite complex in the time domain and generally it requires the solution of a system of differential equations. A very useful simplification of the mathematical procedure results from the use of Fourier transformation. Thereby, by applying the Fourier transforms the transfer function can be defined as reported in this equation.

$$H(\omega) = |H(\omega)|e^{j\phi} \quad 5.5$$

Where $|H(\omega)|$ and ϕ are respectively the modulus and the phase shift of the transfer function. If $x(t)$ is a current and $y(t)$ a voltage, $H(\omega)$ is an impedance value $Z(\omega)$; inversely, if $x(t)$ is a voltage and $y(t)$ a current, the transfer function is an admittance value $Y(\omega) = Z(\omega)^{-1}$ [118]. As a consequence, in terms of electrical analogy, the transfer function in the frequency domain assumes a form similar to Ohm's law. As a matter of fact, this is true if the system obeys to the principles of linear time-invariant systems.

The impedance of an electrochemical system $Z(\omega)$ is a complex number which can be represented either in polar coordinates or in Cartesian coordinates:

$$Z(\omega) = |Z|e^{j\phi} \quad 5.6$$

$$Z(\omega) = ReZ + jImZ \quad 5.7$$

Where $ReZ\ and\ ImZ$ are the real part and the imaginary part of the impedance. The relationship between these quantities are:

$$|Z|^2 = (ReZ)^2 + (ImZ)^2 \quad 5.8$$

$$\phi = arctan\frac{ImZ}{ReZ} \quad 5.9$$

$$ReZ = |Z|cos\phi \quad 5.10$$

$$ImZ = |Z|sin\phi \quad 5.11$$

The graphical representation of the impedance spectrum can be done in Nyquist and Bode plots. In a Nyquist plot the x-axis represents the real part and the y-axis the imaginary part, thus the experimental data is characterized by ReZ, ImZ and ω. The Bode plots displays instead the frequency dependence of modulus and phase and usually is in logarithmic scale. Both plots start from high frequency impedance data to end with the low frequency ones.

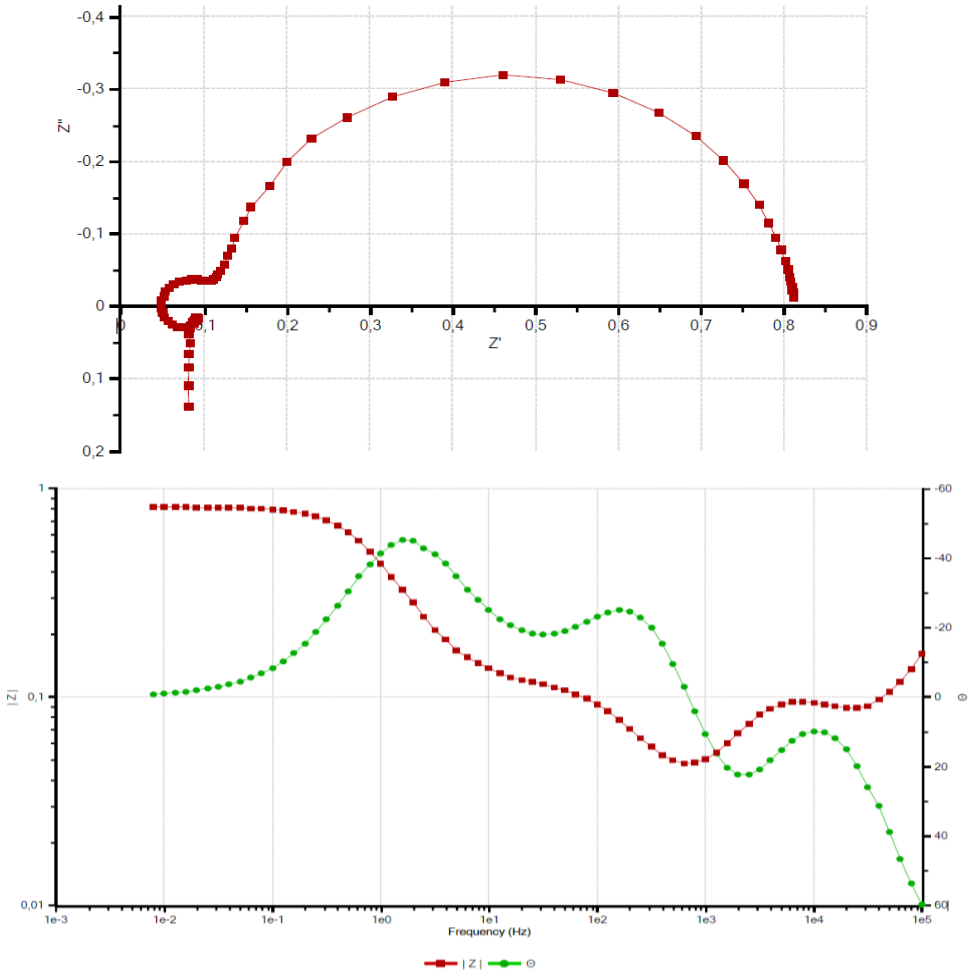

Figure 5.4 Nyquist and Bode plots under potentiostatic mode at 0V, with 60°C and 0.5barg, open cathode.

Electrochemical systems are complex systems where several elementary phenomena occur (transport, adsorption, diffusion, etc.) to end up with the charge transfer at the electrochemical interface. These processes determine the shape of the impedance spectrum.

An impediment to the application of the TF method arises from the assessment of non-linear behaviour in electrochemical systems, strictly linked to the laws which govern the kinetics of mass transport and those of the various electrochemical reactions, as well as the complex couplings between these elementary processes [118]. Moreover, real electrochemical systems behave as non- steady state systems with memory properties [117]. Therefore, the analysis of the impedance through the TF method requires that the system under investigation fulfils the conditions of *causality, linearity, stability, and finiteness*.

5.1.3. Data validation

The determination whether the obtained EIS data are good is fundamental to get a reliable and appropriate interpretation of the impedance data. In fact, EIS data should satisfy the main principles of linear time-invariant systems: linearity, causality, stability, and finiteness.

Linearity : The condition of linearity is satisfied if the amplitude of the perturbation signal is small enough to approach quasi linear conditions for the response. The amplitude should be selected in the linearity domain, which depends on the values of the DC voltage. From the Figure 5.5 it is possible to assess that the maximum acceptable amplitude of the perturbation signal is smaller at low frequency than it is at high frequency. However, a constant amplitude perturbating signal is generally used over the whole frequency range [118] . Note that the low limit of the linearity range comes from the signal-to-noise (S/N) ratio acceptable by the measuring instrument whilst the high limit is determined by the generation of non-linear distortion. Too low perturbation amplitude will result in an unacceptable S/N ratio, so the response is buried in noise and its recognition becomes difficult. Thereby, it is necessary to consider trade-off between linearity and accuracy.

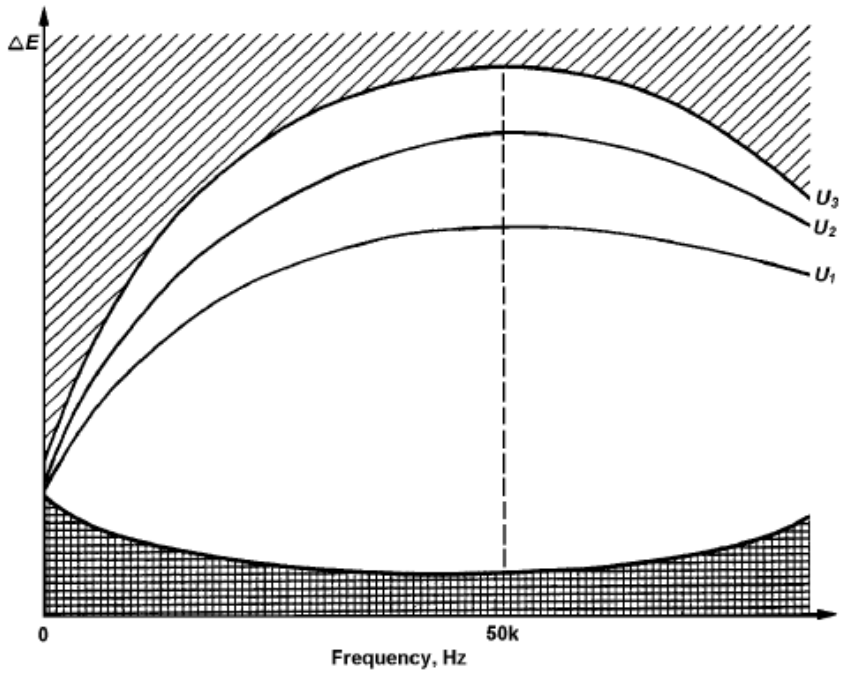

Figure 5.5 Definition of the linearity domain for various values of the DC voltage. The amplitude ΔE of the perturbation signal must be in the white region at a given frequency. [118]

Causality : The response of the system must be completely caused by the perturbating signal, thereby a causal system is not able to predict its future because its future is determined by the last event [119]. Measurement at high frequency are sensible to instrumentation artifacts concerning wires inductances and noise which affect the causality condition.

Finiteness : This condition, also called boundedness, implies that real and imaginary parts of the impedance should take finite values over the entire frequency range. Moreover, the impedance must tend to a constant real value for $\omega \to 0$ and $\omega \to \infty$ [119].

Stability : A system is considered stable if it returns to its original state after removal of the perturbation [119]. Moreover, it is required the steady-state condition, there is to say that the system should be independent from the moment of measurement (time invariant). However, completely stationary systems are difficult to achieve and in general non-stationary systems can be approximates to stationary by limiting the measurement time. Nonetheless, obtaining impedance data is time consuming, especially in low frequency range. Consequently, the stability is compromised and this condition is determined by the drift in the system

with time which can be ascribed to changes in temperature, pressure, concentration and so on and so forth.

In order to check whether these aforementioned conditions are satisfied by the system, impedance data should be subjected to a numerical validation based on the Kramers-Kroning (KK) relations. In fact, if the results obtained from the transformations agree with the experimental data, then it is possible to state that the data are formally corrected and are Kramers-Kroning compliant [119] [120].

The KK relations describe the correlation between the real and the imaginary parts of the impedance as shown in the following equations.

$$Z_{Im}(\omega) = Z''(\omega) = -\left(\frac{2\omega}{\pi}\right)\int_0^{\infty} \frac{Z_{Re}(x) - Z_{Re}(\omega)}{x^2 - \omega^2}\, dx \qquad 5.12$$

$$Z_{Re}(\omega) = Z'(\omega) = Z_{re}(\infty) + \frac{2}{\pi}\int_0^{\infty} \frac{xZ_{Im}(x) - \omega Z_{Im}(\omega)}{x^2 - \omega^2}\, dx \qquad 5.13$$

These equations show that if the real part of the impedance is known over the entire frequency range, its imaginary part is determined, and vice versa; when the imaginary part is given, the real part is completely determined up to the constant $Z_{Re}(\infty)$. In both cases, the degree of convergence between the measured values and the calculated one is an insight of the quality of the measurement [116]. When the measured real part and transformed imaginary part match, or the measured imaginary part match with the transformed real part, this means that data set is valid; instead, corrupted data set are found when neither of these two occurs and in this case invalid data should be rejected since are not suitable for further analysis. Usually, deviations between experimental and transformed data appear at low frequency due to the longer time to gain the data. In general, a criterion for the identification of a good fit comes from the deviation between measured and transformed data that should be below $\pm 1\%$ [115].

The Kramers-Kroning relations are able to determine whether the impedance spectrum of a given system has been influenced by bias errors caused by instrumental artifacts or time-dependent phenomena. Nevertheless, their direct application is not used since the integration of the equations requires impedance spectra measured from 0 Hz to ∞ Hz, which is experimentally impossible due to instrumental limitations or by noise attributable to instability of the electrode [31]. Various methods have been proposed. An approach to overcome this is based on the fact that if an appropriate ECM can be fitted to the experimental data, the data

are assumed to be KK compliant. In other words, the equivalent circuit model satisfies the KK relations implicitly.

The equivalent electrical model used consists of a set of parallel RC circuits in series. This type of structure is called Voigt's structure were the resistors as well as the time constant of the ECM are fitted to a measured impedance spectrum by CNLS fitting. The impedance of the Voigt circuit is described as follows:

$$Z(\omega_k) = R_0 + \sum_{i=1}^{n} \frac{R_i}{1 + \omega_k^2 \tau_i^2} - j \sum_{i=1}^{n} \frac{\omega_k \tau_k R_i}{1 + \omega_k^2 \tau_i^2} \qquad 5.14$$

Using a sufficient number of such RC elements the CPE or Warburg elements can also be approximated. The main drawback of this method is the nonlinear nature of the fit problem, therefore good initial values have to be chosen, and also a proper selection of the weighting to be used for the regression is necessary. Although this approach allows to avoid the integration over an infinite frequency domain, in case of poor fit it is difficult to understand whether this condition is due to inconsistency of the data with KK relations or to the use of an inadequate model or to regression to a local rather than global minimum related to inappropriate initial guess [120].

A modified version of this method has been proposed by Boukamp [121]. The problem related to the nonlinearity of the fit is solved by only fitting the ohmic resistors and pre-setting the time- constants. Hence, the fit problem becomes linear. This method is generally referred as linear KK validity test. In this case, it is necessary to manually pre-set the number of RC-elements to be fitted generating possible situation of under- or over-fitting and therefore leading to ambiguities in the analysis of the obtained results. Schönleber et al. [122] have proposed a strategy on how to automatically choose the number of RC-elements to be fitted for any given impedance spectrum. A tool based on the linear KK test proposed in [121] and the automatic strategy for finding the appropriate number of RC-elements proposed in [122] is the Lin-KK tool [123], that will be used for impedance testing in this thesis. More details will be further discussed in the following chapters. [124]

5.1.4. Equivalent Circuit Modelling

The interpretation of impedance data requires the use of an appropriate model. The information is accumulated in the impedance function, which does not provide a direct measure of all physical phenomena taking place within the system, but it is

more an information property that needs to be extracted through the construction of an appropriate working model [117] .

In principle, modelling of experimental data may be divided into two types: measurement modelling and process modelling [119]. The measurement modelling models the impedance data experimentally obtained by using an exact mathematical model based on a plausible physical theory that predicts theoretical impedance (classical modelling) or by an equivalent electrical circuit which leads to equivalent impedance (structural modelling) [117]. In either these cases, classical or structural modelling, the model parameters are gained by a parametrical identification that foresees the use of statistical methods such as Newton-Marquard, CNLS, simplex, model reduction and others.

In general, the most used approach is Equivalent Circuit Modelling (ECM). The model should be carefully chosen to give the best possible match between the simulated impedance and the measured impedance of the system [116]. The equivalent circuit model (ECM) or equivalent electrical circuit (EEC) consists of impedance elements taken from electrical engineering like resistors, capacitors and inductors as well as specialized electrochemical elements that will be discuss below. A proper combination of the impedance elements describes each physical phenomenon taking place in the system and moreover it provides the shape of the impedance spectrum shown in the Nyquist plot.

As a matter of fact, it is necessary to pay attention that for a given set of impedance data it is possible to use different equivalent circuits, and this may generate ambiguities. Hence, the choice of an adequate EEC needs the knowledge of the whole cell, including the behaviour of each element composing the cell and also the number of elements used should be small in order to avoid the lack of correlation between the impedance elements and the electrochemical processes [116]. Nevertheless, it is necessary to verify the validity of the model that has been constructed. As a rule of thumb, a model is valid when it can fit the impedance spectra obtained under a large variety of conditions.

5.1.4.1. Modelling elements and their physical meaning

Equivalent electrical circuit is a combination of different elements, which are divided in two groups:

Lumped elements: they are electrical elements and can describe only homogeneous systems. Resistors, capacitors and inductors belong to this category.

Frequency dependent elements: they are electrochemical elements, i.e. these are developed for the description of electrochemical processes.

A complete review of lumped and frequency dependent elements is brought in Appendix A:

5.1.4.2. Basic ECMs

Here are presented the basic equivalent circuit models commonly used in electrochemical systems. They are the Randles model and the Voigt's model.

5.1.4.2.1. Randles model

Randles circuit represents the model of a polarizable electrode, in which a single electrochemical reaction occurs at the interface without diffusion limitations. It consists of an ohmic resistance in series with a parallel connection between a double layer capacitance and a charge transfer resistance.

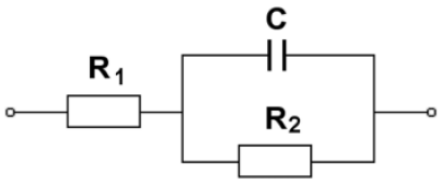

Figure 5.6 Randles model

The impedance diagram is an ideal semicircle as depicted in Figure 5.7. At high frequencies the measured impedance tends to R_Ω while at very low frequency it tends to $R_\Omega + R_{ct}$. Therefore, the high frequency intercept is associated with the electrolyte resistance and the diameter of the semicircle is equal to the charge transfer resistance. The imaginary part of the impedance reaches a maximum value at a frequency denoted as characteristic frequency $\omega_{max} = (R_{ct}C_{dl})^{-1} = \tau^{-1}$ where $\tau = R_{ct}C_{dl}$ is the time constant.

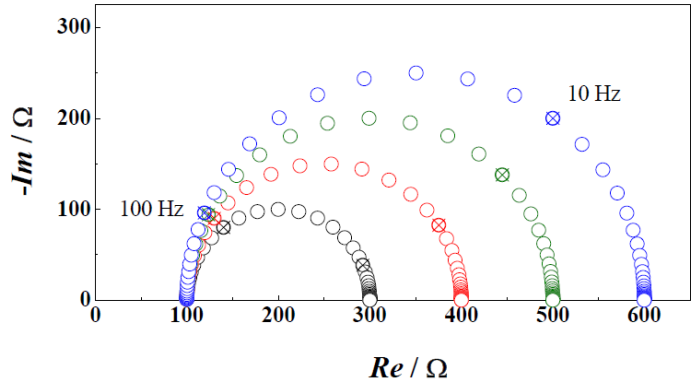

Figure 5.7 Impedance diagram of Polarizable Electrode simulated in the frequency range $10^{3} \div 10^{-3}$ Hz at different values of R_{ct} (R_s = 100 Ohm, C_{dl} = 1E-4 F) [117].

The total impedance is represented by the following equation:

$$Z(\omega) = R_{\Omega} + \frac{R_{ct}}{1 + \omega^2\tau^2} - i\frac{\omega R_{ct}\tau}{1 + \omega^2\tau^2} \qquad 5.15$$

For an electrochemical reaction at open circuit voltage, the charge transfer resistance is given by

$$R_{ct} = \frac{RT}{nFi_0} \qquad 5.16$$

where i_0 is the exchange current, n the number of electrons transferred, F the Faraday constant. Since the exchange current depends on the rate of the reaction, which in turn is potential dependent, the value of the charge transfer resistance has the same dependence. Hence, a variation of R_{ct} with voltage determines a change of the semicircle diameter, of the time constant and thus of the characteristic frequency.

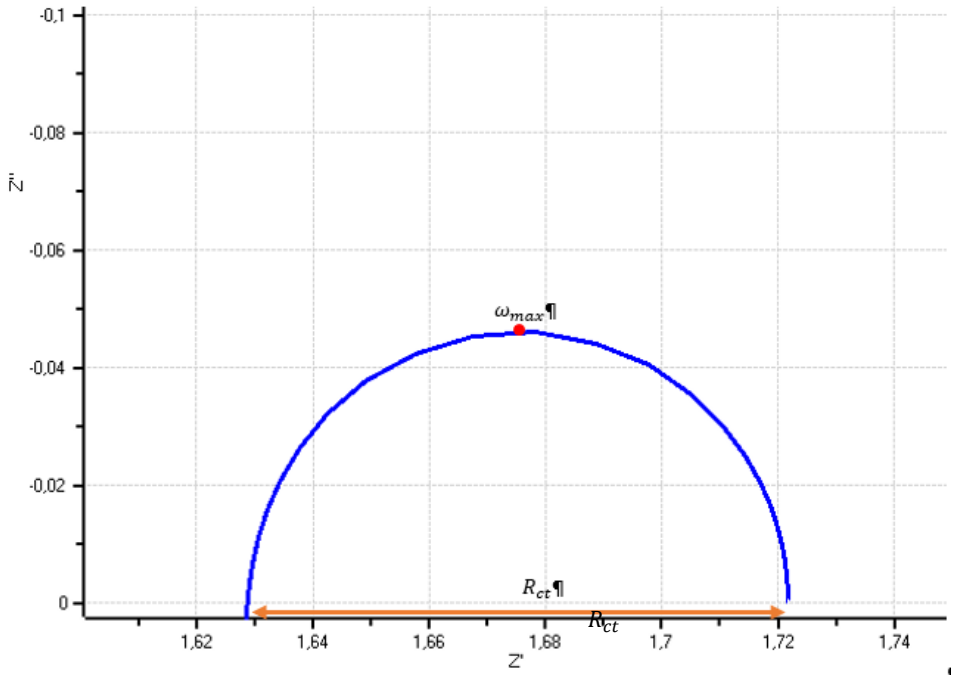

Figure 5.8 Modified Randles circuit

The Randles circuit is mostly used with the capacitance replaced by a CPE. In this case the graphical representation in the Nyquist plot is a depressed semicircle. As before, at high frequencies the impedance tends to R_Ω while at very low frequency it tends to $R_\Omega + R_{ct}$; the parameters of the CPE, n and Q, describe the deformation of the semicircle and its amplitude respectively.

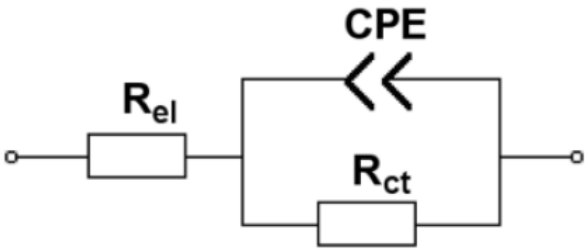

Figure 5.9 Randles with CPE

The impedance expression becomes:

$$Z(\omega) = R_\Omega + \frac{R_{ct} + QR_{ct}^2\omega^n \cos\left(\frac{\pi}{2}n\right)}{1 + 2QR_{ct}\omega^n \cos\left(\frac{\pi}{2}n\right) + Q^2R_{ct}^2\omega^{2n}} - i\frac{QR_{ct}^2\omega^n \sin\left(\frac{\pi}{2}n\right)}{1 + 2QR_{ct}\omega^n \cos\left(\frac{\pi}{2}n\right) + Q^2R_{ct}^2\omega^{2n}} \quad 5.17$$

When polarization is controlled by the combination of kinetic and diffusion processes the circuit model changes, a Warburg element is added in series to the charge transfer resistance (because charge transfer resistance is influenced by diffusion to and from the electrode).

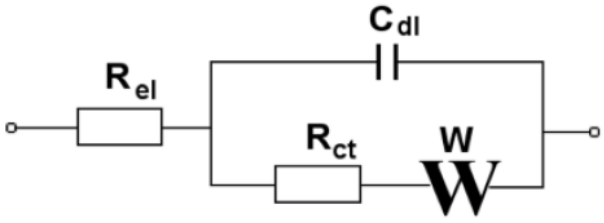

Figure 5.10 circuit with Warburg element

In case of *linear semi-infinite diffusion*, the simple Warburg element is used and therefore the Nyquist plot has a semicircle and a 45° line in the lower frequency region.

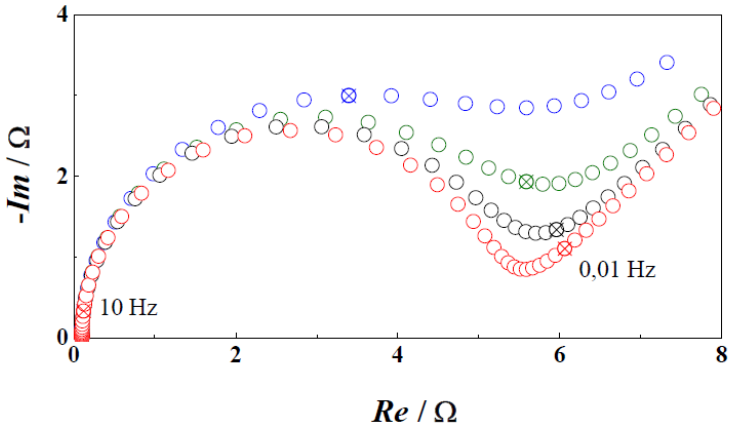

Figure 5.11 Impedance diagram of Randles model at different values simulated in the frequency range $10^3 \div 10^{-3}$ Hz of C_{dl}: 3E 4 F, 1E-3 F, 3E-3 F, 1E-2 F (R_0 = 100 Ohm, R_{ct} = 5000 Ohm, σ = 100) [117].

If linear but finite diffusion is present, the bounded Warburg element is used and the circuit is called bounded Randle circuit.

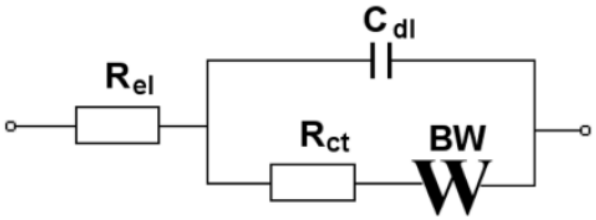

Figure 5.12 circuit with bounded Warburg element

The impedance diagram is characterized by a first semicircle and a 45° line followed by another semicircle. At high frequencies the impedance tends to R_Ω while at very low frequency it tends to $R_\Omega + R_{ct} + R_0$.

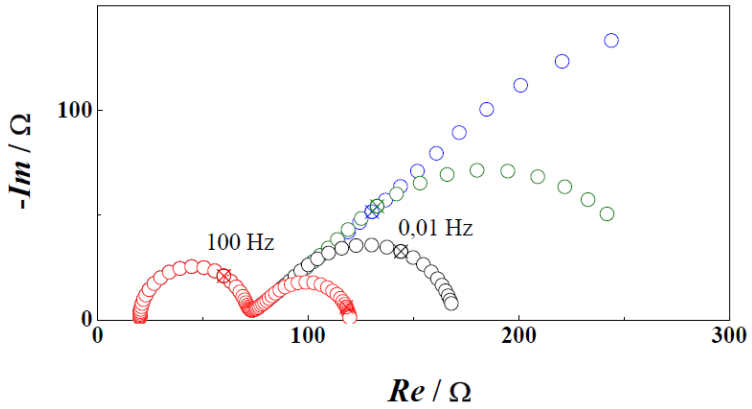

Figure 5.13 Impedance diagram of Bounded Randles model simulated in the frequency range $10^3 \div 10^{-3}$ Hz at different values of R_0: 50 Ohm, 100 Ohm, 200 Ohm, 400 Ohm (R_0 = 20 Ohm, C_{dl}= 1E-4 F, R_{ct} = 50 Ohm, Q = 0.1, n = 0.45) [117].

Another variation of these two circuits is possible by replacing the capacitance with a CPE; the Nyquist plot is unvaried with the only exception of the semicircles which become depressed.

5.1.4.2.2. Voigt's model

The Voigt's model is mostly used to describe solid electrochemical systems, such as electrodes and electrolyte in fuel cells, or electrodes in battery. It consists of several RC circuits in series, each representing a process with a specific time

constant τ. Electrode/electrolyte interface in solid systems is challenging because the electrode reactions involves species coming from the electrode, the electrolyte and the gas phase. Hence, this three-phase boundary is described through the Voigt's model, where every semicircle has a physical meaning. In general, the first two are ascribed to the charge transport through the bulk phase and the grain boundaries of the electrolyte, whereas the third semicircle is due to the electrode response [117] .

The total impedance for n RC circuit in series is calculated as

$$Z(\omega) = \sum_{k=1}^{n} Z_k(\omega) \qquad 5.18$$

$$\mathrm{Z_k}(\omega) = \frac{R_k}{1+\omega^2\tau_k^2} - i\frac{\omega R_k \tau_k}{1+\omega^2\tau_k^2} \qquad 5.19$$

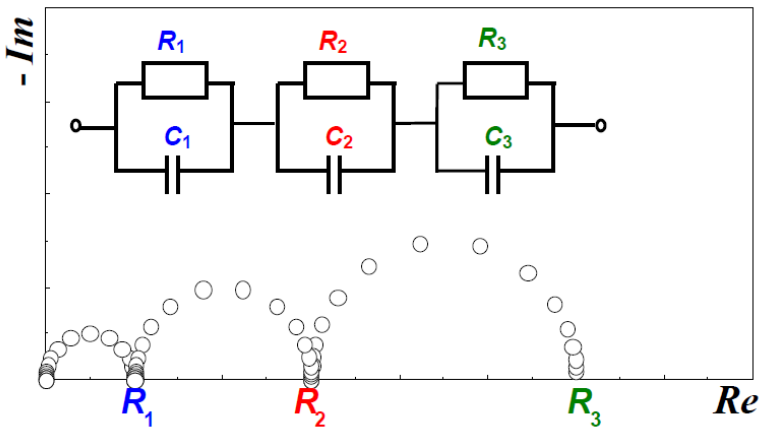

Figure 5.14 Impedance diagram of Voigt's model with three RC in series[117].

When using this model is advisable to see how many time constants are present in the Bode plot. In fact, it can happen that semicircles in the Nyquist plot may overlap because their time constants are very close. Therefore, an impedance spectrum characterized by two-time constants can show in the Nyquist plot only one semicircle.

A modified Voigt's model is possible by replacing the capacitances with CPEs. The impedance diagram is a series of depressed semicircles.

5.1.5. Data fitting

In order to evaluate the parameters of the model, the ECM is fitted to the measured impedance spectra by the Complex Non-linear Least Squares (CNLS) fitting algorithm. As a part of the statistical methods, it deals only with stochastic[1] (random) errors.

The purpose of the method is to find a set of parameters which minimize the objective function defined as:

$$S = \sum_{i=1}^{n} \left\{ w'_i \left[Z'_{i,ex} - Z'_{i,calc} \right]^2 + w''_i \left[Z''_{i,ex} - Z''_{i,calc} \right]^2 \right\} \qquad 5.20$$

where $w_{i,re}$, $w_{i,im}$ are the statistical weights of the real and imaginary components of the impedance Z_i, respectively, and n denotes the number of frequencies in the experimental spectrum. The differences between the experimental impedance and the calculated one are the residuals of the two components of the impedance (real part Z' and imaginary part Z'').

The method, based on the assumption that the distribution of error is normal (Gaussian), is iterative and nonlinear and moreover it requires an initial estimation of the model parameters. To gain a good fit the initial estimation of the parameters must be close as much as possible to the measured values. An inappropriate choice of these parameters may lead to error message from the software, for example "singular matrix", or parameters with high error values. The latter case occurs usually when the algorithm finds a local minimum. In these cases, it is necessary to change the set of initial parameters with new estimated one.

When complicated circuits are used, it is recommended to fit just a part of the whole circuit. Thereby, the elements found are fixed and then additional elements are added as free parameters. Finally, all the parameters should be set as free and thus their final approximation can be gained [119] . Lots of software implement this method and they have similar procedures. The starting point is the initial value estimation for all the model parameters; then the software adjusts the parameters to get the fit. If the goodness of the fit is not satisfactory the process is

[1] The stochastic or random error is intrinsic of each experiment whereas the bias error in the experiment arises from drift and instrumental artifacts [119]. In particular The stochastic errors in impedance measurements arise from an integration of time-domain signals that contain noise originating from the electrochemical cell and the instrumentation [120] .

repeated. Nonetheless, it is still possible to get a poor fit if the ECM is inadequate or the impedance data are affected by noise.

The goodness of the fit depends also on the statistical weight chosen for the evaluation of the parameters. In the following table are listed the possible choices. Since real and imaginary parts of the impedance change by several orders of magnitude when frequency changes, and the impedance is sensitive to low frequency, the unit weighting should never be used. Generally, modulus weighting and proportional weighting are recommended. These are based on an implicit assumption that the relative errors of $Z'_{i,ex}$ and $Z''_{i,ex}$ are proportional either to those quantities themselves or to $|Z_i|$ [125].

Table 2.3 Statistical weighting methodologies.

Method	Weighting
Statistical weighting	$w_i' = \frac{1}{(\sigma_i')^2}$ and $w_i'' = \frac{1}{(\sigma_i'')^2}$
Unit weighting	$w_i' = w_i'' = 1$
Modulus weighting	$w_i' = w_i'' = \frac{1}{\|Z\|^2}$
Proportional weighting	$w_i' = \frac{1}{(Z_i')^2}$ and $w_i'' = \frac{1}{(Z_i'')^2}$

The fitting of the model to the experimental data should provide χ^2 or χ_v^2 and the value of parameter with its standard deviation[2] (or confidence limit).

[2] The variance of a quantity x_k, sampled k=1…n_x times, is given as $\sigma_x^2 = \frac{1}{n_x - 1}\sum_{k=1}^{n_x}(x_k - \mu_x)^2$ where μ_x is the mean of the quantity x_k, while the standard deviation σ_x is given by the square

The minimal value of χ^2 (chi-square) provides a measure of the goodness of the fit of the model to the experimental data and it is defined as:

$$\chi^2 = \sum_{i=1}^{n} \left\{ \left[\frac{Z'_{i,ex} - Z'_{i,calc}}{\sigma_i'} \right]^2 + \left[\frac{Z''_{i,ex} - Z''_{i,calc}}{\sigma_i''} \right]^2 \right\} \quad 5.21$$

The χ_v^2 does the same and it is expressed as

$$\chi_v^2 = \frac{\chi^2}{2n - p} \quad 5.22$$

where p is the number of parameters of the fitted model. This value is more convenient than χ^2 for comparing the results of various fits. The smaller $(2n - p)$ or the larger p at constant n, the larger is χ_v^2 [125] . This χ_v^2 should approach unity when the approximation of the standard deviations are correct.

When the standard deviation of the model parameters is excessively large, it means that the fitting to this parameter is poor. This suggests elimination of the given parameter from the model [125] . Moreover, the residuals should be small and uniformly distributed in the whole range of frequencies considered in the fitting.

To recap, the aim of the fitting of a model to the experimental impedance spectrum is to obtain the smallest χ^2, and a set of model parameters with small standard deviations.

5.1.6. Electrochemical characterization of PEMWE

The following subchapter presents a review of different studies related to the electrochemical characterisation of PEM water electrolysis cells.

Rozain and Millet reported in [126] the results obtained using a MEA consisting of PTFE-reinforced Nafion with unsupported iridium dioxide for the anode catalyst layer (loading 1.5mg/cm2) and carbon-supported platinum for the cathode catalyst layer (0.5mg/cm2). They proposed the equivalent electrical circuit showed in *Fig.26B*, which models:

- charge transfer interface with a parallel connection of the polarization (charge transfer) resistance and the constant phase element

root of the variance. The standard error s_x is the standard deviation scaled by square root of the sample size n_x[120].

- mass transport limitations with a diffusion impedance
- electron flow in the metallic components and ion flow in the membrane with ohmic resistances

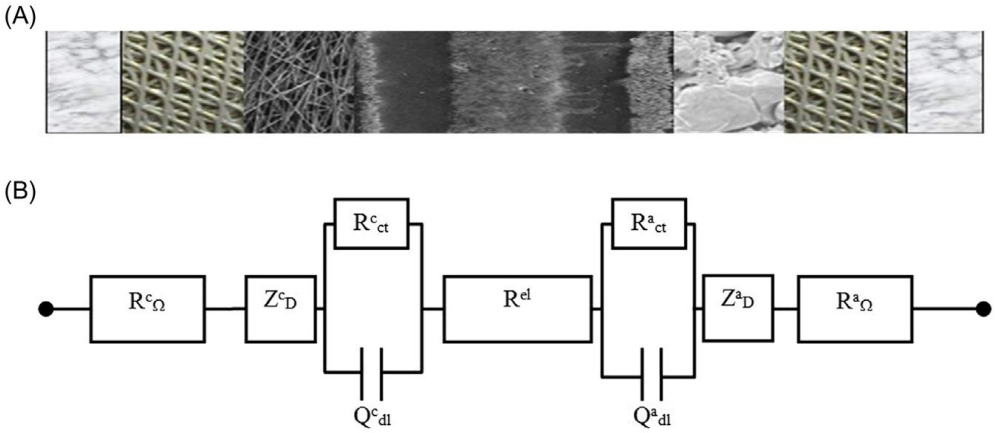

Figure 5.15 (A) Cross section of a PEM water electrolysis cell; (B) equivalent electrical circuit.

The different circuit components are:

R^c_Ω and R^a_Ω $[\Omega/cm^2]$ are current non-dependent electronic resistances of electron-conducting metallic cell components, respectively, in the cathodic and anodic cell compartments.

R^{el} $[\Omega/cm^2]$ is the current non-dependent ionic resistance of the membrane.

R^c_{ct} $[\Omega/cm^2]$ is the current-dependant cathodic charge transfer (polarization) resistance associated with the HER.

R^a_{ct} $[\Omega/cm^2]$ is the current-dependant anodic charge transfer (polarization) resistance associated with the OER.

Q^c_{dl} $[\mathrm{F}/cm^{-2}]$ is the potential-dependant double layer capacitance associated with the cathode/electrolyte interface.

Q^a_{dl} $[\mathrm{F}/cm^{-2}]$ is the potential-dependant double layer capacitance associated with the anode/electrolyte interface.

Z^c_D $[\Omega/cm^2]$ is the current-dependant cathodic diffusion impedance due to H_2 transport away from the cathode.

Z^a_D $[\Omega/cm^2]$ is the current-dependant anodic diffusion impedance due to O_2transport away from the anode and/or to H_2O transport to the anode.

They performed the electrochemical characterization by measuring the polarization curve at $80°C$ and EIS impedance measurements at different DC voltage level (1.4-1.9V) and $80°C$ on a 23 cm^2 PEM electrolytic cell described before.

Impedance spectra obtained had an arc-shape; it is shown that the impedance associated with the HER is negligible and that the two time-constants observed on experimental impedance spectra can both be attributed to the OER. Since no mass transport limitations were evident, the EEC used to fit the results was simplified to a series connection of the ohmic resistance (taking into account both electronic resistances of anode and cathode plus the membrane resistance) and two (RQ) circuits: $R_\Omega\ (R_{HF}Q_{HF})(R_{LF}Q_{LF})$. These elements modelled the single arc attributed to the anode by two semicircles. From the best fit, the polarization resistances at high and low frequency, R_{HF} and R_{LF}, were determined and they were plotted as a function of voltage and temperature. It is found that both polarization resistances decrease with increasing temperature and cell potential. It is shown that charge transfer processes were major cell impedance contributors at voltages up to 1.8-1.9 V whether for cell voltages larger than $1.8 - 1.9\,V$ the impedance became mostly ohmic because R_{HF} and R_{LF} become negligible. This result was in accordance with the polarization curve results in which at high current densities they did not observe mass transport limitations and the current-voltage relationship was almost linear in shape, whereas at low current density the curve was controlled by charge transfer kinetics of anode and cathode.

Van der Merwe at al. [114] identified the losses of a PEM electrolyser by performing EIS measurements in galvanostatic mode. The impedance data recorded were fitted to an ECM consisting of an inductance and an ohmic resistance in series, in turn in series with the parallel between a constant phase element and the series of charge transfer resistance and Warburg element. The Warburg element is used to model mass transfer effects in the cell. The results were verified through polarization curves and Tafel plots. Ohmic losses were individuated by changing only the membrane thickness and keeping unvaried electrocatalyst loadings. As expected, thinner membranes were characterized by lower ohmic resistance. This result is found in accordance with the trend of the polarization curves showing that thicker membrane had a steep slope, so higher ohmic resistance. Activation losses were identified by a change in temperature in the range between 60°C and 80°C. The charge transfer resistance- accounting for activation losses- decreased as temperature increased due to an improvement of kinetics. The effect of mass transport was determined by using two different GDLs

and usually in the Nyquist plot is represented by a second semicircle or a 45° line after the first semicircle.

In another work, van der Merwe et al. [127] investigated through electrochemical impedance spectroscopy, current interruption and current mapping a PEM electrolyser of $25cm^2$, with MEA consisting of Nafion, $1mg\ IrO_2/cm^2$ on the anode and $0.3mg\ Pt/cm^2$ on the cathode. Impedance measurements in galvanostatic mode performed at $0.1A/cm^2, 0.5\ A/cm^2, 1\ A/cm^2$ showed that the ohmic resistance- the high frequency intercept with the real axis on the impedance plot- slightly increased whether the semicircle at intermediate frequencies related to the activation resistance decreased. Finally, mass transfer effect were evident with increasing current densities in the low frequency range. In particular, at $0.5A/cm^2$a small tail is observed indicating that a small amount of mass transfer is occurring; then mass transfer became dominated at $1A/cm^2$. This is seen by the combination of a semicircle and 45° line. The results obtained from EIS measurements were consistent with the CI results.

Dedigama et al. [128] examined using high-speed camera, thermal imaging and electrochemical impedance spectroscopy an optically transparent PEM electrolyser consisted of a $28cm^2$ circular MEA with Nafion 117 and platinum catalyst layers on either side of it. Impedance spectra were obtained at different operating potentials, at different feed water flow rates and were fitted to an equivalent circuit consisting of an ohmic resistance in series with one or two circuit elements- made of a CPE in parallel with a charge transfer resistance. While the first parallel modelled the anode/electrolyte interface, the second is related to mass transfer effect if present in the impedance plot (second semicircle or 45° tail). It was observed that the flow changes from bubbly (many small bubbles) to slug (less but larger bubbles) flow at higher current densities. At high current density- changing the mass flow from low to high values- makes changing the flow from slug to bubbly, decreasing the performance of the electrolyser. This was in accordance with EIS measurements and polarization curves. Near OCV mass flow has little effect on EIS measurements whether at higher potential an increase of the mass flow has a negative effect (low frequency feature increased and internal resistance increased as well). Similar consideration can be done from the polarization curve, in which it was observed a slight decrease in voltage with decreasing flow rate. The main reason is that less heat is removed from the system, so activation overpotential decreased and ionic conductivity of the membrane increased leading to higher performance at lower flow rates. Hence at higher current densities it is better to decrease mass flow rate.

Elsøe et al. [129] investigated the performance of PEMEC at high current densities using EIS measurements in combination with CV, iV-curves and SEM. The PEM electrolyser had an active area of 2.89 cm^2 and it contained a Nafion 117 membrane, anode catalyst layer with 0.3 mg/cm^2 IrO_x and cathode catalyst layer with 0.5 mg/cm^2 platinum supported on carbon. The anode side had a GDL made of two components, a titanium felt and an iridium metal with Nafion binder. The iridium metal is used only to ensure electrical contact between the catalyst layer and the titanium felt. Polarization curves were measured at 53, 61 and 69°C from 0.050 A/cm^2 to 1 A/cm^2 while EIS measurement were realized at 0.07, 0.35, 0.69 and 1 A/cm^2 at 53, 61 and 69°C in the frequency range 100 kHz–0.01 Hz with the alternating current (AC) amplitude of 24.5 mA/cm^2. Higher performance was found at higher temperature due to lower ohmic resistance as confirmed by the EIS measurements at different temperature in which it was found a temperature dependent behaviour of the high frequency intercept with the real axis. Moreover, at fixed temperature, the shape of the spectrum changed with current density. At high current density the impedance spectra showed three arcs indicating three electrochemical processes, thus they used an equivalent circuit model consisting of a resistance-modelling the electrolyte resistance- in series with three R/CPE simulating these three arcs. They suggested that the high frequency arc independent on current density derived from current constrictions- ascribed to bad contact between Nafion and iridium oxide layer and iridium metal layer as supported by SEM- whereas the middle and low frequency features were determined by the interface between IrO_x/Nafion anode catalyst layer causing two capacitive impedances dependent on current density (mid frequency arc decreased while low frequency arc increased with increasing current density), but with total resistive impedance of the two processes constant at current densities from 0.35 A/cm^2. These findings were consistent with results obtained from the polarization curves showing a linear behaviour from 0.35 A/cm^2, meaning that ohmic losses are dominant from 0.35 A/cm^2.

Rasten et al. [130] did studies on powders of iridium oxide (2 $mgIrO_2/cm^2$) as anode catalyst in water electrolysis cells with SPE (active area 5 cm^2). The aim of their work was to develop a high performing water electrolysis cell with low loading of the noble metal oxide catalyst. The catalyst was annealed at different temperatures from $450°C$ to $540°C$ and then studied in an electrolytic cell using cyclic voltammetry, stationary i-V curves, and electrochemical impedance spectroscopy.

The electrochemical results showed that with increasing annealing temperature the electrical conductivity increased whereas the electrocatalytic activity (number of active sites available in the electrode, measured with the capacitance) deteriorated. This was evident in the EIS test performed at $1.49\ V$ with frequency range $10kHz - 10mHz$ on samples with different annealing conditions. The ohmic resistance – including external circuit resistance, resistance of the electrodes and the electrolyte, and contact resistance- decreased up to a constant value with increasing annealing temperature, therefore the electrical conductivity improved. Instead, there was an increase of the diameter of the low frequency arc, which is a measure of the charge transfer resistance and thereby of the catalytic activity of the anode; the latter case was determined by a decrease of the capacitance $[\mu F/cm^2]$ which is in turn due to a worsening of the electrocatalytic activity of the anode. These effects could be explained with the TEM (transmission electron microscopy). TEM revealed an increased crystallinity and size of the particles with increasing annealing temperature. In fact, the particle size growth determined a reduction of the active surface which consequently caused the capacitance reduction (C is a direct measure of the active surface). Meanwhile the higher electrical conductivity was probably related to the higher crystallinity. Furthermore, the impedance measurements performed in the voltage range between $1.54 - 1.61\ V$ with annealed sample showed clearly the presence of two arcs identified in the Bode plot by two-time constants. The time constant associated with the HF arc became more evident with increasing potential whereas that related to the LF range disappeared. The impedance spectra obtained were fitted with an $R_\Omega(R_1Q_1)(R_{dl}Q_{dl})$ circuit where (R_1Q_1) circuit element was attributed by the literature to different phenomena. However, for the researchers it was more likely related to steps in the OER. Optimum annealing conditions were found at 490°C, where the total polarisation reaches a minimum in the high current density range $(1 - 2\ A/cm^2)$, at the actual conditions. Very high performance of a total electrolysis cell can be obtained using a polymer electrolyte with iridium oxide catalyst for the oxygen electrode and platinum for the hydrogen electrode, using totally 2.5 mg of noble metal catalyst per cm^2 MEA area [cit.40].

Rozain et al. [131] also studied the influence of iridium oxide loadings for OER on the overall performance of PEM water electrolyser with active area of $25\ cm^2$ using cyclic voltamperometry, electrochemical impedance spectroscopy and polarization curves. Electrochemical characterizations performed at $80°C$ and atmospheric pressure showed that there is a threshold loading value of $0.5\ \frac{mg}{cm^2}\ IrO_2$ above which the cell voltage does not depend on catalyst loading, i.e., an increment

of the loadings does not produce a further decrease of the voltage. This because the positive effects generated by higher loadings (larger number of catalytic sites, better electronic conductivity through the catalyst layer and improved contact resistance between electrode and backing porous current collector) are counterbalanced by the worsening of the transport of protons through the catalyst layer, caused by the linear increase of the catalyst thickness with higher loadings. This, translated to the EIS results, means that the ohmic resistance (determined by the high frequency intercept with the real axis) measured at $1\ A/cm^2$ remains almost constant in the loadings range $0.5 - 2.6\ mg/cm^2\ \ IrO_2$, while the polarization resistance, taken as the difference between the extrapolated low frequency intercept and the high frequency intercept on the real axis, does not significantly change with IrO_2 loadings. To conclude, below this threshold value the performance of the cell drops quickly and the anode tends to degrade rapidly. Hence a conductive support is needed to keep a good level of performance.

In another work Rozain et al. [132] deepened the influence of iridium oxide as anode catalyst layer in PEMWE by studying the applicability of micro-sized titanium particles as support of IrO_2 particles in the low loading range ($< 0.5\ mg/cm^2\ IrO_2$) in order to increase the electronic conductivity of the anodic catalytic layer. The electrochemical properties of the IrO_2/Ti catalyst were investigated in a $25\ cm^2$ PEM electrolytic cell with $50\ wt.\%IrO_2/Ti$ anodes containing iridium oxide loading ranging from 0.1 to 0.7 mg/cm^2 through the application of CV, EIS and recording polarization curves at 80°C and atmospheric pressure. Regarding EIS measurements, the tests were carried out with DC current level between 0.04-2.00 A/cm^2 in the frequency range $10kHz - 200mHz$. Experimental impedance spectra were fitted using a simple equivalent circuit (L+Rohm+R1//Q1+R2//Q2) where the high frequency equivalent circuit R1//Q1 is attributed to reactions occurring at the cathode, and the low frequency equivalent circuit R2//Q2 is attributed to anodic reactions.

The electrochemical investigation with EIS and i-V curves showed that for IrO_2 loadings below $0.25mg/cm^2$ the addition of titanium particles to the catalyst layer improved the performance with respect to unsupported iridium oxide. This was valid whether they had same or different loadings. However, increasing the loadings when IrO_2/Ti catalyst is used could cause increment of voltage, probably related to the thicker catalyst which introduces mass transport limitations. These results are interrelated with charge transfer kinetics and ohmic resistance of the catalyst layer. At low current density, the voltage drop due to the ohmic resistance of the cell is negligible whereas charge transfer effects are dominant; at high

current density, charge transfer resistance are small, and the voltage drop due to the internal cell resistance is predominant. Therefore, when IrO_2 loadings are below $0.25mg/cm^2$, titanium particles enhanced the electrocatalyst activity (more active sites) and ohmic losses because they favoured an intimate electrical contact between the catalyst layer and the current collector (hence improved electronic conductivity). Meanwhile, with higher loadings the addition of titanium particles determined a thicker catalyst layer which in turn caused the increase of the electronic resistance of the catalytic layer. However, the positive effect of titanium particles found an explanation in SEM and CV: meanwhile small particles are embedded within the catalyst layer, the bigger ones are found to protrude from it, penetrating inside the porosities of the current collector; this contributed to improve the electronic contact between the catalyst layer and the current collector, facilitating the electron transfer hence optimizing the number of active sites [132].

To evaluate the stability of IrO_2/Ti catalyst- the titanium particles in the long-term can oxidize increasing the electrical resistance- they also performed two different ageing-tests. The durability test performed with a PEM electrolytic cell using IrO2/Ti as anode material demonstrated a good stability of the MEA over 1000 h of operation. Using such a low IrO2 loading (0.1 mg cm-2IrO2), the degradation rate measured at 1 A cm-2 was reduced from 180 μV h-1 (measurement made on pure IrO2 anode) down to only 20 μV h-1 for the 50 *wt.*% IrO2/Ti anode [131] A detailed analysis of the electrical properties of the PEM cells during these ageing tests revealed that three main different electrical factors contribute to the degradation of MEA performances: the purely ohmic resistance of the cell, the charge transfer resistance of the anode and the capacity measured at low frequency (this capacity is related to the electrochemically active surface area of the electrodes). The ohmic resistance during the operation at 60°C remained stable or slightly decreased (probably due to membrane thinning) while at 80°C both the ohmic resistance and the charge transfer resistance increased linearly with time. Their degradation was attributed to the oxidation of the titanium current collectors and the resulting increase of the contact resistance between this material and the catalyst layer. The capacity measured at low frequency instead decreased quickly during the first hours of operation and then reached a constant value; this behaviour was attributed to the stress produced by oxygen nucleation within the porous catalyst layer, by bubbling and by erosion of the catalyst particles by water flowing [132].

Lettenmeier et al. [133] did ageing tests on 8-cell stack having MEA from different suppliers operating up to $4\ \mathrm{A/cm^2}$ for more than 750h in a $120\mathrm{cm^2}$ PEM

electrolyser stack. All MEAs had the same membrane Nafion 115 but different anode and cathode catalyst loadings.

The electrochemical characterization was performed recording i-V curves and EIS measurements with additional post-mortem analysis with SEM and AFM. EIS tests were executed at different current densities ($0.025 - 0.35\ A/cm^2$) from 1kHz to 100mHz on each cell of the stack before and after the ageing tests. The EEC used to simulate the impedance data consisted of ohmic resistance in series with two R_{ct}/CPE. The element R_1 represents the ohmic resistance while the two R/CPE elements model the features of HF and LF impedance spectra. The meaning of the two R/CPE circuits finds different possibilities in the literature. If the interpretation given in PEM fuel cell is considered, the HF arc is attributed to the HER at the cathode whereas the LF arc corresponds to the oxygen evolution reaction taking place at the anode. Another interpretation of other groups associates the HF arc with charge transfer processes combined with double layer effects of electrical and/or ionic conductive materials and oxides in the active layer[133]. The latter is supported by Lettenmeier et al. due to the negligible dependence of the HF feature on current density and linear behaviour of the resistance. Polarization curves and impedance spectra were recorded before (T1) and after (T2) operating at 2 A/cm^2 for ca. 500 h, and after 250 h at 4 A/cm^2 (T3).

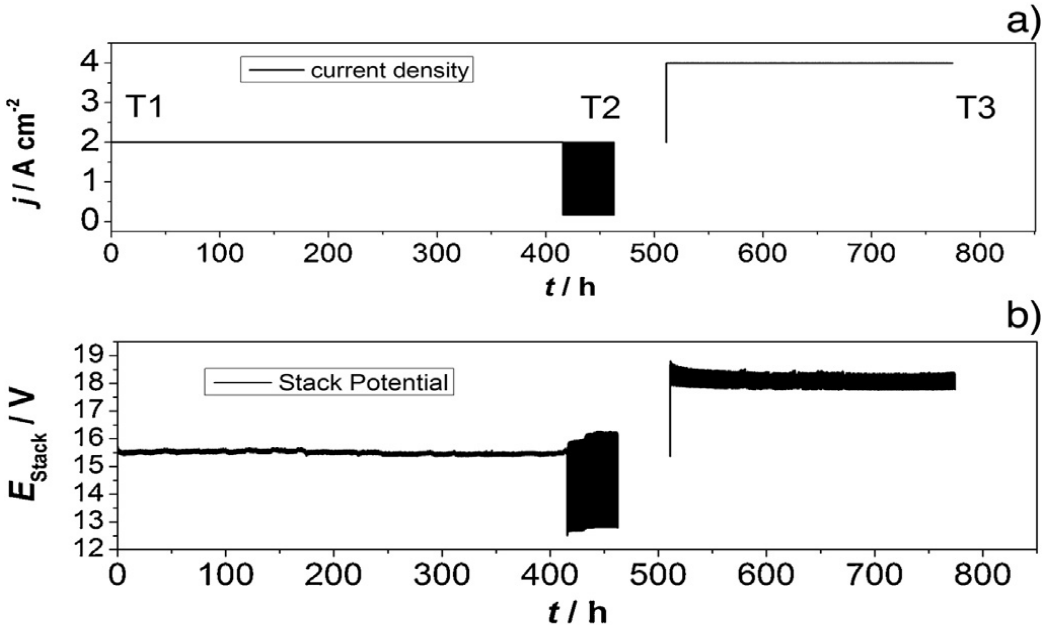

Figure 5.16 Protocol of measurements of the 8-cell 120 cm2 stack: a) Input current density; b) Output stack potential. EIS was measured at the time steps T1, T2 and T3 of the protocol [133].

For all MEAs it was found that the cell voltage decreased during the testing period. The picture below shows that for all MEAs the efficiency is improved because the voltage decreases over time.

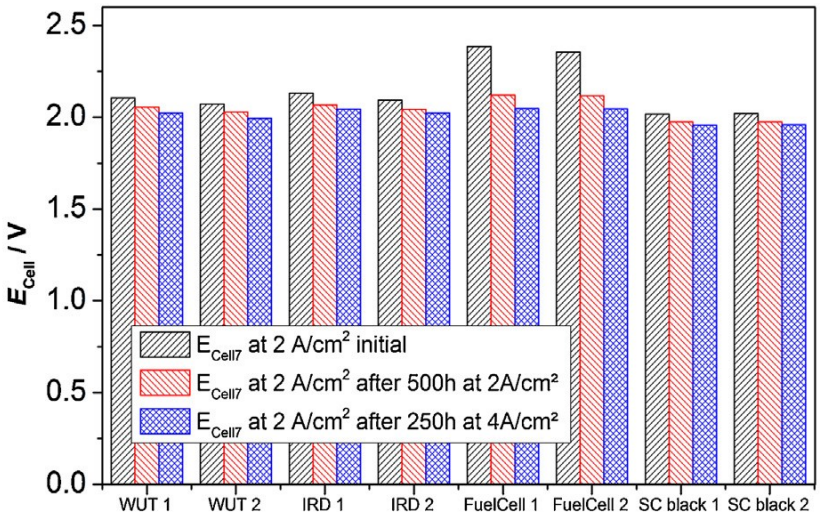

Figure 5.17 E cell of all cells measured at $2\ A/cm^2$ *after T1, T2 and T3* [133].

From a deeper analysis of cell 7, it was found that the ohmic resistance decreased over time whereas the charge transfer resistance increased. The explanation of lower ohmic losses is related to the applied current density (the percentage of decrease increased with increasing operating time) and the increment of activation losses is ascribed to loss in the electrocatalytic properties supported by XPS measurements of DI water resin of the anodic water cycle. Concluding, current density and operation time had an impact on the performance of the PEM electrolyser. The operation at high current density reduced the ohmic drops but long-term operation caused a degradation of the anode. This is supported by post-mortem analysis of the MEAs (SEM and AFM) and water resin (XPS) which revealed a current dependent loss of ionomer and catalyst material in the anode . [133]

Lettenmeier et al. [134] worked on the development of a titanium MPL (macro-porous layer) produced by vacuum plasma spraying (VPS) on the current collector of PEM electrolysers. The aim of the macro-porous layer is to increase the contact surface with the catalyst while improving the water/gas management through a gradient of pore sizes. They found that it enhances the efficiency when operating at high current density by reducing the contact resistance between anode catalyst layer and the current collector of around $20\ m\Omega cm^{-2}$, thus improving the

activation losses and the reactant/product management. The electrochemical characterization (polarization curves and EIS tests) was performed on a 25 cm^2 single PEM electrolyser cells- with a N115 membrane, Ir-based anode and Pt-based cathode- using the porous titanium disc as current collector with and without MPL at 85°C and atmospheric pressure. EIS measurements were realized at different current densities between 0.08 A/cm^2 and 1.2 A/cm^2 in a frequency range of $10kHz - 2mHz$.

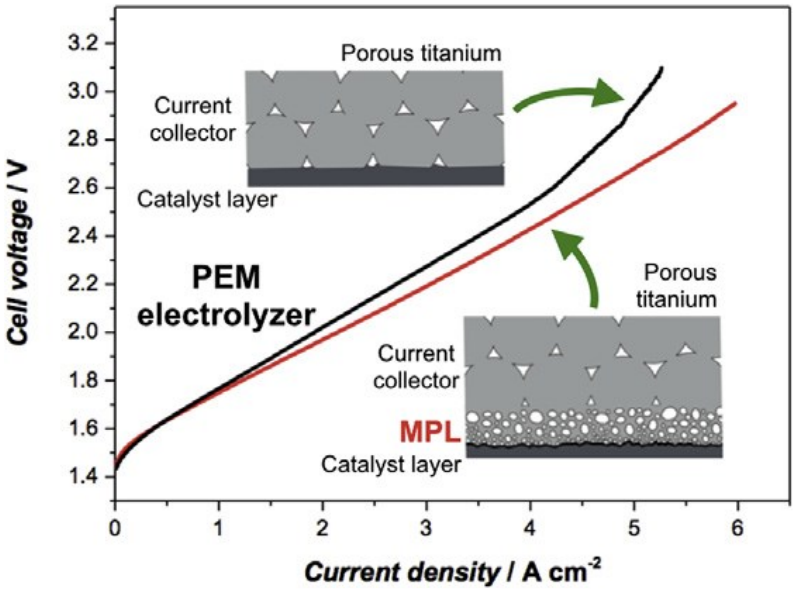

Figure 5.18 Polarization curves of a PEM electrolyser single cell with and without MPL [134]

The EEC used to fit the experimental data consisted of a resistance R_1- associated to the interconnecting elements and membrane- in series with three R/CPE circuit elements modelling the three arcs appearing in the impedance spectra. The circuit element $R_2/CPE2$ models the HF loop related to the interface between MPL and the catalyst layer/ionomer. Meanwhile $R_3/CPE3$ and $R_4/CPE4$ simulate respectively the OER and the mass transport limitation effects. A comparison between impedance spectra measured with and without MPL showed that at high current densities with MPL there is a decrease of R_1 and R_2 , thus of the HF loop, whereas the middle arc representing the kinetics of the oxygen evolution reaction is unvaried. The LF loop did not show a clear trend. Hence, the improvement obtained adding the MPL at high current density is confirmed by EIS results.

Siracusano et al. [135] studied the electrochemical behaviour of a sulfonated polysulfone membrane in a single PEM electrolyzer by linear sweep voltammetry, electrochemical impedance spectroscopy, chrono-amperometry and gas cross-over measurements. The results were compared to those obtained with a PEMWE based on a Nafion 115 reference membrane in order to assess the suitability of SPSf membranes for this application[134]. Both SPSf membrane and Nafion 115 membrane were characterized by same active area of 5 cm^2 and same catalysts with same loadings of 2.5 $mg\ IrO_2/cm^2$ for the anode and 0.4 $mgPt/cm^2$ for the cathode. A comparison of the polarization curves for the electrolysis cells based on SPSf and Nafion 115 membranes at 80°C and atmospheric pressure showed that the cell equipped with Nafion 115 membrane had at 1.8V slightly higher performance (15%) than that of SPSf. This result is verified by EIS test in potentiostatic mode performed at 1.5V and 80°C and atmospheric pressure. Impedance spectra have been fitted with an equivalent circuit consisting of two (RQ) elements- representing HER and OER respectively- in series with the ohmic resistance R_s associated to the electrolyte. Both membranes had similar ohmic resistance, but Nafion membrane showed a lower polarization resistance probably due to a better electrode-membrane interface. This is reasonably related to the presence of Nafion ionomer dispersed in the catalytic layer of the electrodes, which makes the kinetics process faster because it extends the three-phase reaction zone. SPSf membrane is considered a valid alternative to Nafion 115 because, even if Nafion 115 has shown slightly better performance due to higher proton conductivity and improved electrode-membrane interface, their behaviour is comparable. Moreover, other tests such as chrono-amperometric and hydrogen cross-over tests demonstrated that SPSf has good stability and a lower permeability to gas cross-over with respect to Nafion 115, making this type of membrane very promising for the application in high pressure PEM electrolyzers[135].

Siracusano et al. [136] investigated in a PEM electrolyzer a composite Nafion-Sulfated Zirconia ($SZrO_2$) membrane at different temperatures. Its performance was compared to a commercial Nafion 115 membrane of similar thickness. Both membranes were characterized by same active area of 5 cm^2 and same catalysts with same loadings of 2.5 $mg\ IrO_2/cm^2$ for the anode and 0.4 $mgPt/cm^2$ for the cathode. Nafion membranes decrease their proton conductivity at temperature above 100°C. Therefore, incorporation of sulfated zirconia has the aim to enhance its performance under thermal and water management point of view, as its use in fuel cells has demonstrated. In the polarization curves at 80°C and atmospheric pressure it is observed a slightly

different trend between these two different membranes: at low current densities Nafion 115 showed better performance whether Nafion-Sulfated Zirconia performed better at high current densities. These results were consistent with the findings of the EIS test performed at 1.5V and 80°C. From impedance spectra it is found that ohmic resistance of the cell with the composite membrane had lower values (this explains better performance at high current densities where ohmic losses are dominant); instead, the polarization resistance for the cell with bare Nafion was characterized by lower values so better performance in the activation region of the polarization curve. The lower ohmic resistance for the composite membrane is ascribed to the higher humidification level gained with the addition of sulphated Zirconia, whether lower polarization resistance of bare Nafion is related to better catalyst-electrolyte interface. Further, electrochemical characterization at 100°C showed in general better performance of the Nafion-SZrO2 membrane, essentially because sulfated Zirconia promoted higher hydration level determining a decrease of the ohmic resistance; instead, Nafion 115 showed some hydration constraints appearing in the Nyquist plot as a linear slope at high frequencies. In conclusion, composite Nafion-SZrO2 membrane showed better performance principally related to an increase of proton conductivity due to better hydration but it required enhancement of the catalyst-electrode interface affected by the formation of agglomerates which may reduce the adhesion of the catalytic layer on the composite membrane[136].

Su et al. [137] investigated the feasibility of using the catalyst sprayed membrane under illumination (CSMUI) method to prepare low noble metal loading MEAs for PEM water electrolyser. The electrochemical and physical characterization of the MEAs was performed by I-V curves, electrochemical impedance spectroscopy (EIS) and scanning electron microscopy (SEM). It was found that MEA with noble metal loading (NML) of $0.38\ mg/cm^2$ had lower ohmic resistance and negligible mass transport limitations. SEM and EIS measurements revealed that the MEA with low NML has very thin porous cathode and anode CLs that get intimate contact with the electrolyte membrane, which makes a reduced mass transport limitation and lower ohmic resistance of the MEA[136]. They also investigated the influence of the ionomer content in the anode catalyst layer using the MEA with low NML of $0.38\ mg/cm^2$, suggesting that the optimal Nafion content in the anode was 5wt.%. Finally, the durability test showed that MEA with low NML of $0.38\ mg/cm^2$ and 5wt.% Nafion content exhibited good stability in water electrolysis and at a current of $1\ A/cm^2$ its

voltage remained at 1.60 V without significant degradation during the 122 h of testing[137].

Siracusano et al. [138] studied the performance of a 5cm^2 PEM electrolysis cell through polarization curves and electrochemical impedance spectroscopy at different temperatures and catalyst loadings. The results from EIS measurements were obtained by fitting the experimental data to an ECM made of a series resistance- reflecting ohmic phenomena- and two RQ components associated to faradaic processes. The investigation of different cathode loadings consisted of polarization curves at 80°C coupled with EIS tests under voltage control at 1.5V. They observed that polarization curves, with constant anode loading but different cathode catalyst loading, overlap at all current densities, meaning that the cathode loading has no influence on the cell performance. Instead, its effect is visible on the Nyquist plots in which are evident two overlapping semicircles; the one appearing at high frequency is attributed to the cathode because as the cathode loading increases the resistance of the HF arc decreases considerably. On the other hand, the arc occurring at low frequency is attributed to the anode since it has a higher polarization resistance, which does not change with the cathode loading variation. Meanwhile, when the anode loadings is reduced, the polarization resistance at low frequency increases; this reflects in the polarization curves with an increase of voltage at low current densities, which in turn has an influence also at high current density. The study at different temperatures showed that the slope of the polarization curves increases as the temperature decreases. Also, it is observed that the anode benefits much more than membrane from the increase of temperature. Finally, they concluded with a 1000-h durability test carried out at 3 A/cm^2. The test showed a degradation rate of $20\,\mu V/h$ and the anode was identified to contribute to the degradation behaviour since its polarization resistance showed a substantial increase.

Suermann et al [139] proposed an approach to underline degradation mechanisms by using different electrochemical methods including polarization curves and EIS measurements. They suggested that there is an apparent degradation rate coming from the anode, which can be recovered by applying lower potential. Instead, real degradation is related to ohmic and mass transport overpotential occurring at higher current densities and for longer operating times. The degradation test, called constant current test, is performed at 60°C and ambient pressure at two different current densities, 1A/cm2 and 4A/cm2. The CC test last for each constant current density 270 hours, and during the total measurement time electrochemical characterization- iV-curves, EIS measurements under

galvanostatic mode, current interruption- is performed each 30 hours; hence, each 30h CC test has two electrochemical characterization, one at the start and the other at the end. The degradation rate is calculated taking the value obtained at the start of each 30h CC test phase. Another degradation rate is calculated using the end values. The degradation rate based on the start values are considered as the real degradation whereas those obtained with the end values include parts of apparent degradation. It is found that the degradation rate of the 4 A/cm2 sample is higher than those of the 1 A/cm2 sample with $10\mu V/h$. Moreover, degradation rate for the 1A/cm2 sample is mainly due to apparent degradation, hence to the activation overpotential. Concerning the 4A/cm2 sample the degradation rate is related to real degradation, thus to ohmic overpotential. These findings are consistent with the EIS results. While the ohmic resistance stays almost constant for the 1A/cm2 sample at least up to EIS current densities of about 1A/cm2, an increase is measured for the 4 A/cm2 sample. They suggested that the increasing HFR could be caused by cationic contamination of the membrane, dissolution and re-precipitation of the iridium within the membrane or rather by an increase in the interfacial contact resistances between the titanium PTL and the anode and/or the flow field [50]. The difference between the high frequency intercept and the low frequency intercept with the real axis shows a moderate increase for the 1A/cm2 whereas the increase is substantially significant for the 4A/cm2 sample. Therefore, it is verified that at 1A/cm2 the degradation concerns the anode, whereas it is attributed to the membrane at 4A/cm2.

Aßmann et al [140] proposed an accelerated stress test protocol for the evaluation of the PEMWE efficiency and durability. The aim of this type of test is to accelerate the degradation mechanisms by stressors such as high current density, dynamic operation, and shutdown modes. The first step is to individuate the main degradation mechanisms; these are the anode catalyst dissolution, membrane chemical decomposition, and formation of semiconducting oxides on the metal components [140]. Each of these mechanisms is sensible to a determine stressor. The high current density (>1A/cm2) is the most dominant stressor; the use of EIS test confirms that the membrane shows degradation processes when higher current densities are applied. A visible reduction of the ohmic resistance is measured, which is linked to the thinning of the membrane. The latter is caused by a loss of ionomer in the anode catalyst layer. Another cause of performance loss at constant current density is the formation of Ti oxides on the anode Ti-PTL. Other stressors are dynamic operation and shutdown process. Both lead to the corrosion of Pt/C catalyst and to agglomeration of the Pt nanoparticles [140]. Generally, the

degradation rate obtained during dynamic operation is lower compared to the degradation rate under constant operation. They suggested that the ASTs (accelerated stress tests) for PEMWE should include:

- nominal current density operation
- high current density operation, affecting the ionomer content in the anode catalyst layer and membrane, and the Ti-PTL.
- Load cycling, causing degradation of the cathode catalyst layer
- Shutdown process, having an impact on the cathode components.

They concluded that it is also necessary not only to individuate and understand the degradation mechanisms but also to establish a standardized PEMWE testing hardware for the development of ASTs and evaluation of cell components [140].

Alia et al [141] evaluated the anode catalyst losses at low loading and intermittent operation. They observed higher durability losses at low catalyst loading. On the other hand, dynamic operation determined an acceleration of the anode degradation. It is noticed a decreasing of the kinetic performance and an increase of the polarization resistance, both linked to the thinning and deterioration of the anode catalyst layer. Hence, it is suggested that the electrolysers' performance are affected by low catalyst loading and intermittent inputs like renewable source. As a consequence, there is the need of developing components and system controls able to limit these performance losses.

Rakousky et al [142][141] investigated the durability of a PEM water electrolysis cell over 1000h at 80°C and 2A/cm2. Before, during and after the measurement period EIS tests and polarization curves were recorded. They observed an average degradation rate of 194 $\mu V/h$ which accounts for both reversible and irreversible degradation. Using the results of EIS, it is seen an increase of the ohmic resistance from 131 to 157 $m\Omega cm^2$ corresponding to a voltage increase of 52 mV. From the evaluation of the polarization curves obtained during the long term test at 2A/cm2 it is found that of 159 mV increase, 17% (24mV) is caused by the electrode degradation and the remaining 83% (129mV) arises from the total resistance, which takes into account membrane resistance and contact resistances, including the electric resistance of the Ti-PTL. This rise of the total polarization has been assumed to derive from the oxidation of the Ti-PTL. This is experimentally validated using a second cell assembled using Pt-coated Ti-

PTL, that determined a reduction of the degradation rate up to $12\ \mu V/h$ within a period of 380h.

Siracusano et al [143] investigated a set of MEAs, already used for 3500-5700 h in a PEM electrolyser, through EIS measurements and physio-chemical techniques such as SEM, TEM and EDX (energy dispersive X-ray). The MEAs used had same basic components and active area (8cm2) but they were prepared according to different hot-pressing procedures. All MEAs were run at constant current of 1A/cm2 and 55°C and the degradation rate was $3.3\ \mu V/h$. EIS measurements were gained at different current densities and at the end series resistance and polarization resistance are obtained. There was a progressive decrease of the polarization resistance with increasing applied current densities, according to the enhancement in reaction kinetics. However, with prolonged operation, at same current density it is observed an increase in the polarization resistance. On the other hand, the series resistance decreases, due to membrane thinning as assessed by SEM. TEM images of anode and cathode showed that there is an increase of particle size and agglomeration in both sides of the MEA. Moreover, EDX showed Ru dissolution and also the presence of Fe and Ti impurities in the anode, and a decrease of fluorine in the cathode. In conclusion, the main sources of degradation are listed: presence of impurities which affects ionic conductivity and membrane/ionomer degradation; Ru dissolution; Ti plate degradation, related to the release of fluoride species; decrease of ionomer content; membrane thinning and changes in the catalyst/membrane interface, which may affect hydrogen cross-over.

5.2. EIS measurements

5.2.1. EIS test equipment and set-up

In order to perform EIS measurements, it is necessary to have:

- Potentiostat/Galvanostat or a load bank
- Frequency response analyser, FRA
- DC power supply

In Figure 5.19 a schematic EIS measurement configuration shows the connection between potentiostat, FRA and WE cell.

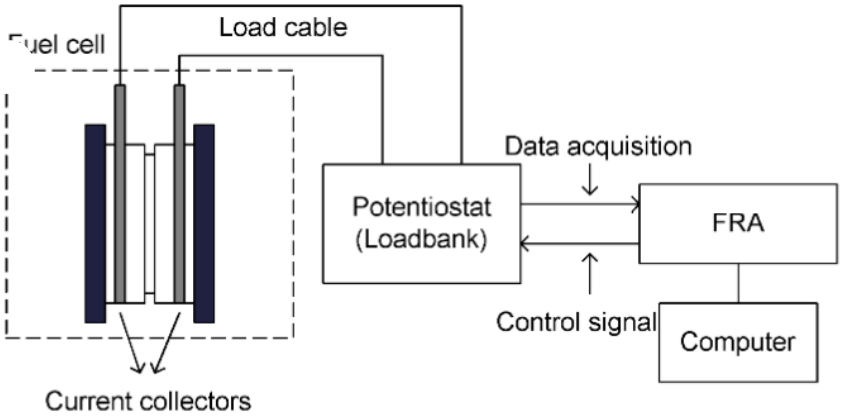

Figure 5.19 Schematic EIS measurement configuration[116].

AC impedance measurements are usually performed by a four-electrode measurement configuration with a working electrode, a counter electrode and two reference /sense electrodes[115]. The WE is the anode (positive electrode), to gain measurements of the current passing through the cell; the CE is the cathode (negative electrode), to provide a voltage or current to drive the cell and the two RE (RE1 and RE2), anode and cathode, to measure the voltage difference between two reference electrode points within the cell. Therefore, a two-wire configuration is performed.

To gain meaningful data from the EIS experiment, reducing as much as possible stochastic and bias errors, it is necessary to pay attention to some important specifications reported in [115]. In particular:

- the test set-up should be connected in such a way as to avoid measuring parasitic current flowing into the load
- the immediate vicinity of the test set-up should be free of electromagnetic sources to avoid interference with the EIS measurement
- low-inductance cables should be used thus they should be shielded, twisted around each other and as short as possible
- cross sections of the CE and WE should be instead as large as possible.

In the EIS experiment, the electrochemical system considered is perturbed with an input signal and the response is measured as an output signal. There are

two options for controlling the perturbation to measured system: one is to control the current perturbation then record the voltage response from the system (galvanostatic mode), the other is to control the voltage perturbation then record the current response (potentiostatic mode) [116]. The working principle for a current control measurement, described below, is equivalent to that of voltage control with the only exception of constant DC value (in this case is a voltage), and input and output signals which are inverted, thus voltage and current respectively. When the leads are all connected, the electrical load is set to a DC constant current. The FRA will generate an AC current perturbation and interrupt the cell through a Potentiostat. The response to the interruption from the cell will enter into the FRA for analysis to obtain the AC impedance spectra [116]. The ratio of the frequency spectra of the response (output) and that of the perturbation (input) gives the impedance in *galvanostatic mode* and the admittance in *potentiostatic mode.* Hence, the complex impedance or admittance can be obtained at the measured frequency by dividing the response by the perturbation. This procedure is repeated again and again, with the frequency of the stimulus swept across the frequency range within the capabilities of the FRA [116] . In this way, it is possible to gain the full impedance spectrum of the electrochemical system under study.

It is necessary to pay attention to the perturbation amplitude. This needs to obey linearity as discussed before, thus it is required a small amplitude of the perturbating signal. However, too low value will result in an unacceptable signal-to-noise ratio making it difficult for the FRA to distinguish between the actual response and the noise arising from random excitations. The figure below from Malkow T et al. [115] lists all the parameters to set up with their recommended value/range.

	Test input	Symbol	Unit	Recommended value / range
	Number of perturbation frequency data per decade of frequency range	*PPD*	-	minimum 3
	Number of perturbation cycles during τ_{ACT} (τ_{ACT} *precedes* τ_{ACS})	n_{ACT}	-	minimum 2 (*)
	Number of perturbation cycles during τ_{ACS} *used to record the* EIS spectra (τ_{ACS} *follows* τ_{ACT})	n_{ACS}	-	minimum 3
	Range of perturbation frequencies	f	Hz	10^{-2}–10^{+6}
Potentiostatic method	load (voltage) perturbation peak-to-peak amplitude	U_{AC}	V	typically 5-10 mV_{rms} to be less than the thermal voltage, U_T (e.g. <30 mV at 80°C cell temperature) (†)
Galvanostatic method	load (current) perturbation peak-to-peak amplitude	I_{AC}	A	0.5% – 5% of I_{DC} (‡)

Figure 5.20 Input parameters and settings for the EIS instrument [115] .

The AC impedance spectrum is graphically represented by the Nyquist plot. Another type of plot is the so called Bode plot. These graphs show the tests output parameters gained from the EIS measurement.

Output	Parameter type	Measurement uncertainty	Sampling rate	
$U_{AC,k}(f)$	primary	± 1%	≥ 20 ($\tau_{ACS}(f)/\tau_{ACT}(f)$)	Galvanostatic method
$I_{AC,k}(f)$	primary	± 1%	≥ 20 ($\tau_{ACS}(f)/\tau_{ACT}(f)$)	Potentiostatic method
$Z_{IM,k}(f)$	secondary	– (*)	–	Nyquist plot (†)
$Z_{RE,k}(f)$	secondary	– (*)	–	Nyquist plot (†)
$\|Z_k\|(f)$	secondary	– (*)	–	Bode plot (‡)
$\theta_k(f)$	secondary	– (*)	–	Bode plot (‡)

Figure 5.21 Output parameters for the EIS measurement [115]

5.2.2. Measurement modes

AC impedance spectroscopy foresees two methods to execute the impedance measurements; these are the potentiostatic mode and the galvanostatic mode. Each mode involves advantages and drawbacks and depending on the application one can result more adequate than the other. In general, the differences in the obtained results are almost invisible to be considered negligible [144] .

With the potentiostatic mode in the operating WE cell an AC voltage perturbation signal is imposed and the response of the system is a current[144]. This method allows to use the whole spectrum provided by the FRA/potentiostat but it should be pay attention to the amplitude of the stimulus for two fundamental reasons. The amplitude must not exceed the maximum current tolerable by the potentiostat otherwise this can drift to an overloading of the cell. Moreover, the amplitude chosen must ensure the linearity of the current response [144]. This explains the recommended amplitude value of the stimulus between $5 - 15\ \mathrm{mV}$ [115]. However, electrolytic cells have lower impedance value ($\approx 1\Omega$) thus even small impedance voltage perturbations may lead to large currents; this may affect negatively the signal-to-noise ratio. When measuring the impedance spectrum in potentiostatic mode the frequency is usually swept in a range between $100\mathrm{kHz}$ and $1\mathrm{mHz}$, and the points per decades are generally 10. Potentiostatic measurements are carried out at different DC voltage levels to have a better representation of the phenomena occurring during the operation of the electrolytic cell. Rozain and Millet [126] performed EIS measurements in the potentiostatic mode at different DC voltages ($1.4 - 1.8\mathrm{V}$) in the $100\ \mathrm{kHz} - 1\mathrm{mHz}$ frequency range to characterize a $23\mathrm{cm}^2$ PEM water electrolysis cell made of Nafion as solid polymer electrolyte, iridium oxide as anodic catalyst and carbon-supported platinum as cathodic catalyst. Dedigama et al. [128] performed EIS characterization of a PEMWE of $28\ \mathrm{cm}^2$ in a constant potentiostatic mode in a frequency range between $100\mathrm{kHz} - 0.1\mathrm{Hz}$ by frequency sweeping in the single sine mode with amplitude of $10\mathrm{mV}$ and 5 frequencies per decade. Siracusano et al. [138] studied a $5\ \mathrm{cm}^2$ PEM electrolytic cell at 1.5V and 1.8V in the frequency from $100\mathrm{kHz} - 100\mathrm{mHz}$ with an AC amplitude pk-pk of $10\mathrm{mV}$.

With the galvanostatic mode the perturbation signal applied is an AC current which spans the cell and hence the response of the system is a voltage [144]. In general, this method is characterized by a frequency range between $200\ \mathrm{kHz}$ and $2\mathrm{mHz}$; moreover, it has the advantage of larger perturbation current amplitude without determining a relevant change in the cell voltage; therefore, it allows a

better control of the current across the cell. In fact, the amplitude value of the current perturbation determines a voltage response of mV, which is tolerated by most instrumentations. Moreover, higher current perturbation improve the signal-to-noise ratio so the EIS measurements are more accurate. Nonetheless, the amplitude of the stimulus is still critical because the response needs to be within the linear regime. In general, it is recommended a value around $0.5 - 5\%$ of the DC value[115]. However, at high current densities, the cell voltage is unstable and this instability could impair the accuracy of the AC impedance measurement, especially for low-frequency measurements. Elsoe et al. [129] chose a frequency range of $100\text{kHz} - 0.01\text{Hz}$, $24.5\ \text{mA/cm}^2$ AC amplitude, and 12 points per decade for the galvanostatic mode measurement of a PEMEC with active electrode area of $2.89\ \text{cm}^2$ at $0.07, 0.35, 0.69, 1\ \text{A/cm}^2$. van der Merwe et al. [26, 38] made impedance measurements on a $25\ \text{cm}^2$ PEM electrolyser in galvanostatic mode with a frequency range of 200 mHz to 200 kHz.

5.2.3. Test procedure

The EIS measurements are carried out with the Energy-Lab XM System Energy-Lab XM System provided by AMETEKSI with Solartron Analytical brand coupled with the software XM-studio ECS. The device consists of a PGSTAT potentiostat/galvanostat, an internal 2A booster and the frequency response analyser, FRA. The system is controlled through the software XM-studio ECS. The Potentiostat/galvanostat enables to perform experiment on the cell. When used on its own it is able to run many types of DC tests, while combined with the FRA it can also measure impedance. It records data with maximum rate of 1M samples/second and it is able to work in a voltage range of $\pm 8\text{V}$ up to $\pm 300\text{mA}$ and 1MHz bandwidth. The internal power booster is used to enhance the capability for testing higher power electrochemical systems, and it is characterized by a maximum output of $\pm 8\text{V}/\pm 2\text{A}$. The FRA allows impedance measurements, it can generate and analyse AC waveform with good accuracy over its range of operation over its full frequency range $10\mu\text{Hz} - 1\text{MHz}$.

Figure 5.22 Energy-Lab XM System.

The test procedure foresees in order:

- the wire connection between the cell and the ModuLab XM,
- the creation of the project in the XM-studio software including the setting of the test input parameters, and finally
- the experiment running.

A proper electrode connection is required. A schematic configuration is reported in Figure 5.23. The potentiostat is connected to the internal booster and the booster is connected to the cell. The CE on the booster is connected to the positive terminal and the WE is connected to the negative terminal. The working and counter wires of the ModuLab XM are connected to the anode (positive electrode) and the cathode (negative electrode) respectively, while the reference wire is connected to both cathode and anode electrodes.

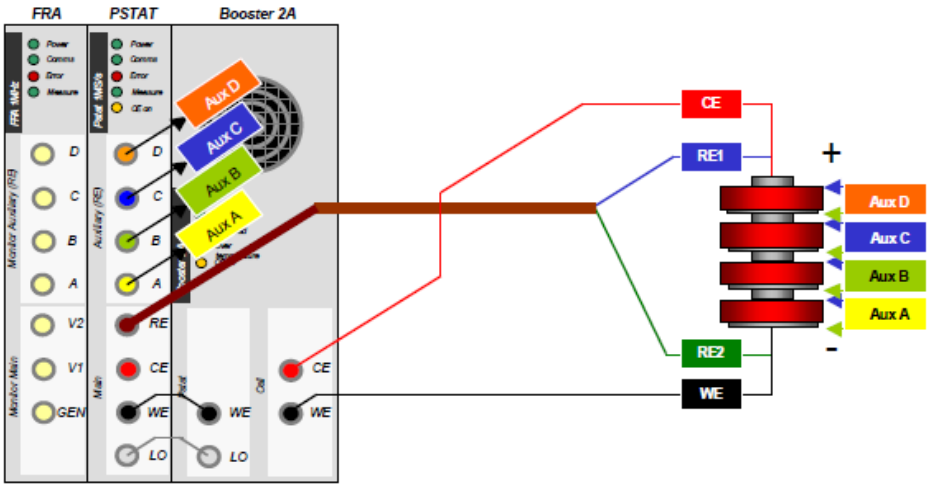

Figure 5.23 Schematic configuration of the connection between the cell and the device.

Prior to the running of the experiment, is the creation of the project in the XM-studio ECS software. This enables to run different experiments named steps: DC voltage control, DC current control, impedance voltage control and impedance current control. The focus of this work is the characterization of the electrolytic cell with the impedance spectroscopy technique thus the steps chosen are the last two: Impedance Voltage Control and Impedance Current Control.

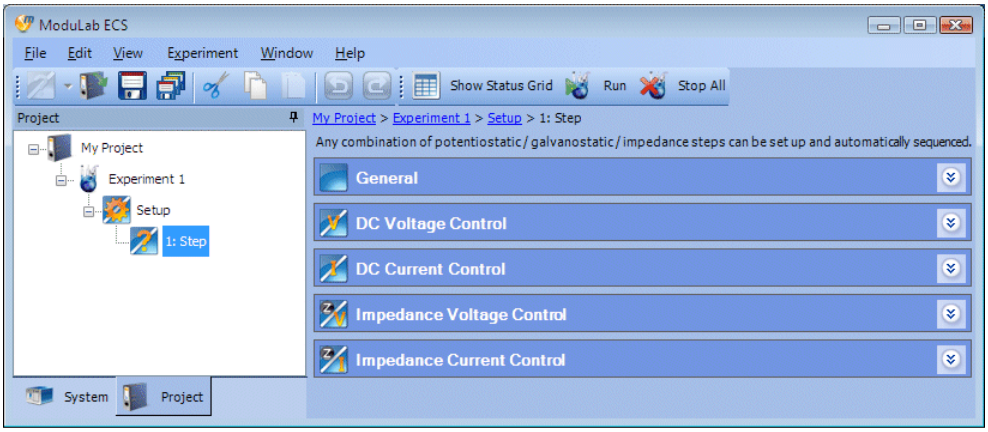

Figure 5.24 Types of experiments in the XM-studio ECS software.

For each step category there is a list of step types among which making the choice. For the impedance voltage control Potentiostatic impedance is selected while for the impedance current control the Galvanostatic impedance. These

represent the two EIS measurement modes performed in this work. Steps are similar for Galvanostatic and potentiostatic cases that is brought in Figure 5.25

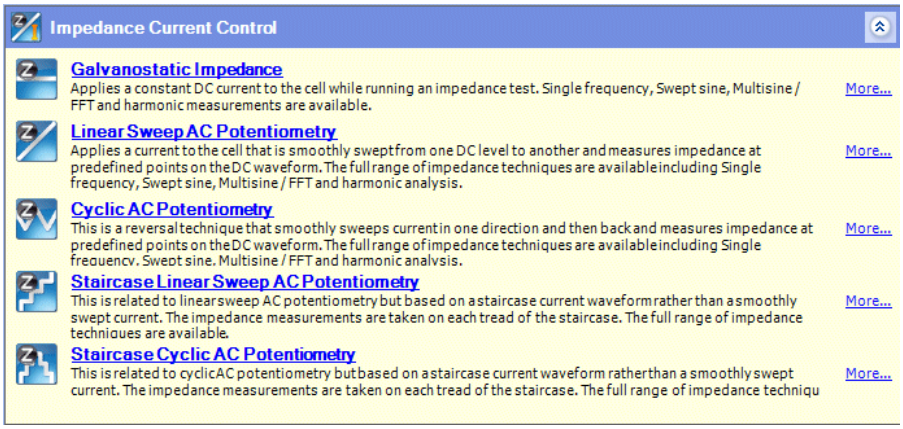

Figure 5.25 Possible step types for *galvanostatic impedance*.

For each EIS measurement mode the first step is the definition of the experiment Setup item consisting of different fields, in particular Hardware Requirement and Cell Setup. The Hardware Requirement specifies the hardware and connection configuration for the experiment while the Cell Setup some specification about electrochemical cell such as the electrode active area, the type of reference electrode, density and equivalent weight.

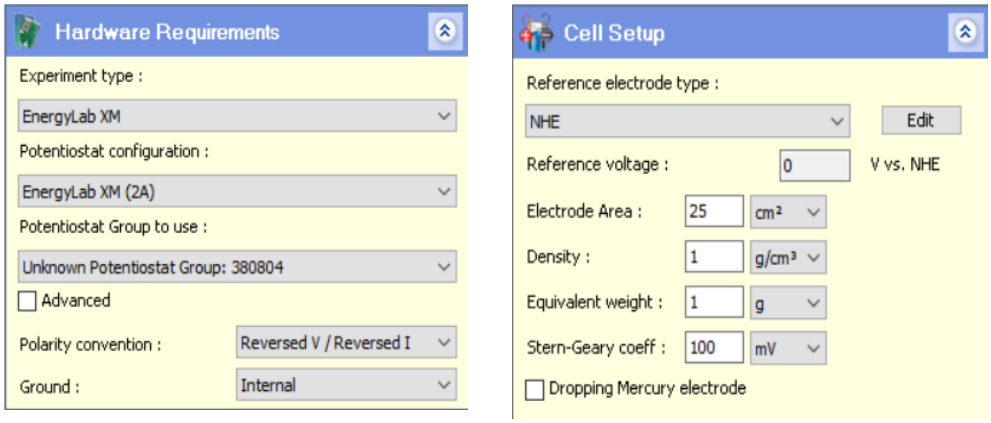

Figure 5.26 Hardware requirements and cell setup example

Thereafter, there is the definition of the test inputs for both the impedance experiments. These are defined into two fundamental sub-screens:

- Scan Setup: this sub-screen specifies values associated with the excitation signal that is applied to the cell.

- Impedance Setup: it specifies the frequency range to be tested since the system superimposes a frequency, or a range of frequencies, on top of the DC scan that has been specified from the Scan Setup.

The Impedance Setup contains several fields to specify as shown in the Figure 5.27. In the Technique the frequency sweep- consisting of a single sinewave swept from the start frequency to the end frequency- is chosen as the type of the AC stimulus. Other possibilities are the single frequency where a single sinewave is applied to the cell at a fixed frequency or the multi-sine where multiple sinewaves, according to a Fast Fourier Transform, are swept from the start frequency to the end frequency. A set of parameters that are set for our experiments are brought in Figure 5.27

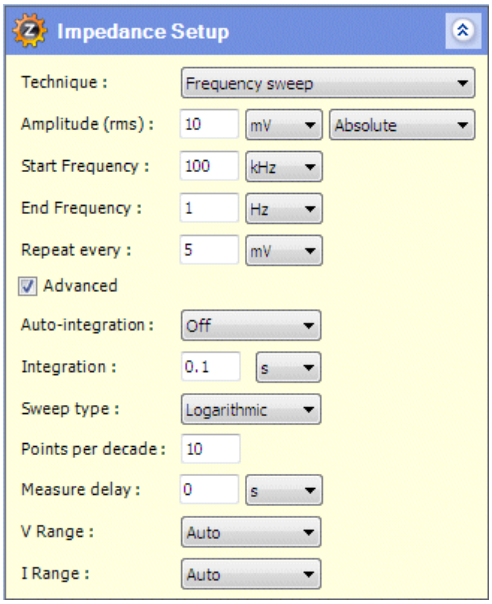

Figure 5.27 Impedance setup.

The amplitude defines the RMS amplitude of the AC signal, maintained at a fixed level during the step. This value is specified in absolute terms without reference to any other values, therefore in both potentiostatic and galvanostatic tests the absolute field is selected. As discussed in the previous section, the amplitude of the stimulus must be carefully chosen to ensure the linearity of the system response but also to provide a reasonable signal-to-noise ratio. Since the Frequency sweep is selected in the frequency field there are two fields representing the Start Frequency and End Frequency of the sweep. Generally, the frequency range used is between $10^{-3} - 10^{6}$.

The signal applied to the FRA can be integrated to reject noise. The effect is to narrow the measurement bandwidth and thus increase the signal-to-noise ratio. Integration increases the measurement time, so there is a trade-off between the accuracy you require and the measurement speed. Auto-integration can be used when there is uncertainty about the degree of interference generated by the cell, so that the integration time is adjusted automatically to obtain a specified statistical accuracy in the measurement result. When auto-integration is off, this field can be used to specify a fixed integration time. The units can be seconds or cycles, and a value in seconds is rounded up to cover the nearest number of whole cycles.

The Sweep type defines the method of variation of frequency during the sweep. Among linear and logarithmic the latter one is chosen. Also, the number of measurement points per decade during a logarithmic sweep should be at least 10.

The other field is the Scan Setup where the DC value of the stimulus is defined. Voltage, or potential as it is otherwise called, is always defined as a difference between two values. For the potentiostatic the potential has to be specified against no obvious reference value; there are many options but the most suitable is the vs. Reference where the value is specified relative to the reference voltage in the Cell Setup. The galvanostatic impedance do not require a referencing method. Once the wires are connected and the project has been created and set, the experiment is run.

5.2.4. Data Quality

The error structure of the measurement data plays a fundamental role in the modelling and fitting steps. Particular attention should be paid to stochastic errors and systematic bias errors. While bias errors can be defined to be those that result inconsistent with the Kramers-Kroning relations, the stochastic errors can be consider under control by selecting suitable experimental parameters. In this regard, the magnitude of the perturbation should be small enough to avoid non-linear response, minimizing stochastic errors [145].

The Lin-KK tool is used to check the Kramers-Kroning compliancy of the impedance spectra. The test result is given as residuals representing the relative deviation between experimental data and an ideal fitting with KK over frequency. Low residuals over the whole frequency range indicate a good quality impedance spectrum, i.e. data are not affected by noise and time- variance. All impedance spectra have been evaluated with Lin-KK tool using complex-fit and RC-auto mode.

Some examples of impedance spectra with good and low quality are reported in the figures below. The first two show valid impedance spectra whereas the last one is considered invalid due to the exhibition of biased residuals, which indicates time-variance.

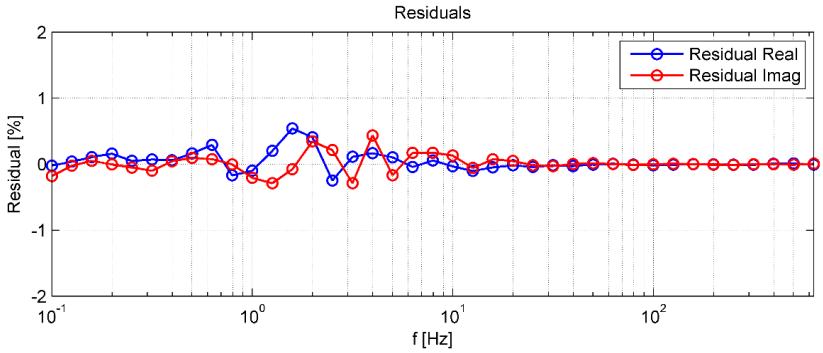

Figure 5.28 Impedance spectrum with low noise and describing a time-invariant system.

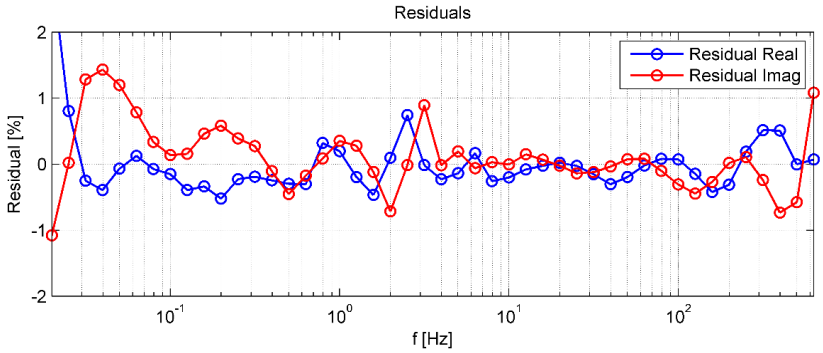

Figure 5.29 Impedance spectrum giving noisy residuals but still acceptable quality.

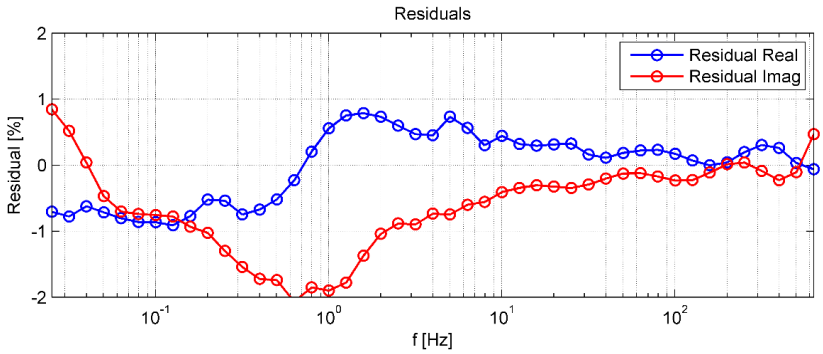

Figure 5.30 Impedance spectrum with time-variant behaviour.

An important stage to improve the identification of the model and its parametrization is the *data pre-processing*, allowing to evaluate the quality of the recorded data. Data pre-processing foresees different steps, in particular data monitoring and filtration [117].

Impedance data are monitored by checking their graphical representation, thus Nyquist and Bode plots. These diagrams can give additional information especially at high frequency where artefact impedance data appear due to wires connected to the cell and cell windings. Electrical leads have self-inductance that produces a typical shape with positive imaginary values (inductive behaviour).

In the filtration stage data points deteriorated by errors are detected and eliminated. Erroneous data are typically outliers, wild points, recorded data coinciding with the electrical grid frequency and harmonics. About the latter, it is known that measurements at frequencies near the power supply frequency, as well as to its harmonics- $50, 100, 150, 250$ Hz, produce erroneous data which should be rejected when possible. Instead, wild points are points that do not obey the general behaviour of a given ensemble of points [117] .

EIS spectra are not corrected for parasite inductive effects determined by wires.

5.3. Modelling

In this subchapter the relevant features of the impedance spectra obtained from the electrolytic cell are presented. Typical circuit elements used to model the impedance spectrum are reported. Further on, the procedure for the development of the equivalent circuit model (ECM) is delineated. Finally, some critical aspects of ECM are discussed.

5.3.1. AC impedance spectra

Impedance measurements on electrolytic cells can give impedance spectra with variable shape. In fact, impedance spectra are affected by the several operating parameters such as current density, voltage, temperature, pressure or relative humidity, or they can change according to catalysts loadings, membrane thickness, additional components to improve the performance and so on. In addition, some features of the impedance spectrum can show stronger correlation to a specific component within the cell or operating parameters may have a different impact depending on the level of ageing of the cell.

Generally, the impedance spectrum of an electrolytic cell consists of one or more semicircles, which usually can also be depressed or incomplete. Furthermore, sometimes it can happen that semicircles merge forming a sort of arc. These arcs or semicircles account for the different processes occurring inside the cell and each of them is characterized by a time constant.

In the impedance spectrum usually three features are observed [144] :

- high frequency (f>1kHz), in which double layer charging effects and proton transport dominate on the faradaic processes of the electrode response.
- mid frequency (1Hz<f<1kHz), related to the electrochemical processes occurring at the electrode/electrolyte interface (so called faradaic processes), so OER at the anode and HER at the cathode.
- low frequency (f<1Hz), which reflects mass transfer limitations due to reactants (H_2O) and products (H_2, O_2) removal or starving in the cell.

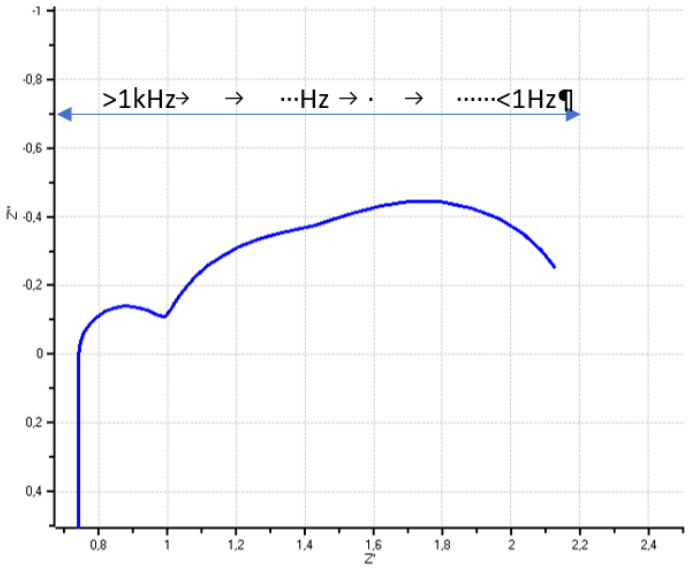

Figure 5.31 frequency range

5.3.1.1. High frequency feature

The high frequency region is potential independent, and it may be attributed to:

- Distributed resistance effects in the electrolyte within the catalyst layer
- MEA structure characteristics

This high-frequency feature- in case of current constrictions- is characterized by combined resistive and capacitive effects and it can be detected as:

- Complete semicircle
- Incomplete semicircle
- Straight line at 45° angle, mostly associated to protonic conductivity limitations in the catalyst layer

Generally, current constriction derives from bad contact between the membrane and the catalyst layer. Bad contact has many causes, principally correlated to the MEA characteristics (catalyst loading, ionomer content, fabrication method, porosity) but all converge to the same consequence, less efficient three phase boundary (TPB). With bad contact a two-phase boundary instead of the three-phase boundary occurs at the anode surface hindering the proton conduction in the electrolyte surface.

The high frequency intercept of the HF feature with the real axis allows to determine an important parameter, the ohmic resistance R_{Ω}, accounting for contact resistances between components and proton/electron transport through electrolyte and conductive components of the cell respectively. A change in the ohmic resistance value is associated to temperature and membrane hydration, as well as variation of the membrane thickness due to degradation issues. It should be noted that in this region it is possible to detect inductive effects due to connecting wires and cell windings that affect the impedance spectrum.

These features- inductive effects, ohmic losses and current constrictions- are modelled through a series connection of different circuit elements. An inductance models inductive effects whether a series resistance is used to simulate ohmic losses. Instead, current constriction appearing as a semicircle at HF- when present- is modelled with a resistance in parallel with a constant phase element (CPE). So, the high frequency feature is simulated by a series connection of inductance, ohmic resistance and parallel between a resistance and a CPE.

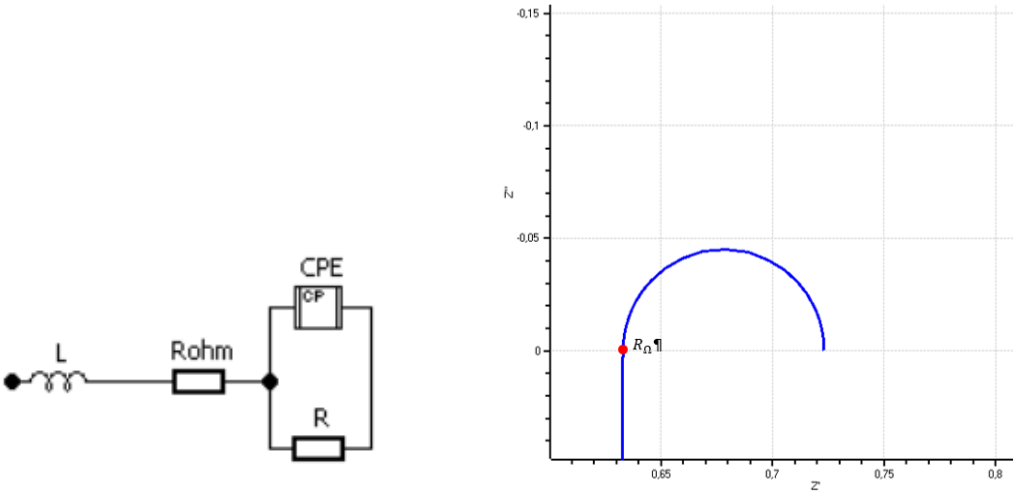

Figure 5.32 CPE and resistance

5.3.1.2. Mid frequency feature

The mid frequency region shows a dependency on potential; in general, it decreases with increasing overpotential due to the rapid increase of the kinetics. It is usually associated to the kinetics of the anode (OER) but in some papers it is also attributed to the HER at the cathode. This mid frequency region appears in the Nyquist plot as one arc or even two more or less merged semicircles. Each of these charge transfer processes is modelled by a parallel of a resistance (called charge transfer resistance) and a CPE.

Figure 5.33 charge transfer resistance and CPE

In general, when only one arc is visible in the mid frequency region in the Nyquist plot (corresponding to a single peak in the same frequency range in the Bode plot), this is modelled with a single $R_{ct}||CPE$; instead, two merged semicircles with two visible peaks in the Bode plot are simulated with two $R_{ct}||CPE$ in series.

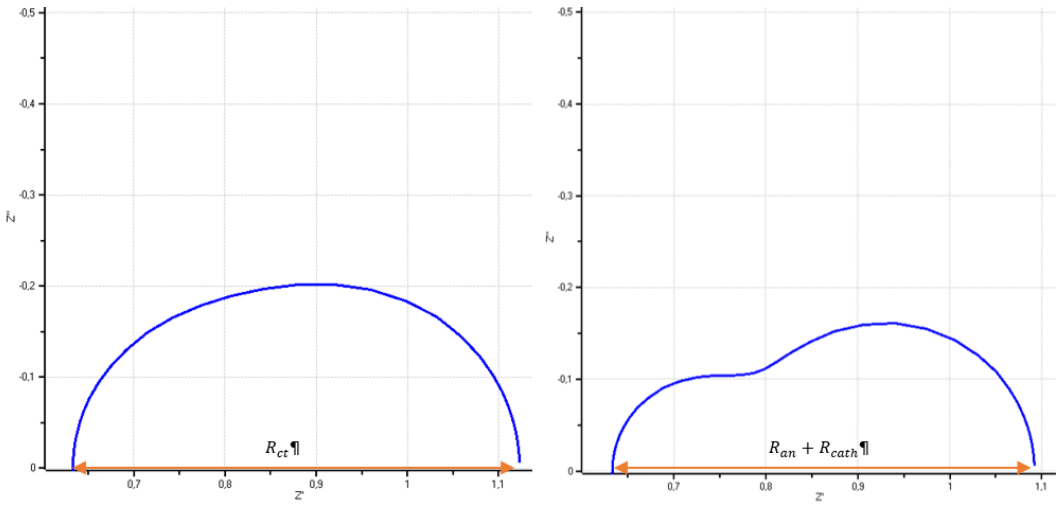

Figure 5.34 R_{ct}, R_{an} and R_{cath}

The charge transfer resistance R_{ct}, corresponding to the diameter of the arc, is associated with the charge transfer mechanism for the electrode reactions (mostly the OER) and it is function of temperature and potential. The constant phase element is mainly used rather than capacitor because by adjusting its parameters it allows to fit data quite well- function very useful in case of overlapping arcs- and moreover, it represents the imperfect nature of electrodes (surface roughness, irregular properties distribution, non-uniform current distribution, etc.). In any case, by using its parameters with maximum frequency or charge transfer resistance, it is possible to determine the capacitance C_{dl} as expressed in equation 5.23.

$$C_{dl} = Q \cdot (\omega_{max})^{n-1} = \frac{(R_{ct}Q)^{\frac{1}{n}}}{R_{ct}} \qquad 5.23$$

The capacitance value gives some insight of the electrode properties, such as catalyst surface area, active sites, catalyst loading and utilization [144]. Higher value of the capacitance means good properties and behaviour of the electrode and it is graphically represented by small semicircles/arcs; in contrast, lower value is related to possible degradation of the electrode with consequently decreasing performance.

5.3.1.3. Low frequency feature

The low frequency feature is also potential dependent, increasing with increasing overpotential and it is related to mass transport limitations. Its graphical

representation at low frequency is generally another semicircle (finite diffusion) rather than a straight line or tail (semi-infinite diffusion) [144]. It is modelled with Warburg elements, which can be added in series to the overall $R_{ct}||CPE$ modelling the mid frequency region or in series only to the charge transfer resistance as shown in *Fig.47*.

Figure 5.35 Warburg elements in series with other elements

To conclude, the number of semicircles/arcs depends on the phenomena occurring in the cell. When only one arc is present probably mass transport limitation are negligible, whereas two or three arcs -more or less pronounced and merged- appear in case of both faradaic and mass transport processes.

5.3.2. Data fitting

5.3.2.1. Qualitative analysis

The impedance spectra are subject to a qualitative analysis. It foresees validation by Kramers Kroning relationships, data pre-processing and structural identification. The aim of the data pre-processing is to individuate and discard data affected by error and noise, wild points, outliers and to delete data affected by inductive effects as well. This first step allows to individuate the frequency range where impedance data are reliable. In the structural identification an inspection of the available complex plane plots provides the number of time constants while the setup of the EIS test- in this case the DC value – can give information about the presence/absence of transport limitations.

5.3.2.2. Parameters initial estimation

A first modelling with the Circle fitting option allows to have an initial estimation of the principal parameters such as resistances, capacitances, at high and low frequencies. This first approximation is useful for the CNLS fit to the model function obtained from the ECM. The Circle fitting method foresees two options

among which make a choice. The Prefit option is selected allowing to fit circles through three points selected in the impedance.

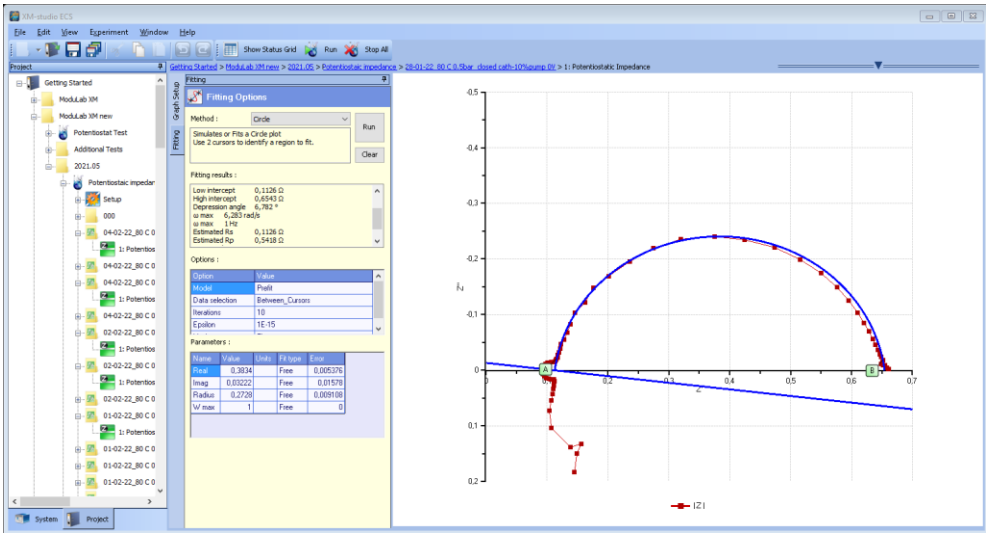

Figure 5.36 fitting of the EIS graphs

5.3.2.3. Model development and CNLS approximation

The model construction and the CNLS approximation to the equivalent circuit model are both performed with the software. To get a good fit of the impedance data a multi-step procedure is carried out.

5.3.2.3.1. ECM construction

On the basis of the qualitative analysis of the impedance diagram the ECM is built using the tool available in the software of Solartron instrument. The ECM usually consists of a series connection of inductance, ohmic resistance and two R||CPE elements.

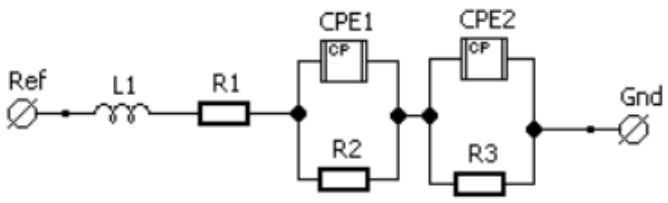

Figure 5.37 Equivalent circuit example

5.3.2.3.2. First approximation

ECM in Figure 5.35 is used to get a first approximation. In this step different parameter such as ohmic resistance R_1 and charge transfer resistances R_2, R_3 are fixed using the values gained by the Circle pre-fit. The CPE has two variables as depicted in Fig.53; TDE represents the Q parameter of the formulas whereas PHIDE represents the exponent n.

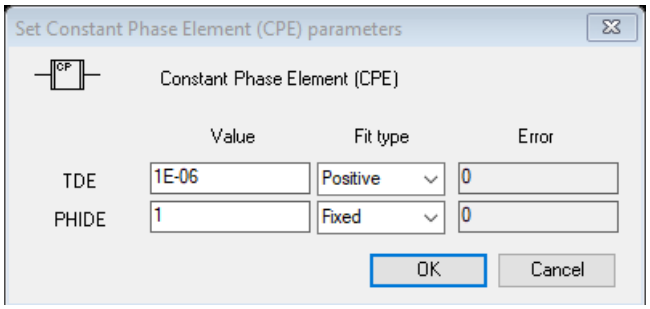

Figure 5.38 CPE set

It is necessary to lock $n = 1$ and leave Q with its default value. Before running the fitting, it is necessary to set the weighting, generally modulus weight is preferred, and also it is important to choose points A and B, which individuate the range of data points to fit in the impedance spectrum.

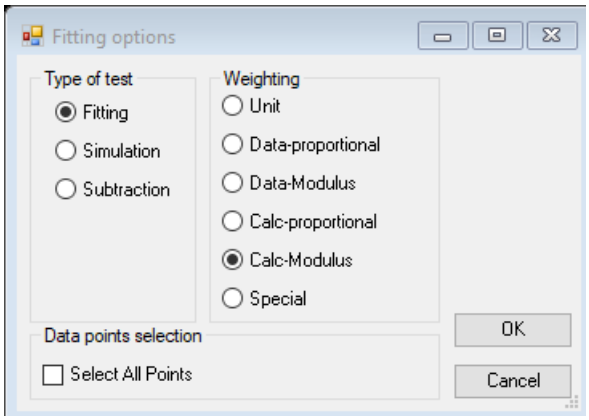

Figure 5.39 Fitting options

Thereafter, it is possible to run the software. After the first run, n in both CPE is unlocked and by running again it is possible to get the first data approximation.

5.3.2.3.3. Analysis of obtained fitting data

It is necessary to note that the anode reaction should occur at lower frequency with respect to the cathode reaction occurring at higher frequency. So, if both anode and cathode reactions are considered, the first Randle element should be related to cathode and the second one to the anode. If from the fitting the opposite is obtained (first Randle element to the anode and second to the cathode) it is necessary to restart again the fitting procedure. If the data obtained from the fitting are consistent with the impedance spectrum it is possible to pass to the next step.

5.3.2.3.4. Build a new circuit adding a Warburg element

Note that if diffusion is present, it should be accounted, hence it is necessary to add a Warburg element usually in parallel to the CPE, since mass transport processes occur in parallel to the charge transfer reaction. The Warburg element used is the so-called short Warburg (W_s), it has three variables: R represents R_0, T is Q and PHI is the exponent n.

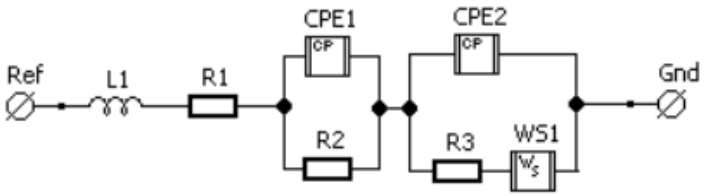

Figure 5.40 alternative ECM

5.3.2.3.5. Get final results

The final ECM is depicted in Figure 5.40. In this case, all the data obtained from the first approximation are fixed whereas in the short Warburg element R_0 is fixed with a small value and n is locked to its default value 0.5.

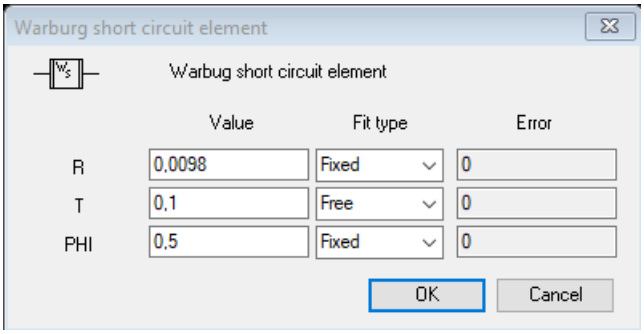

Figure 5.41 Warburg short circuit element

After the run, all the parameters are unlocked and with another running the final results are obtained.

5.3.2.3.6. Ambiguities

The application of equivalent electrical circuits as models shows several ambiguities. ECMs, generally chosen a priori, do not describe the physicochemical properties of the system, they simply reproduce the experimental data whereas physical models not only reproduce but also account for the mechanism occurring at the interface [146]. Hence, this is an incomplete method that needs to be coupled with others. In fact, an EEC containing a sufficient number of elements adequately connected can fit closely the experimental impedance data but at the end the information gained are very limited because the ECM is not clearly based on the physicochemical processes involved in the system.

To overcome the lack of correlation with the physics, only pre-knowledge of the system under study can give some hints on the choice of the circuit elements to get meaningful results. If it is known a priori that a specific process occurs, then it is possible to construct the ECM with elements that could be identified with that process.

It is also important to stress out that the same impedance spectrum may be simulated by different circuits giving rise to difficulties in the interpretation of the experimental data. Orazem et a. [147] presented some examples of ambiguous model identification. Different equivalent circuit models- each modelling to different phenomena (charge transfer, adsorption, diffusion, etc.)- were used to fit two synthetic data samples. The results of the regression of all these models to the synthetic data showed that the models provided acceptable fits to the data. This demonstrates that the phenomena governing the system cannot be identified by the model giving the best fit, but a prior knowledge suggesting a reasonable model is required.

Ambiguities become more relevant with system characterized by several processes, usually modelled with multiple time constant circuits. A circuit with n time constants has at least n solutions for the circuit elements. So, although the equation of the ECM shows a high degree of simulation for each n solutions- i.e., a good fit to the experimental data is achieved- the choice will fall among the most adequate one from a physicochemical point of view [60]. Moreover, it may happen that the contributions of the processes to the impedance spectrum overlap because their time constants are very close. Therefore, there are not visible by simple

inspection of the impedance diagram, thus it is not possible to consider them in the ECM.

Another issue comes from the weakness of the weighting strategy in the CNLS approximation for the model identification. This because the real and imaginary part in the impedance spectra vary over many order of magnitude.

These figures show a clear example of ambiguity in the fitting procedure. Different equivalent circuit models have produced a quite similar fit; all parameters found from the modelling have errors with same order of magnitude hence it is troublesome to choose among the two solutions. Trial one:

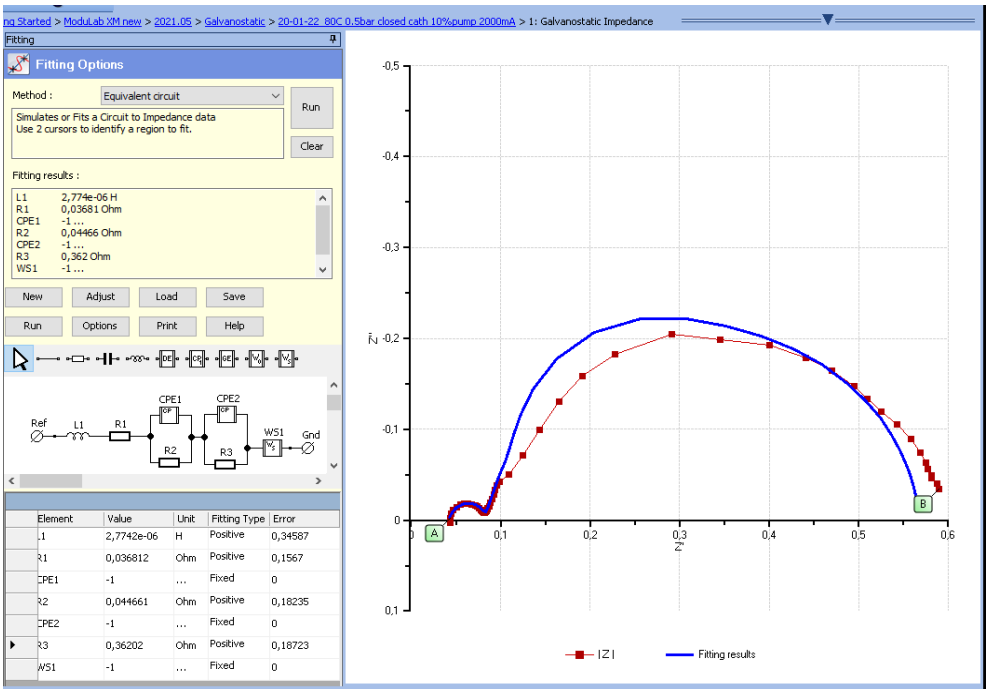

Figure 5.42 fitting trial 1

And the fitting results:

Table 5.1 Fitting results with LR(QR)(QR)WS

Element	Sub-parameters	Value	Error	Fitting
L1		2,77E-06	0,34587	positive
R1		0,036812	0,1567	positive
CPE1	TDE	0,026114	0,53769	positive

	PHIDE	0,94813	0,11356	free
R2		0,044661	0,18235	positive
CPE2	TDE	53,878	0,37091	positive
	PHIDE	0,93802	0,051539	free
R3		0,36202	0,18723	positive
WS1	R	0,12424	0,53275	positive
	T	17,307	0,1158	free
	PHI	0,66556	0,083576	free

Trial 2:

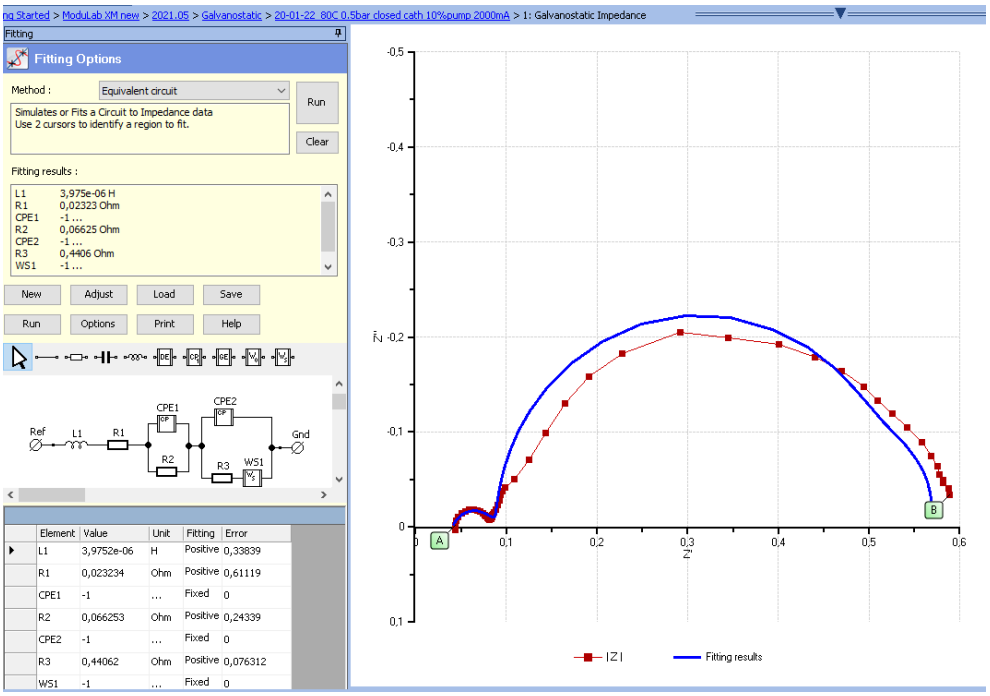

Figure 5.43 fitting trial 2

And the fitting results:

Table 5.2 Fitting results with LR(QR)(QRWS

Element	Sub-parameters	Value	Error	Fitting
L1		3,38E-01	0,33839	positive
R1		0,023234	0,61119	positive

CPE1	TDE	0,071583	0,39248	positive
	PHIDE	0,73087	0,14882	free
R2		0,066253	0,24339	positive
CPE2	TDE	29,869	0,037519	positive
	PHIDE	0,99969	0,030631	free
R3		0,44062	0,076312	positive
WS1	R	0,039049	10,474	positive
	T	19,097	0,70333	free
	PHI	0,61451	0,56276	free

Chapter 6. Results

The electrochemical characterization includes V-I (polarization) curves and electrochemical impedance spectroscopy under potentiostatic and galvanostatic modes. Polarization curves are performed by recording the cell voltage vs. the imposed current density with maximum current density reached of $2\ \mathrm{A/cm^2}$ to prevent damages to the cells.

Electrochemical impedance spectroscopy analysis is carried out using an electrochemical setup consisting of PGSTAT potentiostat/galvanostat (Solartron analytical), an internal 2A booster and the frequency response analyser, FRA, properly connected with the PEM electrolyser as described in the previous chapter. The impedance measurement is performed under potentiostatic and galvanostatic modes. In the potentiostatic mode the AC voltage perturbation signal is superimposed on the DC voltage level. The latter is selected in the range between $0-1.5\mathrm{V}$ while the AC voltage is a single sinewave with amplitude of $10\ \mathrm{mV}$ (RMS) swept in the frequency range of $20\mathrm{kHz}-2\mathrm{mHz}$. In the galvanostatic mode the AC current signal is superimposed on the DC current level, which is selected in the range between $0-2000\mathrm{mA}$. The AC current is again a single sinewave with amplitude of $1000\mathrm{mA}$ (RSM) swept in the frequency range of $10\mathrm{kHz}-1\mathrm{mHz}$. Due to the instrumentation limits, the impedance measurements are executed at low current densities corresponding to the system operation under activation control. Consequently, the impedance analysis allows to observe phenomena principally linked to the electrocatalyst behaviour.

Either polarization curves and EIS tests have been performed at different temperature, pressure, cathode configuration and mass flow rate. Temperature is varied between $40°\mathrm{C}$ and $80°\mathrm{C}$ whereas the relative pressure range is $0.5\mathrm{bar_g}$-$15\ \mathrm{bar_g}$. The cathode configuration is changed by acting on the entrance valve situated at the entrance of the cathode side. In the test bench both anode and cathode have entrance valves which allows water feeding. The aim of changing the configuration of the cathode is to study if there are evident differences on the performance of the cell under different cathode configuration. The mass flow rate is set by varying the chamber percentage of the recirculating pump or by changing manually the needle valve. Whether the recirculating pump or the needle valve is used, the mass flow rate introduced in the system is divided between the entrance of anode and cathode;

thus, both compartments have same mass flow rate considering same losses in the anodic and cathodic circuits. Hence, tests that use the pump have just indicated the pump percentage whereas in case of needle valve the mass flow rate will be exactly given in mL/m^3.

Tests have been performed varying one or more operating parameter, while keeping all the other operating parameters constant. This enables the identification of the several processes occurring within the PEM water electrolyser, which clearly have dependencies on operating parameters. Some more significant tests' typologies are listed below.

- Test performed at constant temperature with different pressure. Cathode open and fixed mass flow rate (imposed with the recirculating pump)
- Tests performed at constant pressure with different temperature. cathode open and fixed mass flow rate (imposed with the recirculating pump)
- Test performed at constant temperature and pressure with different cathode configuration. The mass flow rates is varied between open and closed cathode using the recirculating pump.
- Test performed at constant temperature and pressure with different cathode configuration. The mass flow rate is varied between open and closed cathode using a needle valve.
- Test performed at constant temperature and pressure with different cathode configuration. The mass flow rates kept constant and imposed by the needle valve.

6.1. Cathode configuration

This section presents the results obtained from the tests performed on the PEM electrolytic cell in which two MEAs- having same characteristic but different ageing conditions- were studied. The tests are divided in 2 categories that are based on the physical condition of the cathode inlet port:

- Open cathode tests
- Closed cathode tests

6.1.1. Open vs closed cathode

6.1.1.1. Open cathode configuration

Results gained from the open cathode tests suggest the following assumptions:

- The HF features and the ohmic resistance are not showing a strong dependence on current and/or voltage, but rather they are mostly temperature dependent. These findings suggest that it is not related to kinetics processes but rather to the MEA structure. In particular, it is related to hinder of proton conduction which strictly depends on the characteristics of the membrane electrode assembly, like the presence of big catalyst agglomerates in the active surface of the anode or bad contact between the electrolyte and the anode catalyst layer [129] [148]. However, the attribution of the HF arc is generally troublesome. Some researchers attribute its origin to the HER in the cathode, others correlate this feature to a hinder of the proton conduction in the electrolyte, principally due to the MEA characteristics.
- Considering that in the range 0-2 A (so 0-0,08 A/cm^2 current density) we are in the activation domain and that the LF arc shows a dependence on current density and on voltage, it is suggested that the LF arc is controlled by the charge-transfer kinetics. It means that in the Nyquist plot the LF arc is related to both OER and HER.
- A general improvement is observed as temperature is increased. Instead, pressure determines substantial enhancement at higher temperature rather than at lower. Moreover, it is noticed that when temperature is too high (>71°C) ohmic losses are increased and this is probably related to the loss of humidity. Increasing pressure, at least up to 5 barg, can reduce ohmic resistance at high temperature.

The detail of tests are:

6.1.1.1.1. Constant condition

Test is performed at 60°c, imposed gauge pressure 0.5 barg, with 200 ml/min imposed with a needle valve with open cathode configuration. Note that with open cathode the real pressure in both sides of the cell is given by taking the average between the imposed pressure (exit of the cell) and the pressure at the heater

(entrance of the cell) . During closed cathode the average is taken only for the anode.

The aim of the test to perform electrochemical characterization of the new cell by carrying out EIS measurements. The test is performed at 60°C, 0.5 barg imposed gauge pressure, mass flow rate of 200 mL/min with needle valve and open cathode configuration. Two types of EIS measurements have been used:

- Potentiostatic test, performed at different DC value of voltage (0 V, 0.5 V, 1 V, 1.5 V) vs Reference by varying the frequency from 100 kHz to 0,001 Hz in single sine mode and using a sinusoidal excitation signal of 10 mV root mean square (rms)
- Galvanostatic test, performed at different DC current -0 mA, 1000 mA, 1500 mA, 2000 mA- by varying the frequency from 200 kHz to 0,002 Hz in single sine mode and using a sinusoidal excitation signal of 1000 mA root mean square (rms).

During the test, the cell temperature was 61.5°C whereas the fluid temperature at the heater was 59.2°C; the real gauge pressure in both side of the cell was around 0.9 barg.

6.1.1.1.1.1. Data quality assessment

The Kramers- Kronig (KK) validation shows a general better quality of the measurements under voltage control, whereas those obtained with galvanostatic mode are affected by time variance hence higher residuals are observed. By visual inspection of both Nyquist and Bode plots two-time constants are individuated in both potentiostatic and galvanostatic tests. Hence, the ECM used to model experimental data consists of three elements: LR(QR)(QR).

6.1.1.1.1.2. Modelling

Impedance spectra under voltage control are characterized by an arc at high frequency and a second arc at mid-low frequency. The low frequency features show a dependence on voltage: as the DC value of potential increases this tends to reduce its diameter. Same consideration for tests performed under current control, i.e. the LF arc shows a dependence on the DC current and it tends to reduce as the current density is increased. Details are in Appendix B. Table 0.1

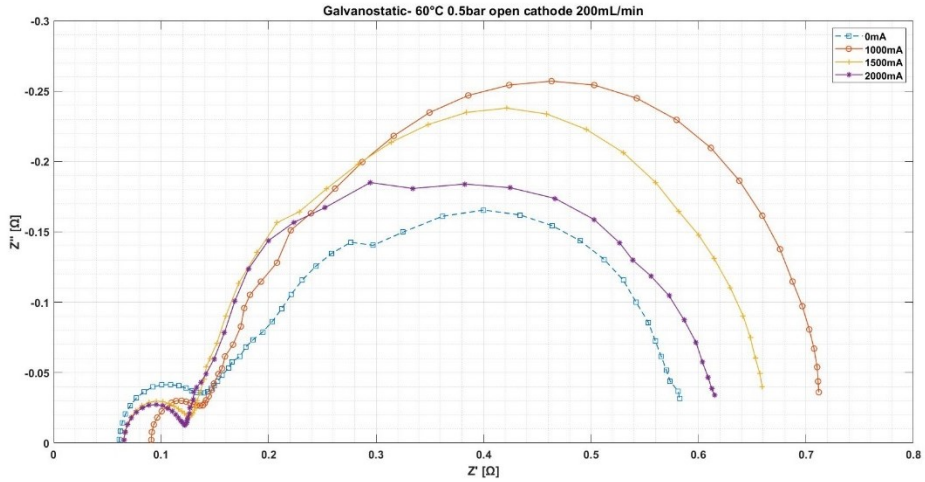

Figure 6.1 Nyquist plot under current control at 60°C 0.5barg open cathode 200mL/min.

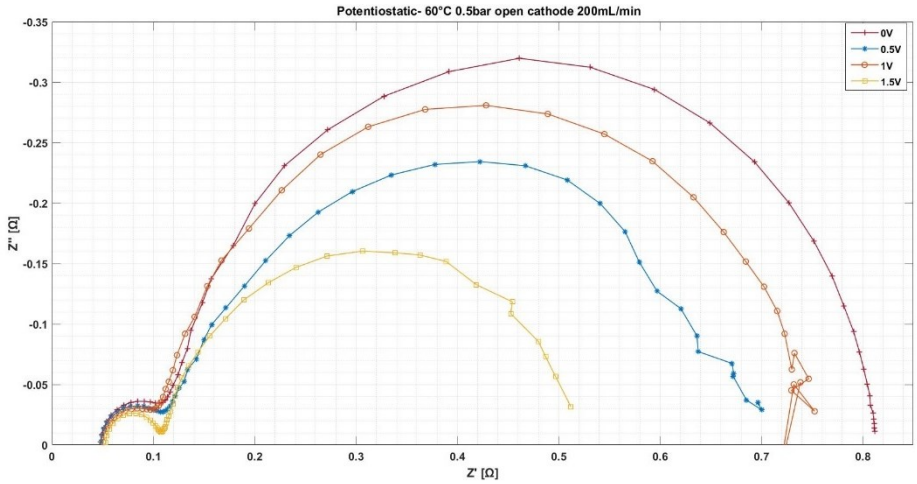

Figure 6.2 Nyquist plot under voltage control at 60°C 0.5barg open cathode 200mL/min.

6.1.1.1.1.3. Discussion

The analysis is focused on the EIS measurements providing good impedance spectra. Hence, 1500 mA and 2000 mA for the galvanostatic mode and the range 0-1.5 V for the potentiostatic mode.

As the current increases in the range 1.5-2 A we have that at LF the charge transfer resistance decreases from 14.4 to 12.3 Ωcm^2 and the capacitance C increase from 1.84 to 3.18 F, so the LF semicircle becomes smaller. Instead, the HF arc in

the same range is characterized by a less dependent behaviour from the current density since it shows very small variation of the charge transfer resistance HF (from 0.13 to 1.34 Ωcm^2) and capacitance (0.025 F), whereas the ohmic resistance is almost constant around 1.69 Ωcm^2.

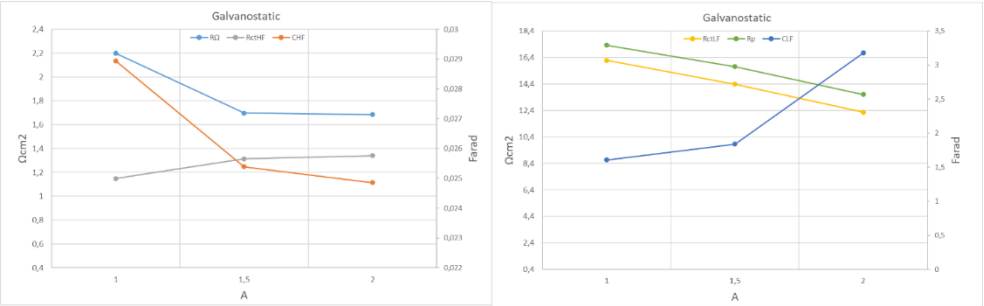

Figure 6.3 Trend of the parameters with galvanostatic mode.

Considering the range 0-1.5 V, it is possible to notice that the ohmic resistance is not varying significantly with voltage (from 1.05 to 1.17 Ωcm^2), whereas as the voltage increases it observed a decrease of the LF arc. About the LF arc, the charge transfer resistance decreases (from 17.4 to 10.3 Ωcm^2) and its capacitance C increases (from 0.37 to 5.37 F). The high frequency arc shows a very slight decrease with voltage: in particular, capacitance is constant around 0.018 F while the charge transfer resistance shows lower value with higher voltage level (from 1.85 to 1.53 Ωcm^2).

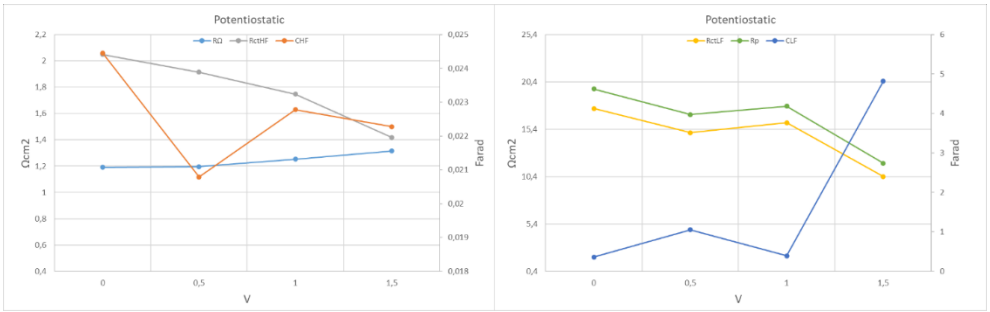

Figure 6.4 Trend of the parameters with potentiostatic mode.

6.1.1.1.2. Effect of temperature

The test is performed at 60°C and 74°C, imposed gauge pressure 0.5barg, with 10% by pump with open cathode configuration

The aim of the test to perform electrochemical characterization of the new cell by carrying out EIS measurements to investigate the temperature effect on the cell impedance. The test consists of two series, first performed at 60°C and the second

at 74°C, both characterized by same operating conditions of 0.5 barg imposed gauge pressure, 10% pump and open cathode configuration. Two types of EIS measurements have been used:

- Potentiostatic test, performed at different DC value of voltage (0 V, 0.5 V, 1 V, 1.5 V) vs Reference by varying the frequency from 100 kHz to 0,001 Hz in single sine mode and using a sinusoidal excitation signal of 10 mV root mean square (rms)
- Galvanostatic test, performed at different DC current -0 mA, 1000 mA, 1500 mA, 2000 mA- by varying the frequency from 200 kHz to 0,002 Hz in single sine mode and using a sinusoidal excitation signal of 1000 mA root mean square (rms).

During the test at 60°C, the cell temperature was 61.3°C whereas the fluid temperature at the heater was 59.7°C; the real gauge pressure in both side of the cell was around 0.6 barg. On the other hand, at 74°C the cell temperature was 74.2°C, fluid temperature 79°C and real gauge pressure was around 0.7 barg.

6.1.1.1.2.1. Data quality assessment

The KK validation shows a general better quality of the measurements under voltage control, whereas those obtained with galvanostatic mode are affected by time variance hence higher residuals. By visual inspection of both Nyquist and Bode plots two time constants are observed in both potentiostatic and galvanostatic tests. The ECM used is LR(QR)(QR).

6.1.1.1.2.2. Modelling

Impedance spectra under voltage control are characterized by an arc at high frequency and a second arc at mid-low frequency. The low frequency features shows a dependence on voltage: as the DC value of potential increases this tends to reduce its diameter. Same consideration for tests performed under current control, i.e. the LF arc shows a dependence on the DC current and it tends to reduce as the current density is increased. Details are in Table 0.2 and Table 0.3.

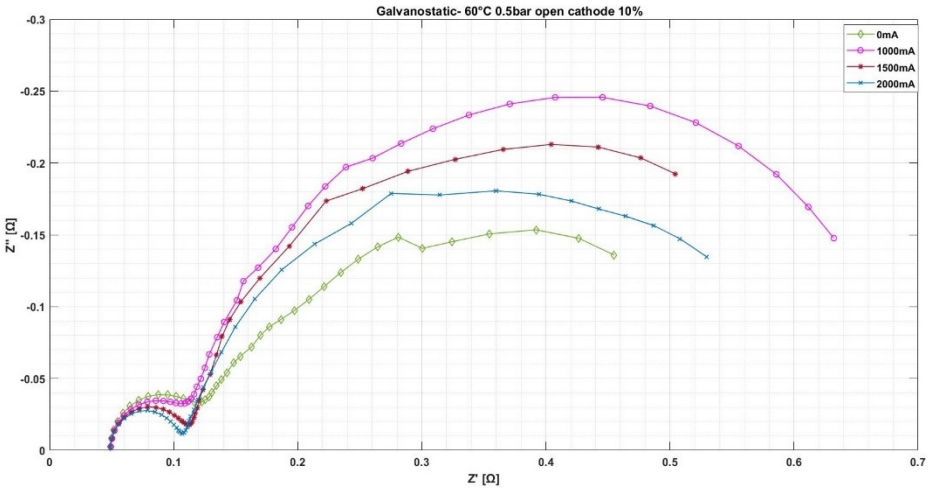

Figure 6.5 Nyquist plot under current control at 60°C 0.5barg open cathode 10%.

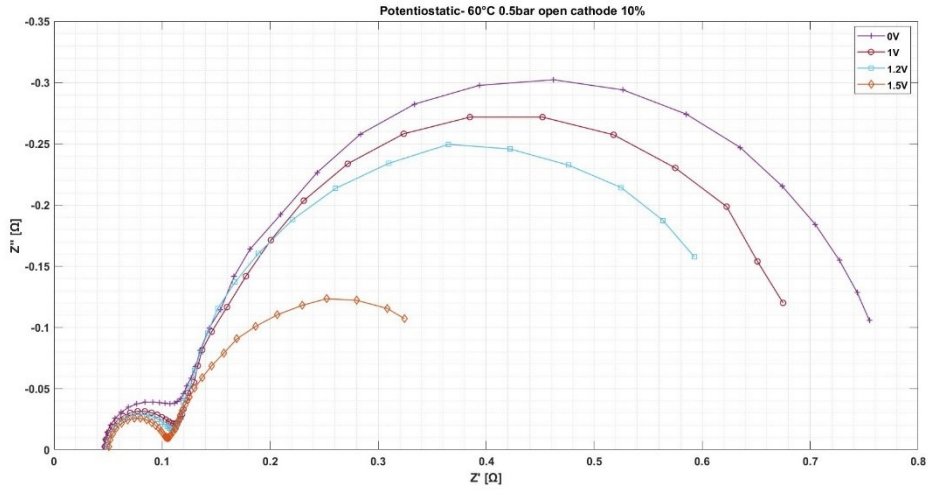

Figure 6.6 Nyquist plot under voltage control at 60°C 0.5barg open cathode 10%.

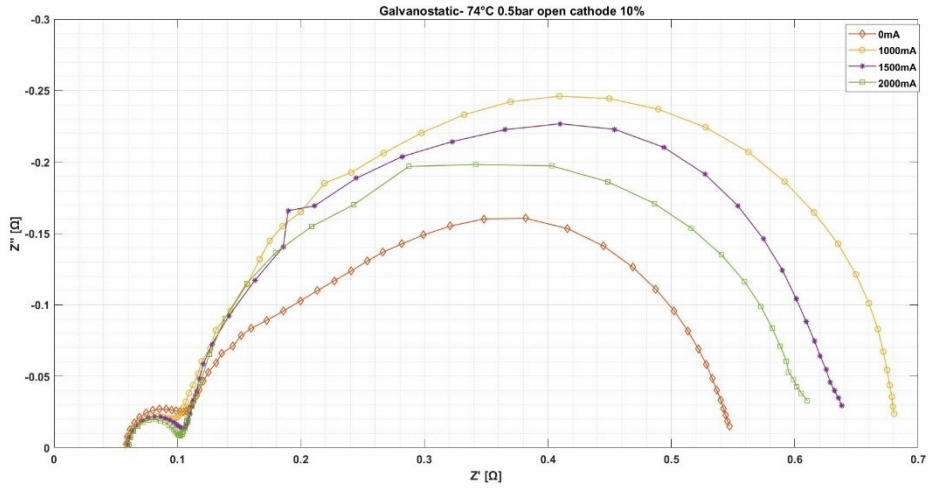

Figure 6.7 Nyquist plot under current control at 74°C 0.5barg open cathode 10%.

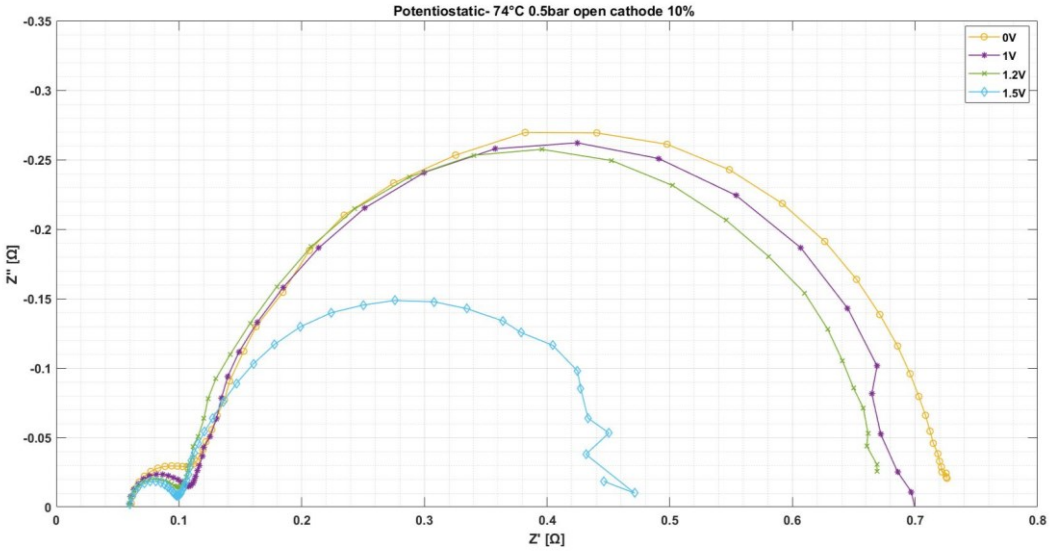

Figure 6.8 Nyquist plot under voltage control at 74°C 0.5barg open cathode 10%.

6.1.1.1.2.3. Discussion

Figures below show the parameters' trend obtained from the fitting results at 60°C and 74°C.

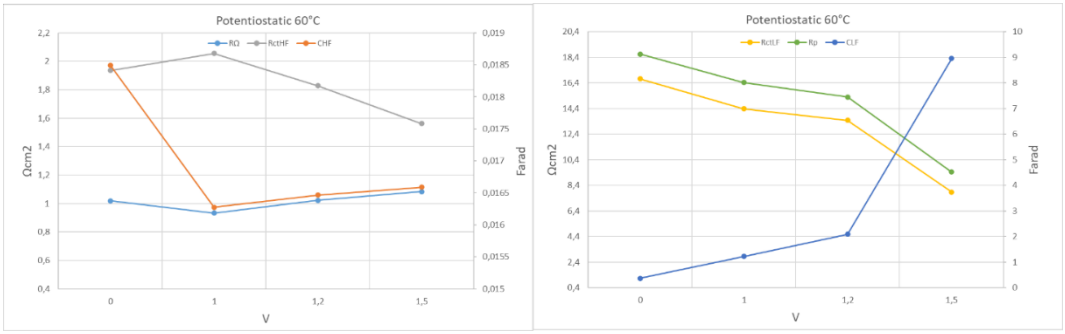

Figure 6.9 Parameters' trend obtained from potentiostatic test at 60°C.

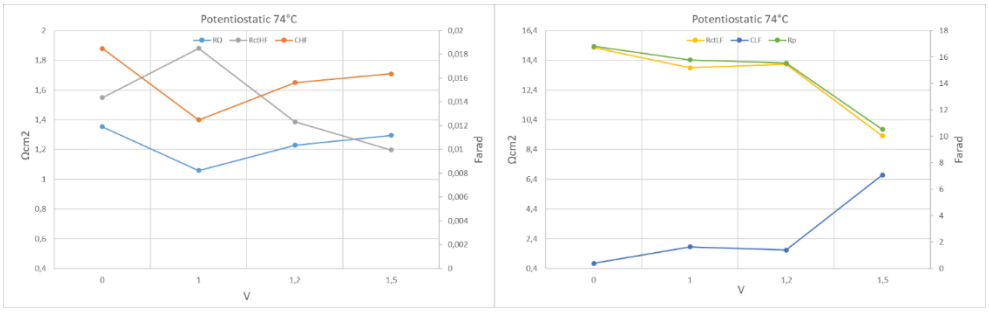

Figure 6.10 Parameters' trend obtained from potentiostatic test at 74°C.

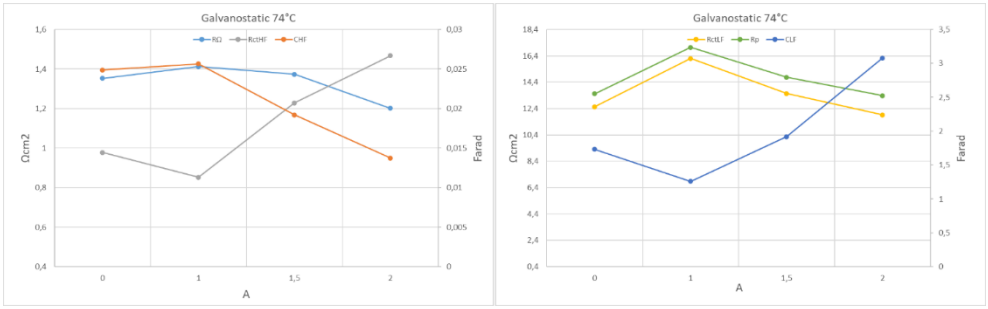

Figure 6.11 Parameters' trend obtained from galvanostatic test at 74°C.

The comparison between the 60°C and 74°C is carried out by considering EIS measurements in the range 0-1.5 V in the potentiostatic mode. Trends show that they have same behaviour as voltage increases, but two parameters-ohmic resistance and charge transfer resistance at HF- have different values. Ohmic resistance is generally smaller whereas charge transfer resistance at high frequency is higher at 60°C; instead, opposite behaviour is observed at 74°C. Nevertheless, both temperatures have similar values of the total polarization resistance and the other parameters do not show relevant variation with temperature.

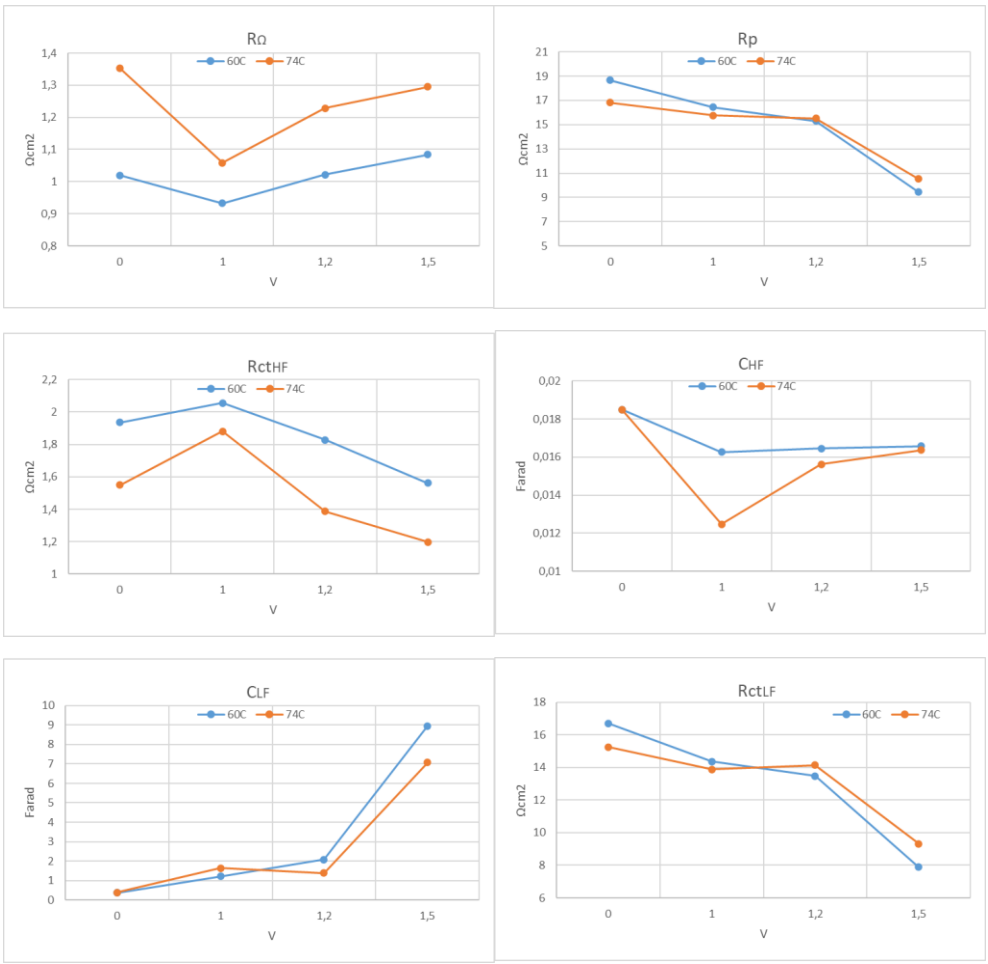

Figure 6.12 Comparison of the parameters gained from potentiostatic measurements between 60°C and 74°C.

Concluding, it is observed that the high frequency arc is particularly affected by temperature whereas the low frequency arc is less temperature dependent although a benefit from higher temperature is noticed.

6.1.1.1.3. Effect of pressure

The test is performed at T=79°C & T=71°C, with open cathode at different gauge pressure. The objective of the experiment is to investigate the influence of temperature and pressure on cell impedance through EIS measurements. The experiment is executed with open cathode at fixed temperature of 79°C, increasing the imposed gauge pressure from 1.4 barg to 7.5 barg. Then, temperature is decreased up to 71°C and kept fixed while imposed gauge pressure is decreased from 7.5 barg to 1.4 barg. EIS measurements are performed after stabilization of

the cell at the desired value of temperature and pressure. Two types of EIS tests have been used:

- Potentiostatic test, performed at 0 DC V vs Open circuit by varying the frequency from 100kHz to 1Hz in single sine mode and using a sinusoidal excitation signal of 10 mV root mean square (rms).
- Galvanostatic test, performed at 0 DC mA by varying the frequency from 200 kHz to 0,2 Hz in single sine mode and using a sinusoidal excitation signal of 1000 mA root mean square (rms).

Note that the real pressure in both sides of the cell is given taking the average between the imposed pressure and the pressure at the heater. Hence, real pressures are different as shown in the Table 0.4.

Real gauge pressure is the same for anode and cathode as depicted in Figure 6.14.

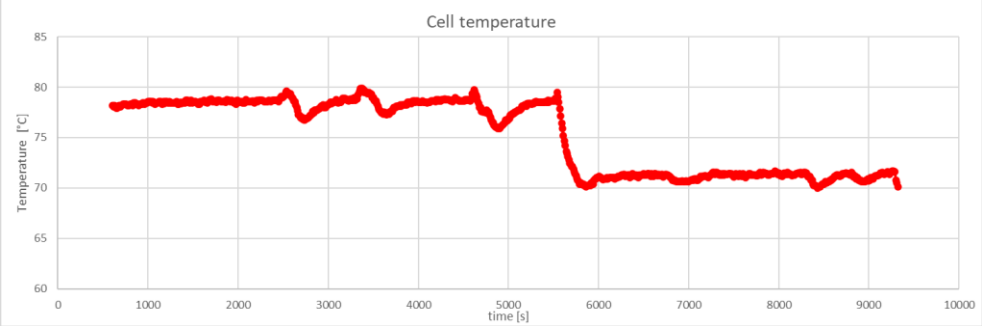

Figure 6.13 Cell temperature measured during the test.

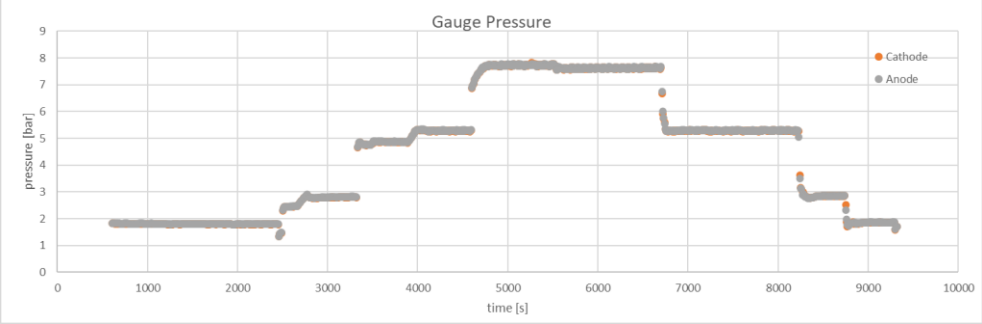

Figure 6.14 Gauge pressure in the anode and cathode measured during the test.

6.1.1.1.3.1. Data quality assessment

The KK validation shows that impedance spectra obtained under voltage control are characterized by residuals in the range ±1%, whereas impedance data gained with galvanostatic tests are affected by time variance. In Nyquist plots it is

observed that the shape is made of a semicircle in the HF and a second incomplete semicircle in the mid frequency region, corresponding to two time constants visible in the Bode plots. Hence, the ECM used to fit is LR(QR)(QR).

6.1.1.1.3.2. Modelling

Figure 6.15 and Figure 6.16 show impedance spectra obtained respectively at 79°C and 71°C at different gauge pressure with potentiostatic tests. The high frequency arc seems not affected by the pressure whereas the second incomplete arc bends down to the real axis with decreasing pressures. The imaginary part of all HF arcs at 79°C reaches a maximum at ω_{max} equal to 158.5 Hz.

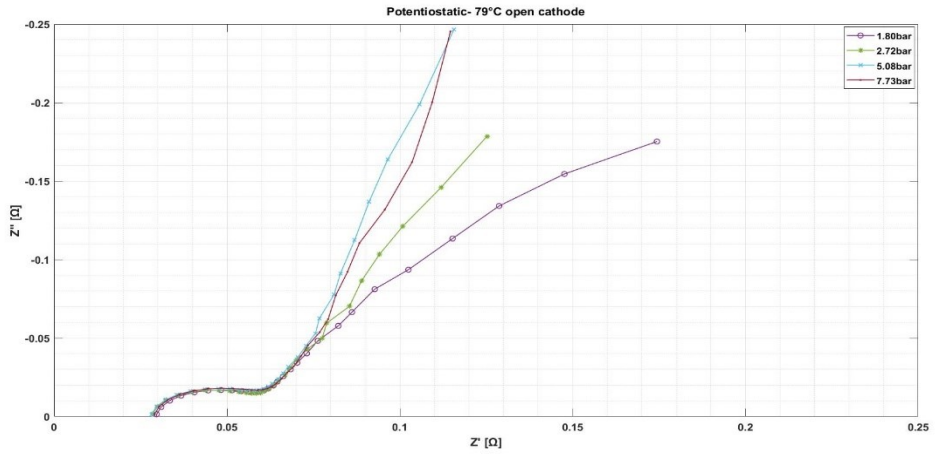

Figure 6.15 Nyquist plot under voltage control at 79°C open cathode at different gauge pressures.

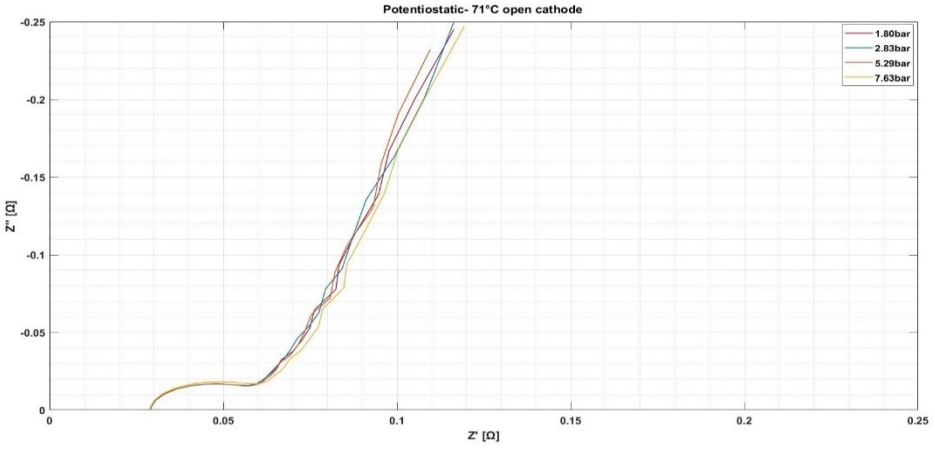

Figure 6.16 Nyquist plot under voltage control at 71°C open cathode at different gauge pressures.

Figure 78 and *79* show impedance spectra obtained respectively at 79°C at different gauge pressure with galvanostatic tests. The high frequency arc is not affected by the pressure as well as the second incomplete arc in the mid frequency region. A tail appears at lower frequencies, maybe it is an insight of a third semicircle. The imaginary part of all HF arcs reaches a maximum at ω_{max} equal to 158.9 Hz.

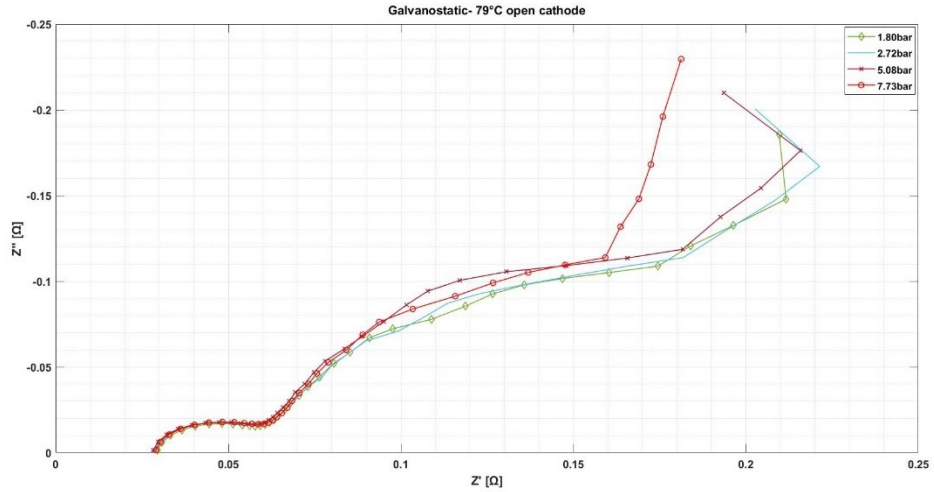

Figure 6.17 Nyquist plot under current control at 79°C open cathode at different gauge pressures.

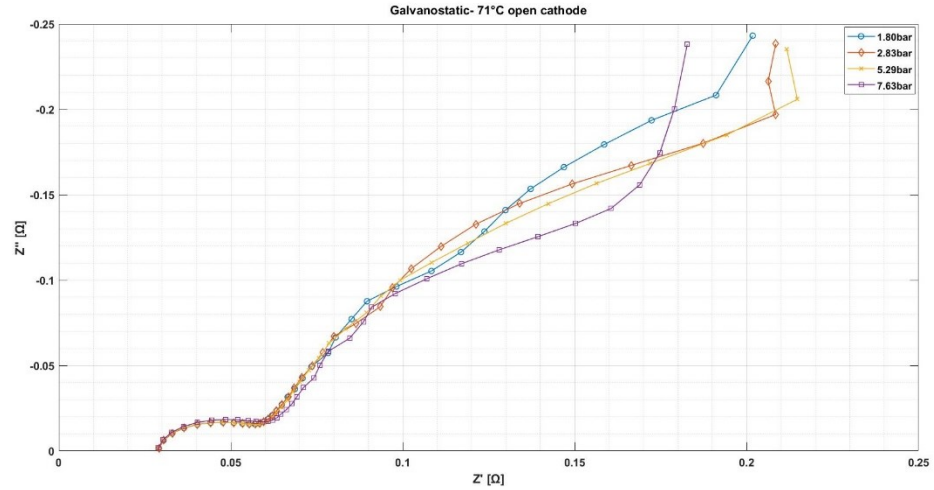

Figure 6.18 Nyquist plot under current control at 71°C open cathode at different gauge pressures.

DISCUSSION

Potentiostatic tests are considered for further analysis. The impedance spectra shows two regions: one at high frequency and another at mid-low frequency. Since the EIS tests are performed using a limited range of frequency (in order to have a fast test), it is not possible to say much about the second region aforementioned. Instead, the high frequency region- represented by the semicircle- can be analysed because we can clearly see the ohmic resistance, intercept of the high frequency arc with the real axes, and the charge transfer resistance, represented by the intercept at mid frequency.

The increase of pressure at 71°C has negligible effects on the high frequency arc; on the other hand, at 79°C it determines a relative decrease of the ohmic resistance (from 0.625 to 0.568 Ωcm^2) as well as the capacitance (from 0.021 to 0.019 F), and an increase of the charge transfer resistance from 0.847 to 0.983 Ωcm^2.

Increasing temperature, considering constant pressure, has a positive effects on capacitance and charge transfer resistance, but it tends to become negligible as pressure increases. Instead, too high temperature (>71°C) causes an increase of the ohmic resistance probably due to dehydration effects, but this negative effects is mitigated by increase of pressure, at least up to 5 barg.

In conclusion, lower pressure and higher temperature have positive effects on the capacitance and the charge transfer resistance (higher capacitance and lower charge transfer resistance), whereas ohmic resistance at high temperature (>70°C) benefits from higher pressure.

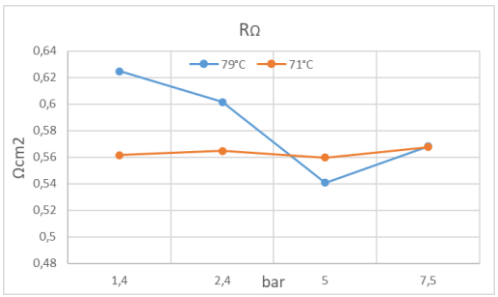

Figure 6.19 Trend of the ohmic resistance at 79°C and 71°C.

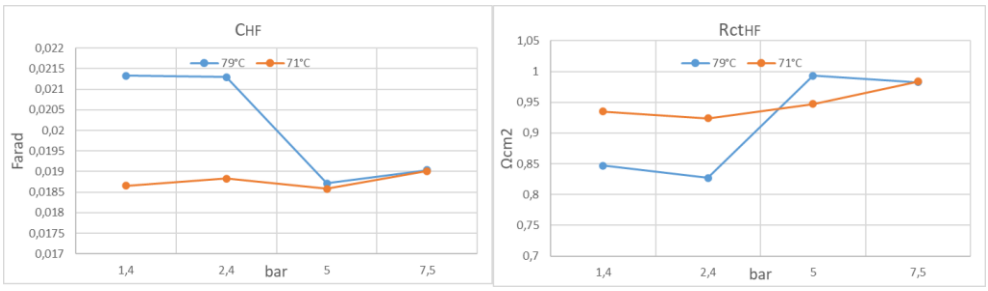

Figure 6.20 Trend of charge transfer resistance and capacitance in the HF region at 79°C and 71°C.

6.1.1.2. closed cathode configuration

EIS tests performed in both modes- potentiostatic and galvanostatic- at different DC value have produced results in accordance with the findings of the open cathode tests: high frequency is current/voltage independent thus related to the MEA structure whereas the mid-low frequency arc is correlated to kinetics process due to its dependence on the current density and voltage. The details of the tests are:

6.1.1.2.1. Constant condition

The test is performed at 60°c, imposed gauge pressure 0.5barg, with 10% mass low rates by pump with closed cathode configuration

The aim of the test to perform electrochemical characterization of the new cell by carrying out polarization curves and EIS measurements. The test is performed at 60°C and 0.5 barg imposed gauge pressure, with closed cathode configuration and 10% pump. Polarization curves are carried out by imposing the current and measuring the voltage whereas two types of EIS measurements have been used:

- Potentiostatic test, performed at different DC value of voltage (0 V, 0.5 V, 1 V, 1.5 V) vs Reference by varying the frequency from 100 kHz to 0,001 Hz in single sine mode and using a sinusoidal excitation signal of 10 mV root mean square (rms)
- Galvanostatic test, performed at different DC current -0 mA, 1000 mA, 1500 mA, 2000 mA- by varying the frequency from 200 kHz to 0,002 Hz in single sine mode and using a sinusoidal excitation signal of 1000 mA root mean square (rms).

During the test the cell temperature was 61.5°C whereas the fluid temperature at the heater was 60°C; the real gauge pressure is 0.75 barg in the anode and 0.4 barg in the cathode.

6.1.1.2.1.1. Data quality assessment

The KK validation shows a general poor quality of the impedance spectra, especially those obtained with galvanostatic tests. Potentiostatic mode has produced impedance measurements with acceptable quality only in the HF range. The ECM used to fit experimental data is LR(QR)(QR) due to the presence of noise at low frequency which makes difficult to get good results.

6.1.1.2.1.2. Modelling

Impedance spectra under voltage control are characterized by an arc at high frequency and a straight line/second incomplete arc at mid-low frequency. The low frequency features shows a dependence on voltage: as the DC value of potential increases this tends to bend down towards the real axis. In fact, at 1.5 V a second arc is clearly visible. Same consideration for tests performed under current control, i.e. the shape changes as the DC value is increased. At 0mA and 1000 mA there are three arcs, one at HF and the others at mid-low frequency. As the DC current is increased up to 2000 mA the arcs become two and the LF arc tends to reduce.

Figures below show the EIS measurements at the end of the tests at 60°C.

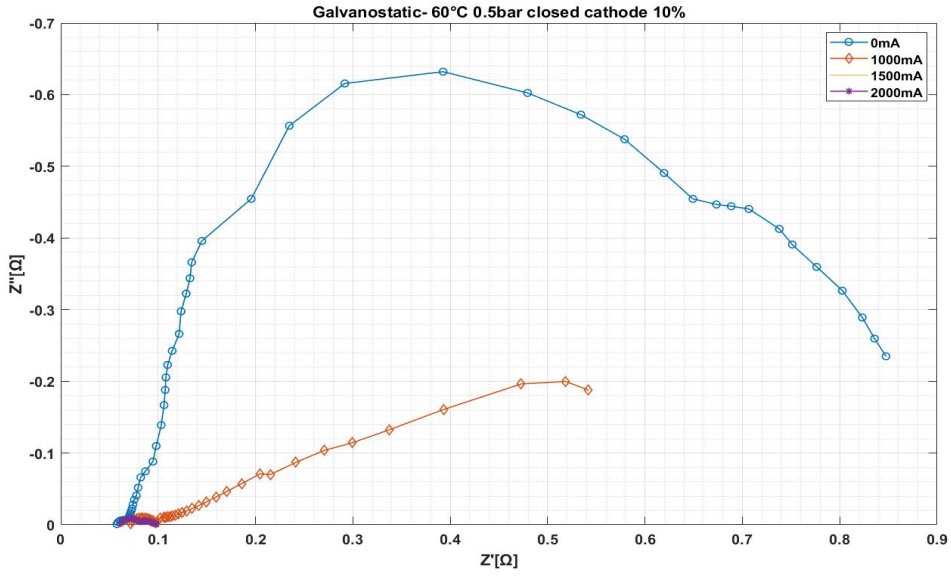

Figure 6.21 Nyquist plot under current control at 60°C 0.5barg closed cathode with 10% pump.

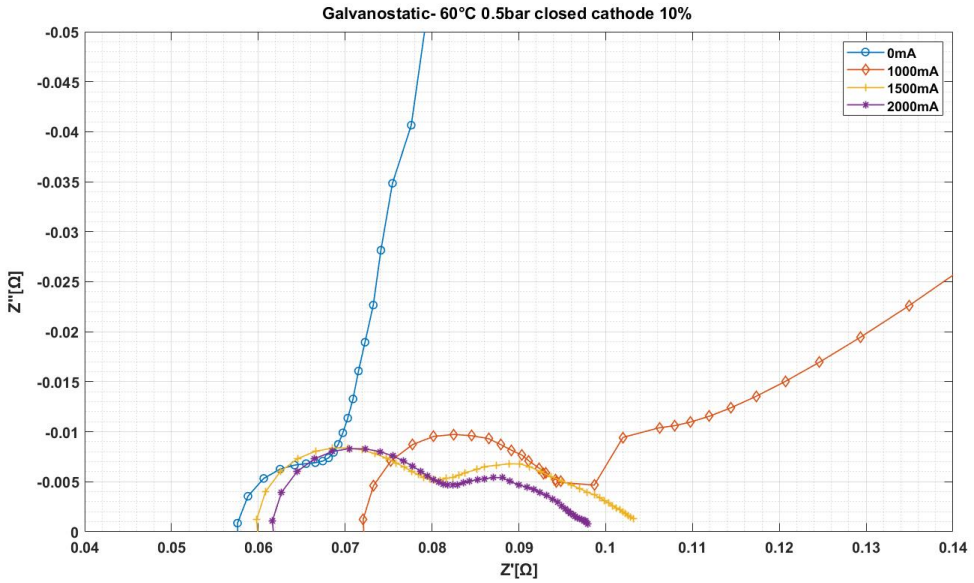

Figure 6.22 Zoom of Nyquist plot under current control at 60°C 0.5barg closed cathode with 10% pump.

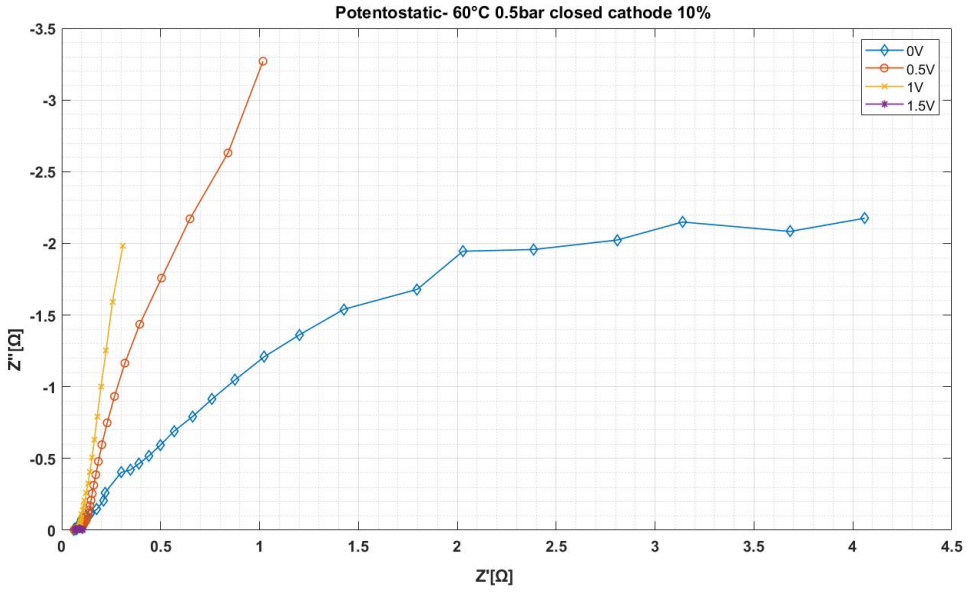

Figure 6.23 Nyquist plot under voltage control at 60°C 0.5barg closed cathode with 10% pump.

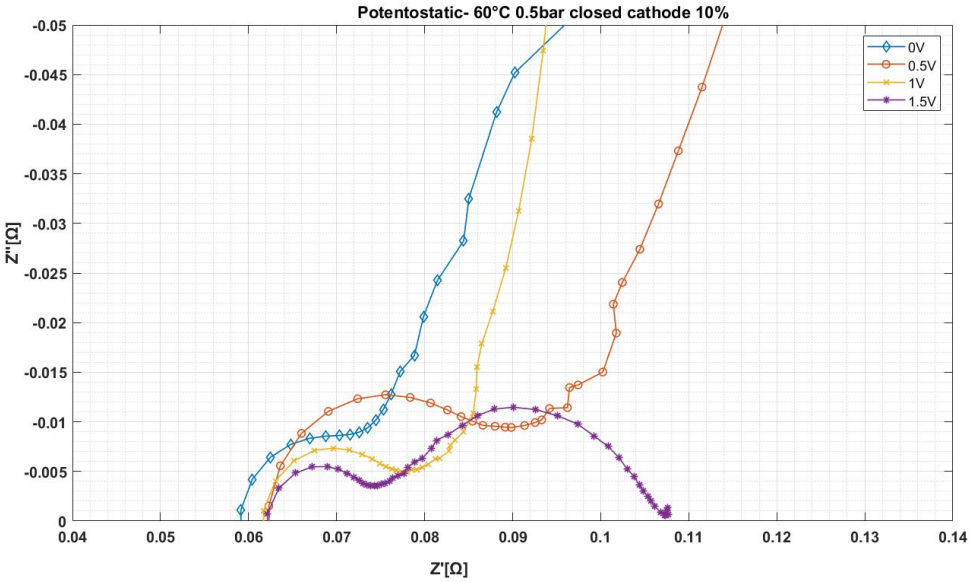

Figure 6.24 Nyquist plot under voltage control at 60°C 0.5barg closed cathode with 10% pump.

The analysis is performed using the results of the potentiostatic tests in the range 0.5-1.5 V done at the end of the test. Considering the range 0.5-1.5V, it is possible to notice that the ohmic resistance is not varying significantly with voltage (from 1.34 to 1.37 Ωcm^2), whereas as the voltage increases, we have that the LF arc bends down to the real axis. Moreover, at LF the charge transfer resistance decreases, and the capacitance C increases, so the LF semicircle becomes smaller. The high frequency arc, characterized by Rct and C, shows a very slight decrease with voltage: in particular, capacitance is increased while the charge transfer resistance shows lower value with higher voltage level. The figures below make a comparison between two types of fitting, ECM and Circle fit. The high difference shown by these trends is probably related to the not perfect modelling of ECM fit to the experimental data.

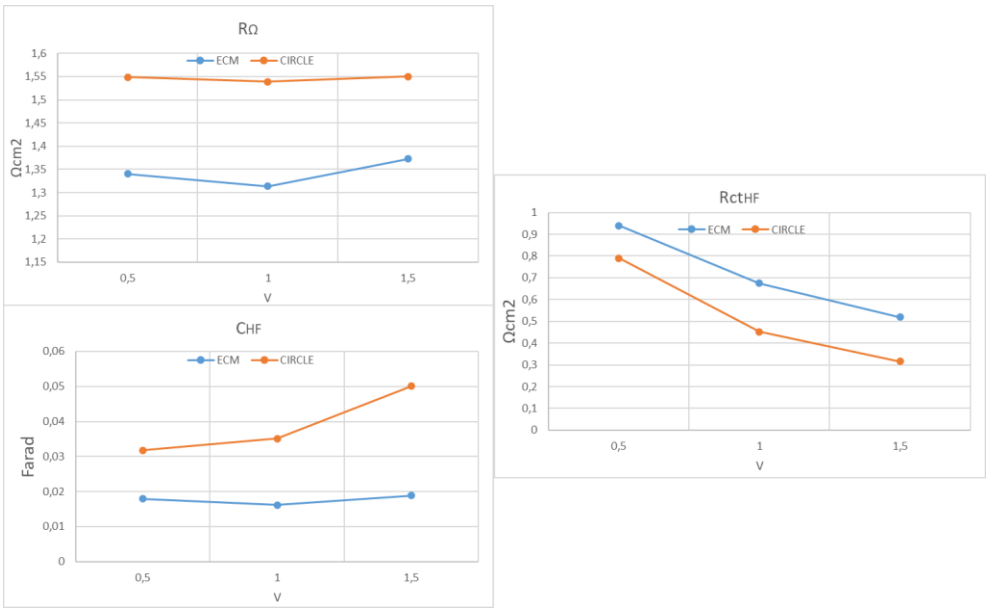

Figure 6.25 Trend of the HF parameters at 60°C and 10%pump.

6.1.1.2.2. Effect of flow rate I

The test is performed at constant current density of 1 A/cm2 with 60°C, 0.5 barg, closed cathode imposing different mass flow rate by recirculating pump. The aim of the experiment is to investigate the influence of mass flow rate on cell impedance at fixed operating condition and with closed cathode. The test is performed at constant current density of 1 A/cm^2 with fixed operating conditions of 60°C and 0,55 barg @ anode -0,44 barg @cathode and different mass flow rates changed by the usage of the pump from 10% to 100%. A change of the mass flow rate by pump causes a variation of the pressure at the heater during the experiment (refer to Table 0.5).

During the experiment two types of EIS tests have been used:

- Potentiostatic test is performed at 0 DC V vs Open circuit by varying the frequency from 100 kHz to 1 Hz in single sine mode and using a sinusoidal excitation signal of 10 mV root mean square (rms);
- Galvanostatic test is performed at 0 DC mA by varying the frequency from 200 kHz to 0,2 Hz in single sine mode and using a sinusoidal excitation signal of 1000 mA root mean square (rms).

6.1.1.2.2.1. Data quality assessment

The KK validation shows that impedance spectra obtained under voltage control are characterized by acceptable values of the residuals, whereas impedance data gained with galvanostatic tests are more affected by biased behaviour. In general, the shape is made of a semicircle in the HF and second incomplete semicircle/straight line in the mid frequency region. Hence, the ECM used to fit is LR(QR)(QR).

6.1.1.2.2.2. Modelling

Figure 6.26 shows impedance spectra obtained with potentiostatic tests. The high frequency intercept with the real axis is not much affected by mass flow rate variation, instead height and diameter of the HF arc show a substantial increase with increasing mass flow rates. The imaginary part of all HF arcs reaches a maximum at ω_{max} equal to 199.5 Hz and it tends to decrease up to 158.9 Hz with increasing mass flow rates. Same considerations can be done on the impedance spectra obtained with galvanostatic tests in Figure 6.27. In this case, the ω_{max} is equal to 200 Hz and it tends to decrease up to 158.9 Hz with increasing mass flow rates.

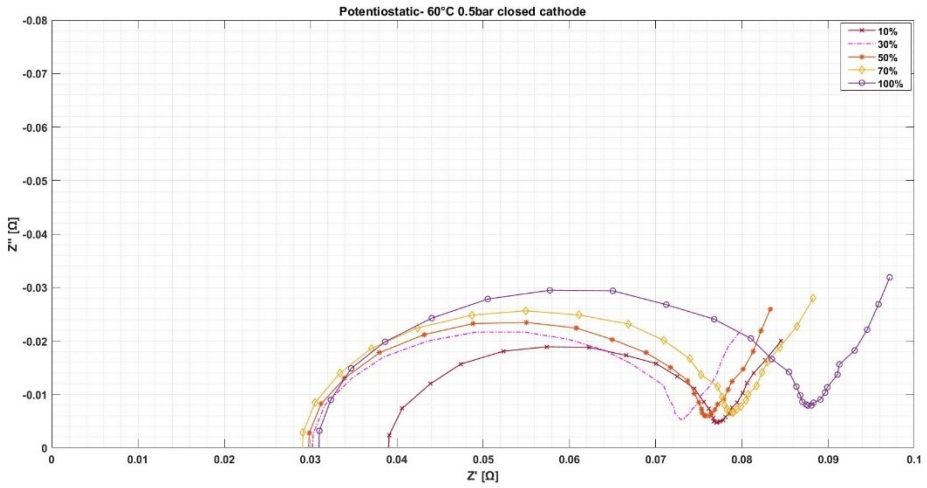

Figure 6.26 Nyquist plot under voltage control at 60°C 0.5barg closed cathode at different percentage of mass flow rates.

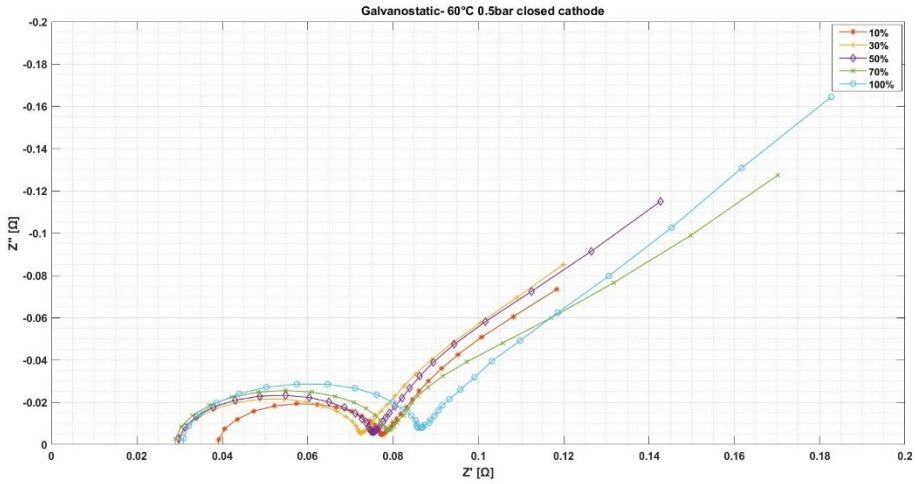

Figure 6.27 Nyquist plot under current control at 60°C 0.5barg closed cathode at different percentage of mass flow rates.

The analysis is carried out by discussing the results obtained from the potentiostatic tests. The impedance spectra show two regions: one at high frequency and another at mid-low frequency. EIS tests are performed using a limited range of frequency, thus only the -HF arc is analysed by measuring the ohmic resistance, intercept of the high frequency arc with the real axes, and the charge transfer resistance, which is the diameter of the high frequency arc.

The increase of mass flow rate determines a relative decrease of the ohmic resistance (from 0.898 to 0.716 Ωcm^2) as well as the capacitance (from 0.0187 to 0.0172 F), and an increase of the charge transfer resistance from 1.010 to 1.447 Ωcm^2. The increase of the charge transfer resistance is higher with respect to the decrease of the ohmic resistance. Hence, it may be assumed that the total polarization resistance is increasing as well; this agree with high values of voltage obtained with higher mass flow rate percentage (higher total polarization resistance means higher voltage).

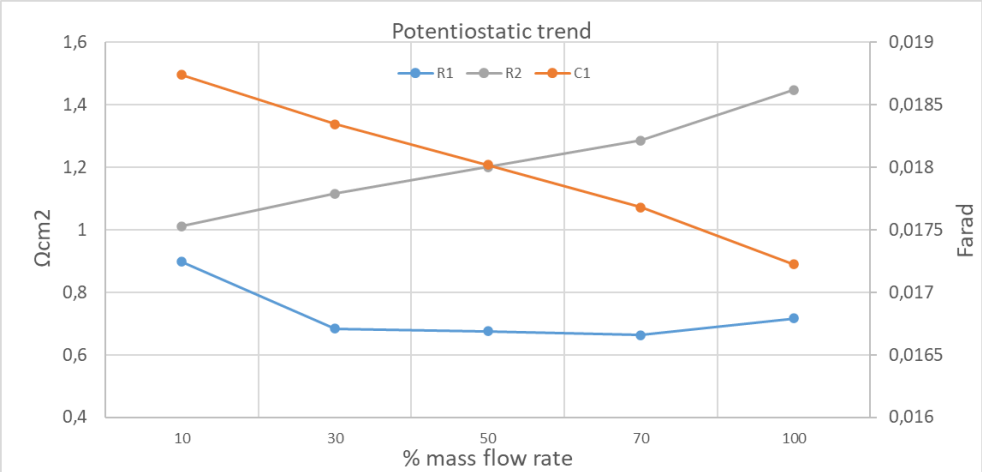

Figure 6.28 Pot trend

The analysis shows that from 10% to 100% of mass flow rate percentage, voltage and pressure at the heater increase instead average cell temperature (61,08°C-61,35°C) is almost constant. Only fluid temperature at the heater is characterized by a decreasing behaviour from 61,8°C up to 59°C, maybe because with higher percentage of the pump the flow is faster and so thermal stabilization is improved. Hence, increasing the percentage of mass flow rate determines an increment of fluid pressure at the heater and a decrease of the temperature at the heater. As a consequence, voltage increases so the cell performance is negatively affected by increment of mass flow rates.

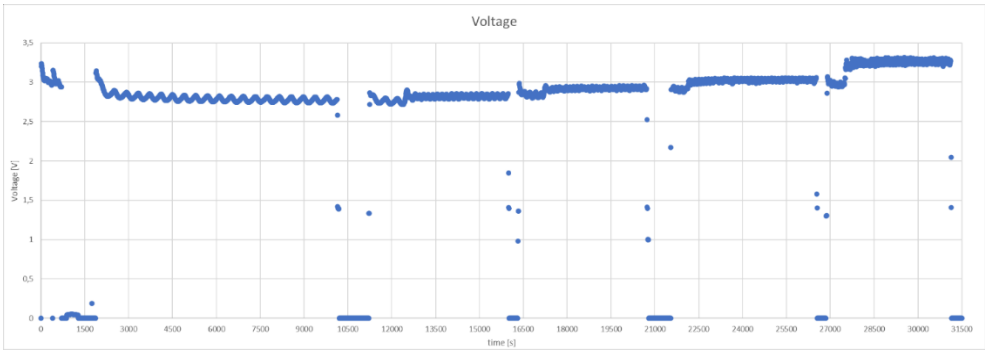

Figure 6.29 Trend of the voltage during the test.

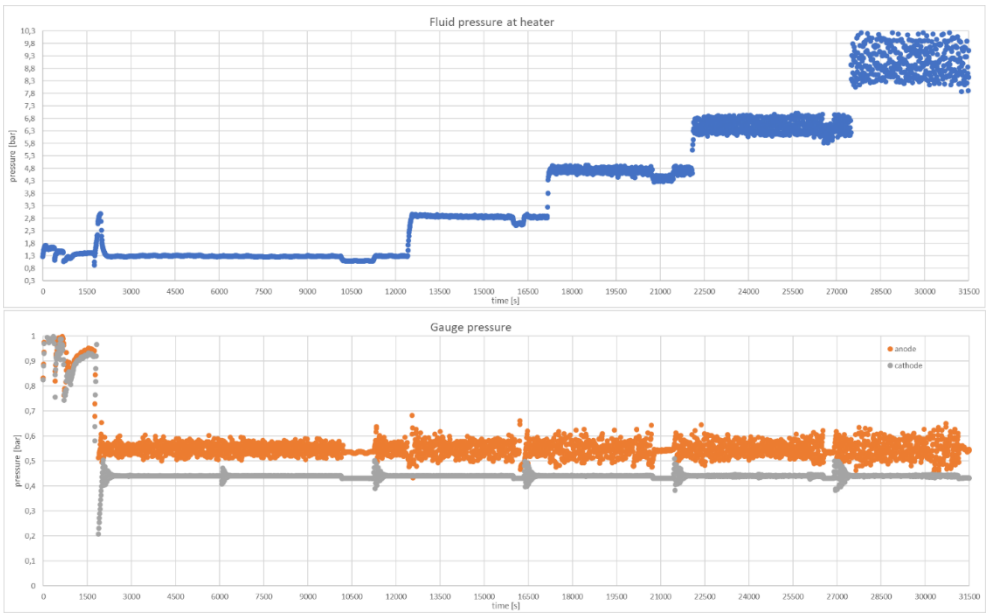

Figure 6.30 Trend of the pressures- anode, cathode, heater- during the test.

In conclusion, with closed cathode at 60°C and with constant current density of 1 A/cm^2, an increase of the mass flow rate determines an increment of pressure which negatively affects the performance of the cell, i.e. higher voltages are measured.

6.1.1.2.3. Effect of flow rate II

The test is performed at 80°c with closed cathode, imposed gauge pressure 0.5 barg, with different mass low rates by pump. The objective of the test is to investigate the effect of mass flow rates on the cell impedance obtained by changing the DC values of the EIS setup. The test is performed at 80°C and 0.5 barg imposed gauge pressure, with closed cathode configuration by imposing the percentage of the chamber displacement of the pump first at 5% then at 20%. Two types of EIS measurements have been used:

- Potentiostatic test, performed at different DC value of voltage (0 V and 1 V) vs Reference by varying the frequency from 100 kHz to 0,001 Hz in single sine mode and using a sinusoidal excitation signal of 10 mV root mean square (rms)
- Galvanostatic test, performed at different DC current -0 mA, 1000 mA, 1500 mA, 2000 mA- by varying the frequency from 200 kHz to 0,002 Hz

in single sine mode and using a sinusoidal excitation signal of 1000 mA root mean square (rms).

During the test with 5% pump, the cell temperature was 79.3°C whereas the fluid temperature at the heater was quite high 85°C; the real gauge pressure was 0.4 barg in the anode and 0.2 barg in the cathode. On the other hand, at 20% the cell temperature was 79.5°C, fluid temperature 80°C and real gauge pressure was around 1 barg and 0.4 barg in the anode and cathode respectively.

6.1.1.2.3.1. Data quality assessment

The KK validation shows that both potentiostatic and galvanostatic modes have some tests with low quality impedance spectra which are invalid so not used in the analysis. By visual inspection of both Nyquist and Bode plots two time constants are observed in the impedance spectra under voltage control and at least two for those obtained with the galvanostatic mode. The ECM used to fit experimental data is LR(QR)(QR) due to the presence of noise at low frequency which makes difficult to get good results.

6.1.1.2.3.2. Modelling

The figure below shows a comparison between impedance spectra obtained with potentiostatic mode at 0 V and 1 V with different percentage of the displacement pump. The shape of the impedance consists of an arc at high frequency and a second incomplete semicircle at mid-low frequency.

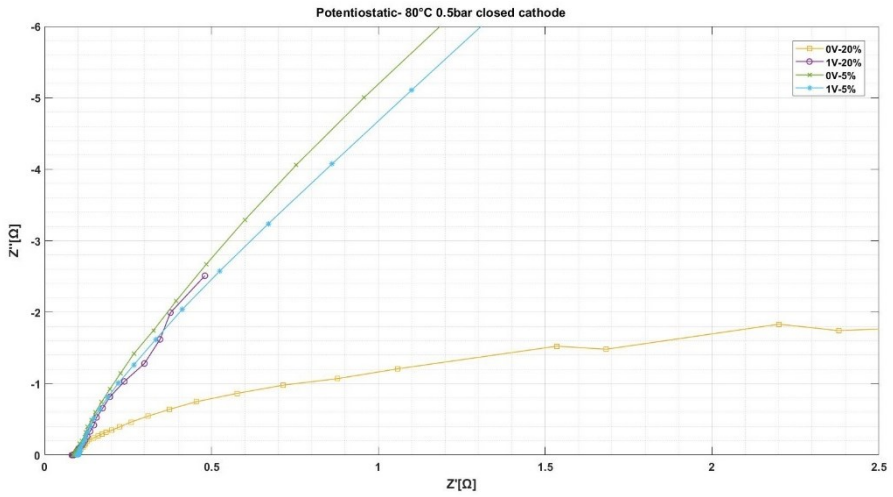

Figure 6.31 Nyquist plot under voltage control at 80°C 0.5barg closed cathode with different mass flow rates.

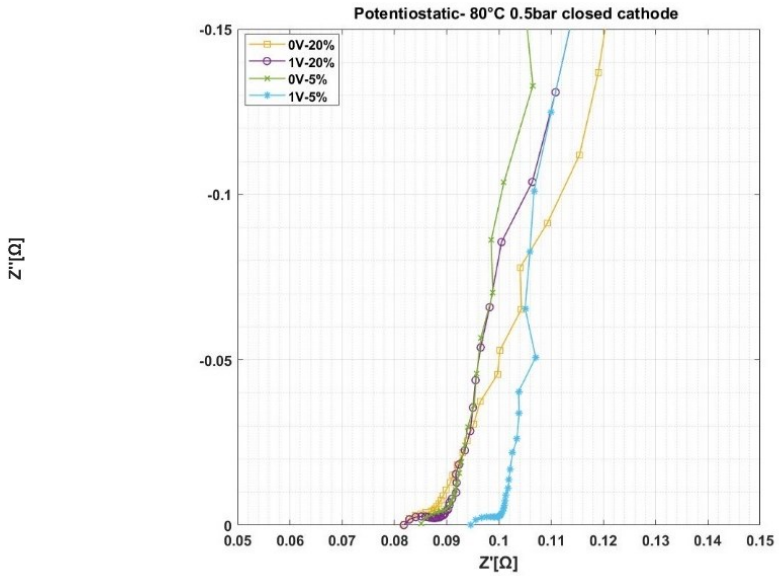

Figure 6.32 Pot CC trend

The figure below shows all impedance spectra measured with galvanostatic tests. The shape changes as the DC value is increased. At 0 mA and 1000 mA there are three arcs, one at HF and the others at mid-low frequency. As the DC current is increased up to 2000 mA the arcs become two and the LF arc tends to reduce as well.

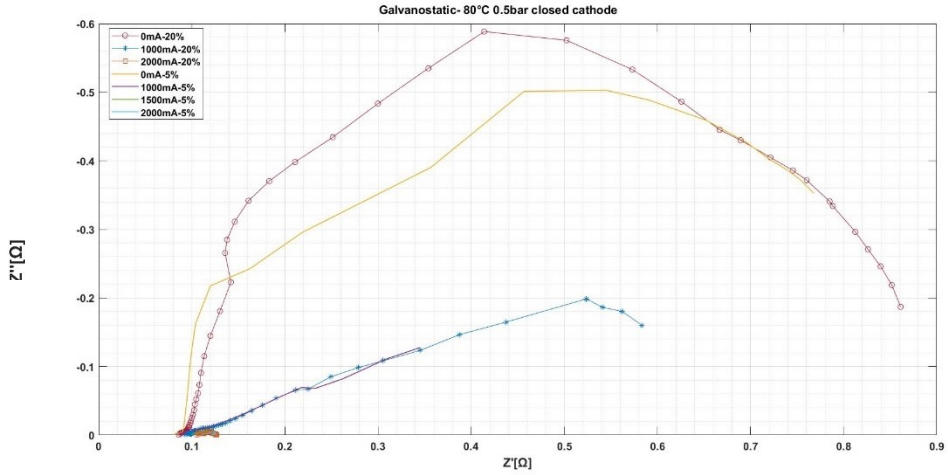

Figure 6.33 Nyquist plot under current control at 80°C 0.5barg closed cathode with different mass flow rates.

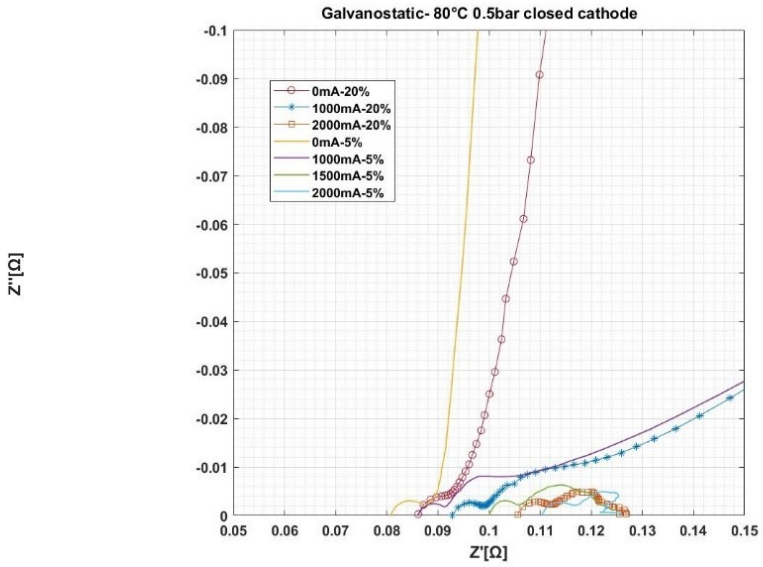

Figure 6.34 Galv trend

Impedance spectra have been fitted only considering the HF region, which shows a relative acceptable quality. Tables with all parameters and their errors are presented in the appendix.

The analysis is made considering only the results obtained by fitting the HF arc of valid impedance spectra measurements under current control, which are characterized by a better quality with respect to those of the potentiostatic mode. It is observed that at low current densities the ohmic resistance decreases sensibly when the mass flow rates are decreased from 20% to 5%. This may be related to lower pressures with low mass flow rate as shown below.

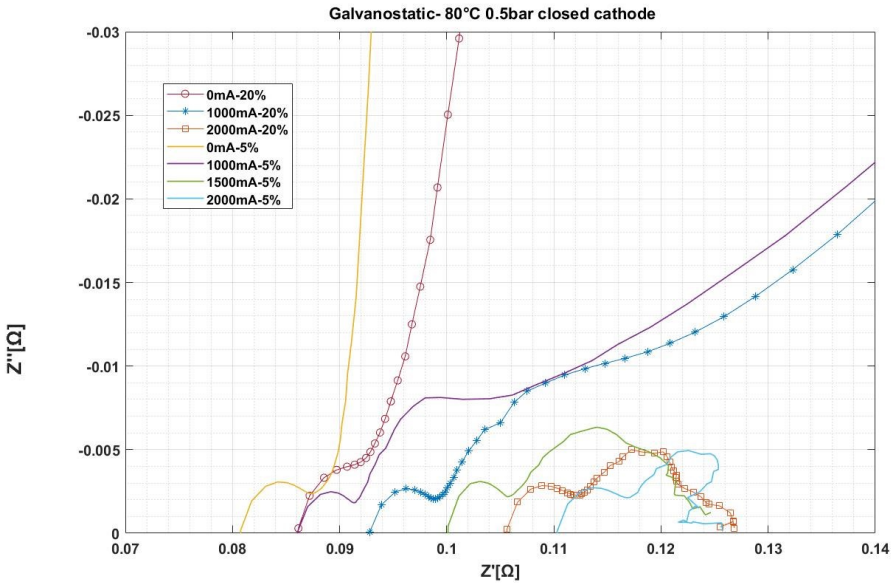

Figure 6.35 Galv CC trend

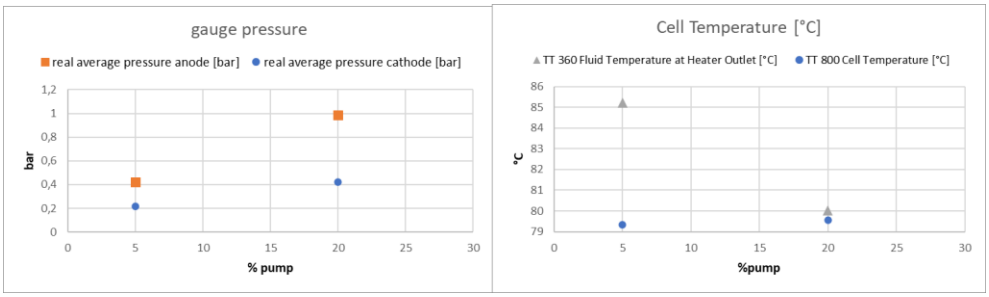

Figure 6.36 P & T

Considering capacitance and charge transfer resistance of the HF arc, these show an unperceivable improvement, i.e., the capacitance slightly increases and the Rct decreases. Instead, qualitatively it is possible to notice equivalent value of the total polarization resistance between the two pump percentage.

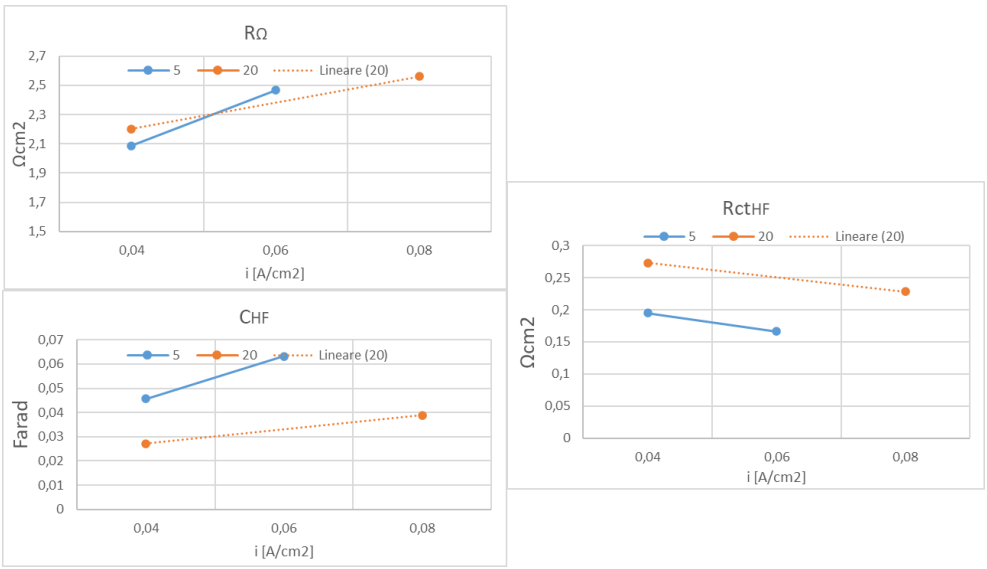

Figure 6.37 resistances trend

In conclusion, at low current densities and higher temperature, lower mass flow rates thus lower pressures can enhance the performance of the cell.

6.1.1.2.4. Effect of temperature, polarization I

The test is performed at 60°c and 80°c with closed cathode, imposed gauge pressure 0.5barg, 105% mass low rate by pump. The aim of the test to perform electrochemical characterization of the new cell by carrying out polarization curves and EIS measurements. The test consists of two series, first performed at 60°C and the second at 80°C, both characterized by same operating conditions of 0.5 barg imposed gauge pressure, 105% pump and closed cathode configuration. Polarization curves were measured by current control up to 1.6 A/cm^2 whereas two types of EIS measurements have been used:

- Potentiostatic test, performed at 0 DC V vs Reference by varying the frequency from 100 kHz to 0,001 Hz in single sine mode and using a sinusoidal excitation signal of 10 mV root mean square (rms)
- Galvanostatic test, performed at 0 DC mA by varying the frequency from 200 kHz to 0,002 Hz in single sine mode and using a sinusoidal excitation signal of 1000 mA root mean square (rms).

During the test performed at 60°C the real gauge pressure at the anode side of the cell is almost 4.6 barg at the anode and 0.44 barg at the cathode, whether the real temperature of the cell is around 61.5°C and fluid temperature at the heater is

59°C. As a matter of fact, during EIS test operating conditions are unvaried. During the test performed at 80°C the real gauge pressure as before is 4.6 barg in the anode and 0.44 barg in the cathode, whether the real temperature of the cell is around 79.6°C and fluid temperature at the heater is 78.1°C. No changes of pressure during EIS tests are 80°C are seen.

6.1.1.2.4.1. Data quality assessment

The KK validation shows a poor quality of the impedance spectra obtained under galvanostatic measurements whereas those obtained with potentiostatic still show high residuals but at least the HF is not much affected by noise or time variance. By visual inspection of both Nyquist and Bode plots two time constants are observed in the measurements under voltage control and at least three under current control. The ECM used to fit experimental data is LR(QR)(QR) due to the presence of noise at low frequency which makes difficult to get good results.

6.1.1.2.4.2. Modelling

The comparison between 60°C and 80°C for both EIS measurements is shown in the figures below.

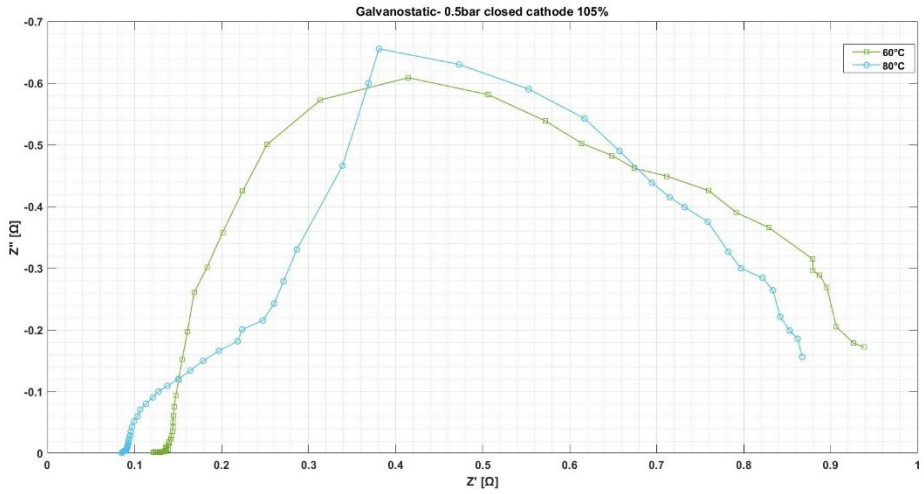

Figure 6.38 Nyquist plot under current control at 0.5barg closed cathode with 105% at different temperatures.

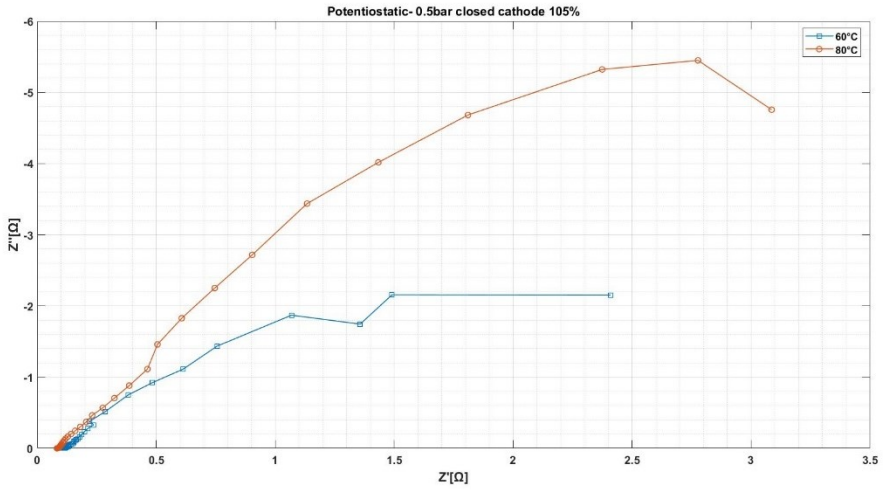

Figure 6.39 Nyquist plot under voltage control at 0.5barg closed cathode with 105% at different temperatures.

Potentiostatic measurements have one semicircle in the HF region and a second incomplete arc in the mid-low frequency range; same behaviour at high frequency for the galvanostatic which instead shows in the mid low frequency range two other arcs, mostly affected by noise. In both EIS modes the HF intercept with the real axis has lower values at 80°C. Impedance spectra of galvanostatic tests are considered only qualitatively due to the KK non-compliant behaviour, hence they have not been fitted. On the other hand, impedance spectra of the potentiostatic mode have been fitted only considering the HF region, which shows a relative acceptable quality. Tables with all parameters and their errors are presented in the appendix.

Results obtained with potentiostatic tests are subject to a verification through a comparison with the iV-curves measured at 60°C and 80°C. Both tests are performed at 0V and they have an arc in the high frequency region and a curved line at low frequencies which can be assumed as an uncompleted arc. As the temperature increases, it is observed a general decrease of the ohmic resistance from $2.572\ \Omega/cm^2$ to $2.012\ \Omega/cm^2$. Instead, capacitance and charge transfer resistance of the HF arc do not show significant variations. The decrease of the ohmic resistance may be related to higher T which has a positive effect on the proton conductivity. The figures below show a comparison between ECM fit and Circle fit. In both cases the trend are the same although there is a small difference between parameters.

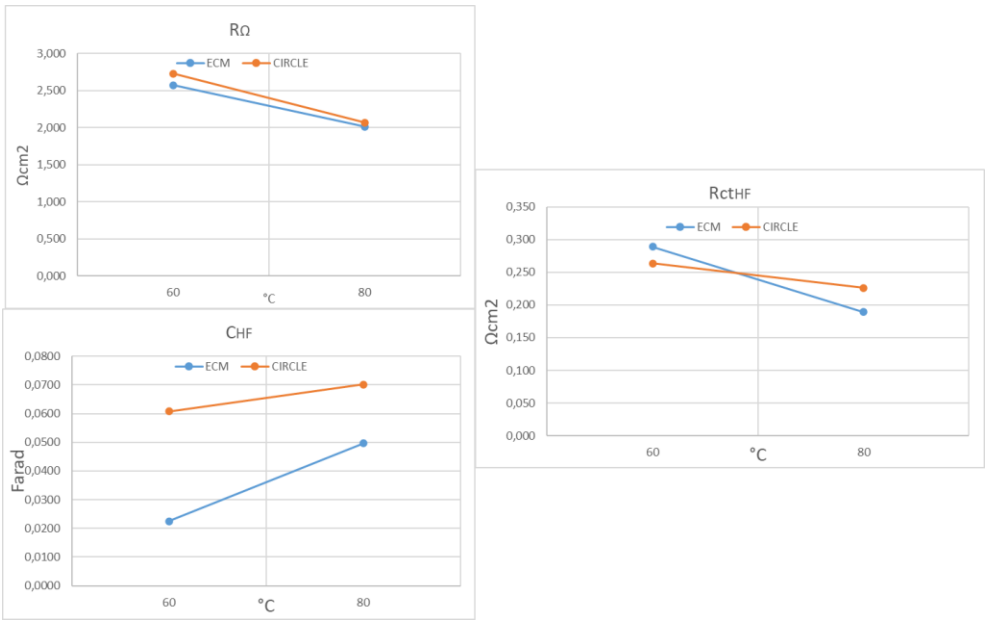

Figure 6.40 resistances trend

Although galvanostatic tests have shown low quality from KK validation, a qualitative analysis can be done. From the Nyquist plot at OCV it is observed that the total polarization resistance and the ohmic resistance are lower at 80°C, hence it suggests that the test at 80°C has lower voltage near the OCV.

The results obtained from EIS measurement under voltage control and the qualitative analysis of galvanostatic tests are in accordance with the polarization curves. The figure below shows a comparison between the two iV-curves, each taken before performing EIS tests. It is observed that at low current density- where activation losses are dominant- high temperature has a positive effect on the cell performance, i.e. lower voltage at 80°C. This trend is opposite at higher current densities where maybe dehydration effects and/or mass transport limitations become more relevant. The latter is a hypothesis because EIS measurements at high current densities or voltages are not possible due to the device limitations.

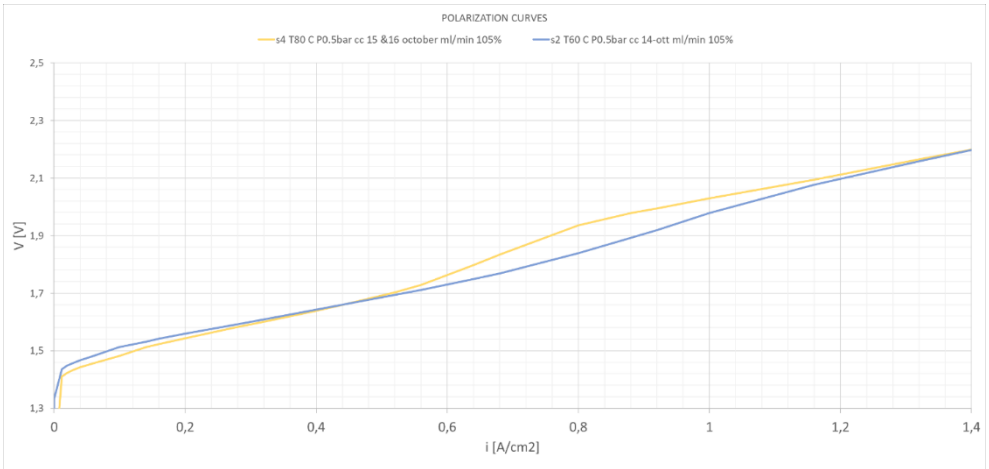

Figure 6.41 Polarization curves at 60°C and 80°C.

6.1.1.2.5. polarization II

The test is performed at 80°C and 60°C, With Closed Cathode, Imposed Gauge Pressure 0.5barg, with 20% Mass Low Rates by Pump. The aim of the test to perform electrochemical characterization of the new cell by carrying out polarization curves and EIS measurements. The test consists of two series, first performed at 80°C and the second at 60°C, both characterized by same operating conditions of 0.5 barg imposed gauge pressure, 20% pump and closed cathode configuration. Polarization curves were measured by current control up to 2 A/cm^2 whereas two types of EIS measurements have been used:

- Potentiostatic test, performed at different DC value of voltage (from 0 V to 1.5 V) vs Reference by varying the frequency from 100 kHz to 0,001 Hz in single sine mode and using a sinusoidal excitation signal of 10 mV root mean square (rms)
- Galvanostatic test, performed at different DC current -0 mA, 1000 mA, 1500 mA, 2000 mA- by varying the frequency from 200 kHz to 0,002 Hz in single sine mode and using a sinusoidal excitation signal of 1000 mA root mean square (rms).

During the test at 80°C, the cell temperature was 79.5° whereas the fluid temperature at the heater was 80.5°C; the real gauge pressure was around 1 barg in the anode and 0.4 barg in the cathode. On the other hand, during the test at 60°C the cell temperature was 61.5°C, fluid temperature 60.8°C and real gauge pressure was 1 barg and 0.4 barg at the anode and cathode respectively.

6.1.1.2.5.1. Data quality assessment

The KK validation shows a general poor quality of the impedance spectra, especially those obtained with galvanostatic tests. Potentiostatic mode has produced impedance measurements with acceptable quality only in the HF range. The main reason of non-validity of the impedance spectra obtained with galvanostatic tests is the time variance of the cell during its execution, as shown in *Figure 98*. In these figures the larger oscillations of pressure individuate when galvanostatic test have been performed.

The number of time constants observed in the graphical representation are two for potentiostatic and at least three for galvanostatic. The ECM used to fit experimental data is LR(QR)(QR) due to the presence of noise at low frequency which makes difficult to get good results.

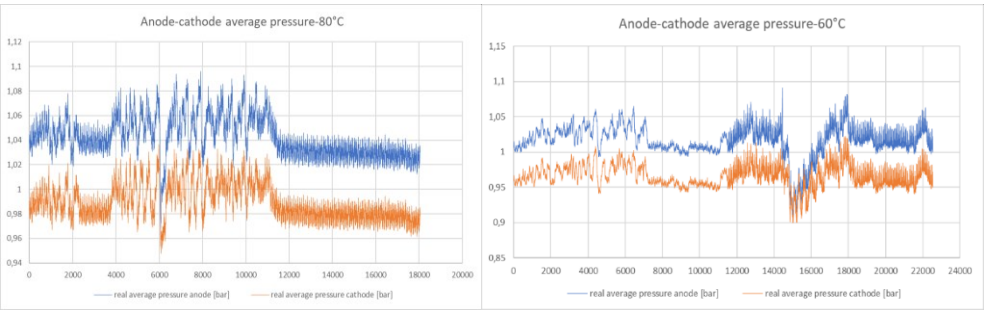

Figure 6.42Trend of pressure during potentiostatic and galvanostatic measurements.

6.1.1.2.5.2. Modelling at 80°C

Nyquist plot below shows the impedance measurement at 80°C, both potentiostatic and galvanostatic. Impedance spectra under voltage control are characterized by an arc at high frequency and a straight line/second incomplete arc at mid-low frequency (some tests were interrupted before reaching the lowest frequency due to noise, this explains the difference in shape at lower frequencies). On the other hand, under current control the shape changes as the DC value is increased. At 0 mA and 1000 mA there are three arcs, one at HF and the others at mid-low frequency. As the DC current is increased up to 2000 mA the arcs become two and the LF arc tends to reduce.

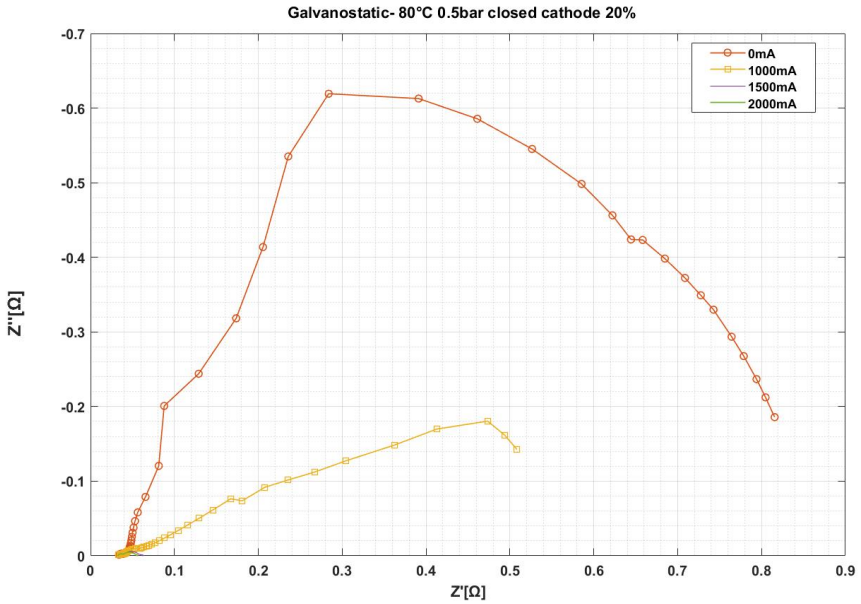

Figure 6.43 Nyquist plot under current control at 80°C 0.5barg closed cathode with 20% pump.

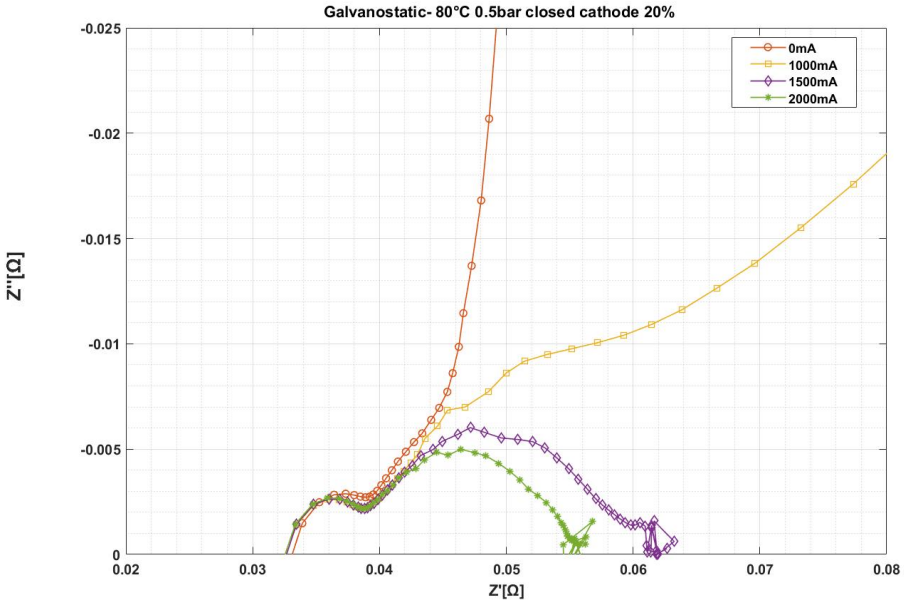

Figure 6.44 Zoom of Nyquist plot under current control at 80°C 0.5barg closed cathode with 20% pump.

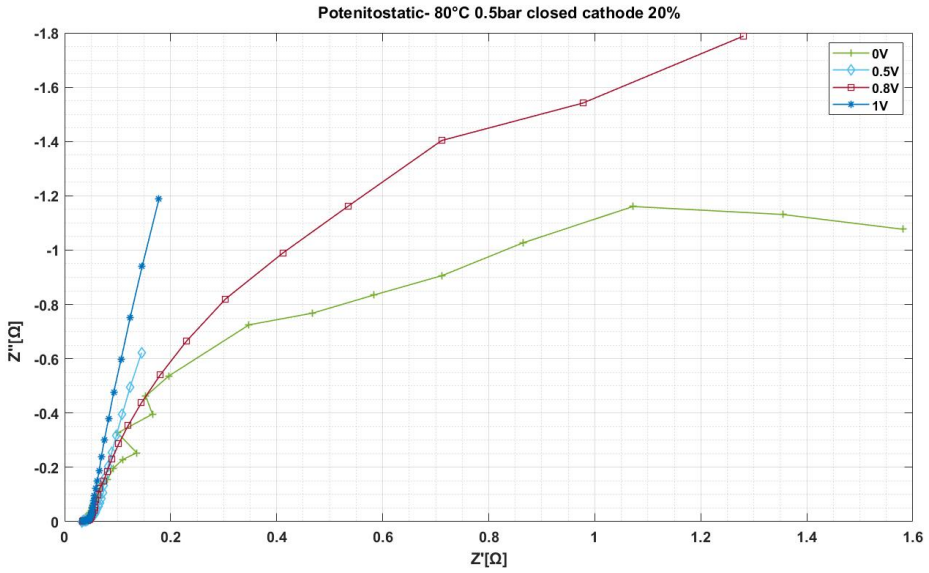

Figure 6.45 Nyquist plot under voltage control at 80°C 0.5barg closed cathode with 20% pump.

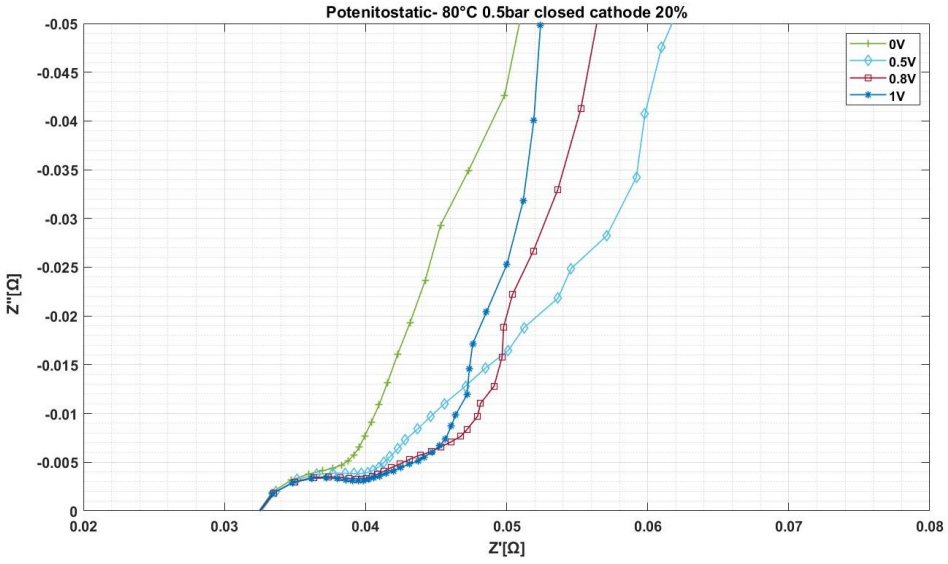

Figure 6.46 Zoom of Nyquist plot under voltage control at 80°C 0.5barg closed cathode with 20% pump.

6.1.1.2.5.3. Modelling at 60°C

Figures below show the EIS measurements at the end of the test at 60°C.

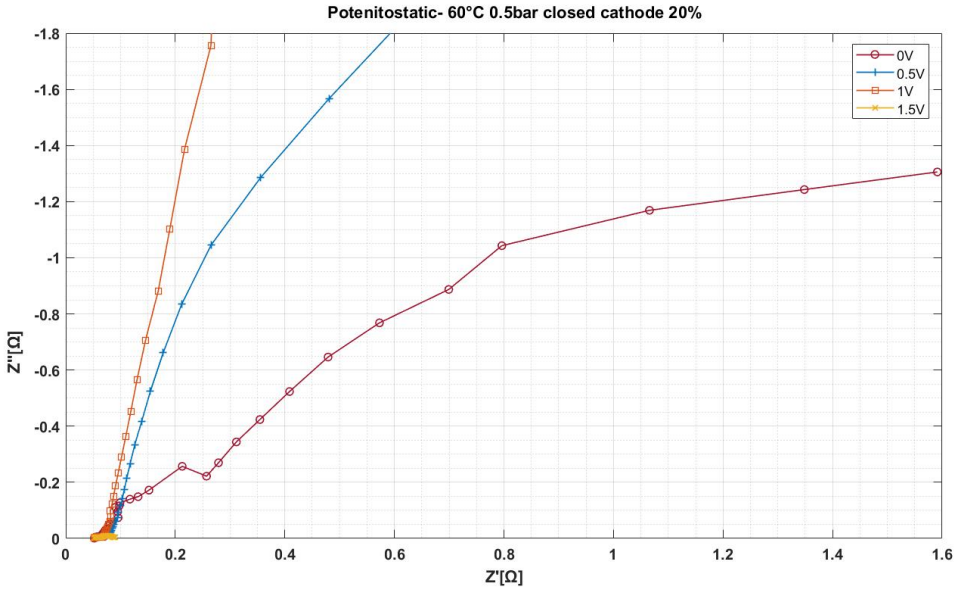

Figure 6.47 Nyquist plot under voltage control at 60°C 0.5barg closed cathode with 20% pump.

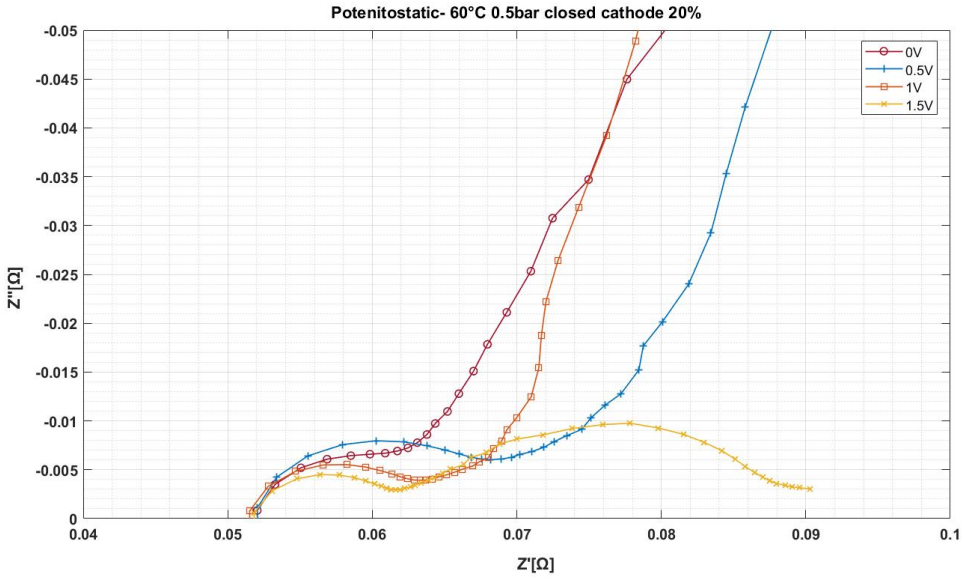

Figure 6.48 Zoom of Nyquist plot under voltage control at 60°C 0.5barg closed cathode with 20% pump.

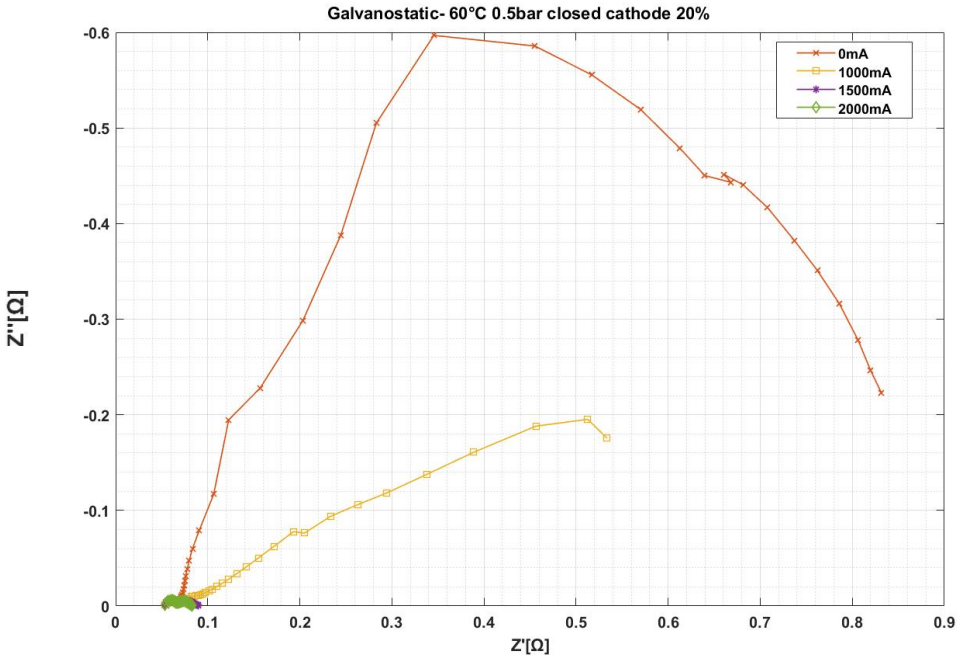

Figure 6.49 Nyquist plot under current control at 60°C 0.5barg closed cathode with 20% pump.

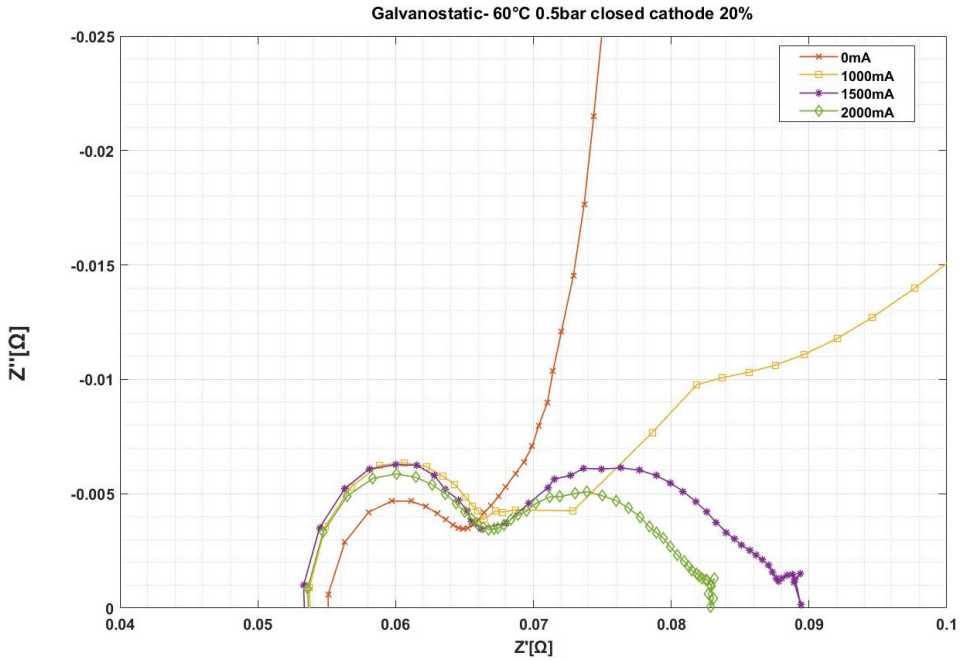

Figure 6.50 Zoom of Nyquist plot under current control at 60°C 0.5barg closed cathode with 20% pump.

Impedance spectra under voltage control are characterized by an arc at high frequency and a straight line/second incomplete arc at mid-low frequency. The low frequency features show a dependence on voltage: as the DC value of potential increases, this tends to bend down towards the real axis. In fact, at 1.5 V a second arc is clearly visible. Same consideration for tests performed under current control, i.e. the shape changes as the DC value is increased.

6.1.1.2.5.4. Considerations on tests performed at 80°C

Results obtained by fitting the impedance spectra measured under current control are analysed from a qualitative point of view. First, it is observed a dependence on current density principally related to the LF arc. As the current density increases it is noticed that the LF arc is characterized by a decrease of charge transfer resistance while its capacitance C increases; so the LF semicircle becomes smaller. Considering that in the range 0-2 A (so 0-0,08 A/cm2 current density) we are in the activation domain and that the LF arc shows a dependence on current density, it is suggested that the LF arc is controlled by the charge-transfer kinetics. It means that in the Nyquist plot the LF arc is related to OER and HER. The presence of noise makes impossible to say if mass transport processes are present.

Instead, the HF arc and the ohmic resistance show an almost constant trend. Hence, it is possible to assess that the HF arc is current independent. This means that is not related to kinetics processes but rather to the MEA structure.

About potentiostatic tests, the analysis of the fitting results concerns only valid spectra which are those obtained in the range 0.5-1 V and it is focused on the HF region of the spectra where quality is higher. It is possible to notice that the ohmic resistance is not varying significantly with voltage (from 0.770 to 0.730 Ωcm^2), the same thing for the HF arc which remains almost constant in this range. In fact, the maximum frequency is constant at 251.2 Hz. Figures below show a comparison between ECM fit and Circle fit. The trend is similar for both types of fit. In the ECM fit mode the result at 0.8 V is considered an outlier due to higher error of the fit.

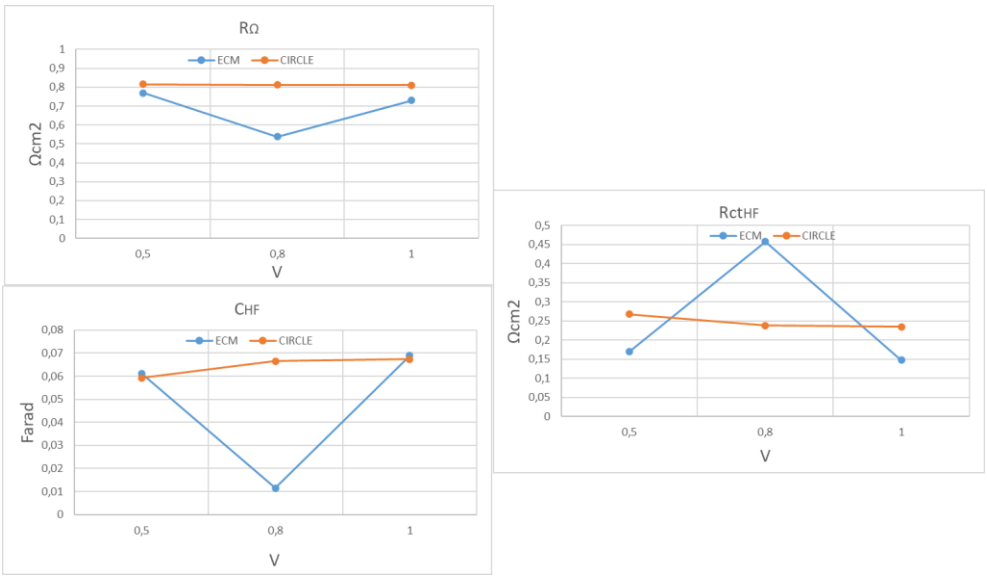

Figure 6.51 Trend of the HF parameters at 60°C with 20%pump.

6.1.1.2.5.5. Considerations on tests performed at 60°C

The analysis is focused on the EIS measurements performed at the end of the test. Only good impedance spectra are considered, thus 1500 mA and 2000 mA for the galvanostatic mode and the range 0.5-1.5 V for the potentiostatic mode.

As the current increases in the range 1.5-2 A we have that at LF the charge transfer resistance decreases from 0.583 to 0.428 Ωcm^2 and the capacitance C is almost constant at 4-4.1 F, so the LF semicircle becomes smaller. Instead, the HF arc in the same range is characterized by an almost constant value of the charge transfer resistance HF (from 0.37 to 0.39 Ωcm^2) and capacitance (from 0.034 to 0.03 F), whereas the ohmic resistance is almost constant around 1.25-1.24 Ωcm^2.

Considering the range 0.5-1.5 V, it is possible to notice that the ohmic resistance is not varying significantly with voltage (from 1.178 to 1.200 Ωcm^2), whereas as the voltage increases, we have that the LF arc bends down to the real axis. Moreover, at LF the charge transfer resistance decreases, and the capacitance C increases, so the LF semicircle becomes smaller. The high frequency arc, characterized by Rct and C, shows a very slight decrease with voltage: in particular, capacitance is increased while the charge transfer resistance shows lower value with higher voltage level.

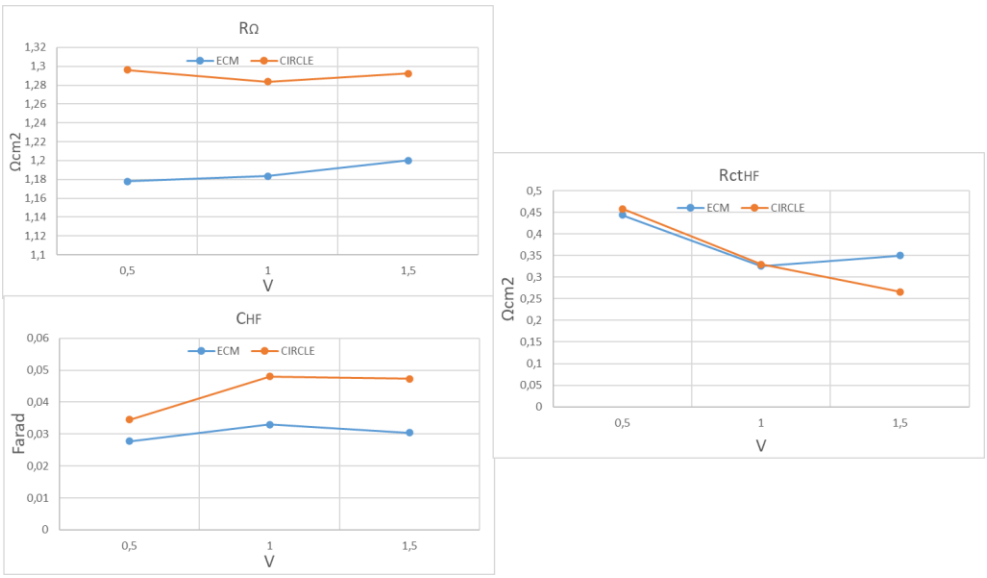

Figure 6.52 Trend of the HF parameters at 80°C with 20%pump.

6.1.1.2.5.6. Comparison Between 80°C And 60°C At 20% Pump

Polarization curves show that the performance of the cell improves at higher temperatures. This result is in accordance with the findings of the EIS tests. First of all, the trends in Figure 6.54 show that the HF feature is improved at higher temperature. Further on, a qualitative comparison between impedance spectra obtained with galvanostatic tests allows to say that total polarization resistance is smaller at 80°C, hence not only the electrolyte benefits from higher temperature but also the anode.

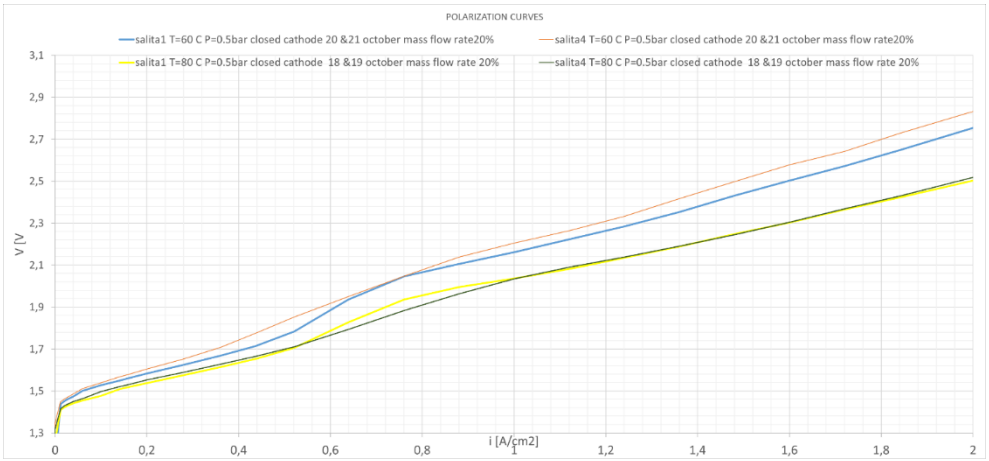

Figure 6.53 polarization curves

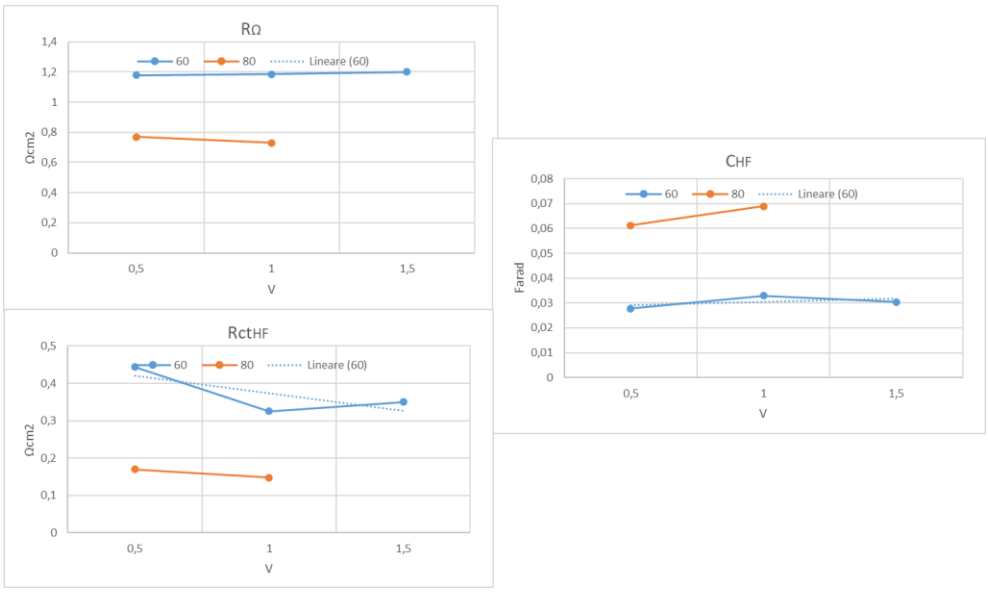

Figure 6.54 Comparison between 80°C and 60°C of the HF parameters with 20%pump.

6.1.2. Comparison of closed vs open cathode

Making a comparison between open and closed cathode configuration at constant temperature in the range 40-60°C, EIS parameters obtained during the open cathode test have better trend. A possible reason is a better thermal stabilization of the system (temperature at the heater has less oscillations). On the other hand, closed cathode seems to perform better at higher temperature (>70°C)- lower value of the charge transfer resistance and capacitance- but still the ohmic resistance is not improving because too higher T cause dehydration effects.

The improvement seen in the open cathode in both cases could be related to the more homogeneous temperature distribution in the housing during the test and improved transport phenomena. EIS tests show that closed cathode has generally a larger high frequency arc which could be related to a worsening of current constrictions.

The details of some performed tests are:

6.1.2.1. Effect of temperature

Tests performed at gauge pressure 1.4 barg, with open/closed cathode at different temperatures. The objective of the experiment is to investigate the influence of temperature and different cathode configurations on the cell impedance by carrying

out EIS tests. It consists of two series: the *first series* is done with *open cathode* with real imposed gauge pressure of 1,84barg in the anode and 1,83barg in the cathode and T going from 70°C to 40°C. The *second series* is done with *closed cathode* with real imposed gauge pressure of 2,38barg in the anode and 1,35barg in the cathode and T going from 50°C up to 80°C. After stabilization of the system at each value of temperature, EIS tests are executed. These are:

- Potentiostatic test, performed at 0 DC V vs Open circuit by varying the frequency from 100kHz to 1Hz in single sine mode and using a sinusoidal excitation signal of 10mV root mean square (rms).
- Galvanostatic test, performed at 0 DC mA by varying the frequency from 200kHz to 0,2Hz in single sine mode and using a sinusoidal excitation signal of 1000 mA root mean square (rms).

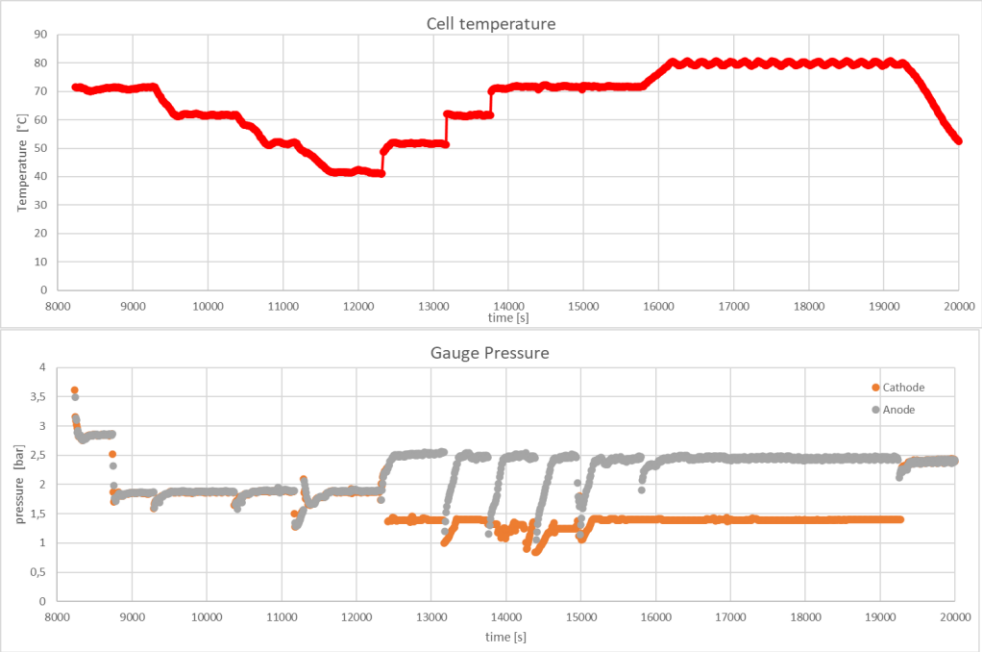

Figure 6.55 Trend of cell temperature and gauge pressure in the anode and cathode.

6.1.2.1.1. Data quality assessment

The KK validation shows that impedance spectra obtained under voltage control are characterized by lower residuals, whereas impedance data gained with galvanostatic tests are affected by time variance of the cell behaviour. In Nyquist spectra the shape is made of a semicircle in the HF and a second incomplete

semicircle/straight line in the mid frequency region, corresponding to two time constants in the Bode plots. Hence, the ECM used to fit is LR(QR)(QR).

6.1.2.1.2. Modelling

Figure 6.56 and Figure 6.57 show impedance spectra obtained with potentiostatic tests, with open and closed cathode respectively. The high frequency arc is not much affected by the temperature in both cathode configurations, whereas the second incomplete arc shows a different behaviour: with open cathode no relevant changes are seen but with closed it bends down to the real axis as temperature decreases. The EIS data obtained with closed cathode at 51°C is in contrast with the trend shown by the other impedance spectra of the same series.

The imaginary part of all HF arcs reaches a maximum at ω_{max} equal to 158.5 Hz for open cathode; for closed cathode is 125.9 Hz, except for 80°C characterized by ω_{max} equal to 158.9 Hz.

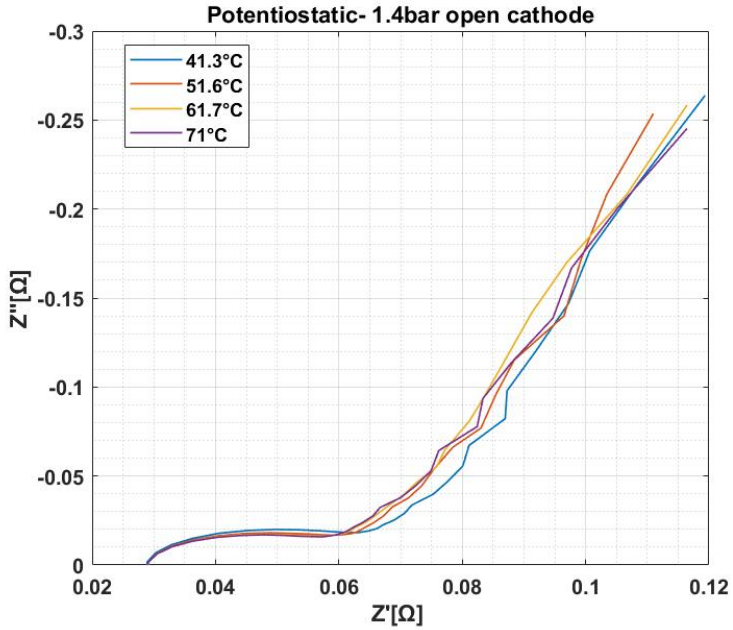

Figure 6.56 Nyquist plot under voltage control at 1.4barg open cathode with different temperatures.

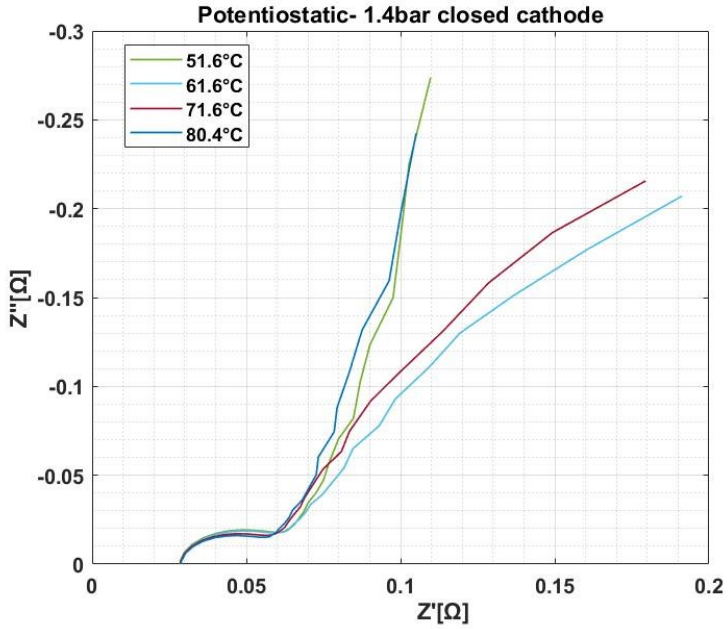

Figure 6.57 Nyquist plot under voltage control at 1.4barg closed cathode with different temperatures.

Figure 6.58 and Figure 6.59 show impedance spectra obtained with open and closed cathode during galvanostatic tests. As before, the high frequency arc is not much affected by temperature in both cathode configurations, whereas the second incomplete arc shows a different behaviour: with open cathode no relevant changes are seen but with closed it bends down to the real axis as temperature decreases. The EIS data at low frequency obtained with closed cathode at 51°C are in contrast with the trend shown by the other impedance spectra of the same series.

The imaginary part of all HF arcs reaches a maximum at ω_{max} equal to 158.5 Hz for open cathode except for 41°C characterized by ω_{max} equal to 126.2 Hz.; for closed cathode is 126.2 Hz at 71°C and 601°C, whereas 80°C and 51°C have ω_{max} equal to 158.9 Hz.

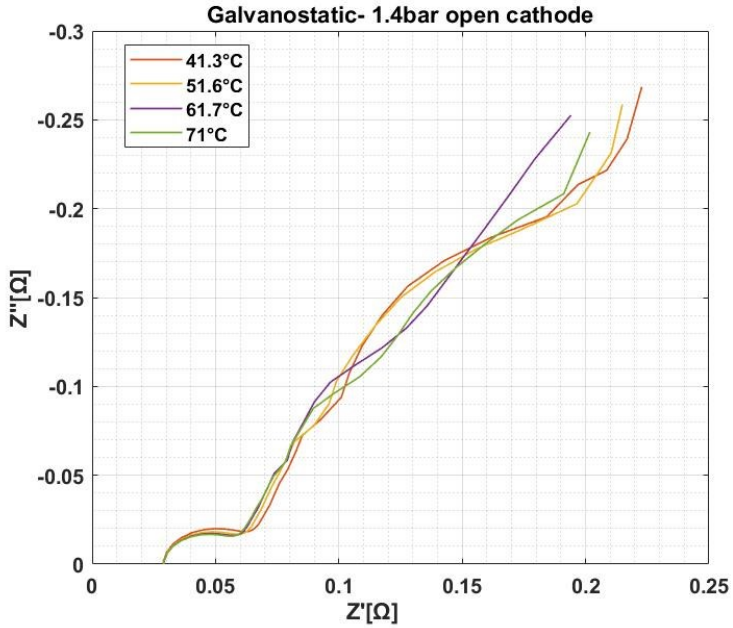

Figure 6.58 Nyquist plot under current control at 1.4barg open cathode with different temperatures.

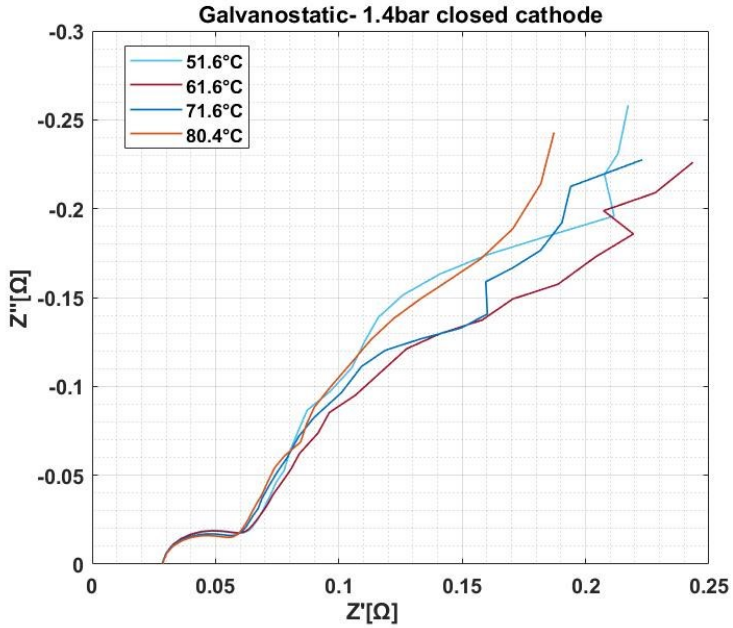

Figure 6.59 Nyquist plot under current control at 1.4barg closed cathode with different temperatures.

Results gained from potentiostatic tests are discussed. It is possible to analyse the high frequency region- represented by the semicircle- by measuring the ohmic resistance, intercept of the high frequency arc with the real axes, and the charge transfer resistance, represented by the intercept at mid frequency.

Considering the effect of temperature, it is observed a clear dependence on T of all parameters. It is noticed a higher dependence during closed cathode whereas during open cathode the variation in the parameters values is negligible. In particular, open cathode shows an enhancement of charge transfer resistance (increment from 0.736 to 0.925 Ωcm^2) and capacitance (from 0.035 to 0.018 F), whereas the ohmic resistance is almost constant. On the other hand, closed cathode in the 51-71°C range shows a worsening of charge transfer resistance (increment from 0.700 to 0.887 Ωcm^2) and capacitance (from 0.0360 to 0.0208 F), whereas the ohmic resistance improves from 0.800 to 0.588 Ωcm^2. Data at 80°C of closed cathode shows an opposite trend, so worsening of the ohmic resistance – maybe due to dehydration effects- and improvement of capacitance and charge transfer resistance.

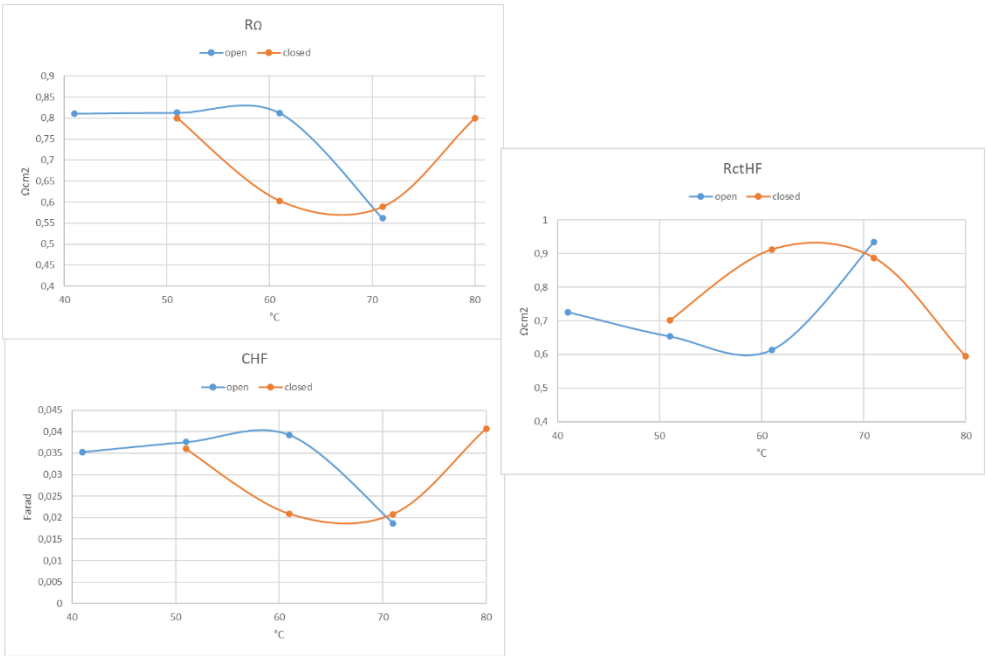

Figure 6.60 Comparison between open and closed cathode of the HF parameters.

In conclusion, open cathode is less affected by the increase of temperature- in the range from 40 to 60°C -with respect to the closed cathode configuration which benefits from an increase of temperature. Making a comparison between

open and closed cathode configuration at constant temperature in the range 40-60°C, EIS parameters obtained during the open cathode test have better trend although it is characterized by higher pressure if compared at constant temperature. A possible reason is a better thermal stabilization of the system (temperature at the heater has less oscillations). On the other hand, closed cathode seems to perform better at higher temperature (>70°C)- lower value of the charge transfer resistance and capacitance- but still the ohmic resistance is not improving because too higher T cause dehydration effects.

6.1.2.2. Effect of flow rate

Tests performed with open/closed cathode with different mass flow rates. The objective is to investigate the influence of the cathode configuration on the cell performance. The only variable changed between open and closed cathode configuration is the mass flow rate; this is done to keep the mass flow rate per channel at the anode side constant between the two configurations. Moreover, two modalities are used to vary the mass flow rate: variation of the pump displacement chamber and usage of the needle valve. On the bases of these two possibilities, two series of experiments are identified:

First series with recirculating pump

1) test executed at 60°C
    - Open, 60% pump- 2,47 barg @anode & 2,42 barg @cathode
    - Closed, 10% pump- 1,73 barg @anode & 1,35 barg @cathode
2) test executed at 80°C
    - Open, 60% pump- 2,36 barg @anode & 2,32 barg @cathode
    - Closed, 10% pump- 1,70 barg @anode & 1,30 barg @cathode

Second series with needle valve

1) test executed at 60°C
    - Open, 200ml/min, 1,65 barg @anode & 1,64 barg @cathode
    - Closed, 100ml/min, 1,56 barg @anode & 1,30 barg @cathode
2) test executed at 70° C
    - Open, 200ml/min, 1,65 barg @anode & 1,64 barg @cathode
    - Closed, 100ml/min, 1,67 barg @anode & 1,36 barg @cathode

3) test executed at 80°C

- Open, 200ml/min, 1,66 barg @anode & 1,67 barg @cathode
- Closed, 100ml/min, 1,59 barg @anode & 1,26 barg @cathode

The electrochemical characterization is performed with polarization curves and EIS measurements. Polarization curves are carried out by imposing the current and measuring the voltage. Two types of EIS tests have been used:

- Potentiostatic test, performed at 0 DC V vs Reference by varying the frequency from 100 kHz to 0,001 Hz in single sine mode and using a sinusoidal excitation signal of 10 mV root mean square (rms)
- Galvanostatic test, performed at 0 DC mA by varying the frequency from 200 kHz to 0,002 Hz in single sine mode and using a sinusoidal excitation signal of 1000 mA root mean square (rms).

For the 1st SERIES:

6.1.2.2.1. Data quality assessment for tests performed at 60°C and 80°C

The KK validation shows impedance spectra of both EIS experiments affected by time variance behaviour, so high residuals values at almost all frequencies. By visual inspection a difference between potentiostatic and galvanostatic modes is observed in both Nyquist and Bode plots. Galvanostatic has produced impedance spectra with three-time constants, whether the potentiostatic has two. In any case, the ECM used to fit is LR(QR)(QR) because the LF range is affected by noise.

6.1.2.2.2. Modelling

1. 60°C open/closed cathode

Figure 6.61 shows Nyquist plots of EIS data measured at 0V. It is possible to notice the presence of an arc at high frequency, and an incomplete second arc in the mid frequency region.

In the closed cathode configuration, it is observed a general increase of HF arc, and a decrease of the second arc; the trend is opposite in case of open cathode. For detailed values refer to Table 0.6 and Table 0.7 in appendix.

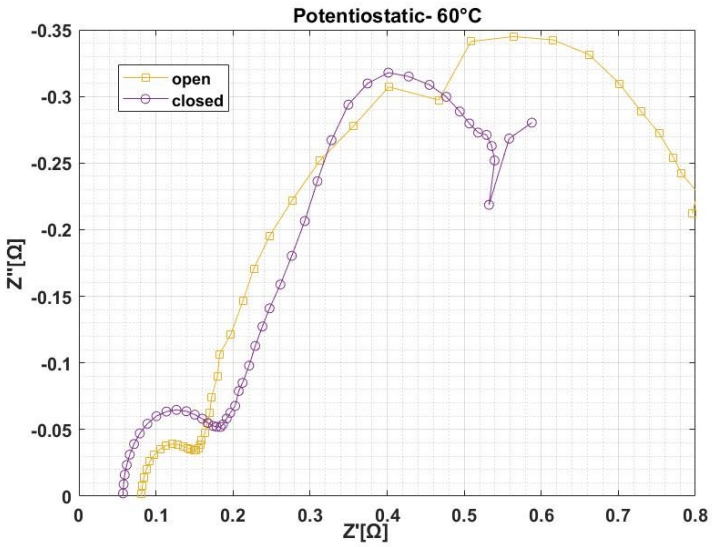

Figure 6.61 Nyquist plot under voltage control at 60°C- open vs closed cathode.

Figure 6.62 shows Nyquist plots of EIS data measured at 0 mA, corresponding to the open circuit voltage of the cell. It is observed the presence of an arc at high frequency, and a second arc in the mid-low frequency region affected by noise. The latter seems made of two merged semicircles. The comparison between open and closed cathode shows that the mid frequency arc is larger in case of open cathode, same consideration for the low frequency region. Instead, the HF arc intercept with the real axis is higher in case of closed cathode.

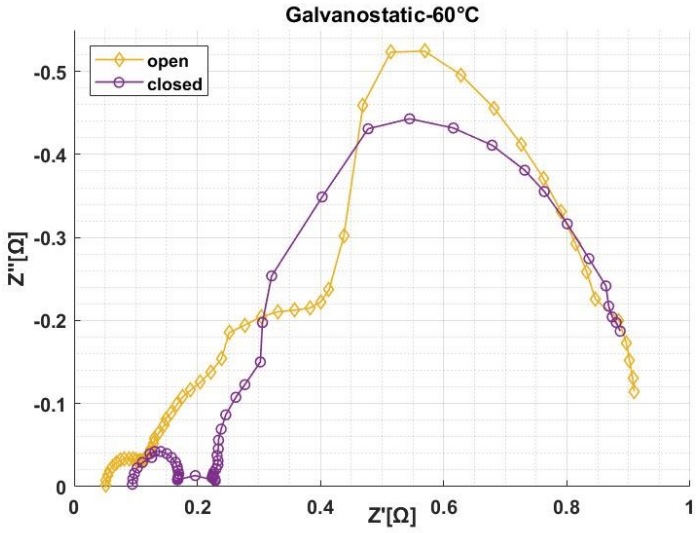

Figure 6.62 Nyquist plot under current control at 60°C- open vs closed cathode.

2. 80°C open/closed cathode

Figure 6.63 shows Nyquist plots of EIS data measured at 0V. It is possible to notice the presence of an arc at high frequency, and an incomplete second arc in the mid frequency region affected by noise. In the closed cathode configuration, it is observed a general increase of HF arc, and a decrease of the second arc; the trend is opposite in case of open cathode. For detailed values refer to Table 0.8 in appendix.

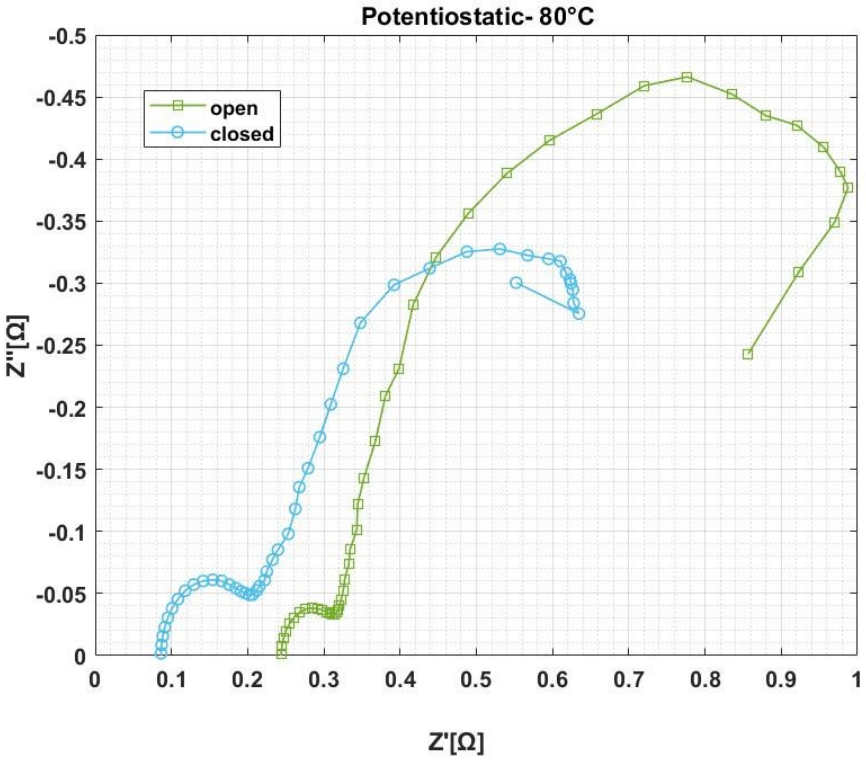

Figure 6.63 Nyquist plot under voltage control at 80°C- open vs closed cathode.

Figure 6.64 shows Nyquist plots of EIS data measured at 0 mA, corresponding to the open circuit voltage of the cell. It is observed the presence of an arc at high frequency, and a second arc in the mid-low frequency region made of two merged semicircles. For detailed values refer to Table 0.9 in appendix.

The comparison between open and closed cathode shows that the mid frequency arc is smaller in case of open cathode, same consideration for the low frequency region. Instead, the HF arc intercept with the real axis is lower in case of closed cathode.

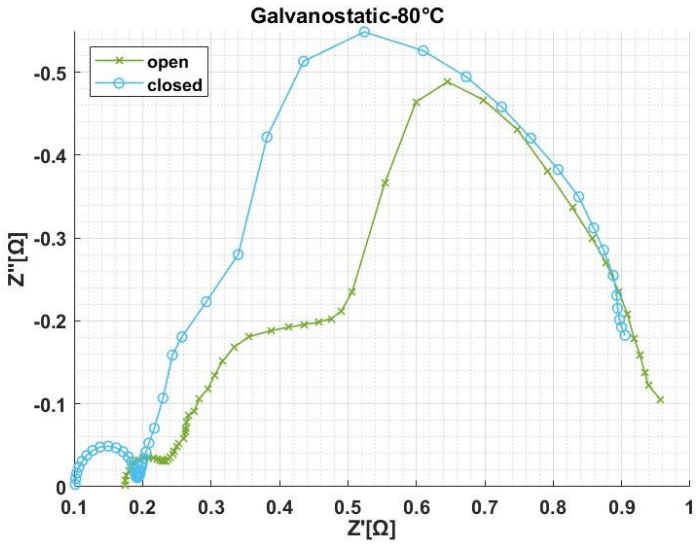

Figure 6.64 Nyquist plot under current control at 80°C- open vs closed cathode.

Table 6.1 Pressure and temperature comparison between open and closed cathode

Average value	**60°C**	**80°C**
T cell open cathode [°C]	61.63	79.47
T cell closed cathode [°C]	61.64	79.64
T fluid open cathode [°C]	58.15	77.37
T fluid closed cathode [°C]	63.14	82.05
Fluid pressure at heater open cathode [bar]	3.51	3.30
Fluid pressure at heater closed cathode [bar]	2.01	1.98

6.1.2.2.3. model validation with iV curves

Considering the test performed at 60°C the presence of noise in both EIS tests do not allow to quantify accurately the parameters gained from the fitting of the experimental data. Nevertheless, from galvanostatic test it seems that near the OCV closed cathode is performing better since it has a lower total polarization resistance- given by the difference between high intercept and low intercept with the real axis - even if the ohmic resistance is higher. The higher value of the ohmic

resistance can have role at higher current densities, where ohmic losses are dominant, determining a lower performance of the closed cathode.

The first observation does not find correspondence in the polarization curves where near the OCV iV curves overlap. Meanwhile higher voltage values at higher current densities are observed for closed cathode in the comparison between iV curves, hence this is in agreement with higher ohmic resistance of the closed cathode.

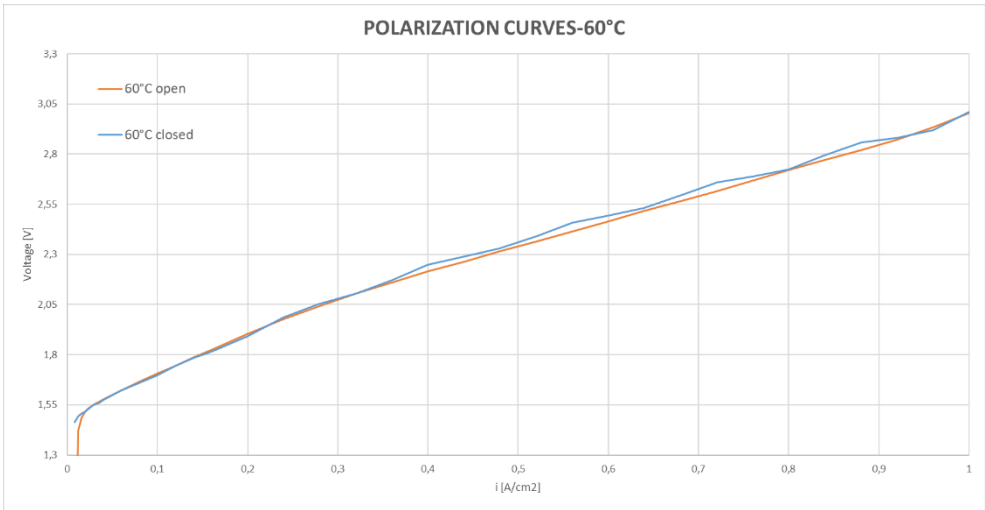

Figure 6.65 Polarization curves at 60°C- open vs closed cathode.

The comparison between the polarization curves at 60°C shows a better performance of the open cathode configuration since its curve is lower with respect to the closed cathode one.

The analysis shows that the cell temperature is the same during open and closed cathode (61.6°C), while fluid temperature and fluid pressure at the heater between open and closed cathode configuration are different. In particular, during open cathode experiment the fluid temperature is lower and pressure is higher compared to closed cathode.

EIS tests at 80°C have produced still low quality impedance spectra but a trend can be seen from galvanostatic results to check the consistency with the polarization curves near the OCV. The most meaningful parameter obtained qualitatively by visual inspection is the polarization resistance, which gives an insight of the activation losses within the cell. It is possible to say that the overall polarization resistance is unvaried between open and closed cathode; only ohmic resistance of the open is higher compared to that of the closed cathode. The higher

ohmic resistance with open cathode should determine lower performance at higher current densities, but this hypothesis is not in agreement with the findings of the polarization curves where it is generally observed a better performance of the open cathode configuration.

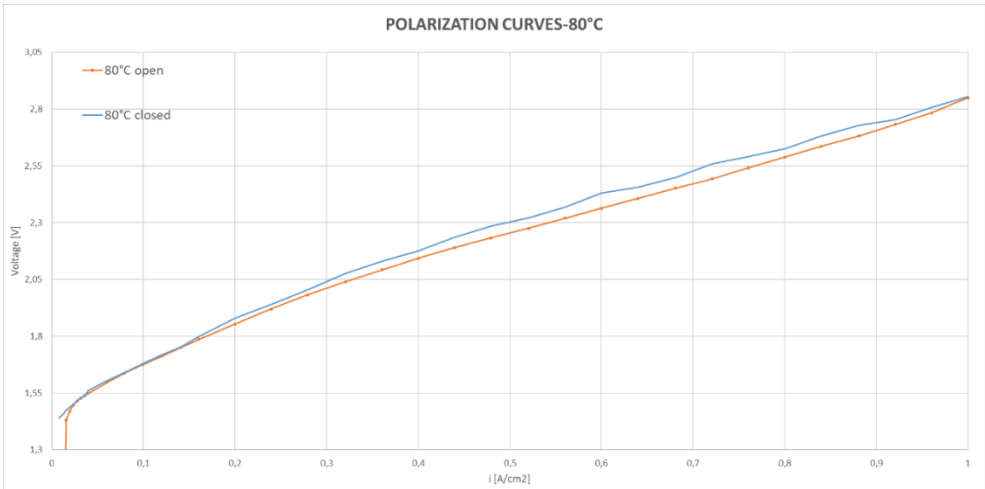

Figure 6.66 Polarization curves at 80°C- open vs closed cathode.

The analysis shows that the cell temperature is around 79,5-79,6°C, instead fluid temperature and fluid pressure at the heater between open and closed cathode configuration are different. In particular, during open cathode experiment the fluid temperature is lower and pressure is higher compared to closed cathode. Again, although the closed cathode has higher T and lower p it shows a lower performance.

For the 2nd SERIES:

6.1.2.2.4. Data quality assessment

The KK validation shows impedance spectra of both EIS experiments affected by time variance behaviour, so high residuals values, mainly larger at lower frequencies. By visual inspection a difference between potentiostatic and galvanostatic modes is observed in both Nyquist and Bode plots. As before, galvanostatic has produced impedance spectra with three-time constants, whether the potentiostatic is characterized by two time constants. In any case, the impedance spectra have poor quality especially at low frequency for both potentiostatic and galvanostatic modes, hence the ECM used to fit is LR(QR)(QR).

6.1.2.2.5. Modelling

1. 60°C open/closed cathode

Figure 6.66 shows Nyquist plots of EIS data measured at 0V. The shape of the impedance spectra changes between open and closed cathode. In the open cathode it is possible to notice the presence of an arc at high frequency, and a second arc in the mid-low frequency region. In the closed cathode configuration, there is a semicircle in the HF region followed by a straight line mostly affected by noise. For detailed values refer to Table Table 0.10 in appendix.

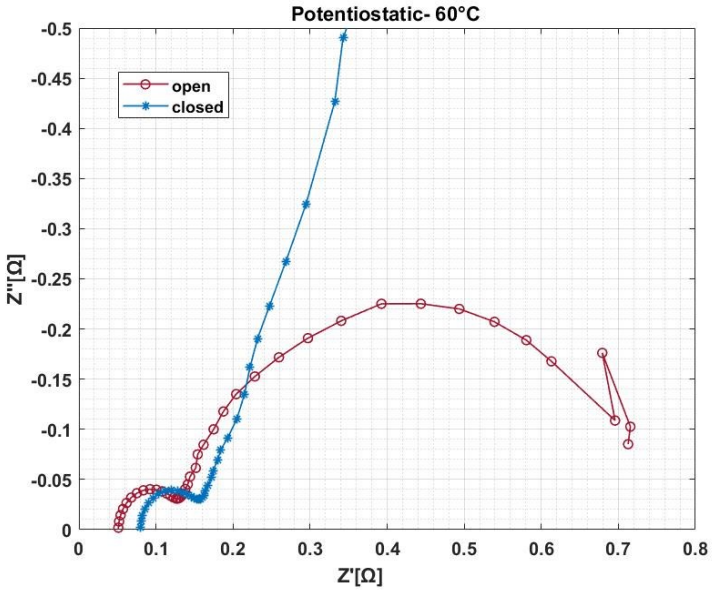

Figure 6.67 Nyquist plot under voltage control at 60°C- open vs closed cathode.

Figure 6.68 shows Nyquist plots of EIS data measured at 0 mA, corresponding to the open circuit voltage of the cell. It is observed the presence of an arc at high frequency, and a second arc- made of two merged semicircles- in the mid-low frequency region affected by noise.

The comparison between open and closed cathode shows that the high frequency arc is smaller in case of open cathode whereas the closed cathode has smaller mid-low frequency arc. For detailed values refer to Table 0.11 in appendix.

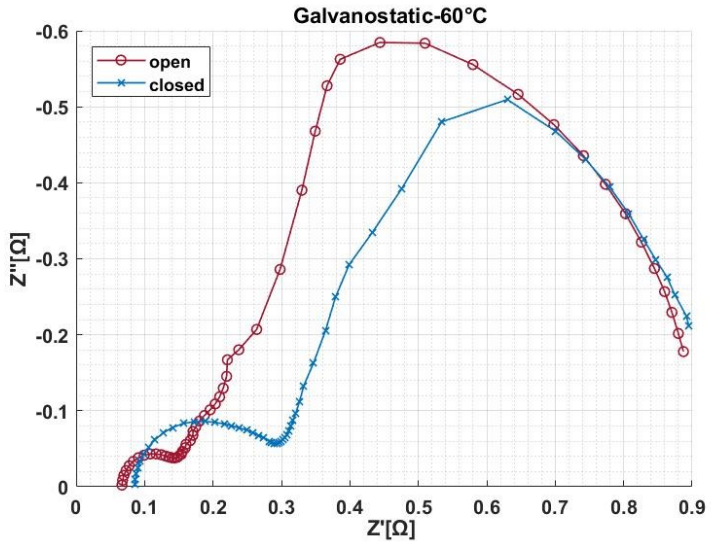

Figure 6.68 Nyquist plot under current control at 60°C- open vs closed cathode.

2. 70°C open/closed cathode

Figure 6.69 shows Nyquist plots of EIS data measured at 0V. The shape of the impedance spectra is similar for both open and closed cathode. It is possible to notice the presence of a small arc at high frequency, and a second incomplete arc in the mid-low frequency region. A lower intercept with the real axis at high frequency is observed for the closed cathode tests. For detailed values refer to Table 0.12 in appendix.

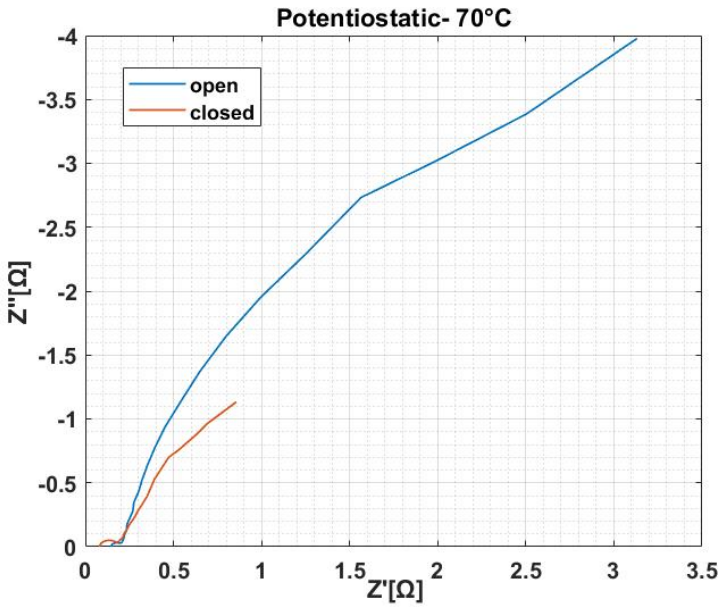

Figure 6.69 Nyquist plot under voltage control at 70°C- open vs closed cathode.

Figure 6.70 shows Nyquist plots of EIS data measured at 0 mA, corresponding to the open circuit voltage of the cell. It is observed the presence of an arc at high frequency, and a second arc in the mid-low frequency region affected by noise.

The comparison between open and closed cathode shows some differences. The impedance spectrum of open shows an incomplete semicircle in the md frequency region, which almost disappears in the closed cathode impedance spectrum. Moreover, the high frequency arc is smaller in case of open cathode whereas the closed cathode has smaller mid frequency arc. For detailed values refer to Table 0.13 in appendix.

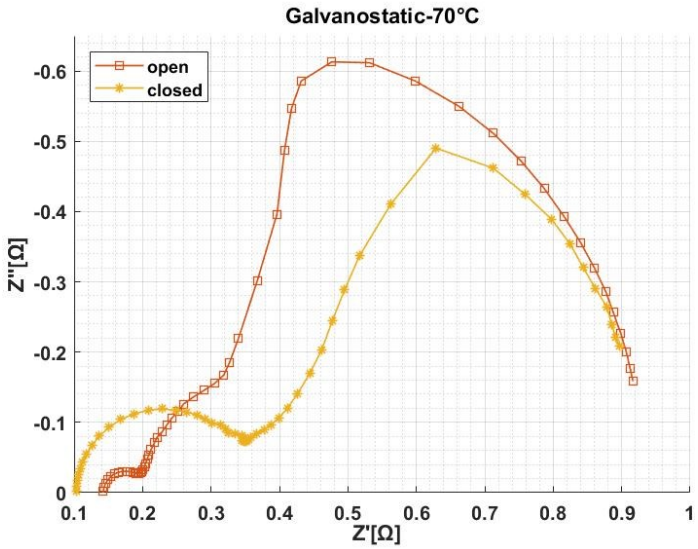

Figure 6.70 Nyquist plot under current control at 70°C- open vs closed cathode.

3. 80°C open/closed cathode

Figure 6.71 shows Nyquist plots of EIS data measured at 0V. The shape of the impedance spectra is similar for both open and closed cathode. It is possible to notice the presence of an arc at high frequency, and a second arc in the mid-low frequency region. The main difference occurs in the mid-low frequency region where the open shows a smaller arc with respect to that appearing in the closed cathode impedance. For detailed values refer to Table 0.14 in appendix.

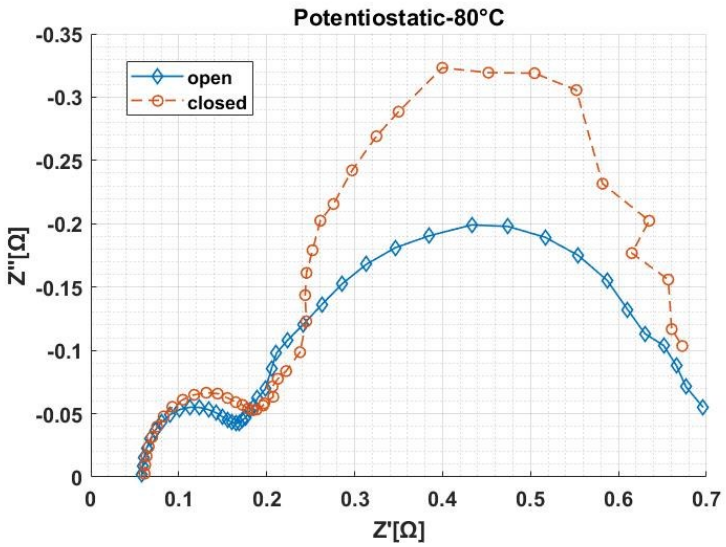

Figure 6.71 Nyquist plot under voltage control at 80°C- open vs closed cathode.

Figure 6.72 shows Nyquist plots of EIS data measured at 0 mA, corresponding to the open circuit voltage of the cell. It is observed the presence of an arc at high frequency, and a second arc in the mid-low frequency region affected by noise.

The comparison between open and closed cathode shows some differences. The impedance spectrum of open shows an incomplete and very small semicircle in the mid frequency region, which disappears in the closed cathode impedance spectrum. The high and low frequency arc do not show significant variations between the two cathode configurations. For detailed values refer to Table 0.15 in appendix.

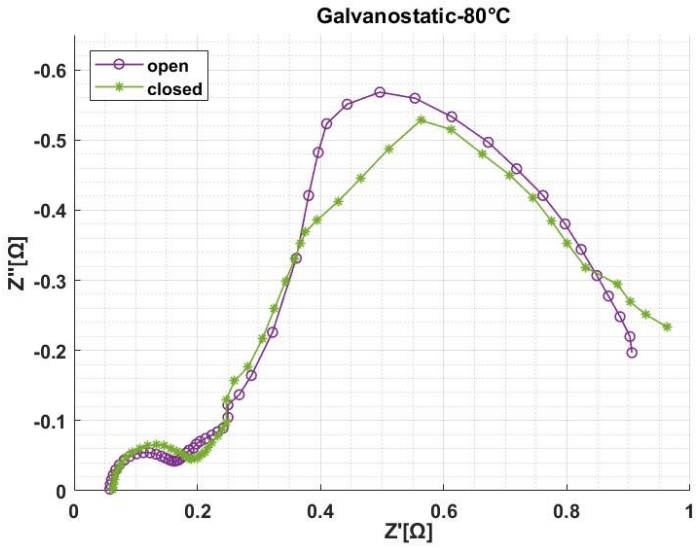

Figure 6.72 Nyquist plot under current control at 80°C- open vs closed cathode.

6.1.2.2.6. model validation with iV curves

Tests performed at 60°C and 70°C under current control show a similar behaviour, i.e the high frequency arc is smaller in case of open cathode whereas the closed cathode has smaller mid-low frequency arc. All EIS tests have shown poor quality in the overall frequency range, but it is possible a qualitative analysis of the impedance spectra gained under galvanostatic mode.

Galvanostatic tests at 60°C shows that closed cathode configuration has lower total polarization resistance; hence it may be assumed a better performance of closed cathode near the OCV. On the other hand, open cathode has lower ohmic resistance which may determine lower voltage value at higher current densities, but this assumption is not in accordance with the polarization results. The comparison between the polarization curves at 60°C shows a better performance of the closed cathode configuration since its curve is slightly lower with respect to the open cathode one. The analysis shows that the cell temperature and fluid pressure at the heater are unvaried –respectively 61,5-61,6°C and 1,99-1,89 barg- while fluid temperature between open and closed cathode configuration is different. In particular, during open cathode experiment the fluid temperature is lower compared to closed cathode.

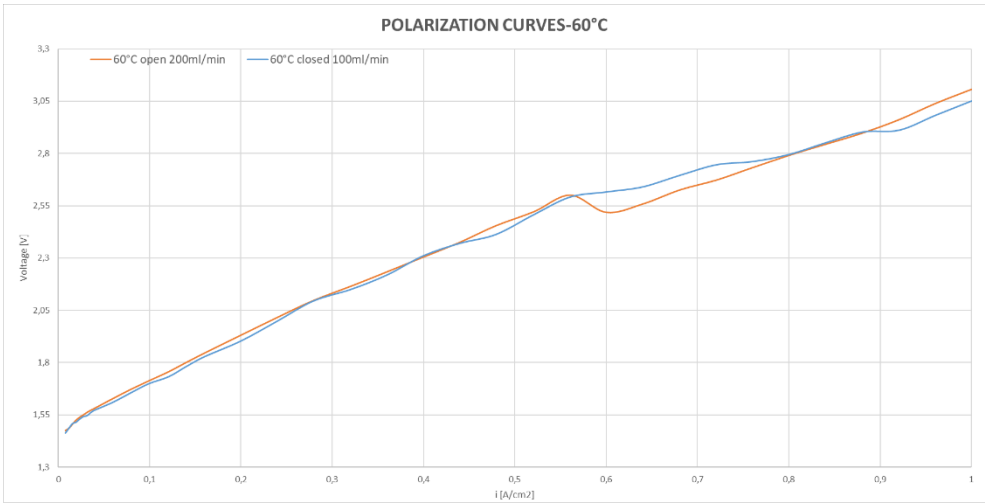

Figure 6.73 Polarization curves at 60°C- open vs closed cathode.

Galvanostatic tests at 70°C shows that both configurations have similar total polarization resistance. However, closed cathode has lower ohmic resistance so this suggests that it has better performance at high current density. The comparison between the polarization curves at 70°C seems to show an overlapping of the two curves. At high current density closed cathode has lower voltage values and hence this finding is in agreement with the previous hypothesis of lower ohmic resistance during closed cathode. The analysis shows that fluid pressure at the heater is around 2 barg, instead fluid temperature and cell temperature between open and closed cathode configuration are different. In particular, during the open cathode experiment both temperatures are lower compared to closed cathode. The higher temperature of the cell during closed cathode with almost unvaried pressure in both sides of the cell for open/closed cathode configuration may be considered the reason of the better performance with respect to the open cathode at higher current densities.

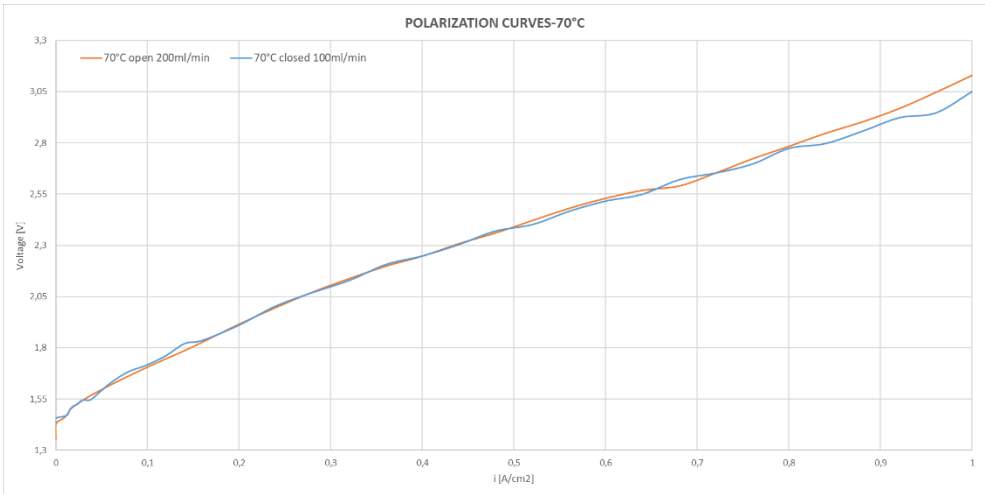

Figure 6.74 Polarization curves at 70°C- open vs closed cathode.

Tests performed at 80°C under current control show that open and closed cathode have similar impedance spectra but the comparison between the polarization curves at 80°C shows generally a better performance of the open cathode configuration since its curve is lower with respect to the closed cathode one. Moreover, it is found that open cathode has a slightly lower value of the ohmic resistance. The analysis shows that the fluid pressure at the heater is around 2 barg, instead fluid temperature and cell temperature between open and closed cathode configuration are different. During the open cathode experiment both temperatures are lower compared to closed cathode.

Table 6.2 Pressure and temperature comparison between open and closed cathode

Average value	**60°C**	**70°C**	**80°C**
T cell open cathode [°C]	61,54	69,36	78,06
T cell closed cathode [°C]	61,62	71,37	79,49
T fluid open cathode [°C]	58,50	67,79	77,75
T fluid closed cathode [°C]	61,48	71,56	79,44
Fluid pressure at heater open cathode [bar]	1,99	2,02	2,04
Fluid pressure at heater closed cathode [bar]	1,89	2,01	1,99

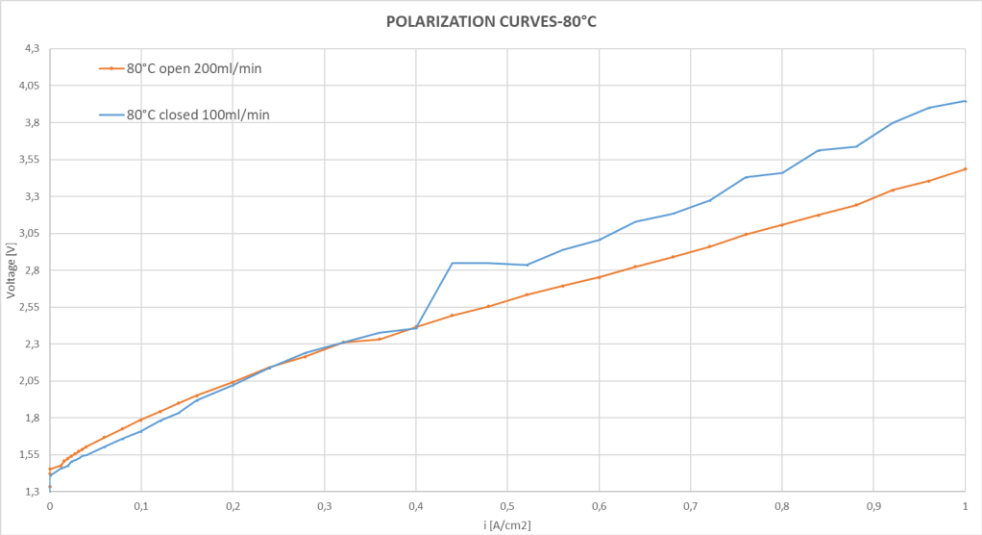

Figure 6.75 Polarization curves at 80°C- open vs closed cathode.

6.2. Degradation test

6.2.1. Basics

PEMWE, as seen, represents the best technology in terms of pure Hydrogen produced. In the next years, it will improve in order to increase the production efficiency and to reduce the disadvantages of this technology. In the Table 6.3 the main characteristics of state-of-the-art are reported. [20] [51]

Table 6.3 Overview of the characteristics regarding PEMWE technology

State-of-the-art Materials & Operating Conditions		
Materials	Membrane	Nafion ® 115/117
	Anode CL	IrO2 / Ir-Ru Ox
	Cathode CL	Pt/C
	Anode GDL	Ti / SS grids
	Cathode GDL	Porous Carbon
	Anode BP	Ti / Ti-coated SS
	Cathode BP	Graphite
	End Plates	SS / Ti

Operating conditions	Temperature [C]	30-80
	Pressure [bar]	1 - 300
	Current density [A/cm2]	0 - 2
	Voltage [V]	1.8 - 2.2
	Efficiency [%]	80 - 90

The relevant improvement regarding PEMWE is the reduction of the cost, since today represent the main disadvantage in to use this technology. However, in order to become an affordable technology, some improvement on used materials will be done. [51]

6.2.1.1. degradation mechanisms

At the present durability, cost and reliability are the main concepts connected to operating conditions of PEMWE. [49] [149] In this sense, lifetime is a key factor to arrive to the commercialization in stationary and mobile application. [150] There are different issues that affect the performances and long-term functioning of the cell. Due to the fact that PEMWE and Fuel Cell (FC) are similar, equal methods are used to characterize these issues. The main issues that can degrade the entire cell are corrosion and contamination. Other issues can occur to Membrane, Catalyst Layer, and BP. [150] [151]

6.2.1.2. Membrane degradation

Membrane is known as the weakest component of the PEMWE considering long term performance. Differently than PEM Fuel Cell (PEMFC), it is always hydrated due to the fact that water is used for electrolysis reaction. [49] Generally, Membrane can be degraded mechanically, chemically, and thermally. The mechanical degradation can be caused by high value of gas pressure or by high compression pressure applied to entire structure of the cell. It was demonstrated that an increase of torque through bolts permits to reduce the voltage and the resistance. In this sense, the performance results better. [109] However, a huge application of pressure to entire system may lead to a mechanical failure of the cell. In this context, it was seen that formation of pinhole can occur in the membrane. These can initiate the propagation of cracks with the reduction of lifetime. High performance are reached when high pressure and high temperature are used. The high pressure can be reached with the circulation of pumped water that can take,

in case of non-uniform circulation, the starvation phenomena with consequent failure of system. [110] Thermal degradation, instead, is due to operating temperature. As said, high temperature permits to reach good performances if compared to low temperature. Nevertheless, if it operates at too low or too high temperature can suffer thermal stresses that affect the membrane structure. In particular, some test are conducted on a membrane and the results showed variations in hydrogen crossover and area resistance. [49] [55] Chemical degradation is, instead, due to a gradual decomposition of polymer constituent the membrane due to contamination of some impurities and other materials contained by water.[111] In feed water the Fe^{2+} ions can be dissolved causing a decrease of proton conductivity and increase of ohmic losses. It results into worst performance of the cell. [33] [143] Another type of contamination can be due to the to dissolution of platinum ions of electrocatalyst into membrane.[152]

During the operation the Oxygen produced in the anode side can pass the membrane going to to the cathode and forming the Hydrogen Peroxide. When these meet the metals ions contained by water, a particular case occurs. It is the Fenton's reaction mechanisms, in which in presence of ferrous ions, like Fe^{2+} and Fe^{3+}, the Hydrogen Peroxide is decomposed into Hydroxil radicals. These tend to attack the membrane with a consequent release of Fluoride ions. The way to measure the chemical degradation consist into measure the fluoride ion content into water exhausted and in particular, the membrane thickness. In fact, Fenton's mechanism tends to accelerate the membrane thinning. The higher the degradation the thinner is the membrane. [49] [153]

6.2.1.3. Catalyst degradation

The membrane, as said, must be covered by precious metals used as catalyst layers in order to increase the rate of reaction. However, these materials operate in harsh conditions and so they can fail, reducing of a lot the durability of cell. There are many effects that affects the durability. In particular, catalyst dissolution, catalyst agglomeration and passivation. These results in a decrease of active surface area that induces to have worst performances. [49]The catalyst dissolution depends mainly on the acid environment. In the case of anode side, it depends on the oxidation of Ir. However, it occurs mainly at high current density or in cyclic load. The dissolution can create serious problems like the reduction of electrochemical surface area (ECSA) and the diffusion of Ir inside the membrane. [133] In cathode side, instead, Pt is more stable than Ir and so it is able to resist to higher value of voltage. Although, after 5500 h of operation, it was demonstrated that Pt ions was

dissolved into membrane, following the dissolution phenomena. In this context, the migration of Pt tends to decrease its activity and anode catalyst surface was blocked from the Pt deposition. [49]Catalyst agglomeration is caused by an increase in size of particles that results in a reduction of ECSA. The agglomeration of catalyst particles tends to deactivate the anode side but observing the system after the operation, no variation in electronic conductivity are found. [133] In this sense, the main contributor of agglomeration is the ionomer loss. Increasing the voltage a degradation of ionomer occurs with a disintegration of catalyst layer.[154]

Cationic contaminations originating from the feed water or cell components can occupy ion exchange sites of the ionomer in the catalyst layer, resulting in an increase of the charge transfer resistance. [49]A reduced activity due to a contamination of the anode with titanium species is observed. [142] Passivation occurs to anode support, and it is also a cause of catalyst layer degradation. It is due to oxidation of metal support, which can block current flow by forming a non-conductive or semiconductive oxide layer. The surface oxidation between the anode support and the interconnect would increase the contact resistance, with consequent increasing of cell overvoltage. [155] In case of IrO2, passivation becomes faster at a higher current density. Additionally, the impurities produced by different degradation phenomena can increase passivation or arriving to destruction of the support. [49]

6.2.1.4. Bipolar plate degradation

One of main causes of cell degradation is corrosion. It can occur in different part of PEMWE cell, in particular Electrocatalyst layer, GDLs and BPs. [156] The BPs are the most influenced in terms of corrosion due to the fact that are made mainly by stainless-steel and so, in them a resistive layer on the surface can appear that can increase the ohmic resistance and reduce the performance. [55] The most used material for BPs is titanium. However, different problems can affect this material. In fact, hydrogen peroxide, that is responsible for membrane degradation, is also able to attack titanium chemically with the formation of an oxide layer on the metal surface and releasing titanium ions. It suffers the Hydrogen, which can form a mixture that can take to embrittlement of material with consequent risk of cracks. The embrittlement occurs mainly at higher temperature, since the formation of hydrides, like TiH2, can happen. Titanium of BPs has the risk to be weakened due to hydride formation. [49] It was demonstrated that the surface of the cathode BP degrades more than the anode one after 1000 h test due to H2 embrittlement.

However, if passivation occurs, an oxide films on the surface is formed that acts as a barrier to hydrogen penetration, and so the phenomena occur very slowly at temperature below 80°C. [157] Due to the fact that it can be corroded in acid environment, other materials were studied to substitute this one. Stainless-steel is the alternative material to substitute titanium, but obviously this one suffers the corrosion at high potential in anode side. [49] To avoid this problem, stainless-steel can be coated with titanium or platinum. [158] Furthermore, a PEMWE stack is tested considering stainless-steel BPs coated with Ti and Pt/Ti. They demonstrated that degradation was reduced after 1000 h operation. [49]

6.2.1.5. Voltage Losses

The previously degradation mechanisms have a direct impact on the cell voltage. To understand the overall degradation over time of PEMWE cell, the increase in voltage is considered. So, a review over the available literature on long-term voltage degradation can be used as starting point to evaluate the crucial parameters influencing the degradation. [159] In this sense, the main literature is reported in Table 6.4.

Table 6.4 Table of different degradation rate

Membrane	**Anode Catalyst Layer**	**Cathode Catalyst Layer**	**Area [cm2]**	**Degradation Rate [µV/h]**	**T [C]**	**I [A/cm2]**	**t [h]**	**Reference**
N117	1.99 mg/cm2 IrO2, Ti	1.31 mg/cm2 Pt black, SGL-24BC	25	5.2	60	0.2 − 1	1000	[160]
N117	1.94 mg/cm2 IrO2, Ti	1.19 mg/cm2 Pt black, SGL-24BC	25	6.2	80	0.2 − 1	1000	[160]
N115	2.5 mg/cm2 Pt unsupported, 0.58mm Ti	2.5 mg/cm2 Pt/Vulcan, 0.95mm Ti	7	92.5	90	0 – 1	4000	[152]
N117	2.25 mg/cm2 IrO2, 1.3mm Ti	0.8 mg/cm2 Pt/C, 2 x TGP-H 120	17.64	194	80	2	1009	[142]
N117	2.25 mg/cm2 IrO2, 1.3mm Pt-coated Ti	0.8 mg/cm2 Pt/C, 2 x TGP-H 120	17.64	12	80	2	350	[142]

N117	2.2 mg/cm2 IrO2, 1.5mm Pt-coated Ti	0.8 mg/cm2 Pt/C, TGP-H120 350μm	17.64	63	80	≥2.5	2000	[161]
N117	2.2 mg/cm2 IrO2, 1.5mm Pt-coated Ti	0.8 mg/cm2 Pt/C, TGP-H120 350μm	17.64	6	80	1 – 2	2000	[161]
N117	2.2 mg/cm2 IrO2, 1.5mm Pt-coated Ti	0.8 mg/cm2 Pt/C, TGP-H120 350μm	17.64	63	80	1 - ≥2.5	2000	[161]
N117	2.25 mg/cm2 IrO2, 1.3mm Ti	0.8 mg/cm2 Pt/C, 2 x TGP-H 120	17.64	0	80	1	1009	[162]
N117	2.25 mg/cm2 IrO2, 1.3mm Ti	0.8 mg/cm2 Pt/C, 2 x TGP-H 120	17.64	65	80	1 – 2	1009	[162]
N117	2.25 mg/cm2 IrO2, 1.3mm Ti	0.8 mg/cm2 Pt/C, 2 x TGP-H 120	17.64	16	80	0 – 2	1009	[162]
N117	2.25 mg/cm2 IrO2, 1.3mm Ti	0.8 mg/cm2 Pt/C, 2 x TGP-H 120	17.64	50	80	0 – 2	1009	[162]
N117	2.78 mg/cm2 Ir, IrO2, 350μm Ti	0.5 mg/cm2 Pt/C, SGL-35DC	2.89	73.6	60	1.5	500	[163] [164]
N115	2.39 mg/cm2 IrO2, 1mm Ti	0.86 mg/cm2 Pt/C, SGL-28BC	25	267	80	2	500	[163] [164]
N115	2.57 mg/cm2 IrO2, 1mm Ti	1.08 mg/cm2 Pt/C, SGL-28BC	25	17	80	0 – 2	500	[163] [164]

As it is possible to see, the voltage degradation rate is dependent on the reference current point. The majority of experiments are conducted at 80◦C. The experiments were performed with different operating conditions. The main condition in which the tests were conducted, was constant current (cc). It means that a certain value of current is fixed and the experiments are performed for a fixed time. However, cycling (cyc) is also another procedure that can be used to evaluate the degradation rate. It consists into applying a cyclic current value that goes from a minimum to a maximum for a certain period of time. In this sense, Rakousky et al. carried the tests both in cc and cyc, and the results are different. From the first a value of 0 μV/h was obtained, while from the second different values was

obtained. This behaviour is due to the fact that cyc test time is different and so, the results were different one from the other. [162] Other tests were carried from the same author in cc condition. However, in this case, the current density was higher than the first tests and fixed at 2 A/cm2. The results showed that degradation rate at higher current density increases of a lot arriving to values of 194 µV/h. [142] Tests both at cc and cyc, changing the values of current densities were performed. In cc tests, the current was fixed to 2.5-3 A/cm2 and the results displayed a value of degradation rate equal to 63 µV/h. Instead, in cyc tests the cyclic current was imposed between 1.0 and 2.0 A/cm2 and low degradation rate was obtained (6 µV/h), when the cyclic current was imposed between 1.0 and 2.5-3.0 A/cm2 the voltage degradation rate obtained was equal to cc test (63 µV/h). [161]

Frensch et al. tested two type of cell for 500 h with different materials for anode and cathode catalyst layers. The test was carried out considering both cc and cyc condition. The first was tested with a fixed current density of 1.5 A/cm2, while the second one was tested with a fixed current density of 2 A/cm2. The results, as expected, showed a higher value of degradation rate in the second case (267 µV/h) rather than the first one (73.6 µV/h). Instead, cyc test was conducted with a cyclic current imposed between 0 - 2 A/cm2 and the result showed lower value of degradation rate (17 µV/h). [163] [164] Considering these tests and Rakousky et al. tests, it is clear that main parameter influencing the degradation rate is the value of current density and not the type operation imposed in the system. In order to prevent the degradation mechanisms can be good to use some coatings able to reduce the effects and the degradation rate. Rakousky et al. demonstrated the effectiveness of Pt-coated on anode side. Thanks to this coating the degradation rate dropped from 194 µV/h to 12 µV/h in cc conditions. [142]

6.2.2. Accelerated tests

In this chapter the effect of designed accelerated degradation tests are compared with a constant load profile. The experiment with the constant load profile at 80°C and 1A/cm2 has been performed for more than 1000 hours and the results show a degradation rate of 12 µV/h. the next step was performing accelerated tests with frequent shutdowns to see the effect of these variations on the degradation rate and on the mechanisms that affect the cell.

6.2.2.1. Frequent shut downs / Dynamic profile

6.2.2.1.1. I

Degradation test performed at 60°C and 80°C, 0.5barg, closed cathode, 10% mass flow rate, constant current density of 0.5 A/cm2:

The degradation test is carried out at a constant current density of 0.5 A/cm^2 and the cell voltage increase over time is monitored. It consists of two series: the first series is performed at 60°C while the second at 80°C; both have an imposed gauge pressure of 0.5barg in the anode and cathode, and closed cathode configuration. During the first series EIS tests have been performed each twelve hours which means two tests each day (early morning and evening) whereas each 24 hours (one test each evening) while performing the second series of the degradation test. Two types of EIS tests have been used:

- Potentiostatic test, performed at 0 DC V by varying the frequency from 100 kHz to 0,001 Hz in single sine mode and using a sinusoidal excitation signal of 10mV root mean square (rms)
- Galvanostatic test, performed at 0 DC mA by varying the frequency from 200 kHz to 0,002 Hz in single sine mode and using a sinusoidal excitation signal of 1000 mA root mean square (rms).

It is expected to have an increase of the cell potential therefore a decrease of the cell performance.

6.2.2.1.1.1. Results of first series

After around 168 h of operation at 0.5 A/cm^2 the cell has shown a degradation rate of 1080 $\mu V/h$.

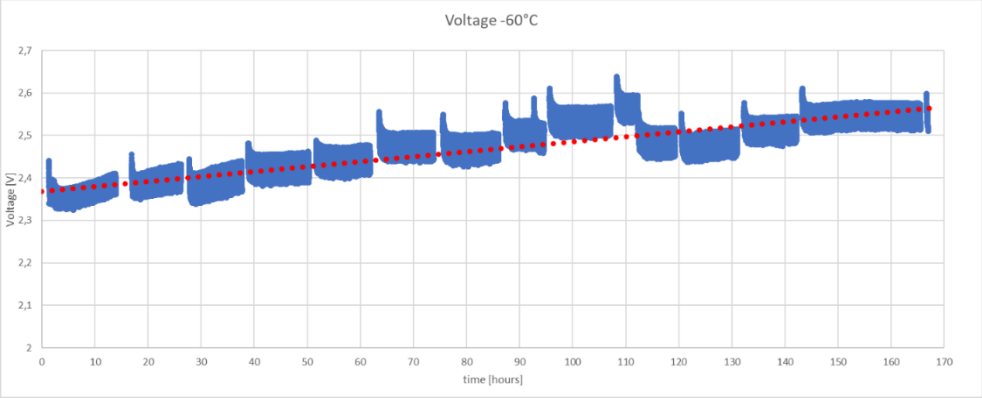

Figure 6.76 Voltage trend during the degradation test at 60°C.

The effective temperature during the experiment oscillates around 61°C whereas the real gauge pressure at the anode and cathode was 0,89 barg and 0,44 barg respectively.

The study shows an increase of pressure at the heater (from 1 to 1.3 barg), instead cell temperature remains in a range of values between 61-61,39°C and fluid temperature at the heater between 61,35-63,32°C.

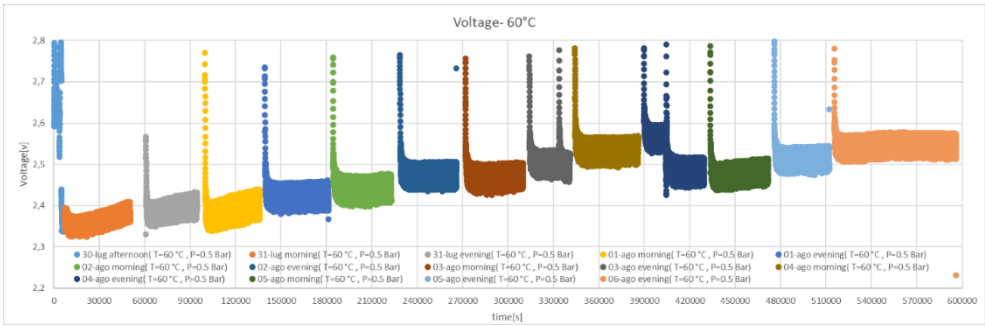

Figure 6.77 V-t

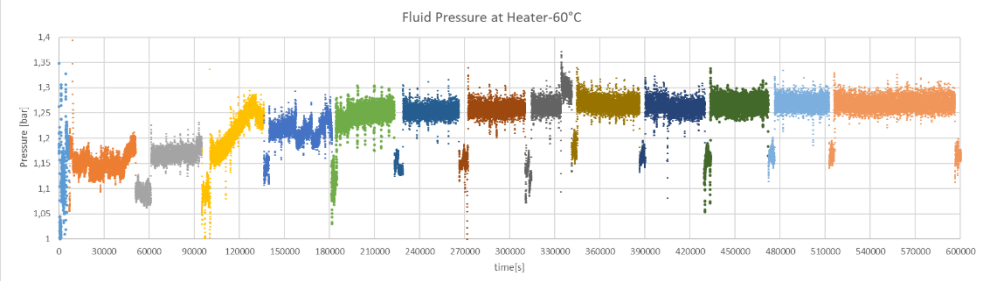

Figure 6.78 P-t

During the experiment there was a fault of the system on 3rd August afternoon that explains the anomaly on the cell voltage. Another remark should be done for the measurement done on 4th August. In the cell voltage graph a steep increase of the voltage is noticed, probably related to a decrease of the pressure at the heater, which also caused a decrease of cell temperature and fluid temperature.

Figure 6.79 and Figure 6.80 show the overall EIS measurements performed under voltage and current control during the degradation test at 60°C.

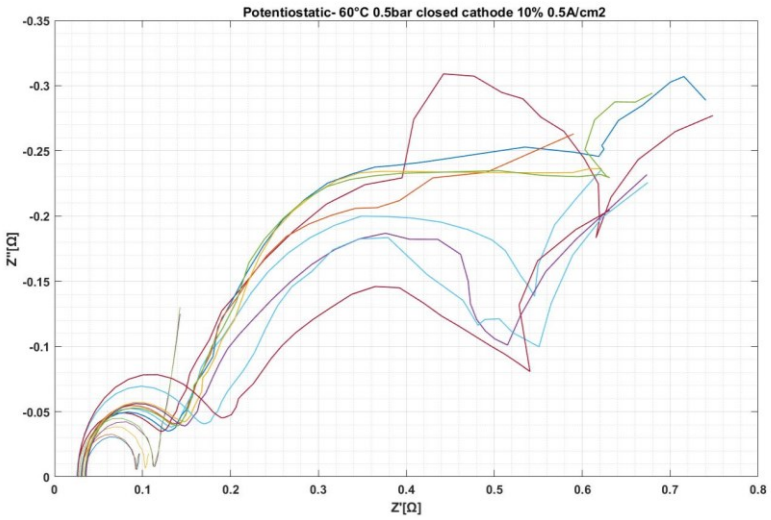

Figure 6.79 All EIS measurements with potentiostatic mode.

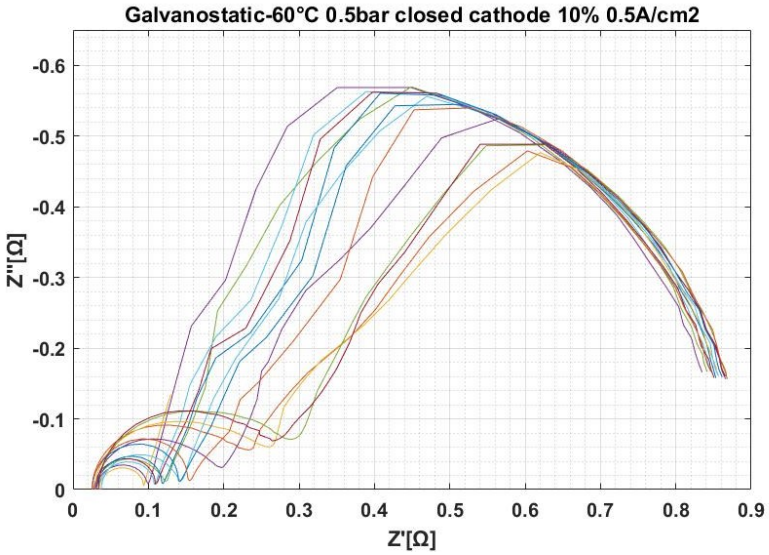

Figure 6.80 All EIS measurements with galvanostatic mode.

6.2.2.1.1.1.1. Data quality assessment

Validation through KK relations shows that impedance spectra obtained with both modes have similar residuals behaviour, i.e. low residuals of high frequency data and larger residuals as data are collected at lower frequencies. This is probably related to the drift of the system during the measurements at low frequency, which are more time consuming.

Impedance spectra showing very high residuals in all frequency range are discarded. These are 2nd, 4th and 5th morning for the potentiostatic and 2nd evening, 3rd 4th and 5th morning for the galvanostatic. Another EIS test not considered due to tripping of the system is the one performed on the 3rd evening.

By visual inspection of the Nyquist and Bode plots it is possible to say that EIS measurements with galvanostatic and potentiostatic mode have produced impedance spectra characterized by at least two-time constants. The low frequency impedance spectra in both modes- particularly in the potentiostatic mode- is affected by noise and/or time variance of the cell behaviour. Consequently, the impedance spectra obtained at lower frequencies is considered only from a qualitative point of view because its approximation to an ECM will probably produce a poor fit. Hence, the impedance spectra are fitted up to where data show a good trend, typically the first semicircle at HF and the initial part of the second semicircle appearing in the mid frequency range. Accordingly, the ECM used is LR(QR)(QR).

6.2.2.1.1.1.2. Modelling

Figure 142 shows Nyquist plots of EIS data measured at 0V, with invalid spectra removed. It is possible to notice the presence of an arc at high frequency, and an incomplete second arc in the mid frequency region. The low frequency data are affected by noise, but it is possible to notice a third semicircle. It is observed a general increase of HF arc, and a decrease of the second arc in favour of an increment of the LF arc even if it is affected by noise.

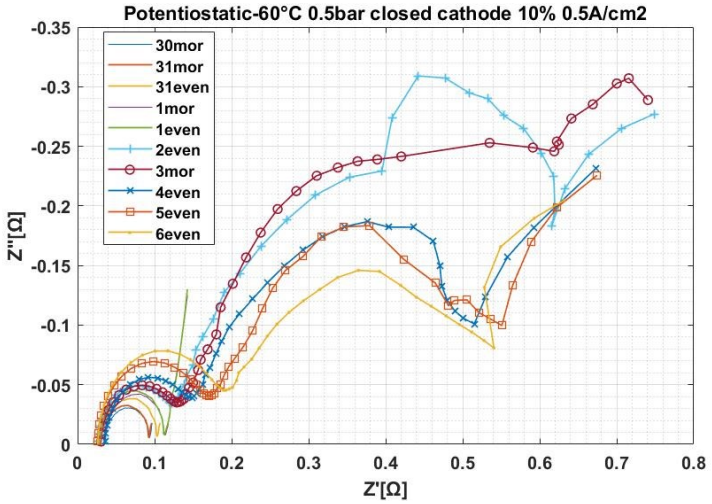

Figure 6.81 EIS measurements with potentiostatic mode- removed invalid impedance spectra.

Figure 143 shows Nyquist plots of EIS data measured at 0 mA, corresponding to the open circuit voltage of the cell, with invalid spectra removed. It is observed the presence of an arc at high frequency, and a second arc in the mid-low frequency region affected by noise. The latter seems to be made of two merged semicircles.

It seems that the HF arc increases but the second arc shows a decreasing behaviour.

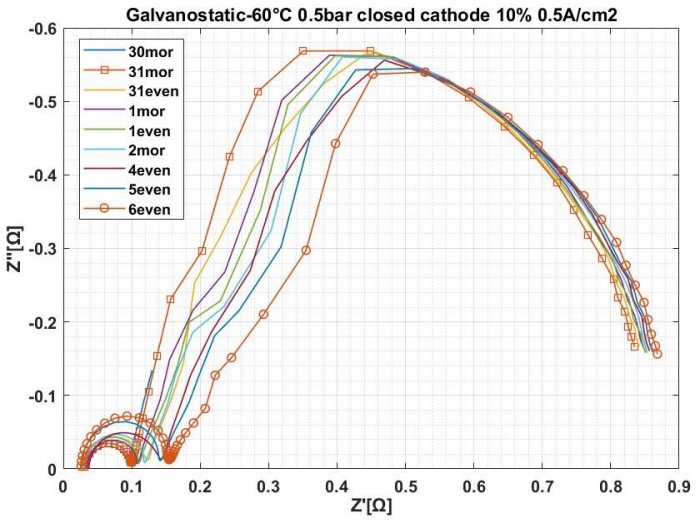

Figure 6.82 EIS measurements with galvanostatic mode- removed invalid impedance spectra.

6.2.2.1.1.1.3. Discussion

The analysis considers both EIS results gained from potentiostatic and galvanostatic modes. The trend of ohmic resistance, high frequency charge transfer resistance and capacitance is shown in:

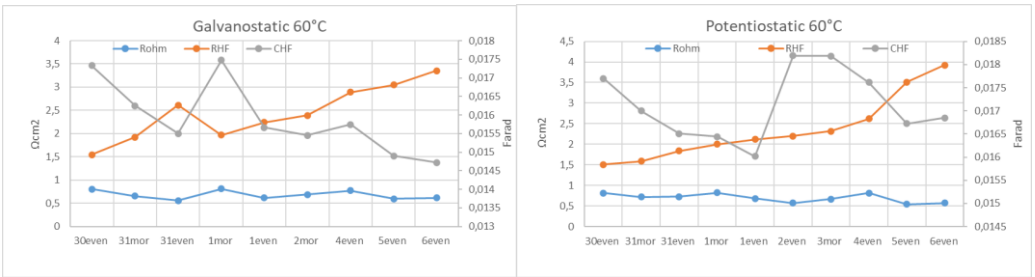

Figure 6.83

For both EIS tests the ohmic resistance seems to have a very slight decrease- although an oscillating behaviour between 0.818-0.542 Ωcm^2 and 0.0806- 0.593 Ωcm^2 is noticed for potentiostatic and galvanostatic respectively- whereas the charge transfer resistance increment is much more evident from 1.51 to 3.92 Ωcm^2 for potentiostatic and 1.55 to 3.35 Ωcm^2 for galvanostatic. The capacitance of the high frequency arc is characterized by a decreasing trend, at least during the first part of the test. Anyway, possible oscillations of the value may be related to time-variance of the system during the whole test but if the start and the end are considered, a decrease can be observed. It is not possible to say much about the low frequency arc due to the presence of noise, particularly in the impedance spectra obtained with voltage control. Hence, it is not possible to gain a quantitative and reliable measurement of the overall polarization resistance. On the other hand, some qualitative considerations can be done for the LF results gained with galvanostatic tests. The low frequency intercept with the real axis seems to show increasing values, hence it is suggested an increase of the total polarization resistance. As it is shown in the figure below, the trend of the total polarization resistance is mainly due to that of the charge transfer resistance of the HF arc.

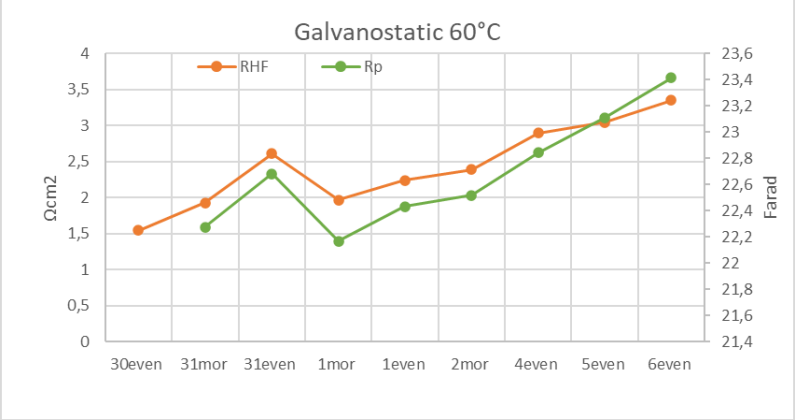

Figure 6.84 Galvanostatic test

Considering the trends of *Figures 144* and *145*, it is assumed that the HF feature is related to current constrictions, whereas the second incomplete semicircle and third one are respectively associated to charge transfer kinetics in the anode and mass transport limitations.

Concluding, the EIS results are in accordance with the increase of voltage during the degradation test. A probable reason of the ohmic resistance decrease (from 0.8 to 0.6 Ωcm^2) is the thinning of the membrane. It is suggested a loss of material from the aged membrane, which can also explain the decrease of the

capacitance at high frequency. A loss of materials or agglomeration of catalyst particles can cause an increase of the distributed contact resistances at the electrolyte/anode interface. This determines current constrictions and thus a lower performance of the cell. About the low frequency region, qualitatively it is possible to say that the larger arc in the galvanostatic tests or the increment of the third arc in the potentiostatic tests may be insights of the anode degradation. Large arcs are characterized by lower value of the capacitance, which in turn is linked to the number of active sites in the electrode surface. A low value of the capacitance demonstrates the occurrence of degradation processes in the catalyst layer. Instead, the presence of a third arc at low frequencies suggests important mass transport limitations, another sign of degradation.

6.2.2.1.1.2. Results second series

After around 135 h of operation at 0.5 A/cm^2 the cell has shown a degradation rate of about 720 $\mu V/h$.

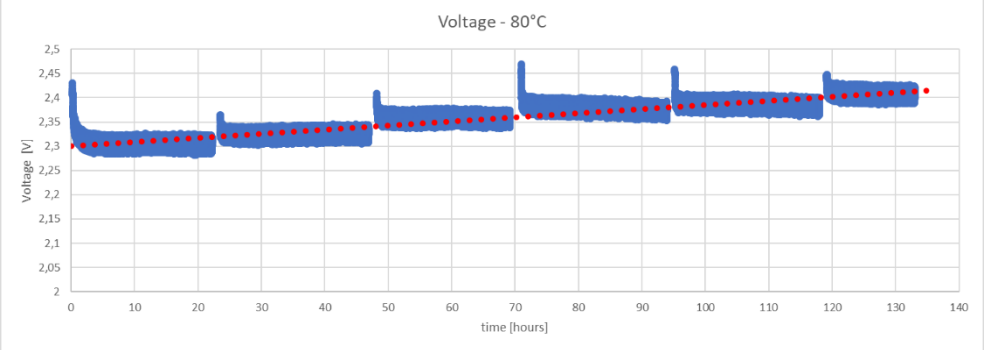

Figure 6.85 Voltage trend during the degradation test at 80°C.

The effective temperature during the experiment oscillates around 79°C whereas real gauge pressure at the anode and cathode was 0,91 barg and 0,44 barg respectively.

The study shows an increase of the cell potential, instead pressure at the heater remains in a range between 1,14 barg-1,29barg, temperature at the heater between 79,3°C -79,8°C and cell temperature remain 79,5°C -79,7°C.

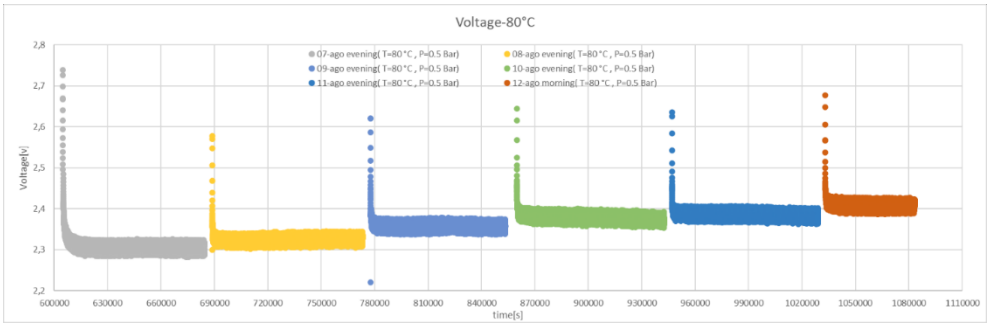

Figure 6.86 V-t

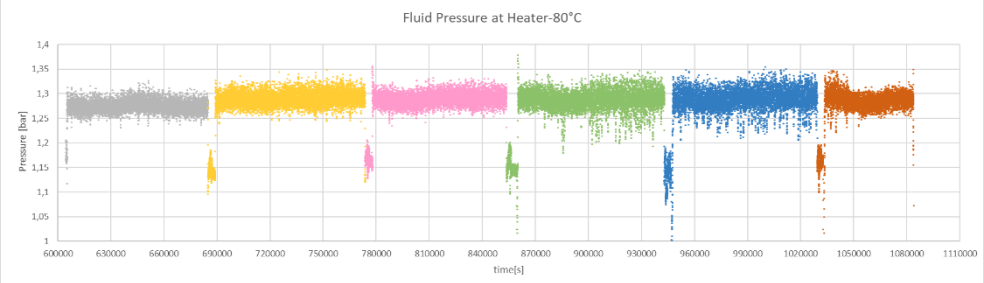

Figure 6.87 P-t

Figures 71 and 72 show the overall EIS measurements performed under voltage and current control during the degradation test.

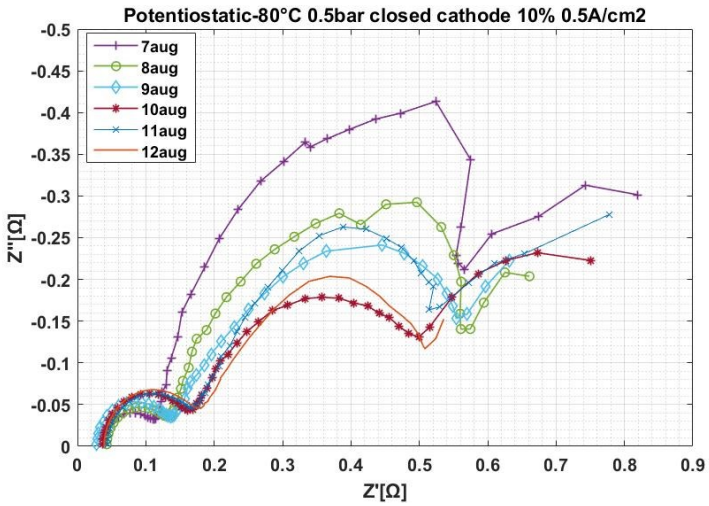

Figure 6.88 EIS measurements with potentiostatic mode.

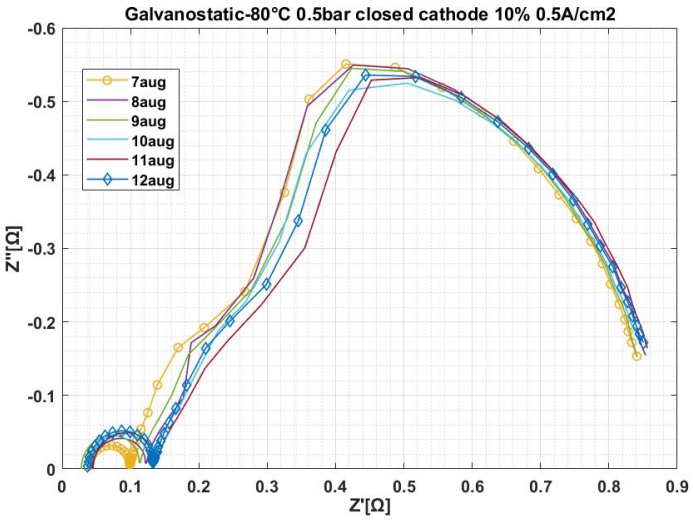

Figure 6.89 All EIS measurements with galvanostatic mode.

6.2.2.1.1.2.1. Data quality assessment

Validation through KK relations shows that impedance spectra obtained with both modes have similar residuals behaviour, i.e. low residuals of high frequency data and larger residuals as data are collected at lower frequencies. Data quality is mostly affected by time variance rather than noise.

By visual inspection of both Nyquist and Bode plots, at least two time constants are individuated, so two distinguishable features are observed: high frequency arc and a mid-frequency arc, mainly affected by noise. As previously said, due to high level of noise the LF data are considered only in a qualitative way. Therefore, the ECM used to fit the experimental data is LR(QR)(QR).

6.2.2.1.1.2.2. Discussion

The analysis is carried out with both EIS results gained from potentiostatic and galvanostatic modes. The trend of ohmic resistance, high frequency charge transfer resistance and capacitance is shown in the figures below.

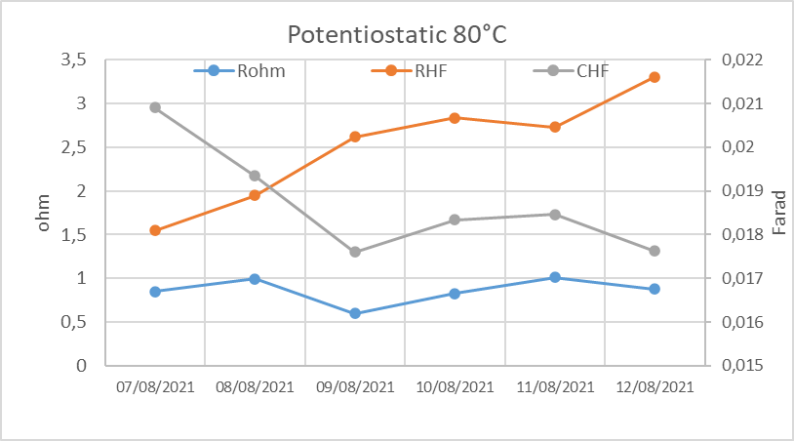

Figure 6.90 Potentiostatic

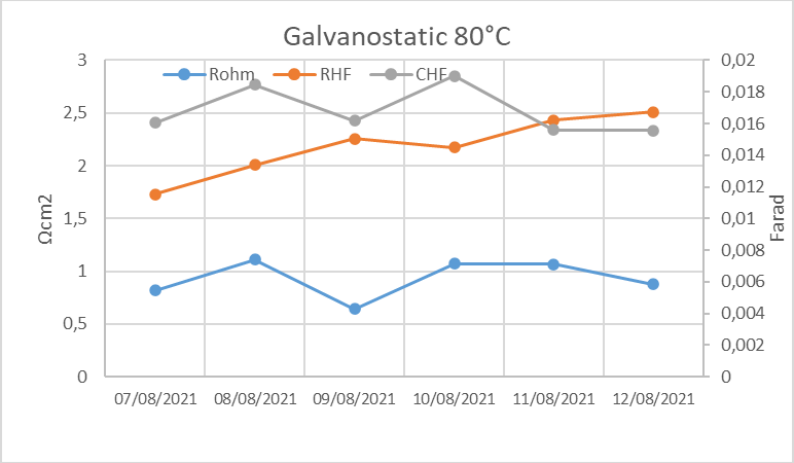

Figure 6.91 Galvanostatic

For both EIS tests the high frequency arc shows a moderate increase: the ohmic resistance seems to oscillate in the between 0.8-1.1 Ωcm^2 whereas there is an evident increment of the charge transfer resistance. Instead, the HF capacitance shows a small decrease, higher in the potentiostatic test (from 0.0209 to 0.0176 F) rather than in the galvanostatic (from 0.0160 to 0.0155). As before, it is possible to get a qualitative trend of the LF feature from the galvanostatic measurements. It is observed an increase of the diameter of the mid-low frequency arc; hence, it can be assumed an increase of the total polarization resistance.

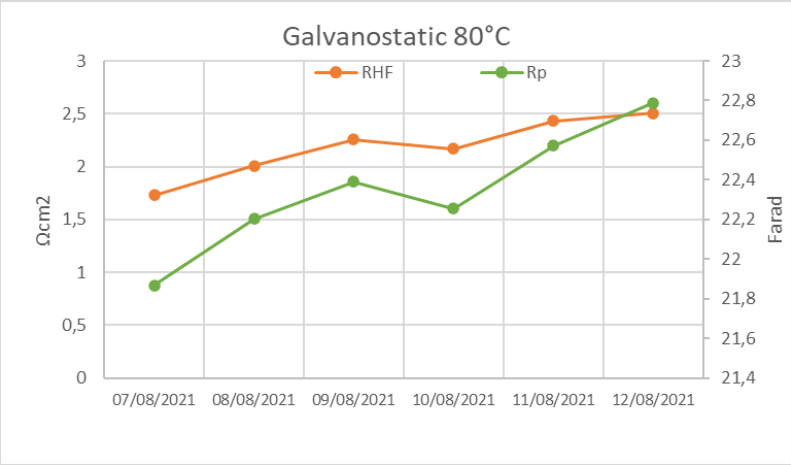

Figure 6.92 Galvanostatic

These results are consistent with the voltage increase during the experiment at 80°C. Therefore, the cell is experiencing degradation mainly of the anode even if some loss of performance are individuated also in the membrane.

6.2.2.1.2. II

Degradation test performed at 80°C, 0.5barg, closed cathode, 10% mass flow rate, constant current density of 1 A/cm2:

The degradation test is carried out at a constant current density of 1 A/cm^2 and the cell voltage increase over time is monitored. It is performed at 80°C, imposed gauge pressure of 0.5barg at the anode and cathode, and closed cathode configuration.

Two types of EIS tests have been used:

- Potentiostatic test is performed at 0 DC V by varying the frequency from 100 kHz to 0,001 Hz in single sine mode and using a sinusoidal excitation signal of 10mV root mean square (rms);
- Galvanostatic test is performed at 0 DC mA by varying the frequency from 200 kHz to 0,002 Hz in single sine mode and using a sinusoidal excitation signal of 1000 mA root mean square (rms).

After around 350 h of operation at 1 A/cm^2 the cell has shown a degradation rate of about 180 $\mu V/h$.

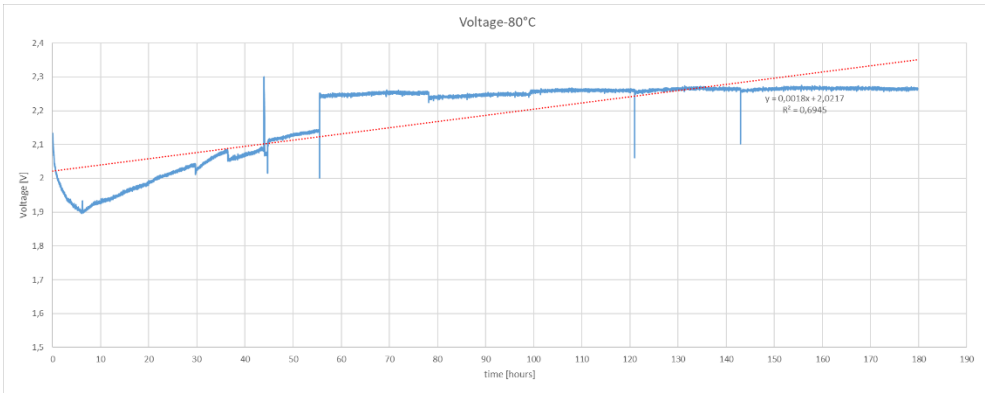

Figure 6.93

The effective temperature during the experiment oscillates around 80°C whereas real gauge pressure at the anode and cathode was 0,95 barg and 0,42 barg respectively. The study shows an increase of the cell potential and of the pressure at the heater; instead, temperature at the heater and cell temperature remain almost unvaried.

6.2.2.1.2.1. Data quality assessment

All impedance spectra are subject to a quality validation through KK relations. It is noticed that impedance measurements gained with galvanostatic mode have quite high residuals due mostly to the instability of the cell during their execution. Conversely, potentiostatic test have provided measurement with lower residuals thus higher quality. A visual inspection of Nyquist and Bode plots clearly show two time constants for the potentiostatic tests and three for the galvanostatic tests.

6.2.2.1.2.2. Modelling

Nyquist plot below shows the impedance spectra measured during potentiostatic tests. Impedance spectra obtained under voltage control are characterized by two semicircles, appearing at high and mid-low frequency respectively. On the other hand, the shape of the impedance spectra produced by galvanostatic tests changes depending on the DC value of the current. Three semicircle are detected at 0mA, one at high frequency and two merged in the mid-low frequency range. As the current increases the mid frequency arc tends to disappear so at the end there are two arcs.

6.2.2.1.2.3. Discussion

The degradation test has a duration of around 350 hours in which the cell behaviour is under dynamic conditions, i.e. several perturbations occur during its execution.

After perturbation the system tends to reach a new equilibrium hence there is always a period of stabilization after each perturbation.

The first part of the test (60 hours) is of stabilization of the cell voltage, then there is the start of the degradation test. At around 120 h there is a perturbation of the cell hence the time lapse up to 200h is of stabilization. After that, the degradation test continues till the end at around 350h.

As a consequence, parts of the test where perturbations and stabilization occur are not considered in the analysis. This means that EIS measurements gained during these part of the test are not considered as well.

The validation with KK relations put in evidence the inconsistency of the impedance spectra measured with galvanostatic mode whereas almost all impedance data under potentiostatic mode showed good quality, i.e. residuals below 0.5%. As a result, only potentiostatic tests are used for the analysis. The EIS tests considered are those shown in the figure below.

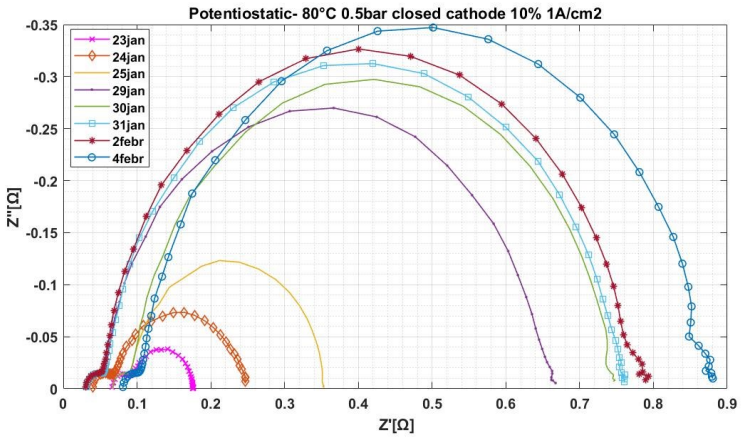

Figure 6.94 Potentiostatic test

It is observed an increase of the low frequency arc whereas the dimension of the high frequency arc seems not to vary. Further on, a third semicircle affected by noise appears at very low frequency as the degradation test goes on.

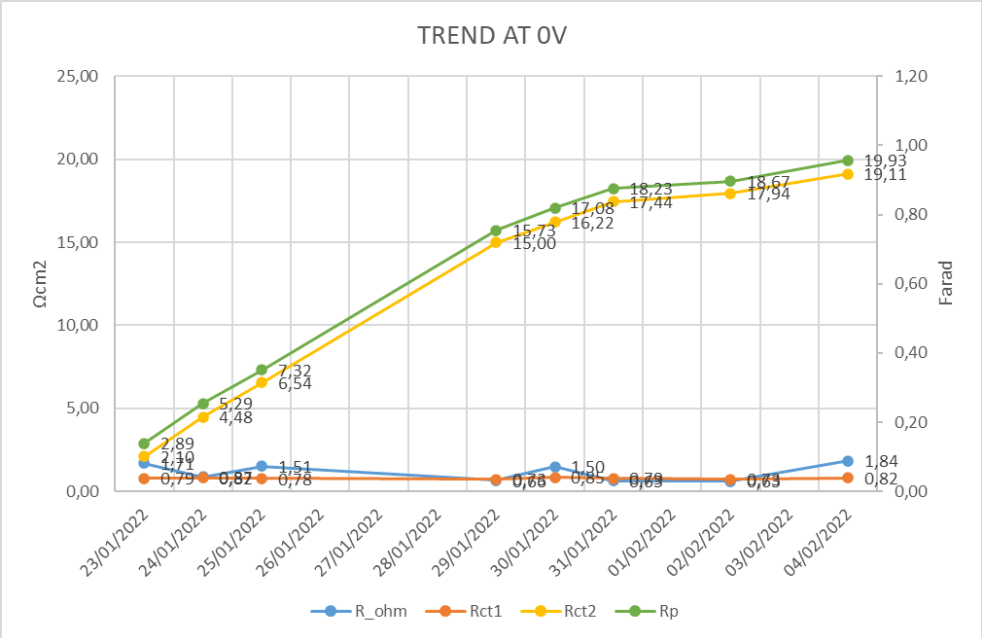

Figure 6.95 trend of resistances

The ohmic resistance shows an oscillating behaviour, so it is not possible to say whether or not a degradation process is occurring in the MEA. Its value goes from a maximum of 1.84 Ωcm^2 and a minimum of 0.63 Ωcm^2. The high frequency arc seems not change during the operation of the cell, the charge transfer resistance is around 0.73-0.82 Ωcm^2 and the capacitance is constant at 0.02 F. What shows a substantial increase is the low frequency arc, i.e. the charge transfer resistance increases from 2.10 to 19.11 Ωcm^2 whereas the capacitance decreases from 0.5 to 0.3 F. As a consequence, the polarization resistance-corresponding to the sum of the diameters of the two arcs- increases from 2.9 to 19.9 Ωcm^2.

The results of the EIS tests shows that a component affected by degradation process is the anode. This is in accordance with the increase of voltage during the degradation test of about 350 mV, corresponding to a degradation rate of 180 µV/h.

6.2.3. Further analysis

A series of Fluoride ion chromatography has been performed which confirmed its direct relation with the conductivity of the demineralized water that is used inside the circuit. As a result, the online control was performed on the values of conductivity to see the effect of the degradation.

After the degradation tests on the mentioned cells, post-mortem analysis using SEM and EDS was performed to have a complete overview about the degradation mechanisms. A sample of the degraded cell after the frequent shut-down profile at 80 degrees Celsius and 1 A/cm2 test is brough in Figure 6.96 , Figure 6.97 , and Figure 6.98.

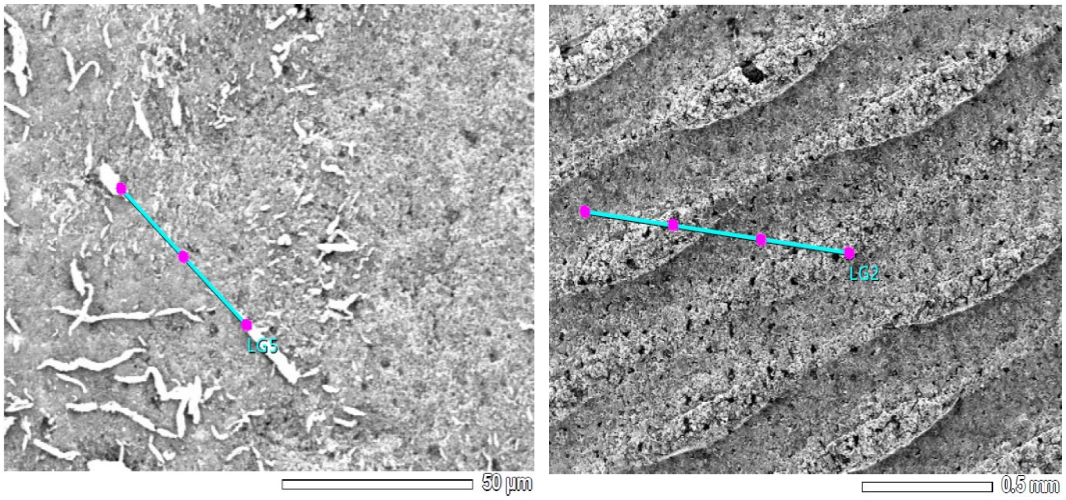

Figure 6.96 Anode SEM: left: as received right: degraded

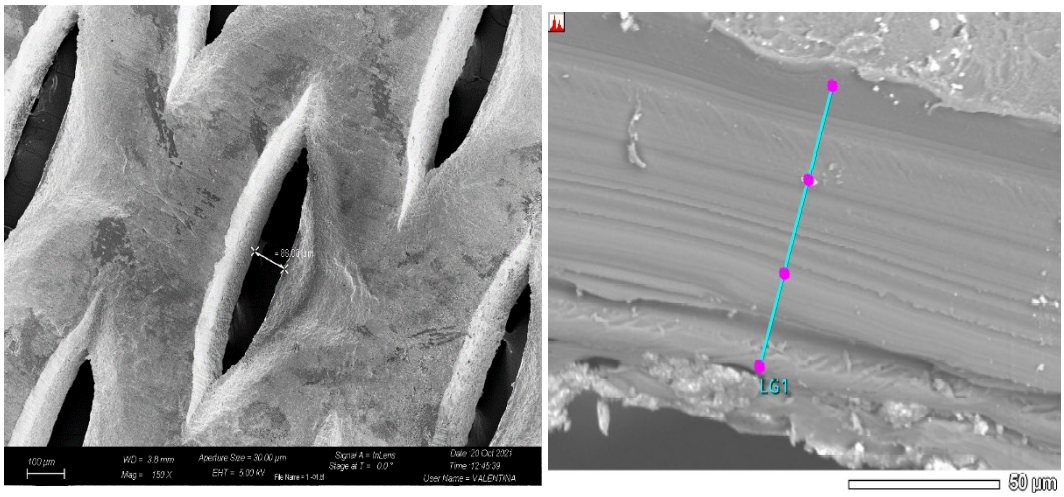

Figure 6.97 oxidized Ti GDL right: degraded membrane thickness

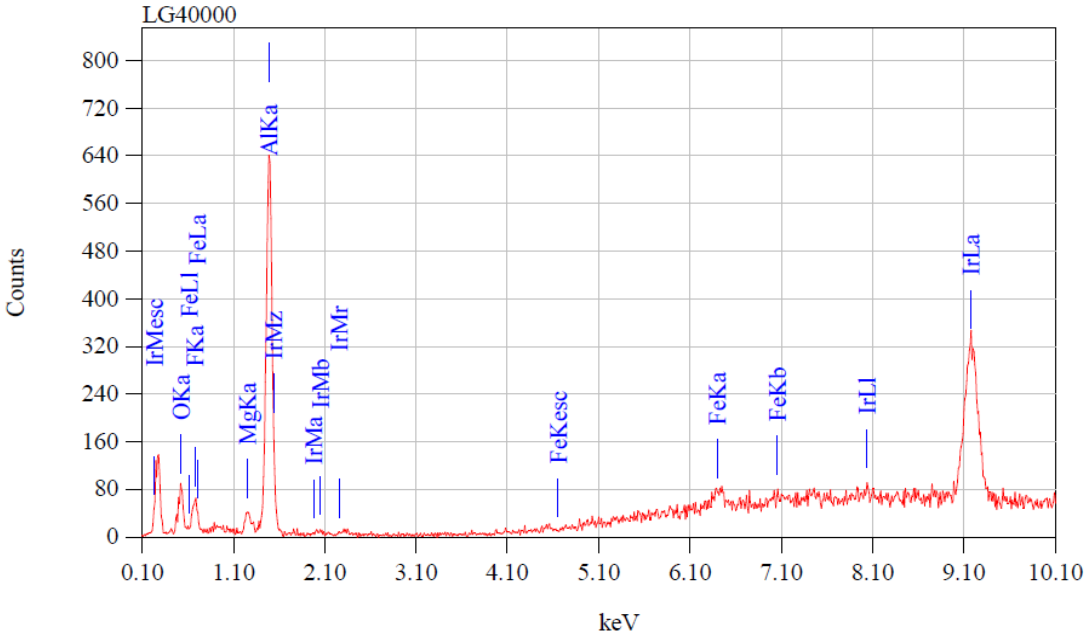

Figure 6.98 EDS of membrane, presence of Iron after degradation test

Some noteworthy results are :

- In Ti gas diffusion layer we see Oxidation which is more evident in anode side due to harsher condition.
- In Membrane electrode assembly (or MEA):
    - We have Presence of Iron which probably come from circuit tubing
    - Membrane thinning is also measured here in Micrometers and can be seen from the presented SEM image.
    - Loss of Fluor from the membrane is also evident with EDS analysis.

This loss of fluor was also Verified with the Fluoride ion chromatography test that was done by sampling the circuit water coming out of cathode at specific time periods.

Chapter 7. Final remarks

7.1. Conclusions and addressed research questions

All said, in the current situation the increase or decrease in the production and use of hydrogen still strongly depends on the policies that are imposed by decision making organizations. In the recent years the energy landscape is changing rapidly, particularly due to the current geopolitical situation. Europe, US and China -some of the world's biggest players in the hydrogen sector- have announced positive changes in their plans. For instance, due to the global energy market disruption caused by the geopolitical conflicts, EU strategies had significant implications on hydrogen production. In the "EU's plan to rapidly reduce dependence on Russian fossil fuels -REPowerEU- hydrogen is receiving more attention along with its derivatives, such as ammonia, methanol, e-kerosene, and e-petrol. While the 2030 target for renewable hydrogen in "Fit for 55" was set at 5.6 Mt, the new REPowerEU strategy has increased the target to 20 Mt, with a purpose to replace 50 bcm of Russian gas. The immense change becomes particularly clear in the planned use of hydrogen by 2030 where this utilization in many important sectors increase some 2 to 5 fold compared to the already ambitious Fit for 55 targets. China's long term plan for hydrogen is another evidence for the growth in the needs for hydrogen production. They intend to arrive at the use of 35 Mt in 2030 (at least 5% of the Chinese energy supply) and 60 Mt in 2050 (10 %). As another example, the U.S. Department of Energy (DOE) has also recently made $7 billion available to fund regional clean hydrogen hubs across the country, which will form a potential key power source in America's future clean energy economy. Hence, although the changes in policies may affect the hydrogen sector rapidly, evidence show that the policies are towards continued and increased support of this sector. Based on these evidence, many market players have already introduced an expansion of electrolyser infrastructures. Such examples can be easily found as gigafactories in Denmark and France.[165][166][167][168][169][170][171]

In this context PEMWE technology represents one of the best choices in terms of environment protection when compared to the traditional methods used to produce this element. Besides, the main advantages of the PEM are its better dynamic behaviour and flexibility in comparison to other electrolyzers.

The performance of PEMWE has been examined in this work from different perspectives such as V-I polarization curve and hydrogen production. Understanding how the performances change requires knowledge of the polarisation curve. After constructing the test rig, electrolytic cell assembly and test bench preparation has been completed in order to conduct the tests. The test bench's primary components, including the temperature and back pressure controllers, have been set up to operate in accordance with the design of experiments. To find the best clamping pressure for the housing of the cell, the pressure paper method has been adopted. The preparation involved carrying out a number of pre-testing steps that directly and indirectly impacted the electrolyser's function. Procedures for assembly, activation, and humidification were done directly on the electrolyzer. Other steps such as thermocouple calibration and temperature controller setting were done in order to guarantee an accurate measurement of the variables. More specifically, after all pre-testing procedures have been conducted, the electrolytic cell has been assembled. The assembly process includes several phases. In order to assemble the MEA along with its GDLs in the cell housing, GDLs have been cut and prepared to the right size. Considering the application and working condition, a gasket material has been chosen and through literature and experimental phases the appropriate thickness of gasket has been found out. In the next phase, the Labview based software has been configured to run the tests. after the assembly of the cell, hydration of the cell is performed. Subsequently a stabilization test was also done to ensure the optimal working condition for the cell. These steps contributed to addressing the first research question mentioned in the sub-chapter 1.4 Research questions addressed

The tests were carried out at various temperatures and pressures by varying the current applied to the cell and selecting between two different configurations: open and closed cathode. The studies were conducted out, in particular, for various temperatures (40-80°C) and pressures (2.5-15barg). The first series of results were voltage-current polarizations which showed that as expected from literature, as the temperature rises, the polarization curve shifts to lower values. Also, the polarization curves are shifted to higher values as the pressure is increased. Considering the obtained values, certain number of oscillations have been seen in the results. The cause could be as a result of various imposed controls working on the cell for example the range of working and delay of the PID controller; i.e. they may have been caused by temperature and pressure controllers' oscillating values. They can also be contributed to external factors acting on the cell and the test bench. In the case of an open cathode configuration, the obtained findings are

reasonably similar to the value of the literature, and in the case of a closed cathode configuration, they are slightly higher. These results contributed to addressing the second research question mentioned in the section 1.4.

The production of hydrogen has also been examined because, together with the polarization curve, it is the outcome that matters the most for a commercial-scale stack. These two outcomes aid in determining whether the MEA and other components are accurately installed and whether the system is operating properly. The closed cathode configuration has been taken into consideration when creating the graphs of hydrogen generation. The values of Hydrogen recorded by the mass flow meter have been studied. The graphs have been created considering the polarization experiment descending from higher current densities to zero. When these production graphs are analyzed, oscillations are visible, but they are caused by the Back Pressure Controller's physics. Additionally, the system's production was compared to the theoretical one, which was computed using the Faraday Law, and it was discovered that the system's rate of production was somewhat lower than the computed one. This is how energy systems often behave. The Faradaic efficiency may be calculated using theoretical and experimental numbers, and it is obvious that it is close to unit, indicating that the system assembly and testing methods have been set up correctly. Moreover, a mass spectroscopy was utilized to understand the percentage of produced hydrogen and oxygen, with excellent results on both the anode and cathode sides.

The 0D mathematical model that was coded on MATLAB® demonstrated the main contributions of voltage for electrolysis processes to be activation and ohmic overpotentials. The ohmic overpotential has a high influence at higher current densities. The validation revealed that the anode and cathode reference exchange current densities are the main impacting ones,and in particular the anode one, has a significant impact on the polarization curve. Numerous fitted parameters have been calculated, and they are extremely close to the values found in the literature. In order to undertake a model validation, three experimental curves for an opened cathode valve configuration at the same pressure (5bar) have been selected. For closed cathode valve design, the same process is carried out with a fixed pressure of 15 bar. In this sense, the curves have merely been fitted while keeping the fitting parameters constant and modifying the temperature. These results contributed to addressing the fourth research question mentioned in the section 1.4.

Multiphysics models were also developed during this work ,i.e. a 2-D multiphysics model that studies the anode compartment as single phase flow, a 2-

D multiphysics model that studied the anode compartment as multi-phase flow and finally 3-D extension of the same models. In the 2D model the results include laminar single-phase and turbulent multiphase flow, while in the 3D model the laminar single-phase and turbulent single-phase flow, and the closed cathode comparison is analysed. The development of the various models demonstrated how the same phenomenon can be analyzed using different techniques. The model that treats the anode compartment flow as a multi-phase flow is undoubtedly the essential part of this work because it captures the interaction between the gas and liquid phases in the slow electrode. The development of this model is driven by both the gap in the literature and the presence of biphasic mixtures in the system, which necessitates the use of a multiphysics model to capture the impact of bubbles on PEMWE performance. The interaction of the gaseous bubbly phase and the liquid phase was thus modeled. In the laminar flow the reported results in the 2D model are, the polarization curve, hydrogen and oxygen concentration, the water concentration with analysis on the water in the membrane and its main concentration factors, potential at the electrodes and at the membrane, local current at the electrodes, temperature distribution, and temperature gradients at anode and cathode. As a result, the velocities of the gaseous and liquid phases, the fraction of gaseous volume relative to the liquid, which is the percentage of volume occupied by bubbles, and the overpotential caused by bubbles are the most important results because they highlight the influence of multiphase flow in an electrolysis process.

The effect of bubbles on the electrochemical process could be simulated and compared to the single phase multiphysics model. Furthermore, the Diffusion overpotential for the two 2-D models with a lower limiting current for the multi-phase treatment was investigated. Another difference between the two 2-D models is the temperature distribution and thermal gradients involved at the interfaces, which show lower values for the multi-phase model. A fitting procedure was also used to validate the model, and the fitted parameter values for both models were close to the values assumed and within the range reported in the literature. The reported results in the 3D models, in addition to those reported in the 2D models, are focused on the comparison of the laminar/turbulent model and open/closed cathode configuration. The main turbulence variables, such as turbulent kinetic energy, specific dissipation rate, and turbulent dynamic viscosity, are presented in the 3D turbulent model analysis. The differences with respect to the 3D laminar model are in the different distribution of the velocity field and vorticity in the anodic channels, where the turbulent flow applies. Another important results in the turbulent model in the different concentrations of water, oxygen and hydrogen, is

that the concentration of hydrogen as a function of channel height is increased compared to the laminar model. This is due to the increase and distribution of turbulent kinetic energy at the interface. The interesting findings with regard to the open/closed cathode configuration are the confirmation of the hypotheses that a closed cathode configuration, which appears to lack water in the cathode channels, causes an increase in temperature due to the lack of a cooling fluid, which in turn causes an increase in the production of hydrogen (with a significant increase in concentration) and polarization of the cell. These results contributed to addressing the fifth research question mentioned in the section 1.4.

Among the different techniques available to study electrolytic systems, AC impedance spectroscopy is one of the most promising, so EIS has been chosen to analyse the cells. The ability to individualize and differentiate phenomena, measure their effect on cell performance, and pinpoint the crucial element are the key benefits. Furthermore, it is a non-destructive method, so it is applied during the operation of the cell. Impedance spectra measured during the performance of EIS tests are then analysed by complex non-linear least square (CNLS) approximation. the spectra is utilized for equivalent circuit model which is to fit the experimental data. The time needed to obtain a complete impedance spectrum is this method's main flaw. Low frequency measurements take a long time, and during that period the system may drift, which may then impact the measurements.

Regarding the EIS results, the results obtained from open cathode measurements suggest attributing the high frequency feature to the properties of the MEA, due to the fact that it is not dependent on current density and voltage. The capacitive behaviour at high frequencies could be due to agglomerated catalysts or poor contact between the anode catalyst layer and the electrolyte. This hypothesis is also supported by the fact that the same behaviour is present in both MEAs that have been tested. The mid-low frequency semicircle, on the other hand, is the result of kinetic processes related to the OER and HER. In this regard, it is assumed that the low frequency feature is primarily associated with the anode, which has sluggish kinetics in comparison to the faster cathode. The open/closed cathode series of experiments shows that open cathode has better performance, most likely due to higher thermal stability. It was also discovered that EIS measurements performed during closed cathode show a more pronounced high frequency arc, implying the presence of more relevant current constrictions. These results contributed to addressing the third research question mentioned in the section 1.4.

Finally, the most time-taking tests performed, are the degradation tests. After performing tests with a base profile of constant current at 1 A/cm^2 which resulted in a degradation of 12 µV/h, the first series of dynamic profile degradation is performed on a MEA at two different temperatures having the same constant current densities of 0.5 A/cm^2. A degradation rate of 1080 µV/h during the 168 hours of test at 60°C and 720 µV/h for the test performed at 80°C with a duration of around 135 hours was found. The higher degradation of the 60°C is related to the higher number of shut downs in the test profile. The results of the impedance spectra indicate that both the anode and the electrolyte are subject to degradation, as both the charge transfer resistances of the HF arc-related to the MEA structure as previously stated- and the low frequency arc-attributed to the anode- have shown increasing behaviour. Regarding the second series performed on the MEA at 80°C and with constant current density of 1 A/cm^2, practically only the anode shows the presence of degradation effects. These results bring the essence of all of the research questions together.

7.2. Future works

Although in this work fundamental goals have been achieved, there are various aspects that can to be improved. First of all, the control system of the test bench can be improved to have a more automated system configuration. in a first phase an automatic water tank refilling system can be installed. Currently the water tank contains approximately 10 litres of demineralized water which for long term degradation tests need a refill once every some days. Another example could be using the already-existing thermocouples at the entrance and exit of anode and cathode sides -in excess to the ones that are present inside the cell housing and inside the flow of input water- and creating a better control on the LabVIEW software to be able to control the temperature of the cell housing more preciously.

Another future step could be installation of other conductivity meters at the entrance of the cell in order to have a comparison with the current conductivity meter at the exit of the cell. Besides, regarding the MATLAB model, more data can be used to improve the fitted parameters.

Regarding the modelling, the integration of the multi-phase flow approach in the anode compartment can be extended to an improved 3-D multiphysics model that completely considers the dimensions of the electrolyzer in order to catch the impact of the bubbles in the electrochemical process in a better way. Furthermore,

other multi-phase flow approaches can be implemented in the multiphysics model to describe higher coalesced agglomerates of gas since the current model treats the gaseous phase as diluted. Moreover, another possible improvement would be to deepen the turbulent motion applied to 2D and 3D models in order to gain a better understanding of the multiphase processes present in the cell and considering applying multiphase models to 3D closed cathode configuration

Regarding the EIS and EEC, a fundamental aspect is to account for the ambiguity related to the equivalent circuit model used to simulate the experimental impedance spectrum. ECMs, generally chosen a priori, do not describe the physiochemical properties of the system. They simply reproduce the experimental data. Only a pre-knowledge of the system under study can help the selection of the ECM to get meaningful results. Consequently, other methods such as distribution of relaxation times (DRT), can assist to the identification of a proper number of circuit element avoiding problem of under- or over fitting as well as lack of correlation with the physics.

Regarding the analysis of output hydrogen and oxygen, apart from the mass spectrometer and the gas analyser that are currently used, dedicated gas analysers with calibrated high precision hydrogen capabilities can also be implemented in future to study the output gasses of the cells in a better way.

Appendix A:

7.3. Modelling elements and their physical meaning

Equivalent electrical circuit is a combination of different elements, which are divided in two groups:

Lumped elements: they are electrical elements and can describe only homogeneous systems. Resistors, capacitors and inductors belong to this category.

Frequency dependent elements: they are electrochemical elements, i.e. these are developed for the description of electrochemical processes.

7.3.1. Lumped elements

7.3.1.1. Resistor

The impedance of a pure resistor, where R is the resistance [Ω], is characterized only by the real part:

$$Z_R(\omega) = R \qquad 0.1$$

In the Nyquist plot it appears as a single point in the real axis.

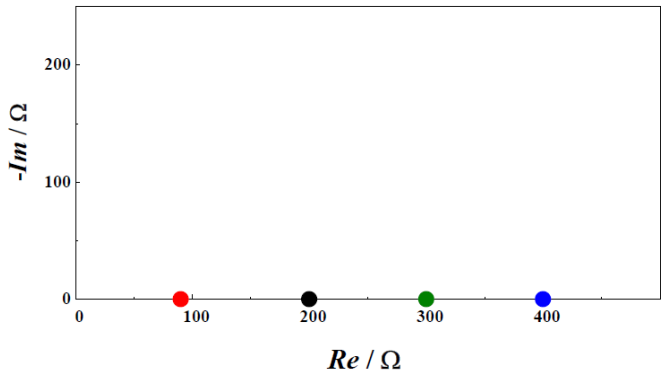

Figure 0.1 Impedance diagram of Resistance simulated in the frequency range $10^3 \div 10^{-3}$ Hz (R = 90 Ohm, 200 Ohm, 300 Ohm, 400 Ohm) [117]

In general, the resistance represents an internal opposition to the occurrence of a process within the system.

In PEM electrolysers it is used to describe:

Proton transport in the electrolytic membrane. It is known *as ionic or membrane resistance* and it is directly proportional to the electrolyte resistivity ρ [Ωcm] and the membrane thickness. The membrane resistance is affected positively by increasing value of temperature since the ionic conductivity $\sigma = 1/\rho$, reciprocal of the resistivity, is temperature dependent. Furthermore, lower value of the ionic resistance is provided by thinner membrane but in this case gas cross-over can occur.

Movement of electrons in the metallic parts and conductors, such as current collectors and wires. Its name is electronic resistance and it is usually negligible in comparison with the membrane resistance.

Electrons transfer at the electrode/electrolyte interface, named *charge-transfer resistance.* It is associated with the charge transfer mechanism for the electrode reactions. In other words, is the resistance that occurs when electrons transfer at the electrode/electrolyte interface. It depends on the potential and temperature as well; an increase of the potential generally determines a decrease of the charge-transfer resistance [116]whereas higher temperature improves kinetics.

The sum of membrane resistance and electronic resistance is called ohmic resistance R_Ω and it is obtained by the intercept of the HF feature with the real axis, whereas the overall resistance to electron crossing the interface at both anode and cathode is called polarization resistance R_p and it is gained by the difference between the intercept of low frequency feature and the intercept of high frequency

feature. The total resistance corresponding to the differential resistance of the polarization curves is given by the intercept of the low frequency feature with the real axis, hence $R_\Omega + R_p$.

7.3.1.2. Capacitor

The impedance of a pure capacitor, where C is the capacitance [F], has only the imaginary part and its value is negative when C is positive.

$$Z_C(\omega) = \frac{1}{j\omega C} \qquad 0.2$$

The behaviour of a pure capacitor is represented in the Nyquist diagram by a line parallel to the negative imaginary axis.

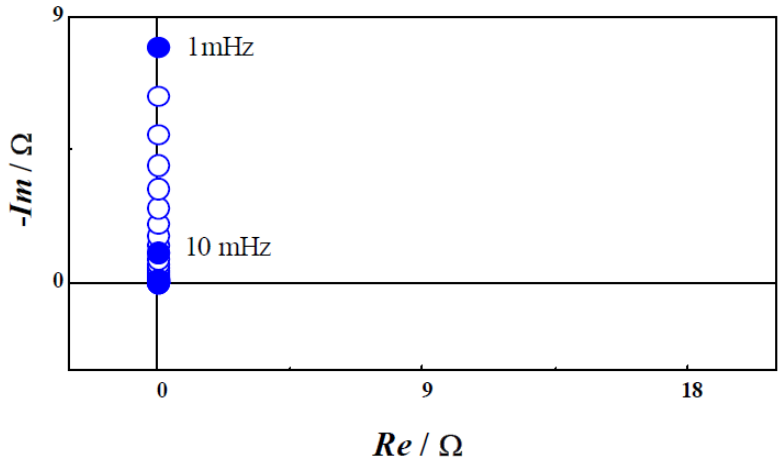

Figure 0.2 Impedance diagram of Capacitance simulated in the frequency range $10^3 \div 10^{-3}$ Hz (C = 1E-3 F) [117].

It is possible to distinguish between bulk capacitance which represents the electric charge stored between the electrodes, and double layer capacitance C_{dl}, arising from an electrical double layer formed at the interface between electrode and electrolyte [172].

7.3.1.3. Inductor

The impedance of a pure inductor, where L is the inductance [H], has only the imaginary part with positive values when L is positive.

$$Z_L(\omega) = j\omega L \qquad 0.3$$

It is used to model the inductive behaviour of wires used for the test performance and its behaviour when considering a pure inductor is represented in the Nyquist diagram by a line parallel to the positive imaginary axis.

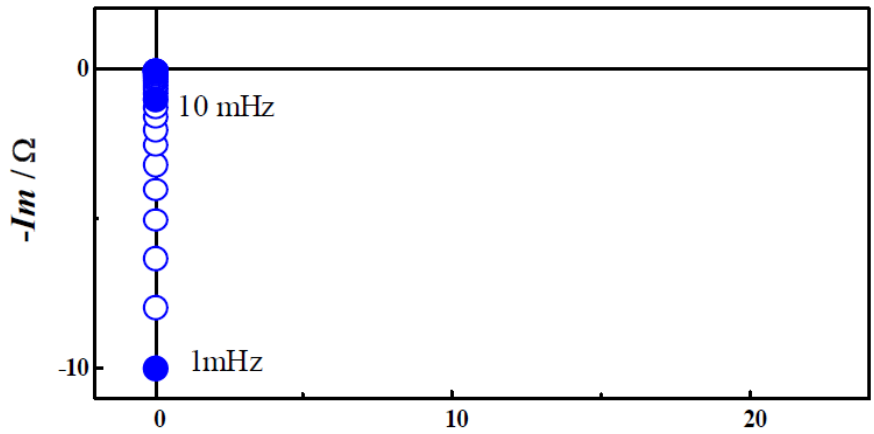

Figure 0.3 Impedance diagram of Inductance simulated in the frequency range $10^{3} \div 10^{-3}$ Hz (L = 1E-3 H) [117].

7.3.2. Frequency-dependent elements

7.3.2.1. Warburg element (W)

It is related to mass transfer in the electrochemical system. It describes linear semi-infinite diffusion. Its impedance is:

$$Z_w(\omega) = \sigma(i\omega)^{-\frac{1}{2}} \qquad 0.4$$

Where σ is known as the Warburg parameter.

Real part and imaginary part of the impedance have same value thus in the Nyquist plot the Warburg impedance is represented by a line with 45° phase shift, and it is not dependent on frequency.

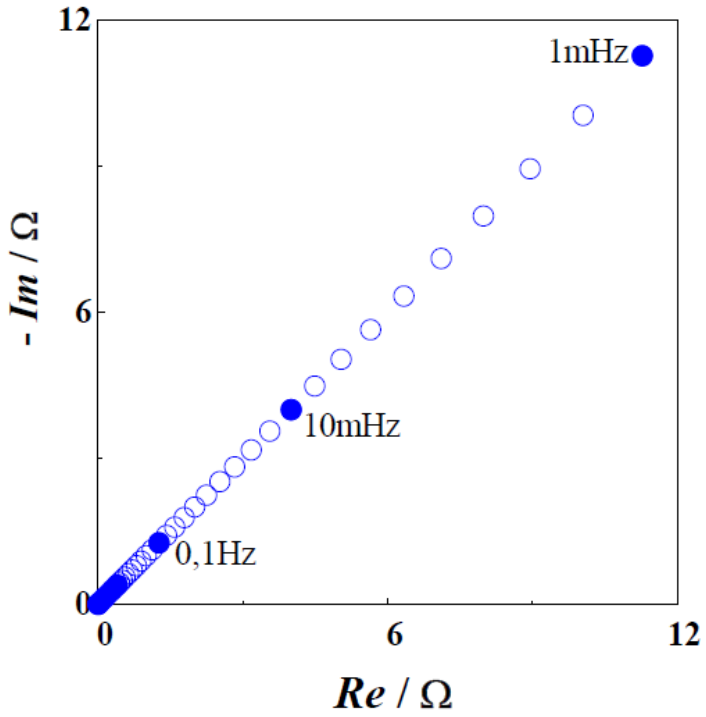

Figure 0.4 Impedance diagram of Warburg element simulated in the frequency range $10^{3} \div 10^{-3}$ Hz (σ = 400 Ω /$s^{1/2}$).

It is important to point out that in real systems diffusion is limited. Hence, a finite diffusion behaviour is generally present, which in the Nyquist plot is represented by a different shape with respect to the standard semi-infinite Warburg impedance. To consider finite diffusion two other type of equivalent circuit elements are used. These are the finite space Warburg (FSW) and finite length Warburg, sometimes called open and short Warburg elements respectively.

The finite space Warburg or open Warburg describes reflective finite diffusion. It tends towards capacitive behaviour at low frequency or in other words the impedance terminates in an open circuit, which corresponds to the reflection.

The finite length Warburg or short Warburg describes transmissive finite diffusion. It terminates in a large resistance at low frequency whether at high frequency the response is almost equal to that of the semi-infinite Warburg, i.e. it looks like a 45° line [116] . The short Warburg is also referred as bounded Warburg impedance and it will be discussed more in detail in the following paragraphs.

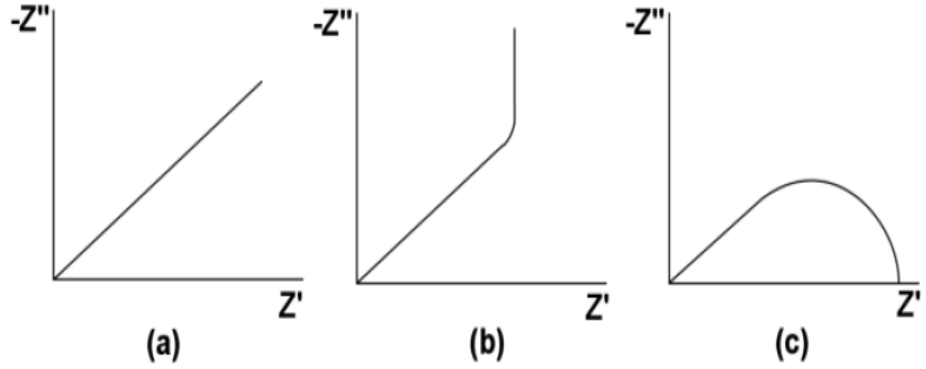

Figure 0.5 Variation of impedance for diffusive systems: a semi-infinite diffusion; b reflective finite diffusion; c transmissive finite diffusion [116]

7.3.2.2. Constant phase element (CPE)

It is a generalised element, it is used to consider the deviations of the double layer from ideal capacitive behaviours which are related to surface roughness and non-uniformly distributed propertied of the irregular electrode surface, as well as varying thickness or composition, non-uniform current distribution. The impedance is described as:

$$Z_{CPE}(\omega) = Q^{-1}(i\omega)^{-n} \qquad 0.5$$

where Q is a factor of proportionality and n is the CPE exponent which characterizes the phase shift. For integral values of n ($n = 1, n = 0, n = -1$) the CPE represents C, R and L respectively. Instead, when $n = 0.5$ it describes the Warburg impedance.

Table 0.1 Physical meaning of the parameter Q with different values of the exponent n.

n	Physical meaning	parameter	units
1	capacitance	C	$F = \Omega^{-1}s$
0	Resistance	R^{-1}	Ω^{-1}
-1	Inductance	L^{-1}	$H^{-1} = \Omega^{-1}s^{-1}$
0.5	Warburg element	σ^{-1}	$\Omega s^{-1/2}$

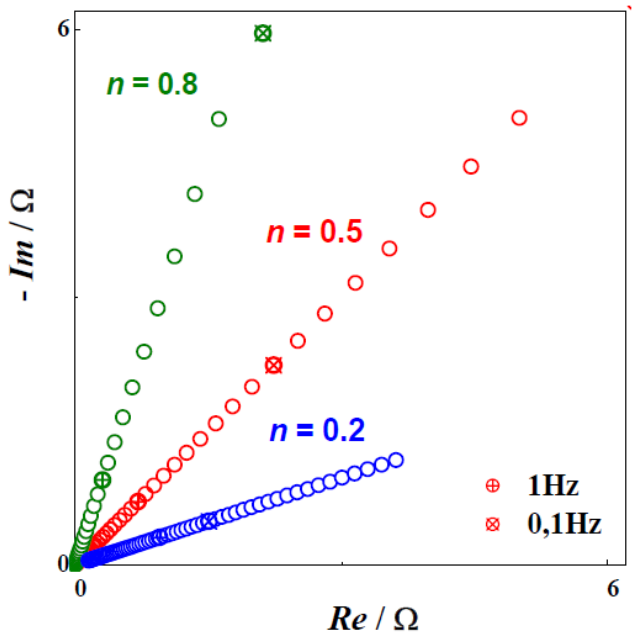

Figure 0.6 Impedance diagram for CPE simulated in the frequency range $10^3 \div 10^{-3}$ Hz at different values of n (Q = 100).

In the Nyquist plot, when a CPE is connected in parallel with R, it is represented by a semicircle with the centre located below the real axis, the so-called depressed semicircle.

7.3.3. Bounded frequency-dependent elements

7.3.3.1. Bounded Warburg element (BW)

It describes linear diffusion in a homogeneous layer with *finite thickness*. It is also denoted as short Warburg element. Its impedance is written as

$$Z_{BW} = \sigma(i\omega)^{-1/2} \tanh\left(\frac{i\omega R_0^2}{\sigma^2}\right)^{1/2} \qquad 0.6$$

Where σ and R_0 are two independent structural parameters. It shows the behaviour of a Warburg element at $\omega \to \infty$ and it tends to a finite value at $\omega \to 0$, therefore it is represented by a 45° line followed by a semicircle.

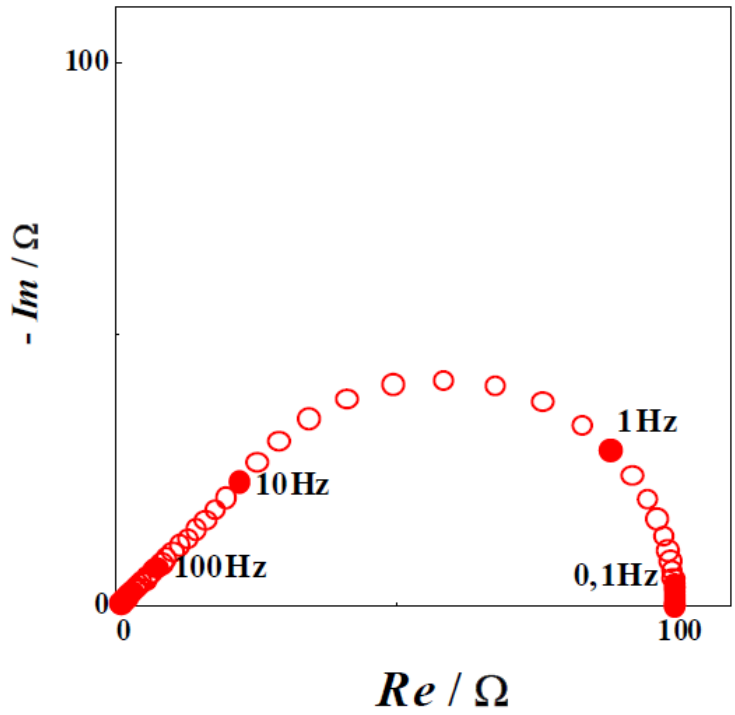

Figure 0.7 Impedance diagram of Bounded Warburg element simulated in the frequency range $10^{3} \div 10^{-3}$ Hz (σ = 0,01 Ω/$s^{1/2}$, R_0= 100 Ω).

7.3.3.2. Bounded constant phase element (BCPE)

It represents the impedance of a bounded homogeneous layer with CPE behaviour. Its impedance is

$$Z_{BCPE} = Q^{-1}(i\omega)^{-n}\tanh(R_0 Q(i\omega)^n) \qquad 0.7$$

where Q, R_0, n are structural parameters.

For n=0.5 it corresponds to linear diffusion in a finite length (BW) and the parameter Q is related to the effective diffusion thickness and to the diffusion coefficient of the diffusing species. The diffusion resistance R_0 is obtained by the intercept of the low frequency feature with the real axis at $\omega \to 0$.

To recap, the BCPE is the most generalised model for homogeneous layers, as it can represent BW as well as CPE with its transformations in R, C, L and W [117].

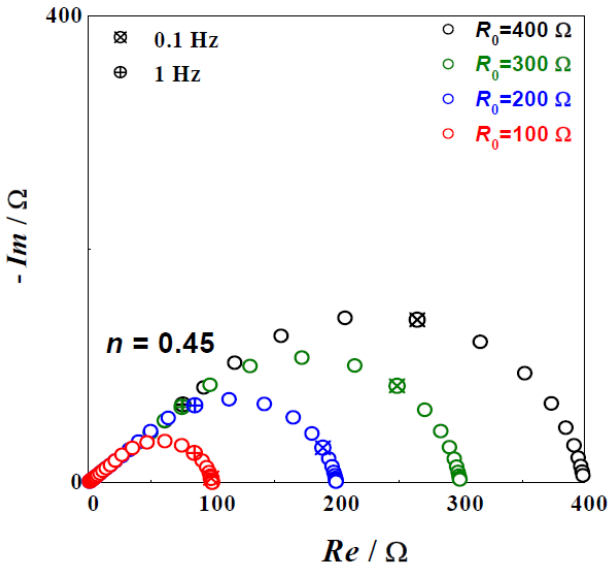

Figure 0.8 Impedance diagram of BCPE simulated in the frequency range $10^3 \div 10^{-3}$ Hz at different values of R_0 (A= 0,01).

The table below summarizes the main impedance elements with their fundamental parameters.

Table 0.2 Description of the impedance elements.

element	name	parameter	units
R	Resistance	R	Ω
C	Capacitance	C	$F = \Omega^{-1}s$
L	Inductance	L	$H = \Omega s$
W	Warburg element	σ	$\Omega s^{-1/2}$
BW	Bounded Warburg	σ	$\Omega s^{-1/2}$
		R_0	Ω
CPE	Constant phase element	Q	$\Omega^{-1}s^n$
		n	$-$
BCPE	Bounded CPE	Q	$\Omega^{-1}s^n$
		n	$-$
		R_0	Ω

Appendix B: data tables

Table 0.1 Characteristic frequency at high and low frequency and correlated time constant for both types of EIS test.

	POTENTIOSTATIC					GALVANOSTATIC			
DC VALUE	ω HF [Hz]	τ HF [s]	ω LF [Hz]	τ LF [s]	DC VALUE	ω HF [Hz]	τ HF [s]	ω LF [Hz]	τ LF [s]
0V	79.43	0.0020	0.631	0.2524	0mA	79.62	0.0020	0.1589	1.0021
0.5V	100	0.0016	0.2512	0.6339	1000mA	100.2	0.0016	0.1589	1.0021
1V	100	0.0016	0.3921	0.4061	1500mA	100.2	0.0016	0.1589	1.0021
1.5V	125.9	0.0013	0.07943	2.0047	2000mA	126.2	0.0013	0.1002	1.5892

Table 0.2 Characteristic frequency at high and low frequency and correlated time constant for both types of EIS test at 60°C.

60°C	POTENTIOSTATIC					GALVANOSTATIC			
DC VALUE	ω HF [Hz]	τ HF [s]	ω LF [Hz]	τ LF [s]	DC VALUE	ω HF [Hz]	τ HF [s]	ω LF [Hz]	τ LF [s]
0V	79.43	0.0020	0.631	0.2524	0mA	79.62	0.0020	0.1262	1.2618
1V	100	0.0016	0.2512	0.6339	1000mA	79.62	0.0020	0.1589	1.0021
1.2V	125.9	0.0013	0.1585	1.0046	1500mA	100.2	0.0016	0.1262	1.2618
1.5V	125.9	0.0013	0.0631	2.5235	2000mA	126.2	0.0013	0.1002	1.5892

Table 0.3 Characteristic frequency at high and low frequency and correlated time constant for both types of EIS test at 74°C.

74°C	POTENTIOSTATIC					GALVANOSTATIC			
DC VALUE	ω HF [Hz]	τ HF [s]	ω LF [Hz]	τ LF [s]	DC VALUE	ω HF [Hz]	τ HF [s]	ω LF [Hz]	τ LF [s]

0V	100	0.0016	0.631	0.2524	*0mA*	100.2	0.0016	0.1589	1.0021
1V	125.9	0.0013	0.1585	1.0046	*1000mA*	126.2	0.0013	0.1589	1.0021
1.2V	158.5	0.0010	0.1995	0.7982	*1500mA*	126.2	0.0013	0.1589	1.0021
1.5V	158.5	0.0010	0.0631	2.5235	*2000mA*	126.2	0.0013	0.1262	1.2618

Table 0.4 Values of pressure during the test.

Imposed gauge pressure	Pressure at the heater @79°C	Real gauge pressure @79°C	Pressure at the heater @71°C	Real gauge pressure @71°C
1.4	2,19	1,8	2,27	1,8
2.4	3,08	2,7	3,28	2,8
5	5,46	5,1	5,70	5,3
7.5	8,08	7,7	8,00	7,6

Table 0.5 Values of temperatures, pressure at the heater and voltage at different percentage of mass flow rates during the test.

	Voltage [V]	**Fluid pressure at heater [bar]**	**Cell Temperature** [°C]	**Fluid Temperature at Heater Outlet [°C]**
10%	2,79	1,31	61,26	61,82
EIS at 10%	-	1,10	61,14	62,03
30%	2,79	2,46	61,30	59,17
EIS at 30%	-	2,57	61,08	58,70
50%	2,87	4,36	61,32	58,71
EIS at 50%	-	4,45	61,23	59,05
70%	3,00	6,32	61,32	58,86
EIS at 70%	-	6,19	61,11	59,10
100%	3,19	8,71	61,34	58,97

EIS at 100%	-	8,86	61,24	59,07

Table 0.6 Characteristic frequency at high and low frequency and correlated time constant for potentiostatic test at 60°C.

POT	ω HF [Hz]	τ HF [s]	ω mid-LF [Hz]	τ mid-low F [s]
open	100	0.001592357	0.3162	0.503591615
closed	63.1	0.002523545	-	-

Table 0.7 Characteristic frequency at high and low frequency and correlated time constant for galvanostatic test at 60°C.

GALV	ω HF [Hz]	τ HF [s]	ω mid-LF [Hz]	τ mid-low F [s]	ω LF [Hz]	τ LF [s]
open	100.2	0.001589178	0.1262	1.261772336	0.05024	3.169499777
closed	126.2	0.001261772	-	-	0.0317	5.023207217

Table 0.8 Characteristic frequency at high and low frequency and correlated time constant for potentiostatic test at 80°C.

POT	ω HF [Hz]	τ HF [s]	ω mid-LF [Hz]	τ mid-LF [s]
open	79.4	0.002005487	0.1585	1.004641443
closed	63.1	0.002523545	0.2512	0.633899955

Table 0.9 Characteristic frequency at high and low frequency and correlated time constant for galvanostatic test at 80°C.

GALV	ω HF [Hz]	τ HF [s]	ω mid-LF [Hz]	τ mid-LF [s]	ω LF [Hz]	τ LF [s]
open	100.2	0.001589178	0.1262	1.261772336	0.05024	3.169499777
closed	100.2	0.001589178	-	-	0.06325	2.517559981

Table 0.10 Characteristic frequency at high and low frequency and correlated time constant for potentiostatic test at 60°C.

POT	ω HF [Hz]	τ HF [s]	ω mid-LF [Hz]	τ mid-LF [s]
open	79.43	0.002005	0.3162	0.503591615
closed	79.43	0.002005	-	-

Table 0.11 Characteristic frequency at high and low frequency and correlated time constant for galvanostatic test at 60°C.

GALV	ω HF [Hz]	τ HF [s]	ω mid-LF [Hz]	τ mid-LF [s]	ω LF [Hz]	τ LF [s]
open	79,62	0,001999946	-	-	0,06325	2,51756
closed	31,7	0,005023207	-	-	0,0317	5,023207

Table 0.12 Characteristic frequency at high and low frequency and correlated time constant for potentiostatic test at 70°C.

POT	ω HF [Hz]	τ HF [s]	ω mid-LF [Hz]	τ mid-LF [s]
open	100	0,0015924	0,01995	7,981737784
closed	63,1	0,0025235	-	-

Table 0.13 Characteristic frequency at high and low frequency and correlated time constant for galvanostatic test at 70°C.

GALV	ω HF [Hz]	τ HF [s]	ω mid-LF [Hz]	τ mid-LF [s]	ω LF [Hz]	τ LF [s]
open	100,2	0,001589178	0,3991	0,398986892	0,06325	2,51756
closed	25,18	0,006323895	-	-	0,0317	5,023207217

Table 0.14 Characteristic frequency at high and low frequency and correlated time constant for potentiostatic test at 80°C.

POT	ω HF [Hz]	τ HF [s]	ω mid-LF [Hz]	τ mid-LF [s]
open	63,1	0,002524	0,3162	0,503592
closed	63,1	0,002524	0,2512	0,6339

Table 0.15 Characteristic frequency at high and low frequency and correlated time constant for galvanostatic test at 80°C.

GALV	ω HF [Hz]	τ HF [s]	ω mid-LF [Hz]	τ mid-LF [s]	ω LF [Hz]	τ LF [s]
open	63,25	0,00251756	-	-	0,7962	0,199995
closed	63,25	0,00251756	-	-	0,05024	3,1695

Bibliography

[1] European Commission, “Stepping up Europe’s 2030 climate ambition Investing in a climate-neutral future for the benefit of our people,” *J. Chem. Inf. Model.*, vol. 53, no. 9, pp. 1689–1699, 2020.

[2] S. Shiva Kumar and V. Himabindu, “Hydrogen production by PEM water electrolysis – A review,” *Mater. Sci. Energy Technol.*, vol. 2, no. 3, pp. 442–454, Dec. 2019, doi: 10.1016/J.MSET.2019.03.002.

[3] T. M. L. Wigley, P. D. Jones, and P. M. Kelly, “Global warming?,” *Nature*, vol. 291, no. 5813, p. 285, 1981, doi: 10.1038/291285a0.

[4] IRENA (2018), “Hydrogen from renewable power: Technology outlook for the energy transition.”

[5] L. B. N. L. Korea Energy Economics Institute, Korea Resource Economics Association, “Policy Modeling for Industrial Energy Use,” 2002, [Online]. Available: https://www.osti.gov/servlets/purl/816777.

[6] J. Chi and H. Yu, “Water electrolysis based on renewable energy for hydrogen production,” *Chinese J. Catal.*, vol. 39, no. 3, pp. 390–394, Mar. 2018, doi: 10.1016/S1872-2067(17)62949-8.

[7] R. R. Dickinson *et al.*, “Power-to-hydrogen and hydrogen-to-X pathways: Opportunities for next generation energy systems,” in *2017 14th International Conference on the European Energy Market (EEM)*, 2017, pp. 1–6, doi: 10.1109/EEM.2017.7981882.

[8] “Electrical Energy Storage | IEC.” Accessed: Jun. 29, 2022. [Online]. Available: https://www.iec.ch/basecamp/electrical-energy-storage.

[9] *IRENA and EC, “Renewable energy prospects for the European Union,.”* 2018.

[10] T. M. Gür, “Review of electrical energy storage technologies, materials and systems: challenges and prospects for large-scale grid storage,” *Energy Environ. Sci.*, vol. 11, no. 10, pp. 2696–2767, 2018, doi: 10.1039/C8EE01419A.

[11] A. G. Olabi, C. Onumaegbu, T. Wilberforce, M. Ramadan, M. A. Abdelkareem, and A. H. Al – Alami, “Critical review of energy storage systems,” *Energy*, vol. 214, p. 118987, 2021, doi: https://doi.org/10.1016/j.energy.2020.118987.

[12] M. Lehner, R. Tichler, H. Steinmüller, and M. Koppe, “Power-to-Gas:

Technology and Business Models," 2014, doi: 10.1007/978-3-319-03995-4.

[13] G. Buffo, P. Marocco, D. Ferrero, A. Lanzini, and M. Santarelli, "Chapter 15 - Power-to-X and power-to-power routes," F. Calise, M. D. D'Accadia, M. Santarelli, A. Lanzini, and D. B. T.-S. H. P. Ferrero, Eds. Academic Press, 2019, pp. 529–557.

[14] IRENA(2020), "Green Hydrogen: A guide to policy making," International Renewable Energy Agency, Abu Dhabi.

[15] IRENA (2019), "Hydrogen: a Renewable Energy Perspective," International Renewable Energy Agency, Abu Dhabi About.

[16] A. Godula-Jopek, "Introduction," in *Hydrogen Production*, John Wiley & Sons, Ltd, 2015, pp. 1–32.

[17] J. Hnát, M. Paidar, and K. Bouzek, "Hydrogen production by electrolysis," *Curr. Trends Futur. Dev. Membr.*, pp. 91–117, Jan. 2020, doi: 10.1016/B978-0-12-817384-8.00005-4.

[18] D. G. Bessarabov Wang, Haijiang,, Li, Hui,, Zhao, Nana,, *PEM electrolysis for hydrogen production : principles and applications*. Boca Raton, Florida: CRC Press, 2016.

[19] L. Barreto, A. Makihira, and K. Riahi, "The hydrogen economy in the 21st century: a sustainable development scenario," *Int. J. Hydrogen Energy*, vol. 28, no. 3, pp. 267–284, Mar. 2003, doi: 10.1016/S0360-3199(02)00074-5.

[20] M. Carmo, D. L. Fritz, J. Mergel, and D. Stolten, "A comprehensive review on PEM water electrolysis," *Int. J. Hydrogen Energy*, vol. 38, no. 12, pp. 4901–4934, Apr. 2013, doi: 10.1016/J.IJHYDENE.2013.01.151.

[21] A. Ursua, L. M. Gandia, and P. Sanchis, "Hydrogen Production From Water Electrolysis: Current Status and Future Trends," *Proc. IEEE*, vol. 100, no. 2, pp. 410–426, 2012, doi: 10.1109/JPROC.2011.2156750.

[22] S. A. Grigoriev and V. N. Fateev, "Hydrogen Production by Water Electrolysis," in *Hydrogen Production Technologies*, John Wiley & Sons, Ltd, 2017, pp. 231–276.

[23] M. Rashid, M. Al Mesfer, H. Naseem, and M. Danish, "Hydrogen Production by Water Electrolysis: A Review of Alkaline Water Electrolysis, PEM Water Electrolysis and High Temperature Water Electrolysis," *Int. J. Eng. Adv. Technol.*, vol. ISSN, pp. 2249–8958, 2015.

[24] J. L. Hall, "Cell components : edited by H.F. Liskins and J.F. Jackson Springer-Verlag Berlin 1985.399 pp. DM 238.," *Phytochemistry*, vol. 26, no. 4, pp. 1235–1236, Jan. 1987, doi: 10.1016/S0031-9422(00)82398-5.

[25] D. S. Falcão and A. M. F. R. Pinto, "A review on PEM electrolyzer modelling: Guidelines for beginners," *J. Clean. Prod.*, vol. 261, p. 121184,

Jul. 2020, doi: 10.1016/J.JCLEPRO.2020.121184.

[26] E. Commission, J. R. Centre, J. Davies, F. Dolci, and E. Weidner, *Historical analysis of FCH 2 JU electrolyser projects : evaluation of contributions towards advancing the state of the art*. Publications Office, 2021.

[27] R. Savinell *et al.*, "A Polymer Electrolyte for Operation at Temperatures up to 200C," *J. Electrochem. Soc.*, vol. 141, no. 4, pp. L46--L48, Apr. 1994, doi: 10.1149/1.2054875.

[28] N. Agmon, "The Grotthuss mechanism," *Chem. Phys. Lett.*, vol. 244, no. 5–6, pp. 456–462, Oct. 1995, doi: 10.1016/0009-2614(95)00905-J.

[29] P. Millet, "PEM Water Electrolysis," *Hydrogen Production*. pp. 63–116, Apr. 13, 2015, doi: https://doi.org/10.1002/9783527676507.ch3.

[30] F. Marangio, M. Pagani, M. Santarelli, and M. Calì, "Concept of a high pressure PEM electrolyser prototype," *Int. J. Hydrogen Energy*, vol. 36, no. 13, pp. 7807–7815, Jul. 2011, doi: 10.1016/J.IJHYDENE.2011.01.091.

[31] H. Ito, T. Maeda, A. Nakano, and H. Takenaka, "Properties of Nafion membranes under PEM water electrolysis conditions," *Int. J. Hydrogen Energy*, vol. 36, no. 17, pp. 10527–10540, Aug. 2011, doi: 10.1016/J.IJHYDENE.2011.05.127.

[32] E. Rozzi, F. D. Minuto, A. Lanzini, and P. Leone, "Green Synthetic Fuels: Renewable Routes for the Conversion of Non-Fossil Feedstocks into Gaseous Fuels and Their End Uses," *Energies*, vol. 13, no. 2, 2020, doi: 10.3390/en13020420.

[33] S. Song, H. Zhang, X. Ma, Z. Shao, R. T. Baker, and B. Yi, "Electrochemical investigation of electrocatalysts for the oxygen evolution reaction in PEM water electrolyzers," *Int. J. Hydrogen Energy*, vol. 33, no. 19, pp. 4955–4961, Oct. 2008, doi: 10.1016/J.IJHYDENE.2008.06.039.

[34] Y. Wang, K. S. Chen, J. Mishler, S. C. Cho, and X. C. Adroher, "A review of polymer electrolyte membrane fuel cells: Technology, applications, and needs on fundamental research," *Appl. Energy*, vol. 88, no. 4, pp. 981–1007, Apr. 2011, doi: 10.1016/J.APENERGY.2010.09.030.

[35] J. Pettersson, B. Ramsey, and D. Harrison, "A review of the latest developments in electrodes for unitised regenerative polymer electrolyte fuel cells," *J. Power Sources*, vol. 157, no. 1, pp. 28–34, Jun. 2006, doi: 10.1016/J.JPOWSOUR.2006.01.059.

[36] S. Toghyani, E. Afshari, E. Baniasadi, and S. A. Atyabi, "Thermal and electrochemical analysis of different flow field patterns in a PEM electrolyzer," *Electrochim. Acta*, vol. 267, pp. 234–245, Mar. 2018, doi: 10.1016/J.ELECTACTA.2018.02.078.

[37] S. H. Wang, J. Peng, W. B. Lui, and J. S. Zhang, "Performance of the gold-plated titanium bipolar plates for the light weight PEM fuel cells," *J. Power Sources*, vol. 162, no. 1, pp. 486–491, Nov. 2006, doi: 10.1016/J.JPOWSOUR.2006.06.084.

[38] M. M. Barzegari, M. Ghadimi, M. Habibnia, M. Momenifar, and K. Mohammadi, "Developed endplate geometry for uniform contact pressure distribution over PEMFC active area," *Iran. J. Hydrog. Fuel Cell*, vol. 7, no. 1, pp. 1–12, 2020, doi: 10.22104/ijhfc.2020.4027.1200.

[39] S. Asghari, M. H. Shahsamandi, and M. R. Ashraf Khorasani, "Design and manufacturing of end plates of a 5 kW PEM fuel cell," *Int. J. Hydrogen Energy*, vol. 35, no. 17, pp. 9291–9297, Sep. 2010, doi: 10.1016/J.IJHYDENE.2010.02.135.

[40] C.-H. Chien, C.-W. Lin, Y.-J. Chao, C. Tong, J. Van Zee, and T.-H. Su, "Variation of Compression of Seals in PEM Fuel Cells BT - Experimental and Applied Mechanics, Volume 6," 2011, pp. 319–327.

[41] L. Frisch, "PEM fuel cell stack sealing using silicone elastomers," *Seal. Technol.*, vol. 2001, no. 93, pp. 7–9, Sep. 2001, doi: 10.1016/S1350-4789(01)80085-4.

[42] P. Millet, "Fundamentals of Water Electrolysis," *Hydrogen Production*. pp. 33–62, Apr. 13, 2015, doi: https://doi.org/10.1002/9783527676507.ch2.

[43] F. Z. Aouali, M. Becherif, H. S. Ramadan, M. Emziane, A. Khellaf, and K. Mohammedi, "Analytical modelling and experimental validation of proton exchange membrane electrolyser for hydrogen production," *Int. J. Hydrogen Energy*, vol. 42, no. 2, pp. 1366–1374, Jan. 2017, doi: 10.1016/J.IJHYDENE.2016.03.101.

[44] M. Santarelli, "Notes of the course: Polygeneration and advanced energy systems."

[45] Z. Abdin, C. J. Webb, and E. M. Gray, "Modelling and simulation of a proton exchange membrane (PEM) electrolyser cell," *Int. J. Hydrogen Energy*, vol. 40, no. 39, pp. 13243–13257, Oct. 2015, doi: 10.1016/J.IJHYDENE.2015.07.129.

[46] J.-M. Le Canut, R. M. Abouatallah, and D. A. Harrington, "Detection of Membrane Drying, Fuel Cell Flooding, and Anode Catalyst Poisoning on PEMFC Stacks by Electrochemical Impedance Spectroscopy," *J. Electrochem. Soc.*, vol. 153, no. 5, p. A857, 2006, doi: 10.1149/1.2179200.

[47] M. Müller *et al.*, "Water management in membrane electrolysis and options for advanced plants," *Int. J. Hydrogen Energy*, vol. 44, no. 21, pp. 10147–10155, Apr. 2019, doi: 10.1016/J.IJHYDENE.2019.02.139.

[48] A. Villagra and P. Millet, "An analysis of PEM water electrolysis cells

operating at elevated current densities," *Int. J. Hydrogen Energy*, vol. 44, no. 20, pp. 9708–9717, Apr. 2019, doi: 10.1016/J.IJHYDENE.2018.11.179.

[49] Q. Feng *et al.*, "A review of proton exchange membrane water electrolysis on degradation mechanisms and mitigation strategies," *J. Power Sources*, vol. 366, pp. 33–55, Oct. 2017, doi: 10.1016/J.JPOWSOUR.2017.09.006.

[50] P. Millet *et al.*, "PEM water electrolyzers: From electrocatalysis to stack development," *Int. J. Hydrogen Energy*, vol. 35, no. 10, pp. 5043–5052, May 2010, doi: 10.1016/J.IJHYDENE.2009.09.015.

[51] A. Godula-Jopek and P. Millet, "Outlook and Summary," *Hydrogen Production*. pp. 383–394, Apr. 13, 2015, doi: https://doi.org/10.1002/9783527676507.ch9.

[52] V. Liso, G. Savoia, S. S. Araya, G. Cinti, and S. K. Kær, "Modelling and Experimental Analysis of a Polymer Electrolyte Membrane Water Electrolysis Cell at Different Operating Temperatures," *Energies* , vol. 11, no. 12. 2018, doi: 10.3390/en11123273.

[53] J. Kai, R. Saito, K. Terabaru, H. Li, H. Nakajima, and K. Ito, "Effect of Temperature on the Performance of Polymer Electrolyte Membrane Water Electrolysis: Numerical Analysis of Electrolysis Voltage Considering Gas/Liquid Two-Phase Flow," *J. Electrochem. Soc.*, vol. 166, no. 4, pp. F246–F254, 2019, doi: 10.1149/2.0521904jes.

[54] T. Oi and Y. Sakaki, "Optimum hydrogen generation capacity and current density of the PEM-type water electrolyzer operated only during the off-peak period of electricity demand," *J. Power Sources*, vol. 129, no. 2, pp. 229–237, Apr. 2004, doi: 10.1016/J.JPOWSOUR.2003.11.050.

[55] U. Babic, M. Suermann, F. N. Büchi, L. Gubler, and T. J. Schmidt, "Critical Review—Identifying Critical Gaps for Polymer Electrolyte Water Electrolysis Development," *J. Electrochem. Soc.*, vol. 164, no. 4, pp. F387–F399, 2017, doi: 10.1149/2.1441704jes.

[56] S. A. Grigoriev *et al.*, "Hydrogen safety aspects related to high-pressure polymer electrolyte membrane water electrolysis," *Int. J. Hydrogen Energy*, vol. 34, no. 14, pp. 5986–5991, Jul. 2009, doi: 10.1016/J.IJHYDENE.2009.01.047.

[57] K. K, B. S, D. F. M, G. S, and C. A, "Blending hydrogen from electrolysis into the European gas grid," no. KJ-NA-30951-EN-N (online), 2022, doi: 10.2760/908387 (online).

[58] G. Tsotridis and A. Pilenga, *EU harmonised protocols for testing of low temperature water electrolysers*. 2021.

[59] D. Bessarbov and P. Millet, *PEM Water Electrolysis V2*. .

[60] G. Tsotridis, A. Pilenga, T. Malkow, and G. De Marco, *EU harmonised polarisation curve test method for low-temperature water electrolysis*. Publications Office, 2018.

[61] Hiden analytical, "Hiden HPR-20 QIC R & D for Advanced Research." 2018.

[62] P. Olivier, C. Bourasseau, and B. Bouamama, "Modelling, simulation and analysis of a PEM electrolysis system," *IFAC-PapersOnLine*, vol. 49, no. 12, pp. 1014–1019, Jan. 2016, doi: 10.1016/J.IFACOL.2016.07.575.

[63] F. Marangio, M. Santarelli, and M. Calì, "Theoretical model and experimental analysis of a high pressure PEM water electrolyser for hydrogen production," *Int. J. Hydrogen Energy*, vol. 34, no. 3, pp. 1143–1158, Feb. 2009, doi: 10.1016/J.IJHYDENE.2008.11.083.

[64] N. Perez, Ed., "Kinetics of Activation Polarization BT - Electrochemistry and Corrosion Science," Boston, MA: Springer US, 2004, pp. 71–120.

[65] T. Thampan, S. Malhotra, J. Zhang, and R. Datta, "PEM fuel cell as a membrane reactor," *Catal. Today*, vol. 67, no. 1–3, pp. 15–32, May 2001, doi: 10.1016/S0920-5861(01)00278-4.

[66] P. Medina and M. Santarelli, "Analysis of water transport in a high pressure PEM electrolyzer," *Int. J. Hydrogen Energy*, vol. 35, no. 11, pp. 5173–5186, Jun. 2010, doi: 10.1016/J.IJHYDENE.2010.02.130.

[67] M. G. Santarelli, M. F. Torchio, and P. Cochis, "Parameters estimation of a PEM fuel cell polarization curve and analysis of their behavior with temperature," *J. Power Sources*, vol. 159, no. 2, pp. 824–835, 2006, doi: 10.1016/j.jpowsour.2005.11.099.

[68] M. Santarelli, P. Medina, and M. Calì, "Fitting regression model and experimental validation for a high-pressure PEM electrolyzer," *Int. J. Hydrogen Energy*, vol. 34, no. 6, pp. 2519–2530, Mar. 2009, doi: 10.1016/J.IJHYDENE.2008.11.036.

[69] C. E. Brennen, *Fundamentals of Multiphase Flow*. Cambridge: Cambridge University Press, 2005.

[70] I. Brevik and H. Sund, "The Kelvin–Helmholtz instability for surface waves in currents of uniform vorticity," *Phys. Fluids A Fluid Dyn.*, vol. 5, no. 7, pp. 1644–1650, Jul. 1993, doi: 10.1063/1.858840.

[71] W. B. Kolb and R. L. Cerro, "The motion of long bubbles in tubes of square cross section*," *Phys. Fluids A Fluid Dyn.*, vol. 5, no. 7, pp. 1549–1557, Jul. 1993, doi: 10.1063/1.858832.

[72] D. J. Nicklin, "Two-phase bubble flow," *Chem. Eng. Sci.*, vol. 17, no. 9, pp. 693–702, 1962, doi: https://doi.org/10.1016/0009-2509(62)85027-1.

[73] Y. Li *et al.*, "In-situ investigation of bubble dynamics and two-phase flow in proton exchange membrane electrolyzer cells," *Int. J. Hydrogen Energy*, vol. 43, no. 24, pp. 11223–11233, 2018, doi: https://doi.org/10.1016/j.ijhydene.2018.05.006.

[74] T. Cubaud and C.-M. Ho, "Transport of bubbles in square microchannels," *Phys. Fluids*, vol. 16, no. 12, pp. 4575–4585, Nov. 2004, doi: 10.1063/1.1813871.

[75] H. Ito *et al.*, "Experimental study on porous current collectors of PEM electrolyzers," *Int. J. Hydrogen Energy*, vol. 37, no. 9, pp. 7418–7428, 2012, doi: https://doi.org/10.1016/j.ijhydene.2012.01.095.

[76] H. Liu, C. O. Vandu, and R. Krishna, "Hydrodynamics of Taylor Flow in Vertical Capillaries: Flow Regimes, Bubble Rise Velocity, Liquid Slug Length, and Pressure Drop," *Ind. Eng. Chem. Res.*, vol. 44, no. 14, pp. 4884–4897, Jul. 2005, doi: 10.1021/ie049307n.

[77] K. E. Ayers, C. Capuano, and E. B. Anderson, "Recent Advances in Cell Cost and Efficiency for PEM-Based Water Electrolysis," *ECS Trans.*, vol. 41, no. 10, pp. 15–22, 2012, doi: 10.1149/1.3684798.

[78] J. O. Majasan, J. I. S. Cho, I. Dedigama, D. Tsaoulidis, P. Shearing, and D. J. L. Brett, "Two-phase flow behaviour and performance of polymer electrolyte membrane electrolysers: Electrochemical and optical characterisation," *Int. J. Hydrogen Energy*, vol. 43, no. 33, pp. 15659–15672, 2018, doi: https://doi.org/10.1016/j.ijhydene.2018.07.003.

[79] M. Zhang, L. Pan, P. Ju, X. Yang, and M. Ishii, "The mechanism of bubbly to slug flow regime transition in air-water two phase flow: A new transition criterion," *Int. J. Heat Mass Transf.*, vol. 108, pp. 1579–1590, 2017, doi: https://doi.org/10.1016/j.ijheatmasstransfer.2017.01.007.

[80] T. Hibiki, T. Takamasa, and M. Ishii, "One-Dimensional Drift-Flux Model and Constitutive Equations for Relative Motion Between Phases in Various Two-Phase Flow Regimes at Microgravity Conditions." pp. 377–386, Apr. 25, 2004, doi: 10.1115/ICONE12-49037.

[81] A. Angulo, P. van der Linde, H. Gardeniers, M. Modestino, and D. Fernández Rivas, "Influence of Bubbles on the Energy Conversion Efficiency of Electrochemical Reactors," *Joule*, vol. 4, no. 3, pp. 555–579, Mar. 2020, doi: 10.1016/j.joule.2020.01.005.

[82] S. S. Hossain, G. Mutschke, A. Bashkatov, and K. Eckert, "The thermocapillary effect on gas bubbles growing on electrodes of different sizes," *Electrochim. Acta*, vol. 353, p. 136461, 2020, doi: https://doi.org/10.1016/j.electacta.2020.136461.

[83] J. C. Garcia-Navarro, M. Schulze, and K. A. Friedrich, "Detecting and

modeling oxygen bubble evolution and detachment in proton exchange membrane water electrolyzers," *Int. J. Hydrogen Energy*, vol. 44, no. 50, pp. 27190–27203, 2019, doi: https://doi.org/10.1016/j.ijhydene.2019.08.253.

[84] Y. Li *et al.*, "High-speed characterization of two-phase flow and bubble dynamics in titanium felt porous media for hydrogen production," *Electrochim. Acta*, vol. 370, p. 137751, 2021, doi: https://doi.org/10.1016/j.electacta.2021.137751.

[85] K. Qian, Z. D. Chen, and J. J. J. Chen, "Bubble coverage and bubble resistance using cells with horizontal electrode," *J. Appl. Electrochem.*, vol. 28, no. 10, pp. 1141–1145, 1998, doi: 10.1023/A:1003447913204.

[86] A. Nouri-Khorasani, E. Tabu Ojong, T. Smolinka, and D. P. Wilkinson, "Model of oxygen bubbles and performance impact in the porous transport layer of PEM water electrolysis cells," *Int. J. Hydrogen Energy*, vol. 42, no. 48, pp. 28665–28680, 2017, doi: https://doi.org/10.1016/j.ijhydene.2017.09.167.

[87] H. Ito *et al.*, "Effect of flow regime of circulating water on a proton exchange membrane electrolyzer," *Int. J. Hydrogen Energy*, vol. 35, no. 18, pp. 9550–9560, 2010, doi: https://doi.org/10.1016/j.ijhydene.2010.06.103.

[88] C. H. Lee, R. Banerjee, F. Arbabi, J. Hinebaugh, and A. Bazylak, "Porous Transport Layer Related Mass Transport Losses in Polymer Electrolyte Membrane Electrolysis: A Review." Jul. 10, 2016, doi: 10.1115/ICNMM2016-7974.

[89] N. Nagai, M. Takeuchi, T. Kimura, and T. Oka, "Existence of optimum space between electrodes on hydrogen production by water electrolysis," *Int. J. Hydrogen Energy*, vol. 28, no. 1, pp. 35–41, 2003, doi: https://doi.org/10.1016/S0360-3199(02)00027-7.

[90] K. Aldas, N. Pehlivanoglu, and M. D. Mat, "Numerical and experimental investigation of two-phase flow in an electrochemical cell," *Int. J. Hydrogen Energy*, vol. 33, no. 14, pp. 3668–3675, 2008, doi: https://doi.org/10.1016/j.ijhydene.2008.04.047.

[91] C. Yan, C. Yan, Y. Shen, L. Sun, and Y. Wang, "Evaluation analysis of correlations for predicting the void fraction and slug velocity of slug flow in an inclined narrow rectangular duct," *Nucl. Eng. Des.*, vol. 273, pp. 155–164, 2014, doi: https://doi.org/10.1016/j.nucengdes.2014.03.019.

[92] T. Hibiki and K. Mishima, "Flow regime transition criteria for upward two-phase flow in vertical narrow rectangular channels," *Nucl. Eng. Des.*, vol. 203, no. 2, pp. 117–131, 2001, doi: https://doi.org/10.1016/S0029-5493(00)00306-X.

[93] A. Roy, S. Watson, and D. Infield, "Comparison of electrical energy efficiency of atmospheric and high-pressure electrolysers," *Int. J. Hydrogen Energy*, vol. 31, no. 14, pp. 1964–1979, 2006, doi: https://doi.org/10.1016/j.ijhydene.2006.01.018.

[94] H. Ito, T. Maeda, A. Nakano, A. Kato, and T. Yoshida, "Influence of pore structural properties of current collectors on the performance of proton exchange membrane electrolyzer," *Electrochim. Acta*, vol. 100, pp. 242–248, 2013, doi: https://doi.org/10.1016/j.electacta.2012.05.068.

[95] S. A. Grigoriev, P. Millet, S. A. Volobuev, and V. N. Fateev, "Optimization of porous current collectors for PEM water electrolysers," *Int. J. Hydrogen Energy*, vol. 34, no. 11, pp. 4968–4973, 2009, doi: https://doi.org/10.1016/j.ijhydene.2008.11.056.

[96] I. Dedigama *et al.*, "In situ diagnostic techniques for characterisation of polymer electrolyte membrane water electrolysers – Flow visualisation and electrochemical impedance spectroscopy," *Int. J. Hydrogen Energy*, vol. 39, no. 9, pp. 4468–4482, 2014, doi: https://doi.org/10.1016/j.ijhydene.2014.01.026.

[97] H. Vogt, "The problem of the departure diameter of bubbles at gas-evolving electrodes," *Electrochim. Acta*, vol. 34, no. 10, pp. 1429–1432, 1989, doi: https://doi.org/10.1016/0013-4686(89)87183-X.

[98] K. Ito *et al.*, "Analysis and visualization of water flow impact on hydrogen production efficiency in solid polymer water electrolyzer under high-pressure condition," *Int. J. Hydrogen Energy*, vol. 40, no. 18, pp. 5995–6003, 2015, doi: https://doi.org/10.1016/j.ijhydene.2015.03.045.

[99] H. Vogt and R. J. Balzer, "The bubble coverage of gas-evolving electrodes in stagnant electrolytes," *Electrochim. Acta*, vol. 50, no. 10, pp. 2073–2079, 2005, doi: https://doi.org/10.1016/j.electacta.2004.09.025.

[100] A. Alexiadis, M. P. Dudukovic, P. Ramachandran, A. Cornell, J. Wanngård, and A. Bokkers, "The Flow Pattern in Single and Multiple Submerged Channels with Gas Evolution at the Electrodes," *Int. J. Chem. Eng.*, vol. 2012, p. 392613, 2012, doi: 10.1155/2012/392613.

[101] J. Nie and Y. Chen, "Numerical modeling of three-dimensional two-phase gas–liquid flow in the flow field plate of a PEM electrolysis cell," *Int. J. Hydrogen Energy*, vol. 35, no. 8, pp. 3183–3197, 2010, doi: https://doi.org/10.1016/j.ijhydene.2010.01.050.

[102] C.-L. Liu, Z. Sun, G.-M. Lu, and J.-G. Yu, "Hydrodynamic characteristics of the two-phase flow field at gas-evolving electrodes: numerical and experimental studies," *R. Soc. Open Sci.*, vol. 5, no. 5, p. 171255, Jun. 2022, doi: 10.1098/rsos.171255.

[103] A. C. Olesen, C. Rømer, and S. K. Kær, "A numerical study of the gas-liquid, two-phase flow maldistribution in the anode of a high pressure PEM water electrolysis cell," *Int. J. Hydrogen Energy*, vol. 41, no. 1, pp. 52–68, 2016, doi: https://doi.org/10.1016/j.ijhydene.2015.09.140.

[104] A. S. Tijani, D. Barr, and A. H. A. Rahim, "Computational Modelling of the Flow Field of An Electrolyzer System using CFD," *Energy Procedia*, vol. 79, pp. 195–203, 2015, doi: https://doi.org/10.1016/j.egypro.2015.11.462.

[105] D. L. Fritz, J. Mergel, and D. Stolten, "PEM Electrolysis Simulation and Validation," *ECS Trans.*, vol. 58, no. 19, pp. 1–9, 2014, doi: 10.1149/05819.0001ecst.

[106] COMSOL Multiphysics, "CFD Module User 's Guide," *COMSOL Multiphysics*, p. 598, 2016, [Online]. Available: https://doc.comsol.com/5.3/doc/com.comsol.help.cfd/CFDModuleUsersGuide.pdf.

[107] D. Ferrero and M. Santarelli, "Investigation of a novel concept for hydrogen production by PEM water electrolysis integrated with multi-junction solar cells," *Energy Convers. Manag.*, vol. 148, pp. 16–29, 2017, doi: https://doi.org/10.1016/j.enconman.2017.05.059.

[108] F. Marangio, M. Santarelli, and M. Calì, "Theoretical model and experimental analysis of a high pressure PEM water electrolyser for hydrogen production," *Int. J. Hydrogen Energy*, vol. 34, no. 3, pp. 1143–1158, 2009, doi: https://doi.org/10.1016/j.ijhydene.2008.11.083.

[109] O. F. Selamet and M. S. Ergoktas, "Effects of bolt torque and contact resistance on the performance of the polymer electrolyte membrane electrolyzers," *J. Power Sources*, vol. 281, pp. 103–113, May 2015, doi: 10.1016/J.JPOWSOUR.2015.01.162.

[110] H. Liu, F. D. Coms, J. Zhang, H. A. Gasteiger, and A. B. LaConti, "Chemical Degradation: Correlations Between Electrolyzer and Fuel Cell Findings BT - Polymer Electrolyte Fuel Cell Durability," F. N. Büchi, M. Inaba, and T. J. Schmidt, Eds. New York, NY: Springer New York, 2009, pp. 71–118.

[111] X. Cheng *et al.*, "A review of PEM hydrogen fuel cell contamination: Impacts, mechanisms, and mitigation," *J. Power Sources*, vol. 165, no. 2, pp. 739–756, 2007, doi: https://doi.org/10.1016/j.jpowsour.2006.12.012.

[112] F. Aubras *et al.*, "Two-dimensional model of low-pressure PEM electrolyser: Two-phase flow regime, electrochemical modelling and experimental validation," *Int. J. Hydrogen Energy*, vol. 42, no. 42, pp. 26203–26216, 2017, doi: https://doi.org/10.1016/j.ijhydene.2017.08.211.

[113] M. Noussan, P. P. Raimondi, R. Scita, and M. Hafner, "The Role of Green

and Blue Hydrogen in the Energy Transition—A Technological and Geopolitical Perspective," *Sustainability* , vol. 13, no. 1. 2021, doi: 10.3390/su13010298.

[114] J. W. van der Merwe, K. R. Uren, G. van Schoor, and D. G. Bessarabov, "A study of the loss characteristics of a single cell PEM electrolyser for pure hydrogen production," *2013 IEEE Int. Conf. Ind. Technol.*, pp. 668–672, 2013.

[115] M. T, P. A, and T. G, "EU harmonised test procedure: electrochemical impedance spectroscopy for water electrolysis cells," no. KJ-NA-29267-EN-N (online),KJ-NA-29267-EN-C (print), 2018, doi: 10.2760/8984 (online),10.2760/67321 (print).

[116] X. Z. Yuan, C. Song, H. Wang, and J. Zhang, "Electrochemical impedance spectroscopy in PEM fuel cells: Fundamentals and applications," *Electrochem. Impedance Spectrosc. PEM Fuel Cells Fundam. Appl.*, pp. 1–420, 2010, doi: 10.1007/978-1-84882-846-9/COVER.

[117] D. Vladikova, "The technique of the differential impedance analysis Part I: Basics of the impedance spectroscopy," Jan. 2004.

[118] C. Gabrielli, "IDENTIFICATION OF ELECTROCHEMICAL PROCESSES BY FREQUENCY RESPONSE ANALYSIS, TECHNICAL REPORT NUMBER 004/83," 1998.

[119] A. Lasia, "Electrochemical impedance spectroscopy and its applications," *Electrochem. Impedance Spectrosc. its Appl.*, vol. 9781461489337, pp. 1–367, Aug. 2014, doi: 10.1007/978-1-4614-8933-7/COVER.

[120] M. E. Orazem and B. Tribollet, *Electrochemical impedance spectroscopy*. .

[121] B. A. Boukamp, "A Linear Kronig-Kramers Transform Test for Immittance Data Validation," *J. Electrochem. Soc.*, vol. 142, no. 6, pp. 1885–1894, 1995, doi: 10.1149/1.2044210.

[122] M. Schönleber, D. Klotz, and E. Ivers-Tiffée, "A Method for Improving the Robustness of linear Kramers-Kronig Validity Tests," *Electrochim. Acta*, vol. 131, pp. 20–27, 2014, doi: https://doi.org/10.1016/j.electacta.2014.01.034.

[123] "IAM-ET - Ausstattung und Software - Lin-KK Tool." https://www.iam.kit.edu/et/Lin-KK.php (accessed Jun. 26, 2022).

[124] M. Schönleber and E. Ivers-Tiffée, "Approximability of impedance spectra by RC elements and implications for impedance analysis," *Electrochem. commun.*, vol. 58, pp. 15–19, Jun. 2015, doi: 10.1016/J.ELECOM.2015.05.018.

[125] P. Zoltowski, "Non-traditional approach to measurement models for

analysis of impedance spectra," *Solid State Ionics*, vol. 176, no. 25, pp. 1979–1986, 2005, doi: https://doi.org/10.1016/j.ssi.2004.11.022.

[126] C. Rozain and P. Millet, "Electrochemical characterization of Polymer Electrolyte Membrane Water Electrolysis Cells," *Electrochim. Acta*, vol. 131, pp. 160–167, 2014, doi: 10.1016/j.electacta.2014.01.099.

[127] J. van der Merwe, K. Uren, G. van Schoor, and D. Bessarabov, "Characterisation tools development for PEM electrolysers," *Int. J. Hydrogen Energy*, vol. 39, no. 26, pp. 14212–14221, 2014, doi: https://doi.org/10.1016/j.ijhydene.2014.02.096.

[128] I. Dedigama *et al.*, "In situ diagnostic techniques for characterisation of polymer electrolyte membrane water electrolysers - Flow visualisation and electrochemical impedance spectroscopy," *Int. J. Hydrogen Energy*, vol. 39, no. 9, pp. 4468–4482, Mar. 2014, doi: 10.1016/J.IJHYDENE.2014.01.026.

[129] K. Elsøe, L. Grahl-Madsen, G. G. Scherer, J. Hjelm, and M. B. Mogensen, "Electrochemical Characterization of a PEMEC Using Impedance Spectroscopy," *J. Electrochem. Soc.*, vol. 164, no. 13, pp. F1419–F1426, 2017, doi: 10.1149/2.0651713jes.

[130] E. Rasten, G. Hagen, and R. Tunold, "Electrocatalysis in water electrolysis with solid polymer electrolyte," *Electrochim. Acta*, vol. 48, no. 25, pp. 3945–3952, 2003, doi: https://doi.org/10.1016/j.electacta.2003.04.001.

[131] C. Rozain, E. Mayousse, N. Guillet, and P. Millet, "Influence of iridium oxide loadings on the performance of PEM water electrolysis cells: Part I–Pure IrO2-based anodes," *Appl. Catal. B Environ.*, vol. 182, no. Complete, pp. 153–160, 2016, doi: 10.1016/j.apcatb.2015.09.013.

[132] C. Rozain, E. Mayousse, N. Guillet, and P. Millet, "Influence of iridium oxide loadings on the performance of PEM water electrolysis cells: Part II – Advanced oxygen electrodes," *Appl. Catal. B Environ.*, vol. 182, pp. 123–131, 2016, doi: https://doi.org/10.1016/j.apcatb.2015.09.011.

[133] P. Lettenmeier *et al.*, "Durable Membrane Electrode Assemblies for Proton Exchange Membrane Electrolyzer Systems Operating at High Current Densities," *Electrochim. Acta*, vol. 210, pp. 502–511, 2016, doi: https://doi.org/10.1016/j.electacta.2016.04.164.

[134] P. Lettenmeier, S. Kolb, F. Burggraf, A. S. Gago, and K. A. Friedrich, "Towards developing a backing layer for proton exchange membrane electrolyzers," *J. Power Sources*, vol. 311, pp. 153–158, 2016, doi: https://doi.org/10.1016/j.jpowsour.2016.01.100.

[135] S. Siracusano, V. Baglio, F. Lufrano, P. Staiti, and A. S. Aricò, "Electrochemical characterization of a PEM water electrolyzer based on a sulfonated polysulfone membrane," *J. Memb. Sci.*, vol. 448, pp. 209–214,

2013, doi: https://doi.org/10.1016/j.memsci.2013.07.058.

[136] S. Siracusano, V. Baglio, M. A. Navarra, S. Panero, V. Antonucci, and A. Aricò, "Investigation of Composite Nafion/Sulfated Zirconia Membrane for Solid Polymer Electrolyte Electrolyzer Applications," *Int. J. Electrochem. Sci.*, vol. 7, Feb. 2012.

[137] H. Su, V. Linkov, and B. J. Bladergroen, "Membrane electrode assemblies with low noble metal loadings for hydrogen production from solid polymer electrolyte water electrolysis," *Int. J. Hydrogen Energy*, vol. 38, no. 23, pp. 9601–9608, 2013, doi: https://doi.org/10.1016/j.ijhydene.2013.05.099.

[138] S. Siracusano, S. Trocino, N. Briguglio, V. Baglio, and A. S. Aricò, "Electrochemical Impedance Spectroscopy as a Diagnostic Tool in Polymer Electrolyte Membrane Electrolysis," *Mater. (Basel, Switzerland)*, vol. 11, no. 8, Aug. 2018, doi: 10.3390/MA11081368.

[139] M. Suermann, B. Bensmann, and R. Hanke-Rauschenbach, "Degradation of Proton Exchange Membrane (PEM) Water Electrolysis Cells: Looking Beyond the Cell Voltage Increase," *J. Electrochem. Soc.*, vol. 166, no. 10, pp. F645–F652, 2019, doi: 10.1149/2.1451910jes.

[140] P. Aßmann, A. S. Gago, P. Gazdzicki, K. A. Friedrich, and M. Wark, "Toward developing accelerated stress tests for proton exchange membrane electrolyzers," *Curr. Opin. Electrochem.*, 2020.

[141] S. M. Alia, S. Stariha, and R. L. Borup, "Electrolyzer Durability at Low Catalyst Loading and with Dynamic Operation," *J. Electrochem. Soc.*, vol. 166, no. 15, pp. F1164–F1172, 2019, doi: 10.1149/2.0231915jes.

[142] C. Rakousky, U. Reimer, K. Wippermann, M. Carmo, W. Lueke, and D. Stolten, "An analysis of degradation phenomena in polymer electrolyte membrane water electrolysis," *J. Power Sources*, vol. 326, pp. 120–128, 2016, doi: https://doi.org/10.1016/j.jpowsour.2016.06.082.

[143] S. Siracusano, N. Van Dijk, R. Backhouse, L. Merlo, V. Baglio, and A. S. Aricò, "Degradation issues of PEM electrolysis MEAs," *Renew. Energy*, vol. 123, pp. 52–57, 2018, doi: https://doi.org/10.1016/j.renene.2018.02.024.

[144] X. Yuan, H. Wang, J. Colin Sun, and J. Zhang, "AC impedance technique in PEM fuel cell diagnosis—A review," *Int. J. Hydrogen Energy*, vol. 32, no. 17, pp. 4365–4380, 2007, doi: https://doi.org/10.1016/j.ijhydene.2007.05.036.

[145] M. E. Orazem and B. Tribollet, "An integrated approach to electrochemical impedance spectroscopy," *Electrochim. Acta*, vol. 53, no. 25, pp. 7360–7366, 2008, doi: https://doi.org/10.1016/j.electacta.2007.10.075.

[146] D. D. Macdonald, "Reflections on the history of electrochemical impedance

spectroscopy," *Electrochim. Acta*, vol. 51, no. 8, pp. 1376–1388, 2006, doi: https://doi.org/10.1016/j.electacta.2005.02.107.

[147] M. E. Orazem, P. Agarwal, and L. H. Garcia-Rubio, "Critical issues associated with interpretation of impedance spectra," *J. Electroanal. Chem.*, vol. 378, no. 1, pp. 51–62, 1994, doi: https://doi.org/10.1016/0022-0728(94)87056-X.

[148] J. Fleig and J. Maier, "The Influence of Current Constriction on the Impedance of Polarizable Electrodes: Application to Fuel Cell Electrodes," *J. Electrochem. Soc.*, vol. 144, no. 11, pp. L302–L305, 1997, doi: 10.1149/1.1838076.

[149] A. Pilenga and G. Tsotridis, *EU harmonised terminology for low temperature water electrolysis for energy storage applications*. Publications Office, 2019.

[150] W. Schmittinger and A. Vahidi, "A review of the main parameters influencing long-term performance and durability of PEM fuel cells," *J. Power Sources*, vol. 180, no. 1, pp. 1–14, May 2008, doi: 10.1016/J.JPOWSOUR.2008.01.070.

[151] F. N. Khatib *et al.*, "Material degradation of components in polymer electrolyte membrane (PEM) electrolytic cell and mitigation mechanisms: A review," *Renew. Sustain. Energy Rev.*, vol. 111, pp. 1–14, Sep. 2019, doi: 10.1016/J.RSER.2019.05.007.

[152] S. A. Grigoriev, K. A. Dzhus, D. G. Bessarabov, and P. Millet, "Failure of PEM water electrolysis cells: Case study involving anode dissolution and membrane thinning," *Int. J. Hydrogen Energy*, vol. 39, no. 35, pp. 20440–20446, 2014, doi: https://doi.org/10.1016/j.ijhydene.2014.05.043.

[153] P. Marocco *et al.*, "Online measurements of fluoride ions in proton exchange membrane water electrolysis through ion chromatography," *J. Power Sources*, vol. 483, p. 229179, 2021, doi: https://doi.org/10.1016/j.jpowsour.2020.229179.

[154] S. Park *et al.*, "Degradation of the Ionic Pathway in a PEM Fuel Cell Cathode," *J. Phys. Chem. C*, vol. 115, no. 45, pp. 22633–22639, Nov. 2011, doi: 10.1021/jp2068599.

[155] S. P. S. Badwal, S. Giddey, and F. T. Ciacchi, "Hydrogen and oxygen generation with polymer electrolyte membrane (PEM)-based electrolytic technology," *Ionics (Kiel).*, vol. 12, no. 1, pp. 7–14, 2006, doi: 10.1007/s11581-006-0002-x.

[156] R. L. Borup, J. R. Davey, F. H. Garzon, D. L. Wood, and M. A. Inbody, "PEM fuel cell electrocatalyst durability measurements," *J. Power Sources*, vol. 163, no. 1, pp. 76–81, 2006, doi:

https://doi.org/10.1016/j.jpowsour.2006.03.009.

[157] P. Lettenmeier, R. Wang, R. Abouatallah, F. Burggraf, A. S. Gago, and K. A. Friedrich, "Coated Stainless Steel Bipolar Plates for Proton Exchange Membrane Electrolyzers," *J. Electrochem. Soc.*, vol. 163, no. 11, pp. F3119–F3124, 2016, doi: 10.1149/2.0141611jes.

[158] A. S. Gago *et al.*, "Protective coatings on stainless steel bipolar plates for proton exchange membrane (PEM) electrolysers," *J. Power Sources*, vol. 307, pp. 815–825, 2016, doi: https://doi.org/10.1016/j.jpowsour.2015.12.071.

[159] M. Bernt, A. Siebel, and H. A. Gasteiger, "Analysis of Voltage Losses in PEM Water Electrolyzers with Low Platinum Group Metal Loadings," *J. Electrochem. Soc.*, vol. 165, no. 5, pp. F305–F314, 2018, doi: 10.1149/2.0641805jes.

[160] F.-O. Frédéric, "Ast Protocols for Pem Water Electrolyis : Insight on Performances and Components Degradation," *2nd Int. Work. Durabiltiy Degrad. Issues PEM Electrolysis Cells Its Components*, 2015.

[161] C. Rakousky, G. P. Keeley, K. Wippermann, M. Carmo, and D. Stolten, "The stability challenge on the pathway to high-current-density polymer electrolyte membrane water electrolyzers," *Electrochim. Acta*, vol. 278, pp. 324–331, 2018, doi: https://doi.org/10.1016/j.electacta.2018.04.154.

[162] C. Rakousky *et al.*, "Polymer electrolyte membrane water electrolysis: Restraining degradation in the presence of fluctuating power," *J. Power Sources*, vol. 342, pp. 38–47, 2017, doi: https://doi.org/10.1016/j.jpowsour.2016.11.118.

[163] S. H. Frensch, F. Fouda-Onana, G. Serre, D. Thoby, S. S. Araya, and S. K. Kær, "Influence of the operation mode on PEM water electrolysis degradation," *Int. J. Hydrogen Energy*, vol. 44, no. 57, pp. 29889–29898, 2019, doi: https://doi.org/10.1016/j.ijhydene.2019.09.169.

[164] S. H. Frensch, A. C. Olesen, S. Simon Araya, and S. K. Kær, "Model-Supported Analysis of Degradation Phenomena of a PEM Water Electrolysis Cell under Dynamic Operation," *ECS Trans.*, vol. 85, no. 11, pp. 37–45, 2018, doi: 10.1149/08511.0037ecst.

[165] "webpage." https://ec.europa.eu/commission/presscorner/detail/en/ip_22_3131.

[166] "webpage." https://www.hydrogen.energy.gov/pdfs/clean-hydrogen-strategy-roadmap.pdf.

[167] "webpage." https://www.warner.senate.gov/public/index.cfm/2022/9/u-s-department-of-energy-announces-history-7-billion-funding-opportunity-to-jump-start-america-s-clean-hydrogen-economy#:~:text=The DOE National

Clean Hydrogen,decarbonization and economic development goals.

[168] “webpage,” [Online]. Available: https://www.csis.org/analysis/china-unveils-its-first-long-term-hydrogen-plan.

[169] “webpage.” https://energypost.eu/how-to-ramp-up-hydrogen-under-the-new-repowereu-targets/.

[170] “webpage,” [Online]. Available: https://www.hydrogen-worldexpo.com/industry_news/plug-power-to-provide-1gw-electrolyser-to-h2-energy/.

[171] “webpage.” https://www.h2bulletin.com/offshore-electrolyser-green-hydrogen/.

[172] M. Sluyters-Rehbach, “Impedances of electrochemical systems: Terminology, nomenclature and representation - Part I: Cells with metal electrodes and liquid solutions (IUPAC Recommendations 1994),” *Pure Appl. Chem.*, vol. 66, no. 9, pp. 1831–1891, 1994, doi: doi:10.1351/pac199466091831.

UPAC Recommendations 1994),” *Pure Appl. Chem.*, vol. 66, no. 9, pp. 1831–1891, 1994, doi: doi:10.1351/pac199466091831.